Improved Glacial Isostatic Adjustment Models for Eastern North America: Implications for Interpreting Vertical Land Motion and Projecting Sea-Level Change

by

Soran Parang

A thesis submitted to the University of Ottawa
in partial fulfillment of the requirements for the degree of

Doctor of Philosophy

at the

Department of Earth and Environmental Sciences
Faculty of Science
University of Ottawa

September 2025

Supervised by:

Prof. Glenn A. Milne

© Soran Parang, Ottawa, Canada, 2025

To my devoted parents, Homayoun and Mahvash

Abstract

Much of the Atlantic coast of North America has been sinking for thousands of years, with maximum rates reaching ~20 cm per century, due to solid earth deformation in response to the deglaciation of the Laurentide Ice Sheet following the Last Glacial Maximum, between approximately 18,000 and 7,000 years ago. This process, known as glacial isostatic adjustment (GIA), is a dominant driver of vertical land motion (VLM) and sea-level change in the region. The research presented in this thesis aims to improve the quantification and understanding of the processes contributing to contemporary and future VLM and gravity change in eastern North America, in order to enhance projections of mean sea-level change and nuisance flooding frequency over the coming decades. A key aspect is to determine optimal GIA model parameters that are consistent with observations of past sea-level change and to better constrain their associated uncertainties, thereby improving the interpretation of long-term gravity change and VLM and refining the GIA component of sea-level projections.

In Chapter 2, we constrain the GIA signal and its uncertainty for southeastern Canada and the northeastern United States using 1,013 paleo relative sea-level (RSL) data points from 38 sites. These data, comprising 544 sea-level index points, 232 marine limiting data points, and 237 terrestrial limiting data points, were compared against output from 14,960 simulations that combine a 1D, spherically symmetric earth model with 34 different North American ice sheet reconstructions. To account for laterally variable earth structure, the 1D GIA modeling results suggest that the region is best represented by two subregions that yield significantly improved fits to the RSL data: (1) HUL, near the center and thickest part of the former Laurentide Ice Sheet, encompassing Hudson Bay, the Ungava Peninsula, and Labrador; and (2) NSNM, located along the former ice margin, including Newfoundland, the St. Lawrence Corridor, New Brunswick and Nova Scotia, and Maine and Massachusetts. This subregional partitioning, inferred from the 1D analysis, was further tested using a 3D finite-volume earth model incorporating lateral viscosity variations based on two shear-wave tomographic models. A central component of this research is the estimation of GIA model uncertainty. Three complementary approaches, including heuristic, nominal Bayesian, and history matching, were used to quantify this uncertainty.

Building on the results of Chapter 2, Chapter 3 delivers the second component of this thesis by isolating and interpreting the processes contributing to contemporary VLM across eastern Canada and the northeastern United States. This chapter evaluates VLM over two timescales, millennial and decadal, across six subregions in the study region. The analysis integrates GNSS-derived VLM rates from 88 stations, late-Holocene RSL reconstructions from 18 sites spanning the past 4,000 years (348 sea-level index points), outputs from regionally constrained GIA models, and GRACE-derived mass change estimates from April 2002 to November 2023. By comparing decadal-scale and millennial-scale VLM estimates, this methodology enables the identification of departures from long-term GIA-driven trends and the interpretation of these deviations in terms of non-GIA processes. The results underscore the dominant role of GIA while also revealing regional contributions from contemporary non-GIA signals, primarily driven by hydrological mass changes. This chapter presents an uncertainty analysis of the VLM signal and GRACE-derived total water storage variations.

Extending the analyses from Chapters 2 and 3, Chapter 4 represents the third original component of this thesis, which aims to evaluate the influence of VLM, particularly its GIA-induced signal, on

regional projections of mean sea-level change and nuisance flooding frequency across eastern Canada and the northeastern United States. This analysis focuses on 25 tide gauge stations across the region and provides projections for the years 2050, 2100, and 2150 CE. Projections of regional mean sea-level changes are developed under three Shared Socioeconomic Pathway (SSP) scenarios, including SSP1-1.9, SSP3-7.0, and SSP5-8.5, and evaluated across three distinct projection cases: (1) full Intergovernmental Panel on Climate Change (IPCC) projections including all components of sea-level change, (2) IPCC projections excluding the VLM signal, and (3) IPCC projections excluding VLM but incorporating regionally optimized GIA-induced VLM rates with associated model uncertainty bounds. Projections of nuisance flooding events are based on harmonic analysis that accounts for local nodal corrections and secular changes in major tidal constituents, while also incorporating projected regional mean sea-level changes under each SSP scenario and projection case. The results generally indicate that incorporating VLM (primarily its GIA signal) substantially modifies projections of both regional mean sea-level change and nuisance flooding frequency, underscoring the critical importance of accounting for the VLM signal in long-term coastal risk assessments in the study region.

Acknowledgements

First and foremost, I would like to express my deepest gratitude to my supervisor, Professor Glenn A. Milne, for his unwavering support, patience, and guidance throughout my PhD journey. From the very beginning, starting in the middle of COVID, Glenn has been a constant source of encouragement, offering not only insightful scientific direction but also genuine understanding and care that went beyond the role of a supervisor. I am truly proud to have had him as my supervisor.

I am also sincerely grateful to my co-supervisors, Dr. John W. Crowley and Dr. Makan A. Karegar, for their invaluable guidance, encouragement, and scientific input throughout my PhD. Their expertise and thoughtful feedback significantly improved the quality of this work, and their support has been instrumental in advancing my research.

I would also like to thank my co-authors and collaborators, Lev Tarasov, Ryan Love, Maryam Yousefi, and Matteo Vacchi, for their contributions and support during the preparation of my manuscripts. I gratefully acknowledge my thesis examination committee, Professors Jeffrey Freymueller, Pascal Audet, Dariush Motazedian, and Claire Perry, for dedicating their time to assess my thesis and for providing valuable feedback that improved the final version.

Table of Contents

1. Introduction **1**
1.1. General overview, motivation, and aims 1
1.2. General overview of GIA 3
1.2.1. GIA mechanism and modelling 4
1.2.1.1. Evolution of GIA modelling 6
1.2.1.2. The sea-level equation 7
1.3. Paleo and contemporary observables 9
1.3.1. Paleo RSL reconstructions 9
1.3.2. Contemporary geodetic observations 10
1.3.2.1. VLM from GNSS measurements 11
1.3.2.2. Mass change signal from GRACE 12
1.4. Recent and future sea-level changes 15
1.5. Contributions and outline of thesis 18

2. Constraining Models of Glacial Isostatic Adjustment in Eastern North America **20**
Abstract 21
2.1. Introduction 21
2.2. Methodology 23
2.2.1. Sea-level dataset 23
2.2.2. 1D GIA model and parameterization 28
2.2.3. Estimation of model parameters 29
2.2.3.1. Estimation of model uncertainty bounds 30
2.2.4. 3D GIA modelling 33
2.3. Results 33
2.3.1. 1D Earth model analysis 34
2.3.1.1. Determination of regional partitioning, optimal parameter sets and model uncertainty 34
2.3.1.2. Regional parameter estimates and data-model fits 39
2.3.1.2.1. Hudson Bay (sites 1-7) 39
2.3.1.2.2. Ungava Peninsula (sites 8-11) 42
2.3.1.2.3. Labrador (sites 12-15) 43
2.3.1.2.4. Newfoundland (sites 16-20) 45
2.3.1.2.5. St. Lawrence Corridor (sites 21-24) 47
2.3.1.2.6. New Brunswick and Nova Scotia (sites 25-34) 48
2.3.1.2.7. Maine and Massachusetts (sites 35-38) 51
2.3.2. 3D Earth model analysis 52
2.3.3. Uncertainty estimation using a history matching approach 55
2.4. Discussion 58
2.5. Summary 61
References 62
Supplementary figures and tables of Chapter 2 68

3. Towards an improved understanding of vertical land motion in eastern North America **109**
Abstract 110

3.1. Introduction 110
3.2. Data and methodology 112
3.2.1. Contemporary observations 112
3.2.1.1. VLM rates from GNSS measurements 112
3.2.1.2. Mass change signal from GRACE 114
3.2.2. Paleo VLM rate estimates 115
3.2.3. GIA model outputs 116
3.3. Results and discussion 116
3.3.1. VLM rates with uncertainty estimates 117
3.3.1.1. Hudson Bay 117
3.3.1.2. Ungava Peninsula and Labrador 119
3.3.1.3. Newfoundland 120
3.3.1.4. St. Lawrence Corridor 121
3.3.1.5. New Brunswick and Nova Scotia 122
3.3.1.6. Maine and Massachusetts 124
3.3.2. Present-day mass change signal with uncertainty estimates 125
3.4. General discussion 132
3.5. Conclusion 135
References 135
Supplementary figures of Chapter 3 140

4. Improved projections of sea-level change and nuisance flooding in central eastern North America: The importance of GIA-induced land motion 163
Abstract 164
4.1. Introduction 164
4.2. Data and methodology 166
4.2.1. GIA-induced VLM signal 166
4.2.2. Regional mean sea-level projections 167
4.2.3. Nuisance flooding analysis 168
4.3. Results and discussion 173
4.3.1. Projections of regional mean sea-level changes 173
4.3.2. Nuisance flooding 176
4.3.2.1. Historic baseline 176
4.3.2.2. Projections 176
4.4. General discussion 184
4.5. Conclusion 186
References 187
Supplementary figures and tables of Chapter 4 192

5. Conclusion 206

Bibliography 212

List of Figures

Figure 1.1. Schematic illustration of glacial isostatic adjustment (GIA) **5**
Figure 1.2. Flowchart illustrating the components and workflow of a GIA model 6
Figure 1.3. Diagram showing how past mean sea levels are inferred using the concept of indicative meaning 9
Figure 1.4. Reconstructed paleo RSL records for site #5 in Hudson Bay 10
Figure 1.5. Sensitivity of GRACE-derived TWS estimates to the applied GIA model 13
Figure 1.6. GMSL rise from satellite altimetry from January 1993 to the present 16
Figure 1.7. Projected global temperature change and GMSL change under five SSPs based on IPCC AR6 16

Figure 2.1. Map showing the spatial distribution of RSL data used in this study **25**
Figure 2.2. RSL reconstructions for the 7 subregions distributed over southeastern Canada and northeastern USA 28
Figure 2.3. Data-model misfit values (δ) for the whole study region 35
Figure 2.4. Data-model misfit values (δ) for the HUL geographic subset 36
Figure 2.5. Data-model misfit values (δ) for the NSNM geographic subset 38
Figure 2.6. Data and modelled RSL curves (optimal and uncertainty bounds) for Hudson Bay 41
Figure 2.7. Data and modelled RSL curves (optimal and uncertainty bounds) for Ungava Peninsula 43
Figure 2.8. Data and modelled RSL curves (optimal and uncertainty bounds) for Labrador 44
Figure 2.9. Data and modelled RSL curves (optimal and uncertainty bounds) for Newfoundland 46
Figure 2.10. Data and modelled RSL curves (optimal and uncertainty bounds) for St. Lawrence Corridor 48
Figure 2.11. Data and modelled RSL curves (optimal and uncertainty bounds) for New Brunswick and Nova Scotia 50
Figure 2.12. Data and modelled RSL curves (optimal and uncertainty bounds) for Maine and Massachusetts 52
Figure 2.13. Differential RSL at 10 ka derived from 3D (based on S40RTS_SL2013) – 1D models 54
Figure 2.14. Difference in the estimated RSL values at 10 ka between the two 3D runs 54
Figure 2.15. Lower and upper bounding models, quantified by the history matching approach 58
Figure 2.S1. RSL data points for site #5 in Hudson Bay before and after radiocarbon re-calibration 70
Figure 2.S2. Map showing the spatial distribution of RSL data used in this study 71
Figure 2.S3. Mean and standard deviation of the 34 North American ice sheet reconstructions at 21 ka BP 72
Figure 2.S4. Mean and standard deviation of the 34 North American ice sheet reconstructions at 10 ka BP 73
Figure 2.S5. Temporal evolution of the ice thickness from 21 ka to the present day based on the 34 North American ice sheet reconstructions 74
Figure 2.S6. Data and modelled RSL curves (optimal and uncertainty bounds) based on the analysis of the entire region 82
Figure 2.S7. Data-model misfit plots (δ) associated with Hudson Bay, Ungava Peninsula, and Labrador 83
Figure 2.S8. Data-model misfit plots (δ) associated with Newfoundland, St. Lawrence Corridor, New Brunswick and Nova Scotia, and Maine and Massachusetts 83
Figure 2.S9. Partitioning the whole study region into 2 geographic subsets based on the data-model misfit analysis 84
Figure 2.S10. Data-model misfit values (δ) for Hudson Bay 85
Figure 2.S11. Data-model misfit values (δ) for Ungava Peninsula 86
Figure 2.S12. Data-model misfit values (δ) for Labrador 87
Figure 2.S13. Data-model misfit values (δ) for Newfoundland 88
Figure 2.S14. Data-model misfit values (δ) for St. Lawrence Corridor 89
Figure 2.S15. Data-model misfit values (δ) for New Brunswick and Nova Scotia 90
Figure 2.S16. Data-model misfit values (δ) for Maine and Massachusetts 91

Figure 2.S17. Data and modelled RSL curves based on the analysis of the entire region from 1D and 3D models 99
Figure 2.S18. Comparison between model uncertainty bounds inferred from history matching and nominal Bayesian approaches for all sites 107
Figure 2.S19. Difference in average ice thickness between two sets of ice history models representing highest and lowest implausibility measures 108

Figure 3.1. Map showing distribution of SLIPs (dating from 4 ka BP to the present day) and GPS stations used for isolating the VLM signal **113**
Figure 3.2. Comparison of VLM rates over millennial and decadal timescales in Hudson Bay 118
Figure 3.3. Comparison of VLM rates over millennial and decadal timescales in the Ungava Peninsula and Labrador 120
Figure 3.4. Comparison of VLM rates over millennial and decadal timescales in Newfoundland 121
Figure 3.5. Comparison of VLM rates over millennial and decadal timescales in St. Lawrence Corridor 122
Figure 3.6. Comparison of VLM rates over millennial and decadal timescales in New Brunswick and Nova Scotia 123
Figure 3.7. Comparison of VLM rates over millennial and decadal timescales in Maine and Massachusetts 125
Figure 3.8. Contemporary GRACE-derived mass change signal and resultant vertical surface displacement (both with uncertainty estimates) in Hudson Bay 127
Figure 3.9. Contemporary GRACE-derived mass change signal and resultant vertical surface displacement (both with uncertainty estimates) in the Ungava Peninsula and Labrador 129
Figure 3.10. Contemporary GRACE-derived mass change signal and resultant vertical surface displacement (both with uncertainty estimates) in the NSNM subregion along the Atlantic coast 131
Figure 3.11. Comparison of RSL rise (in mm/yr) over two different time periods (from 2 ka BP and from 4 ka BP to the present-day) 134
Figure 3.S1. Re-analyzed VLM rate at the “MEGO” GPS station located in Maine and Massachusetts 140
Figure 3.S2. RSL contour maps inferred from the optimal regional GIA model at 4 ka BP for four subregions in the study region 141
Figure 3.S3. Modelled vertical displacement (due to ice mass loss signal associated with Greenland and Canadian Arctic glaciers) at the GPS station “KUUJ” in eastern Hudson Bay 142
Figure 3.S4. RSL curves for three sites in Hudson Bay, derived from the optimal regional GIA model and uncertainty bounds 142
Figure 3.S5. VLM curves for three sites in Hudson Bay, derived from the optimal regional GIA model and uncertainty bounds 143
Figure 3.S6. ΔG + E curves for three sites in Hudson Bay, derived from both RSL and VLM curves 144
Figure 3.S7. RSL curves for sites #1 – #3 in Hudson Bay, illustrating the fit of two models (a postglacial decay model and a linear trend) 145
Figure 3.S8. RSL curves for three sites in Newfoundland, derived from the optimal regional GIA model and uncertainty bounds 146
Figure 3.S9. VLM curves for three sites in Newfoundland, derived from the optimal regional GIA model and uncertainty bounds 147
Figure 3.S10. ΔG + E curves for three sites in Newfoundland, derived from both RSL and VLM curves 148
Figure 3.S11. RSL curves for sites #4, #5, and #6 in Newfoundland, illustrating the best-fit linear trends 149
Figure 3.S12. RSL curves for two sites in St. Lawrence Corridor, derived from the optimal regional GIA model and uncertainty bounds 150
Figure 3.S13. VLM curves for two sites in St. Lawrence Corridor, derived from the optimal regional GIA and uncertainty bounds 150

Figure 3.S14. ΔG + E curves for two sites in St. Lawrence Corridor, derived from both RSL and VLM curves 151
Figure 3.S15. RSL curves for sites #7 and #8 in St. Lawrence Corridor, illustrating the best-fit linear trends 151
Figure 3.S16. RSL curves for six sites in New Brunswick and Nova Scotia, derived from the optimal regional GIA model and uncertainty bounds 152
Figure 3.S17. VLM curves for six sites in New Brunswick and Nova Scotia, derived from the optimal regional GIA model and uncertainty bounds 153
Figure 3.S18. ΔG + E curves for six sites in New Brunswick and Nova Scotia, derived from both RSL and VLM curves 154
Figure 3.S19. RSL curves for sites #9 – #14 in New Brunswick and Nova Scotia, illustrating the best-fit linear trends 155
Figure 3.S20. RSL curves for four sites in Maine and Massachusetts, derived from the optimal regional GIA and uncertainty bounds 156
Figure 3.S21. VLM curves for four sites in Maine and Massachusetts, derived from the optimal regional GIA and uncertainty bounds 157
Figure 3.S22. ΔG + E curves for four sites in Maine and Massachusetts, derived from both RSL and VLM curves 158
Figure 3.S23. RSL curves for sites #15 – #18 in Maine and Massachusetts, illustrating the best-fit linear trends 159
Figure 3.S24. Present-day rates (mm/year) of GIA-induced geoid changes based on optimal regional models 160
Figure 3.S25. Maps showing two primary, independent sources of uncertainty in the GRACE analysis, including uncertainty of the GRACE SHCs and uncertainty of the GIA signal 161
Figure 3.S26. Comparison of RSL rates from CHURCHILL tide gauge observations and GIA model predictions at site #1 in Hudson Bay 162

Figure 4.1. Present-day VLM rates from regionally optimized GIA models for two subregions **167**
Figure 4.2. Locations of the 25 tide gauge stations used in this study 169
Figure 4.3. Secular changes and local nodal modulations in the M2 tidal constituent at two tide-gauge stations (Boston and Churchill) 172
Figure 4.4. Projected regional mean sea-level changes (in mm) relative to the IPCC temporal baseline at four representative tide gauges for 2050, 2100, 2150 under three SSPs and three projection cases 174
Figure 4.5. Nuisance flooding frequency (days per year) at nine tide gauges from 1995 to 2014 176
Figure 4.6. Projected change in annual nuisance flooding days (relative to the 2005) under SSP1-1.9 for the nine tide gauges experiencing historical nuisance flooding 177
Figure 4.7. Projected annual nuisance flooding frequency (days per year) under SSP1-1.9 for the eight Canadian tide gauges without historical nuisance flooding 179
Figure 4.8. Projected annual nuisance flooding frequency (days per year) under SSP1-1.9 for the eight U.S. tide gauges without historical nuisance flooding 179
Figure 4.9. Projected change in annual nuisance flooding days (relative to the 2005 baseline) under SSP3-7.0 for the nine tide gauges experiencing historical nuisance flooding 181
Figure 4.10. Lower bound of projected changes in annual nuisance flooding days (relative to the 2005 baseline) under SSP1-1.9 for the nine tide gauges experiencing historical nuisance flooding 183
Figure 4.11. Upper bound of projected changes in annual nuisance flooding days (relative to the 2005 baseline) under SSP3-7.0 for the nine tide gauges experiencing historical nuisance flooding 183
Figure 4.12. Nuisance flooding frequency (days per year) from 1995 to 2014 for the nine tide gauges experiencing historical nuisance flooding based on reducing climate seasonality impact on SA and SSA 185
Figure 4.S1. Secular changes and local nodal modulations for the M2 tidal constituent at 25 tide gauges 193
Figure 4.S2. Secular changes and local nodal modulations for the N2 tidal constituent at 25 tide gauges 194

Figure 4.S3. Secular changes and local nodal modulations for the K1 tidal constituent at 25 tide gauges 195
Figure 4.S4. Time series of relative sea level at Churchill, derived from annual tide gauge observations from PSMSL 195
Figure 4.S5. Projected regional mean sea-level changes (in mm) relative to the IPCC temporal baseline at 10 Canadian tide gauges for 2050, 2100, 2150 under three SSPs and three projection cases 196
Figure 4.S6. Projected regional mean sea-level changes (in mm) relative to the IPCC temporal baseline at 11 U.S. tide gauges for 2050, 2100, 2150 under three SSPs and three projection cases 198
Figure 4.S7. Projected change in annual nuisance flooding days (relative to the 2005 baseline) under SSP5-8.5 for the nine tide gauges experiencing historical nuisance flooding 199
Figure 4.S8. Projected annual nuisance flooding frequency (days per year) under SSP3-7.0 for the eight Canadian tide gauges without historical nuisance flooding 200
Figure 4.S9. Projected annual nuisance flooding frequency (days per year) under SSP5-8.5 for the eight Canadian tide gauges without historical nuisance flooding 200
Figure 4.S10. Projected annual nuisance flooding frequency (days per year) under SSP3-7.0 for the eight U.S. tide gauges without historical nuisance flooding 201
Figure 4.S11. Projected annual nuisance flooding frequency (days per year) under SSP5-8.5 for the eight U.S. tide gauges without historical nuisance flooding 201
Figure 4.S12. Upper bound of projected changes in annual nuisance flooding days (relative to the 2005 baseline) under SSP5-8.5 for the nine tide gauges with historical nuisance flooding 202
Figure 4.S13. Lower bound of projected annual nuisance flooding frequency (days per year) under SSP1-1.9 for tide gauges without historical nuisance flooding 202
Figure 4.S14. Upper bound of projected annual nuisance flooding frequency (days per year) under SSP3-7.0 for tide gauges without historical nuisance flooding 203
Figure 4.S15. Upper bound of projected annual nuisance flooding frequency (days per year) under SSP5-8.5 for tide gauges without historical nuisance flooding 203
Figure 4.S16. Projected changes in annual nuisance flooding days (relative to the 2005 baseline) under SSP3-7.0 for the nine tide gauges based on reducing climate seasonality impact on SA and SSA 204
Figure 4.S17. Projected annual nuisance flooding frequency (days per year) under SSP3-7.0 for the eight Canadian tide gauges based on reducing climate seasonality impact on SA and SSA 204
Figure 4.S18. Projected annual nuisance flooding frequency (days per year) under SSP3-7.0 for the eight U.S. tide gauges based on reducing climate seasonality impact on SA and SSA 205

List of Tables

Table 2.1. Number of RSL data points, after and before data cleaning, used to constrain the GIA signal **26**
Table 2.2. Earth model parameter sets for the optimal models, bounding models from heuristic approach, and accepted model parameter ranges from nominal Bayesian 38
Table 2.3. Data-model misfit parameter (δ) for 1D model and two 3D runs (using S40RTS and S40RTS_SL2013) for all subregions and the whole study region 55
Table 2.4. Earth-ice model parameter sets associated with the lower and upper bounds from history matching for all subregions 56
Table 2.S1. 34 ice loading history reconstructions with the 'best' and 'worst' 10 models from the history matching analysis 69

Table 4.S1. Latitude, longitude, and station names of tide gauges used in the analysis **192**
Table 4.S2. Number of nuisance flooding days in 2005 at the nine tide gauges experiencing historical nuisance flooding 199

Glossary

A brief glossary of commonly used terms and acronyms referenced in this thesis is provided below.

Acronym	Full term	Definition
EWT	Equivalent Water Thickness	A geophysical unit that converts GRACE/GRACE-FO gravity anomalies into the thickness of a uniform water layer distributed over the Earth's surface. It provides a direct physical measure of changes in terrestrial water storage, ice sheets, and hydrological systems.
GIA	Glacial Isostatic Adjustment	Glacial isostatic adjustment is the process of Earth deformation and sea-level change in response to changes in ice volume. It involves viscoelastic mantle flow, lithospheric flexure, crustal rebound, and associated perturbations to the Earth's gravity field and rotation.
GNSS	Global Navigation Satellite System(s)	Constellations of satellites (including GPS, GLONASS, Galileo, and BeiDou) that provide precise positioning via carrier-phase measurements. In geodesy, GNSS is the primary tool for measuring long-term vertical land motion at millimeter-per-year precision.
GRACE	Gravity Recovery and Climate Experiment	A twin-satellite mission (2002–2017, NASA/DLR) that mapped Earth's time-variable gravity field by measuring inter-satellite distance changes to micrometer precision. GRACE resolved secular mass change processes including ice sheet mass balance, hydrology, and GIA-induced gravity change.
GRACE-FO	GRACE Follow-On	Successor mission launched in 2018 by NASA/GFZ, continuing GRACE's time-variable gravity measurements. It introduced an advanced Laser Ranging Interferometer to complement microwave ranging, improving sensitivity to small gravity perturbations.
IPCC	Intergovernmental Panel on Climate Change	A UN body established in 1988 to assess climate science. The IPCC produces Assessment Reports (ARs), which synthesize global research on climate, sea-level rise, and impacts. Its sea-level projections incorporate process-based and statistical models, and provide baselines for adaptation planning.
LDP(s)	Limiting Data Point(s)	Geological indicators of past sea level that provide one-sided constraints: marine limiting points indicate sea level was above a given elevation, while terrestrial limiting points indicate sea level was below a given elevation.
LGM	Last Glacial Maximum	The last glacial maximum is the point in time during the previous glaciation when global ice volume was at its maximum, and occurred approximately twenty thousand years ago.
LMV	Lower Mantle Viscosity	The viscosity in the lower mantle, defined in our model as a constant viscosity layer from 670 km depth to the core-mantle boundary. See 'Viscosity'.
LT	Lithospheric Thickness	A key parameter in GIA models, representing the effective elastic thickness of the lithosphere, modeled as a high-viscosity (~10^{43} Pas) shell.
MHHW	Mean Higher High Water	The average height of the higher of the two daily high tides observed over a tidal epoch (20 years).
MLLW	Mean Lower Low Water	The average height of the lower of the two daily low tides over a tidal epoch. Used with MHHW to calculate tidal range in nuisance flooding threshold estimation.

MSL	Mean Sea Level	The long-term average sea surface height relative to the land, incorporating both absolute ocean height changes (thermal expansion, ice melt, steric effects) and VLM.
NF	Nuisance Flooding	Also called minor or high-tide flooding. Refers to recurrent, non-storm flooding caused by high tides exceeding locally defined thresholds. Chronic nuisance flooding is defined as ≥50 days per year and represents significant socio-economic impacts.
RSL	Relative Sea Level	Relative sea level is sea level at some time in the past with respect to present-day sea level. RSL reflects the combined influence of absolute sea-surface change and VLM.
SHC(s)	Spherical Harmonic Coefficient(s)	Spherical harmonic coefficients are mathematical parameters that represent Earth's gravity field in terms of a spherical harmonic expansion. In the context of GRACE and GRACE-FO, SHCs are derived from inter-satellite ranging measurements and provide estimates of the mean gravity field over a given time span. These coefficients capture the full combined signal of land hydrology, cryospheric mass changes (ice sheets and glaciers), and solid Earth processes, including GIA.
SLIP(s)	Sea-Level Index Point(s)	Geological indicators with well-constrained age and elevation, providing direct reconstructions of past relative sea level. SLIPs are the most robust paleo RSL data for GIA calibration.
SSP	Shared Socioeconomic Pathway	A set of socio-economic and emission scenarios (e.g., SSP1-1.9, SSP3-7.0, SSP5-8.5) adopted by the IPCC AR6. SSPs provide forcing pathways for global and regional sea-level projections.
TWS	Total Water Storage	The sum of all terrestrial water reservoirs, including groundwater, soil moisture, snow, surface water, glaciers, and water stored in biomass, estimated using GRACE/GRACE-FO observations.
UMV	Upper Mantle Viscosity	The viscosity in the upper mantle, defined in our model as a constant viscosity layer from the base of the lithosphere to a depth of 670 km. See 'Viscosity'.
Viscosity	–	Viscosity is a scalar quantity that relates stress and strain rate, and is a key model parameter. It controls the viscoelastic response of Earth's mantle in GIA models and is expressed in Pas.
VLM	Vertical Land Motion	Vertical displacement of the Earth's solid surface resulting from GIA, tectonics, sediment compaction, groundwater extraction, and anthropogenic loading, as estimated in this thesis using GNSS, paleo–sea-level reconstructions, and GIA models.

1

Introduction

1.1. General overview, motivation, and aims

Sea-level rise is one of the most pressing environmental issues of the 21st century, largely driven by the ongoing effects of anthropogenic climate change. Coastal areas are especially at risk as urban development expands into low-lying regions, increasing exposure to flooding, erosion, and storm surges. In addition to damaging infrastructure, rising sea levels contribute to saltwater intrusion, loss of freshwater resources, degradation of ecosystems, and growing public health risks (Wong et al., 2014). These impacts have far-reaching socio-economic consequences, particularly for vulnerable communities. To plan effective adaptation strategies, decision-makers need accurate projections of sea-level change that account for processes operating on a range of spatial scales, such as ocean dynamics, contemporary vertical land motion (VLM), and glacial isostatic adjustment (GIA) (Spanger-Siegfried et al., 2014; Sweet et al., 2014; Sweet & Park, 2014; Woodworth et al., 2011).

Accurately projecting regional to local sea-level change is challenging because many physical processes interact across various spatial and temporal scales (Milne et al., 2009). Although global mean sea level (GMSL) has been rising at about 3 mm per year in recent decades (Watson et al., 2015), the Intergovernmental Panel on Climate Change (IPCC) projects that this rate could surpass 8 mm per year by the end of the century (Church et al., 2013; Oppenheimer et al., 2019). However, this global average hides large regional and local differences. In some areas, sea-level rise is made worse by land subsidence, while in other places, it is reduced due to land uplift (e.g., Love et al., 2016). As a result, both vertical changes in the sea surface and VLM in coastal regions must be considered.

One of the most important long-term processes influencing VLM and regional sea-level change is GIA. This process refers to the Earth's ongoing response to the melting of continental ice sheets following the Last Glacial Maximum (LGM) around 21,000 years ago (Lambeck et al., 2014). As vast ice sheets such as the Laurentide and Fennoscandian began to melt, mass redistribution caused the previously depressed land to rebound, while peripheral areas experienced subsidence. This dynamic process, involving solid earth deformation and changes in the Earth's gravity field, continues to influence sea levels today (e.g., Spada, 2017; Williams et al., 2024).

In previously glaciated regions such as eastern Canada and the northeastern United States, GIA is an important signal in tide gauge and GNSS (Global Navigation Satellite Systems) records of,

respectively, sea-level change and VLM. For example, ongoing uplift exceeding 10 mm/yr is still observed near the center of the former Laurentide ice sheet, especially around Hudson Bay (Sella et al., 2007). Conversely, in areas peripheral to the ice sheets such as the Atlantic coast of North America, GIA-induced land subsidence contributes to enhanced rates of relative sea-level (RSL) rise. Some areas along the Atlantic coast have been sinking at rates up to 20 cm per century (Love et al., 2016; Spada, 2017), thereby amplifying the impacts of global sea-level rise on these vulnerable regions.

Recent studies have drawn attention to another growing concern: the increasing frequency of minor but recurrent high-water events known as "nuisance flooding" (Moftakhari et al., 2015; Sweet et al., 2014; ten Veldhuis et al., 2010). As sea levels slowly rise, the increased frequency of nuisance flooding can be considered as a "wake-up call" for areas that will be most affected by sea-level rise in the future. Although these events may not cause the catastrophic damage associated with extreme events (e.g., hurricanes), their cumulative effects can severely degrade infrastructure, salinize groundwater, and threaten public health. While this phenomenon has been well documented in parts of the United States, notably along the Atlantic and Gulf Coasts (Karegar et al., 2017; Moftakhari et al., 2015), the extent to which nuisance flooding is affecting or will affect coastal communities in eastern Canada remains poorly studied.

The Atlantic Provinces of Canada, including Newfoundland, New Brunswick, and Nova Scotia, have been identified as high-risk regions for future coastal flooding, partly due to GIA-induced land subsidence (Greenan et al., 2019). However, other factors such as groundwater extraction, dam construction, and regional hydrological cycles may also contribute to VLM in this region. For instance, deviations from GIA-predicted subsidence rates have been observed in areas near the U.S.-Canada border (between Maine and New Hampshire), with contemporary GNSS data revealing uplift trends that contradict geological and GIA-induced estimates (Karegar et al., 2017). One possible explanation involves the James Bay Hydroelectric Project in Quebec, which has altered regional water mass distribution since the 1980s. In this scenario, the accumulation of excess water mass due to damming would cause land subsidence within the impounded region, while surrounding peripheral areas may experience uplift (Reager et al., 2016; Wang et al., 2013). If this hypothesis holds true, it has important implications for understanding VLM and sea-level change across Hudson Bay, the St. Lawrence estuary, and the Atlantic Provinces.

Given the critical need for improved sea-level projections at regional scales and the particular vulnerability of eastern Canada to sea-level-related hazards, the primary goal of the research presented in this thesis is to better constrain and understand the processes contributing to contemporary and future VLM in southeastern Canada and the northeastern United States. This aim is timely given that eastern Canada is experiencing a recent acceleration in sea-level rise due to changes in ocean dynamics (Ezer & Atkinson, 2014) and increasing ice-mass loss (IMBIE team, 2018). In addition, studies analyzing both global and regional sea-level records have found large-scale changes in the long-term trends of diurnal and semidiurnal constituents of tidal high water (Schindelegger et al., 2018), which could potentially affect the frequency of nuisance flooding in eastern Canada. The combination of these factors places this region at increasing risk from both nuisance and storm surge flooding.

To achieve the aim described above, the research presented in this thesis was partitioned into three components. First, it develops refined estimates of GIA model parameter sets that are consistent with observations of past sea-level change in eastern Canada and better constrains the associated model uncertainties. Improving GIA models for this region is essential for quantifying the GIA component of sea-level projections, which is a significant contributor in eastern Canada (Love et al., 2016). Second,

the model output is applied to interpret GNSS observations of VLM and to identify potential discrepancies between paleo and contemporary VLM rates, as well as to more accurately isolate the regional hydrological mass change signal inferred from GRACE (Gravity Recovery and Climate Experiment) measurements that contribute to land surface displacement and reveal the presence of significant non-GIA signals. Third, the results from the first two components are used to quantify the importance of the VLM signal, specifically its GIA component, for projections of mean sea-level change and nuisance flooding frequency, and to enable more accurate quantification of uncertainties in these projections.

This chapter begins with a general overview of GIA, including its physical mechanisms, historical development, and the evolution of GIA modeling frameworks with particular emphasis on the sea-level equation (Section 1.2). Section 1.3 introduces the observations used in this thesis: paleo RSL reconstructions (1.3.1) and geodetic observations (GNSS and GRACE) (1.3.2). Section 1.4 explores past and projected sea-level changes, summarizing the primary contributing processes, the structure of IPCC projections, and the implications for chronic nuisance flooding. Finally, Section 1.5 outlines the main contributions of this thesis and provides a roadmap of the chapters that follow.

1.2. General overview of GIA

GIA is the response of the solid Earth and gravity field to changes in continental (grounded) ice. Since the beginning of the Pleistocene around 3 million years ago, the Northern Hemisphere, particularly North America and Eurasia, has experienced several glacial cycles, mainly occurring every 40,000 to 100,000 years due to changes in Earth-Sun orbit (Shackleton & Opdyke, 1973). During the late Quaternary (past ~800,000 years), massive ice sheets like the Laurentide, Cordilleran, and Innuitian covered much of North America during peak glaciation, with the most recent global LGM occurring around 21,000 years ago (Lambeck et al., 2014). This buildup of ice caused global sea levels to drop by about 130 meters. As the climate warmed, the ice rapidly melted within about 10,000 years, returning the water to the oceans. This redistribution of water mass between continents and oceans led to large-scale earth deformation, changes in the Earth's gravity field and rotation, and, consequently, global sea levels.

Due to the viscoelastic nature of the mantle and lithosphere, deformation continues for many thousands of years after ice loss. Historically, evidence for GIA has been inferred from morphological changes such as shoreline migration, which helped early scientists in the 19th and early 20th centuries develop theories about sea-level change, climate cycles, and earth deformation (e.g., Daly, 1925; Jamieson, 1865; Nansen, 1921). GIA is a process that provides information on various components of the earth system: ice-sheet behavior, sea-level evolution, and the structure of Earth's interior. GIA modelling involves comparing computer simulations with observations, and misfits between these have led to new insights and constraints, such as laterally variable earth structure and feedback between ice dynamics and the solid Earth (Whitehouse, 2018). This has deepened our understanding of both Earth's physical properties and climate history.

GIA processes leave measurable signals across various geophysical and geological records, such as VLM, gravity anomalies, and sea-level changes. Modern measurements such as vertical and horizontal crustal motion from GNSS, RSL trends from tide gauges, and gravity anomalies detected by satellite gravimetry (e.g., GRACE), all reflect ongoing deformation but represent only short segments of the millennial-scale GIA signal. In contrast, paleo RSL data, obtained from geological records, extend across thousands of years, thereby capturing the long-term viscoelastic response of the solid Earth to

past ice mass redistribution (Milne & Shennan, 2013). While modern geodetic and gravimetric measurements are critical for understanding present-day earth surface changes, their interpretation can be ambiguous (e.g., Yousefi et al., 2020). This ambiguity is greatly reduced when these data are interpreted alongside longer-term geological reconstructions. The combination of both contemporary and paleo datasets ensures that GIA models are accurately calibrated and able to simulate both recent and ancient earth responses to surface loading changes. This integrated approach underpins the methodological framework of this thesis (Chapter 3 in particular), providing the foundation for evaluating and refining predictions of VLM and RSL change in this research.

1.2.1. GIA mechanism and modelling

During glaciation, the increasing mass of an ice sheet depresses the underlying crust and mantle, pushing mantle material outward and forming peripheral uplifted regions known as forebulges (see Figure 1.1). This redistribution of internal mass alters Earth's gravitational potential field and causes sea-level variations, as the ocean surface conforms to an equipotential surface, known as the geoid, that represents constant gravitational potential in the absence of atmospheric and oceanic circulation and tides. The growth of ice sheets also draws water mass from the oceans onto the continents, resulting in a surface mass redistribution that further perturbs the gravity field and geoid, independent of earth deformation. As ice sheets melt during deglaciation, the Earth adjusts toward a new isostatic equilibrium. This involves uplift in formerly glaciated regions and resultant subsidence in the peripheral forebulges due to mantle return flow (Figure 1.1). The reversal of solid earth deformation changes the gravity field and, therefore, topography of the sea surface: the decreasing gravitational attraction of the retreating ice causes a regional lowering of the geoid. Simultaneously, the addition of meltwater into the oceans results in a globally uniform rise in sea level known as barystatic sea-level change (e.g., Gregory et al., 2019). The overall impact of these mass redistribution processes is a complex and regionally variable RSL response across the globe (e.g., Clark et al., 1978).

A central component of GIA is the effect of ocean loading, which acts with the ice history to deform the Earth and induce gravitational and rotational changes. Near continental margins, the ocean loading causes vertical displacement patterns known as continental levering (Walcott, 1972), where ocean mass effectively pushes up the adjacent continents while causing subsidence in the ocean basins. This subsidence around continental margins acts to increase the volumetric capacity of the oceans and is an important contributor to the process termed ocean syphoning (Mitrovica & Milne, 2002), which affects global mean RSL through changes in ocean basin volume. Therefore, ocean loading leads to both spatial variations in the sea-level response and contributes to changes in global mean sea level. Another important component of GIA involves Earth’s rotational dynamics. Since any rotating object tends to align its rotation with the axis of maximum moment of inertia, changes in surface water mass distribution from glacial cycles and the resulting deformational and gravitational response modify the Earth’s moment of inertia. This leads to a shift in the orientation of the instantaneous spin axis, a phenomenon known as True Polar Wander (Gross and Vondrák, 1999; Sabadini et al., 1982). These rotational adjustments further affect the shape and gravity field of the Earth and thus influence sea-level patterns on a global scale.

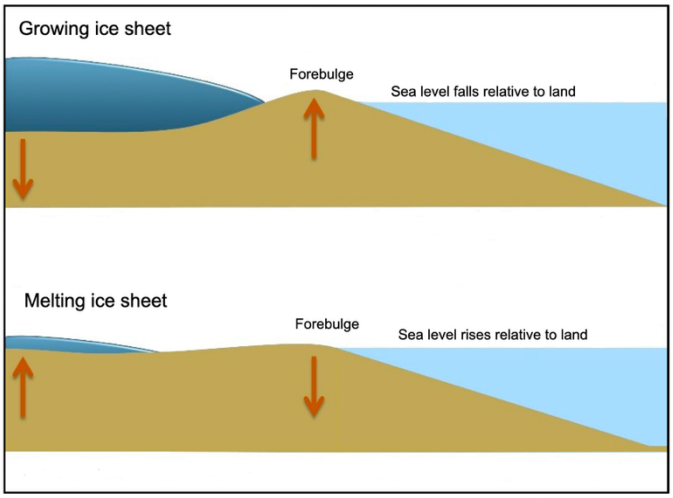


Figure 1.1. Schematic illustration of glacial isostatic adjustment (GIA). During glaciation (top panel), the load of an ice sheet depresses the land beneath it while displacing mantle material outward to form a forebulge, resulting in RSL fall at the forebulge. During deglaciation (bottom panel), land beneath the former ice sheet rebounds while the forebulge collapses, resulting in RSL rise in formerly glaciated regions and subsidence in the peripheral areas. Arrows indicate the direction of VLM (figure adapted from Boon et al., 2018).

Figure 1.2 provides an overview of the general model components and workflow required to simulate the processes described above. This diagram highlights the interconnected roles of surface loading from ice sheets and oceans, the earth structure and rheology, and the resulting deformation and geophysical signals (model outputs). The amplitude of the GIA signal observed in paleo RSL records is primarily controlled by two key factors: the magnitude and distribution of the surface loading from ice and water, and the rheological properties of the Earth's interior. Consequently, GIA modelling studies have generally aimed to constrain (1) the history of ice sheet evolution, and (2) the rheological structure of the Earth (Whitehouse, 2018). Most GIA studies have employed a forward modelling approach, whereby different combinations of earth rheology and ice history are tested to reproduce observational data.

The sea-level equation, the solution of which gives the redistribution of water masses in response to changes in surface loading and the resulting changes in the Earth's gravity field (Farrell & Clark, 1976; Mitrovica & Milne, 2003), is a key component of the forward model. This water mass redistribution is the sea-level response to specified ice and earth model inputs and serves two important roles: (1) it is a component of the surface load and (2) it is one of the primary GIA observables. Once the sea-level equation has been solved, a GIA model produces accurate simulations of many observable fields (Figure 1.2) enabling data-model comparisons to identify the model configuration that minimizes the misfit between model predictions and observations. The optimal parameter sets, representing the best-fitting ice and earth model input parameters, are determined based on these data-model fits. A common challenge is the inherent non-uniqueness of the solution; multiple combinations of ice and earth model input parameters can produce high-quality fits to observations. This ambiguity, combined with observational uncertainties and the simplifying assumptions inherent in the applied models, can lead to significant differences in estimates of the earth rheology (mantle viscosity and lithospheric thickness) and/or deglaciation history. The historical development of GIA modelling, along with the theoretical formulation of the sea-level equation, is presented in the following section.

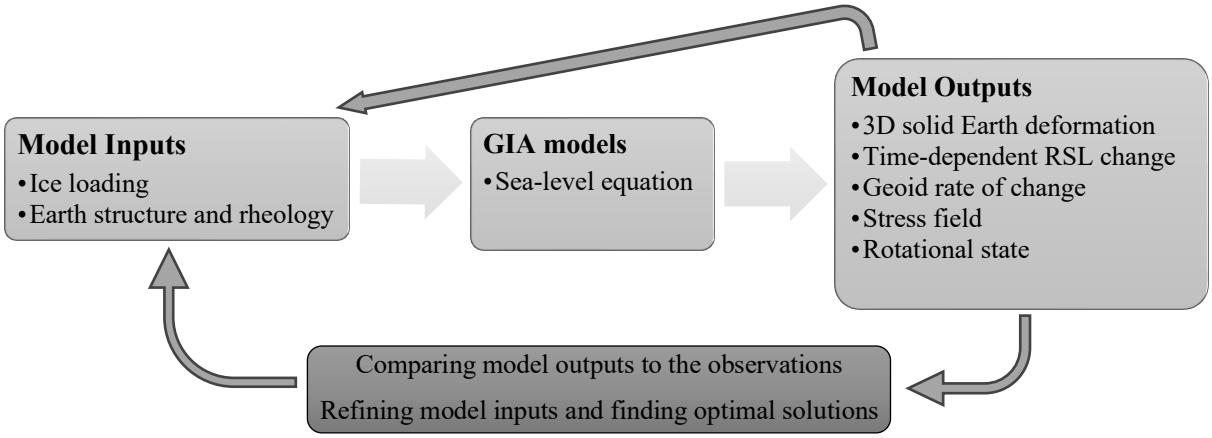


Figure 1.2. Flowchart illustrating the components and workflow of a GIA model. The ice history and earth structure and rheology serve as primary inputs to the GIA model. Common model outputs (right-hand box) are compared with observational data to iteratively refine the model inputs. Solid earth deformation and sea-level change also influence ice sheet evolution, forming a feedback loop that can be addressed in coupled modelling frameworks (Whitehouse et al., 2018).

1.2.1.1. Evolution of GIA modelling

The evolution of GIA modelling has been shaped by several foundational studies beginning in the 1970s. Pioneering work by Peltier (1974) introduced an impulse response formalism based on a Maxwell viscoelastic earth structure. In this approach, Green's functions are computed to characterize the Earth's deformational and gravitational response to a delta function surface mass load. The response to an arbitrary surface load is then obtained by convolving these impulse responses with the full load history. Independently, Farrell and Clark (1976) developed a method to compute sea-level change in response to a pre-defined ice loading history and model of earth rheology using an integral equation framework. Their model assumes a non-rotating Earth with fixed shorelines and a Heaviside-type loading time history, and applies the Green's function approach of Peltier (1974). These two studies form the core of modern GIA modelling frameworks. Subsequent advancements have enhanced these foundational models by, for example, incorporating more complex processes influencing sea-level change, refining ice history inputs, considering more complex (3D) earth structure via numerical modelling (Whitehouse et al., 2018).

A key extension to the original sea level theory is the inclusion of rotational effects. Milne and Mitrovica (1998) developed a treatment for perturbations in the Earth's rotation vector induced by GIA. Other studies have introduced time-varying shorelines, including both direct sea-level impacts and the consideration of marine ice sheets (Milne & Mitrovica, 1998; Mitrovica & Milne, 2003; Peltier, 1998). A further refinement to the sea-level equation was proposed by Dalca et al. (2013) to incorporate the isostatic effects of sediment loading. This extended formulation considers the influence of sediment mass redistribution on both the solid Earth and the gravitational potential, as well as the displacement of ocean water in regions of marine sediment accumulation.

A central issue in GIA modelling is defining the Earth's deformational behaviour. The most widely used rheology is that of a Maxwell solid, which combines elastic and viscous deformation responses. Although it is the simplest physically meaningful rheology, alternatives such as the Burgers model are more complete as it encompasses transient and long-term viscous relaxation (e.g., Ranalli, 1995). Caron

et al. (2017) applied both Maxwell and Burgers rheologies in an inversion of global RSL records to determine optimal average earth viscosity profiles. Notably, they found that Burgers models may lack uniqueness in their solutions. Beyond linear rheologies, laboratory studies suggest that the mantle exhibits non-linear, power-law behaviour under realistic environmental conditions (Karato & Wu, 1993). While many GIA models assume a spherically symmetric Earth with viscosity varying only with depth, more advanced studies incorporate lateral variations in viscosity (e.g., Latychev et al., 2005; Paulson et al., 2005; Wu, 2005). These models are particularly relevant for regions with significant lateral variability in earth structure, such as Antarctica (van der Wal et al., 2015). In these 3D earth models, lateral viscosity variations are most often determined from regional or global seismic velocity models via mineral physics relationships between velocity, density, temperature and viscosity (see above references for further details).

To constrain the earth and ice parameters in GIA models, different approaches have been used. One relies on data or parameterizations that are relatively insensitive to one of the model inputs. For example, postglacial decay time analysis, discussed in Chapter 3, is more sensitive to mantle viscosity than ice history (Kuchar et al., 2019; Mitrovica et al., 2000) and has been used in constructing widely used the series of ICE-XG and VM-Y model pairings (e.g., Peltier, 2004; Peltier et al., 2015). Once a good-fitting viscosity model is determined from the decay time constraints, the ice history is hand-tuned assuming this viscosity model is accurate in other regions. A second approach involves a joint inversion for both ice and earth parameters. Through this approach, scaling factors are applied to initial ice and earth model components to optimize the fit with observations (Caron et al., 2017; Lambeck et al., 2014). This technique was used to develop the global ANU ice model (Lambeck et al., 2014). In general, the optimal earth model parameters vary from region to region. A third approach involves the use of glaciological models to simulate ice sheet evolution based on a specified climate forcing (e.g., Tarasov et al., 2012). These models typically have a large number of parameters and so this approach is more computationally intensive. The benefit is that the resulting ice models are consistent with the ice physics incorporated in the glaciological model.

1.2.1.2. The sea-level equation

The sea-level equation used in modern GIA models describes RSL change $\Delta SL(\theta, \lambda, t)$ as the difference between the change in geoid height $\Delta SS(\theta, \lambda, t)$ and the variation in the height of the solid earth surface (ocean floor) $\Delta R(\theta, \lambda, t)$ written as:

$$\Delta SL(\theta, \lambda, t) = \Delta SS(\theta, \lambda, t) - \Delta R(\theta, \lambda, t) \quad (1.1)$$

where θ and λ are the colatitude and east longitude, respectively, in a spherical coordinate system.

Sea-surface height changes ΔSS are separated into a spatially varying component (ΔG) and a spatially uniform term $E(t)$, giving the extended form of the sea-level equation:

$$\Delta SL(\theta, \lambda, t) = (\Delta G(\theta, \lambda, t) + E(t)) - \Delta R(\theta, \lambda, t) \quad (1.2)$$

The term $E(t)$ represents a time-dependent, spatially uniform shift in sea surface height that ensures mass conservation between the ice sheets and oceans. It consists of two parts: the barystatic sea-level change $E^B(t_j)$ and the ocean syphoning term $E^S(t_j)$. The barystatic component is defined as:

$$E^B(t_j) = -\frac{V_I}{A_o}\frac{\rho_I}{\rho_W} = -\frac{1}{A_o}\frac{\rho_I}{\rho_W}\iint_\Omega \Delta I(\theta', \lambda', t_j) d\Omega \quad (1.3)$$

where A_o is the ocean surface area, ρ_I and ρ_W are the densities of ice and seawater, respectively, V_I is the change in ice volume, and $\Delta I(\theta', \lambda', t_j)$ is the change in ice thickness at location (θ', λ') and time t_j. $d\Omega$ represents the spherical surface integration element.

The ocean syphoning component is expressed by spatial averaging over the ocean area:

$$E^S(t_j) = -\frac{1}{A_o}\langle \Delta G(\theta, \lambda, t) - \Delta R(\theta, \lambda, t)\rangle_O \quad (1.4)$$

The deformation-related terms are computed through spatiotemporal convolutions of the surface load with Green's functions. The vertical displacement of the sea floor $\Delta R(\theta, \lambda, t)$ is given by:

$$\Delta R(\theta, \lambda, t) = \int_{t_f}^{t}\iint_\Omega L(\theta', \lambda', t')\, GF_R(\psi, t - t')\, a^2\, d\Omega\, dt' \quad (1.5)$$

and the perturbation to the gravitational potential $\Delta\Phi(\theta, \lambda, t)$ is:

$$\Delta\Phi(\theta, \lambda, t) = \int_{t_f}^{t}\iint_\Omega L(\theta', \lambda', t')\, GF_\Phi(\psi, t - t')\, a^2\, d\Omega\, dt' \quad (1.6)$$

Here, a is the Earth's radius, ψ is the angular distance between the load point (θ', λ') and the observation point (θ, λ), and $L(\theta', \lambda', t')$ is the surface load at time t', which is composed of ice (ΔI) and ocean (ΔS) load contributions:

$$L(\theta', \lambda', t') = \rho_W \Delta S(\theta', \lambda', t') + \rho_I \Delta I(\theta', \lambda', t') \quad (1.7)$$

The Green's functions GF_R and GF_Φ, which describe the Earth's response to surface mass loading in terms of vertical displacement and gravitational potential, respectively, are written for a linear Maxwell earth rheology as:

$$GF_R(\psi, t) = \frac{a}{M_E}\sum_{n=0}^{\infty}(h_n^V(t) + h_n^E\delta(t))\, P_n(\cos\psi) \quad (1.8)$$

$$GF_\Phi(\psi, t) = \frac{ag}{M_E}\sum_{n=0}^{\infty}(k_n^V(t) + k_n^E\delta(t) + \delta(t))\, P_n(\cos\psi) \quad (1.9)$$

where M_E is the mass of the Earth, g is surface gravitational acceleration, $\delta(t)$ is the Dirac delta function, and P_n is the Legendre polynomial of degree n. The Love numbers h_n and k_n characterize the vertical displacement and gravitational potential perturbation response of the Earth, with superscripts V and E denoting viscous and elastic components, respectively.

Substituting equations (1.3) through (1.6) into equation (1.2), the generalized sea-level equation becomes:

$$\Delta SL(\theta, \lambda, t) = \int_{t_f}^{t}\iint_\Omega L(\theta', \lambda', t')\left(\frac{GF_\Phi(\psi, t - t')}{g} - GF_R(\psi, t - t')\right) a^2\, d\Omega\, dt' - \frac{1}{A_o}\frac{\rho_I}{\rho_W}\iint_\Omega \Delta I_j\, d\Omega - \frac{1}{A_o}\left\langle\int_{t_f}^{t}\iint_\Omega L(\theta', \lambda', t')\left(\frac{GF_\Phi(\psi, t - t')}{g} - GF_R(\psi, t - t')\right) a^2\, d\Omega\, dt'\right\rangle_O \quad (1.10)$$

Using convolution notation (with *), the classical form of the sea-level equation can be compactly represented as:

$$\Delta SL(\theta,\lambda,t) = L * \frac{GF_{\Phi}}{g} - L * GF_R - \frac{1}{A_o}\frac{\rho_I V_I}{\rho_W} - \frac{1}{A_o}\langle L * \frac{GF_{\Phi}}{g} - L * GF_R \rangle_O \quad (1.11)$$

This expression constitutes the traditional sea-level equation introduced by Farrell and Clark (1976). Because ΔSL appears on both sides of the equation (through the ocean loading component in L), it is an implicit formulation and typically requires iterative numerical methods for solution.

1.3. Paleo and contemporary observables

1.3.1. Paleo RSL reconstructions

Paleo RSL datasets are based on a wide variety of indicators to infer past RSL. These indicators are generally classified as either biological or morphological. Biological indicators include fossils of organisms, such as corals, mangroves, foraminifera, diatoms, and pollen, that lived within a known vertical range relative to mean sea level. Morphological indicators consist of coastal landforms shaped by marine processes, including tidal notches, raised beaches, marine deltas, and shore platforms. When such indicators are preserved in situ, their elevation is measured relative to a local datum and interpreted using the concept of indicative meaning, a quantified relationship between the indicator's elevation relative to the tidal range at the time it lived or was formed. This approach, illustrated in Figure 1.3, allows raw observations to be translated into estimates of past mean sea level, which is necessary for direct comparison to GIA model output (e.g., Khan et al., 2015; Shennan, 2015).

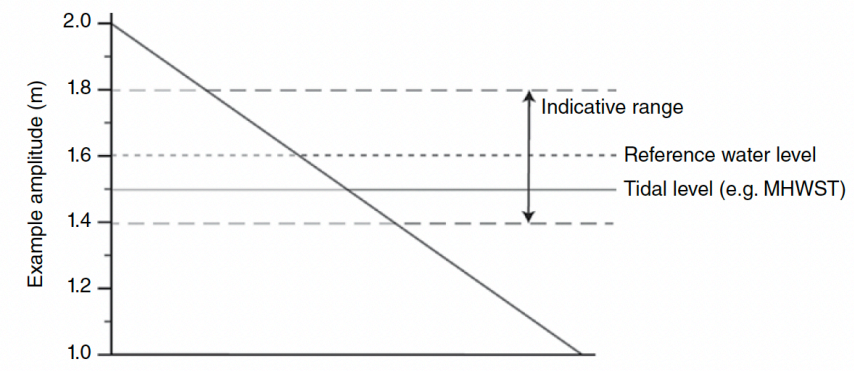


Figure 1.3. The diagram shows how past mean sea levels are inferred using the concept of indicative meaning. The indicative range refers to the vertical height within which a sea-level indicator originally formed, while the indicative meaning is the central height of that range relative to a known tidal datum (e.g., mean high water spring tide, MHWST). By comparing the position of a fossil indicator to its modern counterpart, the change in sea level can be estimated (Edwards, 2013).

Paleo RSL constraints fall into two main categories: sea-level index points (SLIPs) and limiting data points. SLIPs give relatively precise estimates of past sea level, while limiting data points define only the minimum or maximum possible sea level at a given time. For example, terrestrial limiting data points indicate sea level was below the elevation of the indicator, whereas marine limiting data points constrain sea level to have been above the observed elevation (see Figure 1.4). In this research, two regional RSL data compilations are utilized to constrain the regional GIA signal. These compilations

include standardized records of SLIPs and limiting data points derived from the Atlantic coast of the United States (Engelhart & Horton, 2012) and the eastern Canadian coastline (Vacchi et al., 2018). The majority of SLIPs in both regions originate from salt-marsh environments, where biological indicators such as plant macrofossils and microfossil assemblages (e.g., foraminifera and diatoms) are used to infer depositional elevations relative to the tidal frame. Depending on the depositional environment, samples are assigned specific indicative ranges: high marsh environments typically span from Mean High Water (MHW) to Highest Astronomical Tide (HAT); low marsh environments span from Mean Tide Level (MTL) to MHW; and undifferentiated salt-marsh deposits encompass the range from MTL to HAT. In addition to salt-marsh records, SLIPs in the eastern Canadian dataset also include indicators from isolation basins and beach deposits. In addition, terrestrial limiting points are derived from in-situ tree stumps, freshwater peat, isolation basin gyttja, or archaeological coastal settlements, forming above MTL. Marine limiting points are based on in-situ marine shells or marine microfossil assemblages, forming below MTL. To ensure the reliability of these datasets, uncertainty in both the elevation and age of each data point is taken into account. Vertical uncertainty is generally based on the indicative range, while chronological uncertainty comes from radiocarbon dating calibrated consistently across all records. These uncertainties are integrated into the analysis to improve the accuracy of model-data comparisons (e.g., Engelhart and Horton, 2012; Shennan, 2015). To be used in constraining a GIA model, an RSL indicator must have a precisely known location and elevation (with associated uncertainties), an age calibrated using the latest radiocarbon calibration curves (along with its uncertainty), and a clearly defined indicative meaning. The resulting paleo RSL records provide a powerful constraint on GIA models and processes.

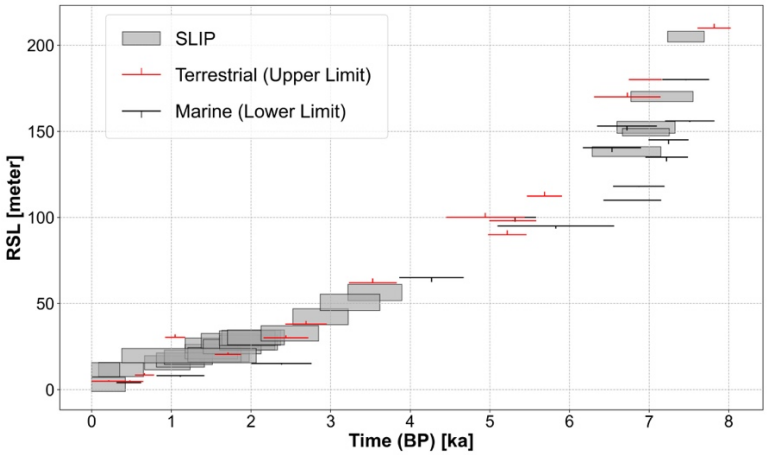


Figure 1.4. Reconstructed paleo RSL records for site #5 in the Hudson Bay (see Chapter 2), illustrating the three primary types of RSL indicators used in this thesis. SLIPs (shown as grey boxes) provide relatively precise estimates of past sea level and are represented with their associated elevation and temporal uncertainties. Terrestrial limiting data (red markers) constrain sea level to have been below the indicator elevation, while marine limiting data (black markers) constrain sea level to have been above. The combination of SLIPs and limiting data improves constraints on past RSL changes and contributes to refining the GIA models. The SLIP boxes indicate ±2σ uncertainty in RSL elevation and age. For limiting data points, the horizontal and vertical bars show ±2σ RSL age uncertainty and one side of the 2σ RSL elevation uncertainty, respectively.

1.3.2. Contemporary geodetic observations

Contemporary geodetic observations, particularly GNSS and GRACE measurements, play a significant role in achieving the overarching aims defined in Section 1.1. GNSS observations provide estimates of present-day VLM, while GRACE measurements complement them by capturing integrated

mass changes over broad spatial scales, providing key insights into both GIA and hydrological processes. By integrating these datasets with paleo observations, this work enhances our understanding of long-term gravity changes and VLM in eastern North America and establishes a framework for assessing discrepancies between millennial-scale and decadal-scale VLM rates. Furthermore, accurately accounting for the GIA signal across these datasets is critical: constraining the GIA signal and its uncertainty not only improves the interpretation of GNSS-derived VLM rates but also enables more accurate extraction of contemporary hydrological mass change signals from GRACE. This has important implications for characterizing total water storage (TWS) variations and refining hydrological models. In addition, geodetic observations can be utilized to constrain the GIA signal itself. To be suitable for GIA model refinement, these observations must first be corrected for other geophysical signals, such as tectonic activity, surface loading from contemporary hydrology or ice mass changes, and instrument-related biases (Argus et al., 2014; Hill et al., 2010).

1.3.2.1. VLM from GNSS measurements

GNSS-based measurements have a long-standing history in constraining GIA models (King et al., 2010). Due to their portability, affordability, and ease of deployment, GNSS instruments have emerged as the most widely used geodetic tools in GIA research. They provide the capacity to monitor present-day land motion across a broad range of geographic settings, with high temporal resolution and growing global coverage. In regions with dense GNSS networks and where non-GIA signals, such as those associated with the global water cycle, atmospheric pressure variations, tectonic activity, or sediment compaction, are well characterized and corrected, GNSS data have proven particularly effective for calibrating GIA models (King et al., 2010). This success is evident in areas such as North America (Sella et al., 2007), Fennoscandia (Lidberg et al., 2007), Antarctica (Thomas et al., 2011), and Greenland (Khan et al., 2016), where robust constraints on past and present surface deformation have improved model-data agreement (e.g., Lidberg et al., 2010; Milne et al., 2001, 2004). However, challenges remain when interpreting GNSS data in regions where other sources of surface deformation overlap with GIA. In particular, ongoing contemporary ice mass loss can contribute to vertical land motion that is difficult to disentangle from the signal associated with the melting of former ice sheets (e.g., Nield et al., 2014). This overlap complicates the separation of past and present contributions to solid Earth deformation and increases the need for careful correction of geodetic signals before they are used in GIA model calibration.

Although horizontal GNSS velocities are generally more precise than vertical rates, often by an order of magnitude (King et al., 2010), the GNSS-derived VLM signal remains the primary geodetic constraint in GIA modeling. This is largely because traditional 1D GIA models neglect lateral Earth structure, which has a strong influence on horizontal motions (Kaufmann et al., 2005). With the emergence of 3D GIA models that incorporate lateral variations, however, horizontal GNSS velocities are now increasingly recognized as a valuable complementary constraint (Vardić et al., 2022). It should be noted that the derivation of accurate VLM rates is complicated by a range of factors that influence the estimation of GNSS velocities. These include differences in analysis strategies, such as the software used to process raw GNSS data, the duration and completeness of the time series, noise characteristics, treatment of position discontinuities, and alignment to a global terrestrial reference frame (Gazeaux et al., 2013; Griffiths & Ray, 2016; Williams, 2003). Among these, identifying and correcting position discontinuities, often caused by antenna replacement artifacts, changes in the antenna environment, errors in station metadata, or seismic events, can have greater impact on velocity estimates and their associated uncertainties. As a result, it is not uncommon for different analysts to report varying velocity solutions for the same GNSS station, even when based on identical raw data (Santamaría-Gómez et al.,

2024). Given these challenges, it is essential to estimate GNSS-derived VLM rates using robust methodologies that explicitly account for discontinuities and noise characteristics.

In the research presented in Chapter 3, present-day VLM is determined using continuous GNSS stations, with velocity estimates based on the Median Interannual Difference Adjusted for Skewness (MIDAS) technique developed by the Nevada Geodetic Laboratory (Blewitt et al., 2016, 2018). MIDAS is a refined form of the Theil-Sen median trend estimator, tailored for high-precision geodetic time series such as GPS/GNSS observations. Unlike conventional least squares regression, which is sensitive to outliers, step discontinuities, seasonal biases, and heteroscedasticity, MIDAS is designed to be resilient to these common issues. MIDAS computes station velocities by selecting coordinate pairs that are exactly one year apart to mitigate seasonal influences and reduce the number of pairings affected by discontinuities. It then filters the slope distribution by removing outliers, those differing by more than two robustly estimated standard deviations from the median. Therefore, the method results in a final robust estimate of both the velocity and its uncertainty. Blind tests on synthetic data and analyses of real-world observations from tectonically stable regions in North America demonstrate that MIDAS yields root-mean-square errors of approximately ±0.3 mm/yr horizontally and ±1.0 mm/yr vertically, outperforming many other automated velocity estimators in terms of bias resistance and statistical realism (Blewitt et al., 2016).

In the context of the research presented in this thesis, MIDAS-derived GNSS velocities are compared against VLM predictions from the regionally constrained GIA models developed in Chapter 2, as well as late-Holocene RSL-based VLM rates (Chapter 3). By examining the residuals between modeled and observed values, we assess the consistency across timescales and investigate the potential influence of other ongoing natural or anthropogenic processes. Where significant discrepancies are observed, they may indicate the presence of additional mass redistribution processes, such as significant changes in the hydrological loading signal, beyond what is explained by GIA alone. This residual signal is further explored using GRACE estimates.

1.3.2.2. Mass change signal from GRACE

Launched in March 2002, the GRACE mission marked a significant advancement in satellite gravimetry by enabling accurate detection of temporal gravity field variations, thereby facilitating studies of global mass redistribution (Tapley et al., 2019). GRACE operates using a twin-satellite configuration, with inter-satellite distances precisely measured via a K-band ranging system, supported by onboard accelerometers, GPS receivers, and star cameras. These measurements are translated into monthly gravity field solutions through data processing systems led by CSR, JPL, and GFZ (Bettadpur, 2018; Dahle et al., 2019). GRACE has provided crucial insights into a wide range of geophysical processes, TWS changes, glacier and ice sheet mass loss, drought and flood monitoring, and sea-level rise (Tapley et al., 2019). In addition, GRACE observations have also contributed to studies of solid earth deformation associated with large earthquakes (J. Li et al., 2016) and GIA (Riva et al., 2009; Tamisiea et al., 2007). The successor mission, GRACE Follow-On (GRACE-FO), launched in May 2018, extends the dataset with improved instrumentation, including a laser ranging interferometer that enhances inter-satellite distance measurements. Although the ~11-month gap between GRACE and GRACE-FO (July 2017–May 2018) limits short-term variability analyses, the continuity of long-term gravity measurements remains largely unaffected (Landerer et al., 2020a; Velicogna et al., 2020).

There are some challenges in quantification of mass variations using GRACE measurements. The coarse spatial resolution (an inter-satellite distance of ~220 km and an orbital altitude of ~500 km,

resulting in an effective spatial resolution no finer than ~300–500 km), uncertainties in satellite accelerometer data, and noise in high-degree and -order spherical harmonic coefficients necessitate spatial filtering and introduce leakage errors, leading to amplitude attenuation and regional signal contamination (Tapley et al., 2019). These limitations are particularly critical for basin-scale hydrological analyses and regional studies. Furthermore, very low-degree coefficients, such as ΔC_{20} (degree-2 zonal coefficient), are poorly estimated, especially during late GRACE and GRACE-FO phases when only one accelerometer was functional (Landerer et al., 2020). To improve the reliability of mass change estimates at the longest spatial wavelengths (mainly associated with ΔC_{20} and ΔC_{30}), the GRACE/GRACE-FO Science Data System recommends substituting these coefficients with independent values derived from satellite laser ranging observations (Loomis, Rachlin, et al., 2019).

For climate-related mass change quantification, solid earth effects, particularly GIA, must be removed from GRACE gravity solutions using model predictions. This step is crucial, as GRACE inherently measures total mass change without distinguishing between surface hydrology and solid earth deformation. Consequently, the accuracy of GIA models directly influences the reliability of derived TWS estimates. Figure 1.5 shows that the spatial pattern and magnitude of the inferred hydrological signal are strongly influenced by the choice of GIA model. This dependency underscores the necessity of regionally optimized GIA models with well-constrained uncertainty bounds.

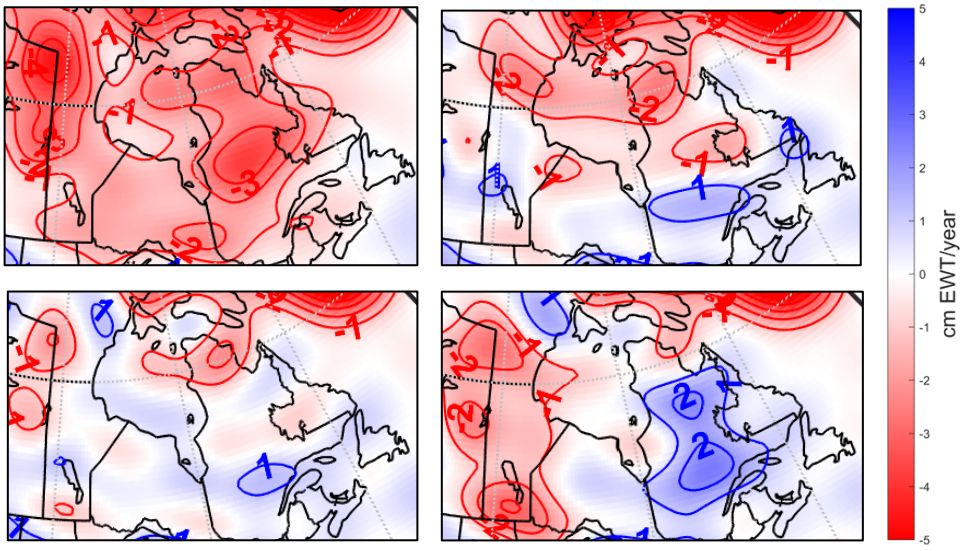


Figure 1.5. Sensitivity of GRACE-derived TWS estimates to the applied GIA model. Spatial patterns of contemporary mass changes are shown after correcting for the GIA signal based on four different models. Variations in both the magnitude and spatial distribution of the inferred hydrological mass change signals highlight the critical role of GIA model in isolating contemporary mass change associated with TWS (figure provided by John Crowley, NRCan).

GRACE observations are typically reported as anomalies in equivalent water thickness (EWT), which represent the integrated response of Earth's gravity field to mass redistribution on or near the surface (Tapley et al., 2004; Wahr et al., 1998). EWT provides a physically meaningful metric by converting gravity field changes into equivalent variations in the thickness of a hypothetical water layer, thereby providing an effective means of assessing total mass changes. After applying corrections for non-hydrological signals (particularly from GIA in our study region), this conversion enables effective quantification of TWS, which encompasses the combined mass contributions of various hydrological reservoirs, including groundwater, soil moisture, surface water bodies (lakes and rivers), snow, ice, and biomass. EWT ($\Delta\sigma$) can be mathematically represented as (Swenson & Wahr, 2002; Wahr et al., 2004):

$$\Delta\sigma(\theta,\lambda) = \frac{a\rho_e}{3\rho_w}\sum_{n=0}^{N_{max}}\left(\frac{2n+1}{1+k_n}\right)\sum_{m=0}^{n}\left\{\left[\Delta C_n^m\cos(m\lambda) + \Delta S_n^m\sin(m\lambda)\right]\overline{P}_n^m(\cos\theta)\right\} \quad (1.12)$$

where θ denotes the colatitude and λ the longitude. The variable a is the Earth's radius, ρ_e is the mean density of the Earth, and ρ_w is the density of water. The term k_n represents the load Love number at degree n and $\overline{P}_n^m$ is the fully normalized associated Legendre function of degree n and order m. The coefficients ΔC_n^m and ΔS_n^m refer to the temporal variations in the monthly Stokes coefficients observed by GRACE (and GRACE-FO), which capture changes in the Earth's gravity field. This formulation allows the transformation of gravity anomalies into EWT changes, enabling the quantification of TWS variations across the globe. Based on the theory of elastic loading, crustal deformation induced by surface water mass changes can be calculated in the spherical harmonics domain. The radial displacement of the Earth's surface, $\Delta h(\theta,\lambda)$, at a given location is expressed as (van Dam et al., 2007; J. Kusche & Schrama, 2005):

$$\Delta h(\theta,\lambda) = a\sum_{n=1}^{N_{max}}\sum_{m=0}^{n}\overline{P}_n^m(\cos\theta)\left[\Delta C_n^m\cos(m\lambda) + \Delta S_n^m\sin(m\lambda)\right]\frac{h_n}{1+k_n} \quad (1.13)$$

Here, the load Love numbers (h_n and k_n) that describe the Earth's elastic response to surface mass loading at spherical harmonic degree n are taken from Wang et al. (2012), based on the Preliminary Reference Earth Model (PREM; Dziewonski & Anderson, 1981), a widely accepted model for earth structure. GRACE/GRACE-FO gravity field solutions are truncated at a maximum degree and order of 60 (N_{max}), which is mainly determined by the satellite orbit configuration, including the satellite altitude and inter-satellite distance. In GRACE/GRACE-FO gravity solutions, spherical harmonic coefficients of degree 2 and higher are typically provided, as the degree-0 and degree-1 coefficients are excluded by definition. The degree-0 term (ΔC_{00}) reflects variations in the total mass of the earth system, which is considered to be constant. The degree-1 terms (ΔC_{10}, ΔC_{11}, and ΔS_{11}) correspond to the three components of geocenter motion, or the displacement between the Earth's center of mass and its center of figure. Since GRACE/GRACE-FO data are defined in the center of mass reference frame, these degree-1 terms are not directly estimated and are instead set to zero in the standard solutions (Crétaux et al., 2002; Swenson et al., 2008).

The solutions based on spherical harmonics suffer from correlated errors, showing north-south "stripe" artifacts, that degrade spatial resolution and limit the utility of GRACE observations for basin-scale or regional hydrological analyses (Seo et al., 2008; Swenson & Wahr, 2006). These stripes originate from correlations between spherical harmonic coefficients of the same order and degree parity. Swenson and Wahr (2006) showed that estimating and removing these correlations significantly reduces striping, although the method could not distinguish such errors from real, stripe-like geophysical signals. To further reduce residual noise, they applied isotropic gaussian smoothing, which also diminished the strength of the true mass change signal. Subsequent methods have been developed to address the trade-off between signal preservation and noise reduction (e.g., Davis et al., 2008; Han et al., 2005; J. Kusche et al., 2009; Jürgen Kusche, 2007; Sasgen et al., 2006). The mass concentration (mascon) technique provides an alternative approach by dividing Earth's surface into predefined spatial blocks and applying mathematical regularization with a priori constraints to stabilize the solution and minimize GRACE's correlated errors (Loomis et al., 2019; Watkins et al., 2015). While mascon solutions effectively reduce stripe artifacts, they may still distort real physical signals and depend on a fixed spatial geometry and prior assumptions, potentially introducing biases (Loomis et al., 2019).

In this thesis (Chapter 3), we utilize the methodology developed by Crowley & Huang (2020) to estimate TWS changes from GRACE. This method provides a significant improvement over earlier destriping approaches by incorporating both statistically significant temporal trends and correlated

spherical harmonic coefficient errors into a joint parametric least-squares framework. The principle of the method relies on: (1) stripe artifacts in GRACE data originate from correlations between spherical harmonic coefficients of the same order and degree parity, and (2) the dominant physical mass anomalies are embedded in the temporal trends of the GRACE data. By taking advantage of the long observational record from GRACE and GRACE-FO (2002–present), the method applies a rigorous F-test at the 99.9% confidence level to identify statistically significant linear, quadratic, annual, and semi-annual components within each coefficient's time series. The joint inversion procedure then fits these temporal components alongside the correlated trends to isolate and remove noise while retaining physically meaningful mass signals. Since the GRACE solutions are corrected for GIA using regionally constrained models with uncertainty bounds, the residual signals, after destriping, more accurately reflect hydrological mass changes.

1.4. Recent and future sea-level changes

Sea-level change is driven by a complex interplay of processes operating over a broad range of temporal and spatial scales. On timescales of tens to hundreds of thousands of years, variations in the Earth's orbit around the sun, known as Milanković cycles, have played a major role in modulating climate and sea level (Ruddiman, 2014). On even longer timescales, plate tectonics and mantle dynamics exert additional control on sea-level evolution (Yokoyama & Purcell, 2021). These climate fluctuations influence sea level directly through changes in the volume of water stored in ice sheets and indirectly via delayed responses such as land deformation from ice and ocean mass redistribution. During the current interglacial period, the Earth's climate peaked in warmth approximately 6,500 years ago, driven mainly by orbital forcing rather than anthropogenic influences (Calvin et al., 2023). Geological records, particularly from marine sediments and coastal deposits, show that GMSL rose rapidly following LGM but slowed significantly by around 7,000–8,000 years ago (Leo et al., 2019).

Since the mid-1800s, increased greenhouse gas emissions from fossil fuel combustion have driven a ~50% rise in atmospheric carbon dioxide, amplifying the Earth's natural greenhouse effect and contributing to a ~1 °C increase in global temperature over the past century (Church et al., 2013). Long-term still water level observations, extending back to the mid-1800s, from tide gauges, which measure the motion of the sea surface relative to the land, suggest global average sea-level rise rates of approximately 1.2 to 1.7 mm/year throughout much of the 20th century (Cazenave & Llovel, 2010; Griggs, 2021). Since 1993, satellite altimetry missions, including TOPEX/Poseidon and the Jason series, have enabled precise global monitoring of absolute sea-level changes. These observations reveal a current GMSL rise rate of ~3.6 ± 0.3 mm/year over the satellite era. Moreover, as Figure 1.6 shows, there has been an acceleration in this rate, estimated at about 1.2 ± 0.5 mm/year per decade, with the rate doubling from 2.1 mm/year during 1993–2003 to 4.1 mm/year during 2013–2023 (Guérou et al., 2023; Nerem et al., 2018).

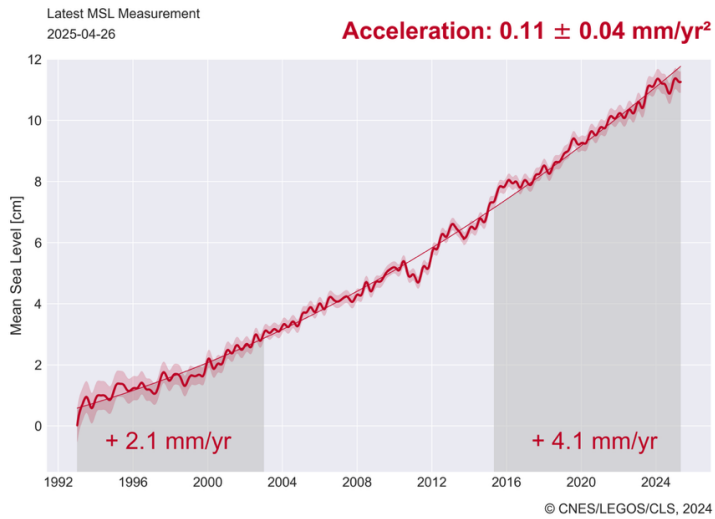


Figure 1.6. GMSL rise from satellite altimetry from January 1993 to the present. The data have been corrected for postglacial rebound, filtered to remove annual and semi-annual signals, and smoothed using a 6-month filter (figure from Aviso+: www.aviso.altimetry.fr).

Tide gauge and satellite altimetry observations have substantially improved our understanding of past and present sea-level variability. However, projecting future sea-level changes remains a key challenge, particularly for regional and local coastal impact assessments. To address this, the Intergovernmental Panel on Climate Change (IPCC) provides comprehensive projections, most recently in its Sixth Assessment Report (AR6), which incorporates the Shared Socioeconomic Pathways (SSPs), a range of future scenarios representing combinations of societal development trajectories and greenhouse gas concentration levels by 2150 (Fox-Kemper et al., 2023). AR6 projections are driven by CMIP6 climate model outputs and a physically based emulator that ensures consistency with assessed climate sensitivity (Forster et al., 2021). The SSPs include SSP1-1.9 (very low emissions), SSP1-2.6 (low), SSP2-4.5 (intermediate), SSP3-7.0 (high), and SSP5-8.5 (very high), with their associated global surface air temperature changes and GMSL rise relative to the baseline illustrated in Figure 1.7 (Lee et al., 2023).

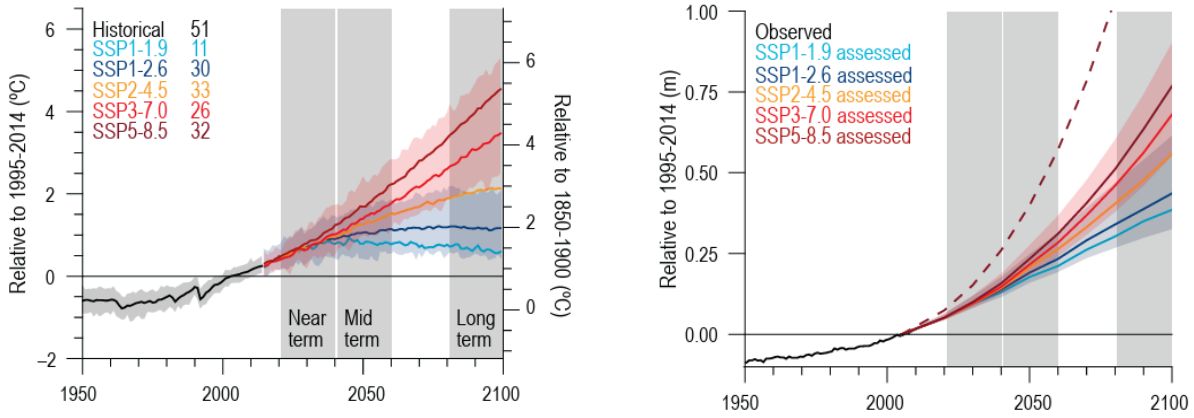


Figure 1.7. Projected global temperature change (left) and GMSL change (right) under five SSPs based on IPCC AR6. Relative to the 1995–2014 baseline, using the 5%–95% confidence intervals as ranges, global mean temperatures are projected to increase between 2.40 and 5.57 °C by the end of the 21st century (2081–2100) under SSP5-8.5, whereas in SSP1-1.9, global temperatures stabilize or even somewhat decline in the second half of the century, spanning a range from 0.13 to 1.25 °C. GMSL change relative to the 1995–2014 baseline is projected to rise by 0.28–0.55 m under SSP1-1.9, and by 0.63–1.02 m under SSP5-8.5 by 2100 (Lee et al., 2023; Tebaldi et al., 2021).

Sea-level projections in the IPCC framework account for multiple contributing processes that operate across global, regional, and local scales. The sterodynamic component combines both steric sea-level change, resulting from thermal expansion of ocean water (thermosteric), salinity variations (halosteric), and ocean circulation (dynamic changes) associated with this density redistribution. Thermosteric expansion, driven by ocean warming, is a major contributor to GMSL rise, whereas halosteric effects are generally negligible at the global scale. Melting of the Greenland and Antarctic ice sheets represents the largest potential contributors to future sea-level rise due to their vast freshwater reservoirs. These ice sheets lose mass through surface melting, iceberg calving, and basal processes. Glaciers also contribute through a long-term imbalance between accumulation and melt, with meltwater sometimes stored temporarily in lakes or closed basins. Land-water storage, which includes water held in rivers, lakes, soil moisture, and snow but excludes glaciers and ice sheets, contributes to sea-level rise through both climate variability and human activities such as groundwater extraction and dam construction. VLM modifies RSL trends and includes elastic responses to contemporary mass redistribution, viscoelastic deformation associated with GIA, tectonic processes, sediment compaction and anthropogenic subsidence (Fox-Kemper et al., 2023). Through the research presented in this thesis, we quantify the contribution of VLM, and specifically the GIA signal, to projections of regional mean sea-level change by integrating output from regionally constrained GIA models into IPCC projections at various tide gauges in our study region (Chapter 4).

Nuisance flooding, also known as high-tide or sunny-day flooding, has become an increasing concern along the U.S. east coast due to ongoing sea-level rise (e.g., Karegar et al., 2017; Moftakhari et al., 2015; Ray & Foster, 2016) and is expected to bring about similar risks in Atlantic Canada as RSL continues to rise. Unlike extreme flood events driven by storms or hurricanes, which have received much attention in past sea-level impact studies (e.g., Hallegatte et al., 2013; Reguero et al., 2015), nuisance flooding is characterized by recurrent, minor inundation events that can occur without storm conditions. These events are often triggered when tidal levels exceed local elevation thresholds, temporarily submerging low-lying infrastructure such as roads, parking lots, and sewer systems (Moftakhari et al., 2015). Though not destructive in the conventional sense, nuisance flooding disrupts daily life, burdens stormwater infrastructure, creates public health hazards, and diminishes economic productivity (e.g., Cherqui et al., 2015; Suarez et al., 2005). The predictability of nuisance flooding makes it an especially useful metric for assessing near-term flood exposure. While extreme storm flooding remains difficult to forecast, nuisance flooding is tightly coupled to astronomical tides and can be predicted in time and space with reasonable accuracy (Moftakhari et al., 2015; Sweet et al., 2014; Wdowinski et al., 2016).

Locations where land elevation is close to local high tide level are particularly vulnerable to recurrent inundation. As regional mean sea level rises, the gap between high tidal datums and established flood thresholds narrows, increasing the likelihood that even moderate tidal fluctuations will exceed minor flood thresholds. Consequently, even modest increases in RSL (which accounts for both absolute sea-level rise and VLM) can lead to a significant rise in the frequency of nuisance flooding events, and over time, may contribute to more severe inundation (Karegar et al., 2017; Kemp & Horton, 2013; Sweet et al., 2014). Long-term observational records have shown that nuisance flooding has increased substantially over the past several decades. A study based on over 70 years of tide gauge data in the United States found a 27% increase in nuisance flooding events in 2019, with the frequency increasing at an exponential rate since 1950, particularly in estuarine regions that have experienced significant changes in tidal characteristics due to anthropogenic alterations of system geometry and river inflow (S. Li et al., 2021). Despite experiencing substantial sea-level change and VLM primarily driven by GIA, eastern Canada remains largely underrepresented in nuisance flooding research. Chapter 4 in this

thesis seeks to address this gap by evaluating the influence of VLM on future nuisance flooding projections at selected tide gauge stations across eastern Canada and the northeastern United States.

1.5. Contributions and outline of thesis

The overarching goal of this thesis is to improve the quantification and understanding of the processes contributing to contemporary and future VLM and gravity change in southeastern Canada and the northeastern United States. This understanding is essential for producing more accurate projections of mean sea-level change and nuisance flooding over the coming decades. As described in Section 1.1, to achieve this aim, three research components are pursued which comprise the three original contributions of this thesis.

Chapter 2 describes the first component of this research, which aims to better constrain the GIA signal and its associated uncertainties across southeastern Canada and the northeastern United States. This effort contributes to a broader scientific initiative aimed at improving GIA models in North America. The regional focus of this chapter is motivated by two factors: the availability of high-quality, recently compiled RSL datasets, and the critical role of GIA as a dominant driver of long-term VLM and contemporary sea-level change in this region. To effectively distinguish long-term GIA-induced land motion from more recent signals driven by hydrological mass changes, this chapter emphasizes the development of improved GIA models with quantified uncertainty for different subregions within the study region. The uncertainty analysis employs two approaches to estimate parametric uncertainty: a heuristic method and a Bayesian framework. These methods explore a large parameter space, comprising 440 different 1D earth viscosity models and 34 ice history models, totaling 14,960 model realizations. This broad exploration enhances the robustness of the derived uncertainty bounds and advances prior efforts by accounting for a wider spectrum of earth structure and ice history configurations.

Chapter 2 considers a third approach to uncertainty quantification that encompasses both parametric and structural sources. By identifying a subset of model parameters that are compatible with the observational constraints, history matching (Tarasov and Goldstein, 2023) provides an alternative way to constrain the GIA model ensemble. Our application of history matching is among the first in the context of paleo sea-level and GIA modelling, and we present it as a potential framework upon which future studies can build. While the core analysis is based on 1D earth models, the chapter also considers the contribution of lateral viscosity variations by including a subset of results from 3D earth models. This component provides a preliminary estimate of model structural error due to the absence of lateral heterogeneity in 1D models and supports the need to account for laterally variable earth structure when constraining the GIA signal across the study region. The output of our GIA modelling, including optimal models and uncertainty bounds, is made available for end users. These include rates of VLM at GNSS stations based on the Nevada Geodetic Laboratory dataset and rates of RSL change at tide gauge locations in the Permanent Service for Mean Sea Level (PSMSL) dataset. These results provide a valuable resource for interpreting contemporary geodetic observations and for improving regional sea-level projections in southeastern Canada and the northeastern United States.

Chapter 3 uses the results of Chapter 2 to deliver the second component of this thesis, which is to isolate and interpret the processes contributing to contemporary VLM across eastern Canada and the northeastern United States. While GIA remains a key driver, the interpretation of contemporary VLM is complicated by the presence of additional signals, particularly those associated with hydrological mass redistribution. This chapter uses temporal variability to evaluate VLM over two timescales, millennial and decadal, across six subregions in the study region. Millennial-scale VLM rates are

estimated from late Holocene RSL reconstructions using the optimal regional GIA models developed in Chapter 2, while decadal-scale rates are derived from GNSS observations. The consistency between these two timescales is assessed for each subregion. Where significant discrepancies exist, the residuals are interpreted as contributions from processes not accounted for by GIA, with a primary focus on regional hydrological mass changes.

To further examine these residuals, GRACE-based mass change estimates are employed. These measurements provide an independent constraint on contemporary surface mass redistribution and are used to validate the spatial and temporal patterns inferred from the VLM comparisons. This chapter presents a comprehensive uncertainty analysis of the VLM signal and provides the first formal application of GIA model uncertainty to quantify the uncertainty in GRACE-derived contemporary mass changes. By identifying and quantifying differences between long-term and contemporary VLM rates, Chapter 3 provides new insight into regional land motion and its implications for sea-level change. To support future research and applications, estimates of VLM with associated uncertainty bounds are provided for each subregion, including rates from GNSS observations and late-Holocene RSL reconstructions. In addition, GRACE-derived estimates of contemporary mass changes, along with their associated uncertainties, are provided for the study region.

Chapter 4 represents the third original component of this thesis, the aim of which is to evaluate the influence of VLM, particularly the component driven by GIA, on regional projections of mean sea-level change and nuisance flooding frequency across eastern Canada and the northeastern United States. This chapter investigates how projected changes in mean sea level and high-tide flooding evolve at 25 tide gauge stations by considering three future time horizons (2050, 2100, and 2150 CE). To evaluate the influence of VLM on these projections, three projection cases are developed: (1) IPCC estimates that include all contributing processes to sea-level change; (2) IPCC estimates from which the VLM signal is excluded; and (3) IPCC estimates that exclude the original VLM component but incorporate a regionally optimized GIA-induced VLM signal along with associated uncertainty bounds, developed in Chapter 2. These projections are produced for three SSP scenarios–SSP1-1.9 (very low emissions), SSP3-7.0 (high emissions), and SSP5-8.5 (very high emissions)–to capture a wide range of possible future climate and socio-economic trajectories.

Nuisance flooding frequency at each station is determined by applying a tidal harmonic analysis to hourly still water level records. This analysis accounts for long-term trends and local nodal corrections for three dominant tidal constituents: M2, N2, and K1. The projected regional mean sea-level changes and nuisance flooding days, each with associated uncertainty bounds and evaluated at 25 tide gauges under three projection cases and SSP scenarios for the years 2050, 2100, and 2150 CE, are provided for future research. As noted above, this is the first study to produce projections of nuisance flooding in eastern Canada. The results will provide valuable information for policymakers and coastal management agencies aiming to design effective mitigation strategies in response to growing flood risks along the Atlantic coasts of eastern Canada and the northeastern United States. In addition, based on the methodology presented in this research, the integration of a regionally constrained GIA signal into the IPCC projection (excluding VLM) can support the extension and refinement of regional mean sea-level change projections in areas with limited observational coverage of VLM (e.g., from GNSS and tide gauges) within GIA-active zones.

2

Constraining Models of Glacial Isostatic Adjustment in Eastern North America

Soran Parang [(1)], Glenn A. Milne [(1)], Lev Tarasov [(2)], Ryan Love [(1)], Maryam Yousefi [(3)], Matteo Vacchi [(4)]

[(1)] Department of Earth and Environmental Sciences, University of Ottawa, Ottawa, ON, Canada
[(2)] Department of Physics and Oceanography, Memorial University, St John's, NL, Canada
[(3)] Canadian Geodetic Survey, Natural Resources Canada, Ottawa, ON, Canada
[(4)] Department of Earth Sciences, Università di Pisa, Pisa, Italy

Citation:

Parang, S., Milne, G. A., Tarasov, L., Love, R., Yousefi, M., & Vacchi, M. (2024). Constraining models of glacial isostatic adjustment in eastern North America. *Quaternary Science Reviews*, *334*, 108708. https://doi.org/10.1016/j.quascirev.2024.108708

Statement of Contribution

This manuscript is my original work, conducted under the supervision of Prof. Glenn A. Milne, who planned and guided the research and aided in manuscript preparation through several rounds of feedback. Lev Tarasov contributed by developing 32 of the ice history reconstructions used in the analysis and collaborated on implementing the history matching approach for model uncertainty quantification. Ryan Love and Maryam Yousefi provided codes for the heuristic uncertainty analysis, and Ryan also offered guidance on executing the Seakon solver for 3D GIA modeling. We used the Vacchi et al. (2018) RSL dataset in this study, and Matteo Vacchi contributed to the radiocarbon recalibration of RSL data points using updated calibration curves. I carried out all model simulations and created all figures presented in the manuscript.

Abstract

We constrain the GIA signal and its uncertainty for southeastern Canada and northeastern USA using 1,013 relative sea-level (RSL) data points distributed over 38 sites from two regional RSL data compilations containing 544 sea-level index points, 232 marine limiting data points, and 237 terrestrial limiting data points. This state-of-the-art dataset was compared to output from 14,960 model runs based on a 1D (spherically-symmetric) Earth model and 34 different North American ice sheet reconstructions. By considering different data subsets (regional partitioning), we found that significantly improved fits can be obtained by separating the data into two larger subregions: the first one close to the central section of the Laurentide ice sheet (including Hudson Bay, Ungava Peninsula, and Labrador), and the second one along the Atlantic coast of Canada and the USA (encompassing Newfoundland, St. Lawrence Corridor, New Brunswick and Nova Scotia, and Maine and Massachusetts). For the first subregion, relatively low lower mantle viscosity (1-2×10^{21} Pas; from the considered range of 1-90×10^{21} Pas) and relatively high upper mantle viscosity (greater than 0.5×10^{21} Pas from the considered range of 0.05-5×10^{21} Pas) for a given ice loading history can provide good quality fits. On the other hand, quality fits for the second subregion require intermediate values for these parameters (specifically, upper mantle viscosity of 0.5-1×10^{21} Pas and lower mantle viscosity of 20-30×10^{21} Pas). When considering model uncertainty bounds, ~91.6% of the observations (928 out of 1013 RSL data points) can be captured, while the remaining residuals (~8.4%) reflect some observational errors (outliers) and systematic error in the model. Given the 1D analysis suggests the existence of significant lateral Earth structure, we explored this aspect via the use of a 3D finite volume Earth model. Considering two realizations of lateral Earth structure based on two shear-wave tomographic models, the 3D results support the spatial partitioning of the whole study region into two larger subregions. However, the 3D model was unable to improve upon the data-model fits obtained with the 1D model, indicating limitations in the models of lateral structure and/or the adopted ice models, which are reconstructed based on 1D Earth models. Finally, our 1D Earth modeling results indicate that, within the first subregion, ice history models with relatively thick ice during the early phase of deglaciation (prior to ~13 ka) and thinner ice in the early Holocene are preferred by the RSL data.

Keywords: Sea-level changes, Glacial isostatic adjustment, Forward modelling, Atlantic coast of Canada, Laterally variable Earth structure, Optimal Earth model parameter sets, Deglaciation history

2.1. Introduction

During the Quaternary, a number of mid-to-high latitude regions experienced repeated glaciation and deglaciation of large ice sheets (e.g., Ehlers and Gibbard, 2007; Lowe et al., 2007; Shackleton and Opdyke, 1973). The response of the solid Earth to this large-scale water mass transfer between ice sheets and oceans is called glacial isostatic adjustment (GIA). GIA is a leading contributor to past and contemporary land motion, gravity and sea-level changes in formerly and presently glaciated regions like North America, Fennoscandia, Greenland and Antarctica. Geophysical models of this process have been compared to a variety of data types to constrain past and contemporary ice sheet evolution and the rheological properties of the Earth's interior (e.g., Lambeck et al., 1998; Milne and Shennan, 2013; Peltier, 2004; Peltier et al., 2022; Spada, 2017; Steffen and Wu, 2011; Wake et al., 2016; Whitehouse, 2018).

Different types of observables can be utilized to constrain the GIA signal over various time scales. Geodetic observations such as global navigation satellite systems (GNSS) measurements of land surface

motion, terrestrial and satellite gravimetry such as the gravity recovery and climate experiment (GRACE), and tide-gauge records of sea-level fluctuations can provide a contemporary snapshot of the GIA signal (e.g., Hill et al., 2010; King et al., 2010; Martín-Español et al., 2016). On longer time scales, paleo relative sea-level (RSL) reconstructions from a wide range of geological evidence have provided powerful constraints on GIA models (e.g., Glueder et al., 2022; Lambeck et al., 1998; Mitrovica et al., 2000; Peltier and Fairbanks, 2006; Simon et al., 2021). High quality regional databases are a primary control on GIA model testing and calibration (e.g., Engelhart and Horton, 2012; Love et al., 2016). The relatively recent HOLSEA initiative (Khan et al., 2019), which defines a standard protocol for producing regional RSL databases, has resulted in an improved availability of high-quality RSL reconstructions that support and facilitate GIA model improvement (including this analysis).

The computer models developed to calculate the various observables associated with GIA are built on the theory developed by Farrell and Clark (1976). This underlying theory, represented in the so-called "sea-level equation", is the basis for most modern GIA modelling studies seeking to accurately calculate sea-level variations in response to ice-ocean surface mass redistribution. We note that more recent studies have developed this theory to incorporate Earth rotation (e.g., Milne and Mitrovica, 1998) and lateral shoreline migration (e.g., Mitrovica and Milne, 2003; Peltier, 1998). In most GIA modelling studies, a spherically symmetric, self-gravitating Earth model with a Maxwell viscoelastic rheology is assumed (Peltier, 1974). Although the model outputs based on this simplified Earth model can often provide good fits to the observations, there is growing evidence that Earth models with 3-D structure (e.g., Austermann et al., 2013; Kaufmann et al., 2005; Latychev et al., 2005; Li et al., 2018; Paulson et al., 2005) and a more complex rheology are necessary (e.g., Baril et al., 2023; Kang et al., 2022; van der Wal et al., 2015, 2013).

There has been a long-term effort to better constrain the GIA signal and improve GIA model input parameters across North America (e.g., Argus et al., 2021; Caron et al., 2018; Lambeck et al., 2017; Peltier et al., 2015; Simon et al., 2016; Tarasov et al., 2012; Zhao, 2013). The work presented here is a continuation of this effort that focuses on eastern Canada but also includes the northeastern United States (Maine and Massachusetts). Our motivation for focusing on this region is twofold: (1) to utilize recently compiled and quality assessed RSL data sets (primarily that of Vacchi et al. (2018) but we also include data from Engelhart and Horton (2012)), (2) as discussed below, GIA is a dominant contributor to long term land subsidence in southeastern Canada and northeastern US and thus is an important driver of contemporary sea-level change (e.g., Davis and Mitrovica, 1996; Love et al., 2016).

Comparison of GNSS measurements of vertical land motion versus those based on reconstructions of RSL on millennial timescales indicates that land subsidence associated with GIA is an important cause of sea-level rise on the eastern seaboard of central North America (Karegar et al., 2016). Consequently, land subsidence (and, therefore, GIA) should be included in assessing sea-level hazard in this region (e.g., Karegar et al., 2017; Love et al., 2016; Zhai et al., 2015). In addition to GIA, other factors, including recent human intervention in water sources (such as excessive groundwater usage and damming) might be significant contributors to vertical land motion in the region (Karegar et al., 2016, 2017). Therefore, an improved GIA model that includes uncertainty estimates is required to separate paleo (GIA) and more recent (hydrological) loading signals.

While quantifying GIA model uncertainty has been largely neglected in many past studies, a growing number of papers have emphasized the importance of this aspect (Caron et al., 2018; Li et al., 2020; Love et al., 2016; Melini and Spada, 2019; Simon et al., 2017; Tarasov and Goldstein, 2023; Tarasov et al., 2012). Quantifying model uncertainty is particularly important in areas where GIA dominates

contemporary land motion and regional sea-level change, as is the case here. In this analysis, we build on past work (Love et al., 2016) to determine model uncertainty bounds based on two different approaches. These approaches focus on quantifying parametric model uncertainty, and so the accuracy of the determined uncertainty bounds is strongly related to the size of the explored parameter space. In this regard, our analysis extends most past work by considering 440 (1D) Earth viscosity models and 34 ice history models for a total of 14,960 parameter sets (model runs). Our large ice model parameter set relies heavily on the analysis of Tarasov et al. (2012).

Our uncertainty analysis considers a third approach that explicitly incorporates estimates of model structural uncertainty in defining a set of model parameters that are compatible with the adopted observational constraints (Tarasov and Goldstein, 2023). Our application of this approach, known as history matching, is one of the first in paleo sea level and GIA modeling studies and, as such, we hope it can be used as an example which future studies can build upon. As noted above, our analysis focuses on the application of 1D Earth viscosity models. An important source of structural error is the (missing) contribution of lateral variations in Earth properties. Therefore, as part of our analysis, we include some results from 3D Earth models to provide a preliminary estimate of this structural error contribution.

As detailed below, our 1D and 3D Earth modeling results indicate the importance of lateral Earth properties across our study region. Several studies have demonstrated the importance of laterally variable Earth structure in North America on GIA model output and inferences of viscosity structure (e.g., Davis et al., 2008; Lau et al., 2018; Li et al., 2020; Paulson et al., 2007, 2005; Wang et al., 2008). In addition, studies based on 1D (spherically symmetric) Earth models (e.g., Engelhart et al., 2011) suggest lateral structure as a primary cause for difficulties in fitting RSL observations. While there are instances where the addition of lateral Earth structure can result in improved fits to the observations (e.g., Kuchar et al., 2019b), it is often the case that 1D models produce equivalent or better fits in near-field regions (e.g., Yousefi et al., 2018). This result likely reflects the fact that the ice models adopted in these studies are developed assuming 1D Earth structure (Li et al., 2020).

In Section 2.2, we describe the RSL data used in our modeling analysis (Section 2.2.1). We also describe the 1D Earth GIA model (2.2.2), methods used to infer optimal model parameters and uncertainty (2.2.3), and, finally, some details of the 3D Earth GIA model (2.2.4). Our results, presented in Section 2.3, are partitioned into those for the 1D Earth model (2.3.1), the 3D Earth model (2.3.2), and the history matching analysis (2.3.3). A general discussion of our main results placed in the context of past work is provided in Section 2.4. Model output (optimal and uncertainty bounds) is made available for end users to quantify the influence of GIA on contemporary vertical land motion (Appendix 1) and RSL (Appendix 2) in our study region.

2.2. Methodology

2.2.1. Sea-level dataset

We have used two regional RSL data compilations for this analysis: one for eastern Canada (Vacchi et al., 2018) and one for the eastern USA (Engelhart and Horton, 2012). Our dataset comprises 38 sites distributed over seven subregions (see Figure 2.1). Sites 1-34 consist of the data compiled by Vacchi et al. (2018), and sites 35-38, associated with Maine and Massachusetts, are from Engelhart and Horton (2012).

All the RSL data points were recalibrated using CALIB 8.2 (Stuiver et al., 2021) with a 2σ range and employing IntCal20 and Marine20 calibration curves (Heaton et al., 2020; Reimer et al., 2020; Stuiver et al., 2021) for terrestrial and marine samples, respectively. Following Vacchi et al. (2018), the marine reservoir correction was assumed to be constant for all marine indicators within a given site. This correction was calculated based on the Marine20 database (Heaton et al., 2020) using the weighted average of all marine samples located within a given site area. For cases where there were no marine samples within a given site, we used the correction of the nearest marine sample to a given RSL data point.

After completion of the calibration process, we removed limiting data points that do not provide any additional constraints on the sea-level reconstruction at each site. This procedure is necessary as these redundant data points do affect the calculated data-model misfit (via the value N in Eq. 2.2). The following criteria were adopted to identify these redundant limiting data points: among several marine (or terrestrial) limiting data points that have significant temporal overlap and do not show sharply falling (or rising) RSL values, we consider only the highest marine (or lowest terrestrial) limiting data points; in some periods in which there is a high density of sea-level index points (SLIPs), we only select those limiting data points that complement the SLIPs, for instance, if they have lower uncertainty than the surrounding SLIPs or fill the time gaps between SLIPs. As a visual example, Figure 2.S1 shows data at site #5 before and after implementation of this limiting data 'cleaning' process and radiocarbon re-calibration.

The total dataset used in this study comprises 1,013 RSL data points, including 544 SLIPs, 232 marine limiting data points, and 237 terrestrial limiting data points, after performing data cleaning (Table 2.1). Following Vacchi et al. (2018) and Engelhart and Horton (2012), we subdivided the sites into seven subregions (Figure 2.2) based on spatial variability in the RSL signature (which reflects the deglaciation chronology) and/or the geomorphological setting (e.g., open coast, estuary, fjord). The number of each data type in individual subregions and the spatial distribution of these data are indicated in Table 2.1 and Figure 2.1, respectively. As described in Section 2.3, we consider data-model fits for both the entire data set as well as the seven subregions identified in Figure 2.2 to examine the potential importance of lateral variability in Earth structure. In the remainder of this section, we provide a brief summary of the data in each of the seven subregions. Additional information can be found in the original publications (Vacchi et al., 2018; Engelhart and Horton, 2012).

Hudson Bay (sites 1-7) is located at the central part of the former Laurentide Ice Sheet, where a continuous RSL fall is clearly recorded during the entire Holocene at each site due to the GIA-induced land uplift. The sea-level indicators for this subregion cover the past ~8.5 ka and limiting data points are significant for constraining the RSL signal during the early- to mid- Holocene. Ungava Peninsula (sites 8-11) is also characterized by uplift, and, therefore, a continuous RSL fall since ~9 ka. However, the limited number of SLIPs in this area does not provide a robust constraint on the spatial variability of RSL across the subregion. Therefore, limiting data points play an important role in constraining the RSL signal at each site. Data from Labrador (sites 12-15) show an RSL fall during the whole Holocene period; however, the RSL signal is constrained exclusively by limiting data points spanning the past ~10 ka (see Figure 2.2).

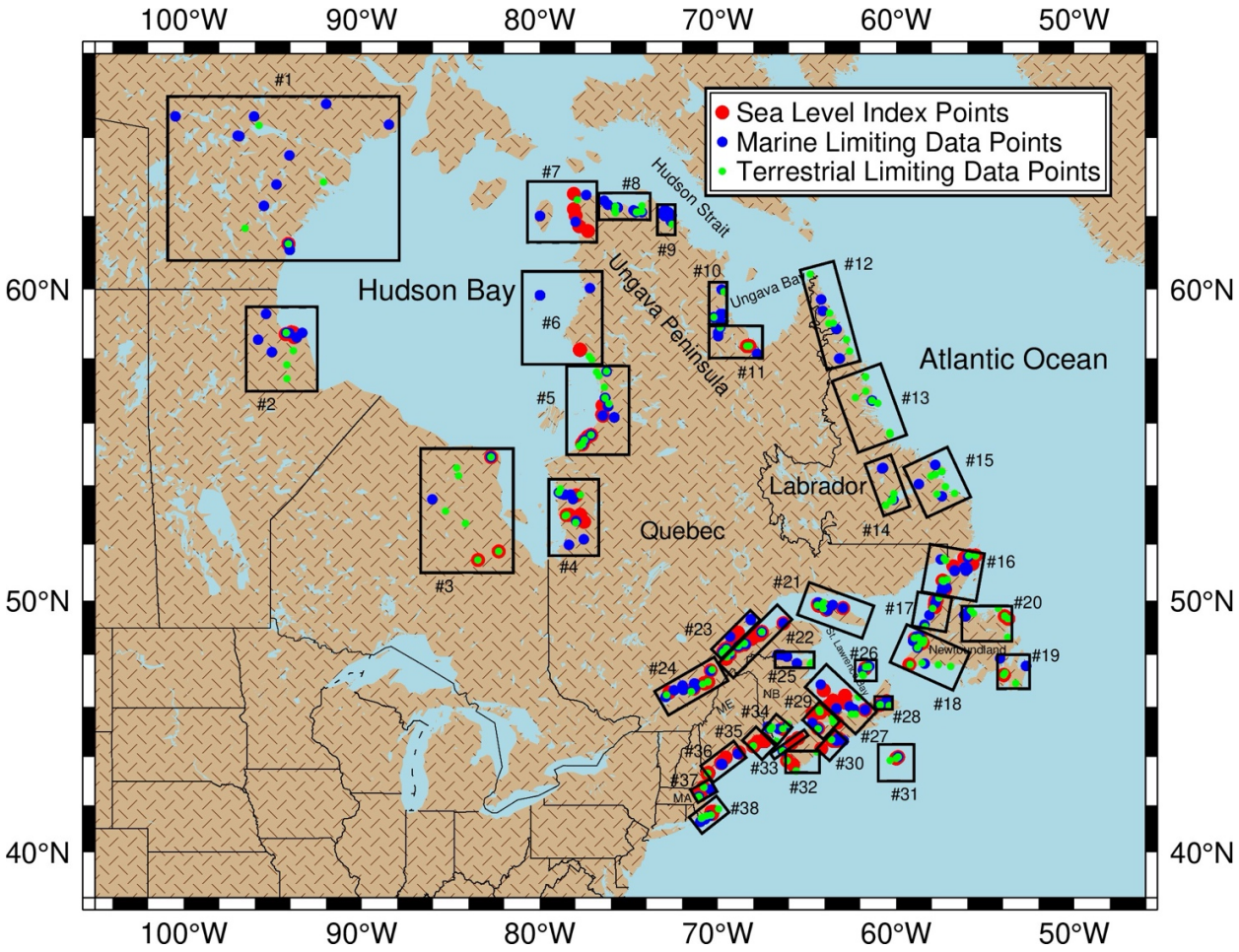


Figure 2.1. Map showing the spatial distribution of RSL data used in this study. The data are grouped into 38 sites (black rectangles) or, more generally, into seven subregions: Hudson Bay (HB, sites 1-7), Ungava Peninsula (UP, sites 8-11), Labrador (LB, sites 12-15), Newfoundland (NF, sites 16-20), St. Lawrence Corridor (SLC, sites 21-24), New Brunswick and Nova Scotia (NN, sites 25-34), and Maine and Massachusetts (MM, sites 35-38). The locations of SLIPs, marine, and terrestrial limiting data points are indicated by red, blue and green circles, respectively. See Table 2.1 for the number of each data type (SLIPs, marine, and terrestrial limiting data points) in each subregion. Additional maps showing this data distribution in more detail are provided in Figure 2.S2.

The RSL data for Newfoundland (sites 16-20) span the past ~16 ka and are mainly comprised of limiting data points. There are two RSL patterns in this subregion: the northwestern part (i.e., site #16; see Figure 2.S2) differs from the rest and can be characterized as an uplifting region such that RSL drops from the mid to late Holocene; at the remaining sites (17-20), the RSL reconstructions show a rapid drop to a lowstand in the early Holocene followed by a continuous RSL rise. This spatially complex RSL history is thought to be associated with forebulge migration and associated hinge line movement from the subsiding southeast coast to the uplifting northwest coastal region (Daly et al., 2007; Shaw and Potter, 2015). The St. Lawrence Corridor (sites 21-24), with a dataset spanning the past ~15 ka, also represents a transitional region in that RSL drops rapidly to current levels during the early-Holocene, followed by a mid-Holocene highstand and a subsequent fall to the present.

RSL data from New Brunswick and Nova Scotia (sites 25-34) span the past ~17 ka and indicate two RSL patterns (see Figure 2.2). Around the coasts of New Brunswick and western Nova Scotia (i.e., sites 25-27, 29, 33, and 34; see Figures 2.S2 and 2.1), RSL falls to a spatially variable early-Holocene lowstand followed by a continuous RSL rise in the remaining Holocene period. In contrast, around

eastern Nova Scotia located at the margin of the former Laurentide Ice Sheet (i.e., sites 28, 30-32), the data show a continuous RSL rise during the Holocene, which indicates that rising global mean sea level (GMSL) and collapse of the peripheral forebulge dominate at these sites. Since this subregion is close to the margin of the Laurentide Ice Sheet at maximum extent, the timing of regional deglaciation is earlier compared to the central areas (e.g., Hudson Bay). Finally, in Maine and Massachusetts (sites 35-38), where the majority of SLIPs are from the past ~6 ka and the RSL history for early-to-mid Holocene stems from limiting data points, there is a non-linear RSL rise during the Holocene.

Table 2.1. The number of RSL data points, after and before (square brackets) data cleaning, used to constrain the GIA signal. Figure 2.1 indicates the spatial distribution of these data.

Subregion	Number of SLIPs	Number of marine limiting data points	Number of terrestrial limiting data points
Hudson Bay	61	62 [114]	45 [68]
Ungava Peninsula	3	33 [61]	16 [18]
Labrador	0	13 [15]	33 [44]
Newfoundland	46	38 [50]	49 [61]
St. Lawrence Corridor	121	36 [59]	24 [53]
New Brunswick and Nova Scotia	171	36 [52]	50 [71]
Maine and Massachusetts	142	14 [39]	20 [40]
Total = 1013 [1289]	**544**	**232 [390]**	**237 [355]**

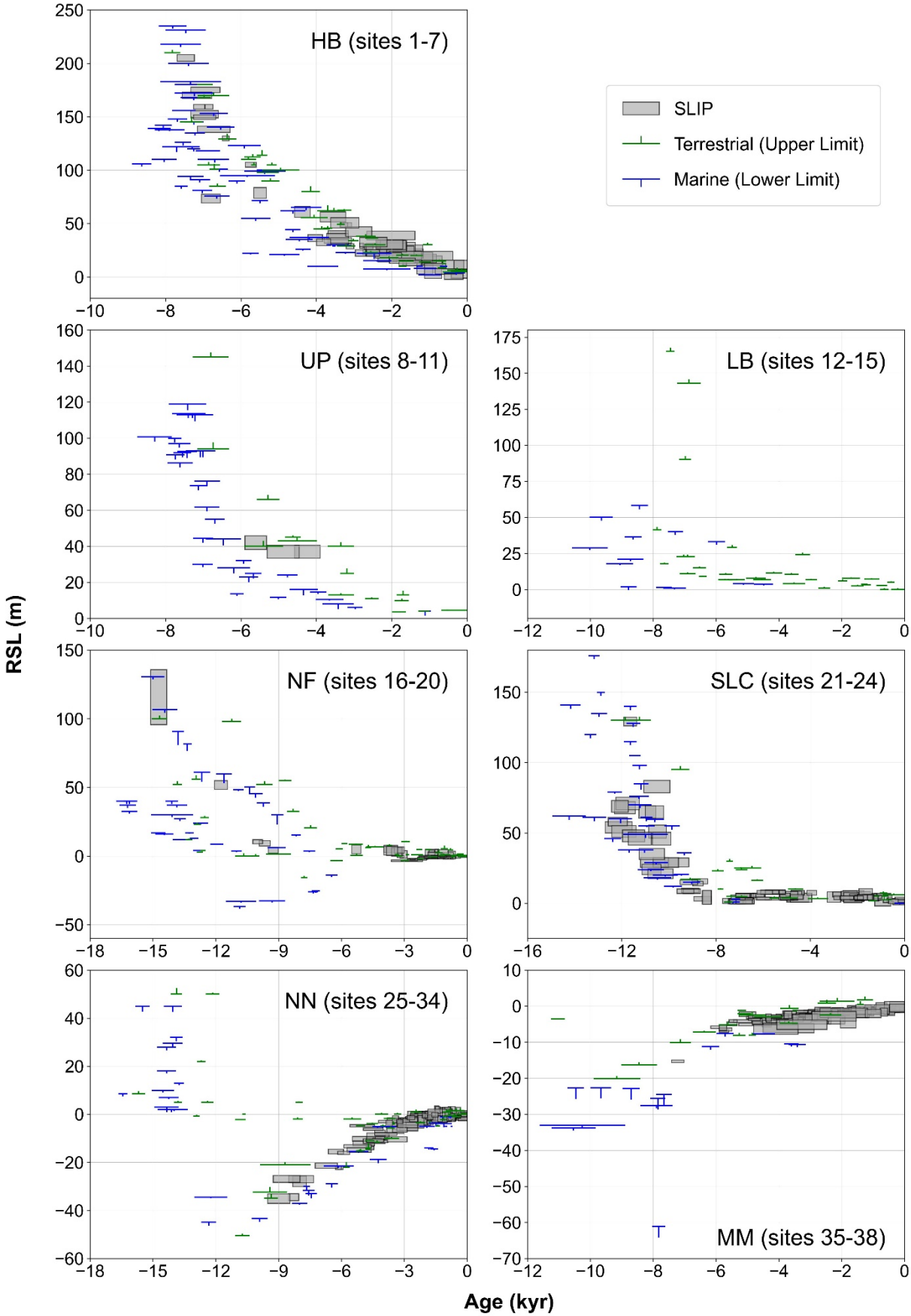


Figure 2.2. Legend on next page.

Figure 2.2. RSL reconstructions for the 7 subregions distributed over southeastern Canada and northeastern USA (see Figure 2.1): Hudson Bay (HB), Ungava Peninsula (UP), Labrador (LB), Newfoundland (NF), St. Lawrence Corridor (SLC), New Brunswick and Nova Scotia (NN), and Maine and Massachusetts (MM). Three symbols indicate the type of sea-level indicator: SLIP, marine (or lower limit of RSL position), and terrestrial (or upper limit of RSL position). The SLIP boxes indicate ±2σ uncertainty in RSL and age. For limiting data points, the horizontal and vertical bars show ±2σ RSL age uncertainty and one side of the 2σ RSL uncertainty, respectively. Figure shows the 'cleaned' version of the database in which redundant limiting data have been removed.

2.2.2. 1D GIA model and parameterization

The 1D GIA model used in this study calculates the response of a compressible Maxwell, spherically symmetric Earth to a loading history, including ice and ocean components, with the ocean load computed in a gravitationally self-consistent manner (Farrell and Clark, 1976; Kendall et al., 2005; Mitrovica and Milne, 2003). The influence of GIA-derived perturbations in the Earth's rotational potential on RSL is included (Milne and Mitrovica, 1998; Mitrovica et al., 2005). Spatial fields are truncated at spherical harmonic degree and order 256, providing a spatial resolution close to that of the ice history models. The density and elastic structure of the model is based on the Preliminary Reference Earth Model (PREM) (Dziewonski and Anderson, 1981). The key input parameters to the GIA modelling are the deglaciation history and Earth viscosity structure, which are generally unknown in advance and typically can be estimated through three approaches: (1) comparing model outputs to different types of observations to constrain the optimal Earth rheology and ice loading history in a given region (e.g., Lambeck et al., 2014, 1998; Love et al., 2016; Milne and Peros, 2013; Peltier et al., 2002; Roy and Peltier, 2015; Yousefi et al., 2018), (2) independently determining the Earth viscosity structure and deploying data for constraining the deglaciation history (e.g., Peltier, 2004), (3) a joint inversion method to constrain the optimal combinations of ice loading history and viscosity structure, providing minimum misfits (e.g., Caron et al., 2017; Lambeck et al., 2017). Based on consideration of the first approach, this research aims to determine a GIA model parameter set that is compatible with observations of past RSL changes and better constrain the uncertainty in these model input parameters for southeastern Canada and northeastern USA. To partly quantify the impact of parametric uncertainty on our results, we consider a broad parameter range for the Earth's viscosity structure and a large suite of ice loading histories. Due to model limitations and assumptions used in the forward modelling and uncertainty in the observations, the solution is not unique, so we have more than one set of optimal model input parameters that can fit the data well.

Three parameters characterize the viscous structure of the Earth model: an outer shell with high viscosity (10^{43} Pas) and varying thickness to simulate an elastic lithosphere (i.e., 46, 71, 96, and 120 km for lithospheric thickness, LT); an upper mantle region with uniform viscosity, extending from the base of lithosphere to 670 km depth; and a lower mantle region with uniform viscosity from 670 km to the core-mantle boundary (i.e., 2885 km). To accommodate the plausible variations in the viscosity structure of the study region, we consider broad parameter ranges for the viscosity space, encompassing 11 values for the upper mantle viscosity (UMV): 0.05, 0.08, 0.1, 0.2, 0.3, 0.5, 0.8, 1, 2, 3, 5 [$\times 10^{21}$ Pas]; and 10 values for the lower mantle viscosity (LMV): 1, 2, 3, 5, 10, 20, 30, 50, 70, 90 [$\times 10^{21}$ Pas].

We have made use of 34 ice history models (see Table 2.S1), consisting of ANU (Lambeck et al., 2017); ICE-6G (Peltier et al., 2015); and a high-variance subset of 32 North American Ice Complex models derived from a physics-based glacial system model, calibrated by regional observations (Tarasov et al., 2012). In addition, the regional North American Ice Complex reconstructions from Tarasov et al. (2012) (referred to as GLAC1D below) were patched into the ICE-5G global model (Peltier, 2004; Love et al., 2016) for RSL computations. We use such a large suite of ice models to

better sample the parametric uncertainty of this model input compared to most previous studies. Figures 2.S3 and 2.S4 display the average thickness and corresponding standard deviation of the 34 ice history models at 21 and 10 ka. Figure 2.S5 illustrates the temporal evolution of ice thickness from 21 ka to the present day for two locations with significant standard deviation values (see white triangles in Figures 2.S3 and 2.S4): southeastern Canada at 21 ka (average position in site #21 from St. Lawrence Corridor) and southern Hudson Bay at 10 ka (average position in site #4 from Hudson Bay). The modeled North American Ice Sheet Complex was at its maximum extent at 21 ka, with the thickest ice situated to the west of Hudson Bay. After 21 ka, there was not a major reduction in ice extent until ~15 ka (see Figure 2.S5). According to all 34 ice history models, the ice extent from eastern Canada and Hudson Bay was completely deglaciated by ~10 and ~7 ka, respectively. In addition, our results indicate that the ice history is less well constrained (i.e., standard deviation of considered ice models is a maximum) in southeastern Canada and northeastern USA at 21 ka (Figure 2.S3) and in the Hudson Bay area at 10 ka (Figure 2.S4).

2.2.3. Estimation of model parameters

Constraining a set of Earth model parameters was carried out through a comparison between GIA model outputs and observations of paleo RSL. Due to the non-uniform distribution of RSL data points in space and time, a spatio-temporal weighting process was conducted on each RSL data type (i.e., SLIPs, marine, and terrestrial limiting data points) separately so that the effect of data clustering on the data-model misfit analysis is reduced (Briggs and Tarasov, 2013). In terms of spatial weighting, the RSL uncertainty of each data point is scaled through the square root of the number of RSL data points in each site divided by the square root of the total number of RSL data points in the associated subregion (e.g., Hudson Bay). For temporal weighting, we considered four time bins based on the temporal distribution of RSL data points, encompassing 0-3, 3-6, 6-9, and older than 9 ka. Similar to the spatial weighting, the RSL age uncertainty is scaled based on the square root of the number of RSL data points falling into each time bin divided by the square root of the total number of RSL data points. The spatio-temporally weighted RSL data were utilized for the misfit analysis to determine optimal GIA model parameters within the explored parameter space.

The misfit analysis was carried out on SLIPs and limiting data points (LDPs in Equation 2.2) separately based on Equations 2.1 and 2.2, respectively (Mitrovica et al., 2000):

$$\delta_{SLIPs} = \frac{1}{N}\sqrt{\sum_{i=1}^{N}\left(\frac{RSL_i^{data}-RSL_i^{model}}{\Delta_{rsl,i}}\right)^2 + \left(\frac{t_i^{data}-t_i^{model}}{\Delta_{t,i}}\right)^2} \qquad (2.1)$$

$$\delta_{LDPs} = \frac{1}{N}\sqrt{\sum_{i=1}^{N}\left(\frac{RSL_i^{data}-RSL_i^{model}}{\Delta_{rsl,i}}\right)^2} \qquad (2.2)$$

Here, RSL_i^{data} and RSL_i^{model} are the observed and predicted RSL for the ith RSL data point; t_i^{data} and t_i^{model} are the observed and predicted RSL age for the ith RSL data point; $\Delta_{t,i}$ and $\Delta_{rsl,i}$ are 1σ age and RSL uncertainties of the ith RSL data point; and N is the total number of SLIPs (in Eq. 2.1) and limiting data points (in Eq. 2.2) in the considered dataset. In Eq. 2.1, the RSL curve is calculated at each SLIP position (i.e., latitude and longitude) and the closest point on this curve to that SLIP, namely RSL_i^{model}, is estimated through the norm-2 distance or Euclidean approach (Mitrovica et al., 2000).

Given that each limiting data point only provides a one-sided bound on RSL, the Euclidean approach cannot always produce an accurate estimate of the closest point on the RSL curve to each limiting data point. Therefore, an alternative approach is used to estimate the misfit value based on limiting data points: two RSL values on the model curve are computed at the minimum and maximum of the age bound of each limiting data point and if at least one of the computed RSL values in the case of marine (or terrestrial) limiting data points is greater (or less) than RSL_i^{data}, the related data-model misfit is considered zero, otherwise it is estimated from Eq. 2.2 at the mid-point of the age uncertainty range. We also considered an approach that involved assigning asymmetric uncertainty bounds to the limiting data such that the marine/terrestrial limiting data had upper/lower uncertainty ranges that were considerably larger than the lower/upper ranges. This approach and the one described above gave close to identical results and so the first method described was applied to generate the final results as it avoids the (non-trivial) task of assigning upper/lower RSL uncertainty ranges to marine/terrestrial limiting data.

To determine the best-fitting Earth model parameters, the data-model misfits are estimated (from Eq. 2.1 and 2.2):

$$\delta = \delta_{SLIPs} + 0.5 \times \delta_{LDPs} \qquad (2.3)$$

For each combination of 440 Earth models and 34 ice loading histories, namely a total of 14,960 Earth-ice model parameter combinations (or model runs). The misfit value based on limiting data is weighted by 0.5 as these data provide only one-sided bounds on RSL and so two limiting data points are required to produce a constraint similar to that of a SLIP.

2.2.3.1. Estimation of model uncertainty bounds

In addition to determining an optimal GIA model parameter set, we estimate the uncertainty associated with this estimate. We utilize the heuristic and nominal Bayesian approaches described by Love et al. (2016), alongside a history matching approach which provides a suite of plausible model parameter values for a defined statistical threshold and explicitly includes the consideration of structural uncertainty in the GIA model (Tarasov and Goldstein, 2023).

In the heuristic approach, the upper and lower bounds are estimated independently by specifying a criterion ([P + (100 - P)/2]% (P = 68.27% for 1σ uncertainty) that defines the minimum percentage of SLIPs that must pass above (for lower bound) or under (for upper bound) a given model run (or parameter set). If the percentage of SLIPs that lie above (or below) a given model curve is greater than the threshold, that model can be considered as a lower (or an upper) bound (Love et al., 2016). Finally, among the possible upper and lower bounding models, the two that provide the minimum misfits (Equations 2.1 and 2.2) are selected as the upper and lower bounding runs. It should be noted that this approach does not always result in one or both bounding models being identified. This can be due to the poor quality of data-model fits for a given dataset, a lack of SLIPs, or a combination of both. For example, this approach did not result in any bounding models for each of the 7 subregions (Figure 2.2) based on 2σ uncertainty (i.e., considering P = 95.45% in the bounding threshold), and so a 1σ P value was used. We also made use of another bounding criterion based on limiting data points, [(100 - P)/2]% for P = 68.27%, to determine whether the lower and upper bounds estimated from the bounding threshold defined by SLIPs are compatible with marine and terrestrial limiting data points.

Because the heuristic approach does not result in bounding models in some regions, we also utilized a Bayesian approach (Love et al., 2016). As per Bayes' rule, the posterior probability (i.e., P(m|d)) is estimated from the prior probability (i.e., P(m)) and the likelihood function (i.e., P(d|m)):

$$P(m|d) = \frac{P(d|m).P(m)}{C} \quad (2.4)$$

$$P(d|m) = e^{-\delta^2} \quad (2.5)$$

Here, δ is the data-model misfit parameter estimated for each Earth model parameter set (Eq. 2.3), *m* is the parameter vector or model configuration, *d* is the observation vector, and *C* is a normalization constant to ensure that posterior probabilities sum to one over the entire model ensemble. The likelihood function showing the closeness of the model outputs to the observations is defined as an exponential function and the prior indicating our knowledge regarding the model parameterization prior to analyzing data is assumed to be uniform. By defining an uncertainty threshold (e.g., 1σ, 2σ, etc.), a sub-ensemble with cumulative posterior probabilities that satisfy this threshold compatible is calculated. From the parameter values within this sub-ensemble, the lower and upper bounds are determined based on the consideration of minimum and maximum modeled RSL values at each site and age. Therefore, the uncertainty bounds in this case represent output from a range of model parameter sets, in contrast to those determined from the heuristic approach where each model bound is based on a distinct parameter set (single model run). Since a 1σ uncertainty range was used in determining the heuristic model bounds, the same threshold was used in calculating the nominal Bayesian bounds. This choice explains why 1σ data uncertainties are shown on figures rather than the more conventional 2σ ranges – Figure 2.2 is the only exception.

When applying the nominal Bayesian approach, we scaled data-model misfit (δ) values in Equation 2.5 to arrive at a preferred scaling factor for each dataset (i.e., all data or a regional subset). This was done to ensure that the uncertainty bounds were consistent with a statistically appropriate number of limiting data – in our case, 68.27% since we have adopted a 1σ uncertainty threshold. The proportion of limiting data points compatible with the inferred bounds was calculated for different scale factors, and the optimal scale factor is the minimum one that satisfies the 1σ uncertainty threshold. This means that the obtained uncertainty bounds are compatible with at least 68.27% of the limiting data points in the dataset being considered.

As a preliminary test of a much more statistically robust approach than traditional Bayesian posterior inference, we use the history matching approach described by Tarasov and Goldstein (2023). This is an approach that focuses on bracketing reality rather than defining an optimal (best-fit or most likely) model parameter set. In our application of this approach, we also seek to define model bounds that are based on a single ice history across the entire region. This contrasts to the heuristic and Bayesian methods described above. A comparison of the results of the three approaches is provided in Section 2.3.4.

While a full history matching analysis would consist of a detailed assessment of model structural uncertainty along with a sequence of iterations, referred to as 'waves', in which the subset of parameter vectors that are deemed plausible are determined with adequate sampling of model parameters (Tarasov and Goldstein, 2023), we apply here a simplified approach in which only a single pass is made to determine a set of tentatively plausible parameter vectors. To be consistent with the nominal Bayesian approach described above, we define an implausibility measure (*IM*) that reflects our definition of data-model misfit (Equations 2.1 and 2.2). For a given parameter vector (i.e., Earth-ice model parameter set),

IM is calculated separately for each SLIP and limiting data point (LDP in Eq. 2.7) using the following equations:

$$IM_{SLIP}^{i} = \sqrt{\frac{\left(RSL_i^{data} - RSL_i^{model}\right)^2}{\Delta_{rsl,i}{}^2 + \sigma_{struct_rsl,i}^2} + \frac{\left(t_i^{data} - t_i^{model}\right)^2}{\Delta_{t,i}{}^2 + \sigma_{struct_t,i}^2}} \qquad (2.6)$$

$$IM_{LDP}^{i} = \sqrt{\frac{\left(RSL_i^{data} - RSL_i^{model}\right)^2}{\Delta_{rsl,i}{}^2 + \sigma_{struct_rsl,i}^2}} \qquad (2.7)$$

Here, $\sigma_{struct_rsl,i}$ and $\sigma_{struct_t,i}$ represent the structural model error at the location and age of the ith RSL data point. The other terms are identical to those utilized in Equations 2.1 and 2.2. The structural uncertainty in the (1D) GIA modeling originates from different sources, for example: the presence of lateral viscosity variations in the study region, the possible influence of non-Maxwellian deformation in the RSL response, and inaccuracy in the ice history reconstructions. In this study, which is largely based on 1D Earth models, we explicitly consider the effect of laterally variable Earth structure as a source of structural uncertainty based on the results from the 3D GIA modelling (Section 2.2.4). Since we do not accurately quantify the structural uncertainty associated with the lateral viscosity variations (we only consider two 3D runs in this study), we provide an estimate that is the average of the two 3D runs at the location and age of each data point. A crude estimate of other contributions to model structural error is 5% of the RSL (height) or age of a given data point. Thus, the model structural error is defined as follows:

$$\sigma_{struct_rsl,i} = \sqrt{(SF_{LV} \times \sigma_{LV}^{i})^2 + (0.05 \times RSL_i^{data})^2} \quad (2.8)$$

$$\sigma_{struct_t,i} = 0.05 \times t_i^{data} \qquad (2.9)$$

Here, σ_{LV}^{i} is the structural uncertainty due to lateral viscosity variations for the ith RSL data point, calculated from the results of 3D GIA modelling as described above. We scaled σ_{LV}^{i} by a value SF_{LV} that is adjusted until an adequate number of plausible parameter vectors is determined across the entire data set (a final value of 1.5 was adopted). This set of plausible parameter vectors is termed "not ruled out yet" (NROY).

Model parameter vectors that result in an implausibility value below a certain threshold across 95% of the complete dataset are accepted as NROY (95% is based on the assumption that *IM* has a continuous unimodal distribution; see Section 3.1 of Tarasov and Goldstein, 2023). We adopt a rejection threshold of 3 which is the minimum value commonly used for history matching (Tarasov and Goldstein, 2023). Since we consider both height and time for SLIPs, the threshold *IM* value is adjusted to $\sqrt{3^2 + 3^2} = \sqrt{18}$. Those troubled by the unimodality assumption should note that this is, in part, offset by the above quadrature of RSL height and time thresholds which would only be strictly justified if height and time residuals were independent, which is clearly not the case. Since the SLIPs and limiting data have a different IM threshold, they are considered separately in determining the NROY parameter set.

The rationale behind the history matching approach, as applied here, is to define model uncertainty bounds based on a uniform ice history for the whole study region (i.e., an ice history model common among all reduced NROY sets), while allowing for varying Earth model parameter vectors between

each subregion (e.g., Hudson Bay versus Newfoundland). Therefore, for ice models that are NROY, the next step is, for each subregion, to identify which parameter vectors produce RSL values that lie, on average, above or below the SLIP data (a regional average of $RSL_i^{model} - RSL_i^{data}$ is computed for this purpose). From these parameter vectors, bounding models for a common ice history model are chosen.

2.2.4. 3D GIA modelling

To assess the importance of lateral viscosity variations in our study region, we apply the 3D GIA model originally presented by Latychev et al. (2005), which computes the GIA response of a self-gravitating, elastically compressible 3D Maxwell viscoelastic Earth to a specified surface loading history using a numerical finite-volume approach. In addition, the influences of rotational feedback and time-varying shorelines are also considered in the computation of solutions and output surface observables, including vertical land motion, gravity perturbation, and RSL. The lateral perturbation of mantle viscosity is superimposed on a reference 1D structure that is the optimal Earth-ice model parameter set determined by the data-model misfit analysis based on the 1D modelling for the whole study region. The lateral viscosity structure is based on a global shear wave velocity model using the following equations (Latychev et al., 2005; Austermann et al., 2013):

$$\delta \ln \rho(r,\theta,\varphi) = \frac{\delta \ln \rho}{\delta \ln v_s}(r)\, \delta \ln v_s(r,\theta,\varphi) \quad (2.10)$$

$$\delta T(r,\theta,\varphi) = -\frac{1}{\alpha(r)} \delta \ln \rho(r,\theta,\varphi) \quad (2.11)$$

$$\eta(r,\theta,\varphi) = \eta_0(r) e^{-\epsilon \delta T(r,\theta,\varphi)} \quad (2.12)$$

Here, r, θ, and φ are the radius, colatitude, and east longitude, respectively. The adopted 3D seismic shear velocity model ($\delta \ln v_s$) is converted to density variations, $\delta \ln \rho$, based on a depth-dependent logarithmic scaling factor, $\frac{\delta \ln \rho}{\delta \ln v_s}(r)$ (see Eq. 2.10). The radial profile of Forte and Woodward (1997) is adopted for the velocity-to-density scaling coefficient that accounts for both anharmonic and elastic effects (Karato, 1993).

According to Eq. 2.11, the temperature variation (δT) is then calculated by scaling the density variation using the depth-dependent thermal expansion coefficient, $\alpha(r)$. The results from Chopelas and Boehler (1992) are adopted here. Finally, the variation in temperature is utilized to compute a 3D viscosity structure (η) through a reference 1D viscosity profile (η_0) and using an exponential function of the scaled temperature variations (with a scaling constant $\varepsilon = 0.04\ ^{\circ}C^{-1}$). We considered two seismic models: S40RTS (Ritsema et al., 2011) and a composite model where S40RTS was replaced by the higher resolution upper mantle model SL2013sv (Schaeffer and Lebedev, 2013). In producing the composite case, the two models were merged over a depth range of several hundred km to avoid adding large and inaccurate velocity gradients.

2.3. Results

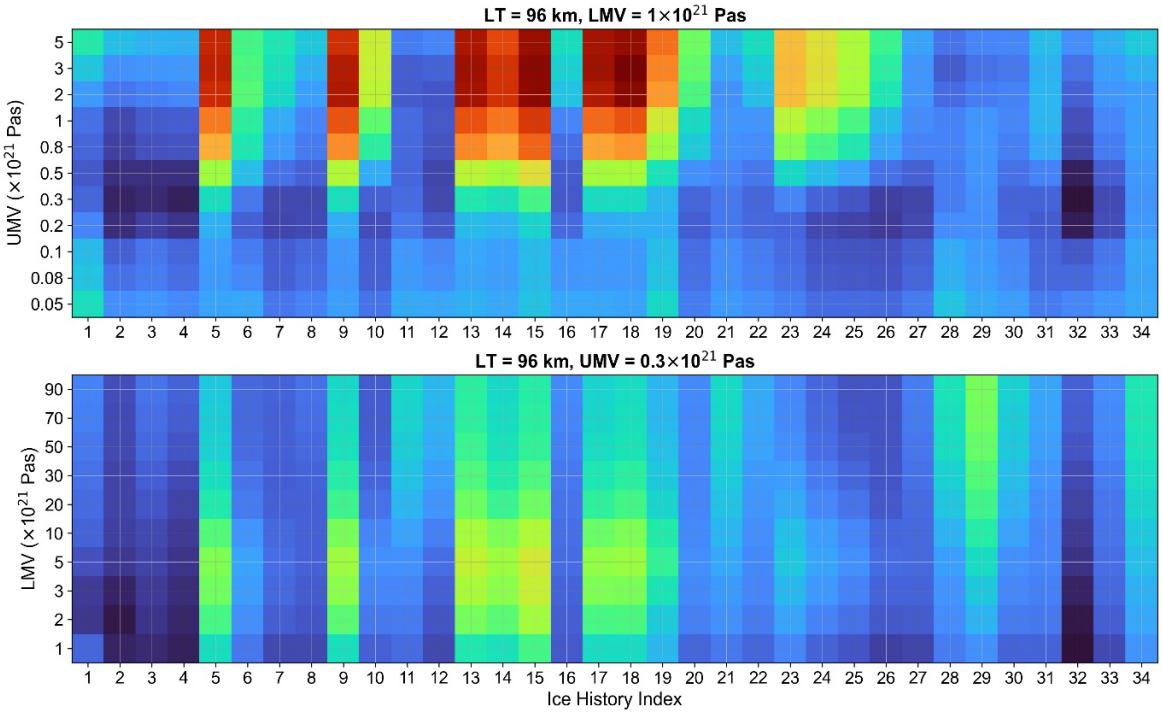
Section 2.3.1 focuses on the determination of optimal model parameters and uncertainty bounds (Section 2.3.1.1) and comparison of model output to observations (2.3.1.2). Section 2.3.1.1 considers the impact of partitioning the dataset into smaller regions to determine if significantly improved fits can be obtained via this partitioning (as a crude way to incorporate the influence of lateral structure). In

Section 2.3.2, the preliminary results of the 3D GIA modelling, based on two seismic tomography models, are presented and compared with the results of the 1D analysis. In Section 2.3.3, we discuss the preliminary results of the history matching approach on determining model uncertainty bounds and compare with those determined using the nominal Bayesian approach. Finally, in Section 2.3.4, we provide a general discussion of our key results with some comparisons to previous work and suggestions of worthwhile avenues for future work.

2.3.1. 1D Earth model analysis

2.3.1.1. Determination of regional partitioning, optimal parameter sets and model uncertainty

We estimated optimal Earth-ice model parameters for the whole study region by determining the parameter set that minimized the data-model misfit parameter (δ) for the complete dataset (SLIPs and limiting data points). Figure 2.3 indicates that the optimal Earth model parameters are: LT = 96 km, UMV = 0.3×10^{21} Pas, LMV = 1×10^{21} Pas, and ice loading history GLAC1D-na8005 (ice model index = 32). Generally, as the lower frame in Figure 2.3 shows, the lowest values for the misfit parameter can be produced for low LMV ($1\text{-}3\times10^{21}$ Pas) and UMV = $0.2\text{-}0.5\times10^{21}$ Pas. We note that good fits were also obtained with ice models 2-4 (Table 2.S1) for similar UMV and LMV ranges (top and middle frames of Figure 2.3). Optimal model curves and uncertainty bounds estimated from the nominal Bayesian approach for the whole study region (sites 1-38) are shown in Figure 2.S6 (no lower bounding model was distinguished using the heuristic approach, so heuristic bounds are not plotted). Figure 2.S6 indicates that the optimal model does not provide a quality fit at most sites between 1-25 (approx.) with the fit at sites 26-38 being, overall, a higher quality in comparison. It is also evident that the estimated model uncertainty is too broad at many sites with the upper/lower bounds often conflicting with terrestrial/marine limiting data points (e.g., site #8). Clearly, the model is struggling to match the large variation in the observed RSL signal across this broad region.



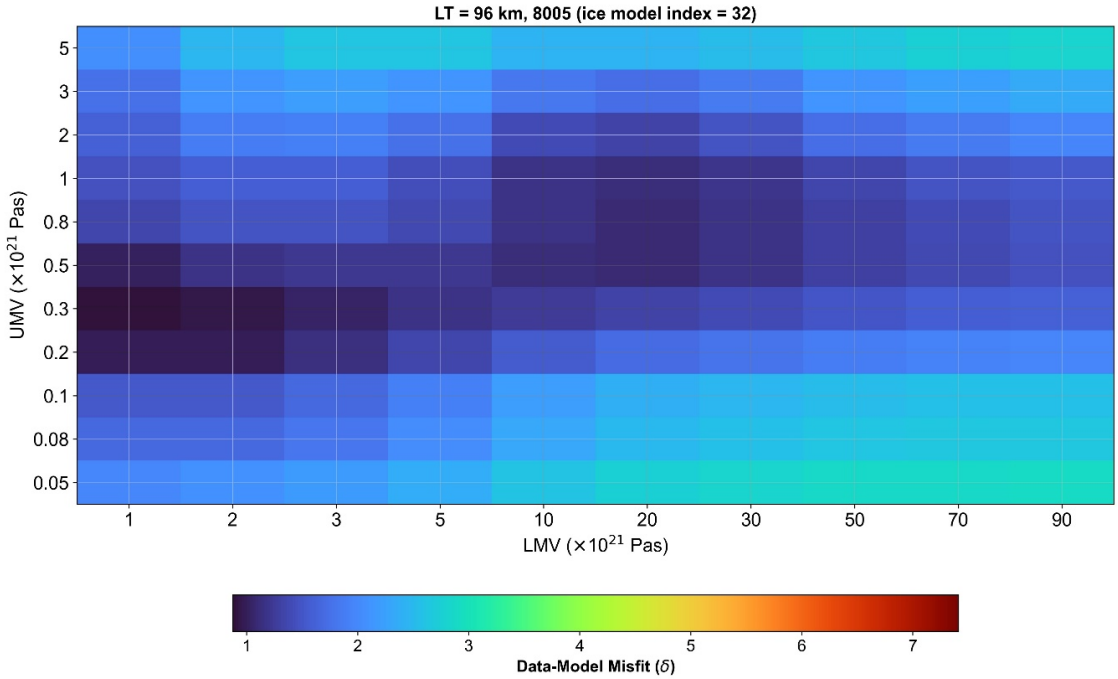


Figure 2.3. Data-model misfit values (δ) for the whole study region as a function of (from top to bottom) UMV and ice loading history when LMV is constant (10^{21} Pas), LMV and ice loading history when UMV is fixed at 0.3×10^{21} Pas, and LMV and UMV for GLAC1D-na8005 (ice history index = 32). In all 3 plots, the lithospheric thickness is 96 km. Note that these plots do not necessarily display all the minimum and maximum values of δ for the parameter space considered.

To determine if spatial partitioning of the data can result in improved fits (as a precursor to the 3D analysis), we identified the optimal Earth model parameter sets for each of the seven subregions (see Section 2.3.1.2) and considered whether there is similarity in the preferred viscosity space and ice loading history between different subregions. A number of ice models can produce good data-model fits for Hudson Bay, Ungava Peninsula, and Labrador for low LMV and intermediate to high UMV values (see Figure 2.S7 for results based on the ANU ice model). Hence, we merged these three subregions into a single, larger subregion (called "HUL"). Moreover, Newfoundland, St. Lawrence Corridor, New Brunswick and Nova Scotia, and Maine and Massachusetts are combined into one subregion (called "NSNM") based on the results of the 1σ-uncertainty analysis because several ice loading histories can provide good fits for intermediate viscosity values in LMV and UMV in each of these subregions (see Figure 2.S8 for results based on the GLAC1D-na8005 ice model). We note that relatively high LMV and UMV values can also provide decent fits. This partitioning of the entire dataset into two larger subregions (illustrated in Figure 2.S9), (i) HUL (sites 1-15; close to the middle part/thickest section of the Laurentide Ice Sheet) and (ii) NSNM (sites 16-38; along the Atlantic coast of Canada and northern USA, close to the ice margin), can result in good quality fits to RSL data that are comparable to those obtained by partitioning into smaller regions, as demonstrated in Section 2.3.1.2. We now proceed to identify optimal model parameters for the expanded subregions HUL and NSNM. A summary of the optimum (and bounding) parameter sets is provided in Table 2.2.

Figure 2.4 indicates misfit analysis results for the HUL subregion (sites 1-15). Each frame shows misfit values while varying two (out of four) model input parameters (see caption for details). The top and middle panels indicate the sensitivity of data-model misfits to variations in the deglaciation history and UMV (top) and LMV (middle). Across the ice models considered, the results indicate a preference

for very low LMV and medium to high UMV. The best fits occur for LMV = 10^{21} Pas, UMV = 2×10^{21} Pas, LT = 120 km, and ice history GLAC1D-na9927 (ice history index = 3) (see bottom frame). This optimal parameter set is somewhat unconventional in that the UMV is double that of the LMV. Of course, when uncertainty in the parameter inference is considered (e.g., see Table 2.2), there are parameter sets that give similar fits in which UMV is lower than LMV (as also evident in Figure 2.4, bottom frame).

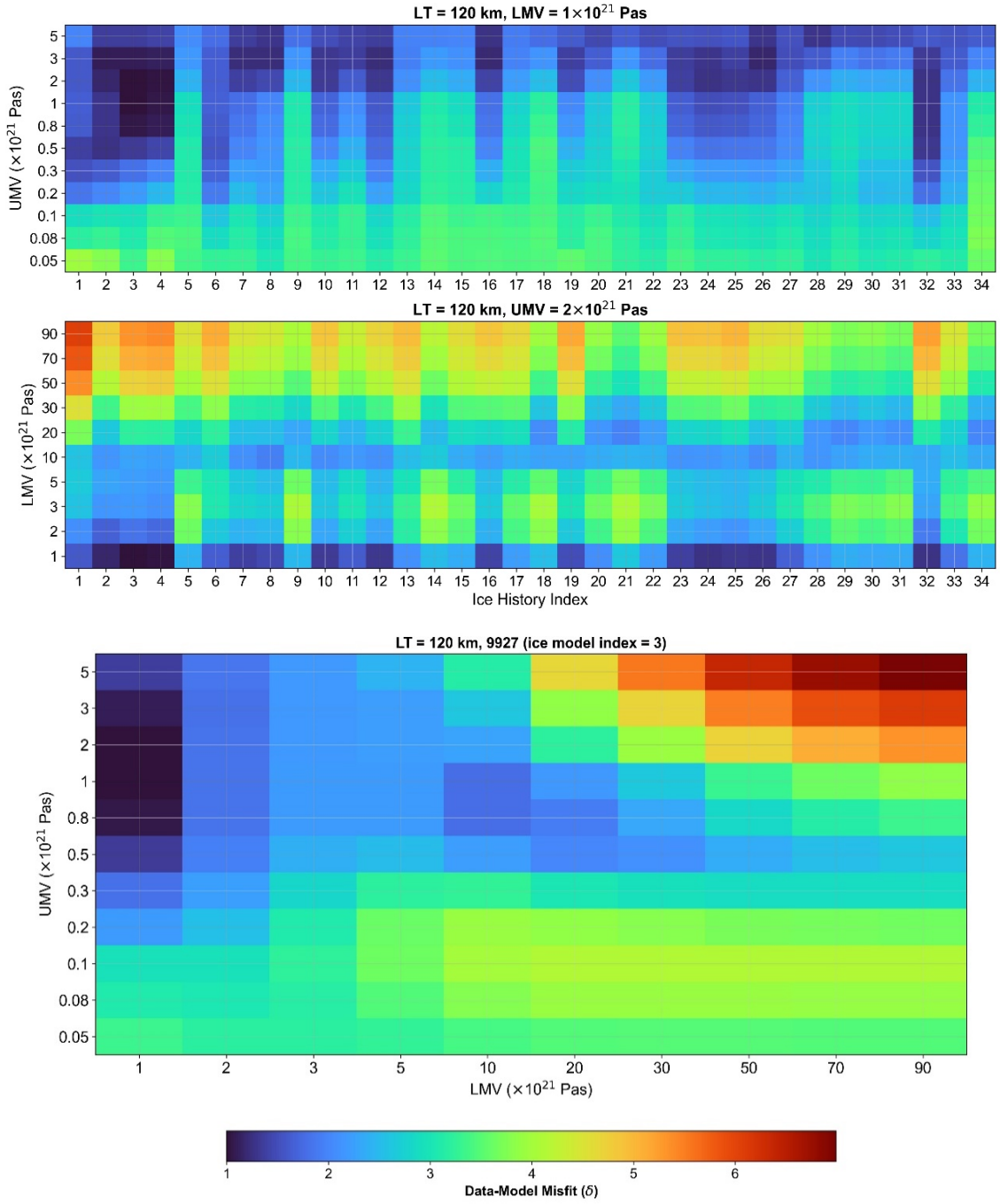
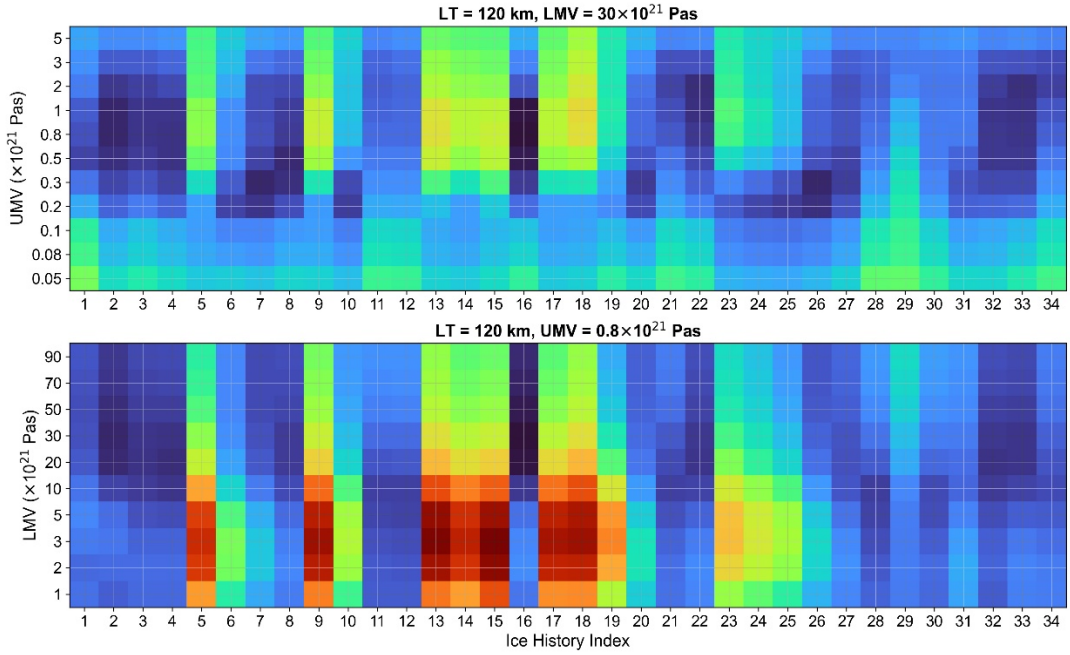


Figure 2.4. Data-model misfit values (δ) for the HUL geographic subset as a function of (from top to bottom) UMV and ice loading history when LMV is constant (10^{21} Pas), LMV and ice loading history when UMV is fixed at 2×10^{21} Pas, and LMV and UMV for GLAC1D-na9927 (ice history index = 3). In all 3 plots, the lithospheric thickness is 120 km. Note that these plots do not necessarily display all the minimum and maximum values of δ for the parameter space considered.

Figure 2.5 indicates the sensitivity of the misfit function (δ) to different model parameters for the NSNM subregion (sites 16-38). The results demonstrate that for the considered parameter ranges, the data-model misfit for this subregion is more sensitive to changes in the deglaciation history compared with the HUL subregion (compare top and middle frames in Figures 2.4 and 2.5; note that the scale bars have different ranges). This reflects the location of NSNM sites being more proximal to the margin of the Laurentide ice sheet compared to HUL sites. The results show that some of the ice models considered (indexes 5, 9, 13-15, 17-18) give very poor fits overall, particularly for relatively low LMV values. In general, intermediate UMV and LMV values result in good fits (specifically, UMV = 0.5-1×10^{21} Pas and LMV = 20-30×10^{21} Pas) (lower frame). This is compatible with the optimal region of UMV-LMV viscosity space when considering the entire dataset (Figure 2.3), indicating that this local minimum is largely associated with the NSNM subregion. Based on the input parameter ranges explored, the optimal Earth model parameter set was determined to be LT = 120 km, UMV = 0.8×10^{21} Pas, LMV = 30×10^{21} Pas, and ice loading history GLAC1D-na1259 (ice model index = 16). Our results suggest a preference for a higher lower mantle viscosity for the NSNM subregion along the eastern coast of Canada (close to the ice margin) compared to the HUL subregion close to the central section (the thickest section) of the ice coverage.



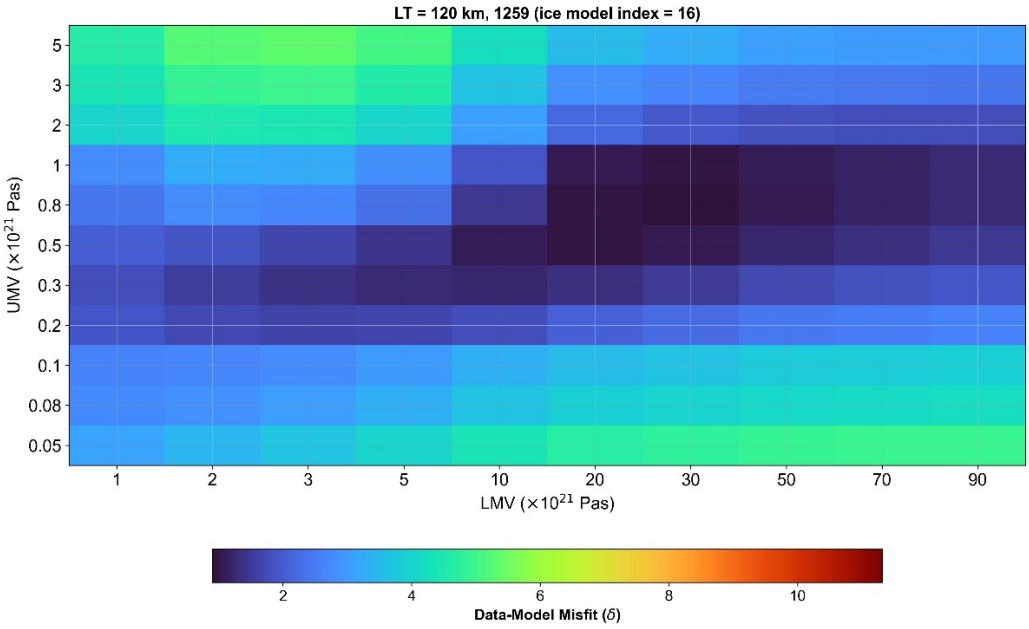


Figure 2.5. Data-model misfit values (δ) for the NSNM geographic subset as a function of (from top to bottom) UMV and ice loading history when LMV is constant (30×10^{21} Pas), LMV and ice loading history when UMV is fixed at 0.8×10^{21} Pas, and LMV and UMV for GLAC1D-na1259 (ice history index = 16). In all 3 plots, the lithospheric thickness is 120 km. Note that these plots do not necessarily display all the minimum and maximum values of δ for the parameter space considered.

The results in this section suggest the presence of lateral variation in Earth viscosity structure between central, near-field regions (HUL) and those closer to ice-marginal, coastal regions (NSNM). This will be explored further in Section 2.3.2 where output from a 3D Earth model is presented.

Table 2.2. Earth model parameter sets for the optimal (minimum misfit) and bounding cases (heuristic approach) for the HUL and NSNM subregions. Accepted model parameter ranges determined from the nominal Bayesian uncertainty analysis are also provided for each subregion. For the HUL region, the LMV values in parentheses appear only once or twice in the accepted sub-ensemble of parameter vectors.

Subregion	**Model**	**Ice loading history**	**LT (km)**	**UMV ($\times10^{21}$ Pas)**	**LMV ($\times10^{21}$ Pas)**
Whole study region	Optimal	GLAC1D-na8005	96	0.3	1
HUL (sites 1-15)	Optimal	GLAC1D-na9927	120	2	1
	Lower bound (heuristic)	ANU	96	0.2	1
	Upper bound (heuristic)	GLAC1D-na1287	71	1	10
	Accepted models/ranges	GLAC1D-na9927, GLAC1D-na9894, GLAC1D-na6439, GLAC1D-na1287, GLAC1D-na1259,	46 - 120	0.2 - 5	1 (2, 30)

		GLAC1D-na6575, GLAC1D-na9852, GLAC1D-na6478, GLAC1D-na8005, GLAC1D-na6318, GLAC1D-na6642, ICE-6G, ANU			
NSNM (sites 16-38)	Optimal	GLAC1D-na1259	120	0.8	30
	Lower bound (heuristic)	GLAC1D-na6053	120	0.8	50
	Upper bound (heuristic)	GLAC1D-na1263	120	0.1	10
	Accepted models/ranges	GLAC1D-na1259, GLAC1D-na8005, GLAC1D-na6575, GLAC1D-na9927, GLAC1D-na9894, GLAC1D-na8025, GLAC1D-na6457, GLAC1D-na6439, GLAC1D-na6244, GLAC1D-na6478, ICE-6G	71 - 120	0.2 - 1	2 - 50

2.3.1.2. Regional parameter estimates and data-model fits

In this section, we assess data-model fits for the optimal and bounding model parameter sets associated with the HUL and NSNM partitioning compared to optimal parameter sets obtained from a more detailed partitioning (i.e., 7 sub-regions, Figures 2.1 and 2.2) to demonstrate that the improvements gained via more detailed partitioning are relatively minor. More importantly, our results show that the model uncertainty bounds for the HUL and NSNM regions bound the optimal model curves (for each subregion; Figure 2.2) at most locations and times.

2.3.1.2.1. Hudson Bay (sites 1-7)

In a broad sense, RSL reconstructions from this subregion have a preference for low LMV and intermediate-high UMV values (see Figure 2.S10, lower frame). This can also be inferred from the middle frame showing the misfit value as a function of ice history and LMV (for the chosen values of LT and UMV) and the upper frame showing the misfit value as a function of ice history and UMV (for the chosen values of LT and LMV). The results show that good fits are achieved by LMV less than about 3×10^{21} Pas and UMV greater than about 0.1×10^{21} Pas. The Earth model parameter vector that produces the best data-model fits is LT = 96 km, UMV = 0.2×10^{21} Pas, LMV = 2×10^{21} Pas, and the ANU ice model (ice history index = 1). However, it is evident from Figure 2.S10 that other parameter vectors can provide good fits to this dataset. For very high UMV and LMV, the data-model fits

associated with all ice history models are poor. In addition, the misfit pattern for Hudson Bay is similar to that for HUL (Figure 2.4) because most SLIPs within HUL (61 out of 64) are from Hudson Bay (and the weight of SLIPs in the misfit analysis is twice that of limiting data points).

Figure 2.6 shows that the optimal model curve for the Hudson Bay dataset (red line) is able to fit the reconstructed RSL records reasonably well, except for a relatively small number of outliers – most notably at sites #3 and #7 where the model fits are poorest. This data-model discrepancy reflects some limitations in both the GIA model (e.g., the presence of lateral viscosity structure) and the RSL dataset (e.g., outliers that require re-assessment such as the anomalously high SLIP at site #3 dating to ~2 ka and the anomalously low SLIP at site #7 dating to ~7 ka). The optimal model curve for this subregion is compatible with the optimal model curve for the larger (HUL) region (orange line) to within the estimated uncertainty bounds at all sites using the heuristic approach (black-dashed lines) and the nominal Bayesian approach (green-dashed lines). A comparison between the optimal model curve obtained from HUL RSL data points and that from only Hudson Bay RSL data points demonstrates that the quality of fit is similar for both parameter sets. The heuristic bounds are wider than the nominal Bayesian bounds in this region, and we note that the heuristic bounds are incompatible with most of the limiting data.

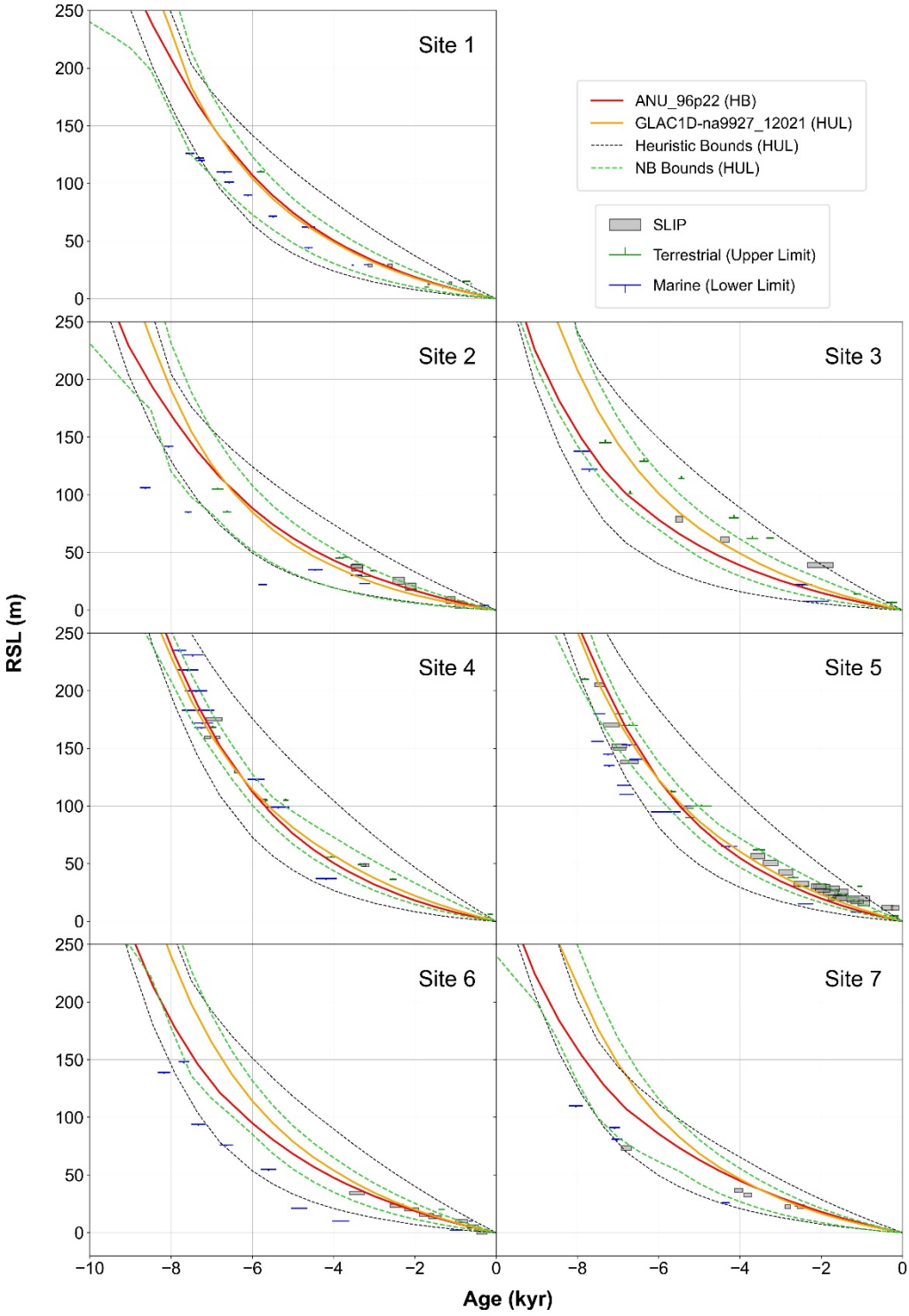


Figure 2.6. The red line shows the optimal modelled RSL estimated from the misfit analysis based on the Hudson Bay (HB) dataset (sites 1-7). The orange line indicates the RSL prediction based on optimal Earth-ice model parameters derived from the analysis of the HUL dataset (sites 1-15, after partitioning the whole study area into two geographic subsets). The upper and lower uncertainty bounds are quantified by the heuristic approach (black-dashed lines) and nominal Bayesian approach (green-dashed lines). RSL curves are plotted at the average position of all RSL data points within each site (see the white diamonds in Figure 2.S2). The dimension of each SLIP box shows ±1σ uncertainty in RSL and age. For limiting data points, the horizontal and vertical bars show ±1σ RSL age uncertainty and one side of the 1σ RSL uncertainty, respectively (the misfit analysis was carried out based on the 1σ uncertainty in RSL and age).

2.3.1.2.2. Ungava Peninsula (sites 8-11)

The sensitivity of the data-model misfit to different model input parameters is shown in Figure 2.S11. Based on the ranges of the input parameters explored, the results indicate that the misfit parameter (δ) has a low sensitivity to changes in UMV and greater sensitivity to changes in LMV and the ice loading history. Compared to Hudson Bay, fewer Earth model parameter sets can fit well the RSL data points, which are mostly limiting data points. For all ice history models, the best fits occur for very low LMV (10^{21} Pas) with some UMV trade-off. Generally speaking, for all ice history models, the data-model fits are poor for very high UMV and LMV as well as for intermediate to high values of UMV and LMV greater than ~2×10^{21} Pas. We note the existence of a local minimum for LMV greater than ~50×10^{21} Pas and UMV of 0.8-1×10^{21} Pas for some ice models (including the optimal model, GLAC1D-na1415).

The optimal parameters for this subregion are LT = 71 km, UMV = 0.5×10^{21} Pas, LMV = 10^{21} Pas, and ice model GLAC1D-na1415 (ice history index = 19). The optimum data-model curve (red line in Figure 2.7) shows that there is a good agreement between the model predictions and observations: the optimal model RSL curve fits well all limiting data points (except for a marine limiting data point at ~4 ka at site #9). The data require a strong curvature of the RSL predictions in the late Holocene, hence the preference for low LMV values. The optimal model curve for Ungava Peninsula (red line) is generally not compatible with the optimal HUL model curve (orange line) when considering the nominal Bayesian uncertainties, but lies close to the lower heuristic bounding model curve at most sites and for most of the time period considered. According to Figure 2.7, at some sites, the optimal Ungava Peninsula model curve provides relatively better fits to some limiting data points (e.g., some terrestrial limiting data points during the late Holocene at site #8) and the regional (HUL) optimal model curve (orange line) can be more compatible with some other RSL data points (e.g., a marine limiting data point and a SLIP at ~4 ka at sites #9 and #11, respectively). Since the number of SLIPs is limited for Ungava Peninsula (only 3 SLIPs at site #11), the heuristic bounding models are not very accurate and are incompatible with some limiting data points. We also note that the heuristic bounds also cross at sites #10 and #11 which does limit their utility for the older data at these sites. This aspect of the heuristic approach relates to the bounds being based on single model runs (parameter sets) that are computed using observations from the larger HUL region. The nominal Bayesian approach avoid this issue but with the caveat that the bounds generally represent output from multiple model runs (based on different parameter sets).

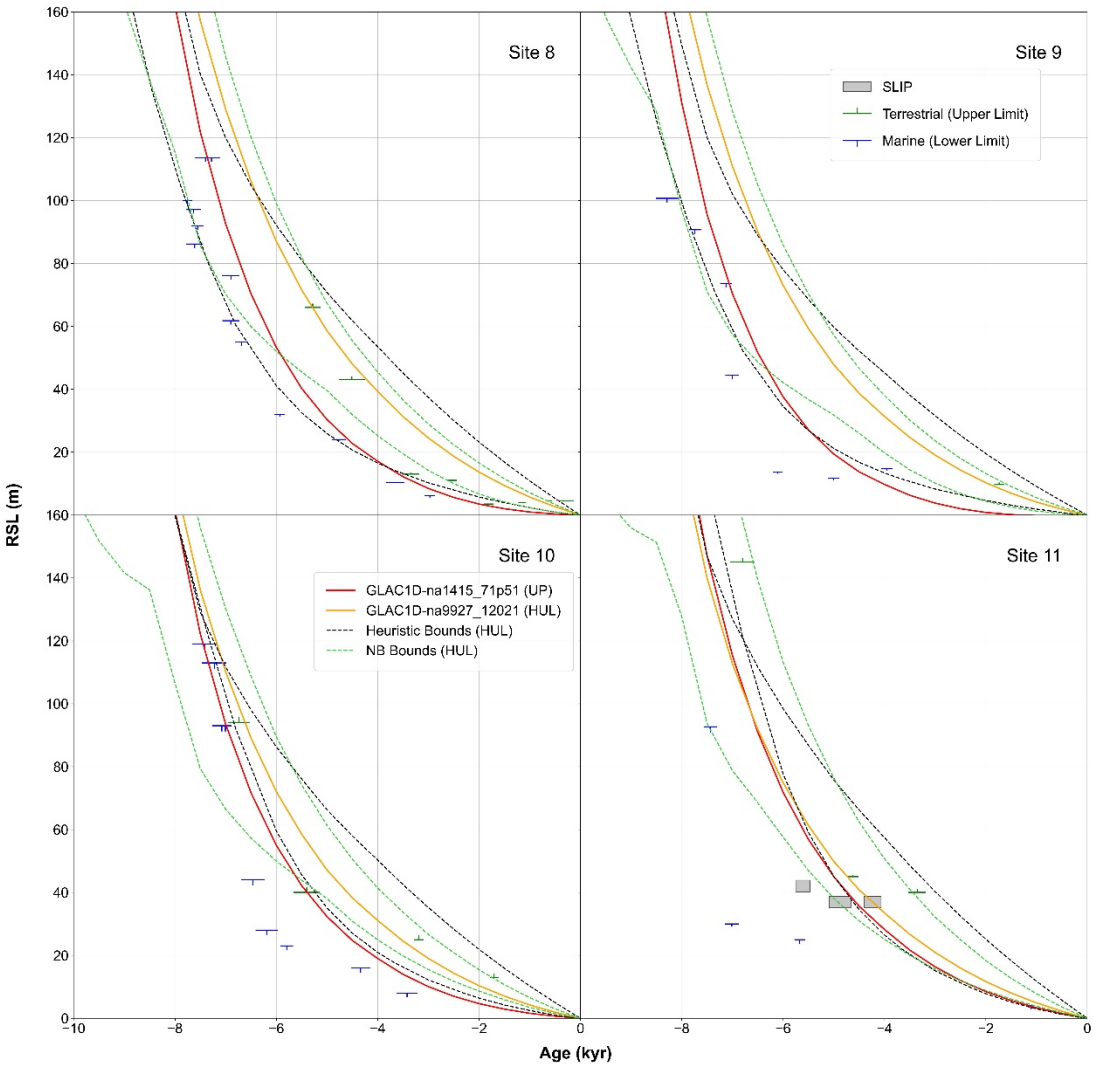


Figure 2.7. The red line shows the optimal modelled RSL estimated from the misfit analysis based on the Ungava Peninsula (UP) dataset (sites 8-11). The orange line indicates the RSL prediction based on optimal Earth-ice model parameters derived from the analysis of the HUL dataset (sites 1-15, after partitioning the whole study area into two geographic subsets). The upper and lower uncertainty bounds are quantified by the heuristic approach (black-dashed lines) and nominal Bayesian approach (green-dashed lines). RSL curves are plotted at the average position of all RSL data points within each site (see the white diamonds in Figure 2.S2). The dimension of each SLIP box shows ±1σ uncertainty in RSL and age. For limiting data points, the horizontal and vertical bars show ±1σ RSL age uncertainty and one side of the 1σ RSL uncertainty, respectively (the misfit analysis was carried out based on the 1σ uncertainty in RSL and age).

2.3.1.2.3. Labrador (sites 12-15)

In this subregion, model constraints are based solely on limiting data points. According to Figure 2.S12, the data-model misfit parameter is less sensitive to changes in UMV and more sensitive to variations in LMV and the deglaciation history. Generally speaking, the better fits are found at very high UMV and LMV values as well as low LMV (1-5×10^{21} Pas) and UMV of 0.2-0.3×10^{21} Pas. The intermediate-high LMV and low-intermediate UMV values, along with low LMV (2-5×10^{21} Pas) and high UMV values (2-5×10^{21} Pas), produce poor fits. The optimal model input parameters are LT = 96 km, UMV = 0.2×10^{21} Pas, LMV = 2×10^{21} Pas, and ice model GLAC1D-na1263 (ice history index = 9).

Figure 2.8 indicates that the optimal GIA model curve for Labrador (red line) provides good a fit to the data with all marine limiting data points being satisfied. There is some incompatibility with some terrestrial limiting data points, however (e.g., a terrestrial limiting data point at ~5.5 ka at site #14). The heuristic model bounds define a narrower range compared to the nominal Bayesian ones at sites #12 and #13. Moreover, the optimal model curve for Labrador lies relatively close to the lower heuristic bounding model at sites #12 and #13. The optimal model curve for Labrador is compatible withs the optimum regional (HUL) curve at sites #12, #13, and #15 and for most of the Holocene at site #14 when considering the nominal Bayesian uncertainty bounds. These uncertainty bounds are not completely compatible with limiting data points (e.g., at site #15, the upper bound is not consistent with some terrestrial limiting data points in the middle Holocene).

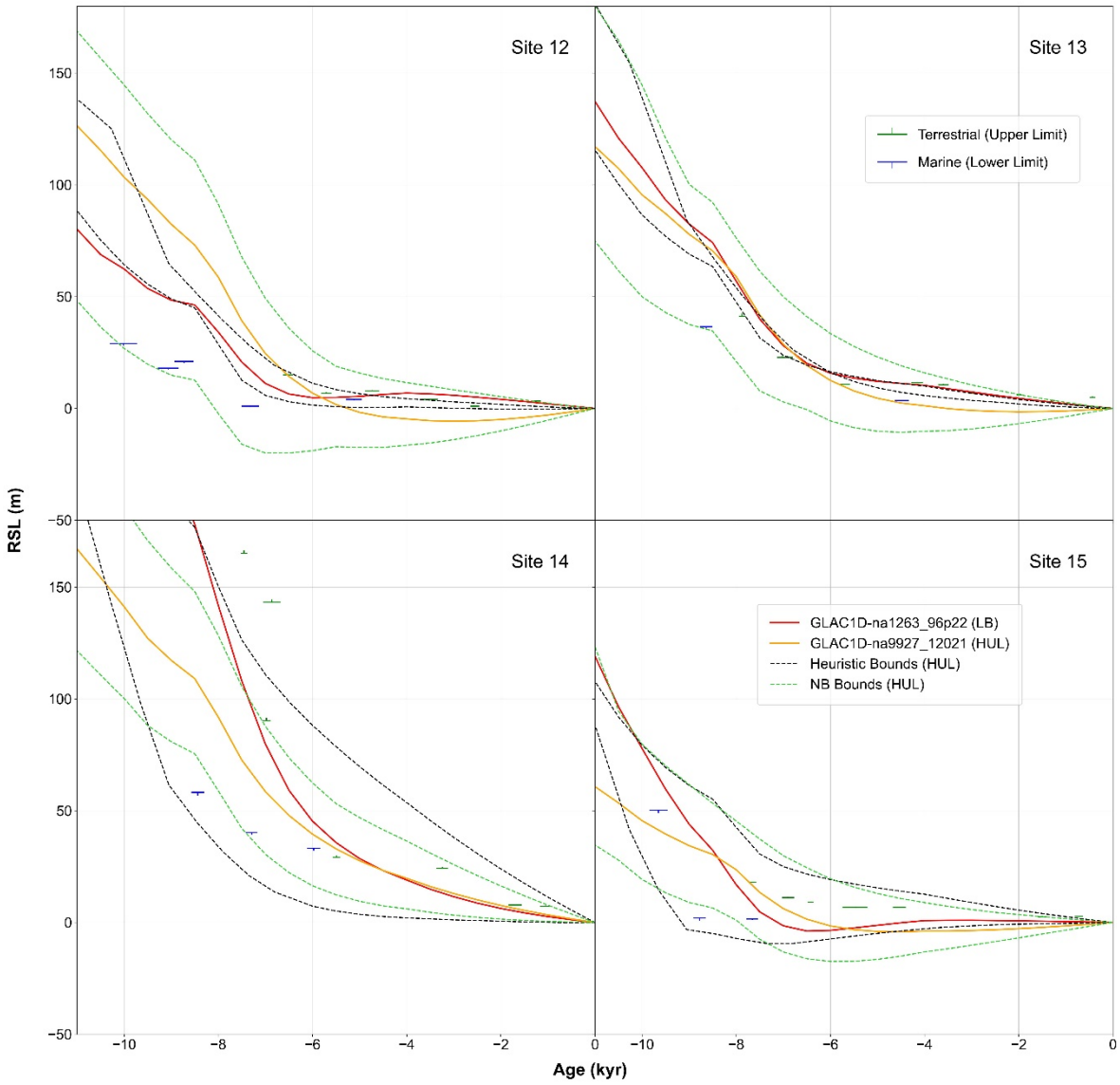


Figure 2.8. The red line shows the optimal modelled RSL estimated from the misfit analysis based on the Labrador (LB) dataset (sites 12-15). The orange line indicates the RSL prediction based on optimal Earth-ice model parameters derived from the analysis of the HUL dataset (sites 1-15, after partitioning the whole study area into two geographic subsets). The upper and lower uncertainty bounds are quantified by the heuristic approach (black-dashed lines) and nominal Bayesian approach (green-dashed lines). RSL curves are plotted at the average position of all RSL data points within each site (see the white diamonds in Figure 2.S2). The dimension of each SLIP box shows ±1σ uncertainty in RSL and age. For limiting data points, the horizontal

and vertical bars show ±1σ RSL age uncertainty and one side of the 1σ RSL uncertainty, respectively (the misfit analysis was carried out based on the 1σ uncertainty in RSL and age).

2.3.1.2.4. Newfoundland (sites 16-20)

Figure 2.S13 shows the sensitivity of the data-model misfit parameter (δ) to changes in each model input parameter. Compared to the subregions mentioned above, the misfit values for this subregion are more sensitive to changes in the ice loading history. As noted above, this reflects the proximity of this location to the ice margin when the ice sheet was at its maximum extent. Moreover, the misfit parameter is less sensitive to changes in LMV relative to variations in UMV. Most ice history models bring about poor fits for UMV of 0.2×10^{21} Pas and less (for all LMV values) as well as low-intermediate LMV and intermediate-high UMV values. In a broad sense, the intermediate UMV space ($0.3\text{-}0.5\times10^{21}$ Pas; for all LMV values) and high UMV and LMV values can result in good fits. The optimal model parameters in this case are: LT = 120 km, UMV = 0.5×10^{21} Pas, LMV = 30×10^{21} Pas, and ice loading history ICE-6G (ice model index = 2).

The model RSL curve associated with the best Earth model parameter set for Newfoundland (red line in Figure 2.9) provides good fits to RSL data points at all sites, except for some inconsistencies. The model cannot capture several marine limiting data points at two sites: #16, during ~8-12 ka; and #18, during ~12-16 ka. It should be noted that these misfits are mainly systematic rather than the existence of some. single, isolated data points as outliers and, therefore, could reflect structural error in the model. It is evident that the optimal model curve obtained from the NSNM dataset (orange line) cannot fit RSL data points at site #16, while the optimal parameter set when considering only the Newfoundland dataset (red line) provides a better fit (the main difference between two optimal models arises from the ice loading history model). At sites #17 and #19, both optimal models (red and orange lines) have the same quality of fit (a SLIP in site #17 at ~12 ka cannot be fit by either optimal model). At site #18, the optimal model curve based on the NSNM dataset provides much better fits to marine limiting data points. Moreover, at site #20, most of the marine limiting data points before the Holocene period are more compatible with the red line. As for Ungava Peninsula (Section 2.3.1.2.2), the heuristic bounding models cross at each site, limiting their utility. Finally, the optimal model is entirely compatible with the optimum regional curve (associated with NSNM) when considering the nominal Bayesian uncertainty bounds.

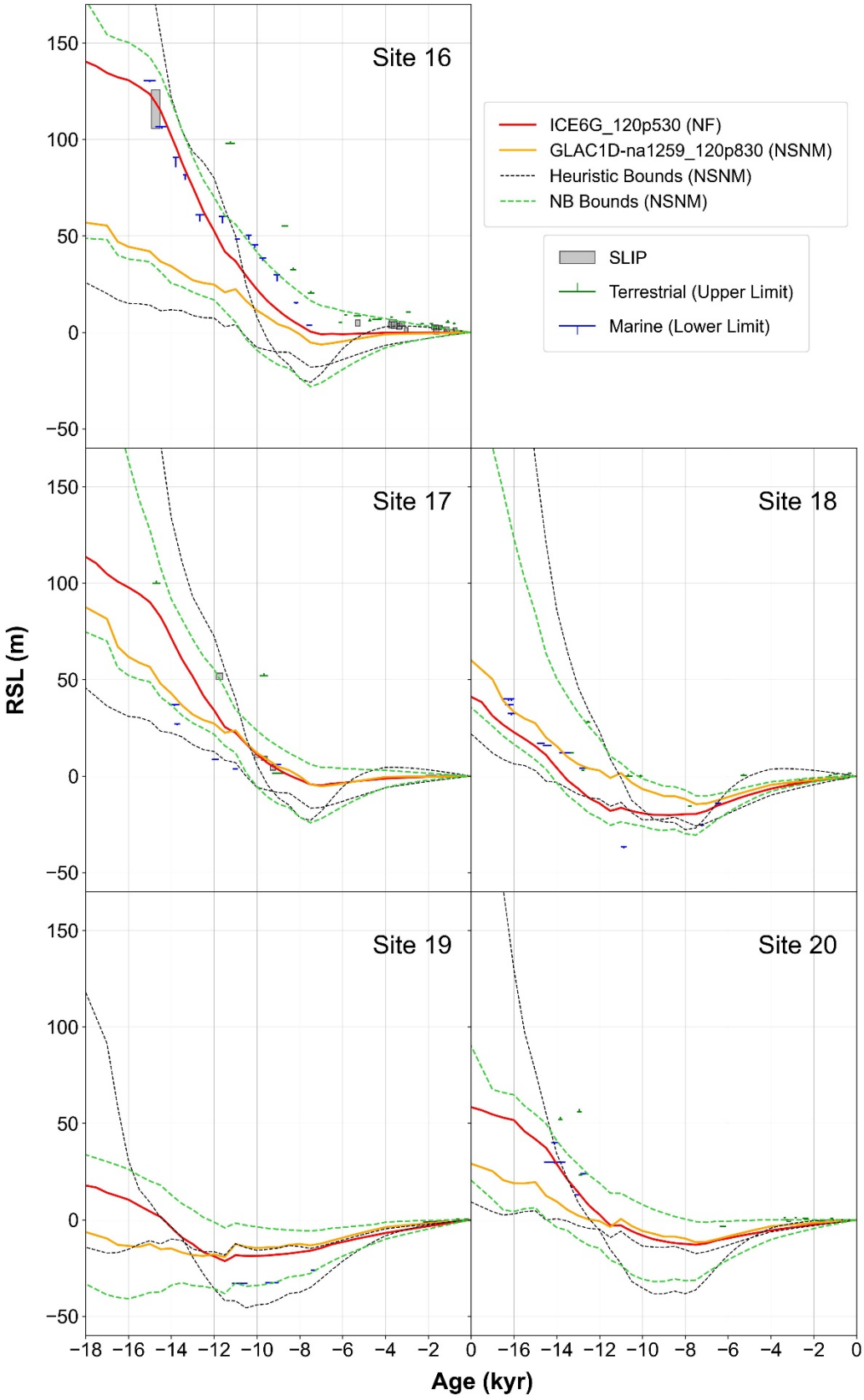


Figure 2.9. The red line shows the optimal modelled RSL estimated from the misfit analysis based on the Newfoundland (NF) dataset (sites 16-20). The orange line indicates the RSL prediction based on optimal Earth-ice model parameters derived from the analysis of the NSNM dataset (sites 16-38, after partitioning the whole

study area into two geographic subsets). The upper and lower uncertainty bounds are quantified by the heuristic approach (black-dashed lines) and nominal Bayesian approach (green-dashed lines). RSL curves are plotted at the average position of all RSL data points within each site (see the white diamonds in Figure 2.S2). The dimension of each SLIP box shows ±1σ uncertainty in RSL and age. For limiting data points, the horizontal and vertical bars show ±1σ RSL age uncertainty and one side of the 1σ RSL uncertainty, respectively (the misfit analysis was carried out based on the 1σ uncertainty in RSL and age).

2.3.1.2.5. St. Lawrence Corridor (sites 21-24)

According to Figure 2.S14, the data-model misfit patterns for this subregion are broadly similar to those for Newfoundland (see Figure 2.S13): good fits are limited to the intermediate UMV space (0.2-0.5×10^{21} Pas; for all LMV values) and relatively high UMV and LMV values. The optimal Earth model parameters for this subregion are estimated to be LT = 46 km, UMV = 0.3×10^{21} Pas, LMV = 10×10^{21} Pas, and ice loading history GLAC1D-na6478 (ice history index = 7). The poorest fits occur at UMV of 0.1×10^{21} Pas and less (for all LMV values) as well as low-intermediate LMV and intermediate-high UMV values. Furthermore, the sensitivity of data-model misfit to changes in LMV is small compared to variations in UMV.

The optimal GIA model curve for this subregion (red line in Figure 2.10) can fit reasonably well the majority of RSL data points, especially limiting data points. However, matching the relatively stable RSL values during the mid-to-late Holocene is a challenge. The relatively broad nominal Bayesian uncertainty bounds (green dashed lines in Figure 2.10) are related to trying to get as close as possible the older SLIPs while still being consistent with limiting data points. Moreover, the optimal model curve for this subregion (red line) is compatible with the NSNM optimum curve (orange line) to within the uncertainty bounds at all sites estimated from the nominal Bayesian approach and all sites except site #24 using the heuristic approach. The optimal model curve obtained from the analysis of the NSNM dataset (orange line) provides relatively better fits to SLIPs within the St. Lawrence Corridor (specifically at sites #21 and #22). Furthermore, both optimal models result in compatible fits to limiting data points, especially the one derived from the misfit analysis on the St. Lawrence Corridor dataset, which produces better fits to marine limiting data points at sites #22 and #24. The nominal Bayesian upper bound is more consistent with the terrestrial limiting data points, but the lower bounds from both approaches provide the same compatibility with marine limiting data points (the heuristic lower bound is more compatible with marine limiting data points at site #21).

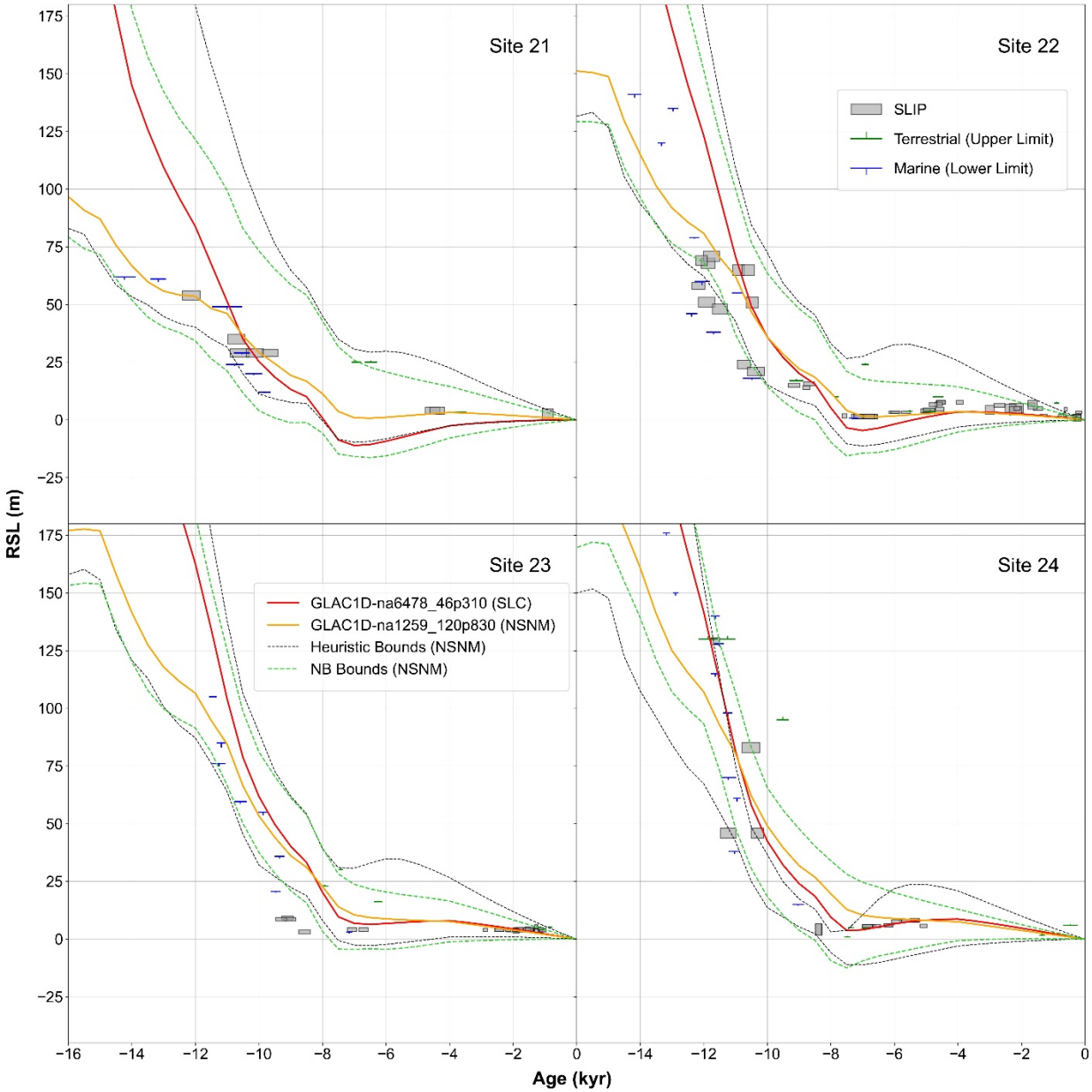


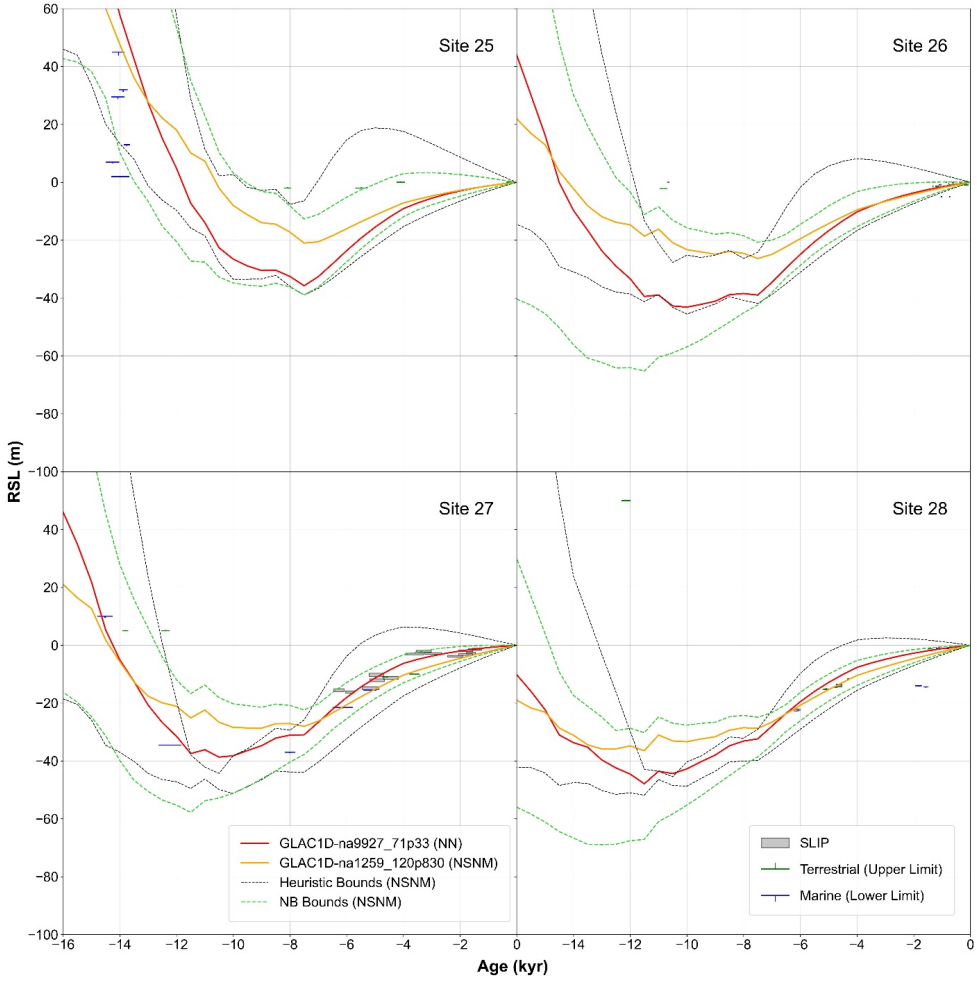
Figure 2.10. The red line shows the optimal modelled RSL estimated from the misfit analysis based on the St. Lawrence Corridor (SLC) dataset (sites 21-24). The orange line indicates the RSL prediction based on optimal Earth-ice model parameters derived from the analysis of the NSNM dataset (sites 16-38, after partitioning the whole study area into two geographic subsets). The upper and lower uncertainty bounds are quantified by the heuristic approach (black-dashed lines) and nominal Bayesian approach (green-dashed lines). RSL curves are plotted at the average position of all RSL data points within each site (see the white diamonds in Figure 2.S2). The dimension of each SLIP box shows ±1σ uncertainty in RSL and age. For limiting data points, the horizontal and vertical bars show ±1σ RSL age uncertainty and one side of the 1σ RSL uncertainty, respectively (the misfit analysis was carried out based on the 1σ uncertainty in RSL and age).

2.3.1.2.6. New Brunswick and Nova Scotia (sites 25-34)

As for other subregions close to the Laurentide ice sheet margin at maximum extent, the data-model misfit plots (Figure 2.S15) indicate pronounced sensitivity to changes in the ice history. In addition, the data-model misfit parameter is less sensitive to changes in LMV space in comparison with variations in UMV. Intermediate values of UMV (especially for low-intermediate LMV space) and relatively high

LMV and UMV values generally provide good fits when considering all ice history models. Similar to Newfoundland and the St. Lawrence Corridor, UMV values less than 0.2×10^{21} Pas (for all LMV values) along with low-intermediate LMV and intermediate-high UMV values result in poor data-model fits. The optimal model parameters are LT = 71 km, UMV = 0.3×10^{21} Pas, LMV = 3×10^{21} Pas, and ice loading history GLAC1D-na9927 (ice history index = 3).

Limiting data points play an important role in constraining the GIA signal during the early-Holocene because most SLIPs are concentrated in the mid- to late-Holocene. The optimal model RSL curve for this subregion (red line in Figure 2.11) can fit well both SLIPs and limiting data points at all sites. This optimal model curve is completely compatible with the regional optimum curve associated with the larger NSNM region to within the nominal Bayesian uncertainty bounds at all sites and is also captured by the heuristic bounding models for most of the time periods during Holocene (at site #31, the heuristic bounds are relatively narrower than the nominal Bayesian ones). The two optimal models (red and orange lines) result in a broadly similar quality of fit across this subregion. In terms of SLIPs, both optimal models bring about the same quality of fit but the red line can better fit some SLIPs during the late Holocene, especially at site #29. In terms of limiting data, there are examples where the parameter set tuned to the larger dataset (NSNM) does a better job. For instance, a marine limiting data point at ~12 ka at site #30 and a terrestrial limiting data point at ~3.5 ka at site #27 are not fit by the red line. The nominal Bayesian bounds capture all SLIPs within each site (the heuristic bounds cannot capture two SLIPs at ~8 ka in site #30) and are highly compatible with limiting data points (although note that the nominal Bayesian lower bound lies below some marine limiting data points at ~14 ka at site #25).



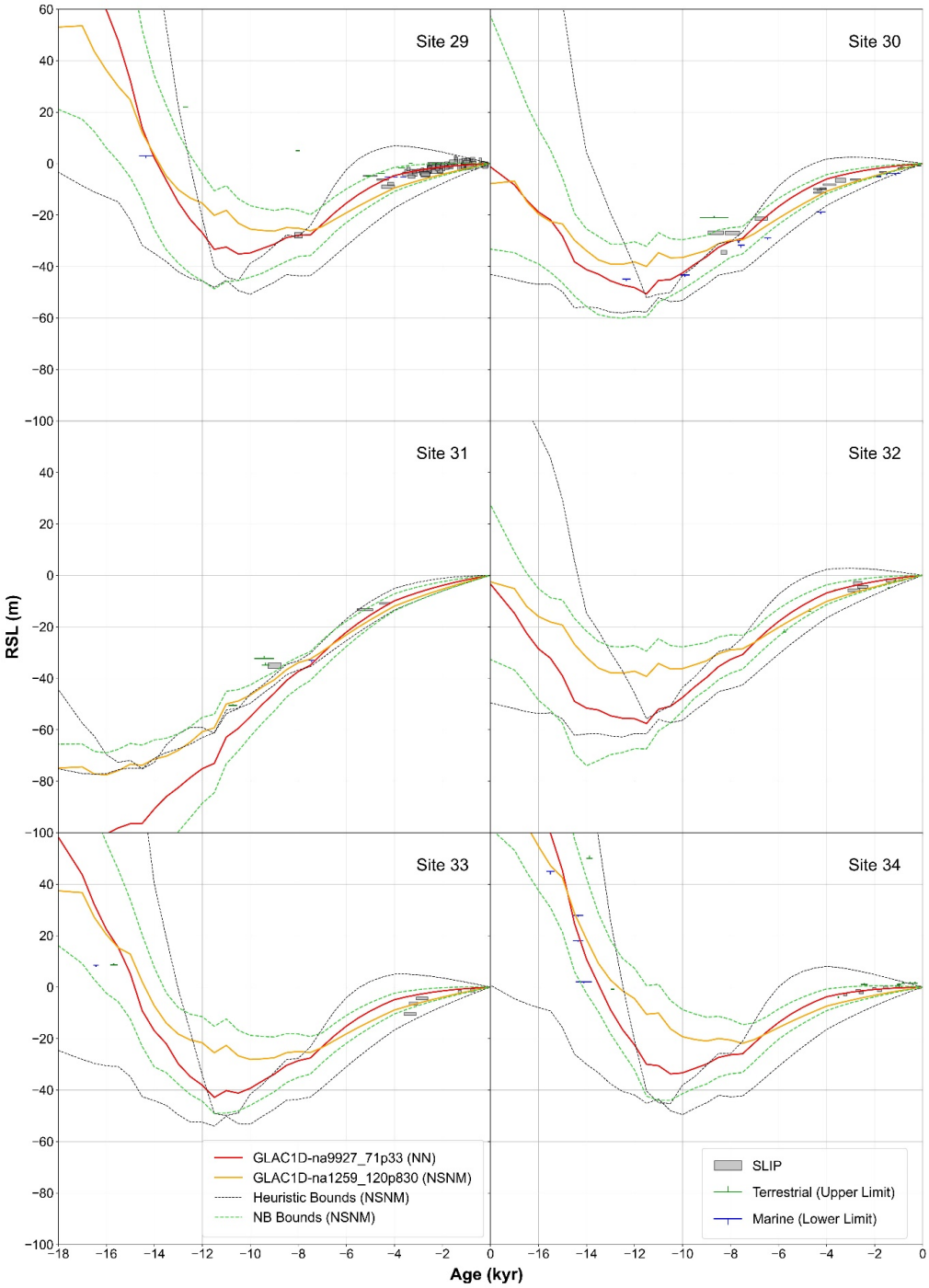


Figure 2.11. The red line shows the optimal modelled RSL estimated from the misfit analysis based on the New Brunswick and Nova Scotia (NN) dataset (sites 25-34). The orange line indicates the RSL prediction based on optimal Earth-ice model parameters derived from the analysis of the NSNM dataset (sites 16-38, after partitioning the whole study area into two geographic subsets). The upper and lower uncertainty bounds are quantified by the heuristic approach (black-dashed lines) and nominal Bayesian approach (green-dashed lines). RSL curves are plotted at the average position of all RSL data points within each site (see the white diamonds in Figure 2.S2). The dimension of each SLIP box shows ±1σ uncertainty in RSL and age. For limiting data points, the horizontal and vertical bars show ±1σ RSL age uncertainty and one side of the 1σ RSL uncertainty, respectively (the misfit analysis was carried out based on the 1σ uncertainty in RSL and age).

2.3.1.2.7. Maine and Massachusetts (sites 35-38)

In this subregion, the data-model misfit parameter (δ) is relatively more sensitive to changes in LMV relative to variations in UMV space (see Figure 2.S16). Due to proximity to the ice margin, this subregion is also relatively sensitive to changes in deglaciation history. The poorest fits for each ice loading history happen for high UMV and low-intermediate LMV values. Generally, high UMV and LMV space bring about the best fits, and there are some regions of viscosity space where decent fits can be achieved when considering all ice models (e.g., for intermediate UMV and low-intermediate LMV values). The minimum misfit is obtained with LT = 71 km, UMV = 3×10^{21} Pas, LMV = 50×10^{21} Pas, and ice loading history GLAC1D-na9894 (ice history index = 4).

The optimal model curve for this subregion generally fits well most RSL data points (see the red line in Figure 2.12). However, in our dataset for this subregion, most SLIPs are concentrated during the mid-to-late Holocene, so they are more straightforward to fit. Roughly speaking, the optimal model RSL curve can fit all limiting data points, but there are a few misfits in terms of SLIPs, most notably at sites #36 and #37, where the red model curve sits too low at, respectively, 6-4 ka and 1-4 ka. In this area the best-fitting regional (NSNM) parameter set produces a curve (orange line) that sits consistently below the red line. This demonstrates the limitation when a larger dataset is considered and so the fits are not optimized, in this case, for Maine and Massachusetts. However, it is important to note that the calculated uncertainty bounds (dashed lines) envelope the red line at sites #36 and #37 and at sites #35 and #38 for most of the time period considered.

Although the heuristic bounds capture all SLIPs within each site, they are not entirely compatible with limiting data points (as discussed in Section 2.2.3.1, the heuristic bounds were estimated using only SLIPs within a given subregion, and limiting data points were used as a useful check to determine whether the estimated lower and upper bounds are compatible with marine and terrestrial limiting data points, respectively). Similarly, the nominal Bayesian bounds can capture all SLIPs within each site (except for the one at ~6 ka in site #35). In contrast to the heuristic upper bound, the nominal Bayesian upper bound is compatible with most terrestrial limiting data points. However, the nominal Bayesian lower bound is not totally consistent with all marine limiting data points (e.g., with two marine limiting data points at ~8 ka in site #36).

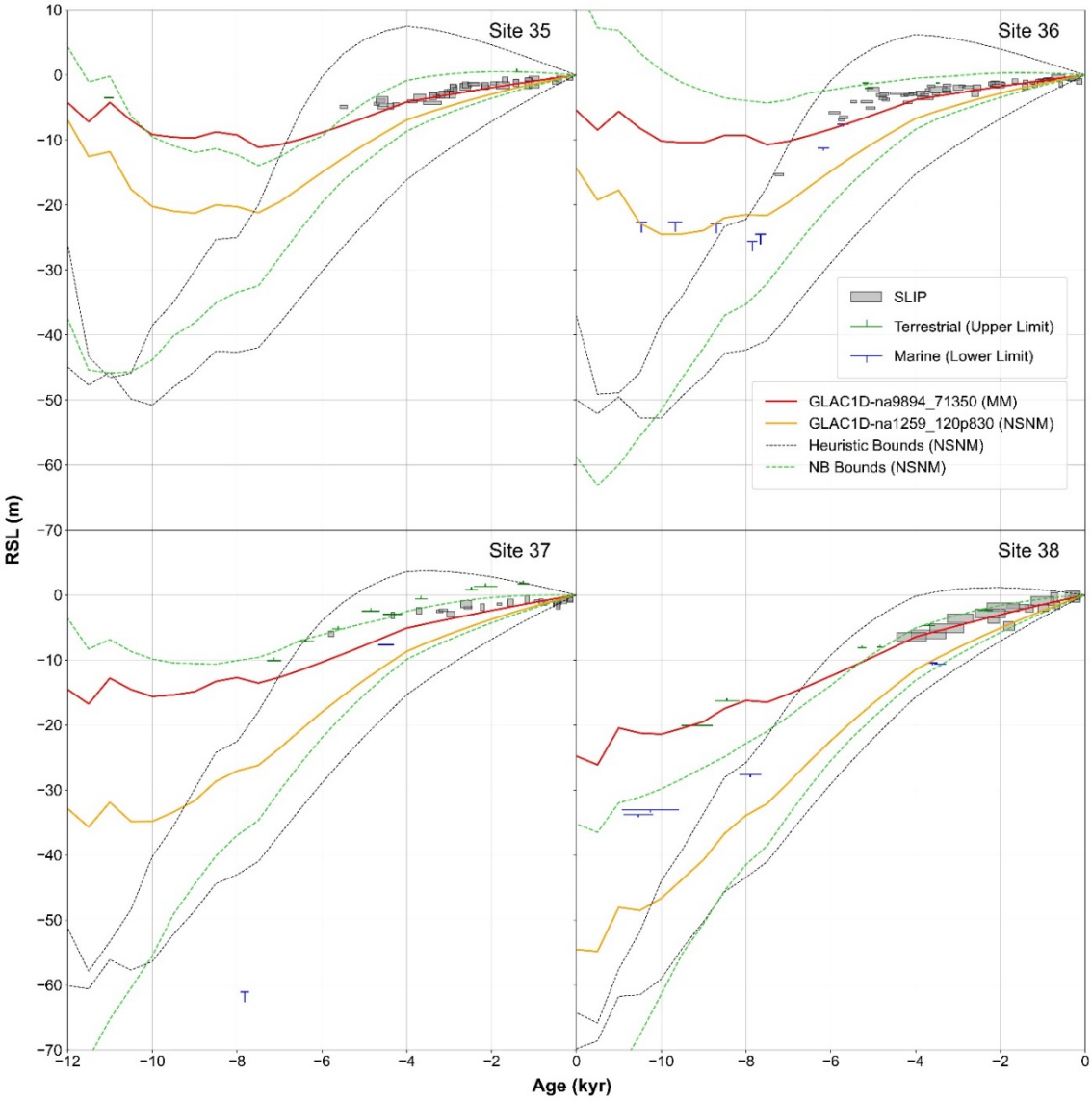


Figure 2.12. The red line shows the optimal modelled RSL estimated from the misfit analysis based on the Maine and Massachusetts (MM) dataset (sites 35-38). The orange line indicates the RSL prediction based on optimal Earth-ice model parameters derived from the analysis of the NSNM dataset (sites 16-38, after partitioning the whole study area into two geographic subsets). The upper and lower uncertainty bounds are quantified by the heuristic approach (black-dashed lines) and nominal Bayesian approach (green-dashed lines). RSL curves are plotted at the average position of all RSL data points within each site (see the white diamonds in Figure 2.S2). The dimension of each SLIP box shows ±1σ uncertainty in RSL and age. For limiting data points, the horizontal and vertical bars show ±1σ RSL age uncertainty and one side of the 1σ RSL uncertainty, respectively (the misfit analysis was carried out based on the 1σ uncertainty in RSL and age).

2.3.2. 3D Earth model analysis

We performed two runs based on one of the optimal Earth model parameter sets obtained for the whole study region from the 1D GIA modelling and data-model misfit analysis: ice history model = ICE-6G, LT = 71 km, UMV = 0.5×10^{21} Pas, LMV = 2×10^{21} Pas. This 1D viscosity profile was used as a reference on which to superimpose lateral viscosity structure using two shear-wave tomographic models (abbreviated to S40RTS and S40RTS_SL2013; see Section 2.2.4). We note that this viscosity

model is not dissimilar to the model used as a reference for developing ICE-6G (i.e., VM5a; Peltier et al., 2015), although it does not include the high viscosity asthenosphere in the VM5a model.

Figure 2.13 illustrates the differential RSL at 10 ka derived from subtracting the 1D model output from the 3D model output based on the S40RTS_SL2013 tomographic model, thus isolating the effect of lateral viscosity structure in our study region. Based on these results, Hudson Bay, Ungava Peninsula, and Labrador show that lateral structure results in a negative shift in predicted RSL, whereas a positive shift is evident in Newfoundland, St. Lawrence Corridor, New Brunswick and Nova Scotia, and Maine and Massachusetts. Figure 2.14 demonstrates that the differences in the estimated RSL values between both 3D models can be significant (a few 10s of meters at 10 ka) in our study region, although they are smaller than the 3D versus 1D RSL differences (Figure 2.13). The time evolution of modelled RSL based on the optimal 1D model and the two 3D models is shown in Figure 2.S17. The results in Figures 2.13 and 2.S17 indicate that the influence of lateral structure can be large and can vary considerably through time. For much of the time period spanned by the data, the differential signal (Figure 2.13) is negative in the continental interior and positive in coastal areas (particularly Newfoundland, St. Lawrence Corridor, New Brunswick and Nova Scotia, and Maine and Massachusetts). This pattern correlates strongly with the data partitioning (into the HUL and NSNM regions) to improve the 1D Earth model fits. Thus, our 3D Earth model results provide independent support for this partitioning.

Table 2.3 provides data-model misfit results for the different data subsets (left column) and output from three different GIA models: the 1D Earth model with parameter set optimized for the entire dataset and the ICE-6G deglaciation history (details provided in caption), and output from the two 3D model experiments described in this section. The results in Table 2.3 indicate that the optimal 1D GIA model generally provides better fits (compared to 3D model output) in most regions. This is not surprising as the Earth model parameters for the 1D case are optimized but this is not necessarily the case for the 3D models. Specifically, the assumed 1D viscosity profile might not provide optimal fits for the chosen lateral viscosity models. This issue is considered in Love et al. (2024).

Improved fits are obtained for the 1D model for the entire dataset and each data type (SLIPs, marine, and terrestrial limiting data points; Table 2.3, second row). The 3D model runs do yield better fits in certain subregions compared to the optimized 1D model output. Regarding SLIPs, the utilization of 3D GIA modeling leads to improved fits for Hudson Bay, Ungava Peninsula, and HUL. In Maine and Massachusetts, when using the S40RTS_SL2013 tomographic model, the quality of fit to SLIPs is comparable to that obtained from 1D modeling. In terms of limiting data points, the 3D runs yield superior fits to marine limiting data points in the majority of subregions. Notably, in the St. Lawrence Corridor and Maine and Massachusetts subregions, the RSL output from 3D GIA modeling exhibits complete alignment with marine limiting data points, which differs from the 1D model. However, when considering terrestrial limiting data points, the 1D GIA model results outperform those from the 3D runs. The very poor fit of the S40RTS 3D run to terrestrial limiting data points in Maine and Massachusetts is mainly due to the single terrestrial limiting data point at ~11 ka and -3 m at site #35 (the uncertainty on this point is very small and so any misfit is weighted highly). In general, considering the total misfit parameter, although the 1D model fits better all RSL data points for most subregions, the 3D runs provide improved fits for Ungava Peninsula (based on both seismic tomographic models) and Maine and Massachusetts (based on the S40RTS_SL2013 tomographic model).

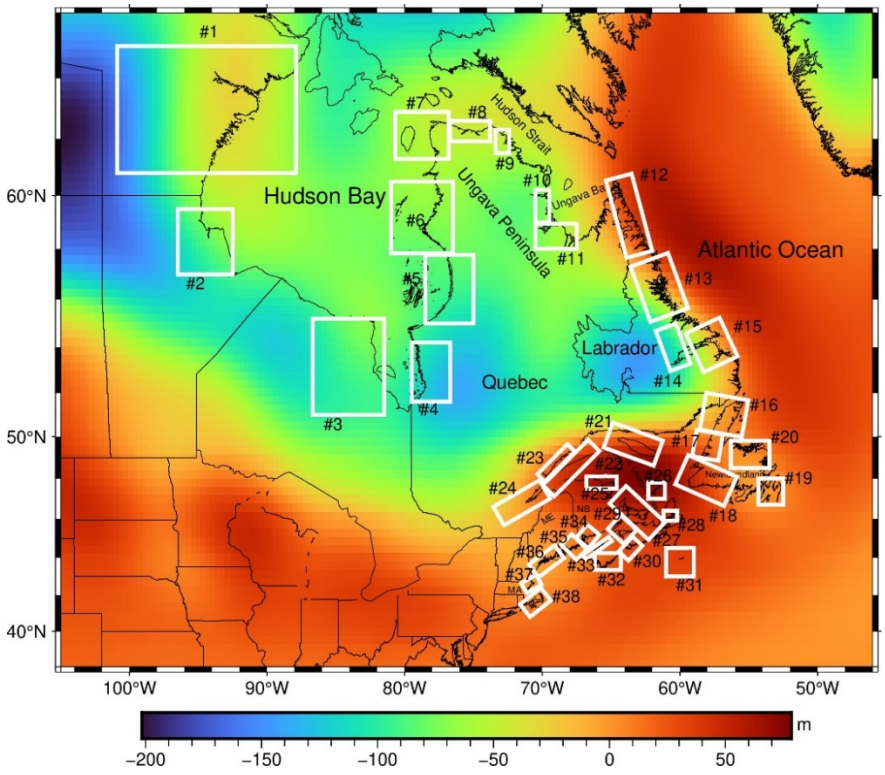


Figure 2.13. Differential RSL at 10 ka derived from subtraction of the RSL output from the 1D model (ice history model = ICE-6G, LT = 71 km, UMV = 0.5×10^{21} Pas, LMV = 2×10^{21} Pas) to that from the 3D model with lateral viscosity variations determined via S40RTS_SL2013 superimposed on the same 1D structure.

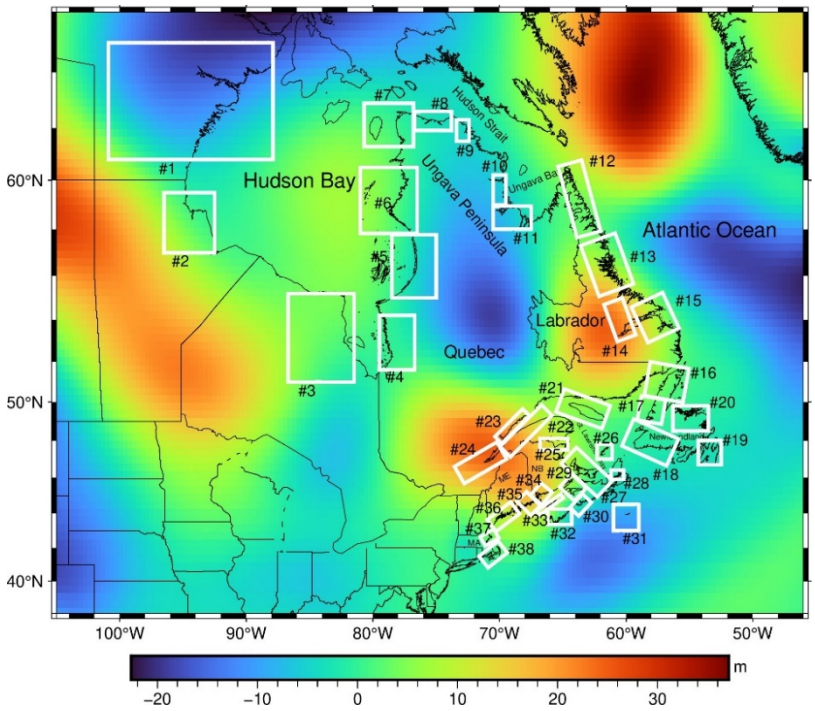


Figure 2.14. Difference in the estimated RSL values at 10 ka between the two 3D runs (see text for details).

Table 2.3. Data-model misfit parameter (δ), inferred from the misfit analysis based on the 1σ uncertainty values for observations (RSL and age), associated with the 1D model (ice history model = ICE-6G, LT = 71 km, UMV = 0.5×10^{21} Pas, LMV = 2×10^{21} Pas) and two 3D runs using S40RTS (3D model 1) and S40RTS_SL2013 (3D model 2), superimposed on the 1D profile (ML and TL stand for marine and terrestrial limiting data points, respectively).

Region	1D model				3D model 1				3D model 2			
	δ^{SLIPs}	δ^{ML}	δ^{TL}	δ^{Total}	δ^{SLIPs}	δ^{ML}	δ^{TL}	δ^{Total}	δ^{SLIPs}	δ^{ML}	δ^{TL}	δ^{Total}
Whole study region	0.222	0.263	1.152	0.929	0.435	0.421	2.934	2.113	0.442	0.39	2.089	1.681
HUL	0.641	0.108	1.637	1.514	0.499	0.911	1.927	1.918	0.472	0.829	1.791	1.782
NSNM	0.241	0.459	1.576	1.258	0.516	0.23	4.688	2.975	0.529	0.189	3.253	2.250
Hudson Bay	0.613	0.210	1.619	1.527	0.505	1.761	1.085	1.929	0.456	1.621	0.877	1.705
Ungava Peninsula	4.618	0	4.966	7.102	2.823	0	5.628	5.637	3.389	0	5.621	6.199
Labrador	-	0	3.228	1.614	-	0	4.636	2.318	-	0	4.135	2.067
Newfoundland	0.810	0.678	2.537	2.417	0.935	0.566	5.675	4.055	0.886	0.697	5.440	3.954
St. Lawrence Corridor	0.648	0.010	1.239	1.273	1.501	0	11.40	7.203	1.374	0	8.797	5.772
New Brunswick and Nova Scotia	0.324	0.756	3.590	2.497	0.609	0.488	7.253	4.479	0.896	0.064	6.311	4.084
Maine and Massachusetts	0.310	2.569	0	1.594	0.420	0	17.90	9.374	0.307	0	1.621	1.117

2.3.3. Uncertainty estimation using a history matching approach

The outcomes from the 3D GIA modeling were used to determine model uncertainty bounds via a history matching approach as described in Section 2.2.3.1. As noted, we consider only a first iteration (or "wave") using this approach and so the results obtained are preliminary. However, they provide an example for future studies to build upon when applying this approach. Furthermore, the results provide self-consistent uncertainty bounds based on a single ice history and so represent a

useful comparison and alternative to the bounds determined using the other two approaches considered here.

Application of the methodology described in Section 2.2.3.1 resulted in an NROY set for the entire dataset of 656 parameter vectors which includes all 34 ice history models. To reduce the number of ice models, we selected a subset of 20 that produced the lowest implausibility values for the SLIPs and limiting data. These 20 models were then used to define model bounds in six subregions as described in Section 2.2.3.1 (Ungava Peninsula and Labrador are combined into a single subregion since there are no SLIPs for Labrador). The ICE6G model resulted in the most symmetric and conservative bounds from these 20 ice models. The Earth model parameter values used in defining the upper and lower model bounds in each subregion (for ICE6G) are defined in Table 2.4.

Table 2.4. The Earth-ice model parameter sets associated with the lower and upper bounds for the six subregions and the ICE6G ice model. The parameters are given in the format LT-UMV-LMV (with LT values in km and viscosity values as 10^{21} Pas).

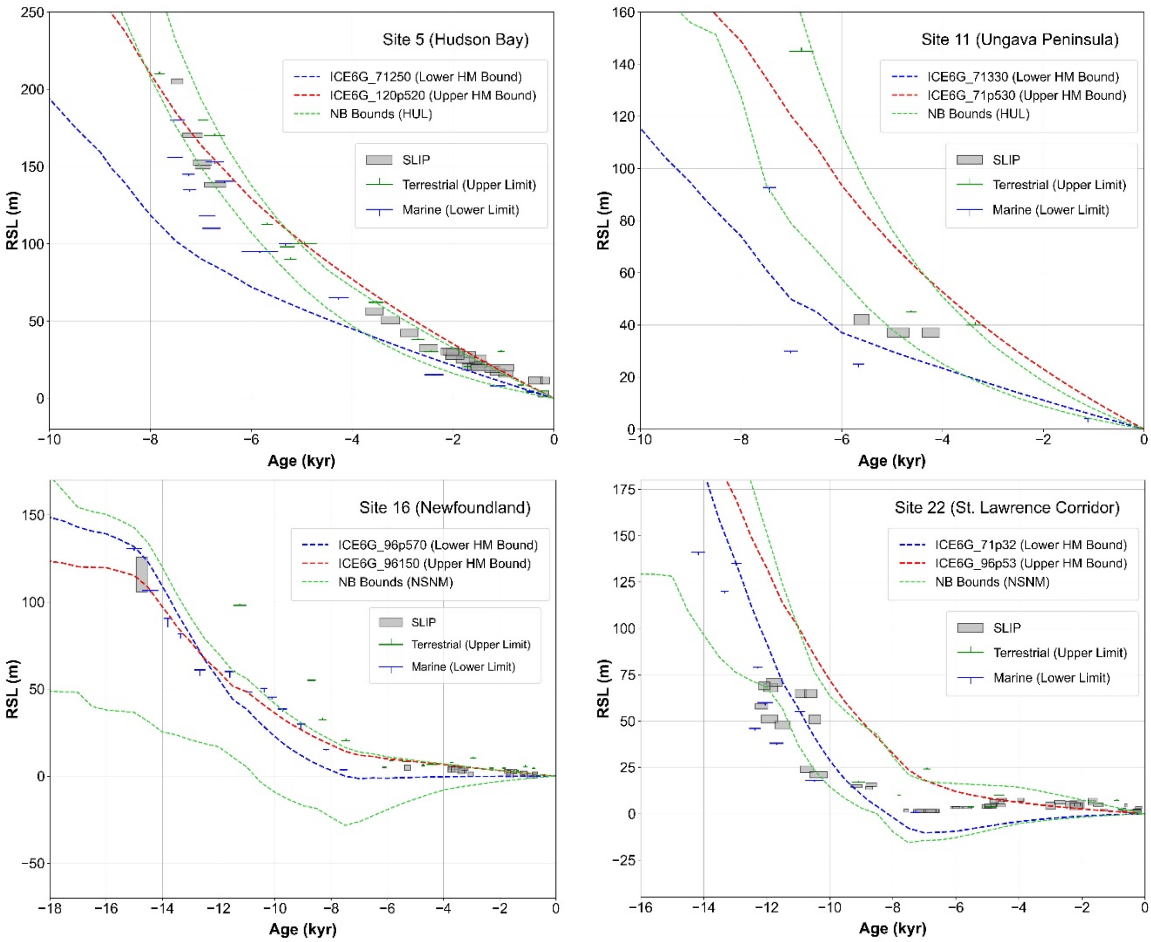
Subregion	Lower bounding model	Upper bounding model
Hudson Bay	71-2-50	120-0.5-20
Ungava Peninsula and Labrador	71-3-30	71-0.5-30
Newfoundland	96-0.5-70	96-1-50
St. Lawrence Corridor	71-0.3-2	96-0.5-3
New Brunswick and Nova Scotia	120-0.5-30	120-0.2-2
Maine and Massachusetts	96-1-50	96-0.3-20

The bounding RSL model curves for each subregion and all sites are provided in Figure 2.S18. Figure 2.15 shows a small subset of these results, with only one site selected from each subregion. For comparison, the nominal Bayesian uncertainty bounds associated with the two larger subregions (HUL and NSNM) are also shown. For Hudson Bay, the history matching approach provides more conservative (wider) uncertainty bounds compared to the nominal Bayesian approach and captures most SLIPs. The upper history matching bound is broadly compatible with most terrestrial limiting data points, but the lower bound sits well below some of the marine limiting data at a number of sites (e.g., site #5; Figure 2.15). The nominal Bayesian bounds are compatible with most limiting data points by design (as this approach includes a scaling to ensure ~68% of the limiting data are compatible with the adopted bounds). For Ungava and Labrador, the history matching bounds are somewhat narrower than those from the nominal Bayesian approach at some sites (e.g., #8 and #9; Figure 2.S18). As the history matching model bounds are identified using SLIPs and there are a very low number of SLIPs in this subregion (3 only), there are sites and time periods where the lower bound lies above the upper bound (e.g., site #12).

For Newfoundland, the history matching bounds are narrower than the nominal Bayesian bounds at all sites. The bounds can capture all SLIPs (except for one SLIP at ~12 ka at site #17; Figure 2.S18) and are broadly compatible with limiting data points. Regarding the St. Lawrence Corridor, the history matching bounds cannot capture all SLIPs within a given site (e.g., SLIPs ranging between ~12 ka and ~10 ka at site #22; Figure 2.15). While the nominal Bayesian bounds capture more SLIPs than the history matching bounds, there remain some that are not captured (sites #22 and #23). In addition, the lower bound obtained using the history matching approach is more compatible with marine limiting data points at all sites compared to the Bayesian results. For New Brunswick and Nova Scotia, the bounding models from history matching are narrower than the nominal Bayesian uncertainty bounds and can capture all SLIPs concentrated in the mid- to late-Holocene. Similarly,

for Maine and Massachusetts, the history matching bounds are narrower and can capture most SLIPs dating from ~6 ka to the present day (e.g., except for some at site #36). They are also compatible with the majority of the limiting data points.

As evident from the results in Figures 2.15 and 2.S18, the history matching approach results in bounds that cross at some sites in some regions (e.g., Newfoundland, Maine and Massachusetts in Figure 2.15). As for the case of the heuristic approach, this reflects the fact that the bounds are based on output from a single model run. This feature is also related to how the model bounds are determined using these methods. For example, the history matching technique isolates upper and lower bounding parameter vectors based on the sign of the average data-model residual for SLIPs in each subregion. Therefore, when the model bounds do cross, it is generally for times where no (or few) SLIPs are present.



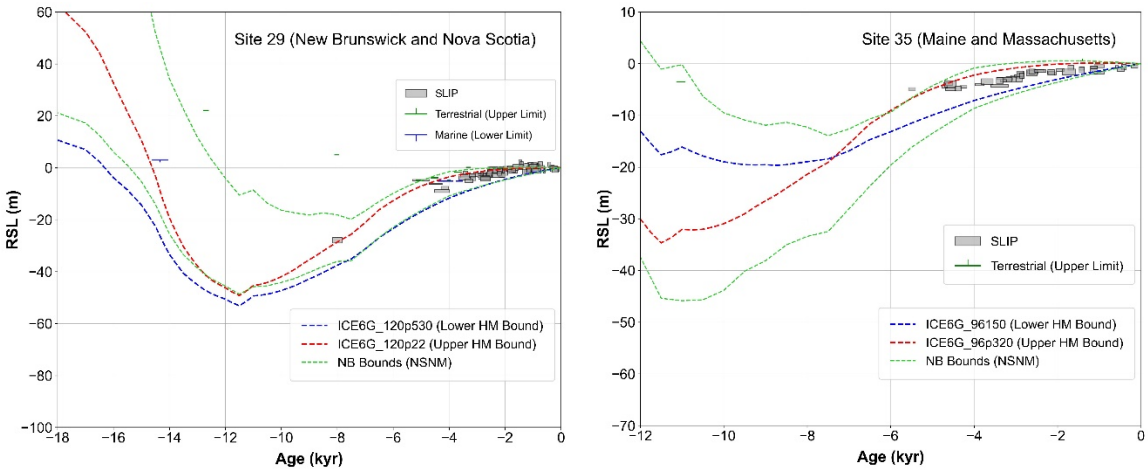


Figure 2.15. The lower and upper bounding models, quantified by the history matching approach (blue- and red-dashed lines, respectively), along with uncertainty bounds from the nominal Bayesian approach (green-dashed lines), are presented for six sites across the entire study region (Hudson Bay, Ungava and Labrador, Newfoundland, St. Lawrence Corridor, Nova Scotia and New Brunswick, Maine and Massachusetts). The uncertainty bounds from the nominal Bayesian approach are based on the regional datasets associated with two larger subregions (i.e., HUL and NSNM). RSL curves were plotted at the average position of all RSL data points within each site (see the white diamonds in Figure 2.S2). The dimension of each SLIP box shows ±1σ uncertainty in RSL and age. For limiting data points, the horizontal and vertical bars show ±1σ RSL age uncertainty and one side of the 1σ RSL uncertainty, respectively (the misfit analysis was carried out based on the 1σ uncertainty in RSL and age).

2.4. Discussion

Based on close to 15,000 forward runs, we constrained a set of optimal Earth model parameters that are most compatible with the adopted paleo RSL dataset (and subsets of this dataset). The results suggest higher UMV in HUL (close to the middle/thickest section of Laurentide Ice Sheet) compared to NSNM (close to the ice margin, along the Atlantic coast), and very low LMV in HUL compared to high LMV in NSNM (see Table 2.2). These distinct Earth model parameter sets reflect the spatial variability of the GIA response that is not accurately captured by a 1D Earth model, and so a single set of optimal Earth model parameters did not provide good quality fits to the entire RSL dataset. These relatively poor fits were evident for a large number (34) of different ice models and so interpreting this spatial variation as being associated with the Earth model appears robust. In addition, the 3D GIA modelling confirms this aspect of our 1D Earth modelling results.

Although our results indicate a significant contribution of lateral Earth properties to the observed RSL signal, the application of a 3D Earth model did not result in improved data-model fits in most regions (Table 2.3). Because only two 3D Earth models were considered, our results are preliminary but, nevertheless, indicate the need to develop improved 3D Earth models for this region. One potential avenue in this regard is the development of more accurate and higher resolution viscosity models based on the joint inversion of regional datasets (e.g., van der Wal et al., 2013). These regional models can be nested into the lower resolution global models (e.g., Goldberg et al., 2016; Yousefi et al., 2021). A major limitation of the 3D Earth modelling is its high computational expense which limits our ability to effectively explore the model parameter space. For example, we adopted the 1D viscosity structure obtained from our 1D analysis in generating 3D Earth models. Given the suggested importance of lateral structure in our study region, which is compatible with previous work (e.g., Lau

et al., 2018; Li et al., 2020), it is possible that this estimate of the 1D structure is biased and not optimal for the adopted models of lateral structure. One interesting development to deal with this issue is the use of Artificial Neural Networks to emulate the output from 3D Earth models (Love et al., 2024).

A central aspect of this analysis is the estimation of model uncertainty. Three different methods were applied to estimate model uncertainty: heuristic and nominal Bayesian approaches (Love et al., 2016) and a partial history matching approach (Tarasov and Goldstein, 2023). There are strengths and weaknesses to each approach. For example, the heuristic and history matching approaches result in model bounds at a given site that are based on single model runs (and so are consistent with the model physics). For the history matching approach, where the bounds are based on a single ice model, this aspect is taken a step further. Depending on the context, a limitation of the incomplete history matching approach (and the heuristic approach) as applied here is that the model bounds cross in some locations, thus limiting their utility for some time periods. The method to determine model uncertainty via nominal Bayesian approach results in bounds that directly reflect the range in predicted RSL (at a given location and time) for the sub-ensemble of accepted parameter vectors. Thus, these bounds lack consistency with the physics of the forward model. Furthermore, our posterior inference is formalistic at best, as the posterior is heavily dependent on the accurate specification of the likelihood. Our likelihood specification ignores the model structural uncertainty (including its highly non-trivial multivariate structure) and is, therefore, incomplete and non-robust.

Regardless of the adopted approach, our results indicate that the model uncertainty is large, varies from region to region, and generally increases with age (Figures 2.6-2.12, 2.S6, and 2.S18). These general findings are compatible with those from other analyses in which aspects of the model uncertainty is quantified (e.g., Li et al., 2020). For the heuristic approach, the upper bound estimated by SLIPs is compatible with terrestrial limiting data points in all subregions. However, the lower bounds within this ensemble cannot satisfy the bounding threshold defined by marine limiting data points in all subregions, originating from some inconsistencies between SLIPs and marine limiting data points, model structural error, and, we suspect, underestimated observational uncertainties.

As a partial application of the history matching approach, our preliminary results show strong potential for this method. Our analysis was limited due to the crude estimate of model structural error and limited sampling of ice sheet chronologies. Furthermore, in defining RSL bounds based on a single ice sheet chronology, we have ignored the structural uncertainty associated with this aspect of the GIA model. As a result, the model bounds are too narrow in some regions (e.g., Newfoundland, Maine and Massachusetts) and are incompatible with a significant portion of limiting data in others (e.g., Hudson Bay). A proper application of history matching would require joint sampling of earth model and ice sheet chronologies, much more complete structural uncertainty assessment, and the use of statistical emulators to enable appropriate parametric sampling over multiple waves (as described in Tarasov and Goldstein, 2023).

Of the three methods considered, the nominal Bayesian approach resulted in model bounds that were best able to capture the SLIPs and remain compatible with most of the limiting data across all subregions (although we note that this latter aspect is implicit in the scaling we applied). While there are clear limitations in this approach (noted above and discussed in Tarasov and Goldstein, 2023), it provides the most conservative and data compatible uncertainty ranges in this analysis. Consequently, the remainder of this discussion will be based on the nominal Bayesian results only.

The model curves (including uncertainty) for our HUL and NSNM data partitioning capture most SLIPs and are compatible with limiting data points within a given site. There are a small number of sites where the nominal Bayesian uncertainty bounds do not capture the RSL observations. These discrepancies can originate from either (i) outliers associated with some single, isolated RSL data point (e.g., the anomalously high SLIP at site #3 dating to ~2 ka BP) or (ii) limitations in the GIA model associated with structural error. As discussed above, model structural error represents various aspects of model physics and parameterization, such as assuming 1D Earth structure or a simple Maxwell rheology. Regarding the latter, recent studies suggest that a non-Newtonian (stress-dependent) rheology results in improved fits in near-field regions where rapid uplift is followed, quite abruptly, by relatively low rates of RSL fall (Kang et al., 2022). The RSL data within the St. Lawrence Corridor (Section 2.3.1.2.5; Figure 2.10) suggest a response with these temporal characteristics. Indeed, Kang et al. (2022) demonstrate improved fits to data in this region when a non-Newtonian viscous response is adopted. Future work that explores these sources of structural error is warranted.

The sub-ensemble of Earth model parameter sets used to define the nominal Bayesian uncertainty ranges (see Table 2.2) are compatible with those from most previous studies, especially for the estimated upper mantle viscosity. There has been an argument on the estimated lower mantle viscosity for decades. In some studies (e.g., Lambeck et al., 2017; Kuchar et al., 2019b), the viscosity of the lower mantle is high (greater than 10^{22} Pas) and in others (e.g., Lau et al., 2016; Peltier et al., 2015; Zhao, 2013), the viscosity of the top third (or all) of the lower mantle is lower ($1.5\text{-}4\times10^{21}$Pas). It is worth mentioning that the approaches and observations applied to constrain the GIA signal in these studies are different, and the study regions are not entirely the same as the one explored here.

Based on observations of vertical land motion and gravity changes, Zhao (2013) suggests an effective lithospheric thickness of 150 km (110-180 km with an 80% confidence level), an upper mantle viscosity of 3.7×10^{20} Pas ($2\text{-}5\times10^{20}$ Pas with a 90% confidence level), and a lower mantle viscosity of 1.9×10^{21} Pas ($1.3\text{-}2.6\times10^{21}$ Pas with a 90% confidence level). These estimates are broadly consistent with those obtained in our study (i.e., LT = 96 km, UMV = 0.3×10^{21} Pas, and LMV = 10^{21} Pas based on analysis of the entire dataset). In addition, our estimated LT and UMV values are in line with those of Lambeck et al. (2017) who determined (with 95% confidence limits): 102 (85-110) km for the effective lithospheric thickness, 5.1×10^{20} ($3.5\text{-}7.5\times10^{20}$) Pas for the upper mantle viscosity, and 1.3×10^{22} ($0.8\text{-}2.8\times10^{22}$) for the lower mantle viscosity.

Comparing the obtained optimal UMV and LMV parameter spaces (when considering the uncertainty bounds) with results from postglacial decay time analyses shows some differences. For example, Kuchar et al. (2019a) demonstrated that for Richmond Gulf (site #5, Figure 2.S2), UMV of $0.3\text{-}0.5\times10^{21}$ Pas and LMV of $5\text{-}50\times10^{21}$ Pas can satisfy the RSL data constraints for the applied ice loading histories. These results are compatible with those of Lau et al. (2016) who performed a more rigorous inversion for viscosity structure using the decay time constraints from this region. The accepted parameter ranges determined using our nominal Bayesian approach are compatible with these previous studies for UMV. This is less clear for the LMV where 81 of the 84 accepted LMV values are 1×10^{21} Pas (with the remainder being 2×10^{21} Pas (twice) and 30×10^{21} Pas). While there is overlap, it is more tenuous for LMV compared to UMV. This apparent discrepancy may be related to the different data sets being used: we consider the entire HUL region and both SLIPs and limiting data points whereas decay time analyses generally consider only SLIPs from one or two sites.

In terms of assessing the ice sheet history models applied in this study, results from our history matching analysis are the most appropriate as they explicitly incorporate estimates of model structural error associated with lateral Earth properties (and so any bias associated with this Earth model aspect should be diminished). We divided our ice model ensemble into two sub-ensembles: 10 with the lowest average *IM* values and 10 with the highest average *IM* values for the complete RSL dataset (Table 2.S1). For these two sub-ensembles, the average ice thickness was computed at four different times (21, 15, 13, and 10 ka) and these averages were then differenced (Figure 2.S19). At 21 ka, the models that are most compatible with the RSL data (lowest *IM* values) exhibit (on average) thicker ice in most of our study region (except for the area from Newfoundland to New Brunswick). This remains the case in a general sense at 15 ka and, to a lesser extent (smaller amplitudes), at 13 ka. However, at 10 ka, the preferred ice models are significantly thinner than the poorer fitting models within Hudson Bay. These results indicate that ice models with thicker ice in our HUL region in the early deglaciation but with thinner ice in the early Holocene gave the best results. This indicates that models with more rapid thinning in the late glacial and/or early Holocene are preferred by the data. Figure 2.S19 also indicates that models with less ice in southeastern Canada (Newfoundland to New Brunswick) are more accurate.

The optimal GIA signal (with its uncertainty bounds) estimated from our study can be used for different applications. For example, the GIA signal can be removed from geodetic measurements (e.g., GRACE satellite gravimetry, GNSS) to better constrain and understand non-GIA processes (e.g., hydrology) contributing to contemporary mass changes and vertical land motion. Our model results can also be used to produce improved projections of mean sea-level change and nuisance flooding in the coming decades (e.g., Karegar et al., 2017; Slangen et al., 2014). Model output with uncertainty based on the nominal Bayesian approach is provided for rates of vertical land motion at GNSS stations in the Nevada Geodetic Laboratory dataset (Blewitt et al., 2018; Appendix 1) and for rates of sea level change at tide gauge stations in the PSMSL dataset (Holgate et al., 2012; Appendix 2).

2.5. Summary

We constrained the GIA signal and its uncertainty for southeastern Canada and northeastern USA using 1,013 RSL data points from two regional RSL data compilations (Vacchi et al., 2018; Engelhart and Horton, 2012) containing 544 SLIPs, 232 marine limiting data points, 237 terrestrial limiting data points, and 14,960 model runs to explore the 4D parameter space (ice model and 3 Earth viscosity model parameters). The quality of data-model fits was assessed for the entire dataset as well as subsets related to a partitioning into 7 subregions (Hudson Bay, Ungava Peninsula, Labrador, Newfoundland, St. Lawrence Corridor, New Brunswick and Nova Scotia, and Maine and Massachusetts).

Each subregion prefers different Earth model parameter sets to produce optimal fits; however, the data in some subregions can be fit relatively well using similar Earth viscosity parameters and ice loading history. Therefore, the whole study region was ultimately partitioned into two larger subregions: (1) HUL close to the middle part/thickest section of Laurentide Ice Sheet (including Hudson Bay, Ungava Peninsula, and Labrador), (2) NSNM along the Atlantic coast of Canada, close to the ice margin (encompassing Newfoundland, St. Lawrence Corridor, New Brunswick and Nova Scotia, and Maine and Massachusetts).

The quality of data-model fits for the HUL-NSNM partitioning is significantly better than that produced for the entire dataset, indicating a considerable contribution to the RSL signal from lateral Earth structure. For the HUL dataset, relatively low LMV (~1-2×10^{21} Pas) and relatively high UMV (greater than 0.5×10^{21} Pas) for a given ice loading history provided good quality fits. In comparison, good quality fits for the NSNM dataset were found for intermediate UMV and LMV values (specifically, UMV = 0.5-1×10^{21} Pas and LMV = 20-30×10^{21} Pas).

Given the evidence for a considerable signal associated with lateral Earth structure, a preliminary 3D Earth modeling analysis was also performed. Two shear-wave tomographic models were considered with a global model of lithosphere thickness variation to determine lateral viscosity structure to be superimposed on the inferred, optimal, 1D profile. The 3D modelling results confirm the spatial partitioning of the whole study region into the two larger subregions (HUL and NSNM) inferred from the 1D GIA modelling. However, the 3D runs did not produce data-model fits that bettered the results based on the 1-D model, suggesting that the models of lateral structure are inaccurate and/or the ice models applied, which were developed using 1D Earth models, are inaccurate. Further work to consider these aspects is recommended.

Model uncertainty bounds were quantified using three different approaches, each with specific strengths and limitations. One common result from all approaches is that model uncertainty is large, as well as spatially and temporally variable, and thus further work is encouraged to produce more accurate and useful estimates for end user communities. Of the approaches considered, uncertainty determined from a nominal Bayesian approach resulted in the more conservative RSL bounds while remaining consistent with most of the data points. When considering these bounds for the optimal parameter sets (for HUL and NSNM), the model results are compatible with ~91.6% of the observations. While some of the data-model residuals are associated with observational outliers, others indicate systematic error in the model, such as departures from the assumed Maxwell rheology.

Finally, on comparing two 10-member sub-ensembles of the 34 ice history models with good versus poor data fits from the history matching analysis, it is evident within the HUL region that models with relatively thick ice during the early phase of deglaciation (pre ~13 ka) and thinner ice in the early Holocene are preferred by the RSL data.

References

Argus, D.F., Peltier, W.R., Blewitt, G., Kreemer, C., 2021. The Viscosity of the Top Third of the Lower Mantle Estimated Using GPS, GRACE, and Relative Sea Level Measurements of Glacial Isostatic Adjustment. J Geophys Res Solid Earth 126. https://doi.org/10.1029/2020JB021537

Austermann, J., Mitrovica, J.X., Latychev, K., Milne, G.A., 2013. Barbados-based estimate of ice volume at Last Glacial Maximum affected by subducted plate. Nat Geosci 6, 553–557. https://doi.org/10.1038/ngeo1859

Baril, A., Garrett, E., Milne, G.A., Gehrels, W.R., Kelley, J.T., 2023. Postglacial relative sea-level changes in the Gulf of Maine, USA: Database compilation, assessment and modelling. Quat Sci Rev 306, 108027. https://doi.org/10.1016/j.quascirev.2023.108027

Blewitt, G., Hammond, W., Kreemer, C., 2018. Harnessing the GPS Data Explosion for Interdisciplinary Science. Eos (Washington DC) 99. https://doi.org/10.1029/2018EO104623

Briggs, R.D., Tarasov, L., 2013. How to evaluate model-derived deglaciation chronologies: a case study using Antarctica. Quat Sci Rev 63, 109–127. https://doi.org/10.1016/j.quascirev.2012.11.021

Caron, L., Ivins, E.R., Larour, E., Adhikari, S., Nilsson, J., Blewitt, G., 2018. GIA Model Statistics for GRACE Hydrology, Cryosphere, and Ocean Science. Geophys Res Lett 45, 2203–2212. https://doi.org/10.1002/2017GL076644

Caron, L., Métivier, L., Greff-Lefftz, M., Fleitout, L., Rouby, H., 2017. Inverting Glacial Isostatic Adjustment signal using Bayesian framework and two linearly relaxing rheologies. Geophys J Int 209, 1126–1147. https://doi.org/10.1093/gji/ggx083

Chopelas, A., Boehler, R., 1992. Thermal expansivity in the lower mantle. Geophys Res Lett 19, 1983–1986. https://doi.org/10.1029/92GL02144

Daly, J.F., Belknap, D.F., Kelley, J.T., Bell, T., 2007. Late Holocene sea-level change around Newfoundland. Can J Earth Sci 44, 1453–1465. https://doi.org/10.1139/e07-036

Davis, J.E., Latychev, K., Mitrovica, J.X., Kendall, R., Tamisiea, M.E., 2008. Glacial isostatic adjustment in 3-D earth models: Implications for the analysis of tide gauge records along the U.S. east coast. J Geodyn 46, 90–94. https://doi.org/10.1016/j.jog.2008.04.007

Davis, J.L., Mitrovica, J.X., 1996. Glacial isostatic adjustment and the anomalous tide gauge record of eastern North America. Nature 379, 331–333. https://doi.org/10.1038/379331a0

Dziewonski, A.M., Anderson, D.L., 1981. Preliminary reference Earth model. Physics of the Earth and Planetary Interiors 25, 297–356. https://doi.org/10.1016/0031-9201(81)90046-7

Ehlers, J., Gibbard, P.L., 2007. The extent and chronology of Cenozoic Global Glaciation. Quaternary International 164–165, 6–20. https://doi.org/10.1016/j.quaint.2006.10.008

Engelhart, S.E., Horton, B.P., 2012. Holocene sea level database for the Atlantic coast of the United States. Quat Sci Rev 54, 12–25. https://doi.org/10.1016/j.quascirev.2011.09.013

Engelhart, S.E., Peltier, W.R., Horton, B.P., 2011. Holocene relative sea-level changes and glacial isostatic adjustment of the U.S. Atlantic coast. Geology 39, 751–754. https://doi.org/10.1130/G31857.1

Farrell, W.E., Clark, J.A., 1976. On Postglacial Sea Level. Geophysical Journal of the Royal Astronomical Society 46, 647–667. https://doi.org/10.1111/j.1365-246X.1976.tb01252.x

Forte, A.M., Woodward, R.L., 1997. Seismic-geodynamic constraints on three-dimensional structure, vertical flow, and heat transfer in the mantle. J Geophys Res Solid Earth 102, 17981–17994. https://doi.org/10.1029/97JB01276

Glueder, A., Mix, A.C., Milne, G.A., Reilly, B.T., Clark, J., Jakobsson, M., Mayer, L., Fallon, S.J., Southon, J., Padman, J., Ross, A., Cronin, T., McKay, J.L., 2022. Calibrated relative sea levels constrain isostatic adjustment and ice history in northwest Greenland. Quat Sci Rev 293, 107700. https://doi.org/10.1016/j.quascirev.2022.107700

Goldberg, S.L., Lau, H.C.P., Mitrovica, J.X., Latychev, K., 2016. The timing of the Black Sea flood event: Insights from modeling of glacial isostatic adjustment. Earth Planet Sci Lett 452, 178–184. https://doi.org/10.1016/j.epsl.2016.06.016

Heaton, T.J., Köhler, P., Butzin, M., Bard, E., Reimer, R.W., Austin, W.E.N., Bronk Ramsey, C., Grootes, P.M., Hughen, K.A., Kromer, B., Reimer, P.J., Adkins, J., Burke, A., Cook, M.S., Olsen, J., Skinner, L.C., 2020. Marine20—The Marine Radiocarbon Age Calibration Curve (0–55,000 cal BP). Radiocarbon 62, 779–820. https://doi.org/10.1017/RDC.2020.68

Hill, E.M., Davis, J.L., Tamisiea, M.E., Lidberg, M., 2010. Combination of geodetic observations and models for glacial isostatic adjustment fields in Fennoscandia. J Geophys Res 115, B07403. https://doi.org/10.1029/2009JB006967

Holgate, S.J., Matthews, A., Woodworth, P.L., Rickards, L.J., Tamisiea, M.E., Bradshaw, E., Foden, P.R., Gordon, K.M., Jevrejeva, S., Pugh, J., 2012. New Data Systems and Products at the Permanent Service for Mean Sea Level. J Coast Res 29, 493–504. https://doi.org/10.2112/JCOASTRES-D-12-00175.1

Kang, K., Zhong, S., Geruo, A., Mao, W., 2022. The effects of non-Newtonian rheology in the upper mantle on relative sea level change and geodetic observables induced by glacial isostatic adjustment process. Geophys J Int 228, 1887–1906. https://doi.org/10.1093/gji/ggab428

Karato, S., 1993. Importance of anelasticity in the interpretation of seismic tomography. Geophys Res Lett 20, 1623–1626. https://doi.org/10.1029/93GL01767

Karegar, M.A., Dixon, T.H., Engelhart, S.E., 2016. Subsidence along the Atlantic Coast of North America: Insights from GPS and late Holocene relative sea level data. Geophys Res Lett 43, 3126–3133. https://doi.org/10.1002/2016GL068015

Karegar, M.A., Dixon, T.H., Malservisi, R., Kusche, J., Engelhart, S.E., 2017. Nuisance Flooding and Relative Sea-Level Rise: the Importance of Present-Day Land Motion. Sci Rep 7, 11197. https://doi.org/10.1038/s41598-017-11544-y

Kaufmann, G., Wu, P., Ivins, E.R., 2005. Lateral viscosity variations beneath Antarctica and their implications on regional rebound motions and seismotectonics. J Geodyn 39, 165–181. https://doi.org/10.1016/j.jog.2004.08.009

Kendall, R.A., Mitrovica, J.X., Milne, G.A., 2005. On post-glacial sea level - II. Numerical formulation and comparative results on spherically symmetric models. Geophys J Int 161, 679–706. https://doi.org/10.1111/j.1365-246X.2005.02553.x

Khan, N.S., Horton, B.P., Engelhart, S., Rovere, A., Vacchi, M., Ashe, E.L., Törnqvist, T.E., Dutton, A., Hijma, M.P., Shennan, I., 2019. Inception of a global atlas of sea levels since the Last Glacial Maximum. Quat Sci Rev 220, 359–371. https://doi.org/10.1016/j.quascirev.2019.07.016

King, M.A., Altamimi, Z., Boehm, J., Bos, M., Dach, R., Elosegui, P., Fund, F., Hernández-Pajares, M., Lavallee, D., Mendes Cerveira, P.J., Penna, N., Riva, R.E.M., Steigenberger, P., van Dam, T., Vittuari, L., Williams, S., Willis, P., 2010. Improved Constraints on Models of Glacial Isostatic Adjustment: A Review of the Contribution of Ground-Based Geodetic Observations. Surv Geophys 31, 465–507. https://doi.org/10.1007/s10712-010-9100-4

Kuchar, J., Milne, G., Hill, A., Tarasov, L., Nordman, M., 2019a. An investigation into the sensitivity of postglacial decay times to uncertainty in the adopted ice history. Geophys J Int. https://doi.org/10.1093/gji/ggz512

Kuchar, J., Milne, G., Latychev, K., 2019b. The importance of lateral Earth structure for North American glacial isostatic adjustment. Earth Planet Sci Lett 512, 236–245. https://doi.org/10.1016/j.epsl.2019.01.046

Lambeck, K., Purcell, A., Zhao, S., 2017. The North American Late Wisconsin ice sheet and mantle viscosity from glacial rebound analyses. Quat Sci Rev 158, 172–210. https://doi.org/10.1016/j.quascirev.2016.11.033

Lambeck, K., Rouby, H., Purcell, A., Sun, Y., Sambridge, M., 2014. Sea level and global ice volumes from the Last Glacial Maximum to the Holocene. Proceedings of the National Academy of Sciences 111, 15296–15303. https://doi.org/10.1073/pnas.1411762111

Lambeck, K., Smither, C., Johnston, P., 1998. Sea-level change, glacial rebound and mantle viscosity fornorthern Europe. Geophys J Int 134, 102–144. https://doi.org/10.1046/j.1365-246x.1998.00541.x

Latychev, K., Mitrovica, J.X., Tromp, J., Tamisiea, M.E., Komatitsch, D., Christara, C.C., 2005. Glacial isostatic adjustment on 3-D Earth models: a finite-volume formulation. Geophys J Int 161, 421–444. https://doi.org/10.1111/j.1365-246X.2005.02536.x

Lau, H.C.P., Austermann, J., Mitrovica, J.X., Crawford, O., Al-Attar, D., Latychev, K., 2018. Inferences of Mantle Viscosity Based on Ice Age Data Sets: The Bias in Radial Viscosity Profiles Due to the Neglect of Laterally Heterogeneous Viscosity Structure. J Geophys Res Solid Earth 123, 7237–7252. https://doi.org/10.1029/2018JB015740

Lau, H.C.P., Mitrovica, J.X., Austermann, J., Crawford, O., Al-Attar, D., Latychev, K., 2016. Inferences of mantle viscosity based on ice age data sets: Radial structure. J Geophys Res Solid Earth 121, 6991–7012. https://doi.org/10.1002/2016JB013043

Li, T., Wu, P., Steffen, H., Wang, H., 2018. In search of laterally heterogeneous viscosity models of glacial isostatic adjustment with the ICE-6G_C global ice history model. Geophys J Int 214, 1191–1205. https://doi.org/10.1093/gji/ggy181

Li, T., Wu, P., Wang, H., Steffen, H., Khan, N.S., Engelhart, S.E., Vacchi, M., Shaw, T.A., Peltier, W.R., Horton, B.P., 2020. Uncertainties of Glacial Isostatic Adjustment Model Predictions in North America Associated With 3D Structure. Geophys Res Lett 47. https://doi.org/10.1029/2020GL087944

Love, R., Milne, G., Ajourlou, P., Parang, S., Tarasov, L., Latychev, K., 2024. A Fast Surrogate Model for 3D-Earth Glacial Isostatic Adjustment using Tensorflow (v2.8.10) Artificial Neural Networks. EGUsphere [preprint]. https://doi.org/https://doi.org/10.5194/egusphere-2023-2491

Love, R., Milne, G.A., Tarasov, L., Engelhart, S.E., Hijma, M.P., Latychev, K., Horton, B.P., Törnqvist, T.E., 2016. The contribution of glacial isostatic adjustment to projections of sea-level change along the Atlantic and Gulf coasts of North America. Earths Future 4, 440–464. https://doi.org/10.1002/2016EF000363

Lowe, J.J., Walker, M.J.C., Porter, S.C., 2007. INTRODUCTION | Understanding Quaternary Climatic Change, in: Encyclopedia of Quaternary Science. Elsevier, pp. 28–39. https://doi.org/10.1016/B0-44-452747-8/00005-3

Martín-Español, A., Zammit-Mangion, A., Clarke, P.J., Flament, T., Helm, V., King, M.A., Luthcke, S.B., Petrie, E., Rémy, F., Schön, N., Wouters, B., Bamber, J.L., 2016. Spatial and temporal Antarctic Ice Sheet mass trends, glacio-isostatic adjustment, and surface processes from a joint inversion of satellite altimeter, gravity, and GPS data. J Geophys Res Earth Surf 121, 182–200. https://doi.org/10.1002/2015JF003550

Melini, D., Spada, G., 2019. Some remarks on Glacial Isostatic Adjustment modelling uncertainties. Geophys J Int 218, 401–413. https://doi.org/10.1093/gji/ggz158

Milne, G., Shennan, I., 2013. SEA LEVEL STUDIES | Isostasy: Glaciation-Induced Sea-Level Change, in: Encyclopedia of Quaternary Science. Elsevier, pp. 452–459. https://doi.org/10.1016/B978-0-444-53643-3.00135-7

Milne, G.A., Mitrovica, J.X., 1998. Postglacial sea-level change on a rotating Earth. Geophys J Int 133, 1–19. https://doi.org/10.1046/j.1365-246X.1998.1331455.x

Milne, G.A., Peros, M., 2013. Data–model comparison of Holocene sea-level change in the circum-Caribbean region. Glob Planet Change 107, 119–131. https://doi.org/10.1016/j.gloplacha.2013.04.014

Mitrovica, J.X., Forte, A.M., Simons, M., 2000. A reappraisal of postglacial decay times from Richmond Gulf and James Bay, Canada. Geophys J Int 142, 783–800. https://doi.org/10.1046/j.1365-246x.2000.00199.x

Mitrovica, J.X., Milne, G.A., 2003. On post-glacial sea level: I. General theory. Geophys J Int 154, 253–267. https://doi.org/10.1046/j.1365-246X.2003.01942.x

Mitrovica, J.X., Wahr, J., Matsuyama, I., Paulson, A., 2005. The rotational stability of an ice-age earth. Geophys J Int 161, 491–506. https://doi.org/10.1111/j.1365-246X.2005.02609.x

Paulson, A., Zhong, S., Wahr, J., 2007. Inference of mantle viscosity from GRACE and relative sea level data. Geophys J Int 171, 497–508. https://doi.org/10.1111/j.1365-246X.2007.03556.x

Paulson, A., Zhong, S., Wahr, J., 2005. Modelling post-glacial rebound with lateral viscosity variations. Geophys J Int 163, 357–371. https://doi.org/10.1111/j.1365-246X.2005.02645.x

Peltier, W.R., 2004. GLOBAL GLACIAL ISOSTASY AND THE SURFACE OF THE ICE-AGE EARTH: The ICE-5G (VM2) Model and GRACE. Annu Rev Earth Planet Sci 32, 111–149. https://doi.org/10.1146/annurev.earth.32.082503.144359

Peltier, W.R., 1998. Postglacial variations in the level of the sea: Implications for climate dynamics and solid-Earth geophysics. Reviews of Geophysics 36, 603–689. https://doi.org/10.1029/98RG02638

Peltier, W.R., 1974. The impulse response of a Maxwell Earth. Reviews of Geophysics 12, 649. https://doi.org/10.1029/RG012i004p00649

Peltier, W.R., Argus, D.F., Drummond, R., 2015. Space geodesy constrains ice age terminal deglaciation: The global ICE-6G_C (VM5a) model. J Geophys Res Solid Earth 120, 450–487. https://doi.org/10.1002/2014JB011176

Peltier, W.R., Fairbanks, R.G., 2006. Global glacial ice volume and Last Glacial Maximum duration from an extended Barbados sea level record. Quat Sci Rev 25, 3322–3337. https://doi.org/10.1016/j.quascirev.2006.04.010

Peltier, W.R., Shennan, I., Drummond, R., Horton, B., 2002. On the postglacial isostatic adjustment of the British Isles and the shallow viscoelastic structure of the Earth. Geophys J Int 148, 443–475. https://doi.org/10.1046/j.1365-246x.2002.01586.x

Peltier, W.R., Wu, P.P.-C., Argus, D.F., Li, T., Velay-Vitow, J., 2022. Glacial isostatic adjustment: physical models and observational constraints. Reports on Progress in Physics 85, 096801. https://doi.org/10.1088/1361-6633/ac805b

Reimer, P.J., Austin, W.E.N., Bard, E., Bayliss, A., Blackwell, P.G., Bronk Ramsey, C., Butzin, M., Cheng, H., Edwards, R.L., Friedrich, M., Grootes, P.M., Guilderson, T.P., Hajdas, I., Heaton, T.J., Hogg, A.G., Hughen, K.A., Kromer, B., Manning, S.W., Muscheler, R., Palmer, J.G., Pearson, C., van der Plicht, J., Reimer, R.W., Richards, D.A., Scott, E.M., Southon, J.R., Turney, C.S.M., Wacker, L., Adolphi, F., Büntgen, U., Capano, M., Fahrni, S.M., Fogtmann-Schulz, A., Friedrich, R., Köhler, P., Kudsk, S., Miyake, F., Olsen, J., Reinig, F., Sakamoto, M., Sookdeo, A., Talamo, S., 2020. The IntCal20 Northern Hemisphere Radiocarbon Age Calibration Curve (0–55 cal kBP). Radiocarbon 62, 725–757. https://doi.org/10.1017/RDC.2020.41

Ritsema, J., Deuss, A., van Heijst, H.J., Woodhouse, J.H., 2011. S40RTS: a degree-40 shear-velocity model for the mantle from new Rayleigh wave dispersion, teleseismic traveltime and normal-mode splitting function measurements. Geophys J Int 184, 1223–1236. https://doi.org/10.1111/j.1365-246X.2010.04884.x

Roy, K., Peltier, W.R., 2015. Glacial isostatic adjustment, relative sea level history and mantle viscosity: reconciling relative sea level model predictions for the U.S. East coast with geological constraints. Geophys J Int 201, 1156–1181. https://doi.org/10.1093/gji/ggv066

Schaeffer, A.J., Lebedev, S., 2013. Global shear speed structure of the upper mantle and transition zone. Geophys J Int 194, 417–449. https://doi.org/10.1093/gji/ggt095

Shackleton, N.J., Opdyke, N.D., 1973. Oxygen Isotope and Palaeomagnetic Stratigraphy of Equatorial Pacific Core V28-238: Oxygen Isotope Temperatures and Ice Volumes on a 10^5 Year and 10^6 Year Scale. Quat Res 3, 39–55. https://doi.org/10.1016/0033-5894(73)90052-5

Shaw, J., Potter, D.P., 2015. Surficial geology, coastal waters, Island of Newfoundland, Newfoundland and Labrador. https://doi.org/10.4095/293728

Simon, K.M., James, T.S., Henton, J.A., Dyke, A.S., 2016. A glacial isostatic adjustment model for the central and northern Laurentide Ice Sheet based on relative sea level and GPS measurements. Geophys J Int 205, 1618–1636. https://doi.org/10.1093/gji/ggw103

Simon, K.M., Riva, R.E.M., Kleinherenbrink, M., Tangdamrongsub, N., 2017. A data-driven model for constraint of present-day glacial isostatic adjustment in North America. Earth Planet Sci Lett 474, 322–333. https://doi.org/10.1016/j.epsl.2017.06.046

Simon, K.M., Riva, R.E.M., Vermeersen, L.L.A., 2021. Constraint of glacial isostatic adjustment in the North Sea with geological relative sea level and GNSS vertical land motion data. Geophys J Int 227, 1168–1180. https://doi.org/10.1093/gji/ggab261

Slangen, A.B.A., Carson, M., Katsman, C.A., van de Wal, R.S.W., Köhl, A., Vermeersen, L.L.A., Stammer, D., 2014. Projecting twenty-first century regional sea-level changes. Clim Change 124, 317–332. https://doi.org/10.1007/s10584-014-1080-9

Spada, G., 2017. Glacial Isostatic Adjustment and Contemporary Sea Level Rise: An Overview. Surv Geophys 38, 153–185. https://doi.org/10.1007/s10712-016-9379-x

Steffen, H., Wu, P., 2011. Glacial isostatic adjustment in Fennoscandia—A review of data and modeling. J Geodyn 52, 169–204. https://doi.org/10.1016/j.jog.2011.03.002

Stuiver, M., Reimer, P.J., Reimer, R.W., 2021. CALIB 8.2 (http://calib.org/).

Tarasov, L., Dyke, A.S., Neal, R.M., Peltier, W.R., 2012. A data-calibrated distribution of deglacial chronologies for the North American ice complex from glaciological modeling. Earth Planet Sci Lett 315–316, 30–40. https://doi.org/10.1016/j.epsl.2011.09.010

Tarasov, L., Goldstein, M., 2023. Assessing uncertainty in past ice and climate evolution: overview, stepping-stones, and challenges. EGUsphere [preprint]. https://doi.org/https://doi.org/10.5194/egusphere-2022-1410

Vacchi, M., Engelhart, S.E., Nikitina, D., Ashe, E.L., Peltier, W.R., Roy, K., Kopp, R.E., Horton, B.P., 2018. Postglacial relative sea-level histories along the eastern Canadian coastline. Quat Sci Rev 201, 124–146. https://doi.org/10.1016/j.quascirev.2018.09.043

van der Wal, W., Barnhoorn, A., Stocchi, P., Gradmann, S., Wu, P., Drury, M., Vermeersen, B., 2013. Glacial isostatic adjustment model with composite 3-D Earth rheology for Fennoscandia. Geophys J Int 194, 61–77. https://doi.org/10.1093/gji/ggt099

van der Wal, W., Whitehouse, P.L., Schrama, E.J.O., 2015. Effect of GIA models with 3D composite mantle viscosity on GRACE mass balance estimates for Antarctica. Earth Planet Sci Lett 414, 134–143. https://doi.org/10.1016/j.epsl.2015.01.001

Wake, L.M., Lecavalier, B.S., Bevis, M., 2016. Glacial Isostatic Adjustment (GIA) in Greenland: a Review. Curr Clim Change Rep 2, 101–111. https://doi.org/10.1007/s40641-016-0040-z

Wang, H., Wu, P., van der Wal, W., 2008. Using postglacial sea level, crustal velocities and gravity-rate-of-change to constrain the influence of thermal effects on mantle lateral heterogeneities. J Geodyn 46, 104–117. https://doi.org/10.1016/j.jog.2008.03.003

Whitehouse, P.L., 2018. Glacial isostatic adjustment modelling: historical perspectives, recent advances, and future directions. Earth Surface Dynamics 6, 401–429. https://doi.org/10.5194/esurf-6-401-2018

Yousefi, M., Milne, G.A., Latychev, K., 2021. Glacial isostatic adjustment of the Pacific Coast of North America: the influence of lateral Earth structure. Geophys J Int 226, 91–113. https://doi.org/10.1093/gji/ggab053

Yousefi, M., Milne, G.A., Love, R., Tarasov, L., 2018. Glacial isostatic adjustment along the Pacific coast of central North America. Quat Sci Rev 193, 288–311. https://doi.org/10.1016/j.quascirev.2018.06.017

Zhai, L., Greenan, B.J.W., Hunter, J., James, T.S., Han, G., MacAulay, P., Henton, J.A., 2015. Estimating Sea-Level Allowances for Atlantic Canada using the Fifth Assessment Report of the IPCC. Atmosphere-Ocean 53, 476–490. https://doi.org/10.1080/07055900.2015.1106401

Zhao, S., 2013. Lithosphere thickness and mantle viscosity estimated from joint inversion of GPS and GRACE-derived radial deformation and gravity rates in North America. Geophys J Int 194, 1455–1472. https://doi.org/10.1093/gji/ggt212

Supplementary figures and tables of Chapter 2

Contents of this section

Table 2.S1 and Figures 2.S1 to 2.S19. This supplemental section contains additional tables and figures that complement material in the main text. All of the tables and figures below are referred to in the main text. See captions for further details.

Additional supplementary material

Appendix 1 - Model output of vertical land motion rate at GPS stations in the Nevada Geodetic Laboratory database.

Appendix 2 - Model output of sea level rate at tide gauge stations in the Proudman Service for Mean Sea Level database.

https://doi.org/10.1016/j.quascirev.2024.108708

Table 2.S1. The 34 ice loading history reconstructions used in this study (Lambeck et al., 2017; Peltier et al., 2015; Tarasov et al., 2012). The 'best' and 'worst' 10 models from the history matching analysis (based on calculated *IM* values; see Equations 2.6 and 2.7) are identified by * and † symbols, respectively. These are the two ice model ensembles used to generate the results in Figure 2.S19.

Ice model index	Ice history model
1	ANU*
2	ICE-6G*
3	GLAC1D-na9927†
4	GLAC1D-na9894*
5	GLAC1D-na1246
6	GLAC1D-na4247
7	GLAC1D-na6478†
8	GLAC1D-na6575†
9	GLAC1D-na1263
10	GLAC1D-na8038†
11	GLAC1D-na9394
12	GLAC1D-na9852†
13	GLAC1D-na1087
14	GLAC1D-na1243
15	GLAC1D-na1250†
16	GLAC1D-na1259*
17	GLAC1D-na1279
18	GLAC1D-na1287
19	GLAC1D-na1415
20	GLAC1D-na5962
21	GLAC1D-na6053*
22	GLAC1D-na6244*
23	GLAC1D-na6317
24	GLAC1D-na6318
25	GLAC1D-na6321
26	GLAC1D-na6439†
27	GLAC1D-na6457
28	GLAC1D-na6642*
29	GLAC1D-na7042†
30	GLAC1D-na7221†
31	GLAC1D-na7239†
32	GLAC1D-na8005*
33	GLAC1D-na8025*
34	GLAC1D-na8034*

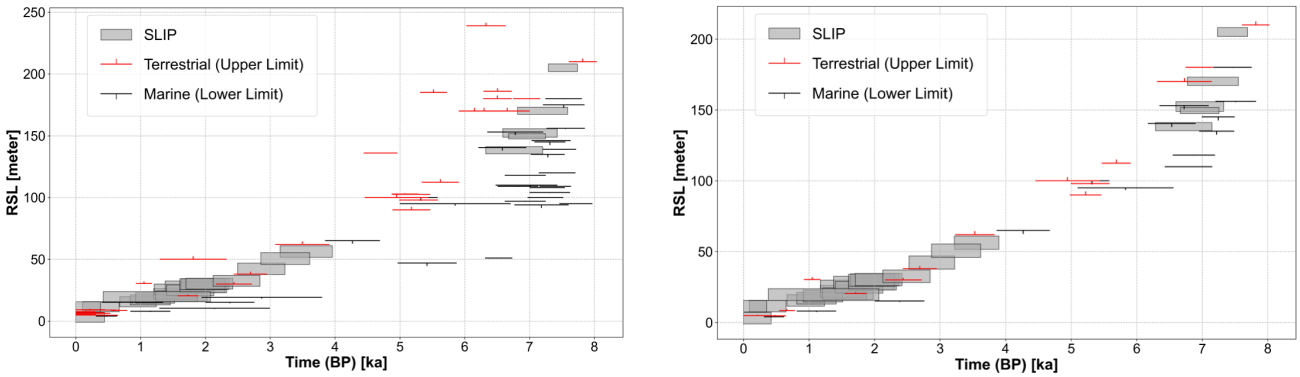


Figure 2.S1. Left: raw RSL data points for site #5 in Hudson Bay; right: after radiocarbon re-calibration and data cleaning. The SLIP boxes indicate ±2σ uncertainty in RSL and age. For limiting data points, the horizontal and vertical bars show ±2σ RSL age uncertainty and one side of the 2σ RSL uncertainty, respectively.

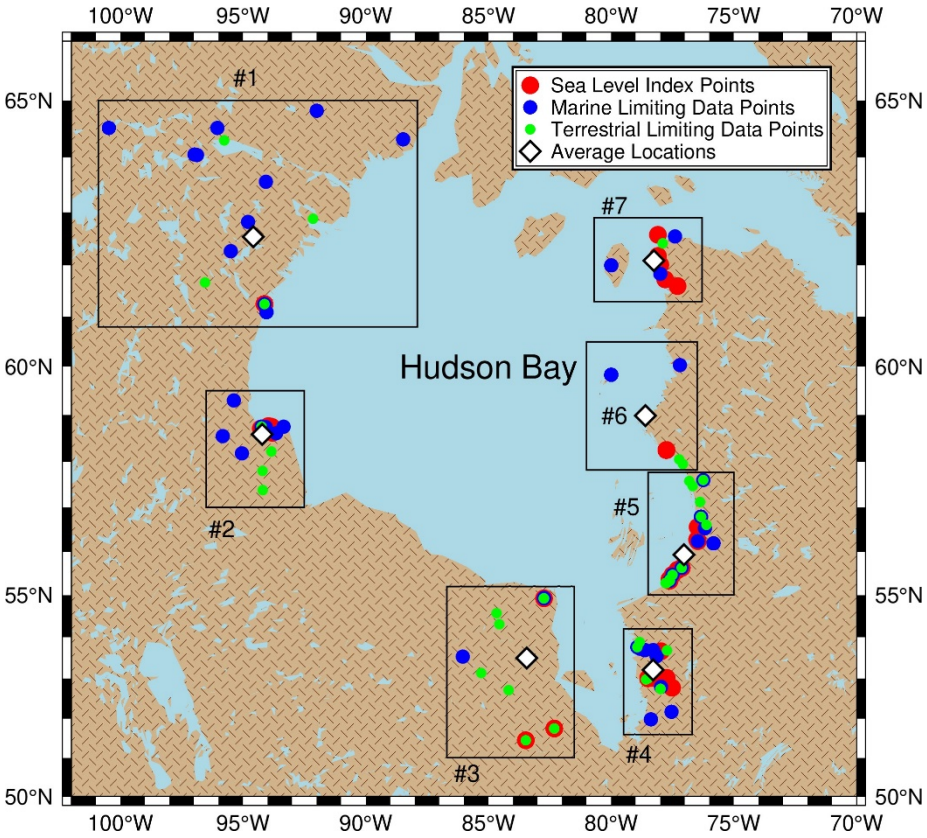


Figure 2.S2. Legend on next page.

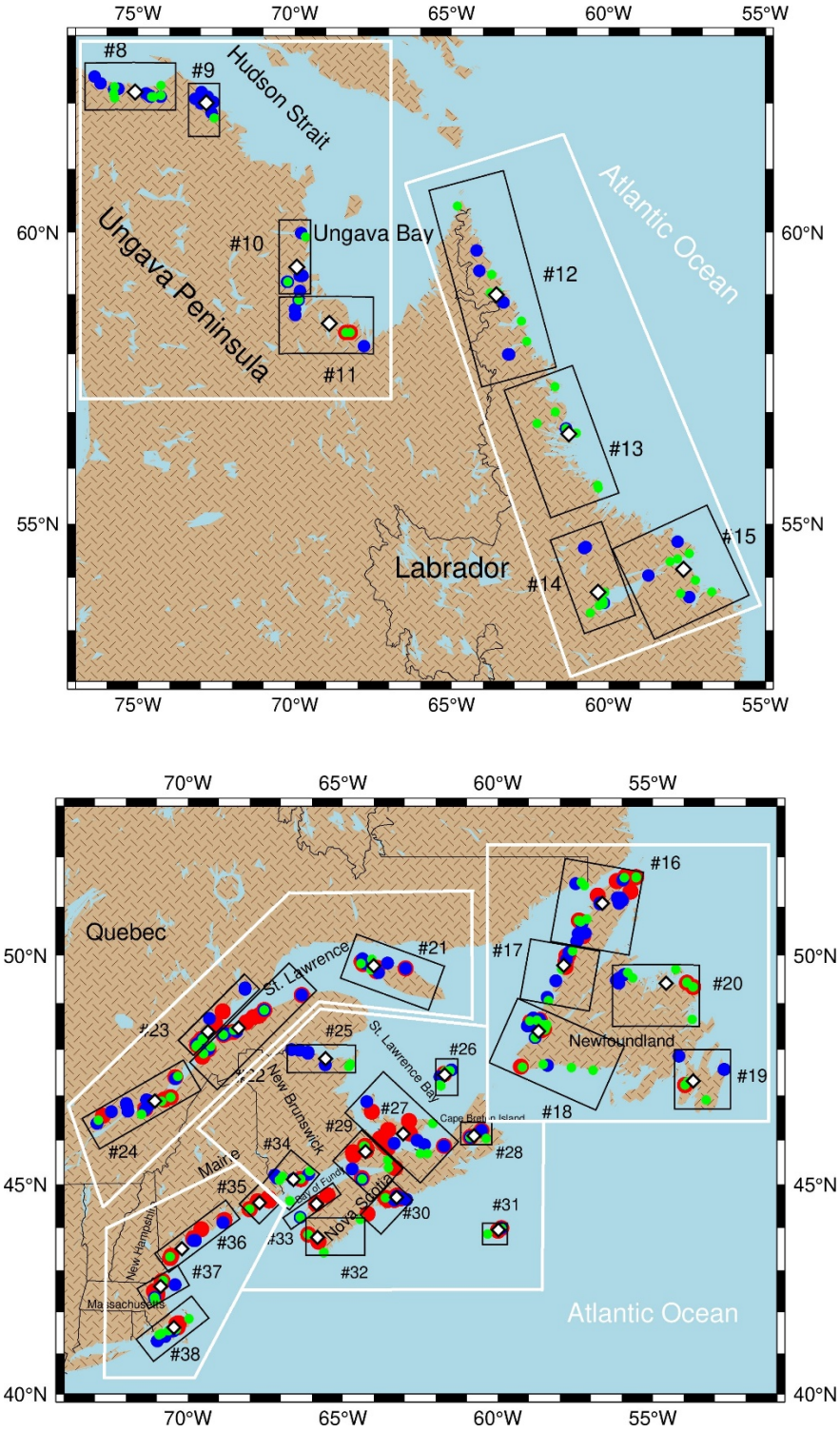


Figure 2.S2. Map showing the spatial distribution of RSL data used in this study. The top, middle and bottom frames show sites 1-7 (Hudson Bay), sites 8-15 (including Ungava Peninsula and Labrador), and sites 16-38 (including Newfoundland, St. Lawrence Corridor, New Brunswick and Nova Scotia, and Maine and Massachusetts), respectively. The locations of SLIPs, marine, and terrestrial limiting data points are indicated by red, blue and green circles, respectively. The white diamond in each site gives the average position of all paleo RSL observations; these points are the locations at which data-model curves are generated for visual comparison between model curves and observations.

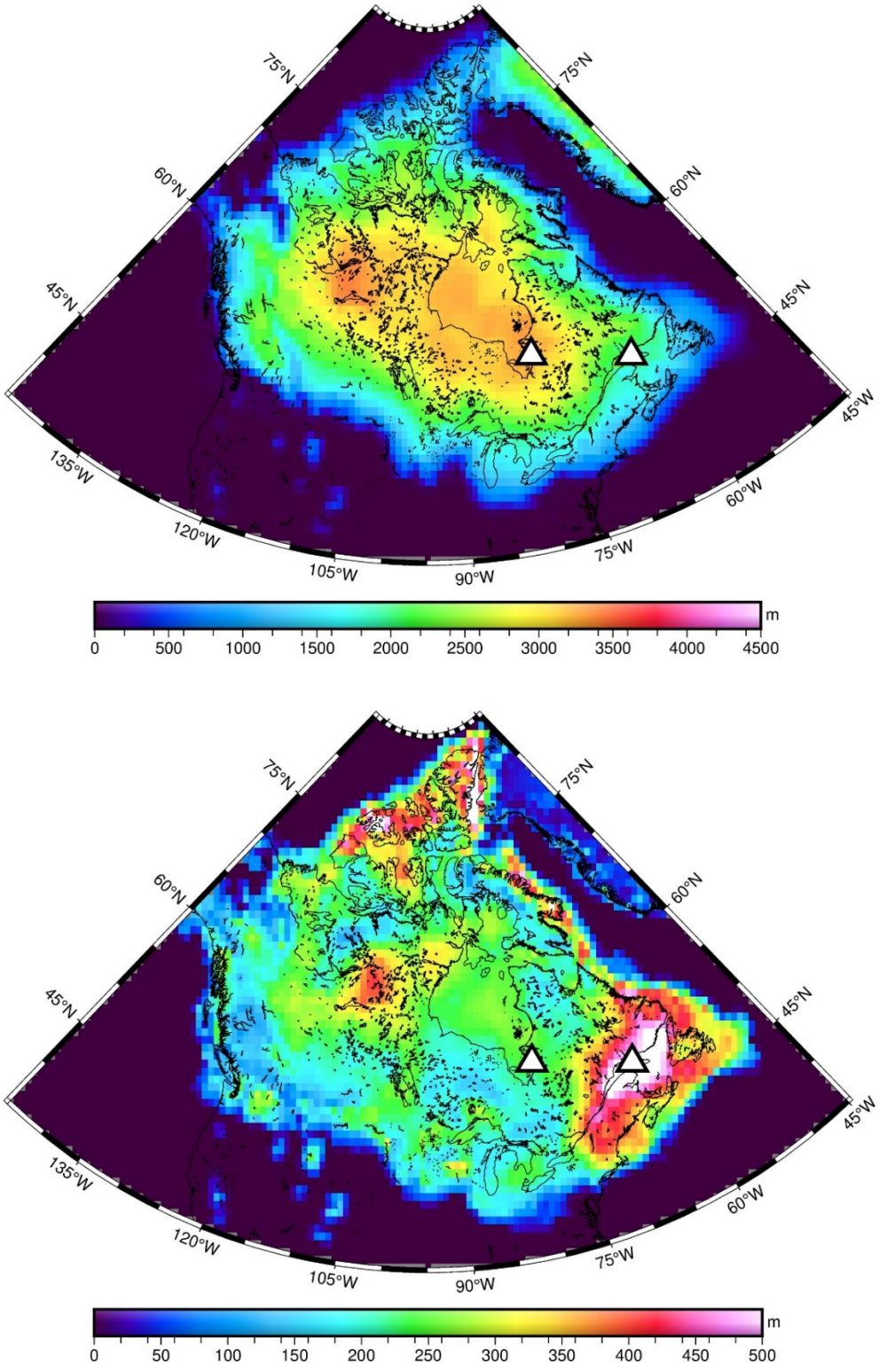


Figure 2.S3. The mean (top frame) and standard deviation (bottom frame) of the 34 North American ice sheet reconstructions (see Table 2.S1) adopted in this study for the time 21 ka. White triangles indicate the locations (average position in site #4 from Hudson Bay and site #21 from St. Lawrence Corridor) of the ice thickness time series in Figure 2.S5.

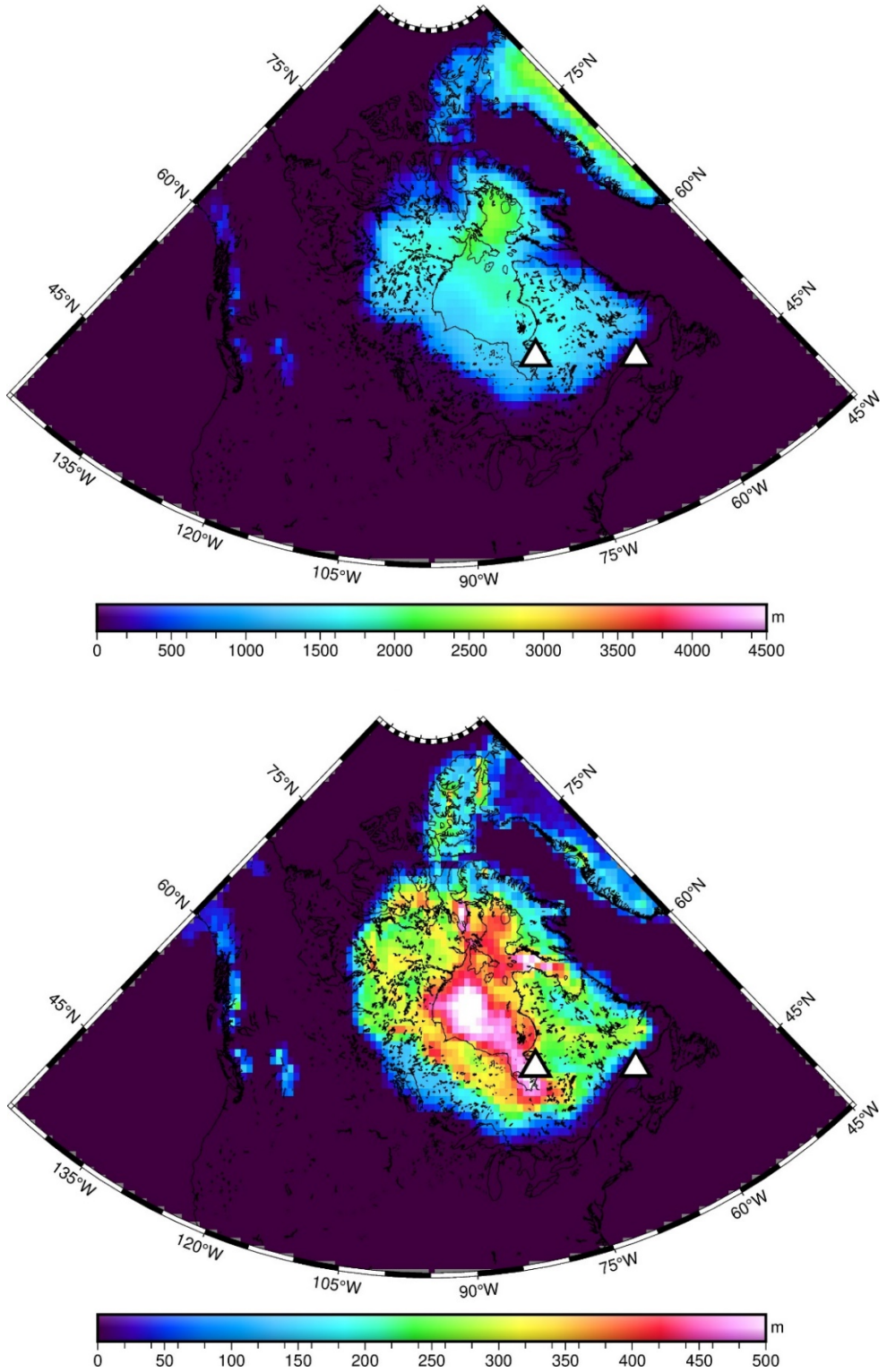


Figure 2.S4. The mean (top frame) and standard deviation (bottom frame) of the 34 North American ice sheet reconstructions (see Table 2.S1) adopted in this study for the time 10 ka. White triangles indicate the locations (average position in site #4 from Hudson Bay and site #21 from St. Lawrence Corridor) of the ice thickness time series in Figure 2.S5.

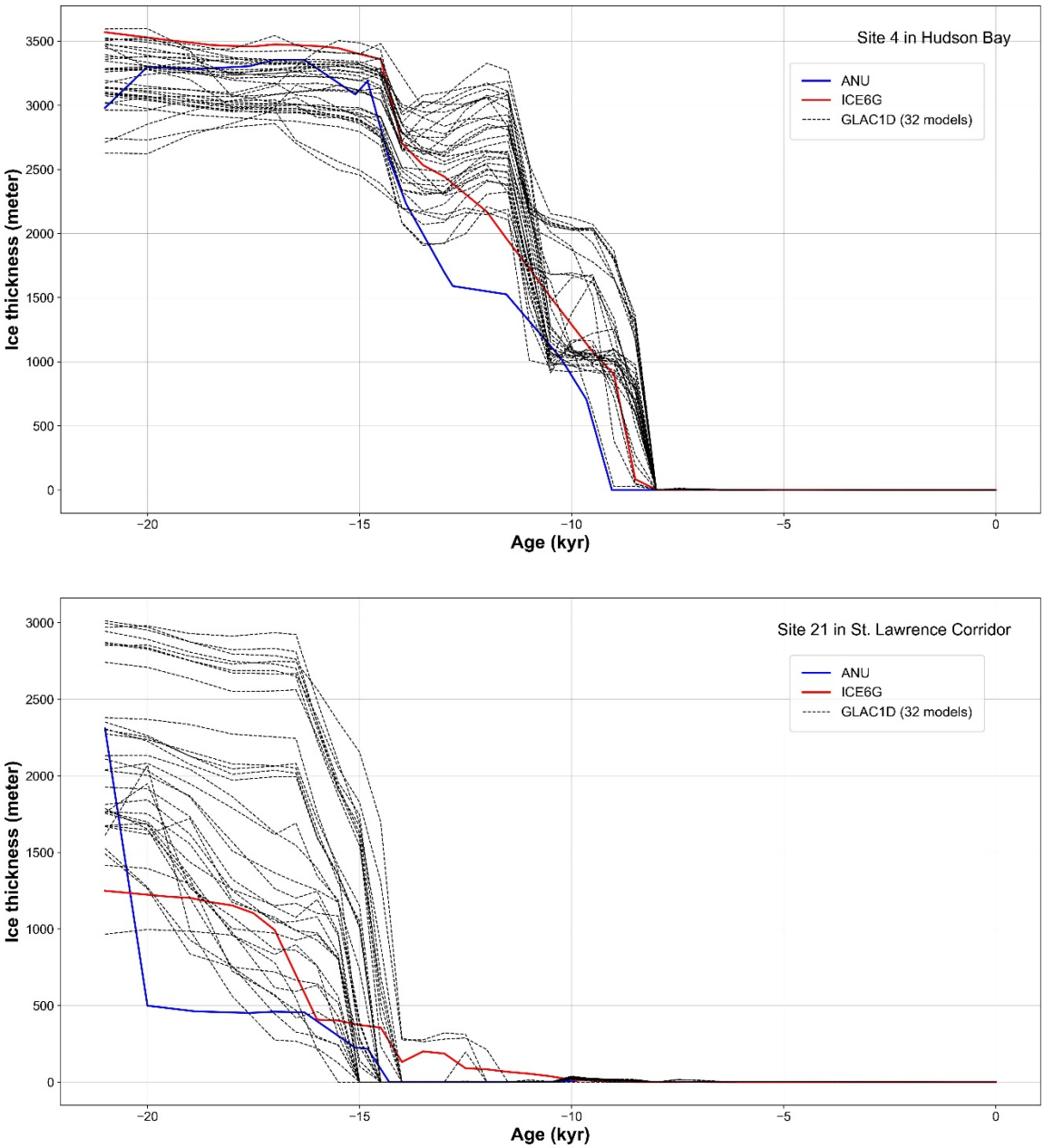


Figure 2.S5. Temporal evolution of the ice thickness from 21 ka to the present day based on the 34 ice history models adopted in this study for two locations (see white triangles in Figures 2.S3 and 2.S4): average position in site #4 from Hudson Bay (top frame) and average position in site #21 from St. Lawrence Corridor (bottom frame).

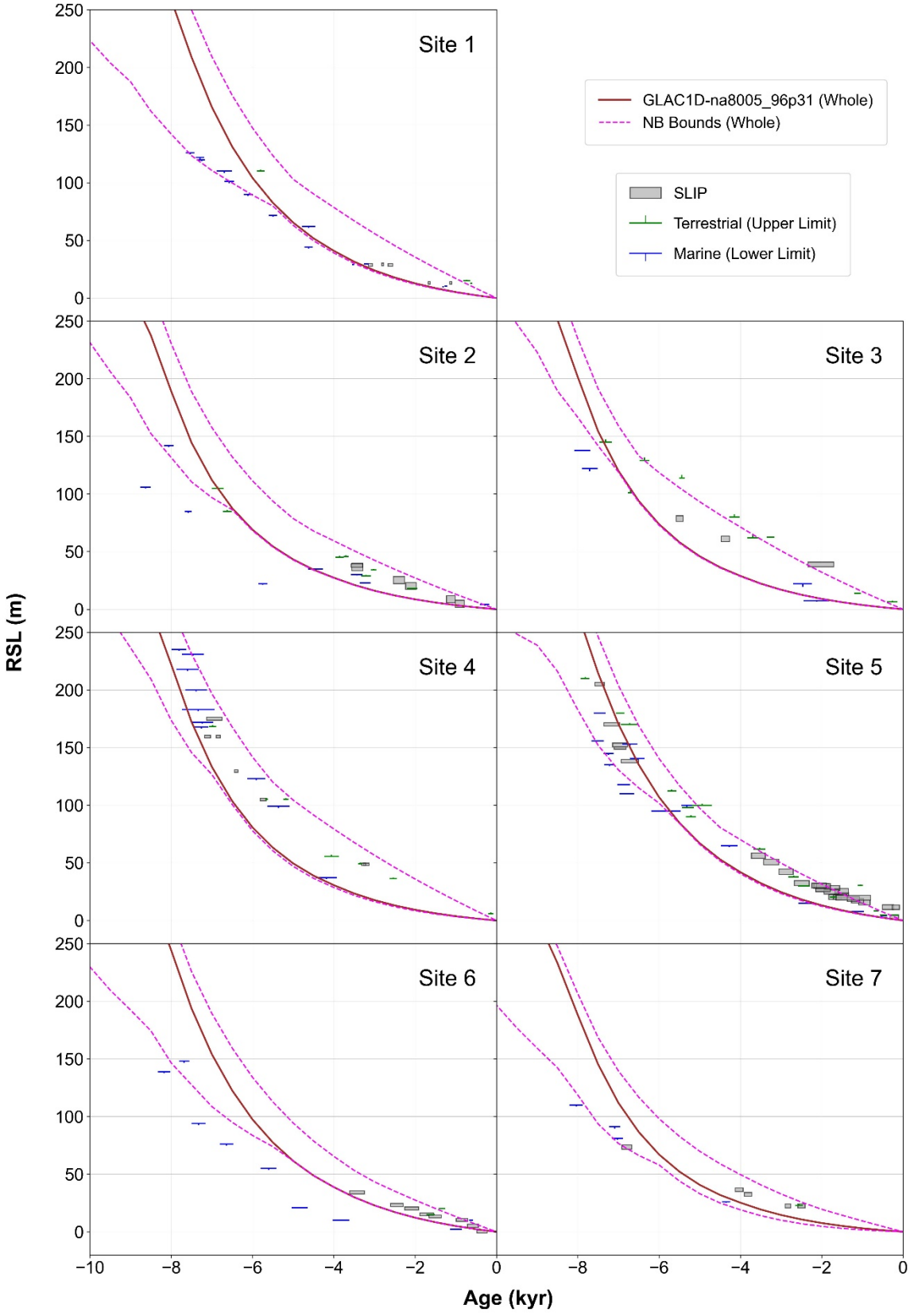


Figure 2.S6. Legend on Page 82.

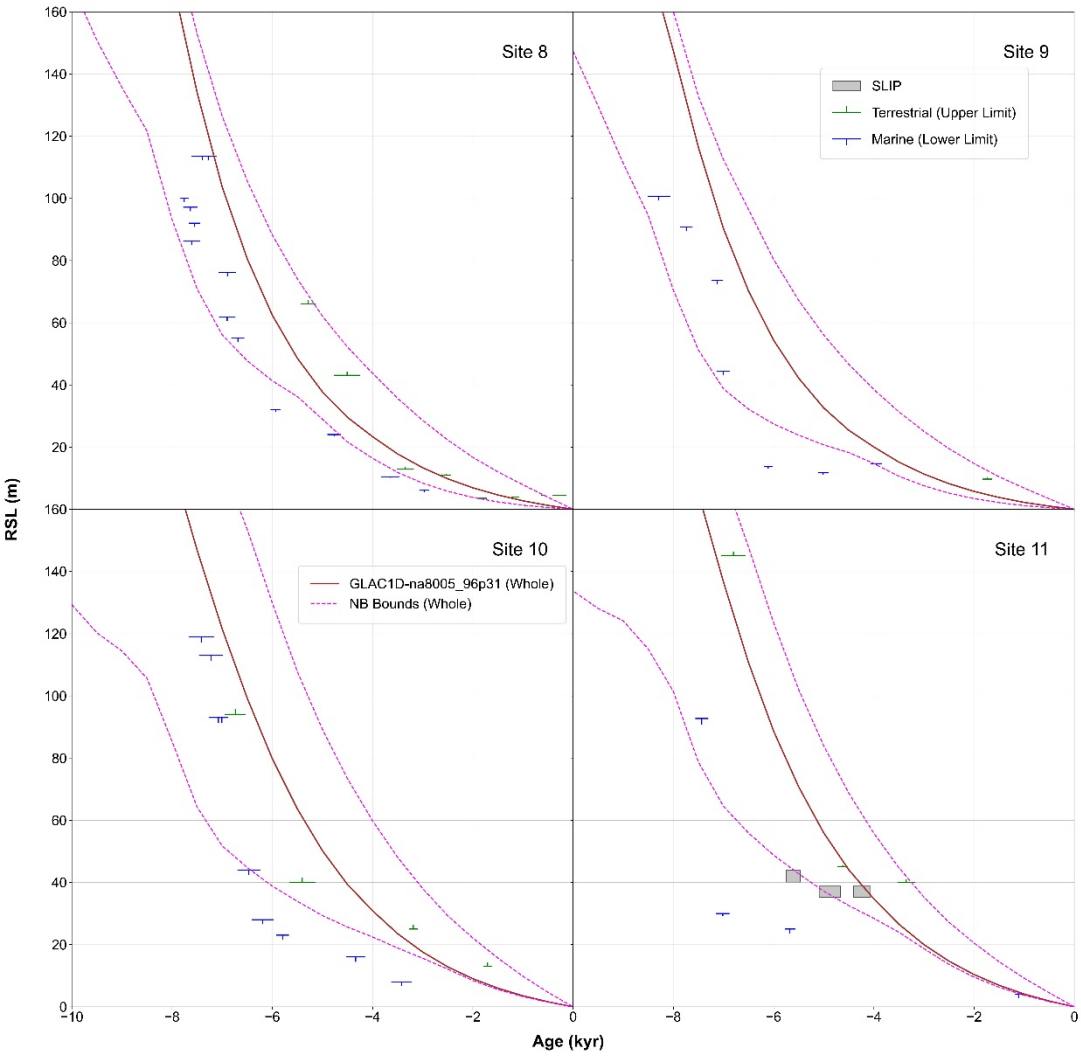


Figure 2.S6. Legend on Page 82.

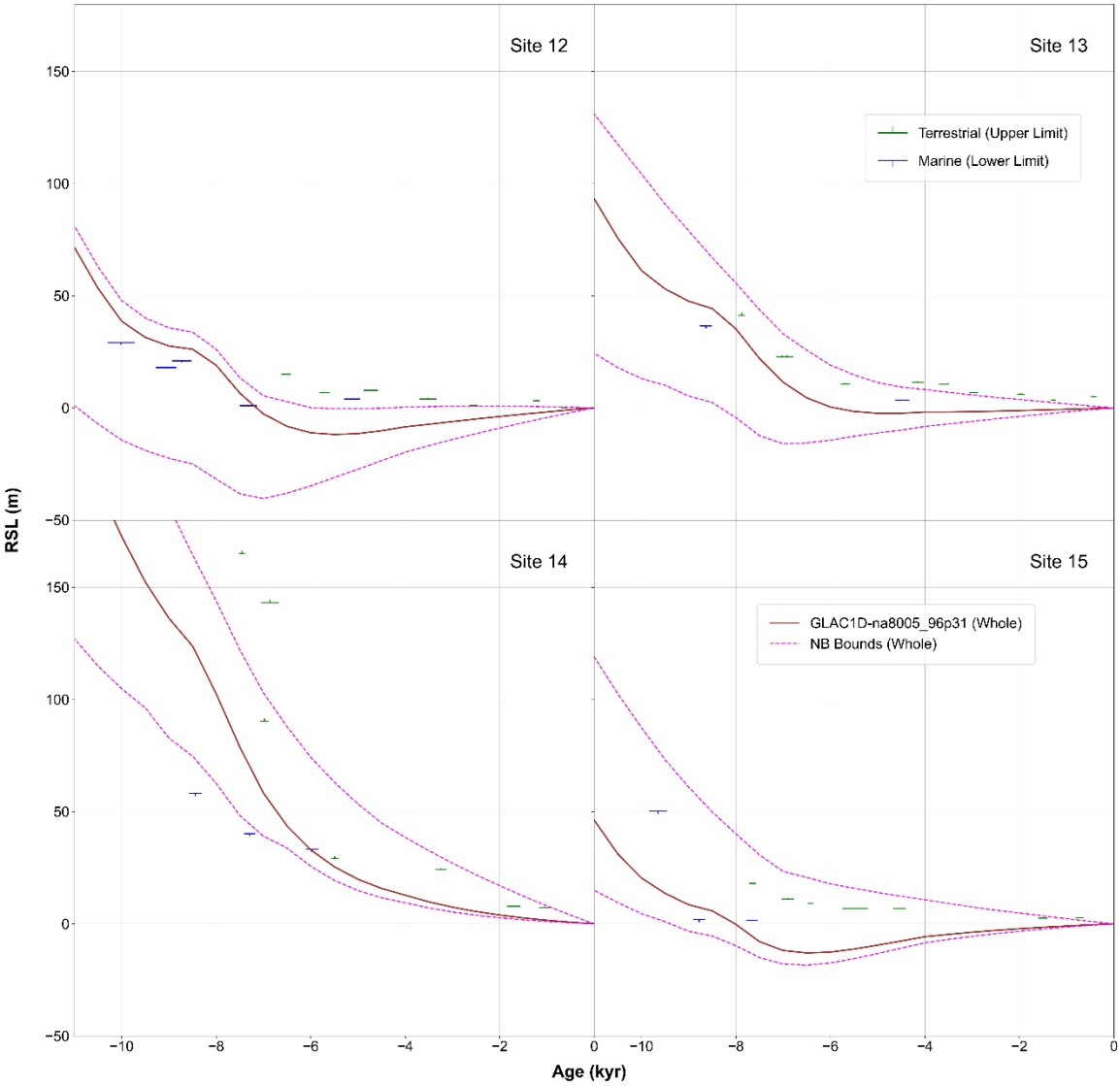


Figure 2.S6. Legend on Page 82.

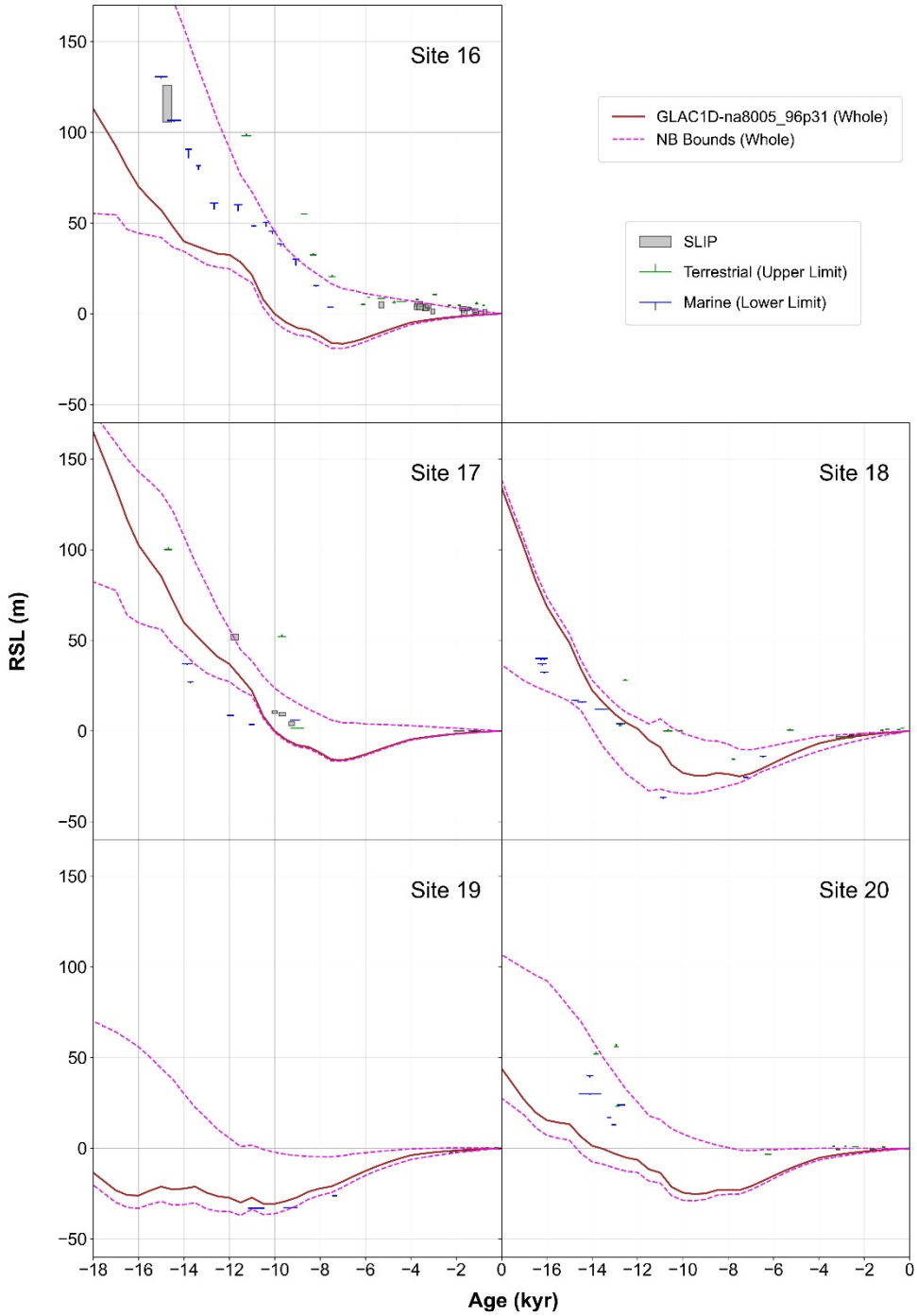


Figure 2.S6. Legend on Page 82.

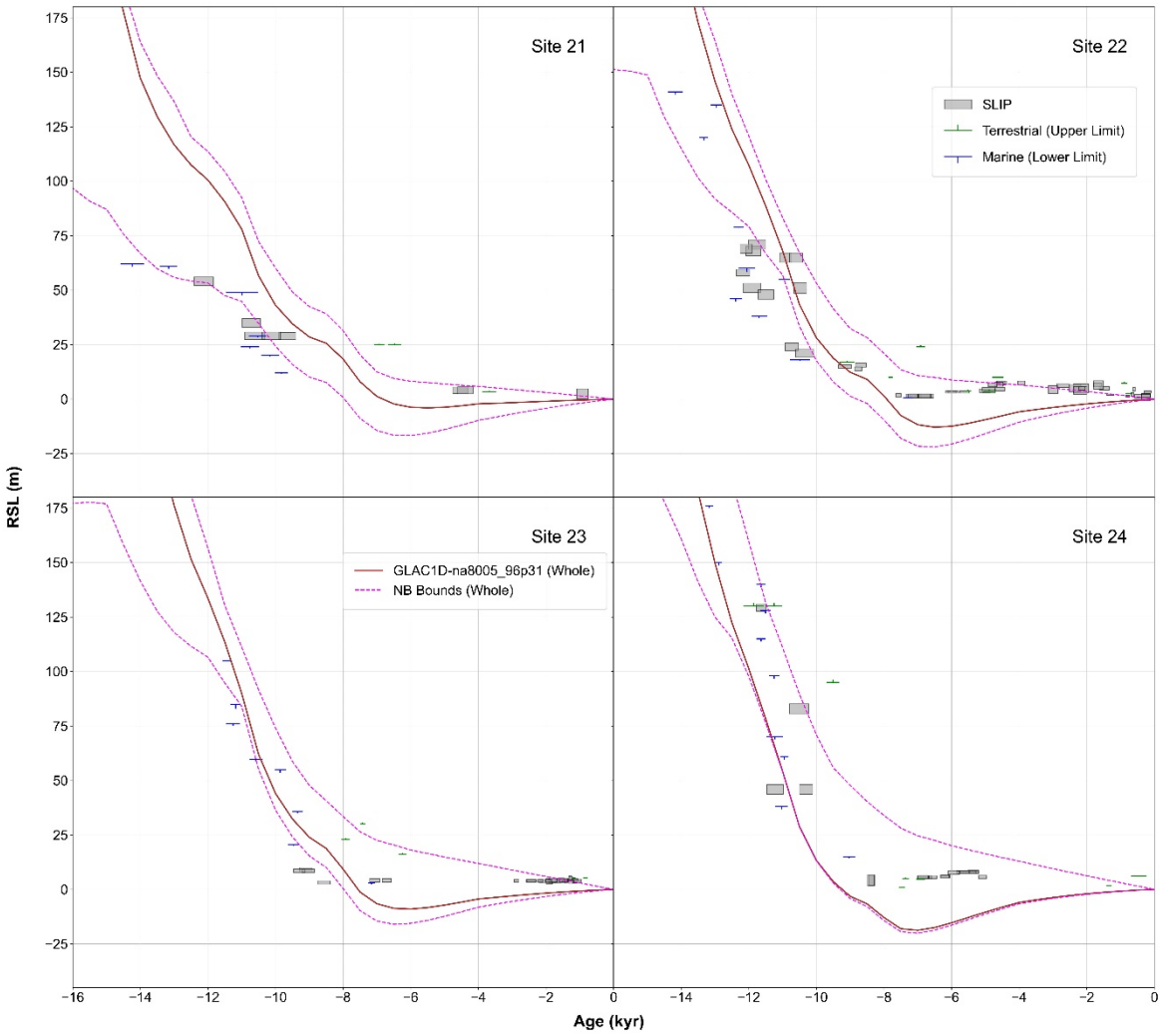


Figure 2.S6. Legend on Page 82.

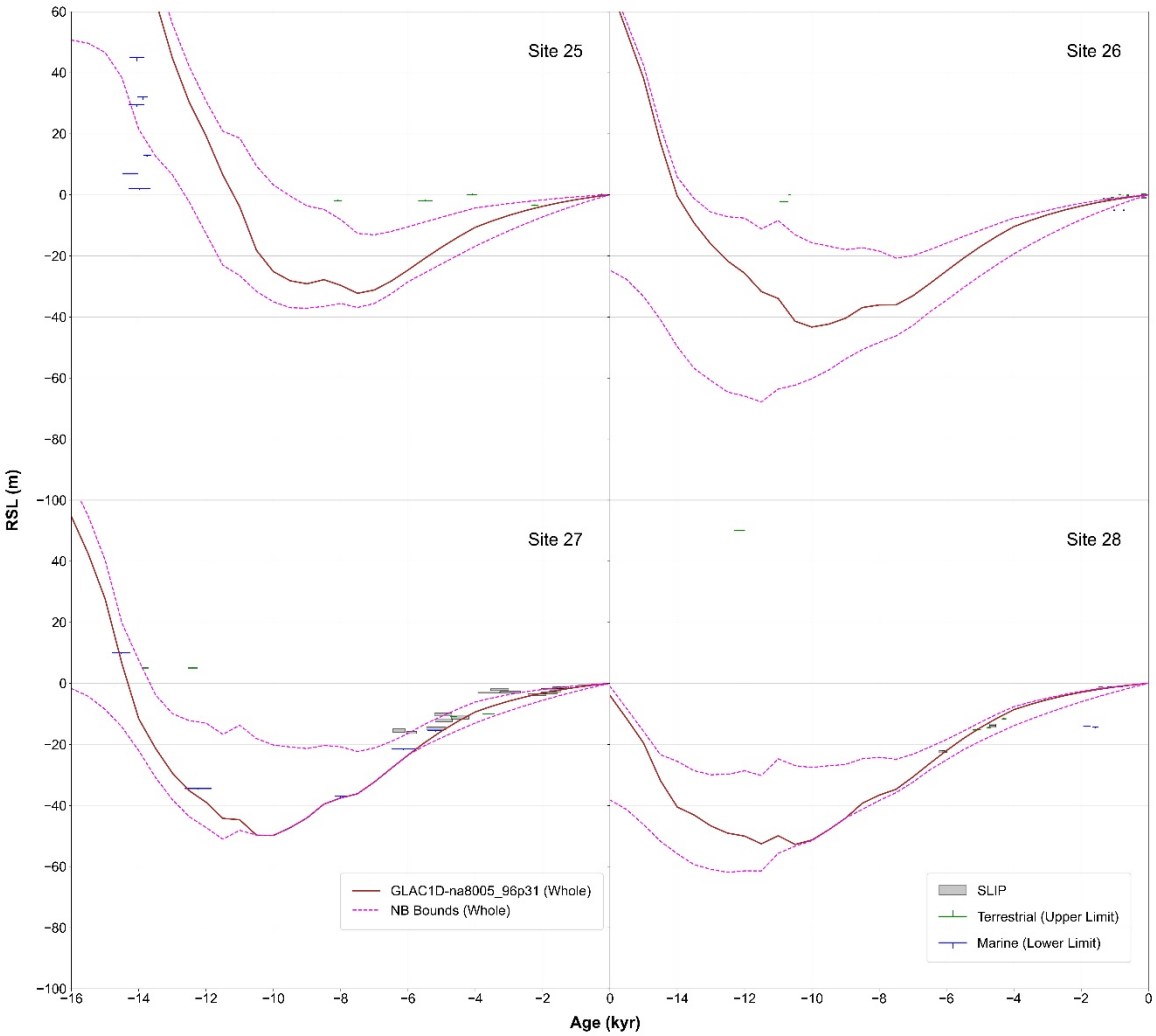


Figure 2.S6. Legend on Page 82.

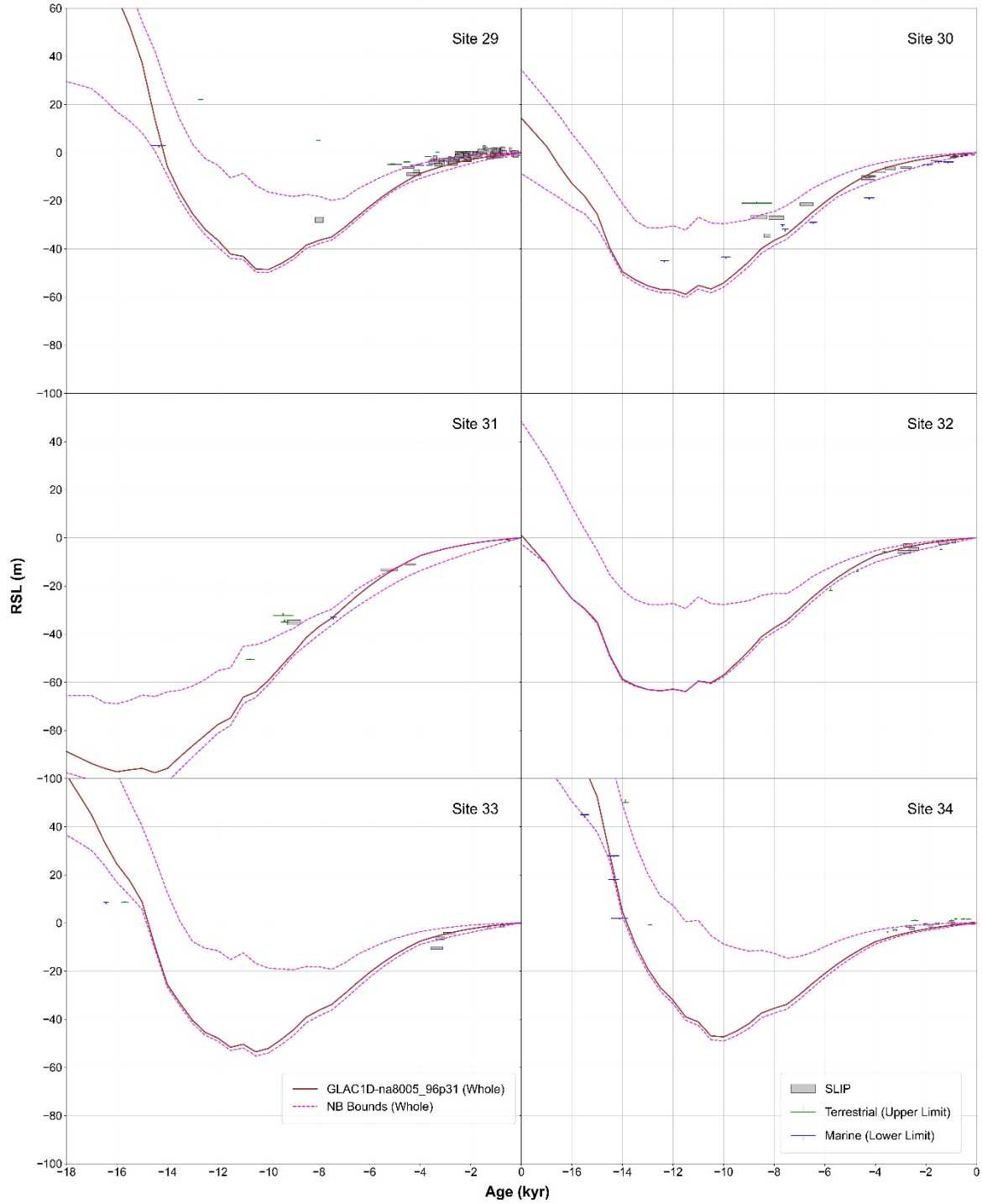


Figure 2.S6. Legend on Page 82.

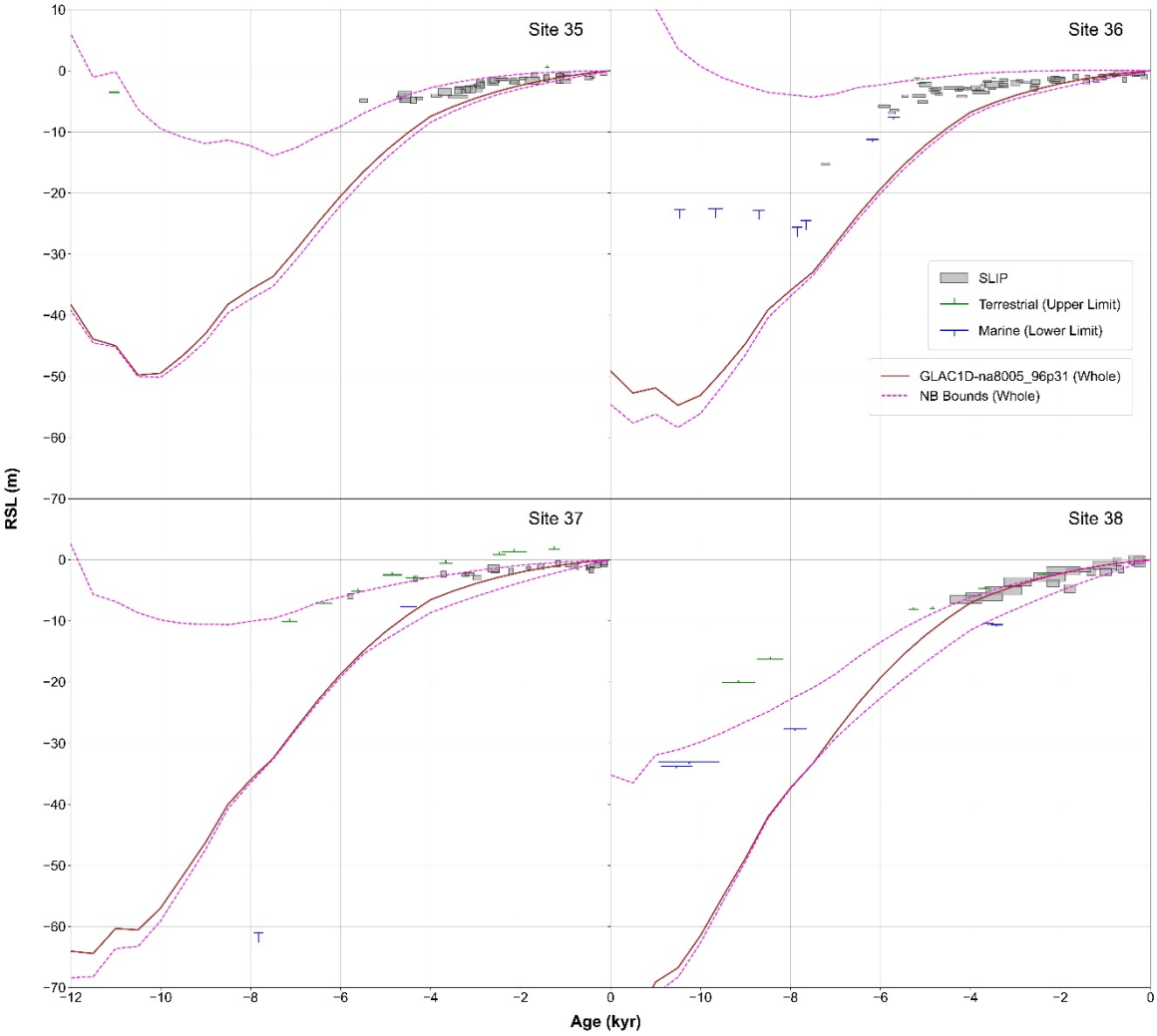


Figure 2.S6. The purple-solid line shows the optimal modelled RSL estimated from the data-model misfit analysis based on the whole dataset (sites 1-38). The upper and lower uncertainty bounds (purple-dashed lines) are quantified by the nominal Bayesian approach based on consideration of the 1σ uncertainty for determination of a sub-ensemble of the highest-probability Earth model parameter sets. RSL curves were plotted at the average position of all RSL data points within each site (see the white diamonds in Figure 2.S2). The dimension of each SLIP box shows ±1σ uncertainty in RSL and age. For limiting data points, the horizontal and vertical bars show ±1σ RSL age uncertainty and one side of the 1σ RSL uncertainty, respectively (the misfit analysis was carried out based on the 1σ uncertainty in RSL and age).

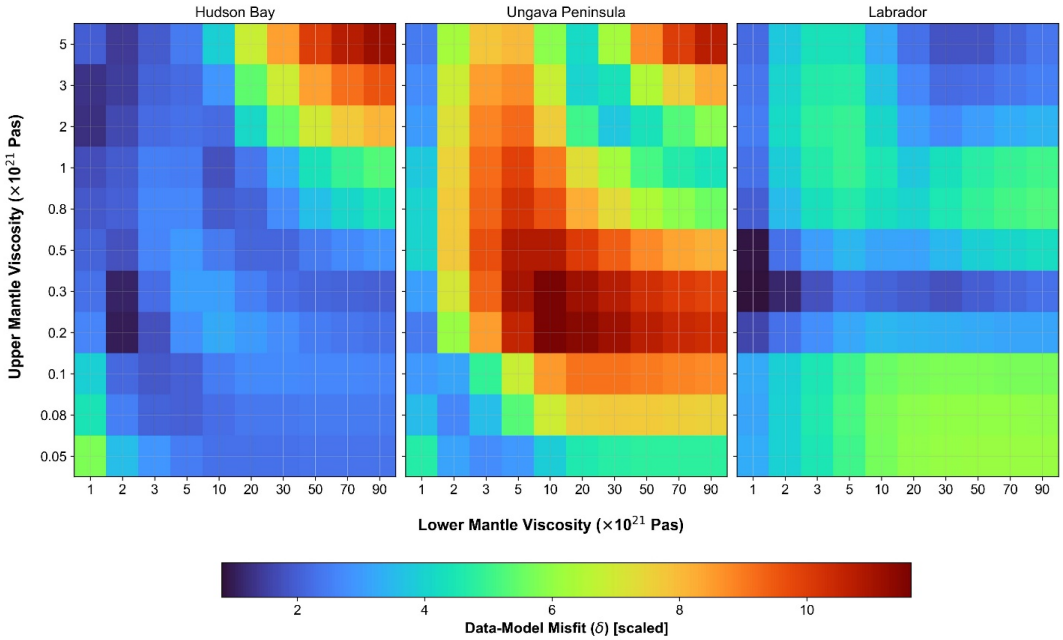


Figure 2.S7. The data-model misfit plots (δ) associated with Hudson Bay (left), Ungava Peninsula (middle), and Labrador (right), estimated by the misfit analysis for the ANU ice history model (LT is 96 km in all plots).

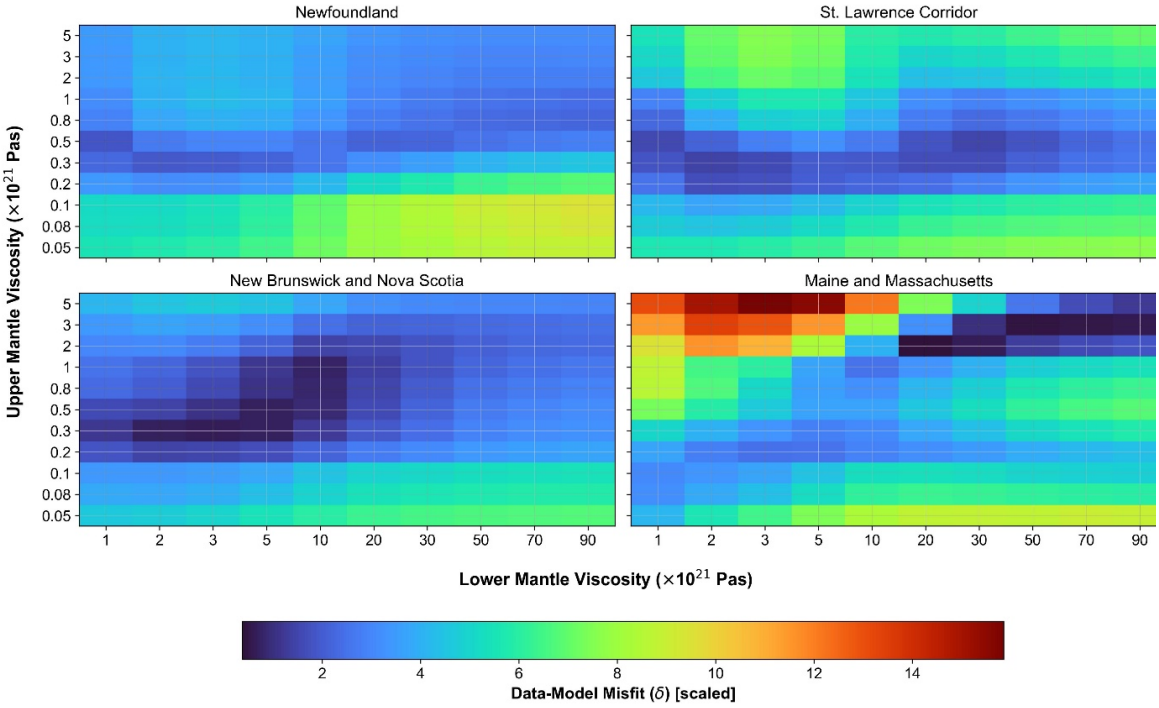


Figure 2.S8. The data-model misfit plots (δ) associated with Newfoundland (top left), St. Lawrence Corridor (top right), New Brunswick and Nova Scotia (bottom left) and Maine and Massachusetts (bottom right), estimated by the misfit analysis for ice history GLAC1D-na8005 (LT is 96 km in all plots).

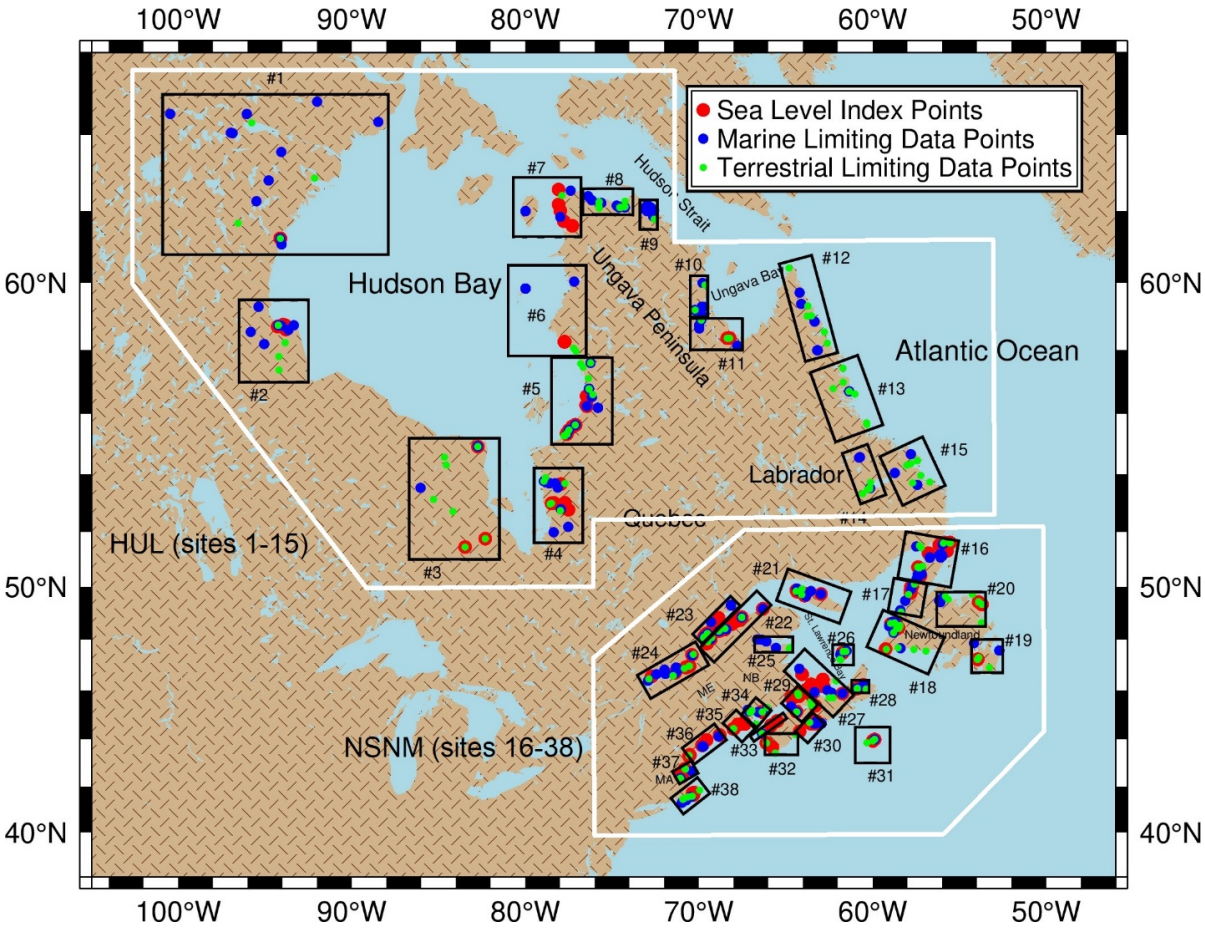


Figure 2.S9. Partitioning the whole study region into 2 geographic subsets based on the data-model misfit analysis. HUL (sites 1-15) includes 3 subregions: Hudson Bay, Ungava Peninsula, and Labrador. NSNM (sites 16-38) comprises 4 subregions: Newfoundland, St. Lawrence Corridor, New Brunswick and Nova Scotia, and Maine and Massachusetts.

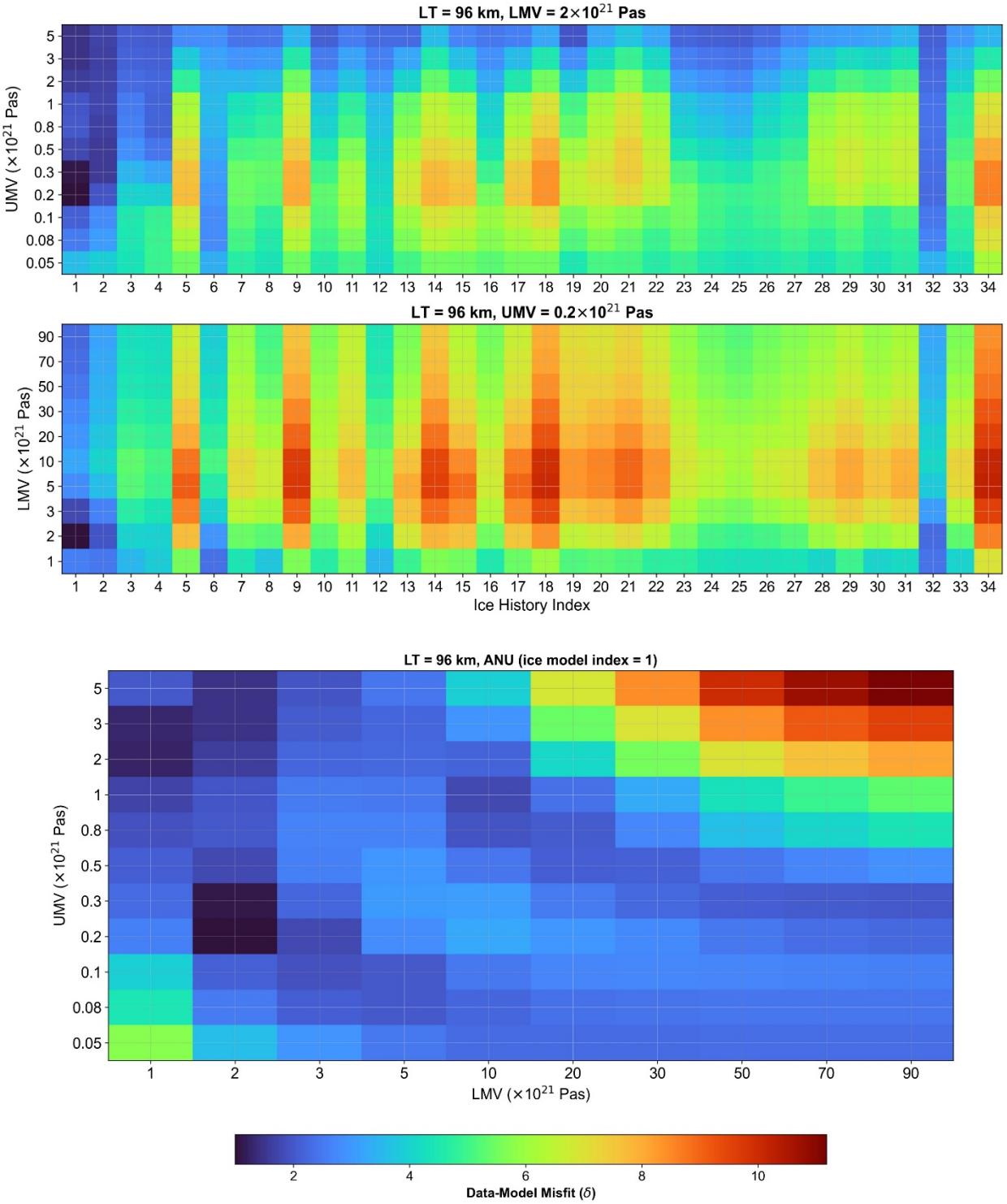


Figure 2.S10. Data-model misfit values (δ) for Hudson Bay as a function of (from top to bottom) UMV and ice loading history when LMV is constant (2×10^{21} Pas), LMV and ice loading history when UMV is fixed at 0.2×10^{21} Pas, and LMV and UMV for the ANU ice model (ice history index = 1). In all 3 plots, the lithospheric thickness is 96 km. Note that these plots do not necessarily display all the minimum and maximum values of δ for the parameter space considered.

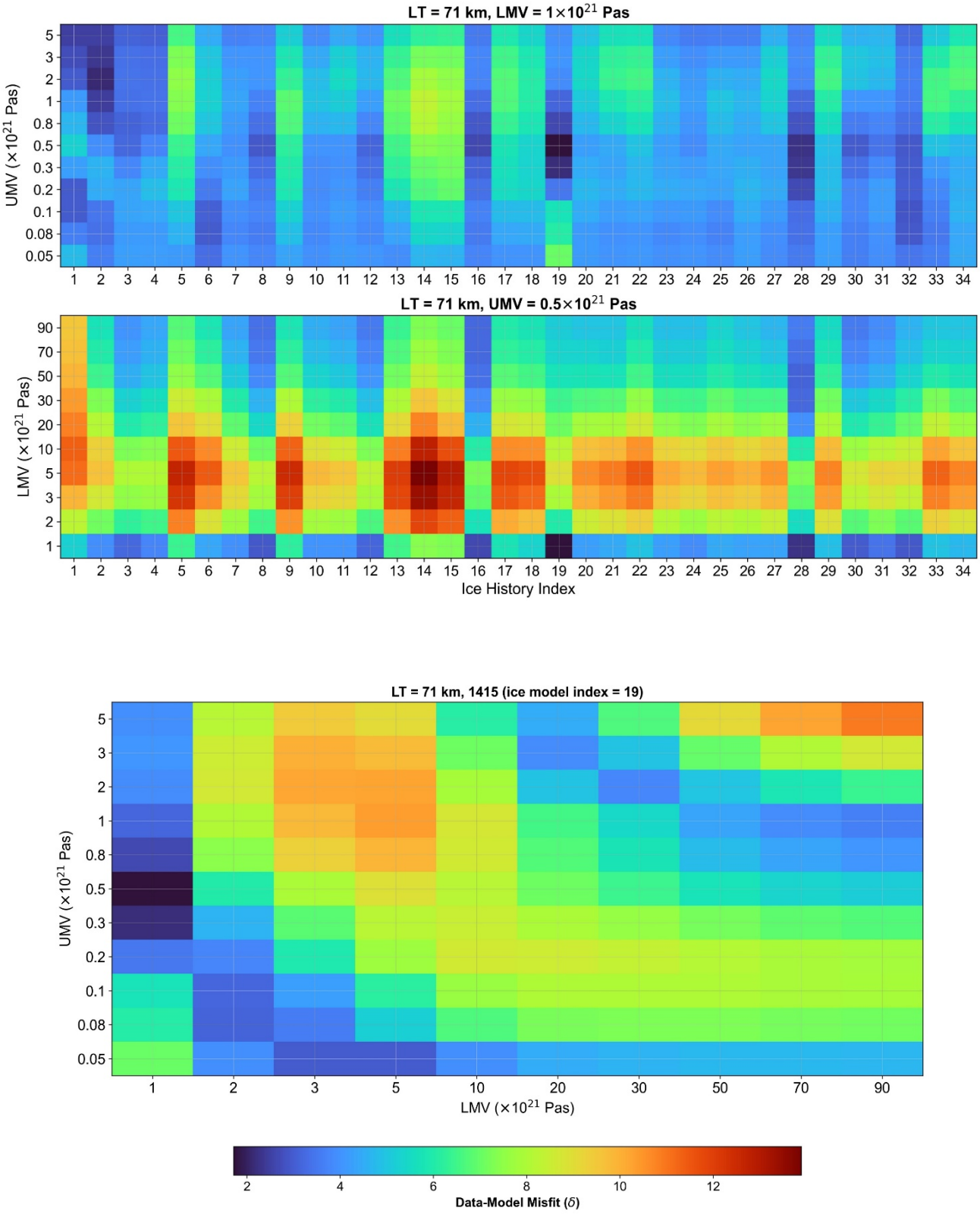


Figure 2.S11. Data-model misfit values (δ) for Ungava Peninsula as a function of (from top to bottom) UMV and ice loading history when LMV is constant (10^{21} Pas), LMV and ice loading history when UMV is fixed at 0.5×10^{21} Pas, and LMV and UMV for GLAC1D-na1415 (ice history index = 19). In all 3 plots, the lithospheric thickness is 71 km. Note that these plots do not necessarily display all the minimum and maximum values of δ for the parameter space considered.

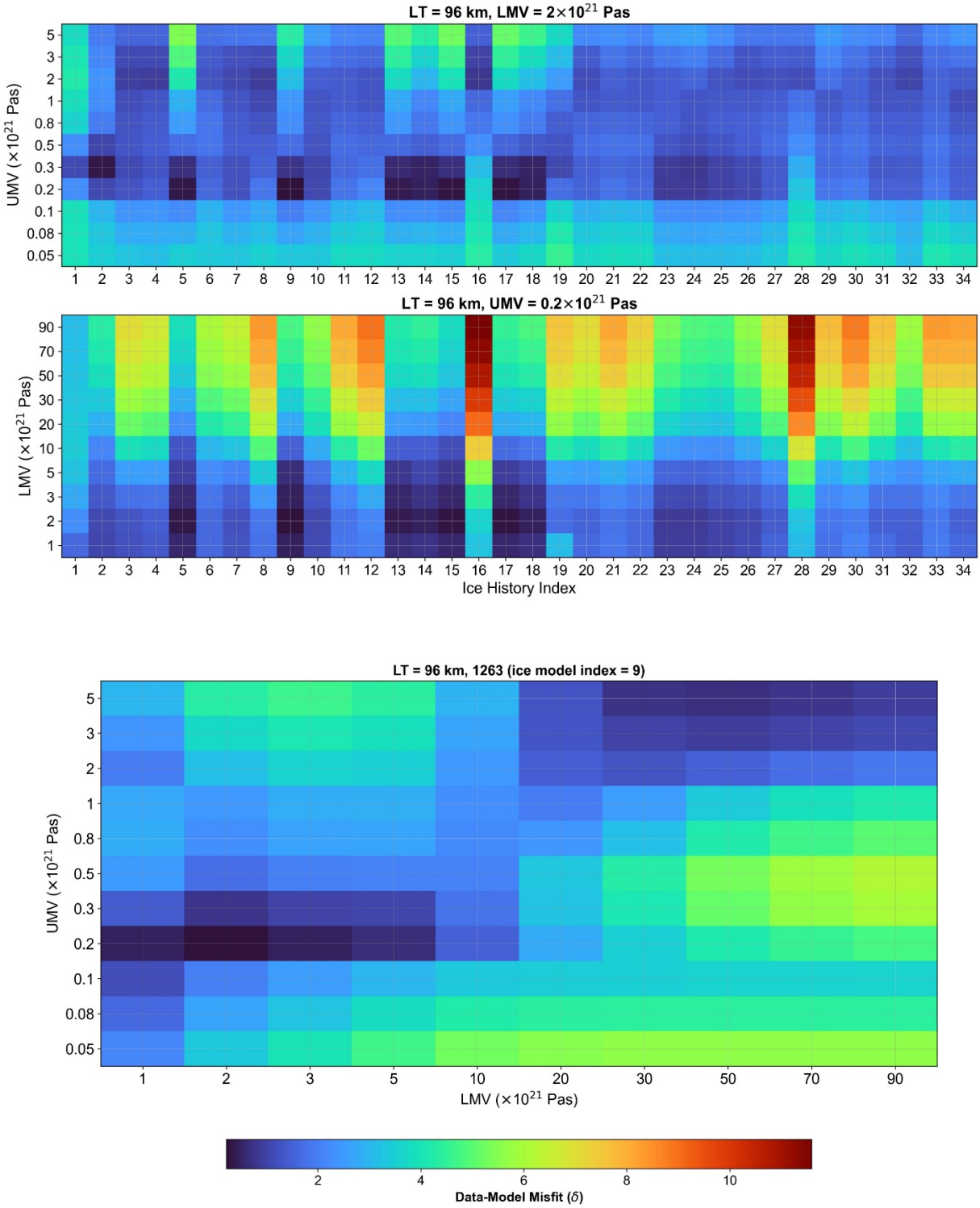


Figure 2.S12. Data-model misfit values (δ) for Labrador as a function of (from top to bottom) UMV and ice loading history when LMV is constant (2×10^{21} Pas), LMV and ice loading history when UMV is fixed at 0.2×10^{21} Pas, and LMV and UMV for GLAC1D-na1263 (ice history index = 9). In all 3 plots, the lithospheric thickness is 96 km. Note that these plots do not necessarily display all the minimum and maximum values of δ for the parameter space considered.

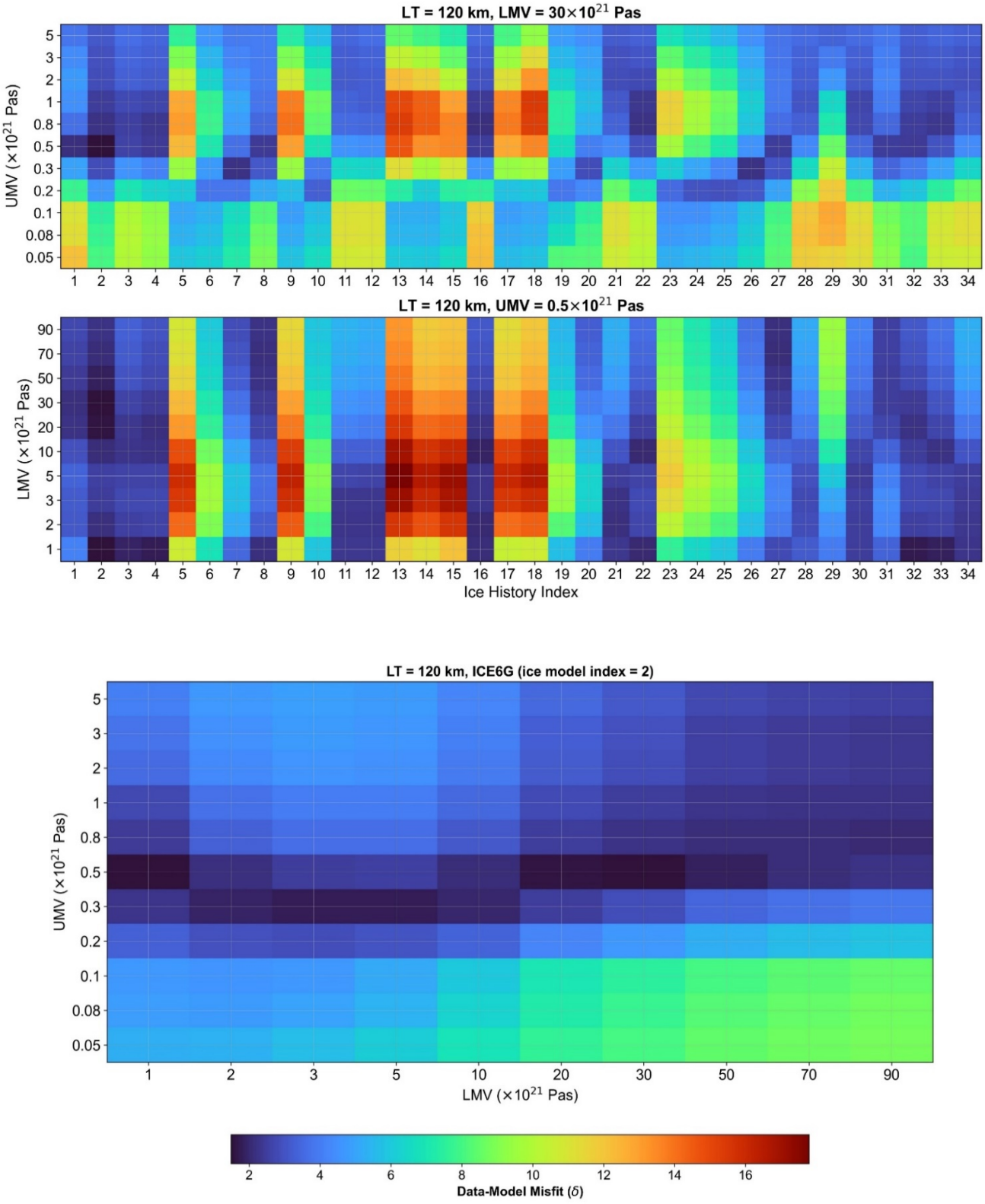


Figure 2.S13. Data-model misfit values (δ) for Newfoundland as a function of (from top to bottom) UMV and ice loading history when LMV is constant (30×10^{21} Pas), LMV and ice loading history when UMV is fixed at 0.5×10^{21} Pas, and LMV and UMV for ICE-6G (ice history index = 2). In all 3 plots, the lithospheric thickness is 120 km. Note that these plots do not necessarily display all the minimum and maximum values of δ for the parameter space considered.

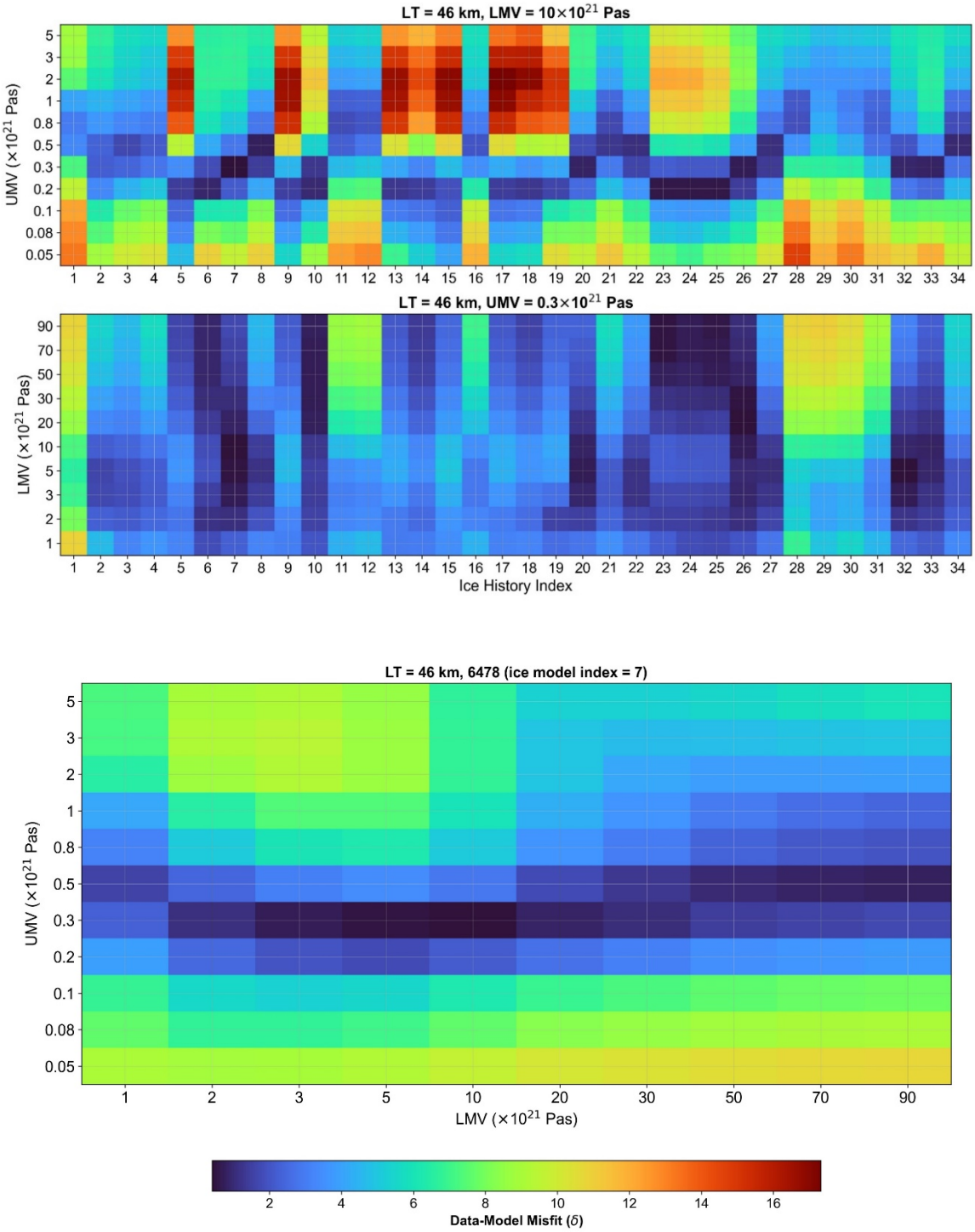


Figure 2.S14. Data-model misfit values (δ) for St. Lawrence Corridor as a function of (from top to bottom) UMV and ice loading history when LMV is constant (10^{22} Pas), LMV and ice loading history when UMV is fixed at 0.3×10^{21} Pas, and LMV and UMV for GLAC1D-na6478 (ice history index = 7). In all 3 plots, the lithospheric thickness is 46 km. Note that these plots do not necessarily display all the minimum and maximum values of δ for the parameter space considered.

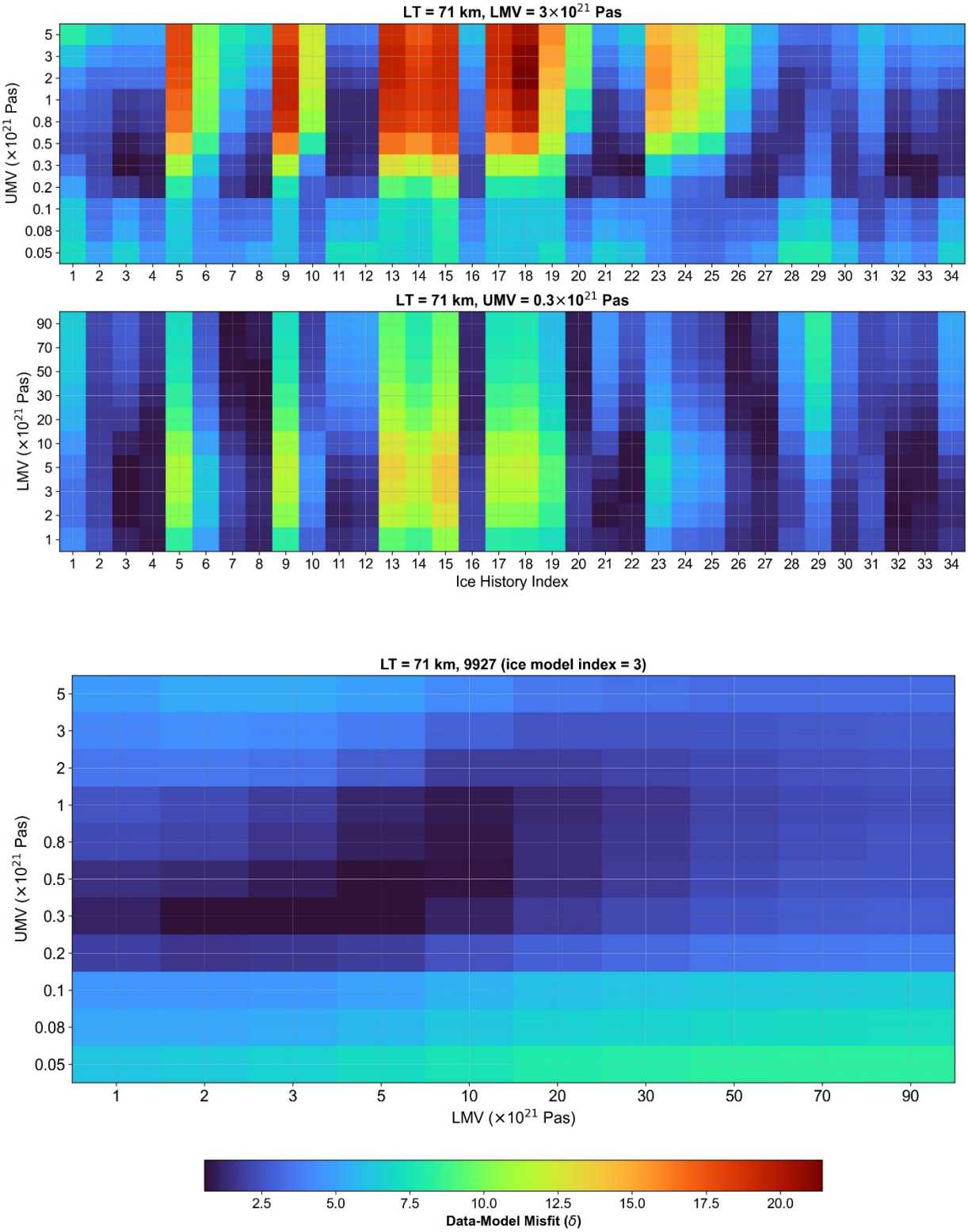


Figure 2.S15. Data-model misfit values (δ) for New Brunswick and Nova Scotia as a function of (from top to bottom) UMV and ice loading history when LMV is constant (3×10^{21} Pas), LMV and ice loading history when UMV is fixed at 0.3×10^{21} Pas, and LMV and UMV for GLAC1D-na9927 (ice history index = 3). In all 3 plots, the lithospheric thickness is 71 km. Note that these plots do not necessarily display all the minimum and maximum values of δ for the parameter space considered.

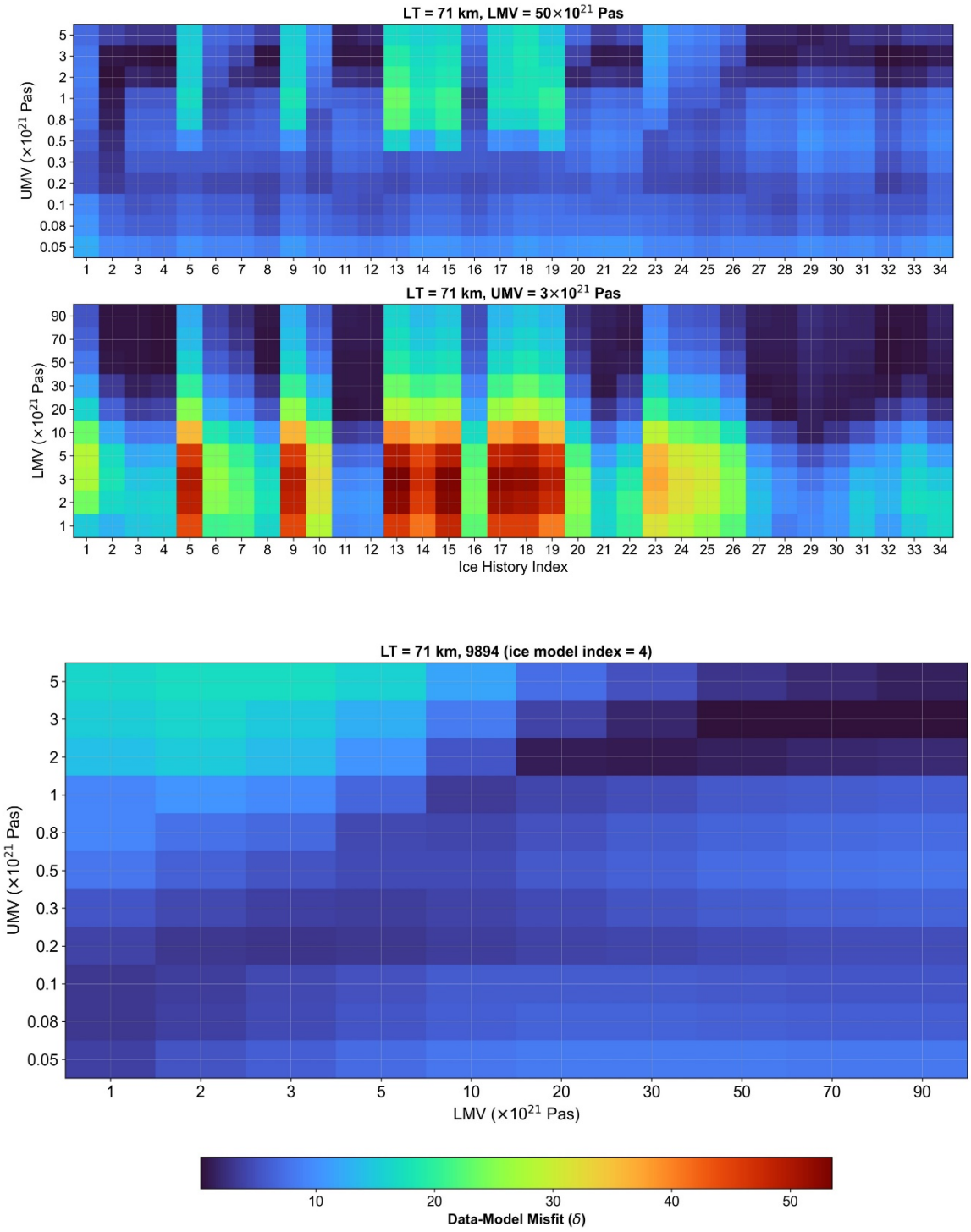


Figure 2.S16. Data-model misfit values (δ) for Maine and Massachusetts as a function of (from top to bottom) UMV and ice loading history when LMV is constant (50×10^{21} Pas), LMV and ice loading history when UMV is fixed at 3×10^{21} Pas, and LMV and UMV for GLAC1D-na9894 (ice history index = 4). In all 3 plots, the lithospheric thickness is 71 km. Note that these plots do not necessarily display all the minimum and maximum values of δ for the parameter space considered.

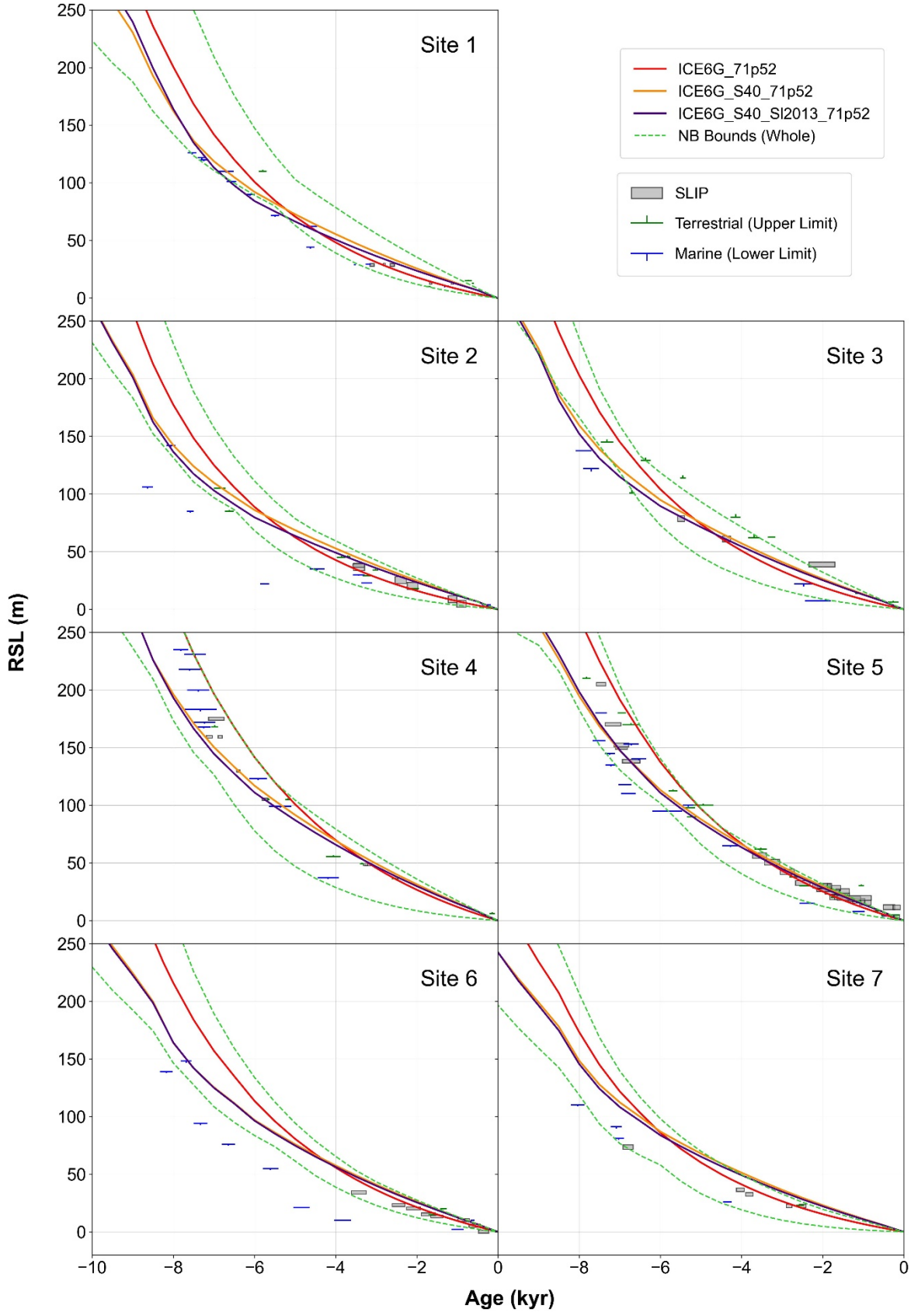


Figure 2.S17. Legend on Page 99.

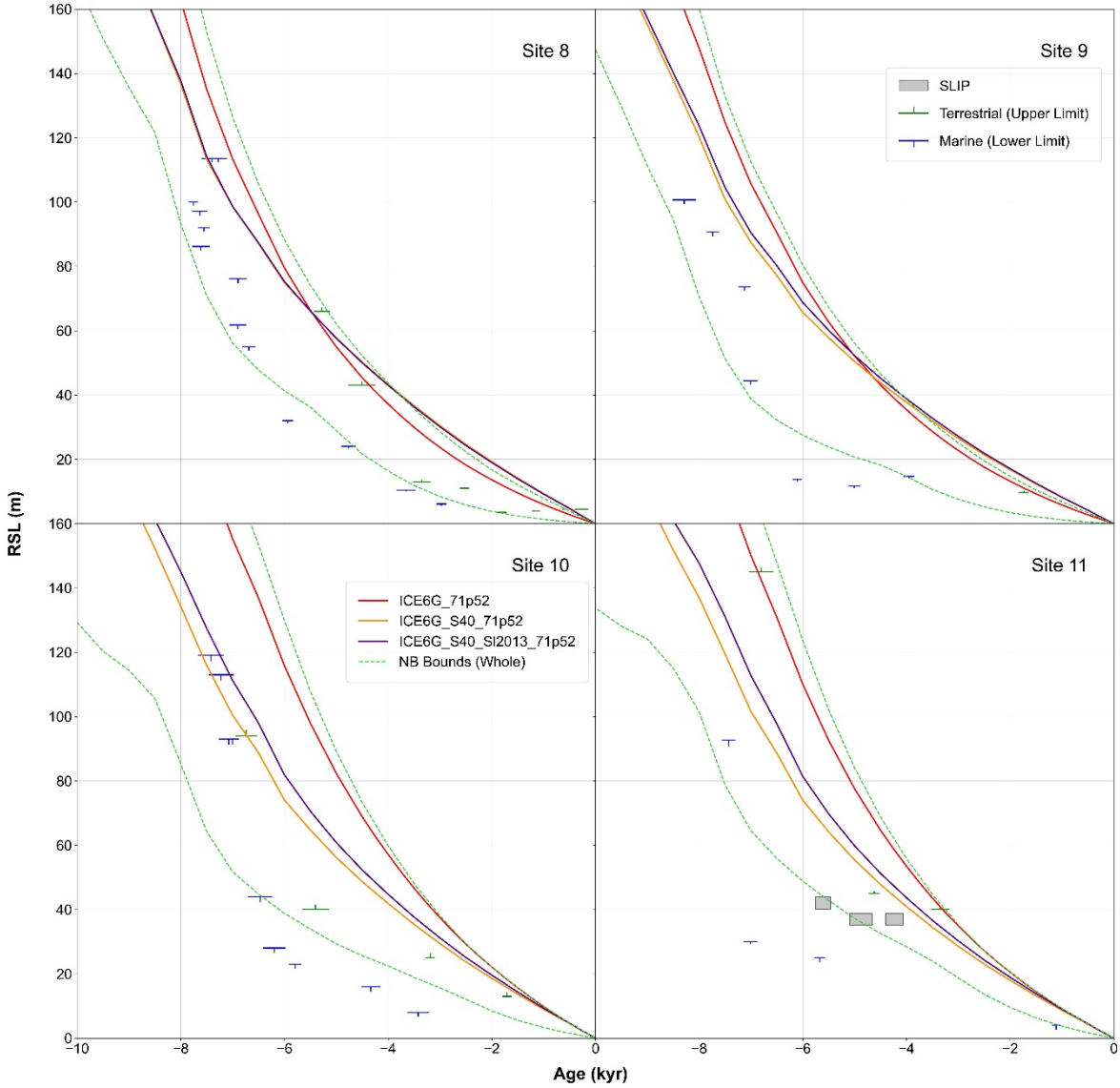


Figure 2.S17. Legend on Page 99.

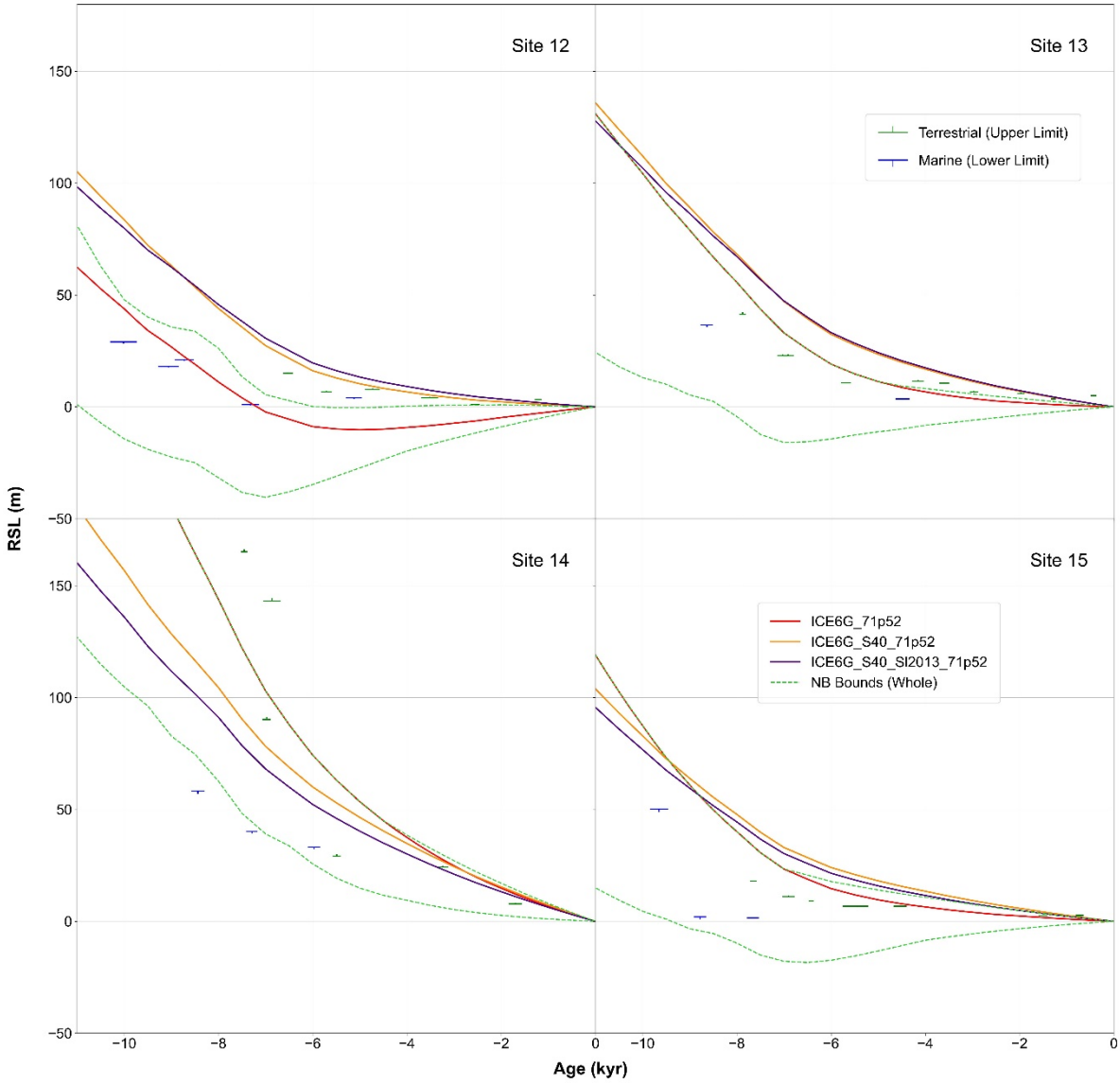


Figure 2.S17. Legend on Page 99.

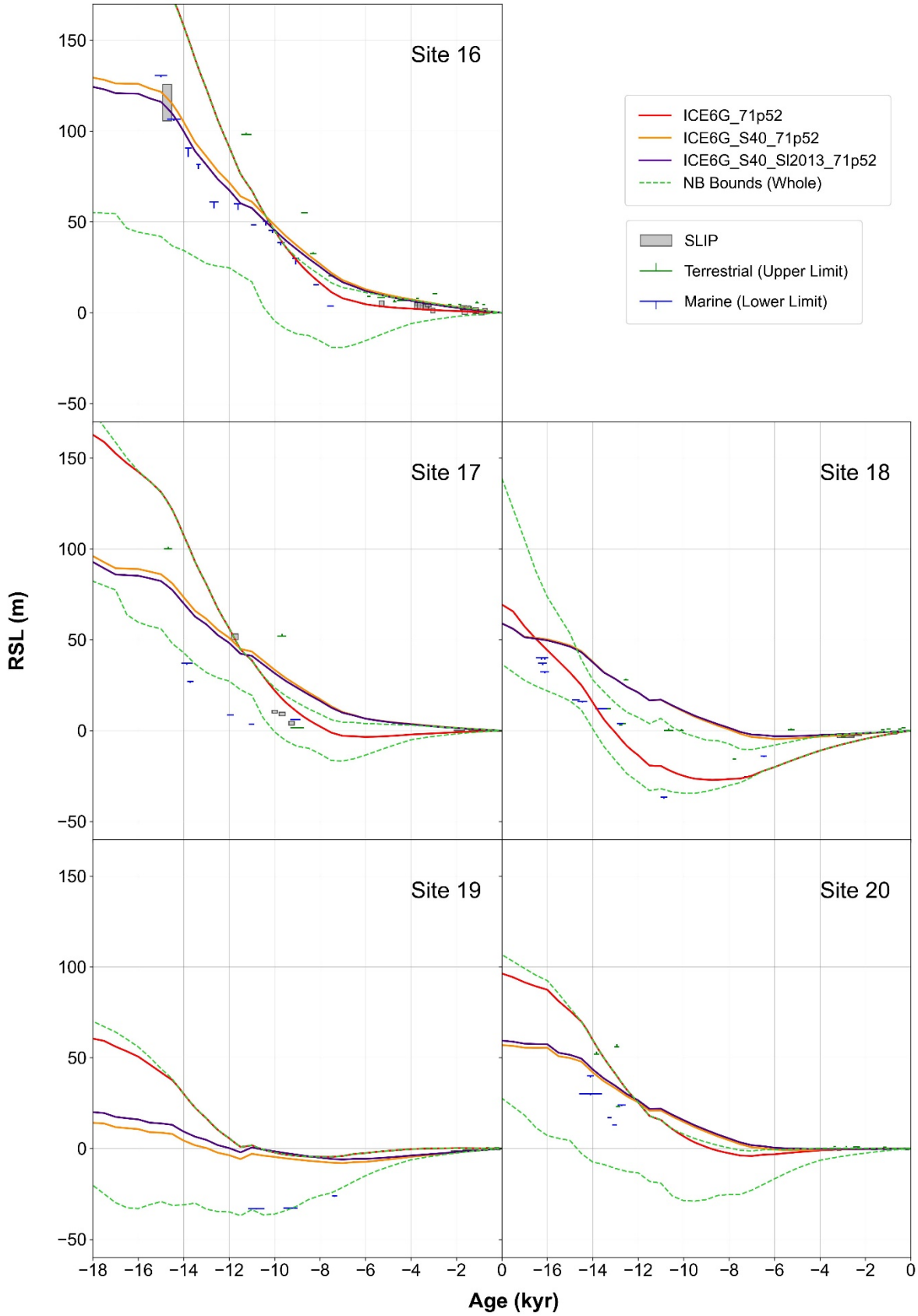


Figure 2.S17. Legend on Page 99.

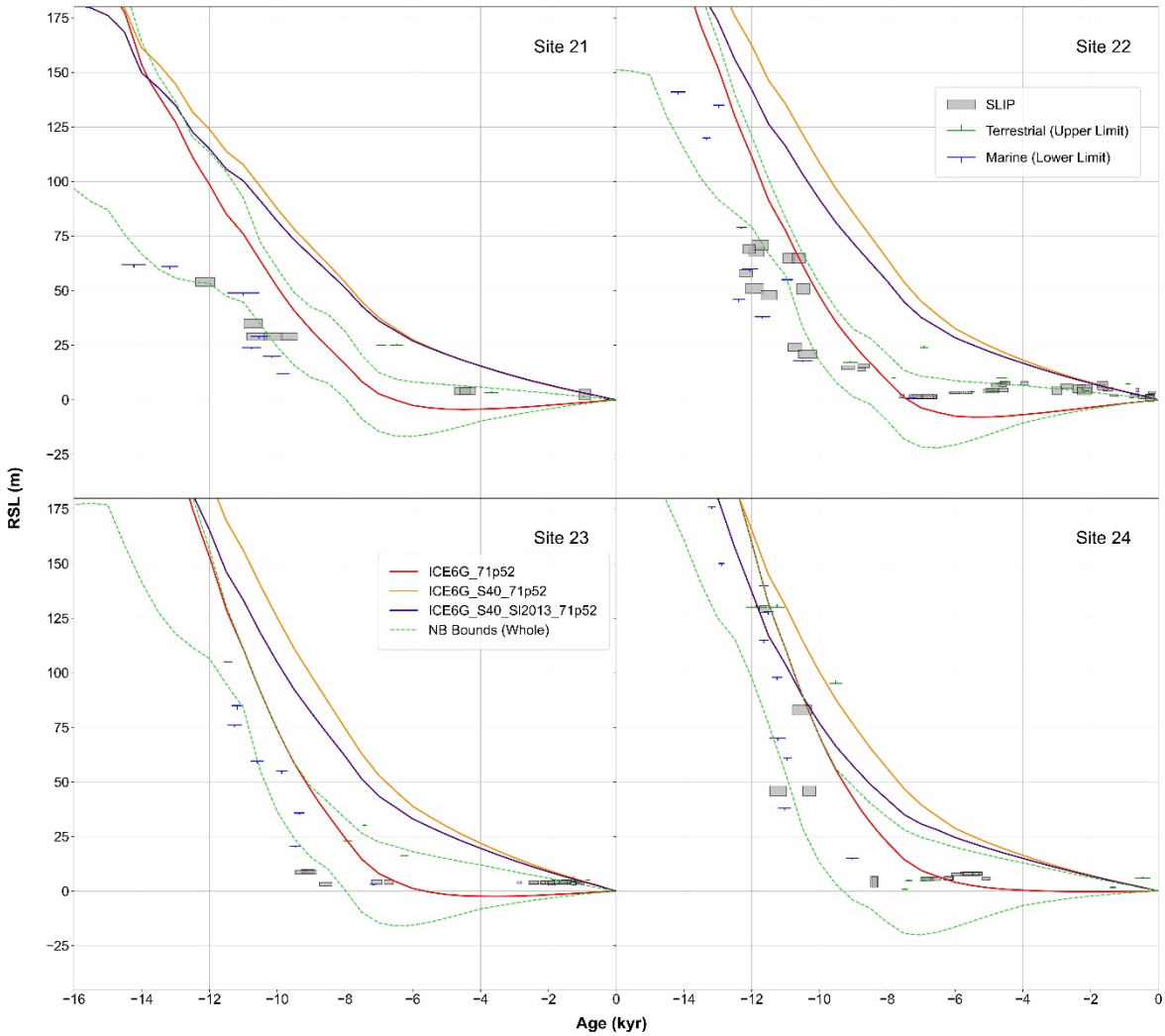


Figure 2.S17. Legend on Page 99.

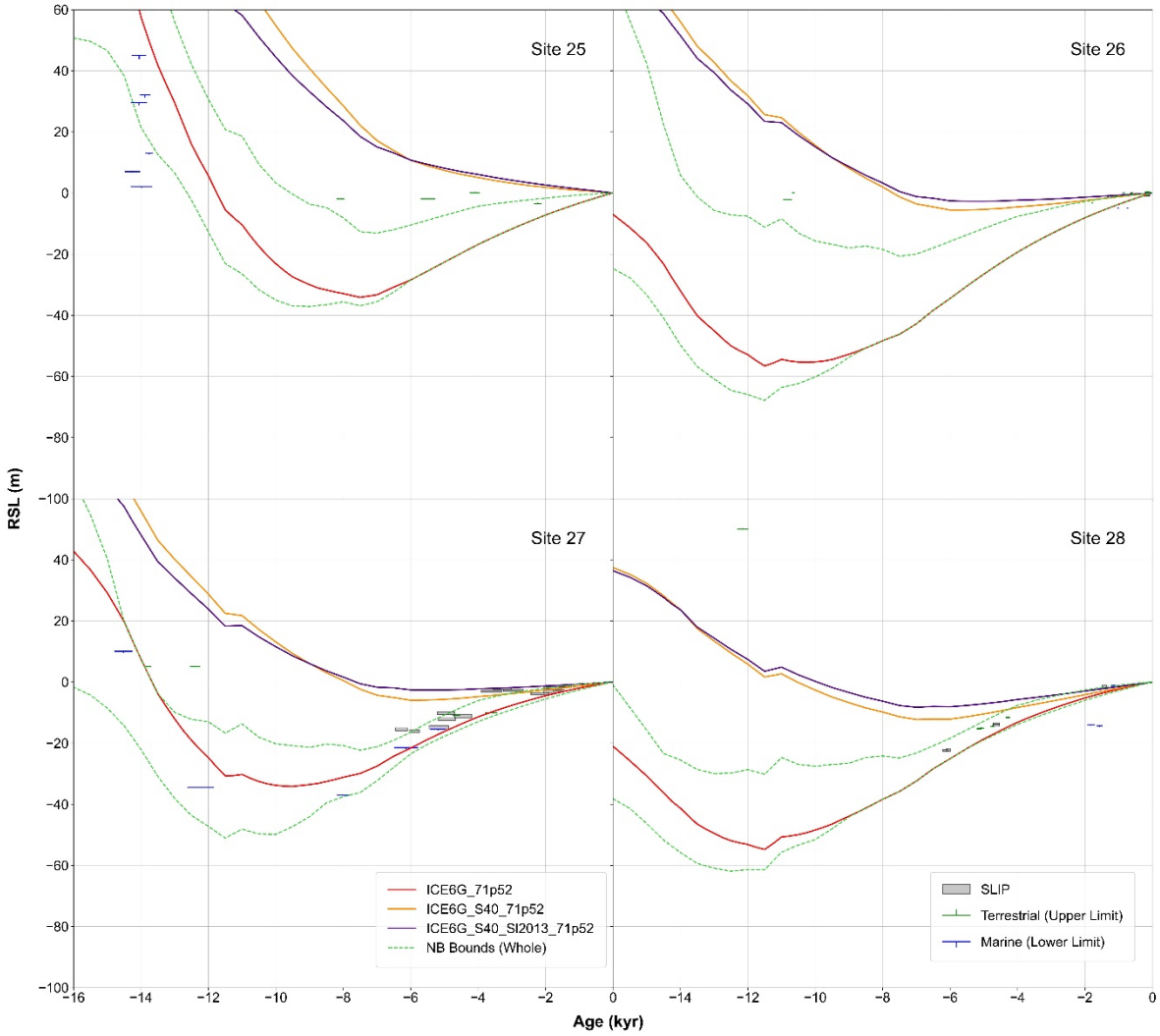


Figure 2.S17. Legend on Page 99.

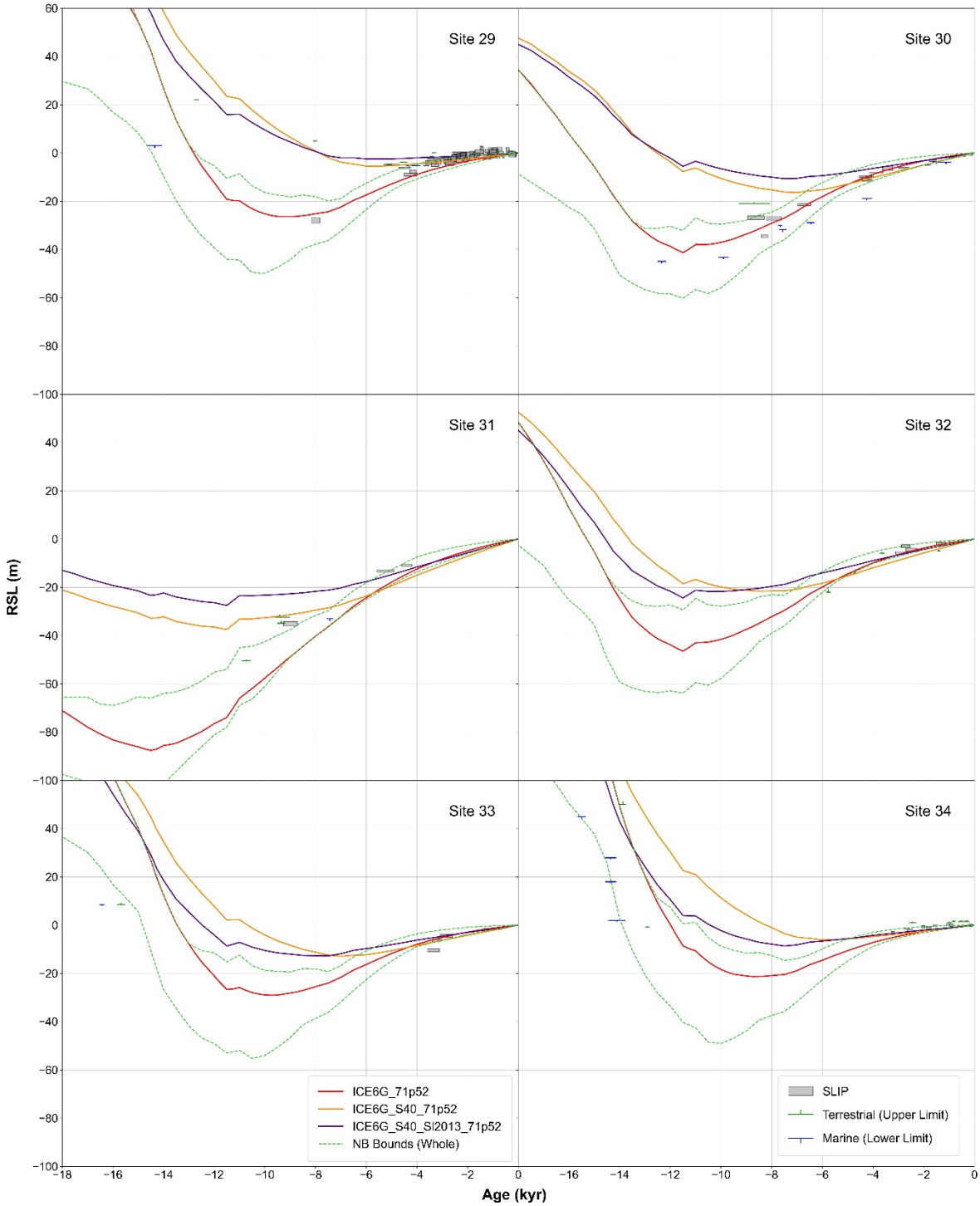


Figure 2.S17. Legend on Page 99.

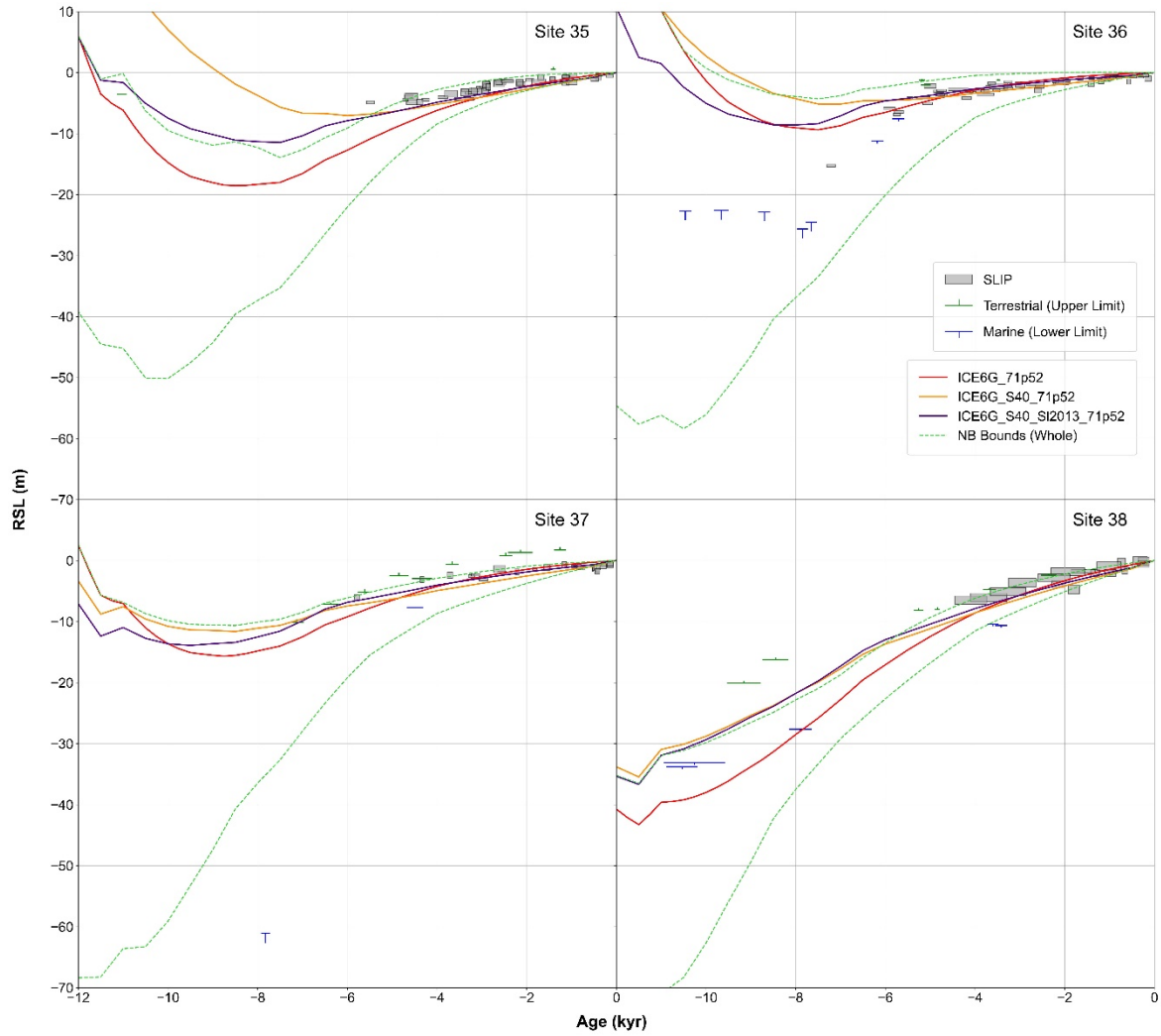


Figure 2.S17. The red-solid line shows the optimal modelled RSL estimated from the data-model misfit analysis based on the whole dataset (sites 1-38) and the 1D modelling (ice history model = ICE-6G, LT = 71 km, UMV = 0.5×10^{21} Pas, LMV = 2×10^{21} Pas). The orange-solid and blue-solid lines indicate the modelled RSL quantified from two 3D GIA runs (to incorporate the effect of lateral viscosity perturbations using shear-wave tomographic models superimposed on the 1D profile) based on S40RTS and S40RTS_SL2013, respectively. The upper and lower uncertainty bounds (green-dashed lines) are quantified by the nominal Bayesian approach based on consideration of the 1σ uncertainty for determination of a sub-ensemble of the highest-probability Earth model parameter sets. RSL curves were plotted at the average position of all RSL data points within each site (see the white diamonds in Figure 2.S2). The dimension of each SLIP box shows ±1σ uncertainty in RSL and age. For limiting data points, the horizontal and vertical bars show ±1σ RSL age uncertainty and one side of the 1σ RSL uncertainty, respectively (the misfit analysis was carried out based on the 1σ uncertainty in RSL and age).

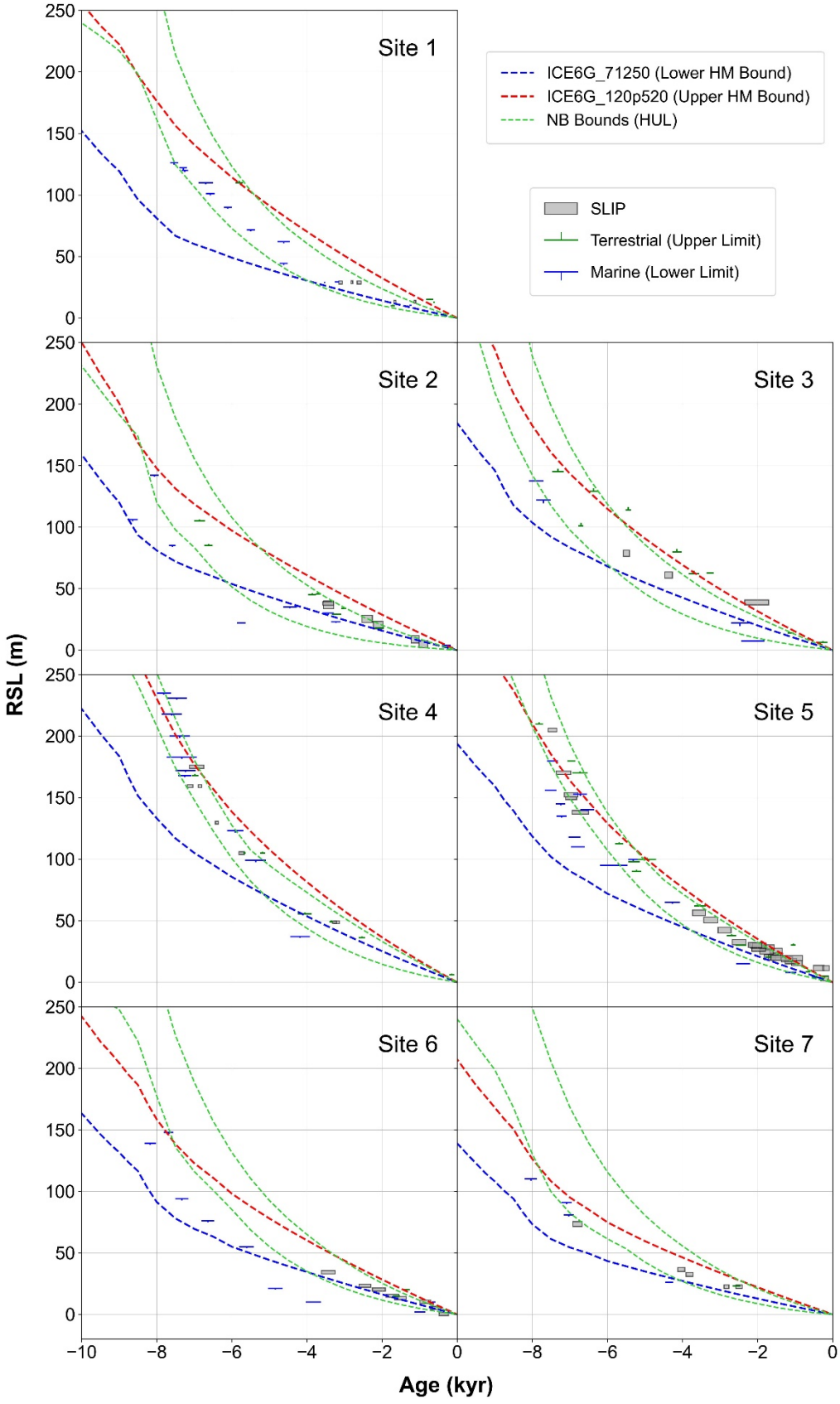


Figure 2.S18. Legend on Page 107.

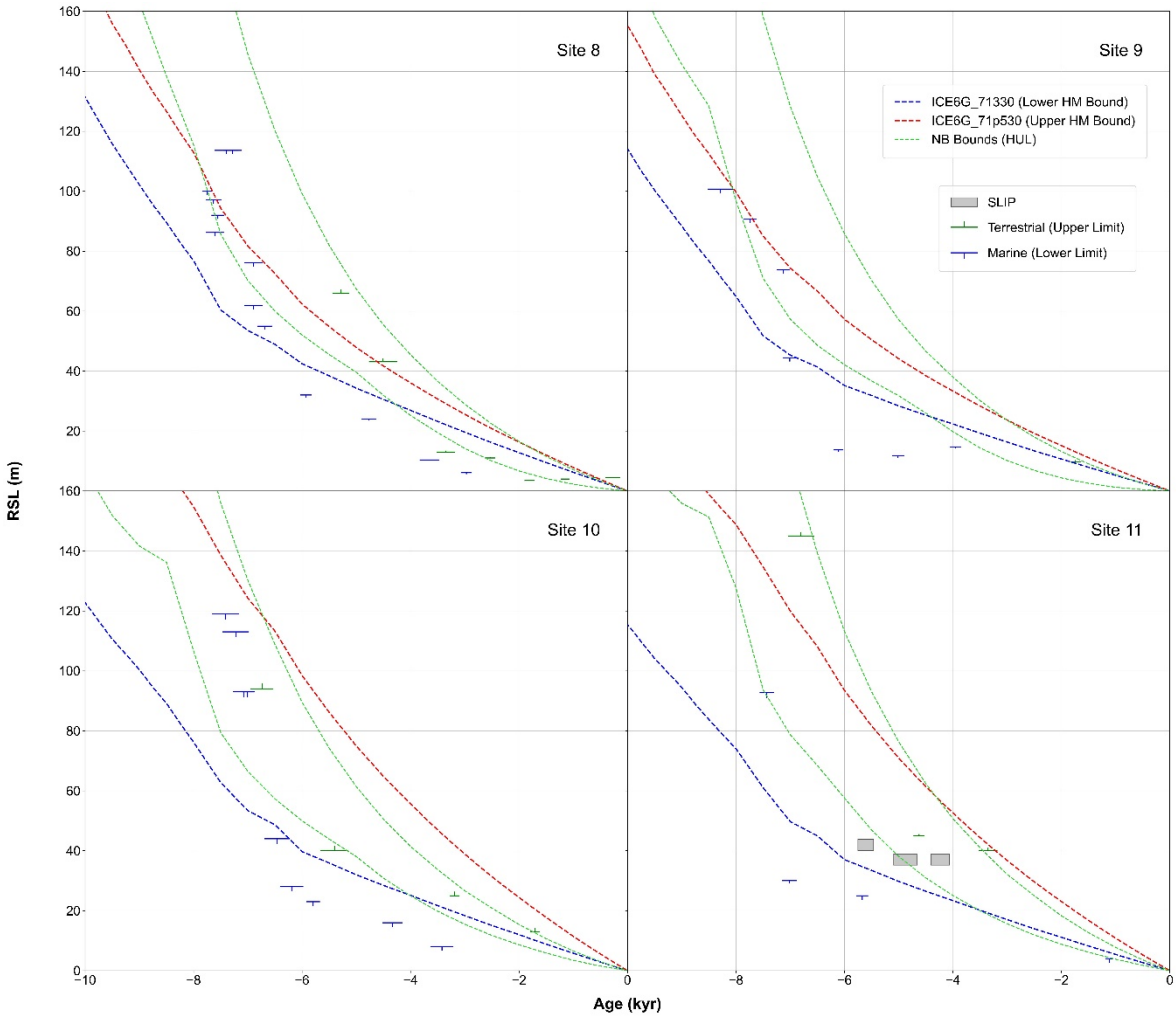


Figure 2.S18. Legend on Page 107.

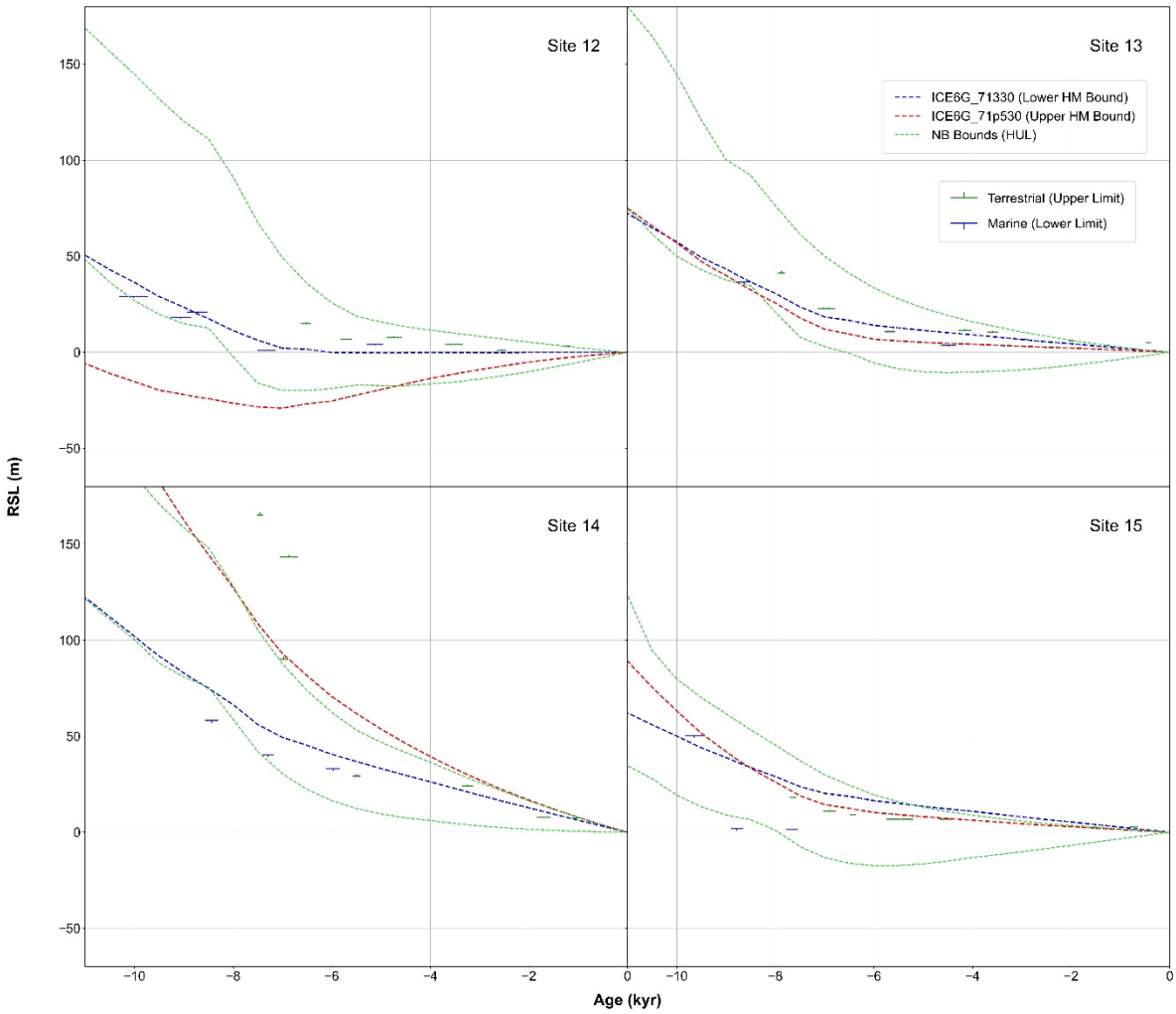


Figure 2.S18. Legend on Page 107.

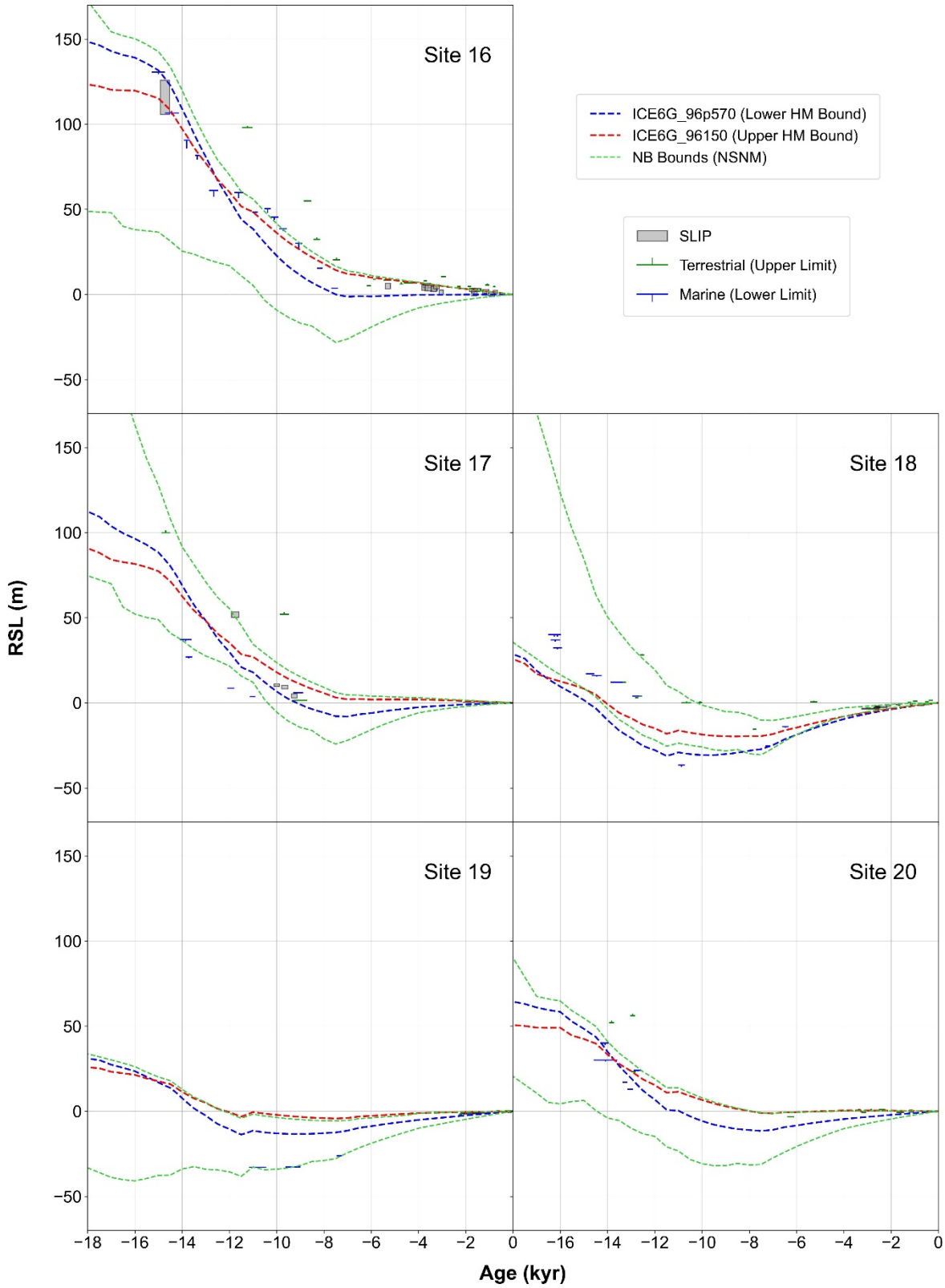


Figure 2.S18. Legend on Page 107.

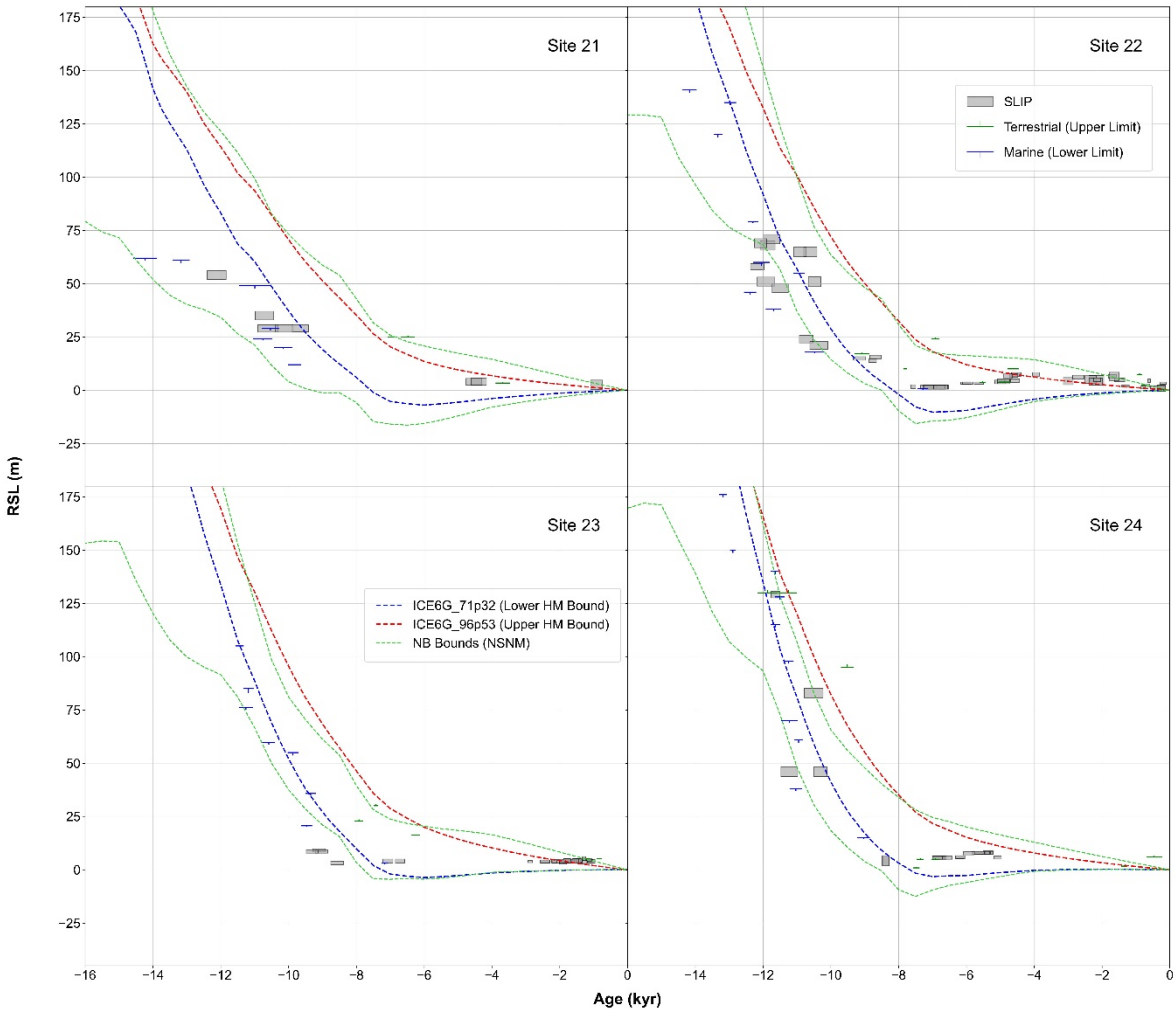


Figure 2.S18. Legend on Page 107.

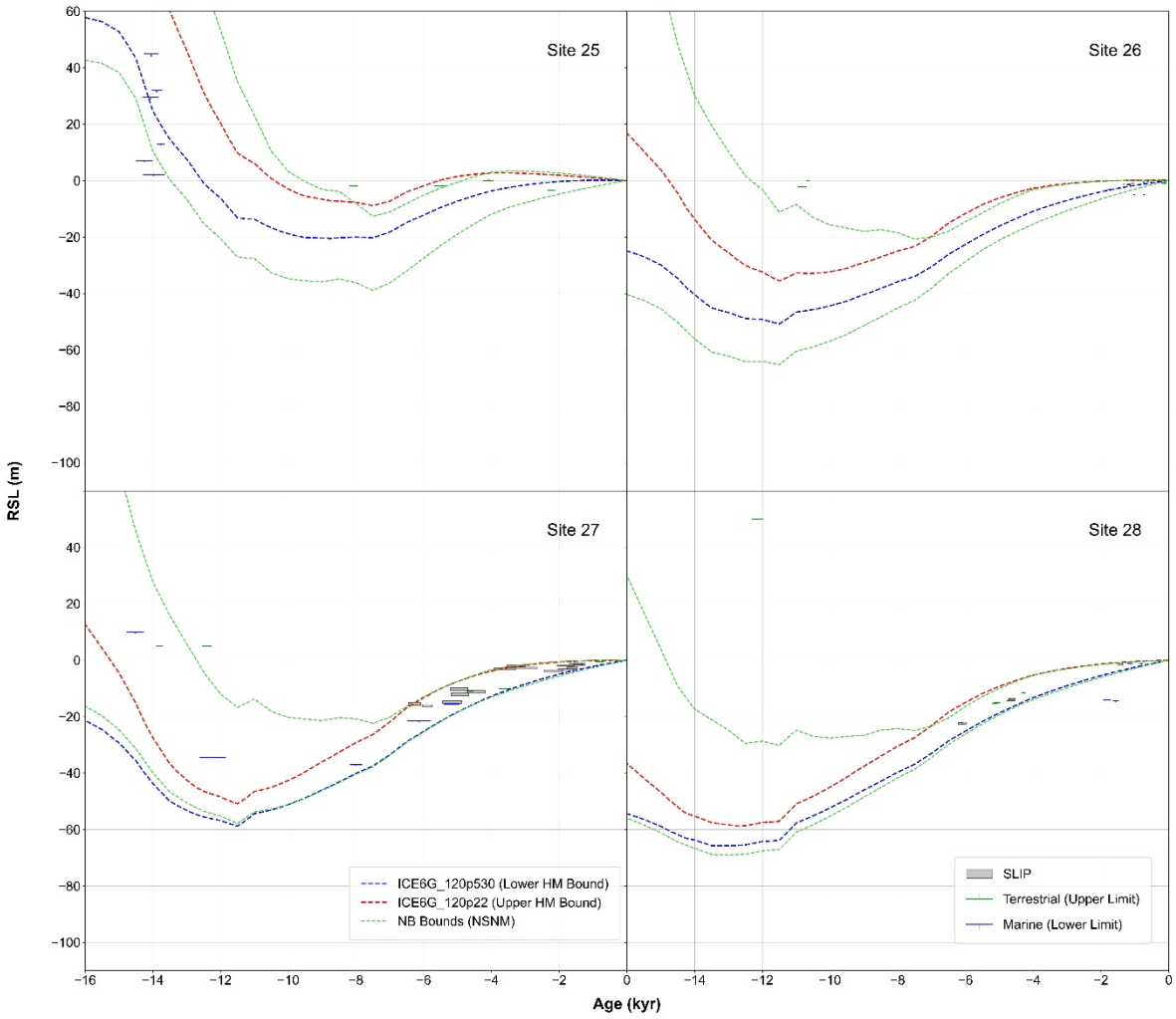


Figure 2.S18. Legend on Page 107.

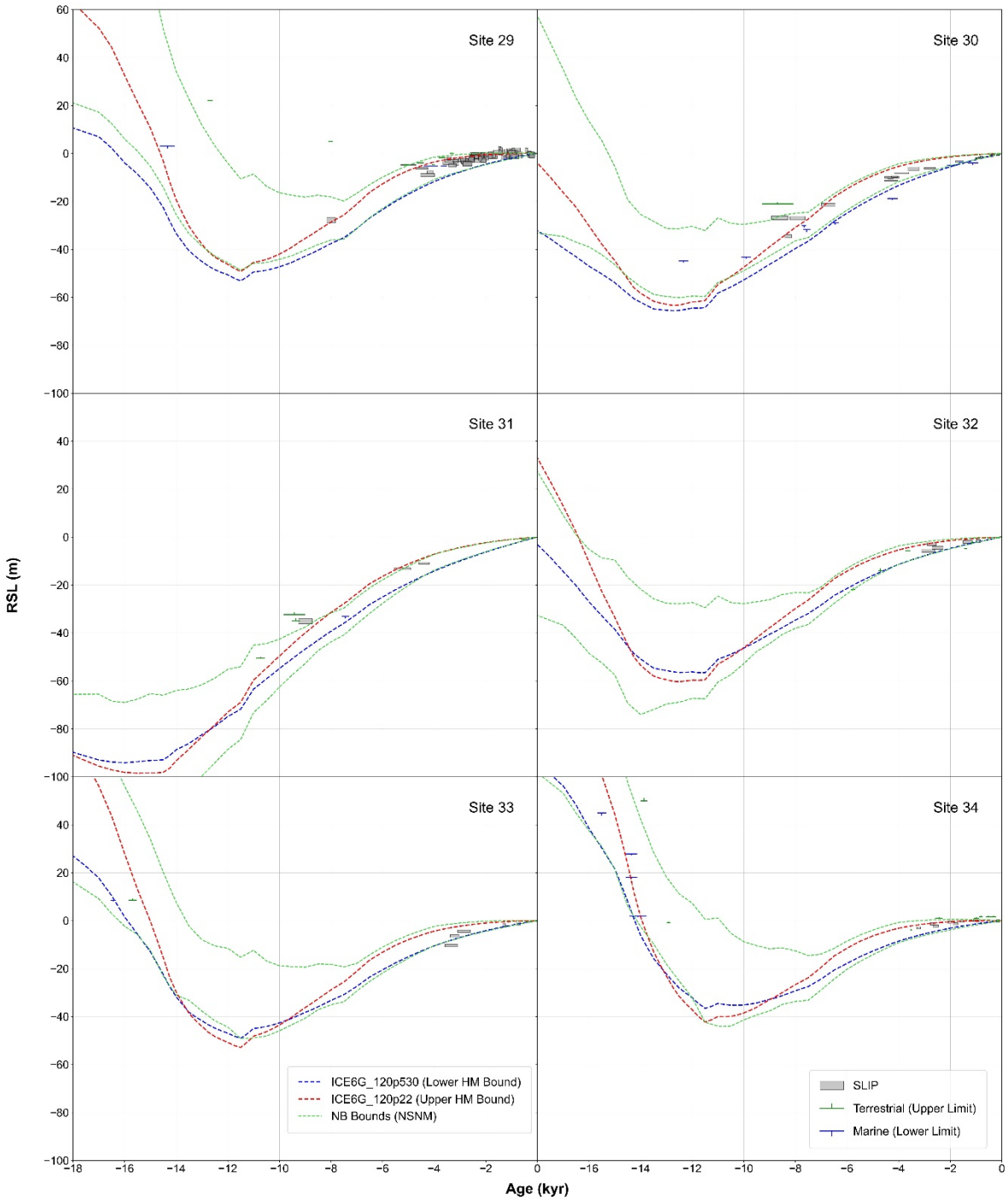


Figure 2.S18. Legend on Page 107.

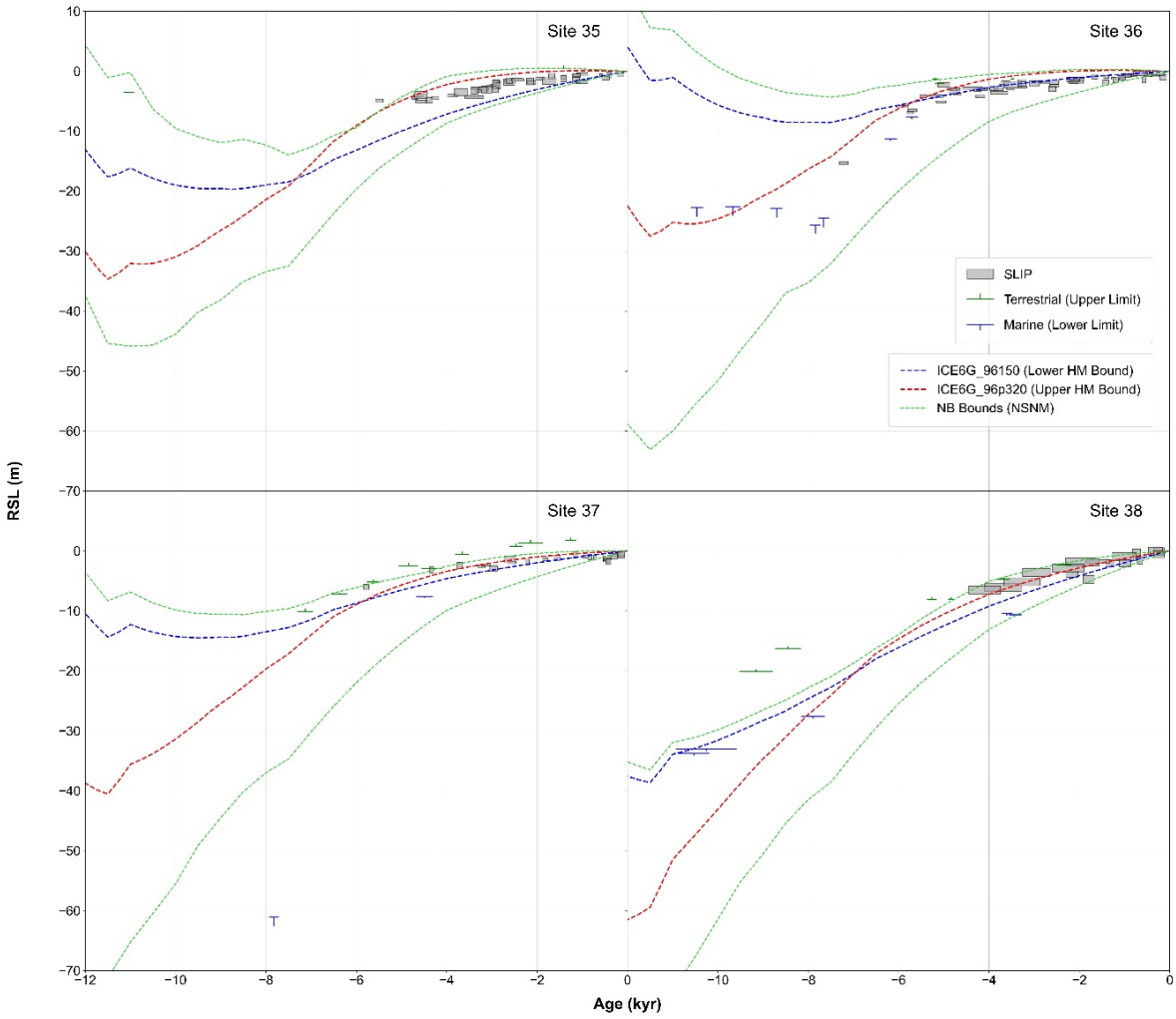


Figure 2.S18. The lower and upper bounding models, quantified by the history matching approach (blue- and red-dashed lines, respectively), are depicted along with uncertainty bounds from the nominal Bayesian approach (green-dashed lines) for sites 1-38 across the entire study region. The uncertainty bounds from the nominal Bayesian approach are based on the regional datasets associated with two larger subregions (i.e., HUL and NSNM). RSL curves were plotted at the average position of all RSL data points within each site (see the white diamonds in Figure 2.S2). The dimension of each SLIP box shows ±1σ uncertainty in RSL and age. For limiting data points, the horizontal and vertical bars show ±1σ RSL age uncertainty and one side of the 1σ RSL uncertainty, respectively (the misfit analysis was carried out based on the 1σ uncertainty in RSL and age).

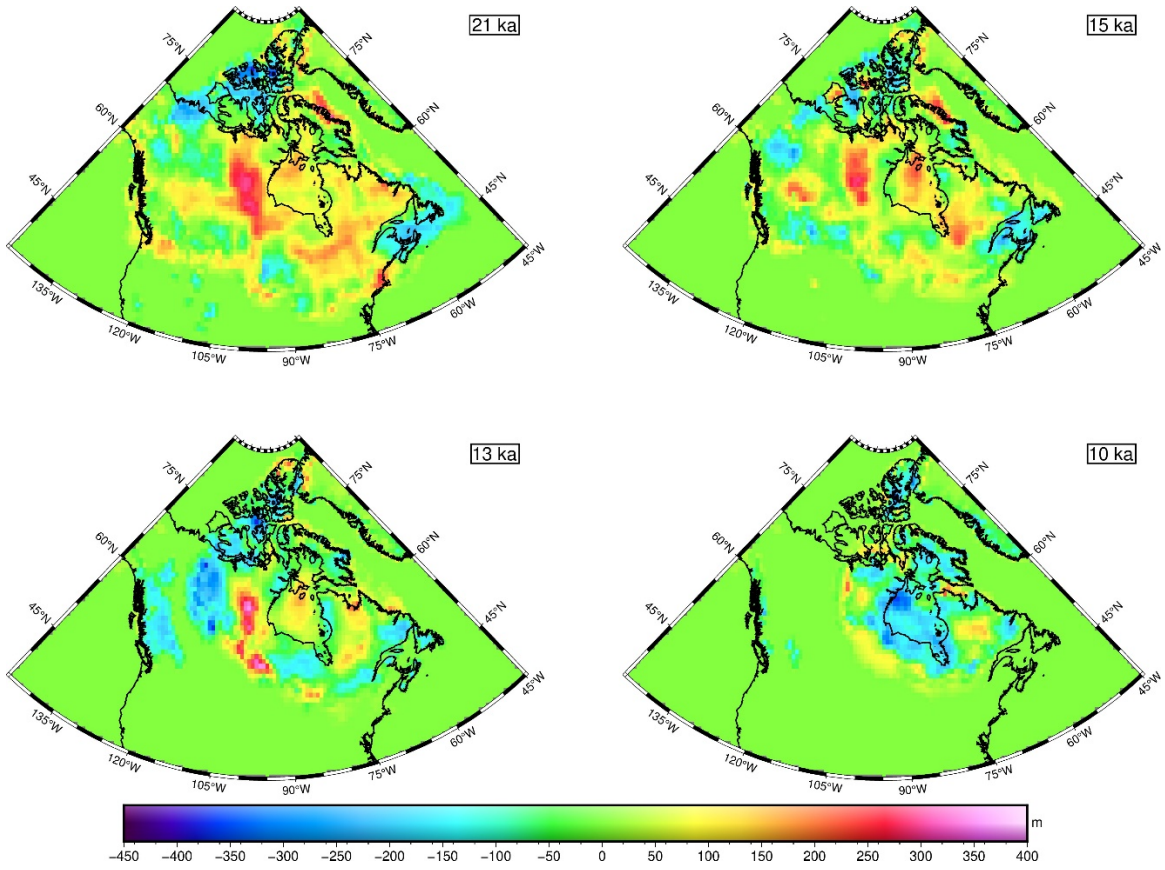


Figure 2.S19. The difference in average ice thickness between two sets of ice history models highlighted in Table 2.S1 for four time steps: 21, 15, 13, and 10 ka. This difference illustrates the subtraction of the average ice thickness calculated by the 10 ice models with the highest *IM* values from that inferred by the 10 ice models with the lowest *IM* values.

3

Towards an improved understanding of vertical land motion in eastern North America

Soran Parang [(1)], Glenn A. Milne [(1)], John W. Crowley [(2)], Makan A. Karegar [(3)]

[(1)] Department of Earth and Environmental Sciences, University of Ottawa, Ottawa, Canada
[(2)] Canadian Geodetic Survey, Natural Resources Canada, Ottawa, ON, Canada
[(3)] Institute of Geodesy and Geoinformation, University of Bonn, Bonn, Germany

Statement of Contribution

This manuscript is my original work, conducted under the supervision of Prof. Glenn A. Milne, who planned and guided the research and provided several rounds of feedback during manuscript preparation. John W. Crowley supervised the GRACE analysis and provided the code used in his processing methodology. Makan A. Karegar contributed to the GNSS analysis by providing code for offset detection and removal, as well as feedback on the analysis. I carried out all analyses and created all figures presented in the manuscript.

Abstract

Much of the Atlantic coast of North America has been sinking for thousands of years, at a maximum rate of ~20 cm per century, due to solid Earth deformation caused by the deglaciation of the Laurentide Ice Sheet—a process known as glacial isostatic adjustment (GIA). In addition to GIA, other factors such as hydrological mass redistribution may also contribute significantly to the vertical land motion (VLM) signal in this region. The primary aim of this research is to better constrain and understand the processes driving contemporary VLM in southeastern Canada and the northeastern USA. We integrate decadal-scale and millennial-scale VLM estimates to assess spatial and temporal variations across six subregions: Hudson Bay, the Ungava Peninsula and Labrador, Newfoundland, the St. Lawrence Corridor, New Brunswick and Nova Scotia, and Maine and Massachusetts. Our methodology incorporates contemporary VLM rates derived from the Global Navigation Satellite System (GNSS/GPS) time series at 88 stations, paleo VLM rates from 348 late-Holocene relative sea-level (RSL) reconstructions spanning the last 4,000 years across 18 sites, regionally optimized GIA model outputs, and contemporary mass change estimates (April 2002–November 2023) from the Gravity Recovery and Climate Experiment (GRACE). Our study is the first to comprehensively quantify uncertainty in GRACE mass change estimates associated with GIA by using a combination of Bayesian and Monte Carlo approaches. A primary goal of this work is to identify departures from long-term trends associated with GIA and seek to understand these in terms of contemporary hydrological signals. Our results highlight the dominance of GIA as the primary driver of VLM in the study region, while also identifying contributions from non-GIA processes. The analysis reveals broad agreement between millennial-scale and decadal-scale rates at most sites, and GRACE estimates show no significant hydrological mass change signals from either natural or anthropogenic causes in the region. Our findings challenge a previous hypothesis suggesting substantial anthropogenic hydrological impacts on VLM in the study region—specifically, excessive water mass accumulation associated with the James Bay Hydroelectric Project in southeastern Hudson Bay. Our results indicate that uncertainty in the GIA signal is a primary limiting factor and so future work seeking to reduce this uncertainty is encouraged. Finally, our results underscore the importance of considering a range of datasets and model outputs to seek consistency across multiple constraints and thus improve accuracy of signal interpretation.

Keywords: Vertical land motion, Glacial isostatic adjustment, Relative sea level, Uncertainty analysis, Geodetic measurements, Eastern North America, Sea level index points, Mass change signal, Paleo and contemporary rates

3.1. Introduction

Determining future sea-level changes and understanding long-term geophysical processes, especially in areas influenced by glacial isostatic adjustment (GIA), depend on an understanding of the vertical land motion (VLM) (Woodworth et al., 2019). Much of the Atlantic coast of North America has been sinking for thousands of years at a maximum rate of 20 cm per century due to GIA, which is a response to the deglaciation of the Laurentide ice sheet (LIS) following the last glacial maximum (LGM), approximately 18,000 to 7,000 years ago. Postglacial rebound caused uplift in ice covered areas as the LIS receded, whereas forebulge collapse caused subsidence in ice marginal and peripheral areas (e.g., Davis & Mitrovica, 1996; Mitrovica & Milne, 2003; Peltier, 1998). While the Atlantic coast undergoes land subsidence and accompanying sea-level rise due to GIA, areas close to the former ice center show land uplift and associated sea-level fall (e.g., Ding et al., 2019; Simon E. Engelhart & Horton, 2012; Love et al., 2016; Parang et al., 2024; Sella et al., 2007; Vacchi et al., 2018; van der Wal et al., 2009; Williams et al., 2024).

Apart from GIA, other processes—such as tectonic activity, sediment compaction, anthropogenic impacts (e.g., groundwater extraction and damming), and hydrological mass redistribution—also contribute to VLM, complicating the interpretation of this signal. Different modelling methodologies and datasets have been employed in recent research to enhance our comprehension of VLM and its implications. Geodetic measurements from techniques like Global Navigation Satellite Systems (GNSS/GPS) and Interferometric Synthetic Aperture Radar (InSAR), as well as RSL changes captured by tide gauges and deduced from geological reconstructions, are utilized to constrain the VLM signal (e.g., Huang et al., 2022; Schumacher et al., 2018; Sella et al., 2007; C.-Y. Wang et al., 2024; Yousefi et al., 2020). These datasets provide complementary insights: RSL observations capture the combined effects of land motion and changes in sea surface height, whereas geodetic techniques such as GNSS and InSAR directly measure land surface displacement, including contributions from slow processes like GIA and secular tectonic changes, as well as shorter-term and recent processes such as anthropogenic factors and hydrological changes (e.g., Bouin & Wöppelmann, 2010; Bürgmann et al., 2000; S. Engelhart et al., 2011; Kemp et al., 2011; Santamaría-Gómez et al., 2012; Shirzaei et al., 2020; Woodworth et al., 2019). In addition, integrating these measurements with estimates of the contemporary mass redistribution signal from the Gravity Recovery and Climate Experiment (GRACE) observations provides a more comprehensive understanding of the VLM signal at regional and local scales (Frederikse et al., 2019; Pan et al., 2023).

The observed VLM trends in the U.S. and Canada exhibit spatial and temporal variability, influenced by the combined effects of hydrological mass changes, GIA, and potentially unaccounted-for geological or anthropogenic factors (Frederikse et al., 2019). Karegar et al. (2017) compared measurements of contemporary land motion from geodetic methods to estimates of sea-level change over the past few thousand years from geological records along the Atlantic coast of the USA and identified locations where anthropogenic effects are significant. A key finding of this study is that while GIA is the dominant process driving land subsidence in most areas, large deviations from this signal can occur due to the influence of anthropogenic activity impacting hydrological processes. One such area is between Maine (45°N) and New Hampshire (43°N), near the Canadian provinces, where GPS data indicate uplift of 7.5 cm/century, but geological data and a GIA model show slow subsidence of 10 cm/century. The cause of this discrepancy remains unclear. One hypothesis is that increasing water mass accumulation, associated with the James Bay Hydroelectric Project in Quebec, may be a contributing factor. This project, initiated in the 1980s, involves a series of large dams on rivers draining into Hudson Bay. If this hypothesis is correct, it has important implications for land motion and sea-level change within Hudson Bay, the St. Lawrence estuary, and the Atlantic Provinces.

Therefore, accurately constraining the VLM signal in eastern Canada is crucial, but interpreting the contemporary VLM signal is challenging due to the various contributing processes. Additionally, the existing literature addressing this issue is limited. The primary aim of this study is to better constrain and understand the processes contributing to contemporary and future VLM and gravity changes in southeastern Canada and the northeastern USA. This study uses the temporal variability to isolate the VLM signal and provides estimates of decadal-scale and millennial-scale VLM rates at selected sites across six subregions: Hudson Bay, the Ungava Peninsula and Labrador, Newfoundland, the St. Lawrence Corridor, New Brunswick and Nova Scotia, and Maine and Massachusetts. The contemporary VLM rates are derived from GNSS measurements and the paleo VLM rates are based on late-Holocene RSL reconstructions and optimal regional GIA models developed for each subregion. A key aspect is verifying the consistency among these estimates to evaluate our understanding of VLM in this region. Any discrepancies between paleo and contemporary VLM rates are identified for each subregion, and the residual signals are interpreted in terms of other processes, primarily associated with

regional hydrological changes. Compared to previous studies (e.g., Karegar et al., 2016, 2017), our work employs new GIA model constraints and GRACE estimates to separate GIA from hydrological signals. GRACE estimates of mass change are utilized to validate inferences drawn from the comparison of paleo and contemporary VLM rates (i.e., residual VLM signals) and to assess whether significant contemporary hydrological mass change signals exist in the study region, specifically testing the hypothesis stated by Karegar et al. (2017).

For historical reconstructions and future sea-level change projections to be more accurate, the sources of VLM uncertainty, including errors from geodetic VLM estimates (e.g., GNSS), GIA models, and terrestrial reference frame realizations, need to be thoroughly addressed (Santamaría-Gómez et al., 2017). According to Bouin & Wöppelmann (2010), local tectonics and regional misfits in global GIA models are the causes of the differences between postglacial rebound predictions from models and GPS-derived velocities, as well as tide gauge data. They found that GPS-induced VLM rates were consistently higher than those predicted by the ICE-5G model in eastern Canada (by 2–3 mm/year), underscoring the need for improved GIA models. Given that GIA is the dominant source of uncertainty in our study region (Eicker et al., 2024; Parang et al., 2024), we build upon the results developed in Chapter 2, which constrained the regional GIA signal and its corresponding uncertainty bounds for eastern North America using approximately 15,000 Earth-ice model parameter sets and approaches that account for parametric and structural uncertainties in GIA modelling. This study represents a comprehensive uncertainty analysis of the VLM signal and is the first to formally incorporate GIA model uncertainty into GRACE estimates of contemporary mass changes. Our findings will contribute to produce improved projections of mean sea-level changes and flooding risks in the coming decades, providing valuable insights for regional mitigation strategies.

In Section 3.2, we describe the datasets and methodologies employed in our analysis. This includes contemporary VLM and mass change signals derived from GNSS and GRACE, respectively (Section 3.2.1); paleo VLM signal inferred from late-Holocene RSL changes (Section 3.2.2); and estimates based on GIA model outputs (Section 3.2.3). Section 3.3 presents our results, divided into the analysis of VLM rates (Section 3.3.1) and contemporary mass change estimation (Section 3.3.2). Finally, Section 3.4 provides a general discussion of our key findings in the context of previous studies, as well as the limitations that can inspire future research. The VLM rates with uncertainty bounds (Appendix 1) from (1) GNSS time series, (2) GIA model predictions, and (3) late-Holocene RSL changes, as well as the contemporary mass changes from GRACE with uncertainty estimates (Appendix 2), are made available for our study region.

3.2. Data and methodology

3.2.1. Contemporary observations

3.2.1.1. VLM rates from GNSS measurements

The GPS VLM rates and associated uncertainties were sourced from the Nevada Geodetic Laboratory. These rates were determined using the Median Interannual Difference Adjusted for Skewness (MIDAS) method (Blewitt et al., 2018). This approach ensures a reliable estimation of GPS station velocities, addressing common issues such as step discontinuities, outliers, seasonal effects, and time-dependent noise (or heteroscedasticity) (Blewitt et al., 2018). We also carried out a separate analysis on Nevada Geodetic Laboratory GPS time series and recalculated the VLM rates after correcting for remaining outliers (Wdowinski et al., 1997) and predefined jumps based on a least

squares adjustment model that accounts for bias, annual and semi-annual trends, and offsets (see Figure 3.S1).

To accurately estimate VLM rates corresponding to locations with RSL data points, we selected GPS stations co-located with sea-level index points (SLIPs) dating from 4 ka before present (BP) (Section 3.2.2), and for which the associated VLM rate uncertainty values are less than 1 mm/year. For sites within New Brunswick, Nova Scotia, Maine, and Massachusetts, where multiple GPS stations were available and significant spatial variability or gradients existed in the RSL signal between GPS stations and SLIPs (see Figure 3.S2 for RSL contour maps at 4 ka BP for four subregions in the study region), we prioritized GPS stations located as close as possible to the average positions of the SLIPs to ensure consistent spatial representation (see site #9 in Figure 3.S2 as an example of the GPS stations selected). In cases where the number of GPS stations was insufficient to directly represent the spatial characteristics of the RSL signal, VLM corrections were applied to the GPS rates to account for the spatial gradient in the RSL signal (see site #4 in Figure 3.S2). These corrections were derived using the optimal regional GIA models, which provided a reliable basis for adjusting the GPS-derived rates. For the Ungava Peninsula and Labrador, where no SLIPs exist from 4 ka BP, we considered all available GPS stations with VLM rate uncertainty less than 1 mm/year. This selection process resulted in a total of 88 GPS time series being used in this analysis (see blue diamonds in Figure 3.1).

In central eastern North America, the solid Earth shows an elastic response to the contemporary ice mass loss from Greenland and the Canadian Arctic region, influencing geodetic measurements. Not accounting for this elastic signal in GPS rates can bias VLM estimates, particularly for stations at higher latitudes such as Hudson Bay, Ungava Peninsula, and Labrador. In this study, to distinguish the effects of contemporary ice mass loss from other VLM sources (e.g., GIA) measured by GPS, we utilize the results of Riva et al. (2017), which also consider changes in Earth's rotation. The GPS-derived VLM rates are corrected for this elastic signal by estimating a linear trend through the VLM times series provided by Riva et al. (2017) for the period 2000 – 2014 CE (see Figure 3.S3).

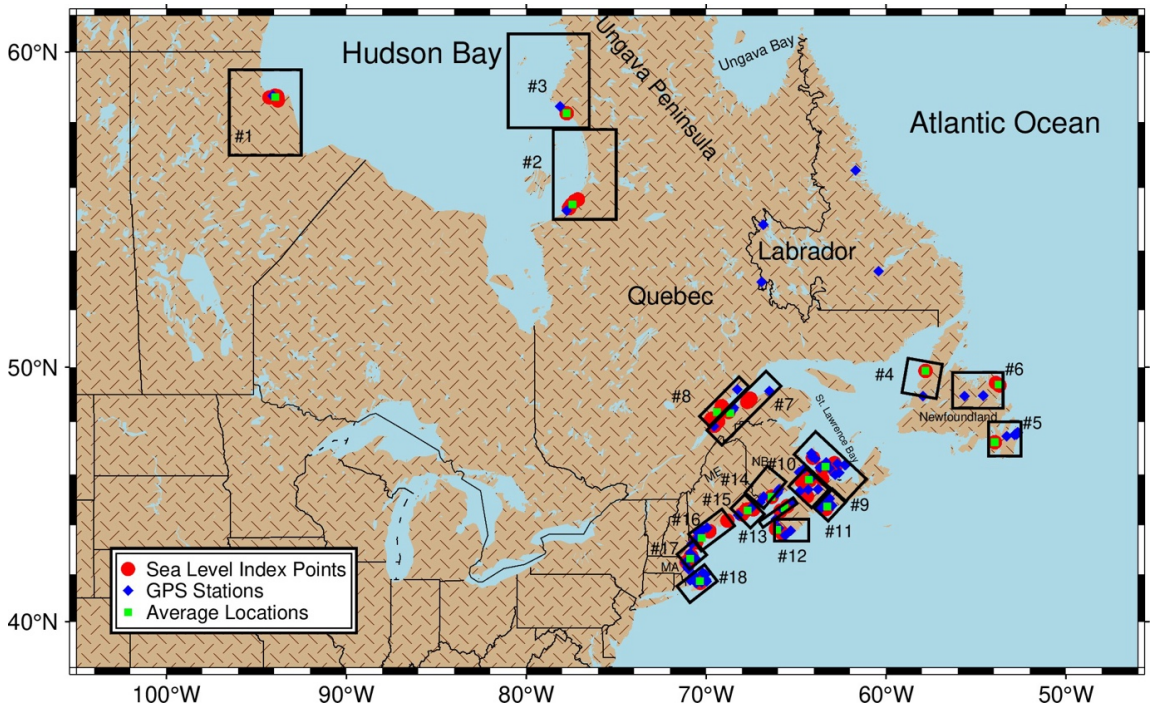


Figure 3.1. Red circles represent the spatial distribution of SLIPs dating from 4 ka BP to the present day. The

data are grouped into 18 sites (black rectangles) across five subregions: Hudson Bay (HB, sites #1 – #3), Newfoundland (NF, sites #4 – #6), St. Lawrence Corridor (SLC, sites #7 and #8), New Brunswick and Nova Scotia (NN, sites #9 – #14), and Maine and Massachusetts (MM, sites #15 – #18). Blue diamonds indicate the GPS stations co-located with SLIPs at each site. For the Ungava Peninsula and Labrador, due to the absence of SLIPs over 4 ka BP, all available GPS stations (4 stations) are included in the VLM analysis. Green squares mark the average locations (average latitude and longitude) calculated from all SLIPs within each site, where the parameters of ΔRSL, ΔVLM, and ΔG are estimated (see Equation 3.1).

3.2.1.2. Mass change signal from GRACE

In this study, the contemporary mass change estimates from GRACE are obtained using a novel least-squares method developed by Crowley & Huang (2020). This method models spherical harmonic coefficients (SHCs) with constant, linear, quadratic, annual, and semi-annual components. It simultaneously estimates both correlated errors (stripes) and significant temporal trends in SHCs, efficiently removing stripes without significant signal attenuation or spatial distortions. Statistically significant temporal trends in each SHC are identified using an F-test, and trends failing to meet the 99.9% confidence level are set to zero (Crowley & Huang, 2020). This method is applied to the GRACE RL06 and GRACE-FO RL062 (level 2) spherical harmonic solutions from the Center for Space Research (CSR) at the University of Texas at Austin, covering the period from April 2002 to November 2023, extending up to degree and order 60.

Accurately isolating the present-day hydrological mass change signal or total water storage (TWS) variations from GRACE estimates in eastern North America is mainly dependent on constraining the GIA signal and its uncertainty in this area (Caron et al., 2018; Eicker et al., 2024; T. Li et al., 2020; Parang et al., 2024). The GRACE estimates are corrected for the GIA signal using optimal GIA models developed for each subregion in our study area, based on the results inferred from Chapter 2 (see Section 3.2.3). The present-day rates of GIA-originated geoid changes from 100 years ago to the present are estimated from GIA models after removing the effects of syphoning and barystatic sea-level changes (see Section 3.2.2 for more details), namely degree and order zero in the spherical harmonic coefficients of the geoid change.

Monthly mass changes are derived by converting geoid changes (destriped and corrected for GIA) to mass changes, with a mean field subtracted from the monthly solutions to obtain monthly mass anomalies, which are presented in surface density units of equivalent water thickness (EWT). In addition, due to the proximity of our study region to Greenland, the potential Gibbs ringing (or spectral leakage) effect is removed from mass change estimates. We also estimate the uncertainty of the inferred contemporary mass change signal by considering two main, independent sources of uncertainty in the analysis: (1) the standard deviations of the GRACE SHCs, and (2) the uncertainty of the GIA signal, which is the dominant source of uncertainty in our study region. The standard deviations of SHCs are calculated based on the standard deviation of the time-series residuals after eliminating linear, quadratic, annual, and semi-annual trends (Crowley & Huang, 2020). The uncertainty bounds of the GIA signal (removed from GRACE solutions) in each subregion are constrained by the sub-ensemble of the highest-probability GIA models determined using a Bayesian approach (see Chapter 2).

Both sources of uncertainty are converted into mass changes (in EWT) and quantified in the spatial domain using a Monte Carlo sampling approach. In this approach, we generate 1,000 realizations of the GRACE-derived SHCs by adding normally distributed random noise to each coefficient, scaled by its standard deviation. Each simulated realization is processed to generate spatial grids using spherical

harmonic transformations and the Schmidt-normalized associated Legendre polynomials (Wieczorek & Simons, 2007). The uncertainty for each grid cell is calculated as the standard deviation of all realizations for that grid cell. For GIA-related uncertainty, the mean and standard deviation values are computed for the cosine and sine coefficients of each degree and order based on the Bayesian sub-ensemble of the highest-probability models. Using these means and standard deviations, the contribution of GIA uncertainty to the mass change signal is estimated through the same approach applied to the GRACE-derived SHCs. Finally, the overall uncertainty of the GRACE mass change signal is determined by combining the uncertainties from SHCs and GIA in quadrature, following the principles of error propagation.

Additionally, the inferred mass change associated with variations in surface mass density over time (expressed in EWT) is converted into the corresponding vertical surface displacement. This is done using SHCs derived from the analysis, which have been destriped, corrected for GIA, and processed to remove Gibbs ringing effects. Elastic load Love numbers from Wang et al. (2012) are also applied, following the methodology detailed by van Dam et al. (2007) and Kusche & Schrama (2005) and utilized in recent studies (e.g., Fang et al., 2021; S. Li et al., 2020). The uncertainty in the resultant elastic displacement of the Earth's surface is estimated using the same approach as that employed for estimating the uncertainty in the contemporary mass change signal, but it is based on equations that convert geoid anomalies to vertical surface displacement, as described by Farrell (1972) and Wahr et al. (1998). Finally, the estimated elastic displacement signal can be compared to the residual signal obtained from the difference between paleo and contemporary VLM rates to assess whether the GRACE estimates support the findings from the VLM rate analysis.

3.2.2. Paleo VLM rate estimates

The estimation of the average millennial-scale VLM rate from late-Holocene RSL change at a given site is based on available SLIPs of age 4 ka BP or younger. We consider only SLIPs from the quality-assessed datasets of Engelhart & Horton (2012) and Vacchi et al. (2018) (updated using the most recent radiocarbon calibration curves, as discussed in Chapter 2). The 4 ka to present time frame provides enough data at several sites for accurate regression analysis while also reducing the impact of uncertainty in global ice melt on the VLM rate estimates (Engelhart et al., 2009; Karegar et al., 2016; Shennan & Horton, 2002; Yousefi et al., 2020). This ensures that the observed changes are more indicative of regional/local processes and less strongly influenced by uncertainty in global sea-level variations (Hallmann et al., 2018).

To determine temporal changes in VLM rates, we selected sites with sufficient SLIPs in the 4 ka to present time window and where GPS stations are co-located. At a given site, the average VLM rate is estimated from the rate of late-Holocene RSL change:

$$\Delta VLM(\varphi_{avg}, \lambda_{avg}) = \Delta G(\varphi_{avg}, \lambda_{avg}) + E - \Delta RSL(\varphi_{avg}, \lambda_{avg}) \quad (3.1)$$

Here, ΔVLM is the average VLM rate at a given site and calculated at the average position of the SLIP locations (see green squares in Figure 3.1), defined by the average latitude (φ_{avg}) and average longitude (λ_{avg}). ΔRSL is the rate inferred from the SLIPs and ΔG is the contribution to this rate from regional variations in geoid height change, which, we assume, are dominated by GIA at most sites in our study region. Finally, E is a globally uniform contribution to the rate of sea surface height change associated with barystatic sea level change (Gregory et al., 2019) and ocean syphoning (Mitrovica & Peltier, 1991; Mitrovica & Milne, 2002). The terms ΔG and E and their uncertainty were determined

using output from a GIA model (see Section 3.2.3). Equation 3.1 does not explicitly consider sea-surface height change associated with variations in ocean density and circulation (sterodynamic sea-level change; Gregory et al., 2019). There are limited observations to constrain this signal over the late Holocene and so we assume its contribution has been negligible at the locations considered in this analysis.

In Equation 3.1, ΔRSL is estimated by determining the best-fitting function for the SLIPs using total least squares adjustment (orthogonal distance regression), which takes into account the uncertainties in both RSL elevation and age. The best-fitting function is chosen to be linear at all sites except for those in Hudson Bay, where the reconstructed RSL changes often display an exponential form (e.g., Mitrovica et al., 2000; Mitrovica & Peltier, 1995; Walcott, 1980) and can be represented well by:

$$RSL(t) = A\left(e^{\frac{t}{\tau}} - 1\right) + c \quad (3.2)$$

Here, RSL represents the relative sea level at time t. The parameter A governs the amplitude of the sea level change, while τ signifies the decay time, which represents how quickly sea level changes over time. The parameter c accounts for potential vertical shifts due to systematic errors or uncertainties, such as displacements caused by particularly strong storm surges. In Hudson Bay, only one site (site #2; Figure 3.1) has a sufficient number of SLIPs over the past 4 ka to make use of the exponential model (Equation 3.2). There are insufficient SLIPs at sites #1 and #3 to apply Equation 3.2 and so a linear function was adopted on SLIPs over the past 2 ka. For the Ungava Peninsula and Labrador, there are no SLIPs over 4 ka BP co-located with GPS stations, therefore, the paleo VLM rates are determined from a GIA model at the locations of the GPS stations (Section 3.2.3). Overall, 18 sites were selected in our study region (Figure 3.1), comprising a total of 348 SLIPs and 88 GNSS time series.

3.2.3. GIA model outputs

As noted above, we use output from a GIA model to determine the ΔG and E terms in Equation 3.1, and to generate VLM rates to compare to GNSS-determined rates in the Ungava Peninsula and Labrador where there are no SLIPs. We adopt the regionally optimized GIA models developed in Chapter 2. These models include optimal values for the elastic thickness of the lithosphere (LT), upper mantle viscosity (UMV), lower mantle viscosity (LMV), and the optimal ice history model (refer to Section 2.2.3 in Chapter 2). We utilize the GLAC1D-na9927 ice history model (Tarasov et al., 2012), with parameters LT = 120 km, UMV = 2×10^{21} Pas, and LMV = 10^{21} Pas, as the optimal GIA model parameter set for Hudson Bay, Ungava Peninsula, and Labrador. For other subregions along the eastern coast (i.e., NSNM), we employ the GLAC1D-na1259 ice history model (Tarasov et al., 2012), with parameters LT = 120 km, UMV = 0.8×10^{21} Pas, and LMV = 30×10^{21} Pas. Additionally, uncertainty bounds for the GIA model outputs were estimated using a Bayesian approach, which utilizes the sub-ensemble of the highest-probability model parameters (refer to Table 2.2 in Chapter 2).

3.3. Results and discussion

In Section 3.3.1, we present the decadal-scale VLM rates, derived from GNSS measurements (refer to Section 3.2.1.1), and the millennial-scale VLM rates, inferred from GIA models and late-Holocene RSL changes (refer to Section 3.2.2), along with their associated uncertainties across six subregions in southeastern Canada and northeastern USA. By comparing the paleo and contemporary VLM rates, taking into account the respective uncertainty bounds, we assess whether there is broad compatibility in VLM rates within each subregion. Additionally, Section 3.3.2 provides GRACE estimates of the

contemporary mass change signal, including uncertainty ranges (refer to Section 3.2.1.2) for each subregion, to complement the analysis of VLM rates. The residual signal, determined by the difference between paleo and contemporary VLM rates, is interpreted in terms of any significant contemporary signals (i.e., non-GIA or hydrological mass change signals) in each subregion.

3.3.1. VLM rates with uncertainty estimates

3.3.1.1. Hudson Bay

As mentioned in Section 3.2.2, only three sites in Hudson Bay (see Figure 3.2) qualify for estimating VLM rates based on late-Holocene RSL changes. The contemporary VLM rates are obtained from GPS measurements at five stations. In contrast, the paleo VLM rates are inferred using the optimal GIA model (refer to Section 3.2.3) applied at the locations of the GPS stations within each site, as well as from late-Holocene RSL changes at the average location of these data within each site (indicated by green squares in Figure 3.2). Figures 3.S4 and 3.S5 display the RSL and VLM curves (orange lines) derived from the optimal regional GIA model (GLAC1D-na9927_12021), along with the model uncertainty bounds (green dashed lines) as determined using the Bayesian approach (a sub-ensemble of the highest-probability models). Because Hudson Bay is situated in a near-field region, close to the thickest part of the LIS at LGM, RSL falls as the solid Earth undergoes uplift. Both curves are employed to estimate the $\Delta G + E$ term based on Equation 3.1 (see Figure 3.S6). Figure 3.S7 illustrates the paleo rates of RSL changes at three sites. As outlined in Section 3.2.2, the rate for site #2 is estimated using two methods: (1) fitting an exponential function (red line) derived from the postglacial decay time analysis to the SLIPs over 4 ka BP (see Equation 3.2), and (2) fitting a linear trend (blue dashed line) to the SLIPs over 2 ka BP. For sites #1 and #3, the rate is estimated solely through a linear regression applied to the SLIPs over 2 ka BP. The RSL change rate at site #2 from the exponential decay function (-8.512 ± 2.532 mm/yr) is lower than the rate over the last 2,000 years (-11.45 ± 1.842 mm/yr); however, the uncertainties indicate that while the rates are different, their ranges do overlap. In addition, over the last 2,000 years, site #1 has experienced a somewhat higher rate of RSL change than sites #2 and #3. However, the overlapping uncertainties among these sites indicate an overall consistent regional pattern of RSL change during this period, with site #1 likely being influenced by localized factors.

The estimated rate of paleo RSL change and the estimate of $\Delta G + E$ (Figure 3.S6) are applied in Equation 3.1 to calculate the average millennial-scale VLM rate for each site. Figure 3.2 presents the VLM rates along with their estimated 1σ uncertainty ranges. It is important to note that the relatively large uncertainty ranges for the GIA-derived rates are estimated from a subset of 84 GIA models, determined by the Bayesian approach, that provide a good fit to paleo RSL observations within Hudson Bay, where the GIA signal is strong and the primary contributor to VLM (see Chapter 2).

For site #1, the GIA rate from the optimal regional model (5.364 mm/year, with an uncertainty range of 2.172 to 10.034 mm/year) is lower than the VLM rates inferred from late-Holocene RSL changes and GNSS time series. The average VLM rate derived from three GPS stations is 9.661 ± 0.550 mm/year, and it overlaps with the upper bound of the GIA-induced rate. In contrast, the RSL-derived VLM rate is higher; when considering uncertainty ranges, the residual signal is at least ~0.7 mm/year. This residual, if accurate, would indicate a contemporary localized loading signal causing subsidence, and it will be assessed in terms of the hydrological mass change signal based on GRACE estimates in Section 3.3.2. Therefore, although the GNSS rates align with the upper bound of the GIA-induced rate, the higher VLM rate inferred from SLIPs indicates the presence of potential site-specific processes that require further investigation. It should be noted that the Bayesian approach used to estimate the GIA

uncertainty bounds accounts only for the parametric uncertainty in the modeling, while other sources of uncertainty, mainly associated with structural uncertainty, may also play an important role in this area. Furthermore, the limited number of SLIPs available for estimating the RSL rate at this site (only four SLIPs over the past 2 ka) may be another contributing factor to this residual.

At site #2, the GPS-derived VLM rate (12.73 ± 0.52 mm/yr) is in good agreement with the late-Holocene VLM rate from the linear model (12.21 ± 1.85 mm/yr). The GIA model rate (ranging from 6.46 to 11.82 mm/yr, with an optimal rate of 9.82 mm/yr) is lower than the VLM rates derived from both the late-Holocene RSL changes based on linear regression and GPS measurements but falls within the lower bound of the uncertainty range for the paleo rate from SLIPs over 2 ka BP. Additionally, it is very close to the GPS rates (the difference is 0.39 mm/yr when considering their uncertainty bounds). The late-Holocene VLM rate from the postglacial decay time analysis (9.27 ± 2.53 mm/yr) compares well with the GIA model rates. Overall, while there is some variability in the rates, the noted discrepancies are considered minor given the relatively large uncertainty ranges (and that they are 1σ ranges).

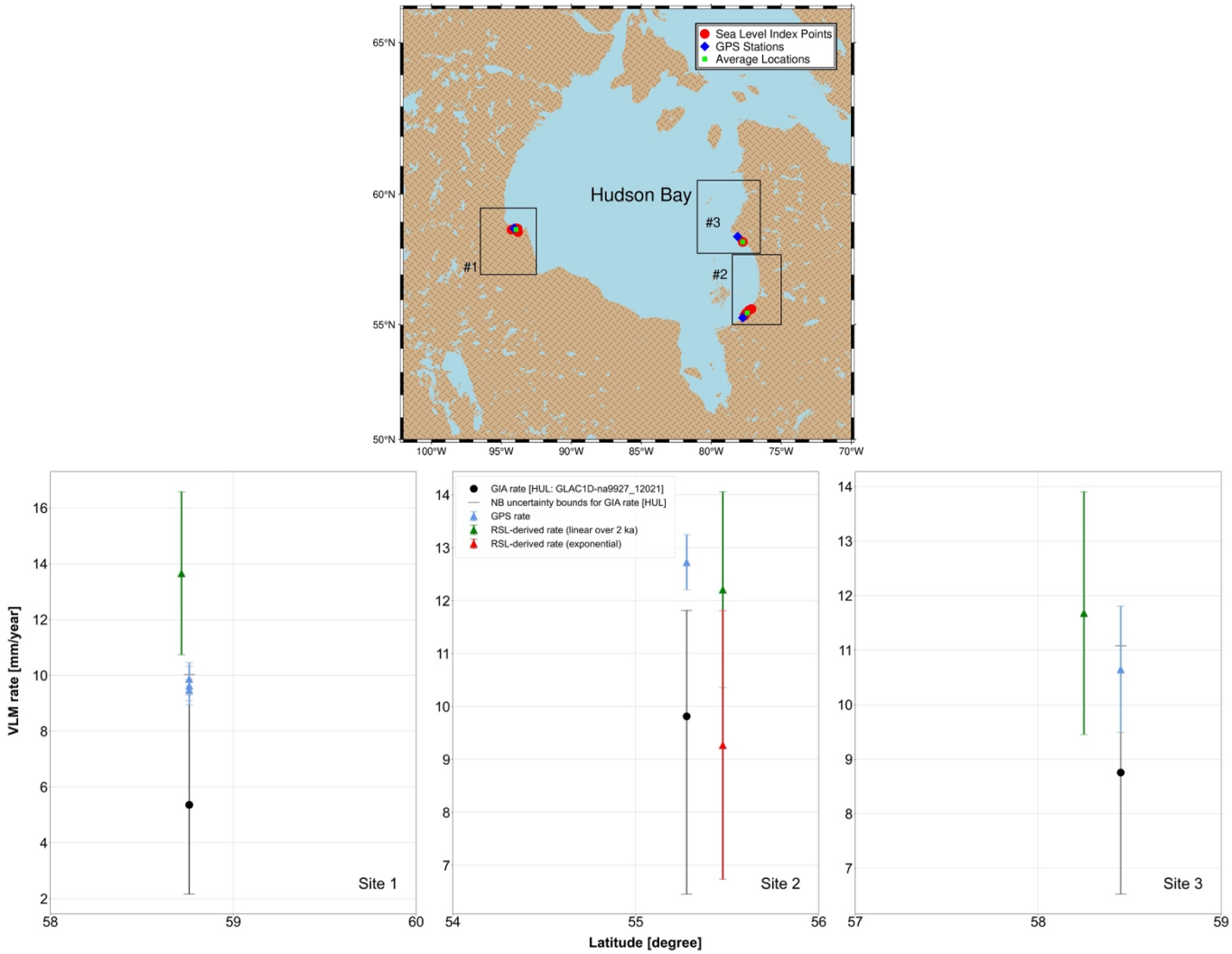


Figure 3.2. Top panel depicting the sites in Hudson Bay that were considered for the VLM rate analysis. Red circles represent the spatial distribution of SLIPs dating from 4 ka BP to the present day. Blue diamonds indicate the GPS stations co-located with SLIPs at each site. Green squares mark the average locations (average latitude and longitude) calculated from all SLIPs within each site, where the parameters of ΔRSL, ΔVLM, and ΔG are estimated (see Equation 3.1). Bottom panel compares paleo and contemporary VLM rates at three sites in Hudson Bay. The decadal-scale rates, represented by blue triangles, are derived

from GPS measurements, while the millennial-scale rates are inferred from GIA modelling (black circles) and late-Holocene RSL changes using both linear regression (green triangles) and postglacial decay time analysis (red triangles) over the past 2,000 and 4,000 years, respectively. The error bars indicate 1σ uncertainty bounds for each estimate. The x-axis shows the latitudes (in degrees) of the locations where the VLM rates are determined. The late-Holocene VLM rates are estimated at the average location within each site, and the GIA-induced rates correspond to the locations of GPS stations.

For site #3, the GPS-derived VLM rate (10.65 ± 1.16 mm/yr) is somewhat lower than the VLM rate from late-Holocene RSL changes based on a linear regression (11.68 ± 2.22 mm/yr), but it falls within the uncertainty bounds of the RSL-induced estimate. The GIA model rate (ranging from 6.53 to 11.07 mm/yr, with an optimal rate of 8.76 mm/yr) is lower than both the GPS and RSL-induced rates but remains within the uncertainty range of the GPS rate and the lower bound of the VLM rate from SLIPs over 2 ka BP. We conclude that the different VLM rate estimates in Hudson Bay are broadly compatible.

3.3.1.2. Ungava Peninsula and Labrador

In this subregion, there are no SLIPs younger than 4 ka BP, so the millennial-scale VLM rates are based solely on the GIA model outputs, and so all available GPS stations (see Figure 3.3) in this subregion are used for the contemporary VLM rates. Figure 3.3 illustrates the comparison between GPS-derived (blue triangles) and GIA model-predicted (black circles) VLM rates with the related uncertainty bounds for the four GNSS stations in this subregion. The results indicate generally strong agreement between the contemporary and paleo VLM rates. At the stations located at 52.94° and 54.83° latitude, the GPS rates of approximately 10.22 mm/yr and 10.03 mm/yr, respectively, are closely aligned with the GIA predictions, falling well within the GIA model uncertainty bounds. This indicates that GIA is likely the primary driver of land motion at these locations. At the 53.30° latitude station, the GPS rate of 4.54 mm/yr is slightly higher than the GIA-predicted rate of 3.67 mm/yr, but still within the uncertainty range, suggesting a reasonable alignment between the two. The only discrepancy is observed at the station located at 56.53° latitude, where the GPS rate of 3 ± 0.4 mm/yr contrasts with the GIA model rate of -0.51 mm/yr (ranging from -1.5 to 1.13 mm/yr). This difference suggests that either the millennial-scale rate has significant contributions from processes not related to GIA, such as local tectonic activity, and/or there are significant contributions to the contemporary rate not accounted for in the applied model (Section 3.2.1.1; Riva et al. 2017). The proximity of this GPS station ("NAIN") to Greenland and the Canadian Arctic region results in a relatively large contribution from contemporary ice mass loss (1.07 mm/yr). The model rate applied to remove this signal is based on a timeseries extending to 2014 CE (Figure 3.S3) whereas the GNSS time series extends to 2019 CE (from 1997).

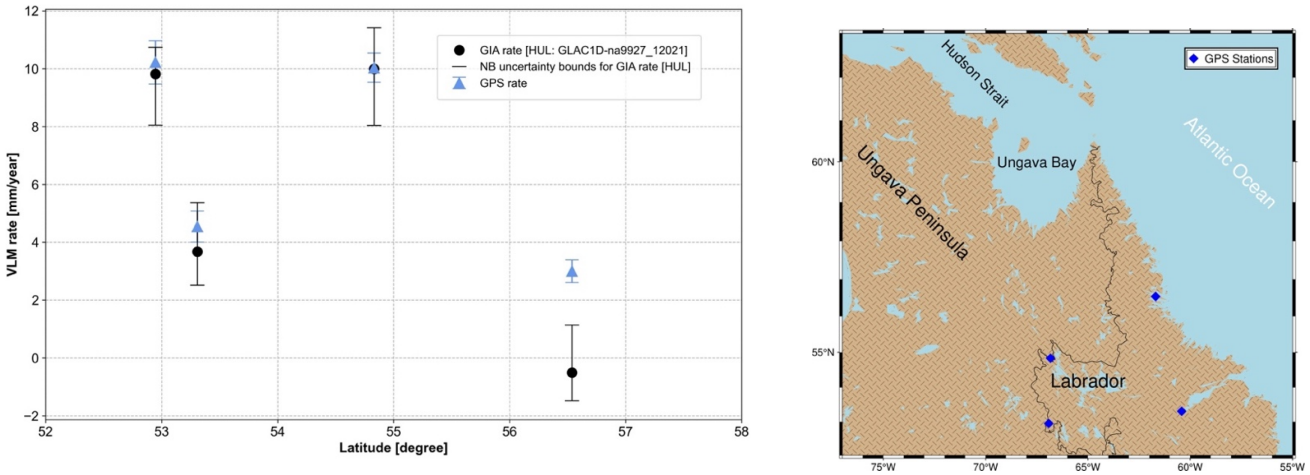


Figure 3.3. Legend on next page.

Figure 3.3. Right panel: Map of the Ungava Peninsula and Labrador showing the locations of GPS stations (indicated by blue diamonds) used for the VLM rate analysis. Left panel: Comparison of decadal-scale VLM rates derived from GPS observations (blue triangles) and millennial-scale VLM rates from GIA model predictions (black circles) for four GPS stations located in the Ungava Peninsula and Labrador subregion. The error bars indicate 1σ uncertainty bounds for each estimate. The GIA rates are based on the optimal regional GIA model (GLAC1D-na9927_12021), with the associated uncertainty bounds inferred from a Bayesian approach. The x-axis shows the latitudes (in degrees) of the GPS stations where the VLM rates are determined.

3.3.1.3. Newfoundland

The analysis of VLM rates for this subregion is inferred from data at three specific sites (see sites #4, #5, and #6 in Figure 3.4). To estimate the millennial-scale VLM rates based on Equation 3.1, as demonstrated in Figures 3.S8 and 3.S9, the optimal regional GIA model (GLAC1D-na1259_120p830) is utilized for the modelled RSL and VLM time series. The model uncertainty bounds (green dashed lines) are determined using the Bayesian approach, based on a sub-ensemble of 71 GIA models that provide good fits. Across all three sites, the best-fit model curves (orange lines) show a rising/falling RSL/VLM trend over the past 6,000 years. Figure 3.S10 shows the $\Delta G + E$ term with the respective uncertainty, estimated based on Equation 3.1 using the RSL and VLM curves. In addition, the paleo rate of RSL change at each site is determined by a linear regression applied to SLIPs over 4 ka BP (Figure 3.S11). The different VLM estimates (Figure 3.4) indicate broad compatibility between the paleo and contemporary rates at each site, suggesting that GIA is the dominant geodynamic process and the applied signal for contemporary mass loss is accurate.

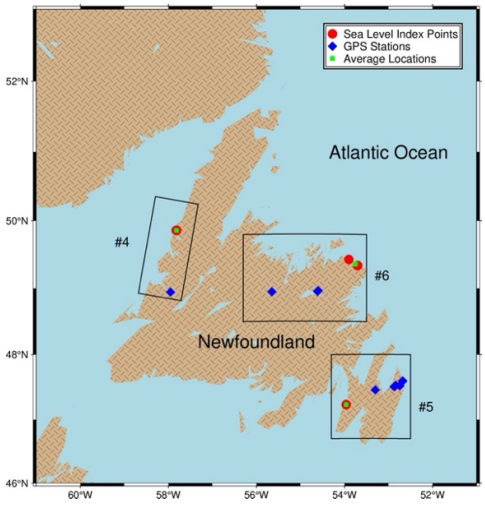


Figure 3.4 (continued). Legend on next page.

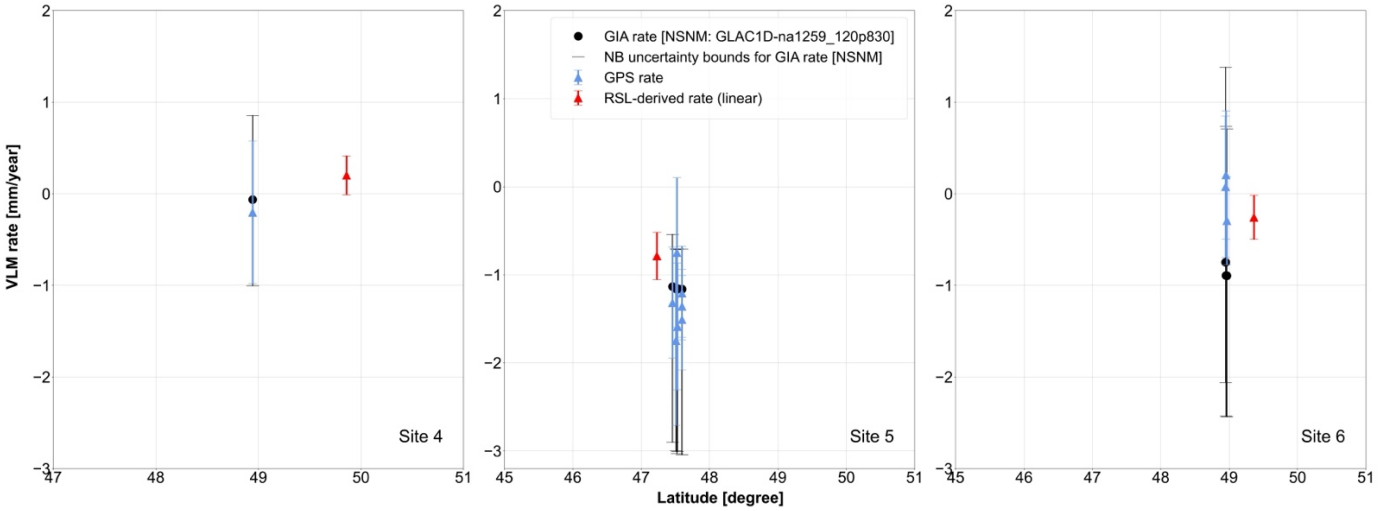


Figure 3.4. Top panel depicting the sites in Newfoundland that were considered for the VLM rate analysis. Red circles represent the spatial distribution of SLIPs dating from 4 ka BP to the present day. Blue diamonds indicate the GPS stations co-located with SLIPs at each site. Green squares mark the average locations (average latitude and longitude) calculated from all SLIPs within each site, where the parameters of ΔRSL, ΔVLM, and ΔG are estimated (see Equation 3.1). Bottom panel compares paleo and contemporary VLM rates at three sites in Newfoundland. The decadal-scale rates, represented by blue triangles, are derived from GPS measurements, while the millennial-scale rates are inferred from GIA modelling (black circles) and late-Holocene RSL changes using a linear regression over the past 4,000 years (red triangles). The error bars indicate 1σ uncertainty bounds for each estimate. The x-axis shows the latitudes (in degrees) of the locations where the VLM rates are determined. The late-Holocene VLM rates are estimated at the average location within each site, and the GIA-induced rates correspond to the locations of GPS stations.

3.3.1.4. St. Lawrence Corridor

As indicated in Figure 3.5, two RSL sites (sites #7 and #8) in this subregion are utilized for the paleo VLM rate analysis, with a total of 5 GNSS stations available to constrain contemporary rates within these sites. The GIA model rates are calculated using the same parameter values as those for Newfoundland (Section 3.2.3). Figures 3.S12 and 3.S13 respectively show the modeled optimal RSL and VLM curves (orange lines) with uncertainty bounds (green dashed lines) applied for the estimation of the $\Delta G + E$ term in Equation 3.1 (see Figure 3.S14). As demonstrated in Figure 3.S12, at site #7, from 4 ka BP to the present day, the modeled RSL begins to gradually decrease, consistently aligning with the SLIPs, suggesting that the RSL fall is primarily driven by GIA. Similarly, at site #8, the modelled RSL reveals a general declining trend from 4 ka BP to the present, while the SLIPs display greater variability compared to site #7, indicating that other localized factors, such as changes in sedimentation rates, may also be influencing the RSL. Figure 3.S15 provides the RSL trend estimates.

A comparison of the VLM rate estimates is shown in Figure 3.5. At site #7, the GIA-induced VLM rate estimates range between 1 and 2 mm/yr with wide uncertainty bounds (-1 – 4 mm/yr). The VLM rates from GPS measurements range between 0 and 3 mm/yr when considering the associated uncertainty ranges, and so overlap with those of the GIA-induced rates. The rate inferred from SLIPs over 4 ka BP is slightly above 2 mm/yr, with its uncertainty range overlapping with the rates estimated from GPS and GIA model predictions. Therefore, the decadal-scale and millennial-scale estimates of VLM rates are compatible at site #7, suggesting no significant contemporary non-GIA signal. At site #8, the VLM rates from GPS and the optimal regional GIA model are compatible. However, the VLM rate derived from late-Holocene RSL changes is lower (although overlaps with the GIA model rate

uncertainty). The different between the RSL-derived and GNSS VLM rates is 2-3 mm/yr and so worthy of further investigation.

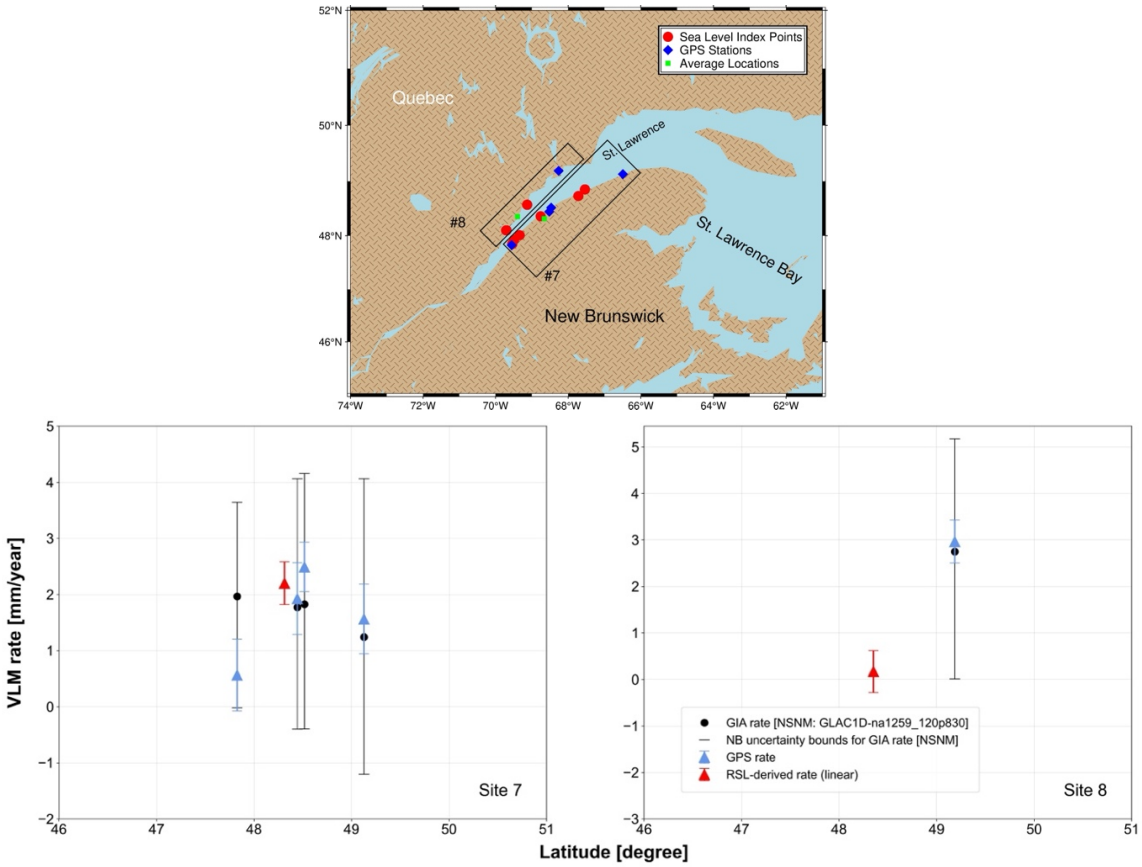


Figure 3.5. Top panel depicting the sites in St. Lawrence Corridor that were considered for the VLM rate analysis. Red circles represent the spatial distribution of SLIPs dating from 4 ka BP to the present day. Blue diamonds indicate the GPS stations co-located with SLIPs at each site. Green squares mark the average locations (average latitude and longitude) calculated from all SLIPs within each site, where the parameters of ΔRSL, ΔVLM, and ΔG are estimated (see Equation 3.1). Bottom panel compares paleo and contemporary VLM rates at two sites in St. Lawrence Corridor. The decadal-scale rates, represented by blue triangles, are derived from GPS measurements, while the millennial-scale rates are inferred from GIA modelling (black circles) and late-Holocene RSL changes using a linear regression over the past 4,000 years (red triangles). The error bars indicate 1σ uncertainty bounds for each estimate. The x-axis shows the latitudes (in degrees) of the locations where the VLM rates are determined. The late-Holocene VLM rates are estimated at the average location within each site, and the GIA-induced rates correspond to the locations of GPS stations.

3.3.1.5. New Brunswick and Nova Scotia

In this subregion, according to Figure 3.6, a comparison of paleo and contemporary rates of VLM is conducted at six sites (sites #9 – #14). The modelled RSL, VLM, and $\Delta G + E$ curves (Figures 3.S16 – 3.S18) are computed using the regional GIA model parameter sets developed for the eastern subregions (NSNM; see Section 3.2.3). Figure 3.S17 indicates significant land subsidence across all sites, corresponding to the observed RSL rise shown in Figure 3.S16, which highlights the impact of GIA-driven VLM in these areas. Figure 3.S19 shows that although all sites exhibit an increasing RSL trend, site #13 has the most rapid rise (3.036 ± 0.248 mm/yr), while site #14 has the slowest (1.027 ± 0.114 mm/yr). This variation in RSL changes across sites reflects differences in the GIA response and other site-specific geophysical processes.

As demonstrated in Figure 3.6, at each site, the GPS-derived rates are broadly consistent with the GIA-induced rates, as the overlapping uncertainty bounds indicate a reasonable level of agreement. In addition, at all sites except for site #13, the late-Holocene VLM rates from SLIPs over 4 ka BP show a strong agreement with both the GPS-derived and GIA-related rates, falling within the associated uncertainty ranges and indicating substantial consistency. Conversely, at site #13, the late-Holocene VLM rate differs by less than ~1 mm/yr from the rates derived from the GIA model outputs and GPS, with no overlap in their uncertainty ranges. This discrepancy might suggest the presence of additional local factors influencing the RSL or a limitation in the rate estimation due to the insufficient number of SLIPs at this site (5 SLIPs; see Figure 3.S19) to robustly determine the rate through linear trend fitting.

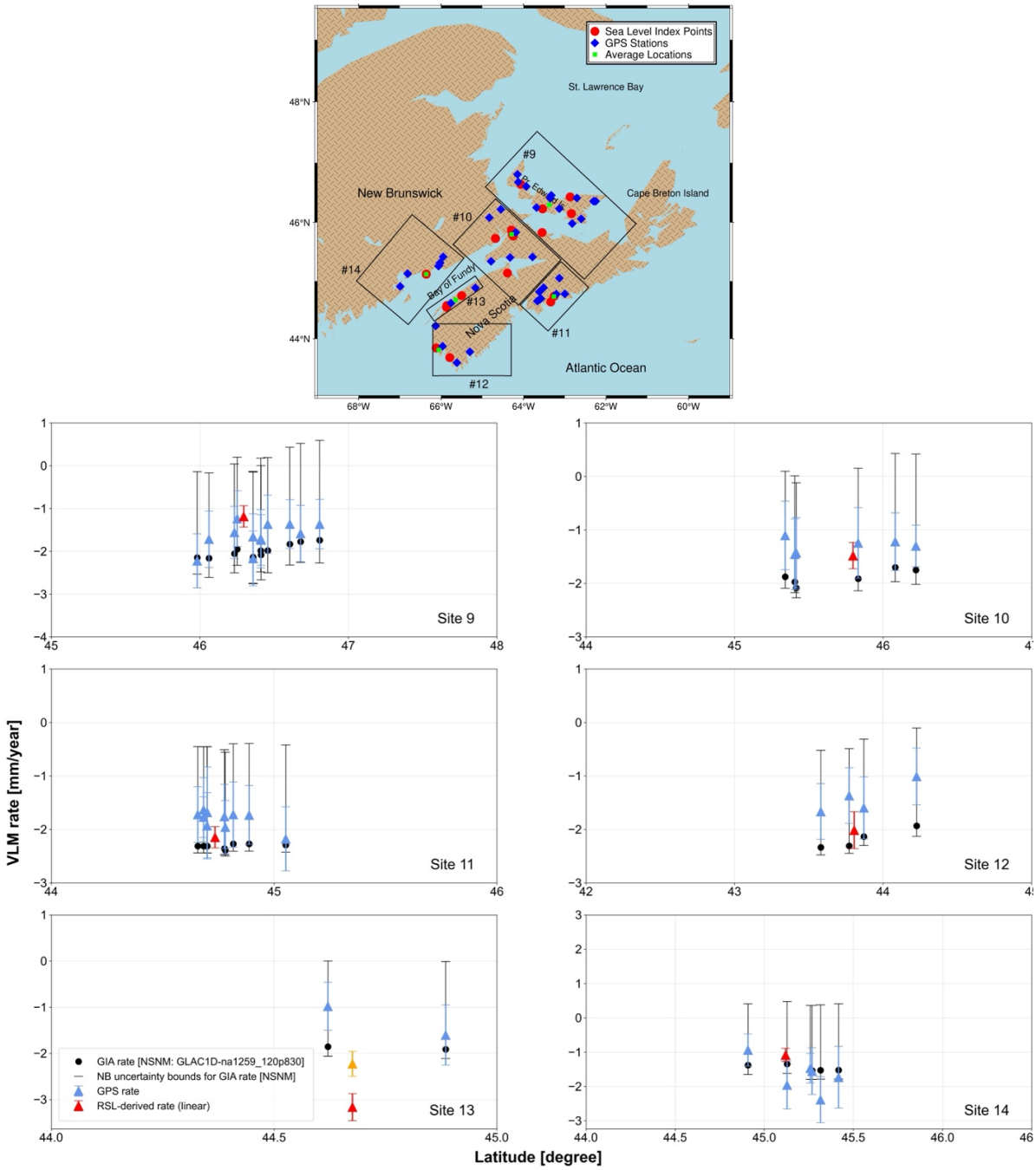


Figure 3.6. Top panel depicting the sites in New Brunswick and Nova Scotia that were considered for the VLM rate analysis. Red circles represent the spatial distribution of SLIPs dating from 4 ka BP to the present day.

Blue diamonds indicate the GPS stations co-located with SLIPs at each site. Green squares mark the average locations (average latitude and longitude) calculated from all SLIPs within each site, where the parameters of ΔRSL, ΔVLM, and ΔG are estimated (see Equation 3.1). Bottom panel compares paleo and contemporary VLM rates at six sites in New Brunswick and Nova Scotia. The decadal-scale rates, represented by blue triangles, are derived from GPS measurements, while the millennial-scale rates are inferred from GIA modelling (black circles) and late-Holocene RSL changes using a linear regression over the past 4,000 years (red triangles). The error bars indicate 1σ uncertainty bounds for each estimate. The x-axis shows the latitudes (in degrees) of the locations where the VLM rates are determined. The late-Holocene VLM rates are estimated at the average location within each site, and the GIA-induced rates correspond to the locations of GPS stations. At site #13, the orange triangle shows the VLM rate from the late-Holocene RSL changes after removal of the SLIP with an age of ~3 ka BP and RSL of ~-10 m, which lies below the lower NB bound and another SLIP with a similar age (see Figure 3.S16).

3.3.1.6. Maine and Massachusetts

The comparison between decadal-scale and millennial-scale rates of VLM, along with their associated uncertainty estimates, across four sites (sites #15 – #18) in Maine and Massachusetts is shown in Figure 3.7. As discussed in Section 3.2.3, the optimal regional GIA model (GLAC1D-na1259_120p830), along with a sub-ensemble of 71 highest-probability model parameter sets, is used to estimate the RSL, VLM, and $\Delta G + E$ time series (see Figures 3.S20 – 3.S22). Figures 3.S20 and 3.S21 demonstrate that the interplay between RSL rise and land subsidence at all sites highlights the dominant role of GIA in long-term sea level changes and solid Earth displacement in this subregion. In addition, the best-fit linear regression to the SLIPs over 4 ka BP (blue dashed lines in Figure 3.S23) indicates that the highest RSL rise is observed at site #18, with a rate of 1.75 ± 0.197 mm/yr, while the lowest is at site #17, with a rate of 0.52 ± 0.061 mm/yr. Overall, according to Figure 3.7, the uncertainty bounds for all three rates inferred from GPS, GIA modelling, and late-Holocene RSL changes overlap considerably at each site, indicating that the differences in magnitude are within the acceptable range of uncertainty. Therefore, the results suggest a broad compatibility between paleo and contemporary rates in interpreting subsidence at each site.

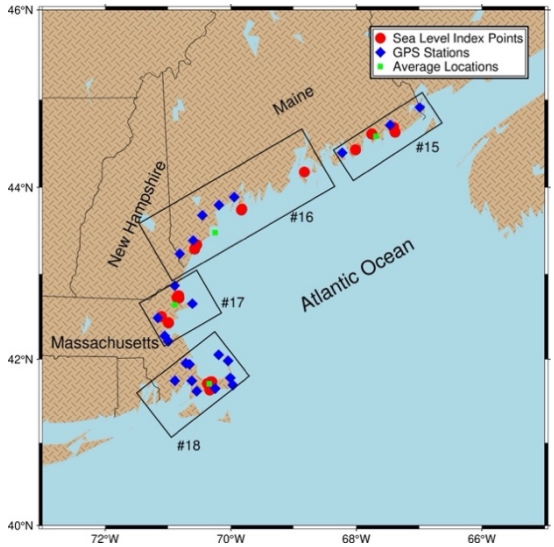


Figure 3.7 (continued). Legend on next page.

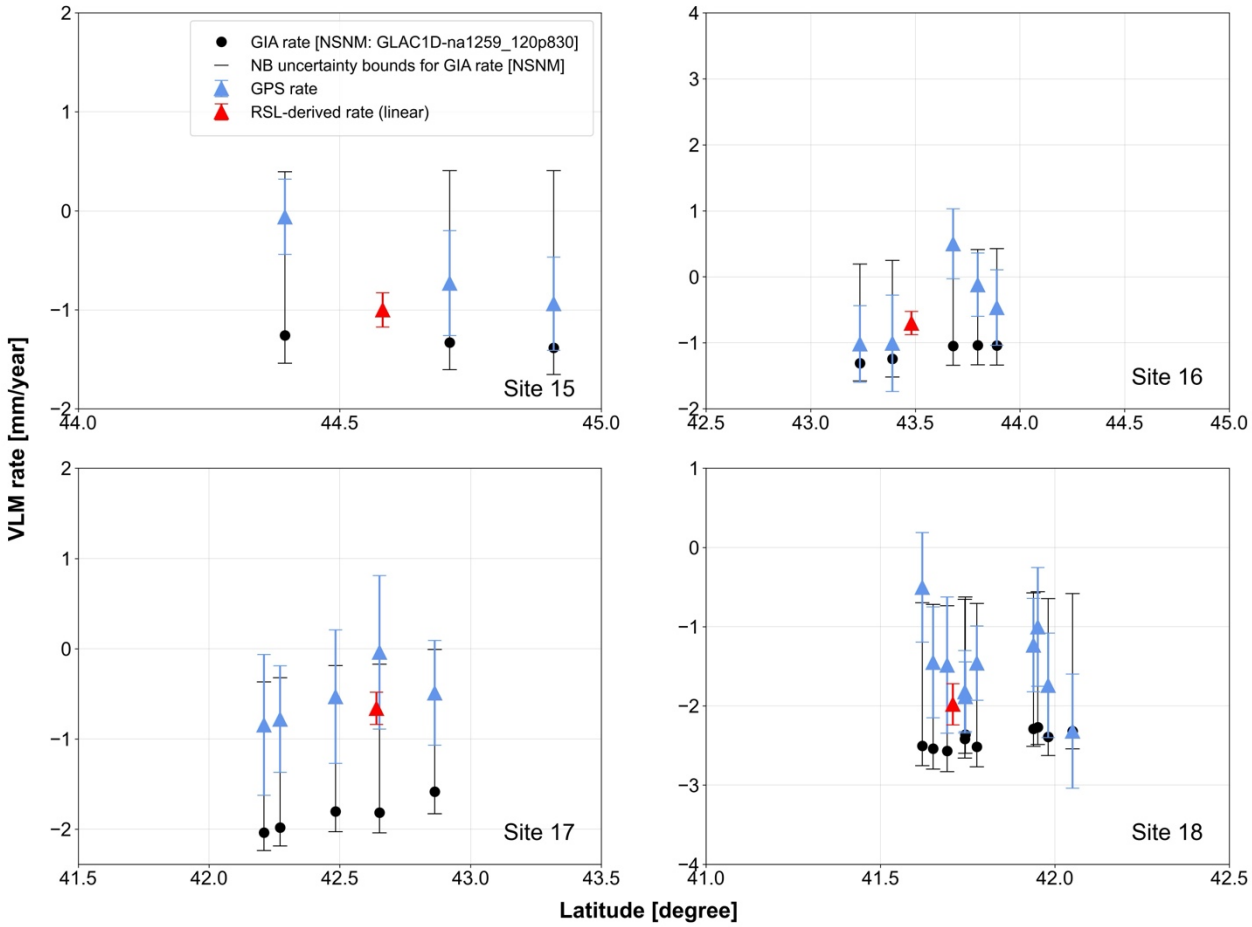


Figure 3.7. Top panel depicting the sites in Maine and Massachusetts that were considered for the VLM rate analysis. Red circles represent the spatial distribution of SLIPs dating from 4 ka BP to the present day. Blue diamonds indicate the GPS stations co-located with SLIPs at each site. Green squares mark the average locations (average latitude and longitude) calculated from all SLIPs within each site, where the parameters of ΔRSL, ΔVLM, and ΔG are estimated (see Equation 3.1). Bottom panel compares paleo and contemporary VLM rates at four sites in Maine and Massachusetts. The decadal-scale rates, represented by blue triangles, are derived from GPS measurements, while the millennial-scale rates are inferred from GIA modelling (black circles) and late-Holocene RSL changes using a linear regression over the past 4,000 years (red triangles). The error bars indicate 1σ uncertainty bounds for each estimate. The x-axis shows the latitudes (in degrees) of the locations where the VLM rates are determined. The late-Holocene VLM rates are estimated at the average location within each site, and the GIA-induced rates correspond to the locations of GPS stations.

3.3.2. Present-day mass change signal with uncertainty estimates

As discussed in Section 3.3.1, the VLM analysis results indicate that, for each subregion, there is a general agreement between paleo and contemporary rates, within the bounds of uncertainty estimates. This suggests that there is no significant contemporary (non-GIA) signal attributable to present-day hydrological mass changes. In this section, GRACE estimates of contemporary mass changes and the resultant vertical surface displacement, along with their respective uncertainties (see Section 3.2.1.2 for methodology), are evaluated for each subregion to determine if the inferred present-day mass change signal supports the VLM rate analysis results.

The GRACE estimates for each subregion are corrected for the GIA signal using present-day rates of GIA-induced geoid changes (see Figure 3.S24), derived from optimal regional models, which were also used to estimate GIA-driven VLM rates. Figure 3.8 provides a complete view of the contemporary

mass change signal, the resulting vertical surface displacement, and their associated uncertainties in the Hudson Bay region. The map of contemporary mass change (top left), primarily associated with TWS variations from April 2002 to November 2023, shows that southeastern Hudson Bay experiences a slight mass gain, represented by a yellow-red gradient, with values reaching approximately 13 mm EWT/yr. This mass increase is associated with a subsidence rate of up to -0.3 mm/yr, as depicted in the vertical surface displacement map (bottom left). Additionally, western and southwestern Hudson Bay show more significant mass gain, indicated by orange and red shades. In contrast, parts of eastern and northeastern Hudson Bay exhibit minor mass loss, less than -3 mm EWT/yr. This modest mass loss results in an uplift rate of under 0.5 mm/yr in the eastern region, with a higher rate in the northeast, possibly due to minimal mass changes and ongoing elastic displacement linked to contemporary ice mass loss in Greenland. Overall, these mass changes and the associated vertical surface displacement rates indicate relatively minor hydrological loading signal across Hudson Bay.

The uncertainty map of the contemporary mass change signal (top right), estimated from the uncertainties in both GRACE SHCs and the GIA signal (see Figure 3.S25), reveals that the southern areas of Hudson Bay have the lowest uncertainty, with values between 1.8 and 2 mm EWT/yr. In comparison, the northern areas have slightly higher uncertainty, ranging from 2.3 to 2.5 mm EWT/yr. The uncertainty in the corresponding elastic displacement of the Earth's surface (bottom right) averages approximately 0.055 mm/yr over Hudson Bay, with slightly higher values in the northern regions. Therefore, when accounting for uncertainty estimates, the vertical surface displacement caused by present-day mass changes falls within the range of residual VLM signals discussed in Section 3.3.1.1. An important takeaway is that the overall magnitude of the contemporary mass change signal, along with its uncertainty estimate, is not substantial enough to result in significant discrepancies between paleo and contemporary rates of VLM. This suggests no large present-day hydrological mass change signal in Hudson Bay.

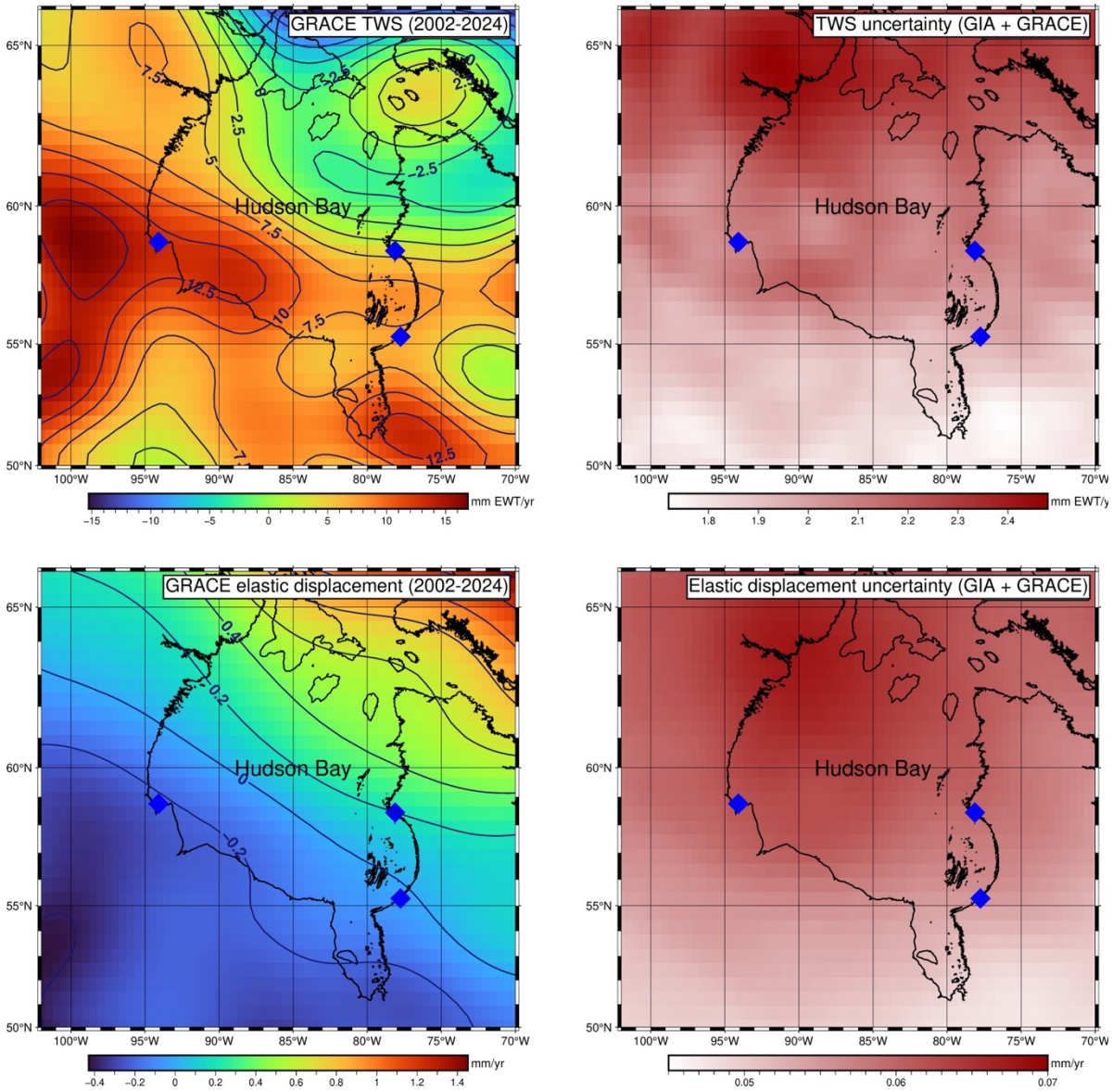


Figure 3.8. Contemporary GRACE-derived mass change signal, corresponding vertical surface displacement, and associated uncertainties in the Hudson Bay region from April 2002 to November 2023, corrected for GIA, destriped, with Gibbs ringing effects removed. (Top left) Contemporary mass changes (mm EWT/yr), primarily associated with TWS variations, show a slight mass gain in southeastern, western, and southwestern Hudson Bay, and small mass loss in parts of the eastern and northeastern regions. (Top right) Uncertainty estimates (mm EWT/yr) for the GRACE mass change signal, with the lowest uncertainty observed in southern Hudson Bay, indicating confidence in the mass change signal in this area. The GRACE TWS uncertainty estimates are derived from (1) uncertainty in the GIA signal, the dominant source of uncertainty in this area, and (2) standard deviations of the GRACE SHCs based on the standard deviation of the time-series residuals (see Figure 3.S25). (Bottom left) Elastic displacement (mm/yr) resulting from contemporary mass changes, where mass gain in southeastern Hudson Bay corresponds to subsidence, and mass loss in the northeastern region results in uplift. (Bottom right) Uncertainty in elastic displacement (mm/yr), estimated using the same approach as for the uncertainty in the contemporary mass change signal, shows slightly higher values in the northern regions. The contour intervals for contemporary mass changes (top left) and elastic displacement (bottom left) are 2.5 mm EWT/yr and 0.2 mm/yr, respectively. Blue diamonds indicate the GPS stations used in the VLM rate analysis.

As shown in Figure 3.9, the top-left map highlights the contemporary mass change signal, primarily influenced by TWS variations from April 2002 to November 2023 across the Ungava Peninsula and Labrador subregion. In general, this area exhibits a slight mass gain, reaching up to about 15 mm EWT/yr, most notably in the southeastern Ungava Peninsula and northern Labrador (indicated by dark red shades). Further inland, towards northern Ungava Peninsula and southern Labrador, the mass gain signal weakens, with a minor mass loss of around -5 mm EWT/yr observed in northern Ungava Peninsula. The slight mass change across this subregion contributes to a minor vertical surface displacement (as shown in the bottom-left map), with an uplift rate reaching approximately 0.6 mm/yr, particularly along the coastal areas of northern Ungava Peninsula. The uncertainty in the mass change signal (top right) is relatively uniform across the Ungava Peninsula and Labrador, generally ranging from approximately 1.7 to 2.2 mm EWT/yr. Higher uncertainty values appear near the coastline and in the northern areas of the Ungava Peninsula, likely due to the variability of hydrological mass loss processes and the influence of Greenland's ice loss signal. In contrast, central and southern Labrador shows the lowest uncertainty values.

The uncertainty in the elastic displacement signal (bottom right) is relatively consistent across the subregion, averaging approximately 0.055 mm/yr, with slightly higher values in the northern areas of the Ungava Peninsula. These estimates suggest that, in addition to GIA, the observed displacement across the subregion is influenced by recent mass changes and their associated elastic responses. However, further evaluation of the Greenland ice mass loss signal is necessary to accurately interpret the specific magnitude of land displacement in these areas. Based on the VLM rate analysis results (refer to Section 3.3.1.2), the GPS measurements indicate slightly higher uplift rates than those predicted by the GIA model outputs, particularly at the GPS station located at latitude 56.53° N (“NAIN”). The GRACE estimates imply that the residual signal is also attributable to contemporary mass changes in the region, specifically in response to TWS variations. For instance, the resultant vertical surface displacement and its associated uncertainty at the “NAIN” station can partly capture this residual signal. These findings suggest that, similar to Hudson Bay, the overall magnitude of contemporary mass changes, alongside their associated uncertainty estimates, does not imply drastic hydrological mass changes across the Ungava Peninsula and Labrador.

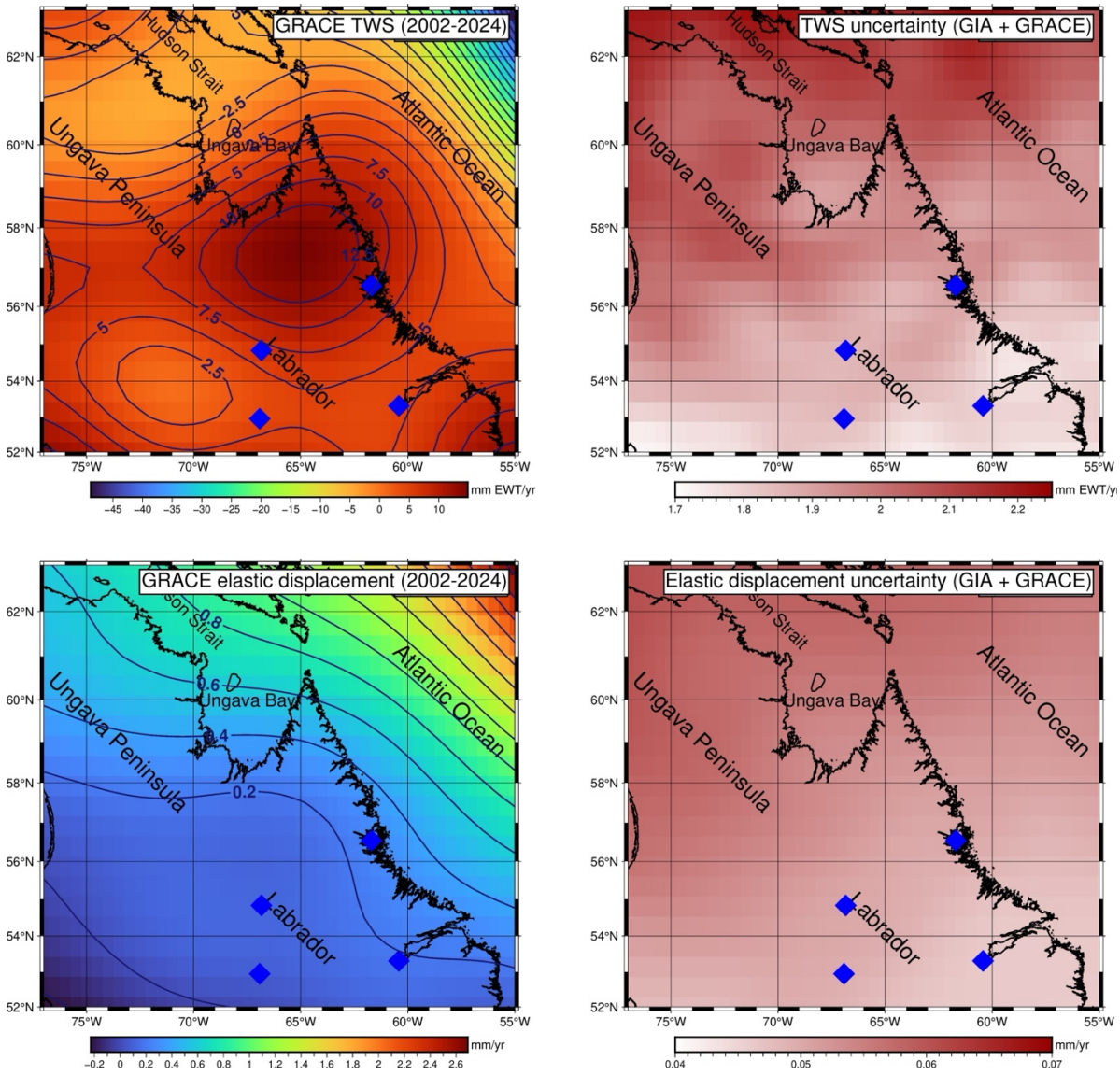


Figure 3.9. Contemporary GRACE-derived mass change signal, corresponding vertical surface displacement, and associated uncertainties in the Ungava Peninsula and Labrador subregion from April 2002 to November 2023, corrected for GIA, destriped, and with Gibbs ringing effects removed. (Top left) Contemporary mass changes (mm EWT/yr), primarily associated with TWS variations, show a slight mass gain (up to 15 mm EWT/yr) in the southeastern Ungava Peninsula and northern Labrador and minor mass loss (~-5 mm EWT/yr) in northern Ungava Peninsula. (Top right) Uncertainty estimates (mm EWT/yr) for the GRACE mass change signal range from approximately 1.7 to 2.2 mm EWT/yr, with higher uncertainty values near the coastline and in the northern areas of the Ungava Peninsula, and lower uncertainty values in central and southern Labrador. The GRACE TWS uncertainty estimates are derived from (1) uncertainty in the GIA signal, the dominant source of uncertainty in this area, and (2) standard deviations of the GRACE SHCs based on the standard deviation of the time-series residuals (see Figure 3.S25). (Bottom left) Elastic displacement (mm/yr) resulting from contemporary mass changes reaches up to ~0.6 mm/yr along the northern areas of the Ungava Peninsula. (Bottom right) Uncertainty in elastic displacement (mm/yr), estimated using the same approach as for the uncertainty in the contemporary mass change signal, is relatively consistent across the subregion, with slightly higher uncertainty in the northern areas of the Ungava Peninsula. The contour intervals for contemporary mass changes (top left) and elastic displacement (bottom left) are 2.5 mm EWT/yr and 0.2 mm/yr, respectively. Blue diamonds indicate the GPS stations used in the VLM rate analysis.

Figure 3.10 presents the GRACE-derived contemporary mass change signal (primarily associated with TWS variations) and the resulting vertical displacement signal, along with their associated uncertainties, for the period from April 2002 to November 2023 across four subregions in southeastern Canada and the northeastern USA: Newfoundland, the St. Lawrence Corridor, New Brunswick and Nova Scotia, and Maine and Massachusetts. In Newfoundland, the contemporary mass change signal (top-left panel) ranges from about -3 mm EWT/yr in the southwestern regions to approximately 9 mm EWT/yr along the northeastern coast. This gradient suggests a net reduction in TWS towards the west, likely influenced by local hydrological factors. The elastic displacement signal (bottom-left panel) displays a slight uplift, with rates between roughly 0.2 and 0.4 mm/yr, reflecting the effects of mass variations on the land surface. Uncertainty in the mass change signal (top-right panel) spans from about 2.4 to 2.5 mm EWT/yr, with slightly higher uncertainties near the northeastern coast, potentially due to fluctuations in the hydrological mass change. In the St. Lawrence Corridor, the northern section shows slight mass gains of up to approximately 5 mm EWT/yr, while the southern part experiences a minor mass loss of around -3 mm EWT/yr. This distribution suggests that hydrological processes in the north contribute to mass gains, in contrast to slight reductions in the south. The elastic displacement signal indicates a slight uplift across the corridor, with rates generally between 0.3 and 0.4 mm/yr. The uncertainty in TWS estimates is relatively consistent, averaging around 2.5 mm EWT/yr, with a slight increase near the western boundaries. In New Brunswick and Nova Scotia, TWS variations indicate an increase in mass, particularly in central Nova Scotia, reaching approximately 5 mm EWT/yr. In contrast, parts of New Brunswick near the Maine border exhibit minor decreases of around -2 mm EWT/yr.

The elastic displacement map shows largely neutral/slight uplift, reaching up to ~0.3 mm/yr in northern parts of New Brunswick. These observations imply that local hydrological processes may be causing slight changes in the contemporary mass signal but have a limited effect on vertical surface displacement. The uncertainty in the mass change signal is relatively uniform across this subregion, ranging between 2.4 and 2.5 mm EWT/yr, providing a moderately reliable assessment of mass changes. For Maine and Massachusetts, the TWS map highlights minor mass losses in Maine (up to approximately -3 mm EWT/yr) and minor increases in Massachusetts (up to around 6 mm EWT/yr), indicating contrasting hydrological processes between the two states. The elastic displacement map shows a slight uplift in central Maine of about 0.2 mm/yr and neutral to minor land subsidence in Massachusetts, likely resulting from localized changes in water storage mass. The uncertainty in the contemporary mass change signal is approximately 2.5 mm EWT/yr, with minimal regional variation. In addition, the average uncertainty in the elastic displacement signal across all four subregions (bottom-right panel) is approximately 0.15 mm/year, indicating an acceptable confidence level in interpreting the elastic displacement signal, with a signal-to-noise ratio greater than 1. Overall, when comparing the GRACE-derived results in Figure 3.10 with those from the VLM rate analysis (as presented in Sections 3.3.1.3 – 3.3.1.6), no significant discrepancies are observed across the four subregions, supporting the conclusion that GIA remains the dominant factor influencing VLM in these areas. The GRACE-based TWS and displacement rates align with the residual signals observed in VLM rates, suggesting that contemporary hydrological mass changes have a limited impact on VLM.

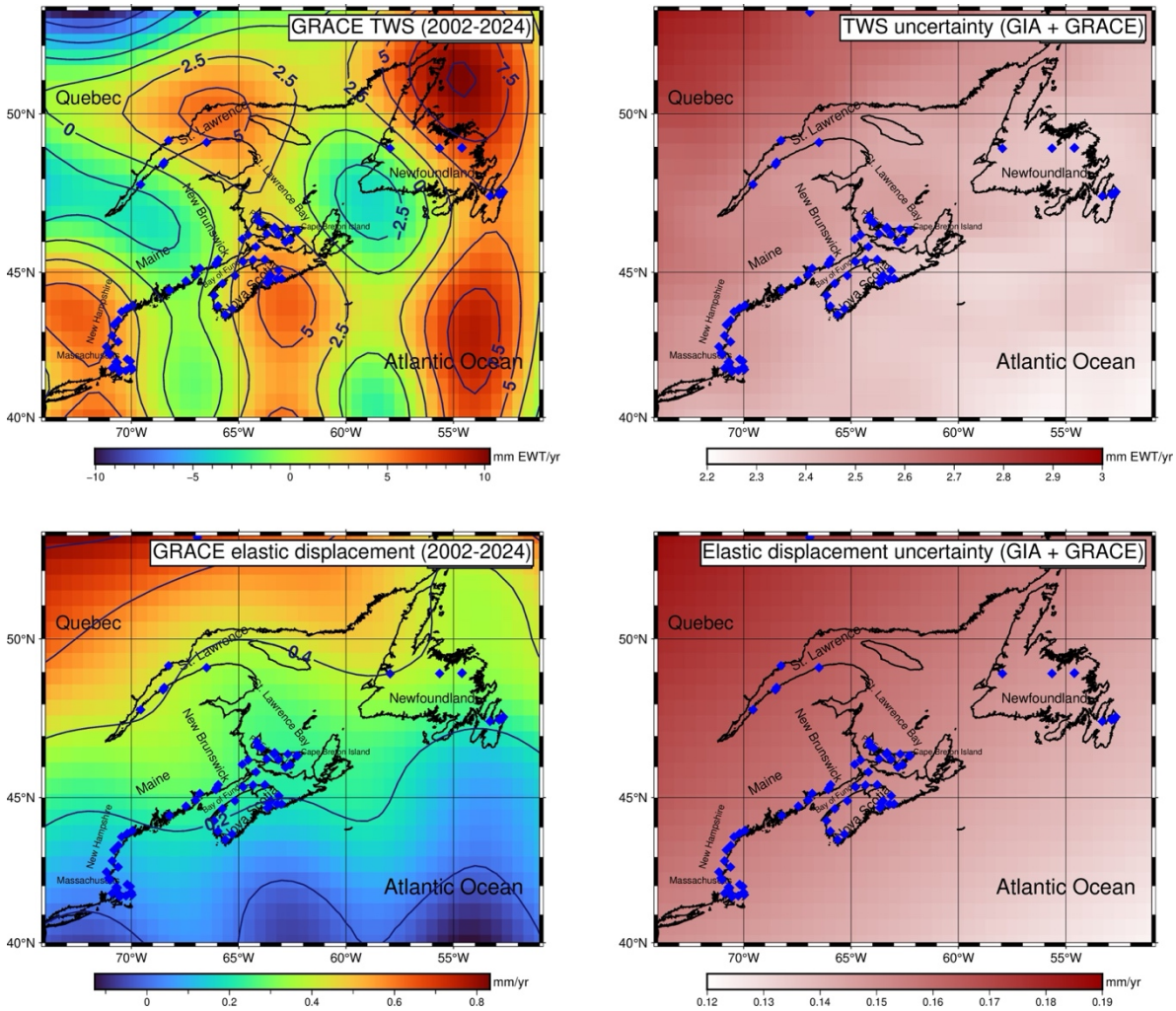


Figure 3.10. The contemporary GRACE-derived mass change signal, corresponding vertical surface displacement, and associated uncertainties from April 2002 to November 2023 across four subregions in southeastern Canada and northeastern USA (including Newfoundland, St. Lawrence Corridor, New Brunswick and Nova Scotia, and Maine and Massachusetts), corrected for GIA, destriped, and with Gibbs ringing effects removed. (Top left) Contemporary mass changes (mm EWT/yr), primarily associated with TWS variations, show fluctuation across subregions: Newfoundland has a gradient from -3 mm EWT/yr in the southwest to 9 mm EWT/yr in the northeast; St. Lawrence Corridor sees gains up to 5 mm EWT/yr in the north and losses around -3 mm EWT/yr in the south; New Brunswick and Nova Scotia exhibit central mass increases (5 mm EWT/yr) and minor decreases (-2 mm EWT/yr) near Maine; Maine shows losses up to -3 mm EWT/yr, while Massachusetts has slight gains (~6 mm EWT/yr). (Top right) Uncertainty estimates (mm EWT/yr) for the GRACE mass change signal range from 2.4 to 2.5 mm EWT/yr across subregions. The GRACE TWS uncertainty estimates are derived from (1) uncertainty in the GIA signal, the dominant source of uncertainty in this area, and (2) standard deviations of the GRACE SHCs based on the standard deviation of the time-series residuals (see Figure 3.S25). (Bottom left) Elastic displacement (mm/yr) signal due to contemporary mass changes shows a slight uplift in Newfoundland (0.2 to 0.4 mm/yr), a general uplift across the St. Lawrence Corridor (0.3 to 0.4 mm/yr), neutral to minor uplift (~0.3 mm/yr) in New Brunswick and Nova Scotia, and a slight uplift in central Maine (~0.2 mm/yr) with neutral to minor subsidence in Massachusetts. (Bottom right) Uncertainty in elastic displacement (mm/yr), estimated using the same approach as for the uncertainty in the contemporary mass change signal, is ~0.15 mm/yr across subregions. The contour intervals for contemporary mass changes (top left) and elastic displacement (bottom left) are 2.5 mm EWT/yr and 0.2 mm/yr, respectively. Blue diamonds indicate the GPS stations used in the VLM rate analysis.

3.4. General discussion

This study underscores the interaction between long-term geophysical processes and present-day hydrological mass changes based on a thorough analysis of VLM rates across six subregions in northeastern USA and southeastern Canada. We assessed the temporal and spatial variability of VLM by combining the millennial-scale and decadal-scale VLM estimates with contemporary mass change signals. Our results indicate both the contributions of non-GIA processes and the importance of GIA as the main driver of VLM in our study region.

A major contribution of this study is the utilization of the optimal regional GIA models with model uncertainty bounds to more precisely constrain the GIA model outputs in eastern North America. This study improves the accuracy of VLM modelling by building on the work presented in Chapter 2, which accounted for the implications of the laterally variable Earth structure in the GIA modelling. Our comprehensive uncertainty analysis for the VLM signal addresses gaps identified in previous studies (e.g., Bouin & Wöppelmann, 2010; Santamaría-Gómez et al., 2017). Additionally, this study is the first to provide the uncertainty in the GRACE mass change estimates based on accounting for uncertainty in the GIA signal, which has an important role in the interpretation of GRACE-derived secular mass changes (Caron et al., 2018; Eicker et al., 2024). Therefore, based on the applied methodology, the residual signal between paleo and contemporary VLM rates is reliably interpreted and the potential biases associated with the GIA correction in estimating the contemporary mass change signal from GRACE are minimized.

Our findings significantly improve upon those of Karegar et al. (2017), who hypothesized that the anthropogenic impacts of the James Bay Hydroelectric Project in southeastern Hudson Bay have led to excessive water mass accumulation in this area, contributing to notable departures of contemporary VLM rates from the long-term GIA-induced rates along some parts of the Atlantic coast of North America, particularly near the Canadian provinces. They reported contemporary uplift rates derived from GPS measurements in Maine and Massachusetts that were inconsistent with GIA-induced land subsidence, which was inferred from a single global model (ICE-6G-VM5a). However, our uncertainty-inclusive approach, which integrates independent measurements capturing different temporal scales, indicates a broad compatibility between paleo and contemporary VLM rates in different subregions. Furthermore, the contemporary hydrological mass change signal in Hudson Bay is not large enough to cause a modern peripheral bulge. Our GRACE analysis, which covered the period from April 2002 to November 2023, also found no significant hydrological mass change signals originating from either natural causes or anthropogenic effects in other subregions. In addition, the residual VLM signal can be captured by the contemporary mass changes derived from GRACE, supporting the conclusion that GIA remains the dominant driver of VLM in our study region, with small contributions from hydrological processes.

Apart from the improvements and new contributions made in this study, several limitations should be considered. The important limitation is the sparse distribution of GNSS stations in our study region, particularly in Hudson Bay and the Ungava Peninsula and Labrador, which limits our analysis on the localized variations of the decadal-scale VLM rates. Based on the criteria used for selecting GNSS stations within each site (see Section 3.2.1.1), the spatial bias between GPS- and RSL-derived VLM rates is minimized, and the differences mainly originate from temporal changes. In addition, the length of the GNSS time series at some sites is relatively short, such as the single GPS station available at site #3 in Hudson Bay ("INUQ" station) with a length of ~5 years, and it may add some bias into the inferred rates and affect its reliability for temporal comparisons (e.g., with GRACE estimates derived from

measurements spanning 22 years). Moreover, the small number (or absence) of SLIPs over 4 ka BP at some sites can be another limitation in our VLM analysis. For instance, as discussed in Section 3.2.2, for the postglacial decay time analysis, which is a more reliable model in Hudson Bay, there are insufficient SLIPs over 4 ka BP at sites #1 and #3. For this reason, the VLM rates from the late-Holocene RSL reconstructions at these sites are based on fitting a linear model to SLIPs over 2 ka BP, which may introduce some bias. Another subregion in which this limitation can be important is the Ungava Peninsula and Labrador, where the VLM rate analysis relies exclusively on GNSS time series and GIA model predictions. It should be noted that GIA rates are in a reference frame with the origin at the center of mass of the solid Earth, while the reference frame for the GNSS rates has the origin at the center of mass of the total Earth system. However, the effect of the origin transformation on the GNSS VLM rates is less than ~0.2 mm/yr (Schumacher et al., 2018), and this small value can be accounted for within the uncertainty ranges.

Despite the broad compatibility between decadal-scale and millennial-scale VLM rates in our study region, a few sites require further investigation. As discussed in Section 3.3.1.1, at site #1 in western Hudson Bay, the uplift rates derived from GNSS time series and late-Holocene RSL changes are both larger (by ~5 mm/yr) than the GIA-induced VLM rate from the optimal regional model. However, the upper bound of the GIA-induced rates captures the GPS rates, showing the significance of uncertainty estimates in the VLM analysis. Similarly, as shown in Figure 3.S26, the RSL fall rate from the CHURCHILL tide gauge station, co-located with the GPS stations at this site, is larger than that from the optimal regional GIA model, although the corresponding lower bound captures the tide gauge rate. Apart from the insufficient number of SLIPs, which can affect the estimation of RSL-induced VLM rates, there are also limitations in GIA modeling, mainly associated with structural uncertainty, such as inaccuracies in the ice history models, the effects of lateral viscosity structure, and limitations in the applied physical model (Maxwell rheology) (see Chapter 2). This source of uncertainty in GIA modeling can also influence the estimation of sea-surface height changes ($\Delta G + E$; see Section 3.2.2) and serve as a source of uncertainty in VLM rates derived from late-Holocene RSL changes. In addition, the larger VLM rate derived from late-Holocene RSL changes compared to that from the GNSS time series at this site may result from significant hydrological mass changes that occurred before the GRACE period (April 2002 – November 2023).

Removing the elastic uplift signal caused by the contemporary ice mass loss associated with Greenland and Canadian Arctic glaciers from the GNSS time series may introduce another source of uncertainty, as the applied model (Riva et al., 2017) does not capture this signal after 2014 CE. This could potentially explain the higher GNSS-derived VLM rates at some sites, particularly in Hudson Bay and the Ungava Peninsula and Labrador. It should be noted that the rate of RSL change estimated from SLIPs can be impacted by an anomalous SLIP, as observed at site #13. By removing the SLIP at an age of ~3 ka BP and RSL of ~-10 m, which lies below the lower NB bound and another SLIP with a similar age (see Figure 3.S16), the RSL-induced VLM rate becomes smaller (by ~1 mm/yr). Although this rate remains lower than the VLM rates derived from GNSS time series and GIA model predictions, when considering the uncertainty bounds, the RSL-induced VLM rate aligns with the other estimates. In terms of the impact of different time frames on the estimation of late-Holocene VLM rates, we considered two time periods: (1) from 2 ka BP to the present-day and (2) from 4 ka BP to the present-day, across sites #10, #11, and #18, where there are sufficient SLIPs for both periods to enable robust regression analysis. As demonstrated in Figure 3.11, the rates of RSL changes (see the right panel), estimated from the best-fit linear model and total least squares adjustment, at all three sites for both time frames, are within a range of ±1 mm/yr difference while intersecting the 1:1 line. Furthermore, after removing the contribution of sea-surface height change ($\Delta G + E$), along with the corresponding

uncertainty—which is similar for both time frames—from the RSL rate of change, the inferred late-Holocene VLM rates (see the left panel) align with each other when considering the uncertainty bounds. Therefore, the comparable rates between both time frames confirm that most of the ice-equivalent meltwater influence on global mean sea level rise occurred before 4 ka BP, and its contribution is minimal (less than 1 meter) after 4 ka BP (e.g., Engelhart & Horton, 2012; Hallmann et al., 2018; Lambeck et al., 2014), indicating a stronger representation of regional/local processes.

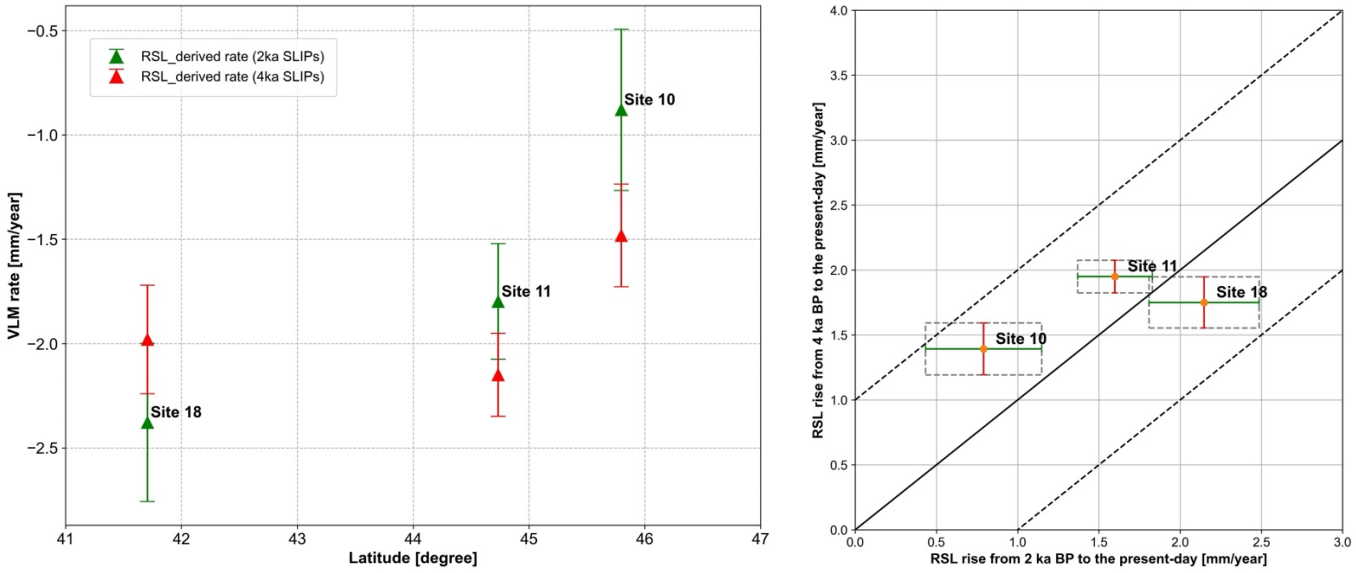


Figure 3.11. The right panel shows the comparison of RSL rise (in mm/yr) over two different time periods: (1) from 2 ka BP to the present-day (green bars) and (2) from 4 ka BP to the present-day (red bars), across sites #10, #11, and #18. The rate of RSL change for each time frame is estimated from SLIPs using the best-fit linear trend through total least squares adjustment (see the red and blue dashed lines in Figures 3.S19 and 3.S23). The solid and dashed black lines represent no change in rate and a 1 mm/yr difference, respectively. The left panel compares the late-Holocene VLM rates derived from SLIPs over the past 2 ka (green triangles) and the past 4 ka (red triangles) across three sites. To remove the influence of sea-surface height change ($\Delta G + E$ term in Equation 3.1) from the inferred RSL rates shown in the right panel, the optimal regional GIA model (GLAC1D-na1259_120p830) and its model uncertainty bounds are applied. The rates are estimated at the average location of SLIPs within each site. The error bars represent 1σ uncertainty bounds for each estimate.

In summary, the results from this study improve the understanding of VLM and its underlying causes in eastern North America, providing valuable insights for regional sea-level change projections and adaptation planning. Building on these findings, future studies should enhance the spatial and temporal resolutions of contemporary VLM measurements by expanding GNSS stations and incorporating InSAR technique, especially in subregions with sparse coverage, such as Hudson Bay, and the Ungava Peninsula and Labrador. Moreover, for these subregions, where the elastic signal from contemporary ice mass loss has a larger contribution, updating and extending the work of Riva et al. (2017) using datasets from after 2014 can provide a better constraint on the regional contemporary VLM signal. Our comprehension of VLM in the study region will be further broadened by enhancing the regional GIA models (with uncertainty bounds) through accounting for structural uncertainties in the modeling. Additionally, using high-resolution regional/local hydrological models to extend the temporal scope for constraining the contemporary hydrological mass change signal to periods before GRACE will also contribute to this advancement.

3.5. Conclusion

This study provides a comprehensive analysis of VLM in southeastern Canada and the northeastern USA, addressing both decadal-scale and millennial-scale rates. By integrating GNSS measurements, late-Holocene RSL changes, GRACE-derived contemporary mass change estimates, and regionally optimized GIA models, this research captures the temporal and spatial variability of the VLM signal across six subregions. A key contribution of this work is its uncertainty-inclusive approach, which enhances the interpretation of the VLM signal and its impacts for regional geophysical processes and sea-level change projections.

In this study, we deployed different and complementary measurements to estimate VLM rates and assess their uncertainty. Contemporary VLM rates were derived from the Nevada Geodetic Laboratory GNSS time series at 88 stations, processed using the MIDAS method, analyzed for remaining outliers and jumps based on a least squares adjustment model, and corrected for the elastic displacement signal caused by contemporary ice mass loss from Greenland and Canadian Arctic glaciers. Millennial-scale VLM rates were estimated from 348 late-Holocene SLIPs across 18 sites, selected from quality-assessed datasets and analyzed using regression models. GIA contributions to the VLM signal were constrained by regionally optimized models incorporating refined Earth structure and ice history parameters. Uncertainty bounds for the GIA model outputs were quantified using a Bayesian approach based on a sub-ensemble of the highest-probability model parameters. GRACE SHCs spanning from April 2002 to November 2023 were analyzed to estimate contemporary mass change signals, corrected for GIA using the same regionally optimized models. For the first time, the uncertainty in GRACE-derived mass change estimates was quantified by incorporating a contribution from the uncertainty in the GIA signal, based on Monte Carlo and Bayesian approaches.

The findings show that GIA is the predominant driver of VLM across all subregions and there is a broad compatibility between paleo and contemporary rates. In Hudson Bay, VLM rates inferred from late-Holocene SLIPs and GNSS time series largely align with GIA-induced rates, although localized discrepancies suggest contributions from other site-specific processes (e.g., pre-GRACE hydrological mass changes). In the Ungava Peninsula and Labrador, where SLIPs were unavailable, contemporary GNSS-derived rates closely matched GIA-predicted rates, showing the dominant contribution of the GIA signal in this subregion. In Newfoundland, the St. Lawrence Corridor, New Brunswick and Nova Scotia, and Maine and Massachusetts, VLM rates derived from GNSS time series, late-Holocene RSL reconstructions, and GIA model predictions were consistent within their uncertainty bounds, indicating minimal contributions from non-GIA processes. GRACE-derived mass change estimates also demonstrate no significant hydrological mass change signals originating from either natural causes or anthropogenic effects in our study region, supporting the conclusion that GIA remains the dominant driver of VLM, with small contributions from hydrological processes.

References

Blewitt, G., Hammond, W., & Kreemer, C. (2018). Harnessing the GPS Data Explosion for Interdisciplinary Science. *Eos*, *99*. https://doi.org/10.1029/2018EO104623

Bouin, M. N., & Wöppelmann, G. (2010). Land motion estimates from GPS at tide gauges: a geophysical evaluation. *Geophysical Journal International*, *180*(1), 193–209. https://doi.org/10.1111/j.1365-246X.2009.04411.x

Bürgmann, R., Rosen, P. A., & Fielding, E. J. (2000). Synthetic Aperture Radar Interferometry to Measure Earth's Surface Topography and Its Deformation. *Annual Review of Earth and Planetary Sciences*, *28*(1), 169–209. https://doi.org/10.1146/annurev.earth.28.1.169

Caron, L., Ivins, E. R., Larour, E., Adhikari, S., Nilsson, J., & Blewitt, G. (2018). GIA Model Statistics for GRACE Hydrology, Cryosphere, and Ocean Science. *Geophysical Research Letters*, *45*(5), 2203–2212. https://doi.org/10.1002/2017GL076644

Crowley, J. W., & Huang, J. (2020). A least-squares method for estimating the correlated error of GRACE models. *Geophysical Journal International*, *221*(3), 1736–1749. https://doi.org/10.1093/gji/ggaa104

van Dam, T., Wahr, J., & Lavallée, D. (2007). A comparison of annual vertical crustal displacements from GPS and Gravity Recovery and Climate Experiment (GRACE) over Europe. *Journal of Geophysical Research: Solid Earth*, *112*(B3). https://doi.org/10.1029/2006JB004335

Davis, J. L., & Mitrovica, J. X. (1996). Glacial isostatic adjustment and the anomalous tide gauge record of eastern North America. *Nature*, *379*(6563), 331–333. https://doi.org/10.1038/379331a0

Ding, K., Freymueller, J. T., He, P., Wang, Q., & Xu, C. (2019). Glacial Isostatic Adjustment, Intraplate Strain, and Relative Sea Level Changes in the Eastern United States. *Journal of Geophysical Research: Solid Earth*, *124*(6), 6056–6071. https://doi.org/10.1029/2018JB017060

Eicker, A., Schawohl, L., Middendorf, K., Bagge, M., Jensen, L., & Dobslaw, H. (2024). Influence of GIA Uncertainty on Climate Model Evaluation With GRACE/GRACE-FO Satellite Gravimetry Data. *Journal of Geophysical Research: Solid Earth*, *129*(5). https://doi.org/10.1029/2023JB027769

Engelhart, S., Horton, B., & Kemp, A. (2011). HOLOCENE SEA-LEVEL CHANGES ALONG THE UNITED STATES' ATLANTIC COAST. *Oceanography*, *24*(2), 70–79. https://doi.org/10.5670/oceanog.2011.28

Engelhart, S. E., Horton, B. P., Douglas, B. C., Peltier, W. R., & Tornqvist, T. E. (2009). Spatial variability of late Holocene and 20th century sea-level rise along the Atlantic coast of the United States. *Geology*, *37*(12), 1115–1118. https://doi.org/10.1130/G30360A.1

Engelhart, Simon E., & Horton, B. P. (2012). Holocene sea level database for the Atlantic coast of the United States. *Quaternary Science Reviews*, *54*, 12–25. https://doi.org/10.1016/j.quascirev.2011.09.013

Fang, J., He, M., Luan, W., & Jiao, J. (2021). Crustal vertical deformation of Amazon Basin derived from GPS and GRACE/GFO data over past two decades. *Geodesy and Geodynamics*, *12*(6), 441–450. https://doi.org/10.1016/j.geog.2021.09.002

Farrell, W. E. (1972). Deformation of the Earth by surface loads. *Reviews of Geophysics*, *10*(3), 761–797. https://doi.org/10.1029/RG010i003p00761

Frederikse, T., Landerer, F. W., & Caron, L. (2019a). The imprints of contemporary mass redistribution on local sea level and vertical land motion observations. *Solid Earth*, *10*(6), 1971–1987. https://doi.org/10.5194/se-10-1971-2019

Frederikse, T., Landerer, F. W., & Caron, L. (2019b). The imprints of contemporary mass redistribution on local sea level and vertical land motion observations. *Solid Earth*, *10*(6), 1971–1987. https://doi.org/10.5194/se-10-1971-2019

Gregory, J. M., Griffies, S. M., Hughes, C. W., Lowe, J. A., Church, J. A., Fukimori, I., et al. (2019). Concepts and Terminology for Sea Level: Mean, Variability and Change, Both Local and Global. *Surveys in Geophysics*, *40*(6), 1251–1289. https://doi.org/10.1007/s10712-019-09525-z

Hallmann, N., Camoin, G., Eisenhauer, A., Botella, A., Milne, G. A., Vella, C., et al. (2018). Ice volume and climate changes from a 6000 year sea-level record in French Polynesia. *Nature Communications*, *9*(1), 285. https://doi.org/10.1038/s41467-017-02695-7

Huang, S. A., Sauber, J. M., & Ray, R. (2022). Mapping Vertical Land Motion in Challenging Terrain: Six-Year Trends on Tutuila Island, American Samoa, With PS-InSAR, GPS, Tide Gauge, and Satellite Altimetry Data. *Geophysical Research Letters*, *49*(23). https://doi.org/10.1029/2022GL101363

Karegar, M. A., Dixon, T. H., & Engelhart, S. E. (2016). Subsidence along the Atlantic Coast of North America: Insights from GPS and late Holocene relative sea level data. *Geophysical Research Letters*, *43*(7), 3126–3133. https://doi.org/10.1002/2016GL068015

Karegar, M. A., Dixon, T. H., Malservisi, R., Kusche, J., & Engelhart, S. E. (2017). Nuisance Flooding and Relative Sea-Level Rise: the Importance of Present-Day Land Motion. *Scientific Reports*, *7*(1), 11197. https://doi.org/10.1038/s41598-017-11544-y

Kemp, A. C., Horton, B. P., Donnelly, J. P., Mann, M. E., Vermeer, M., & Rahmstorf, S. (2011). Climate related sea-level variations over the past two millennia. *Proceedings of the National Academy of Sciences*, *108*(27), 11017–11022. https://doi.org/10.1073/pnas.1015619108

Kusche, J., & Schrama, E. J. O. (2005). Surface mass redistribution inversion from global GPS deformation and Gravity Recovery and Climate Experiment (GRACE) gravity data. *Journal of Geophysical Research: Solid Earth*, *110*(B9). https://doi.org/10.1029/2004JB003556

Lambeck, K., Rouby, H., Purcell, A., Sun, Y., & Sambridge, M. (2014). Sea level and global ice volumes from the Last Glacial Maximum to the Holocene. *Proceedings of the National Academy of Sciences*, *111*(43), 15296–15303. https://doi.org/10.1073/pnas.1411762111

Li, S., Shen, W., Pan, Y., & Zhang, T. (2020). Surface seasonal mass changes and vertical crustal deformation in North China from GPS and GRACE measurements. *Geodesy and Geodynamics*, *11*(1), 46–55. https://doi.org/10.1016/j.geog.2019.05.002

Li, T., Wu, P., Wang, H., Steffen, H., Khan, N. S., Engelhart, S. E., et al. (2020). Uncertainties of Glacial Isostatic Adjustment Model Predictions in North America Associated With 3D Structure. *Geophysical Research Letters*, *47*(10). https://doi.org/10.1029/2020GL087944

Love, R., Milne, G. A., Tarasov, L., Engelhart, S. E., Hijma, M. P., Latychev, K., et al. (2016). The contribution of glacial isostatic adjustment to projections of sea-level change along the Atlantic and Gulf coasts of North America. *Earth's Future*, *4*(10), 440–464. https://doi.org/10.1002/2016EF000363

Mitrovica, J. X., & Peltier, W. R. (1991). On postglacial geoid subsidence over the equatorial oceans. *Journal of Geophysical Research: Solid Earth*, *96*(B12), 20053–20071. https://doi.org/10.1029/91JB01284

Mitrovica, J. X., & Peltier, W. R. (1995). Constraints on mantle viscosity based upon the inversion of post-glacial uplift data from the Hudson Bay region. *Geophysical Journal International*, *122*(2), 353–377. https://doi.org/10.1111/j.1365-246X.1995.tb07002.x

Mitrovica, J. X., Forte, A. M., & Simons, M. (2000). A reappraisal of postglacial decay times from Richmond Gulf and James Bay, Canada. *Geophysical Journal International*, *142*(3), 783–800. https://doi.org/10.1046/j.1365-246x.2000.00199.x

Mitrovica, Jerry X., & Milne, G. A. (2003). On post-glacial sea level: I. General theory. *Geophysical Journal International*, *154*(2), 253–267. https://doi.org/10.1046/j.1365-246X.2003.01942.x

Mitrovica, J.X., & Milne, G. A. (2002). On the origin of late Holocene sea-level highstands within equatorial ocean basins. *Quaternary Science Reviews*, *21*(20–22), 2179–2190. https://doi.org/10.1016/S0277-3791(02)00080-X

Pan, Y., Jiang, W., Ding, H., Shum, C. K., Jiao, J., Xiao, Y., & Wu, Q. (2023). Interannual variability of vertical land motion over High Mountain Central Asia from GPS and GRACE/GRACE-FO observations. *GPS Solutions*, *27*(4), 168. https://doi.org/10.1007/s10291-023-01511-8

Parang, S., Milne, G. A., Tarasov, L., Love, R., Yousefi, M., & Vacchi, M. (2024). Constraining models of glacial isostatic adjustment in eastern North America. *Quaternary Science Reviews*, *334*, 108708. https://doi.org/10.1016/j.quascirev.2024.108708

Peltier, W. R. (1998). Postglacial variations in the level of the sea: Implications for climate dynamics and solid-Earth geophysics. *Reviews of Geophysics*, *36*(4), 603–689. https://doi.org/10.1029/98RG02638

Riva, R. E. M., Frederikse, T., King, M. A., Marzeion, B., & van den Broeke, M. R. (2017). Brief communication: The global signature of post-1900 land ice wastage on vertical land motion. *The Cryosphere*, *11*(3), 1327–1332. https://doi.org/10.5194/tc-11-1327-2017

Santamaría-Gómez, A., Gravelle, M., Collilieux, X., Guichard, M., Míguez, B. M., Tiphaneau, P., & Wöppelmann, G. (2012). Mitigating the effects of vertical land motion in tide gauge records using a state-of-the-art GPS velocity field. *Global and Planetary Change*, *98–99*, 6–17. https://doi.org/10.1016/j.gloplacha.2012.07.007

Santamaría-Gómez, Alvaro, Gravelle, M., Dangendorf, S., Marcos, M., Spada, G., & Wöppelmann, G. (2017). Uncertainty of the 20th century sea-level rise due to vertical land motion errors. *Earth and Planetary Science Letters*, *473*, 24–32. https://doi.org/10.1016/j.epsl.2017.05.038

Schumacher, M., King, M. A., Rougier, J., Sha, Z., Khan, S. A., & Bamber, J. L. (2018). A new global GPS data set for testing and improving modelled GIA uplift rates. *Geophysical Journal International*, *214*(3), 2164–2176. https://doi.org/10.1093/gji/ggy235

Sella, G. F., Stein, S., Dixon, T. H., Craymer, M., James, T. S., Mazzotti, S., & Dokka, R. K. (2007). Observation of glacial isostatic adjustment in "stable" North America with GPS. *Geophysical Research Letters*, *34*(2). https://doi.org/10.1029/2006GL027081

Shennan, I., & Horton, B. (2002). Holocene land- and sea-level changes in Great Britain. *Journal of Quaternary Science*, *17*(5–6), 511–526. https://doi.org/10.1002/jqs.710

Shirzaei, M., Freymueller, J., Törnqvist, T. E., Galloway, D. L., Dura, T., & Minderhoud, P. S. J. (2020). Measuring, modelling and projecting coastal land subsidence. *Nature Reviews Earth & Environment*, *2*(1), 40–58. https://doi.org/10.1038/s43017-020-00115-x

Tarasov, L., Dyke, A. S., Neal, R. M., & Peltier, W. R. (2012). A data-calibrated distribution of deglacial chronologies for the North American ice complex from glaciological modeling. *Earth and Planetary Science Letters*, *315–316*, 30–40. https://doi.org/10.1016/j.epsl.2011.09.010

Vacchi, M., Engelhart, S. E., Nikitina, D., Ashe, E. L., Peltier, W. R., Roy, K., et al. (2018). Postglacial relative sea-level histories along the eastern Canadian coastline. *Quaternary Science Reviews*, *201*, 124–146. https://doi.org/10.1016/j.quascirev.2018.09.043

Wahr, J., Molenaar, M., & Bryan, F. (1998). Time variability of the Earth's gravity field: Hydrological and oceanic effects and their possible detection using GRACE. *Journal of Geophysical Research: Solid Earth*, *103*(B12), 30205–30229. https://doi.org/10.1029/98JB02844

van der Wal, W., Braun, A., Wu, P., & Sideris, M. G. (2009). Prediction of decadal slope changes in Canada by glacial isostatic adjustment modellingThis article is one of a series of papers published in this Special Issue on the theme *GEODESY* . *Canadian Journal of Earth Sciences*, *46*(8), 587–595. https://doi.org/10.1139/E09-044

Walcott, R. I. (1980). Rheological models and observational data of glacial isostatic rebound. *N.-A. Mörner (Ed.), Earth Rheology, Isostasy, and Eustasy, Wiley*, 3–10.

Wang, C.-Y., Lin, Y. N., Hwang, C., & Shum, C. K. (2024). Observing glacial isostatic adjustment by PSInSAR in southern Hudson Bay. *Remote Sensing of Environment*, *304*, 114023. https://doi.org/10.1016/j.rse.2024.114023

Wang, H., Xiang, L., Jia, L., Jiang, L., Wang, Z., Hu, B., & Gao, P. (2012). Load Love numbers and Green's functions for elastic Earth models PREM, iasp91, ak135, and modified models with refined crustal structure from Crust 2.0. *Computers & Geosciences*, *49*, 190–199. https://doi.org/10.1016/j.cageo.2012.06.022

Wdowinski, S., Bock, Y., Zhang, J., Fang, P., & Genrich, J. (1997). Southern California permanent GPS geodetic array: Spatial filtering of daily positions for estimating coseismic and postseismic displacements induced by the 1992 Landers earthquake. *Journal of Geophysical Research: Solid Earth*, *102*(B8), 18057–18070. https://doi.org/10.1029/97JB01378

Wieczorek, M. A., & Simons, F. J. (2007). Minimum-Variance Multitaper Spectral Estimation on the Sphere. *Journal of Fourier Analysis and Applications*, *13*(6), 665–692. https://doi.org/10.1007/s00041-006-6904-1

Williams, K., Stamps, D. S., Melini, D., & Spada, G. (2024). Vertical Displacements and Sea-Level Changes in Eastern North America Driven by Glacial Isostatic Adjustment: An Ensemble Modeling Approach. *Journal of Geophysical Research: Solid Earth*, *129*(10). https://doi.org/10.1029/2023JB028250

Woodworth, P. L., Melet, A., Marcos, M., Ray, R. D., Wöppelmann, G., Sasaki, Y. N., et al. (2019). Forcing Factors Affecting Sea Level Changes at the Coast. *Surveys in Geophysics*, *40*(6), 1351–1397. https://doi.org/10.1007/s10712-019-09531-1

Yousefi, M., Milne, G., Li, S., Wang, K., & Bartholet, A. (2020). Constraining Interseismic Deformation of the Cascadia Subduction Zone: New Insights From Estimates of Vertical Land Motion Over Different Timescales. *Journal of Geophysical Research: Solid Earth*, *125*(3). https://doi.org/10.1029/2019JB018248

Supplementary figures of Chapter 3

Contents of this section

Figures 3.S1 to 3.S26. This supplemental section contains additional figures that complement material in the main text. All of the figures below are referred to in the main text. See captions for further details.

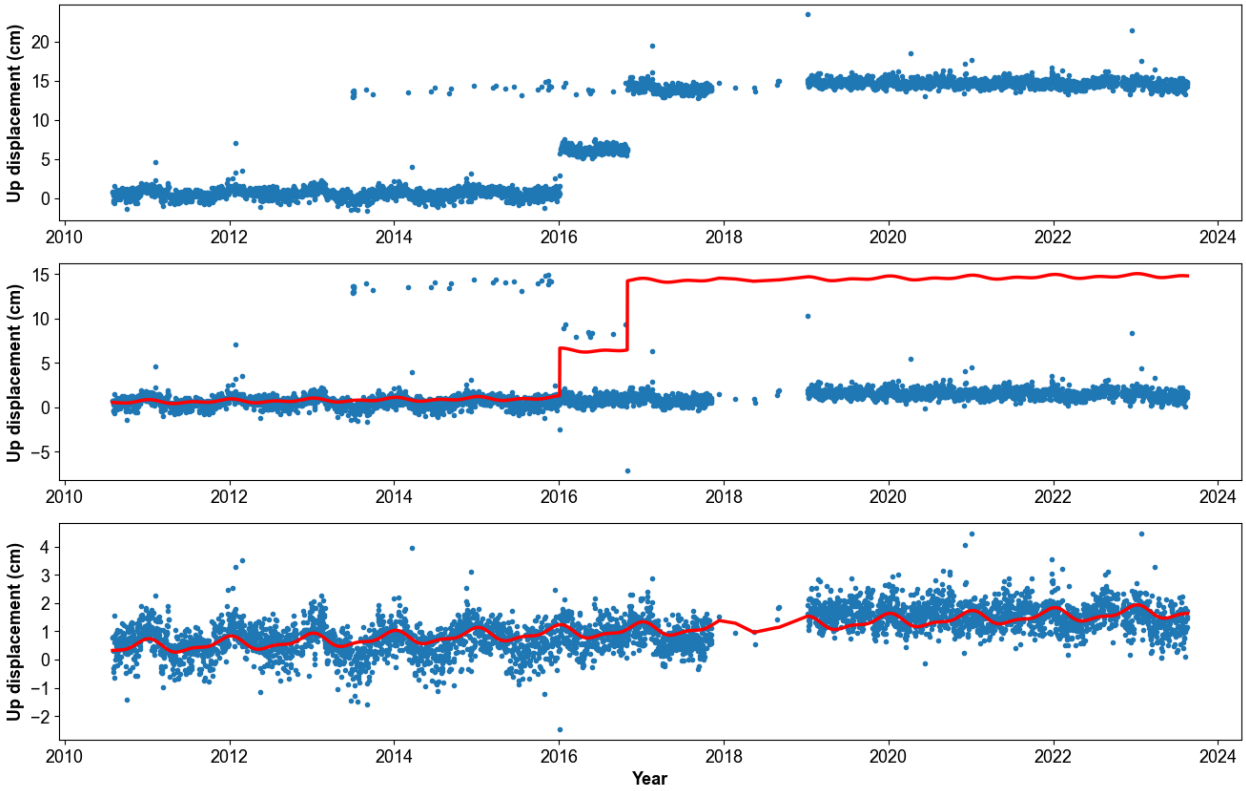


Figure 3.S1. Re-analyzed VLM rate at the "MEGO" GPS station located in the Maine and Massachusetts subregion. The NGL GNSS vertical displacement time series is corrected for outliers and jumps based on a least squares adjustment model. Top panel shows the original GNSS time series. Middle panel displays the offset-corrected time series based on the least squares adjustment model. Bottom panel shows the cleaned time series after removing 43 outliers (inferred VLM rate of 1 mm/yr).

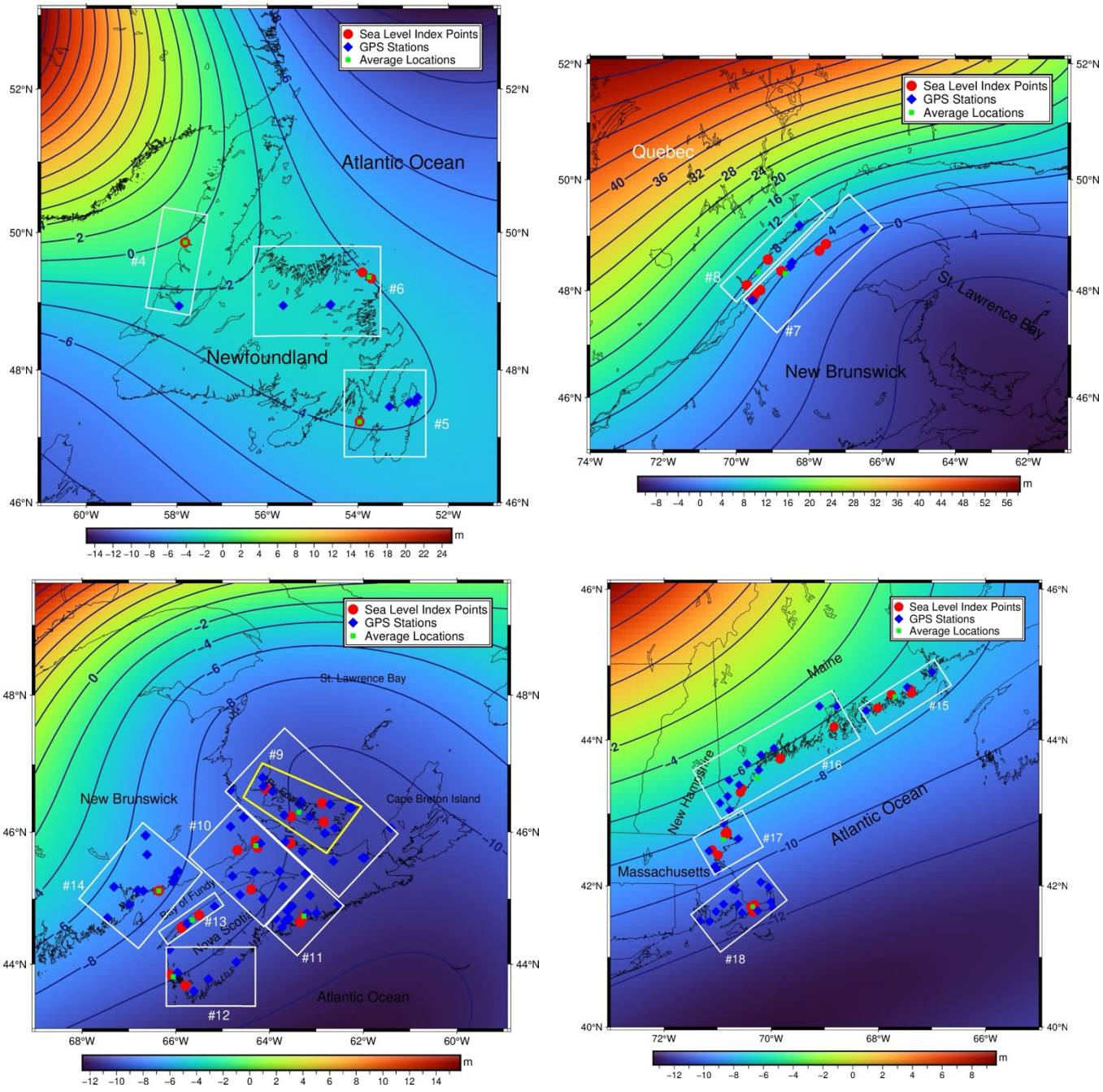


Figure 3.S2. RSL contour maps inferred from the optimal regional GIA model (GLAC1D-na1259_120p830) at 4 ka BP for four subregions in the study region: Newfoundland (top left), the St. Lawrence Corridor (top right), New Brunswick and Nova Scotia (bottom left), and Maine and Massachusetts (bottom right). Red circles represent the spatial distribution of SLIPs dating from 4 ka BP to the present day. Blue diamonds indicate GPS stations co-located with SLIPs at each site. Green squares mark the average locations (average latitude and longitude) calculated from all SLIPs within each site. For sites located within two subregions (New Brunswick and Nova Scotia, and Maine and Massachusetts), where multiple GPS stations are available, GPS stations are selected based on their proximity to the average positions of the SLIPs, taking into account the spatial variability of the RSL signal. The yellow polygon inside site #9 highlights the selected GPS stations.

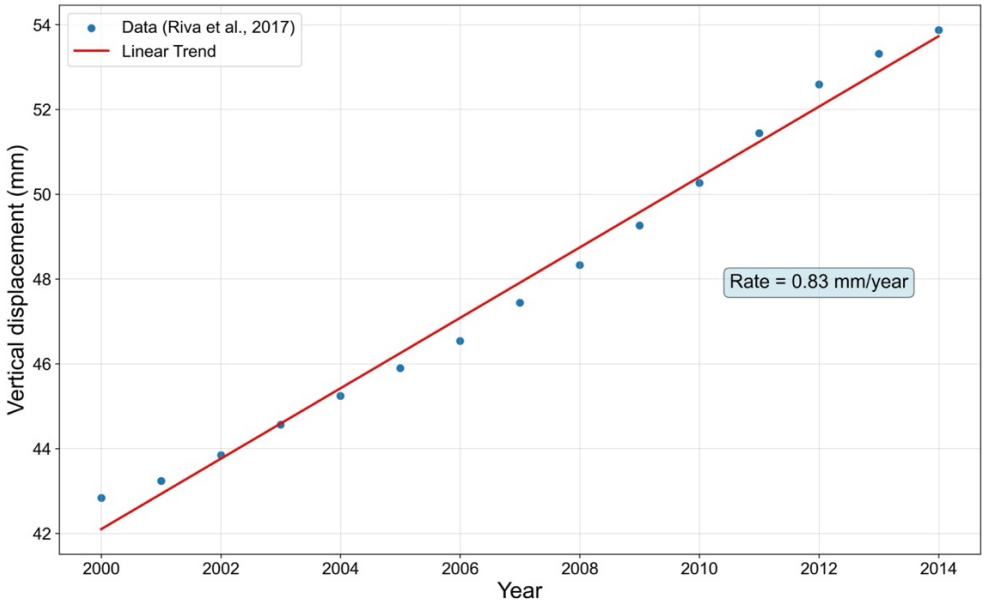


Figure 3.S3. Modelled vertical displacement at the GPS station "KUUJ" in eastern Hudson Bay (located at site #2). The rate is estimated by fitting a linear trend through the vertical displacement time series (2000 – 2014) using ordinary least squares adjustment.

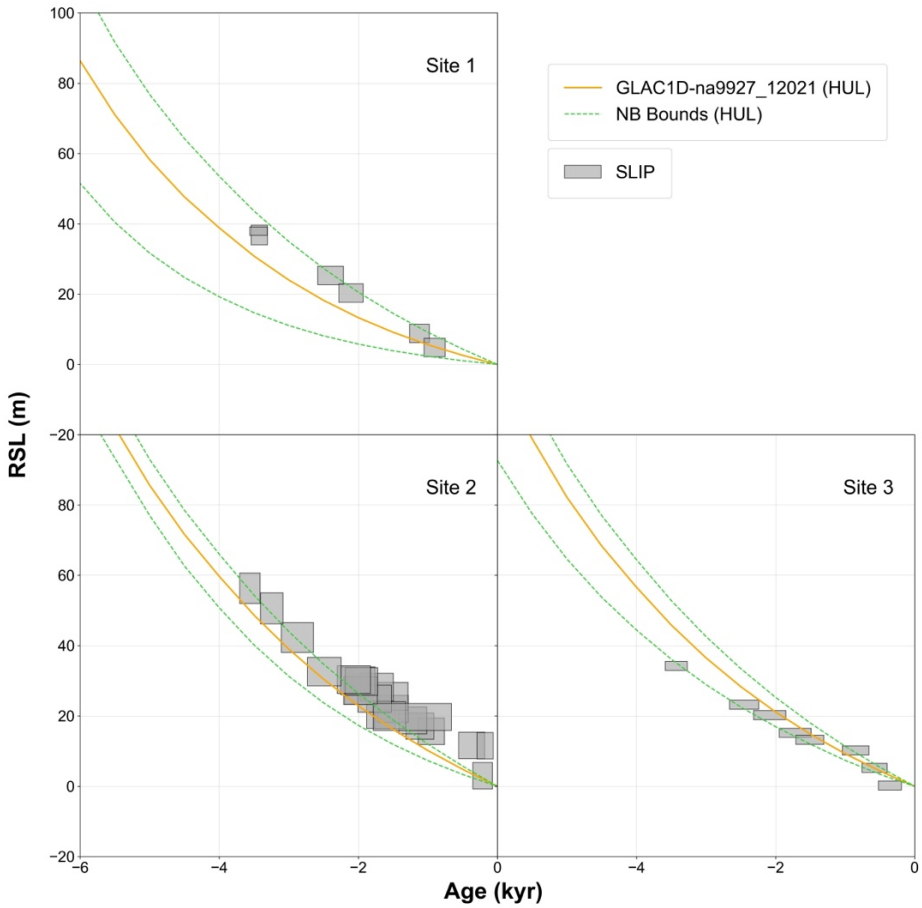


Figure 3.S4. RSL curves for three sites in Hudson Bay, derived from the optimal regional GIA model (GLAC1D-na9927_12021; orange lines) with uncertainty bounds (green dashed lines) from a Bayesian (so-called Nominal Bayesian or NB) approach using a sub-ensemble of the highest-probability GIA models.

Shaded gray boxes represent SLIPs over 4 ka BP. The curves illustrate the RSL evolution at the average locations (green squares in Figure 3.2) over the past 6,000 years (kyr) for sites #1 – #3. The close alignment between the SLIPs and the model predictions indicates that the GIA model effectively captures the regional RSL changes. The uncertainty bounds provide a range of possible trajectories, with most scenarios supporting a consistent declining trend, highlighting the model's reliability in reconstructing past sea level variations in this region.

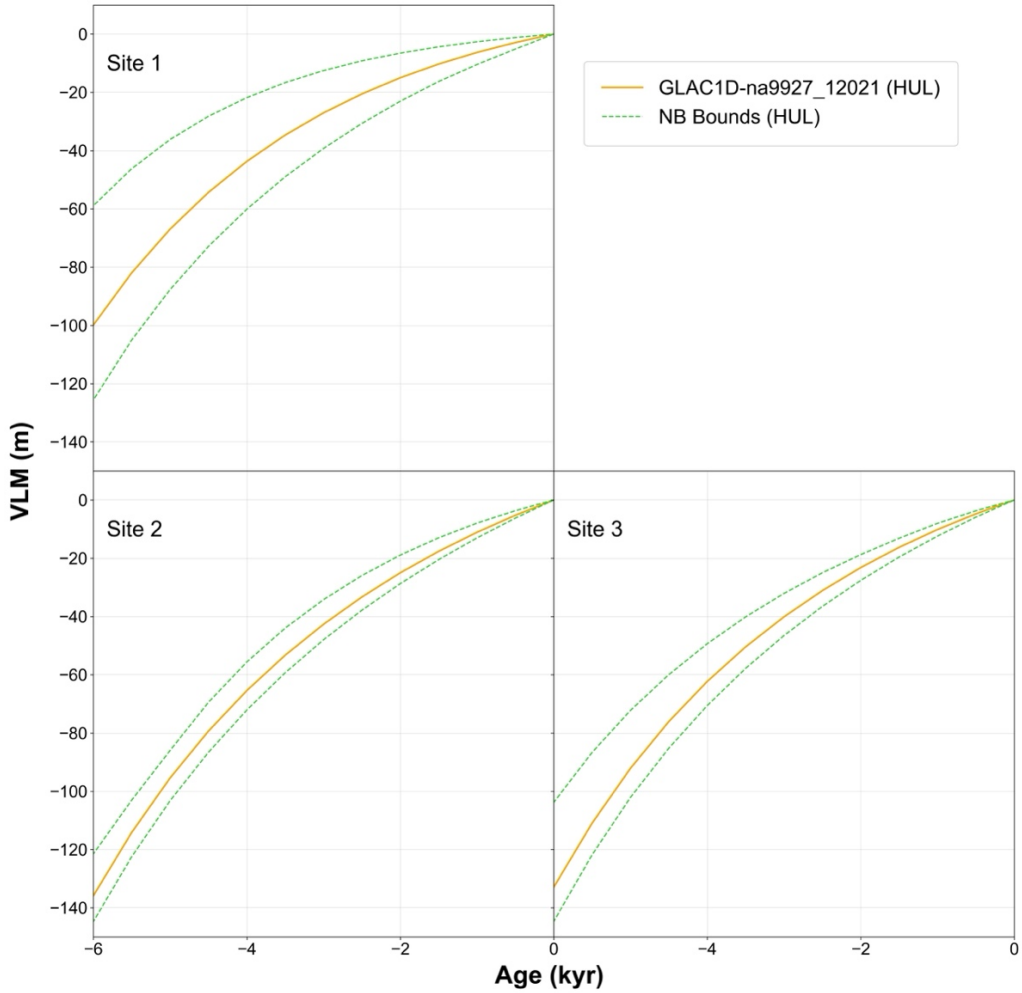


Figure 3.S5. VLM curves for three sites in Hudson Bay, derived from the optimal regional GIA model (GLAC1D-na9927_12021; orange lines) with uncertainty bounds (green dashed lines) from a Bayesian (so-called Nominal Bayesian or NB) approach using a sub-ensemble of the highest-probability GIA models. The curves illustrate the VLM evolution at the average locations (green squares in Figure 3.2) over the past 6,000 years (kyr) for sites #1 – #3. The model results show a consistent trend of land uplift, reflecting the long-term response to glacial unloading. The close agreement between the model predictions and the uncertainty bounds underscores the robustness of the GIA model in reconstructing VLM in this region.

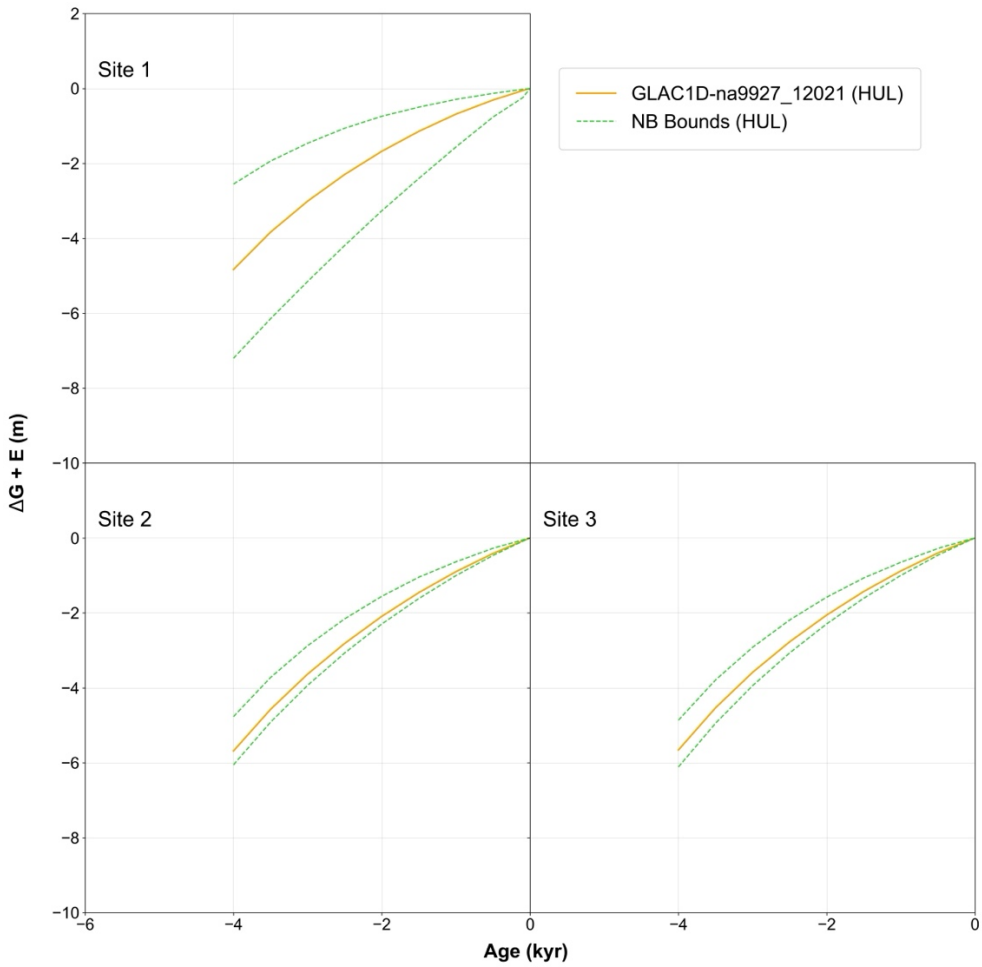


Figure 3.S6. $\Delta G + E$ curves for three sites in Hudson Bay, derived from both RSL and VLM curves presented in Figures 3.S4 and 3.S5 using Equation 3.1. The $\Delta G + E$ term is inferred from the optimal regional GIA model (GLAC1D-na9927_12021; orange lines), with uncertainty bounds (green dashed lines) determined using a Bayesian (so-called Nominal Bayesian or NB) approach with a sub-ensemble of the highest-probability GIA models. The curves illustrate the combined spatially varying geoid-height change (ΔG) and spatially uniform height shift (E) over the past 4,000 years (kyr) at the average locations (green squares in Figure 3.2) for sites #1 – #3. The close agreement between the model outputs and the uncertainty bounds underscores the robustness of the GIA model in estimating these combined geophysical effects in this region.

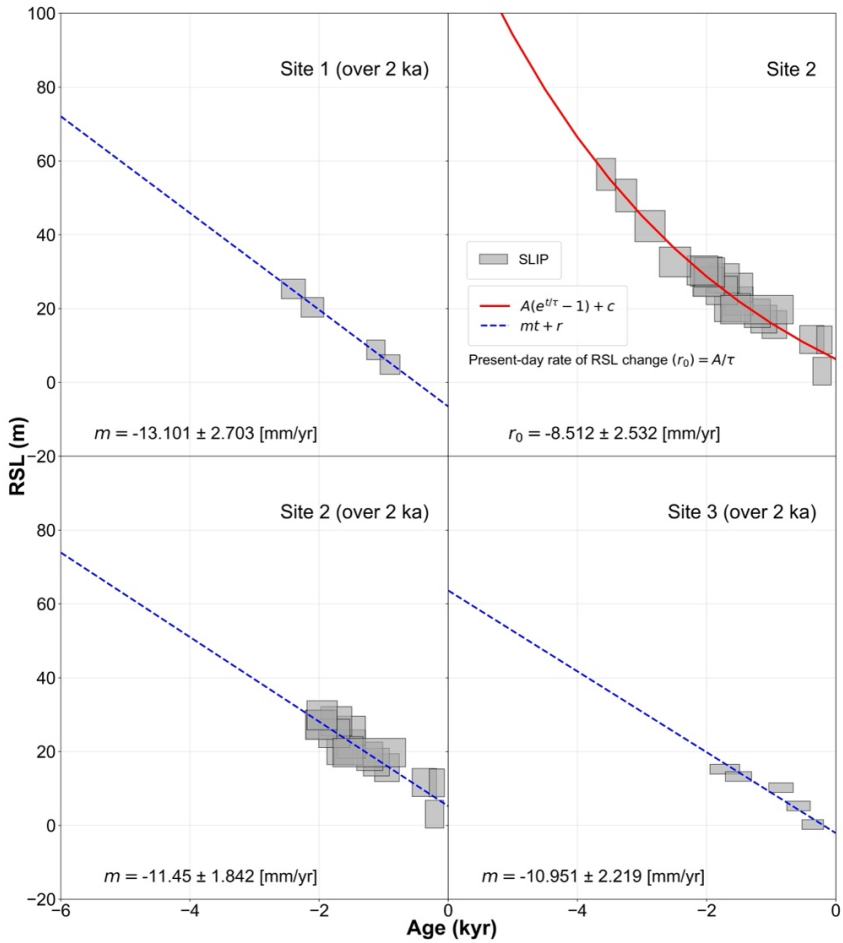


Figure 3.S7. RSL curves for sites #1 – #3 in Hudson Bay, illustrating the fit of two models: a postglacial decay model and a linear trend. The top-right panel (for site #2) shows the RSL curve fitted with an exponential decay model (red line; see Equation 3.2), where the present-day rate of RSL change (r_0) is given by A/τ. The other panels show linear regression fits ($m \times t + r$; blue dashed lines) for the last 2,000 years for sites #1 – #3, with slopes (m) representing the average RSL rate of change. The shaded gray boxes denote SLIPs, which provide observational constraints. The calculated rates and uncertainties highlight the temporal changes in RSL and the consistency of these trends across both models and three sites.

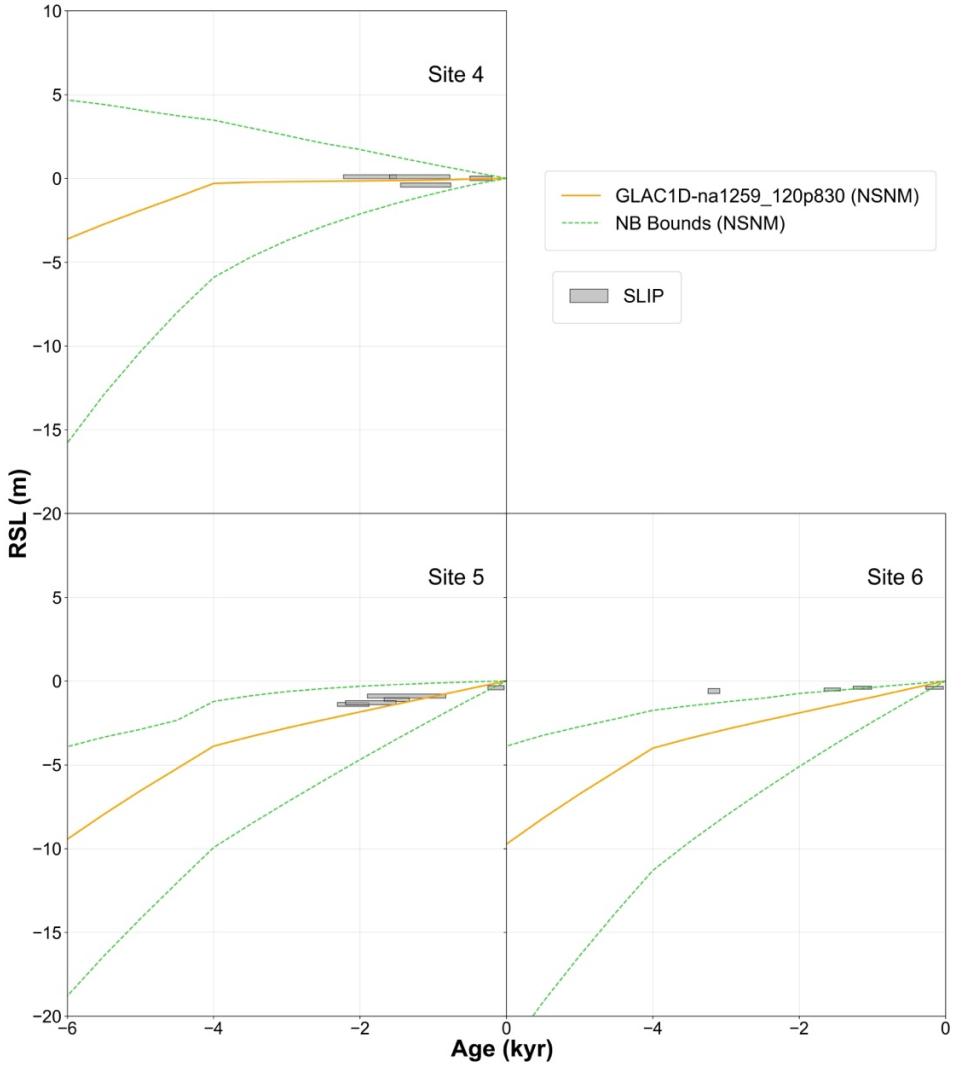


Figure 3.S8. RSL curves for three sites in Newfoundland, derived from the optimal regional GIA model (GLAC1D-na1259_120p830; orange lines) with uncertainty bounds (green dashed lines) from a Bayesian (so-called Nominal Bayesian or NB) approach using a sub-ensemble of the highest-probability GIA models. Shaded gray boxes represent SLIPs over 4 ka BP. The curves illustrate the RSL evolution at the average locations (green squares in Figure 3.4) over the past 6,000 years (kyr) for sites #4, #5, and #6. The close alignment between the SLIPs and the model predictions indicates that the GIA model effectively captures the regional RSL changes.

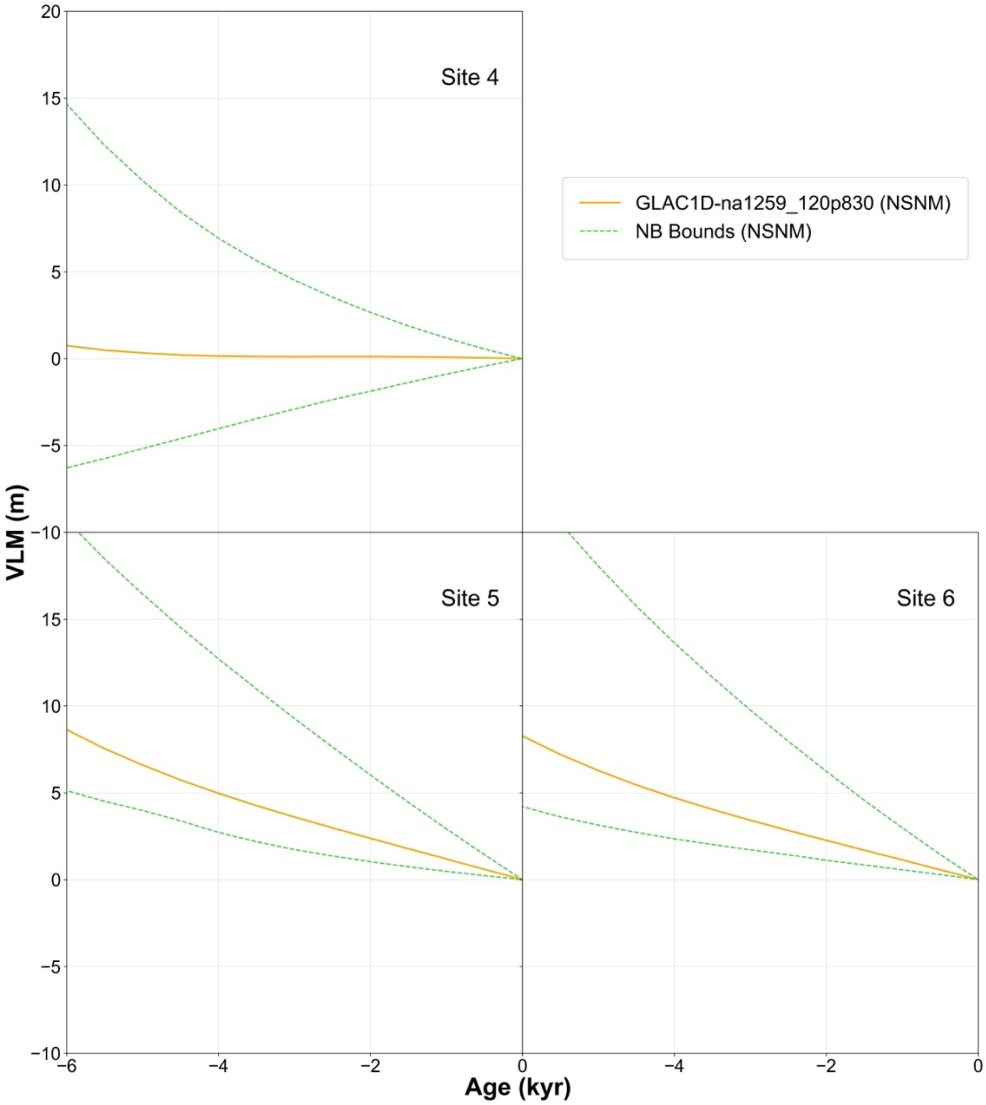


Figure 3.S9. VLM curves for three sites in Newfoundland, derived from the optimal regional GIA model (GLAC1D-na1259_120p830; orange lines) with uncertainty bounds (green dashed lines) from a Bayesian (so-called Nominal Bayesian or NB) approach using a sub-ensemble of the highest-probability GIA models. The curves illustrate the VLM evolution at the average locations (green squares in Figure 3.4) over the past 6,000 years (kyr) for sites #4, #5, and #6.

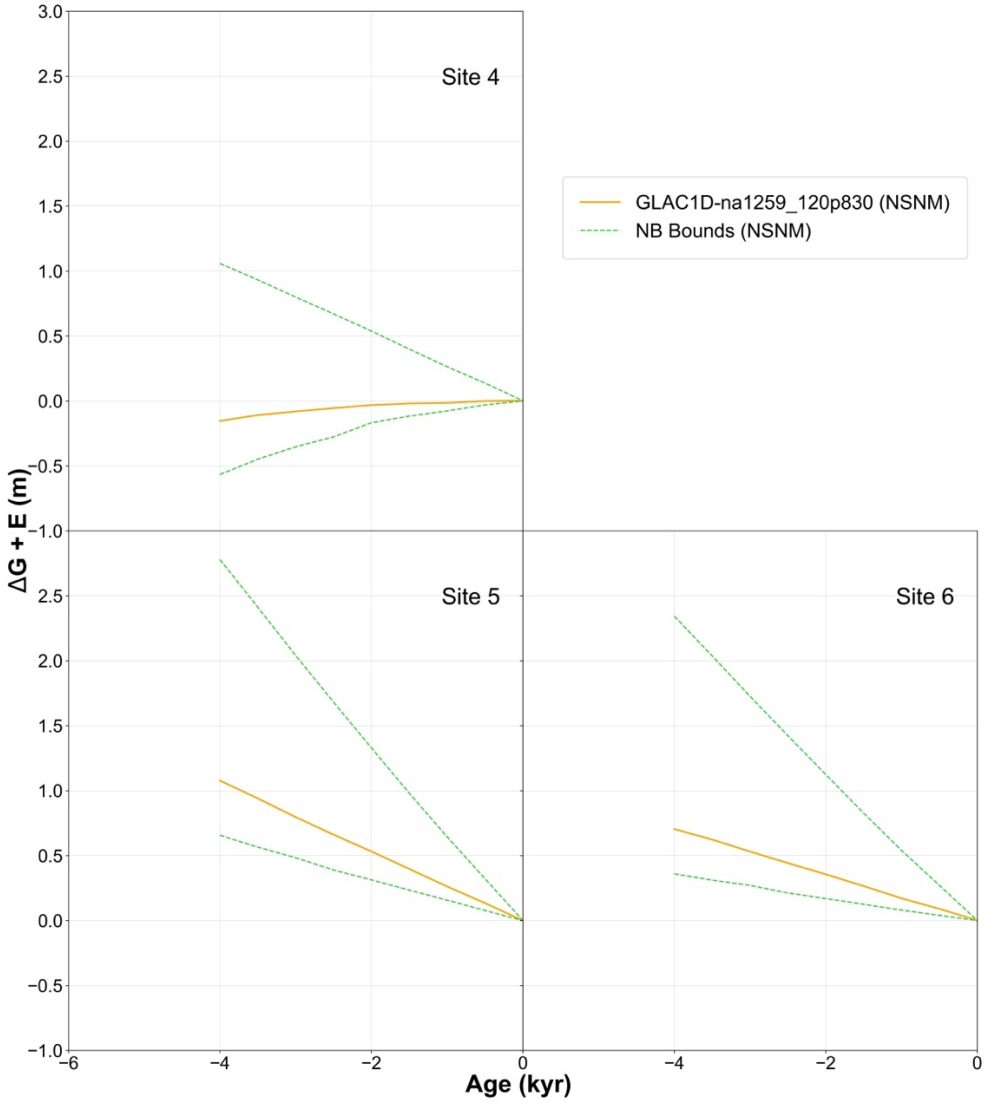


Figure 3.S10. $\Delta G + E$ curves for three sites in Newfoundland, derived from both RSL and VLM curves presented in Figures 3.S8 and 3.S9 using Equation 3.1. The $\Delta G + E$ term is inferred from the optimal regional GIA model (GLAC1D-na1259_120p830; orange lines), with uncertainty bounds (green dashed lines) determined using a Bayesian (so-called Nominal Bayesian or NB) approach with a sub-ensemble of the highest-probability GIA models. The curves illustrate the combined spatially varying geoid-height change (ΔG) and spatially uniform height shift (E) over the past 4,000 years (kyr) at the average locations (green squares in Figure 3.4) for sites #4, #5, and #6.

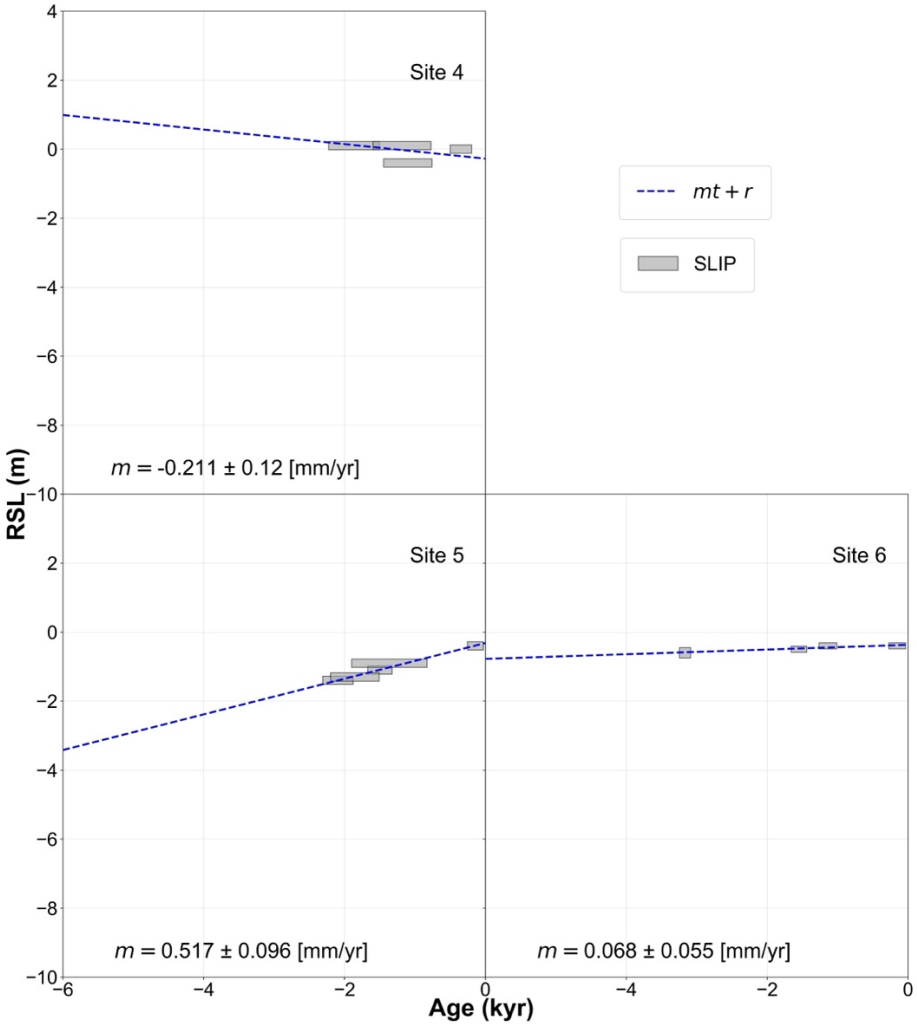


Figure 3.S11. RSL curves for sites #4, #5, and #6 in Newfoundland, illustrating the best-fit linear trends obtained by total least squares adjustment (orthogonal distance regression). The panels show linear regression fits ($m \times t + r$; blue dashed lines) for the last 4,000 years, with slopes (m) representing the average RSL rate of change. The shaded gray boxes denote SLIPs, which provide observational constraints. The resulting slope estimates indicate varying rates of RSL changes: an RSL fall in site #4, an RSL rise in site #5, and a relatively stable RSL in site #6 with a minor RSL rise.

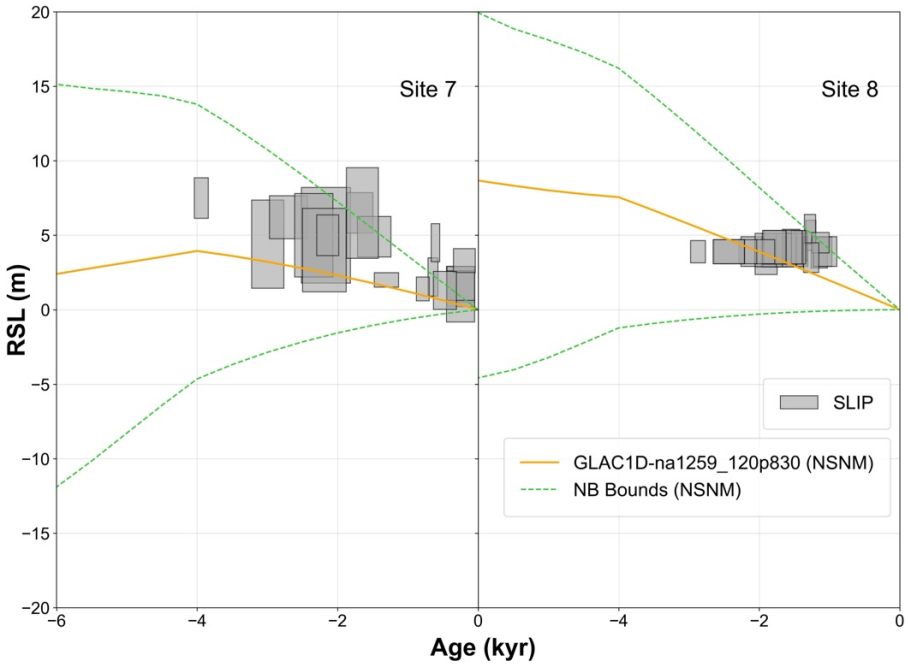


Figure 3.S12. RSL curves for two sites in St. Lawrence Corridor, derived from the optimal regional GIA model (GLAC1D-na1259_120p830; orange lines) with uncertainty bounds (green dashed lines) from a Bayesian (so-called Nominal Bayesian or NB) approach using a sub-ensemble of the highest-probability GIA models. Shaded gray boxes represent SLIPs over 4 ka BP. The curves illustrate the RSL evolution at the average locations (green squares in Figure 3.5) over the past 6,000 years (kyr) for sites #7 and #8. The close alignment between the SLIPs and the model predictions indicates that the GIA model effectively captures the regional RSL changes.

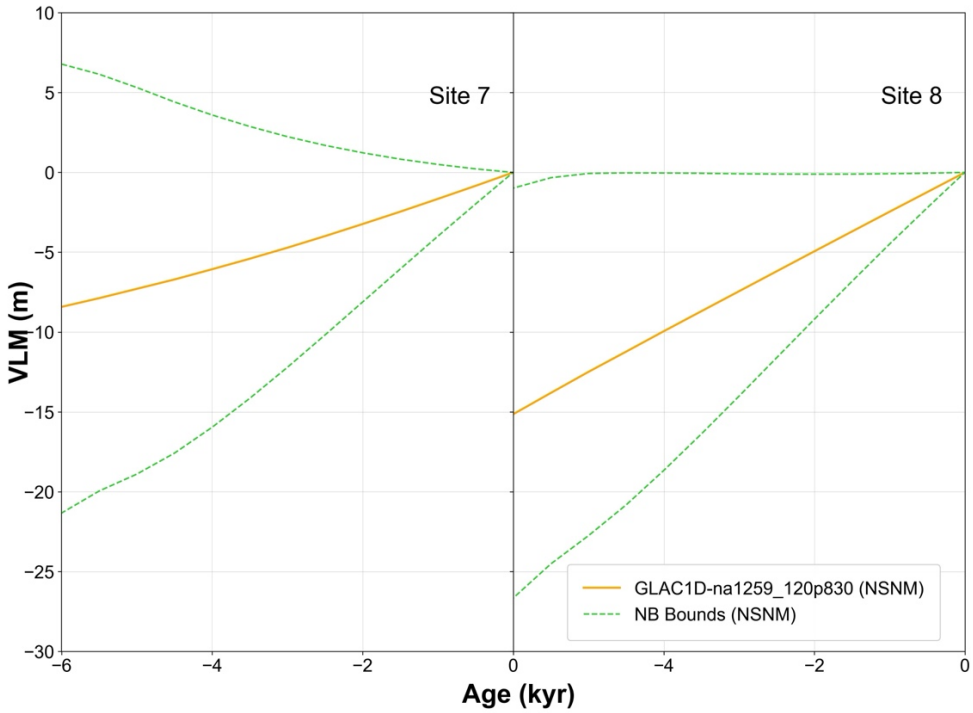


Figure 3.S13. VLM curves for two sites in St. Lawrence Corridor, derived from the optimal regional GIA model (GLAC1D-na1259_120p830; orange lines) with uncertainty bounds (green dashed lines) from a Bayesian (so-called Nominal Bayesian or NB) approach using a sub-ensemble of the highest-probability GIA models. The curves illustrate the VLM evolution at the average locations (green squares in Figure 3.5) over the past 6,000 years (kyr) for sites #7 and #8.

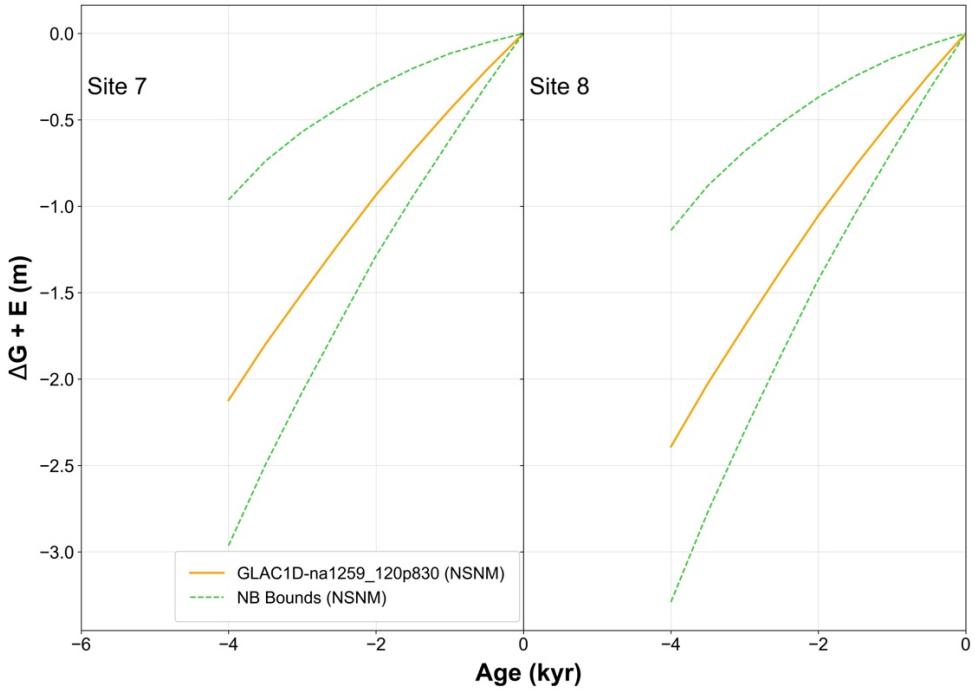


Figure 3.S14. $\Delta G + E$ curves for two sites in St. Lawrence Corridor, derived from both RSL and VLM curves presented in Figures 3.S12 and 3.S13 using Equation 3.1. The $\Delta G + E$ term is inferred from the optimal regional GIA model (GLAC1D-na1259_120p830; orange lines), with uncertainty bounds (green dashed lines) determined using a Bayesian (so-called Nominal Bayesian or NB) approach with a sub-ensemble of the highest-probability GIA models. The curves illustrate the combined spatially varying geoid-height change (ΔG) and spatially uniform height shift (E) over the past 4,000 years (kyr) at the average locations (green squares in Figure 3.5) for sites #7 and #8.

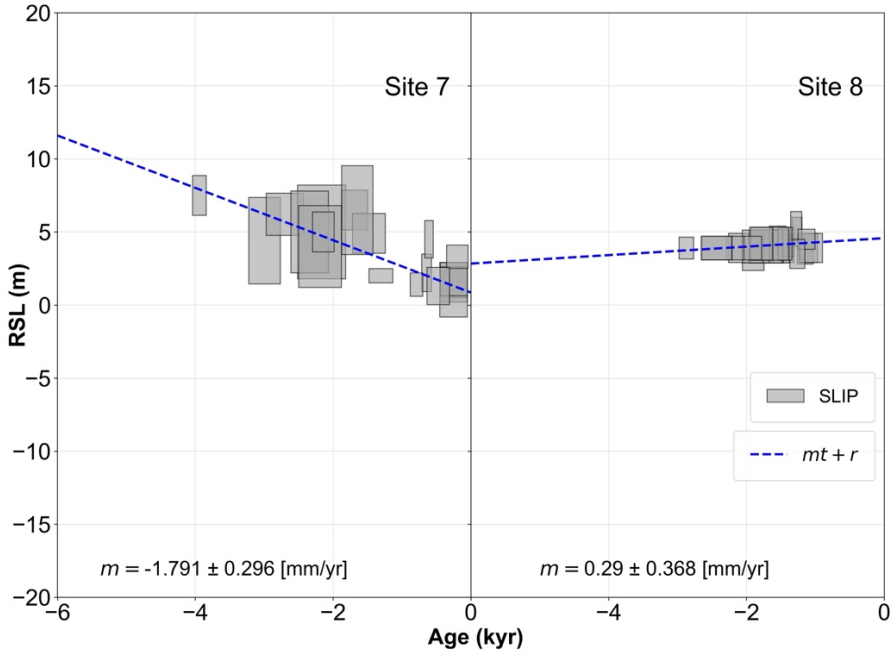


Figure 3.S15. RSL curves for sites #7 and #8 in St. Lawrence Corridor, illustrating the best-fit linear trends obtained by total least squares adjustment (orthogonal distance regression). The panels show linear regression fits ($m \times t + r$; blue dashed lines) for the last 4,000 years, with slopes (m) representing the average RSL rate of change. The shaded gray boxes denote SLIPs, which provide observational constraints. The resulting slope estimates indicate varying rates of RSL changes: an RSL fall in site #7 and a minor RSL rise in site #8.

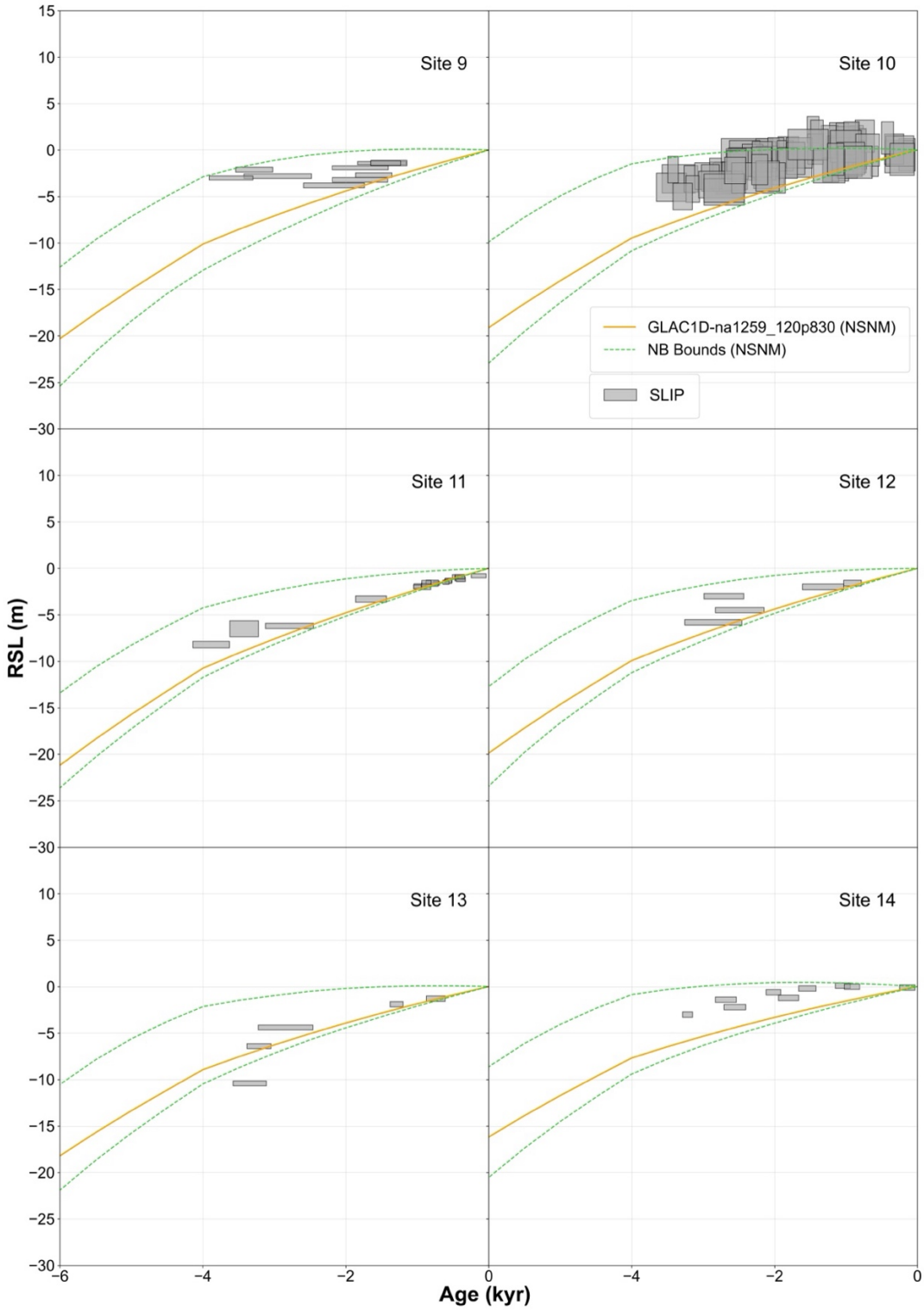


Figure 3.S16. RSL curves for six sites in New Brunswick and Nova Scotia, derived from the optimal regional GIA model (GLAC1D-na1259_120p830; orange lines) with uncertainty bounds (green dashed lines) from a Bayesian (so-called Nominal Bayesian or NB) approach using a sub-ensemble of the highest-probability GIA models. Shaded gray boxes represent SLIPs over 4 ka BP. The curves illustrate the RSL evolution at the average locations (green squares in Figure 3.6) over the past 6,000 years (kyr) for sites #9 – #14. The close alignment between the SLIPs and the model predictions indicates that the GIA model effectively captures the regional RSL changes.

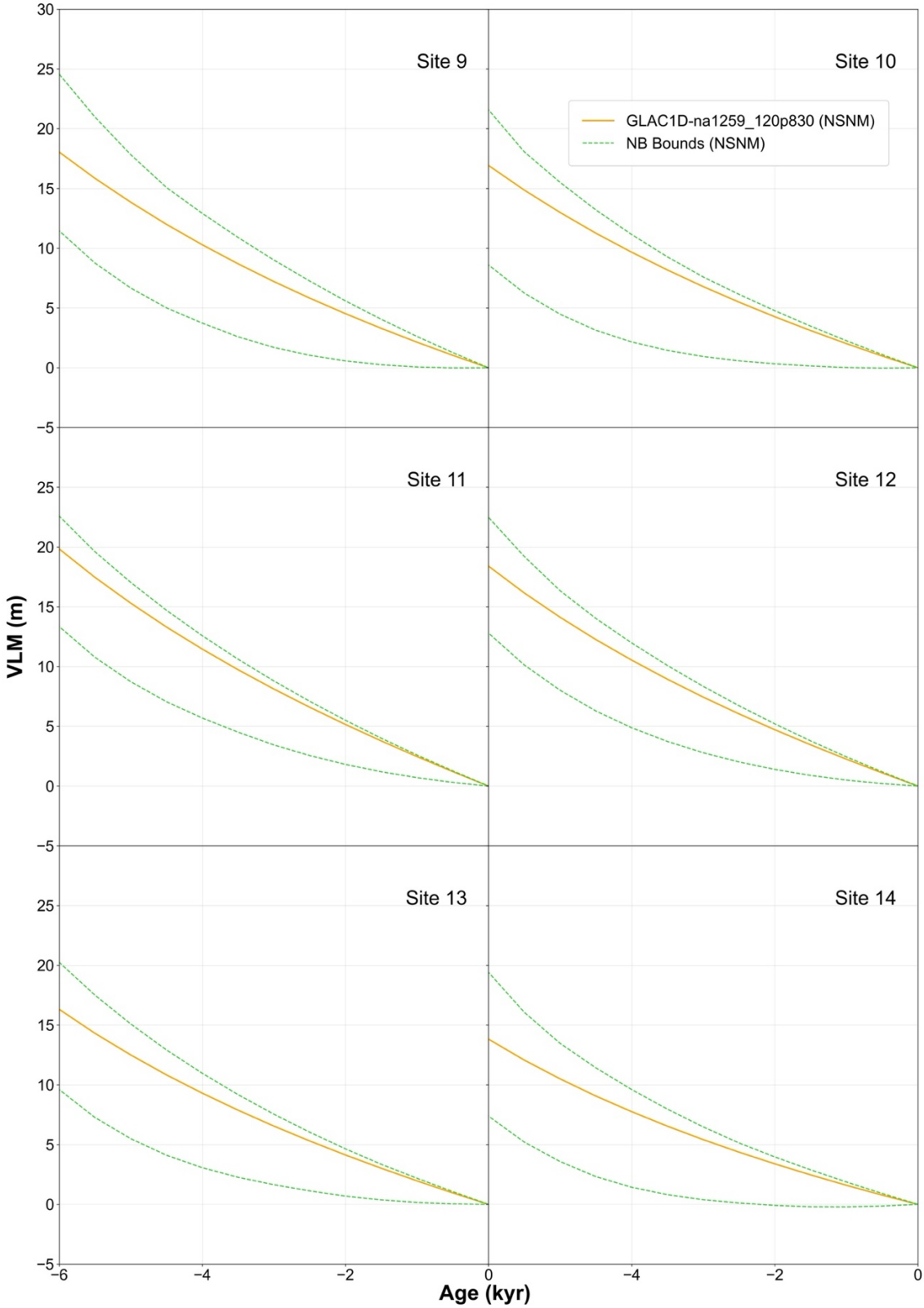


Figure 3.S17. VLM curves for six sites in New Brunswick and Nova Scotia, derived from the optimal regional GIA model (GLAC1D-na1259_120p830; orange lines) with uncertainty bounds (green dashed lines) from a Bayesian (so-called Nominal Bayesian or NB) approach using a sub-ensemble of the highest-probability GIA models. The curves illustrate the VLM evolution at the average locations (green squares in Figure 3.6) over the past 6,000 years (kyr) for sites #9 – #14.

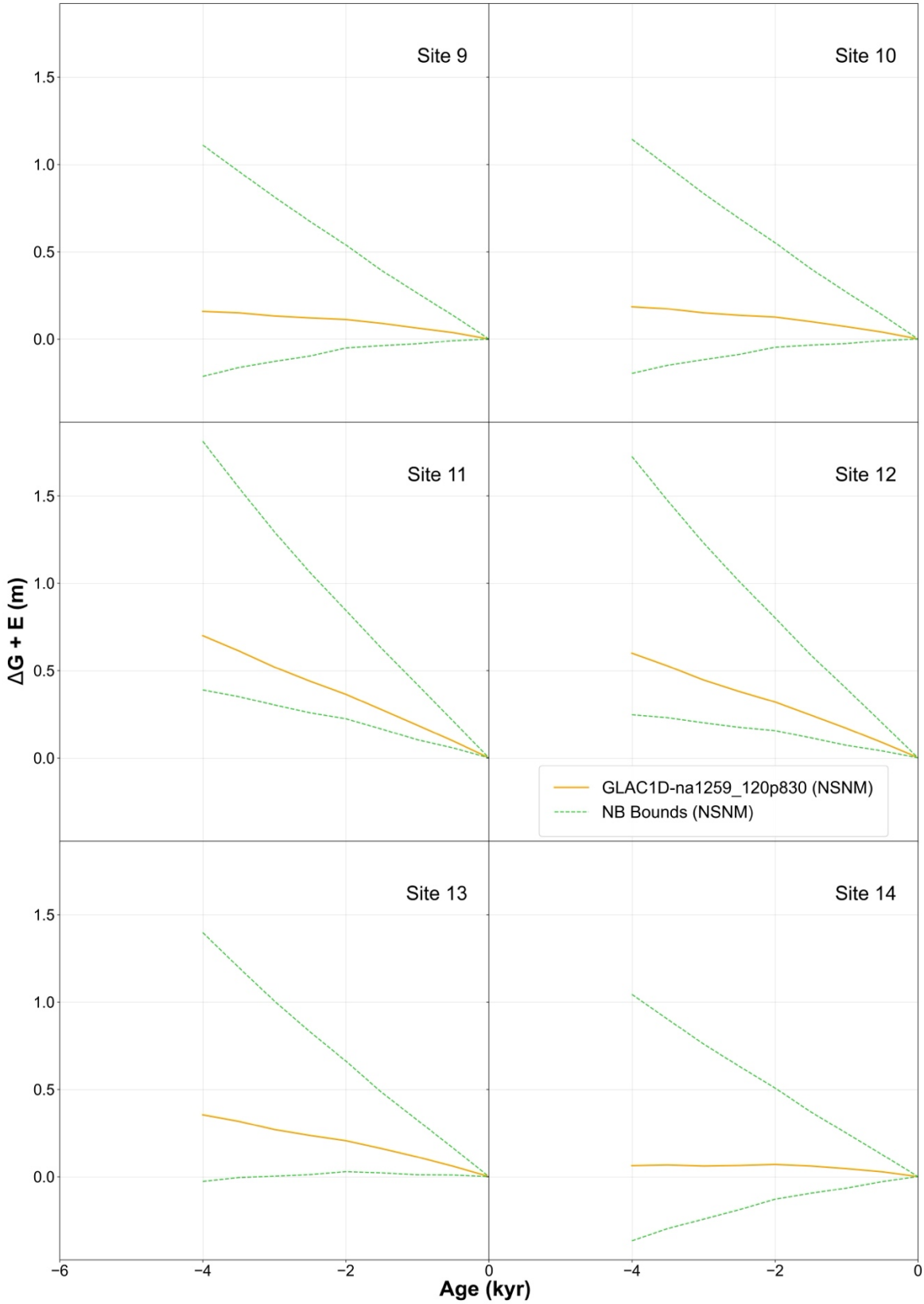


Figure 3.S18. *ΔG + E* curves for six sites in New Brunswick and Nova Scotia, derived from both RSL and VLM curves presented in Figures 3.S16 and 3.S17 using Equation 3.1. The *ΔG + E* term is inferred from the optimal regional GIA model (GLAC1D-na1259_120p830; orange lines), with uncertainty bounds (green dashed lines) determined using a Bayesian (so-called Nominal Bayesian or NB) approach with a sub-ensemble of the highest-probability GIA models. The curves illustrate the combined spatially varying geoid-height

change (ΔG) and spatially uniform height shift (E) over the past 4,000 years (kyr) at the average locations (green squares in Figure 3.6) for sites #9 – #14.

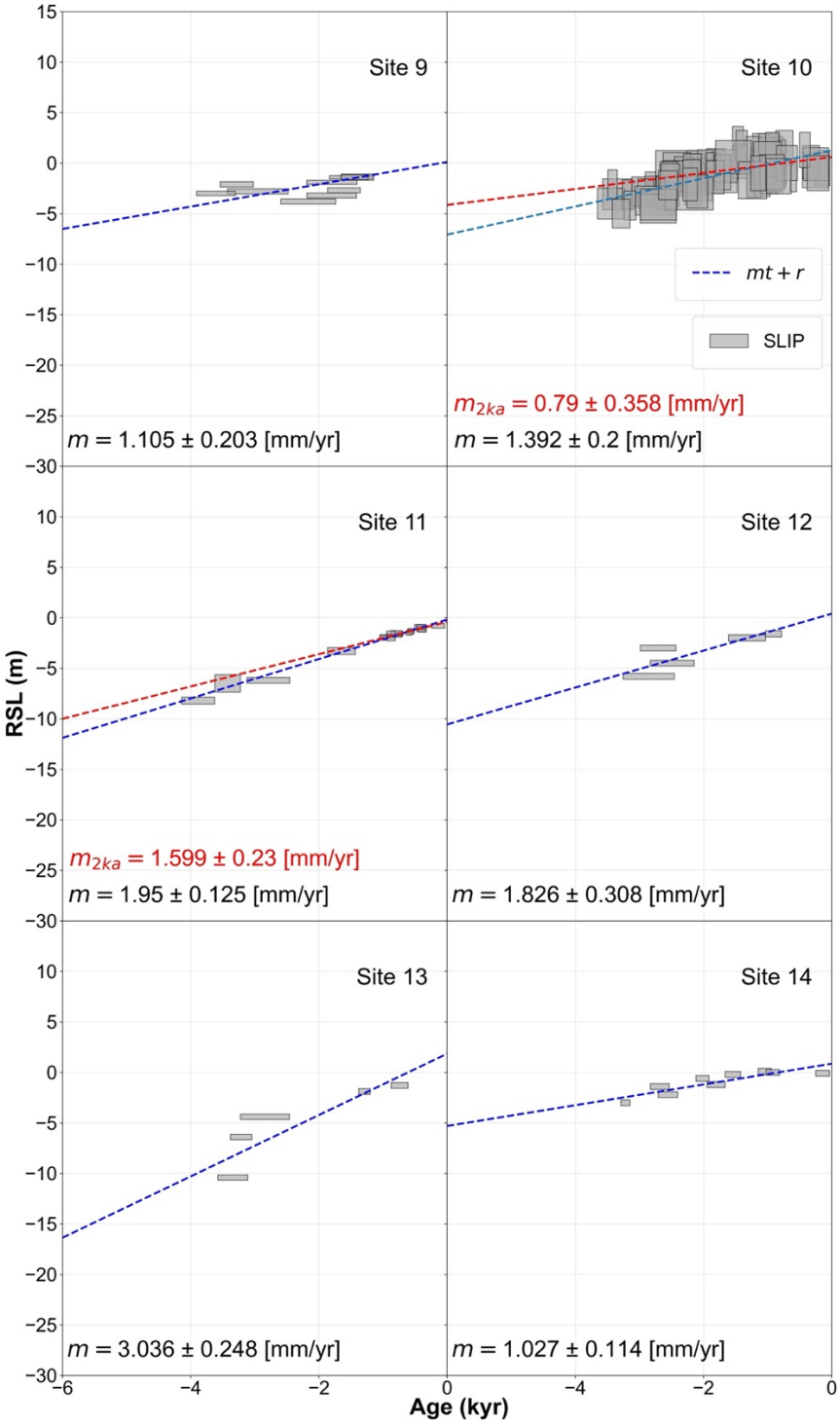


Figure 3.S19. RSL curves for sites #9 – #14 in New Brunswick and Nova Scotia, illustrating the best-fit linear trends obtained by total least squares adjustment (orthogonal distance regression). The panels show linear regression fits ($m \times t + r$; blue dashed lines) for the last 4,000 years, with slopes (m) representing the average RSL rate of change. The shaded gray boxes denote SLIPs, which provide observational constraints. The resulting slope estimates indicate varying rates of RSL rise across the sites. At sites #10 and #11, the red dashed line indicates the linear regression fit for SLIPs over the last 2,000 years (the inferred rates for sites #10 and #11 are 0.79 ± 0.358 mm/yr and 1.599 ± 0.23 mm/yr, respectively).

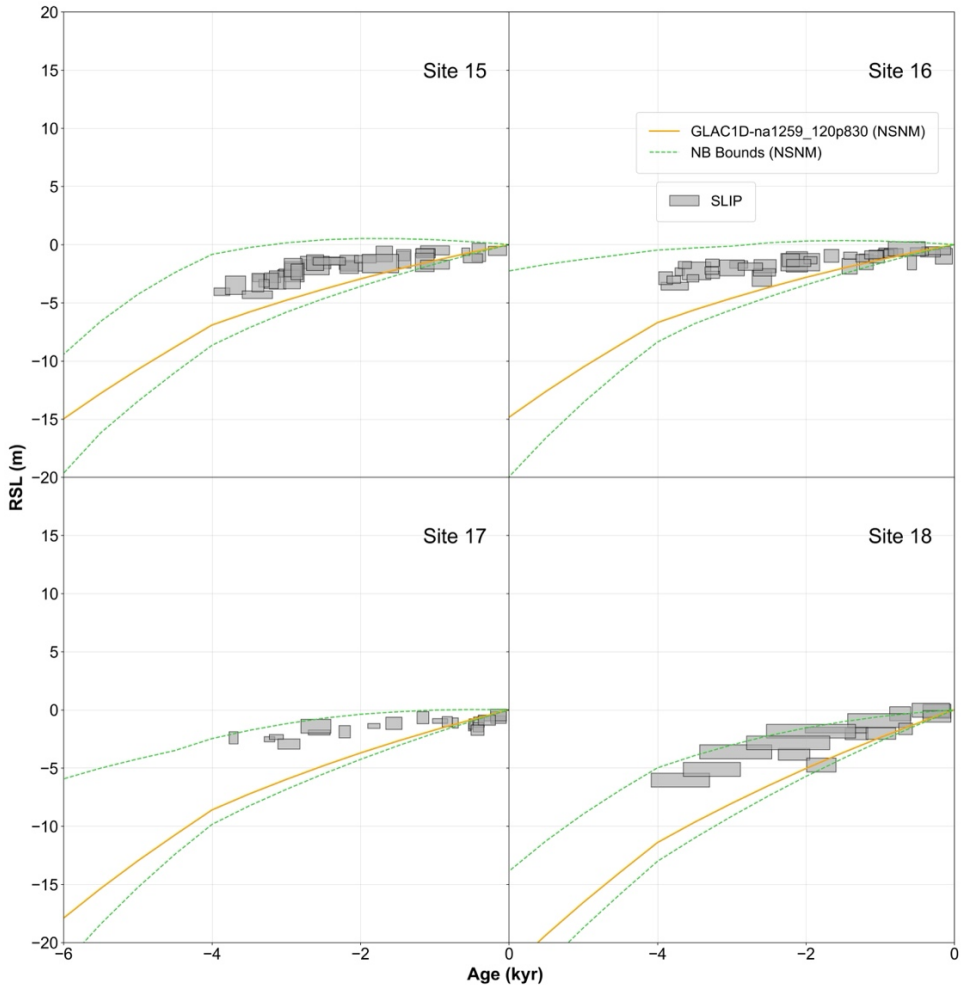


Figure 3.S20. RSL curves for four sites in Maine and Massachusetts, derived from the optimal regional GIA model (GLAC1D-na1259_120p830; orange lines) with uncertainty bounds (green dashed lines) from a Bayesian (so-called Nominal Bayesian or NB) approach using a sub-ensemble of the highest-probability GIA models. Shaded gray boxes represent SLIPs over 4 ka BP. The curves illustrate the RSL evolution at the average locations (green squares in Figure 3.7) over the past 6,000 years (kyr) for sites #15 – #18. The close alignment between the SLIPs and the model predictions indicates that the GIA model effectively captures the regional RSL changes.

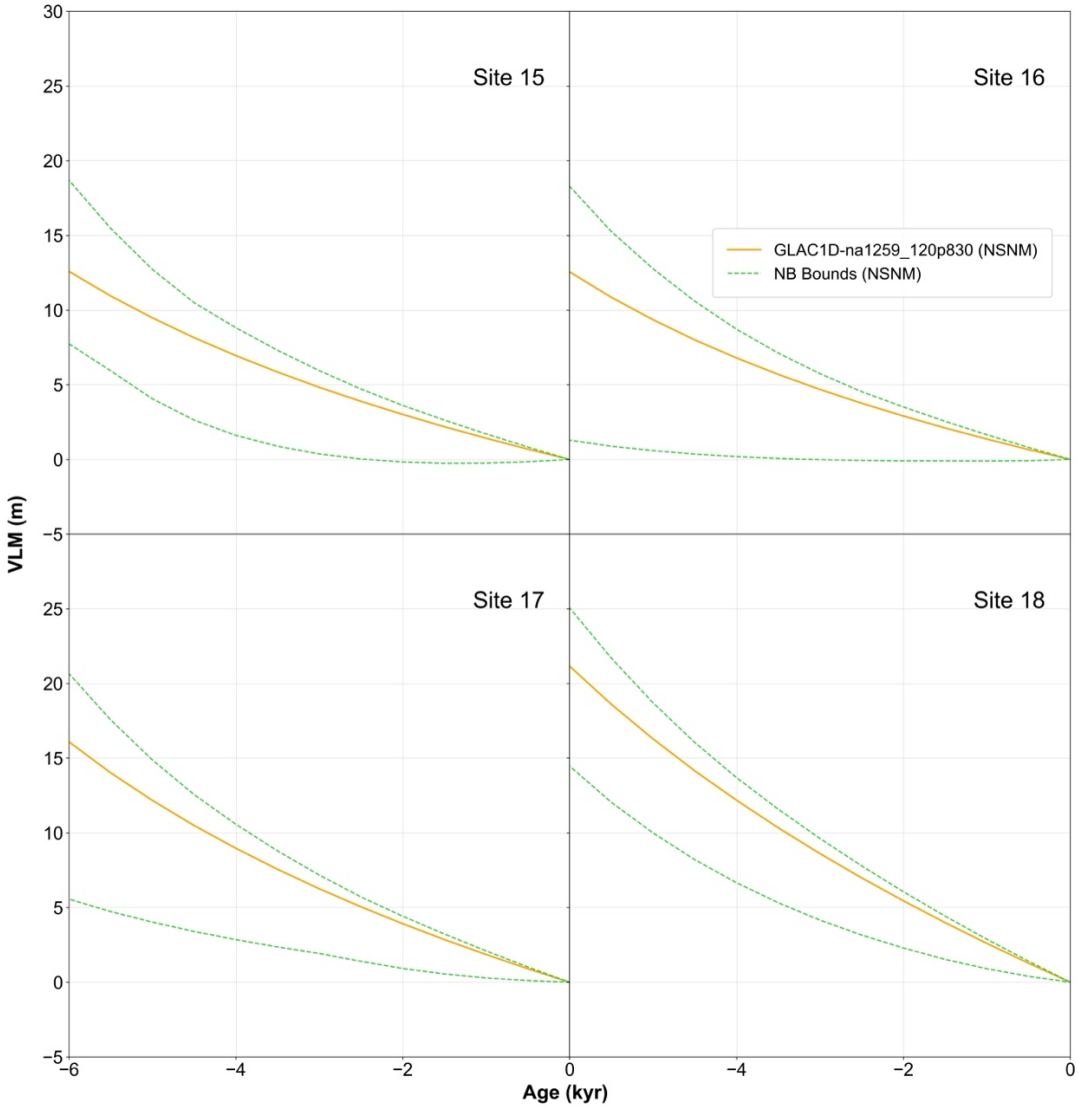


Figure 3.S21. VLM curves for four sites in Maine and Massachusetts, derived from the optimal regional GIA model (GLAC1D-na1259_120p830; orange lines) with uncertainty bounds (green dashed lines) from a Bayesian (so-called Nominal Bayesian or NB) approach using a sub-ensemble of the highest-probability GIA models. The curves illustrate the VLM evolution at the average locations (green squares in Figure 3.7) over the past 6,000 years (kyr) for sites #15 – #18.

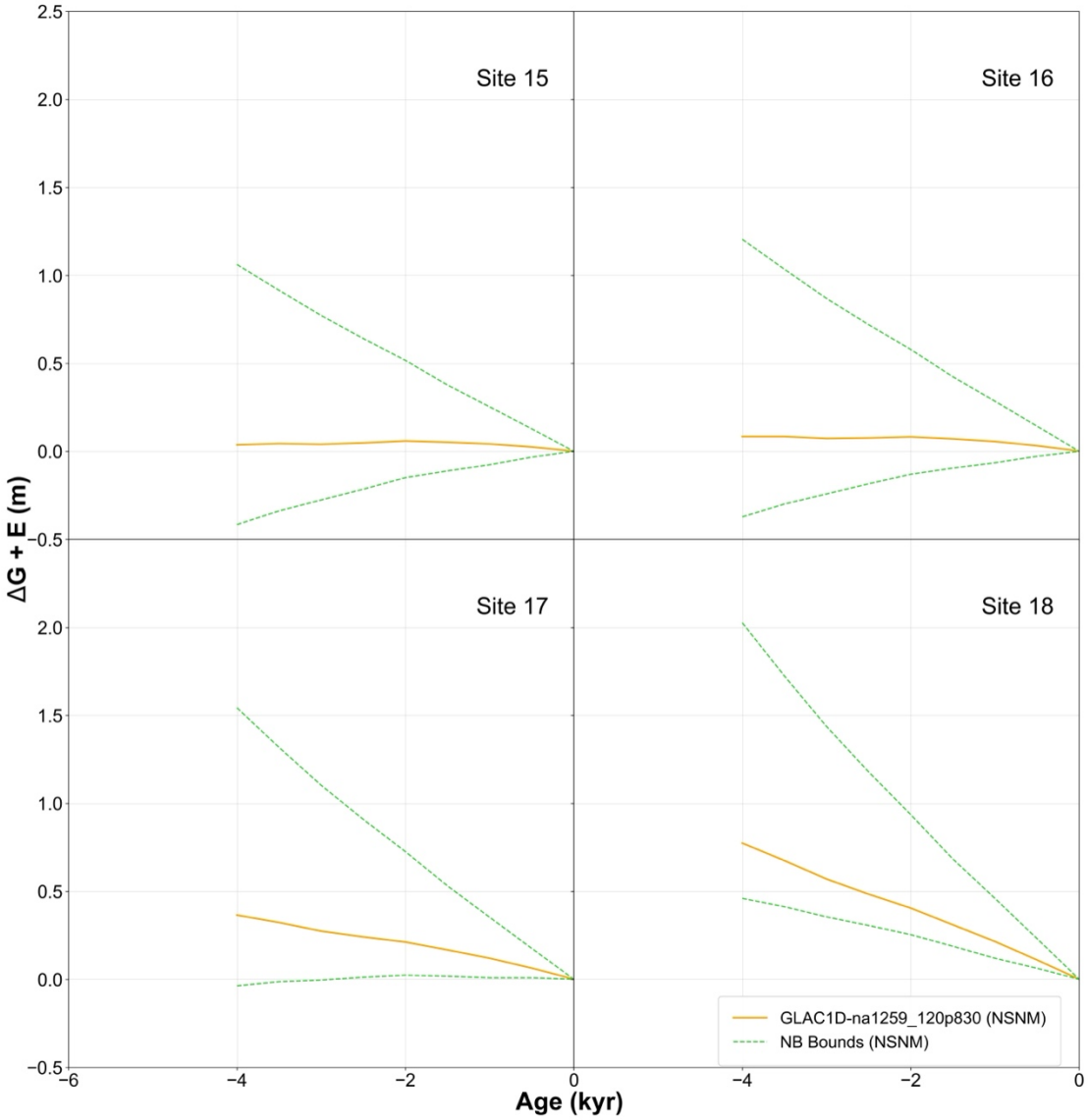


Figure 3.S22. *ΔG + E* curves for four sites in Maine and Massachusetts, derived from both RSL and VLM curves presented in Figures 3.S20 and 3.S21 using Equation 3.1. The *ΔG + E* term is inferred from the optimal regional GIA model (GLAC1D-na1259_120p830; orange lines), with uncertainty bounds (green dashed lines) determined using a Bayesian (so-called Nominal Bayesian or NB) approach with a sub-ensemble of the highest-probability GIA models. The curves illustrate the combined spatially varying geoid-height change (*ΔG*) and spatially uniform height shift (*E*) over the past 4,000 years (kyr) at the average locations (green squares in Figure 3.7) for sites #15 – #18.

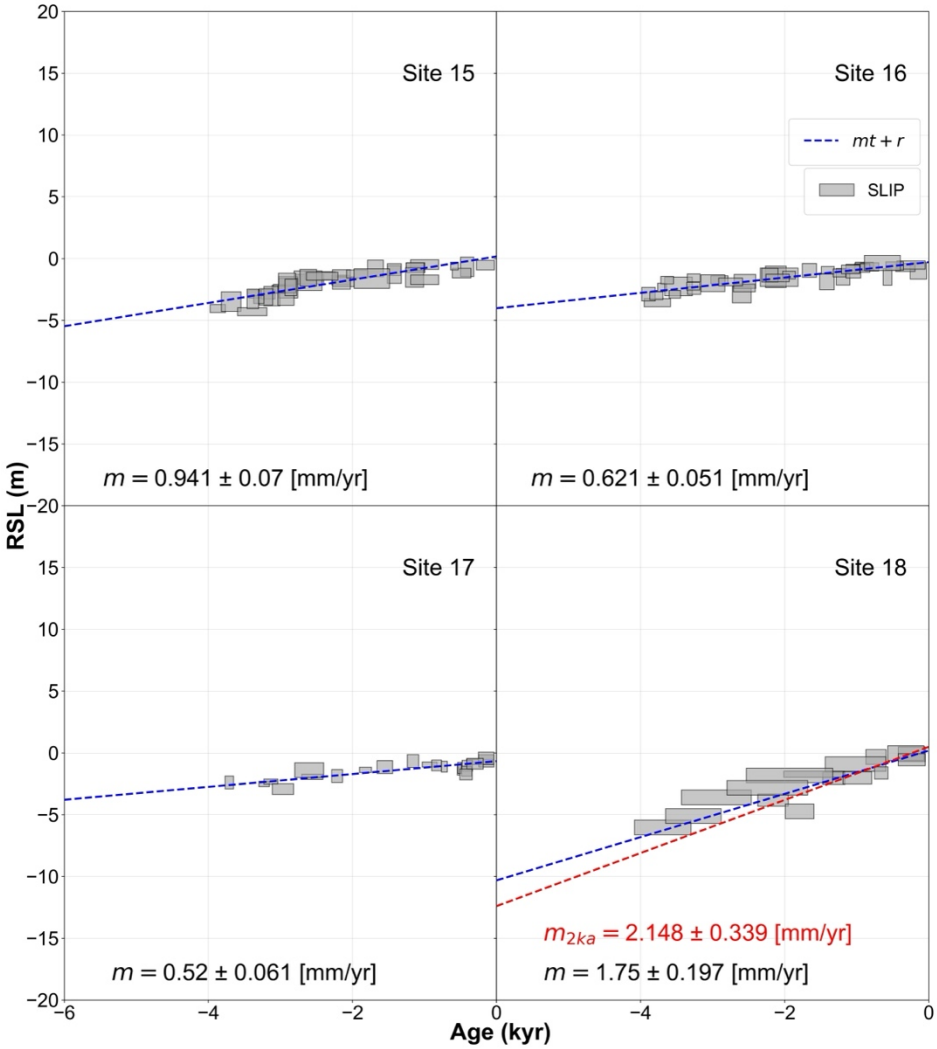


Figure 3.S23. RSL curves for sites #15 – #18 in Maine and Massachusetts, illustrating the best-fit linear trends obtained by total least squares adjustment (orthogonal distance regression). The panels show linear regression fits ($m \times t + r$; blue dashed lines) for the last 4,000 years, with slopes (m) representing the average RSL rate of change. The shaded gray boxes denote SLIPs, which provide observational constraints. The resulting slope estimates indicate varying rates of RSL rise across the sites. At site #18, the red dashed line indicates the linear regression fit for SLIPs over the last 2,000 years (the inferred rate is 2.148 ± 0.339 mm/yr).

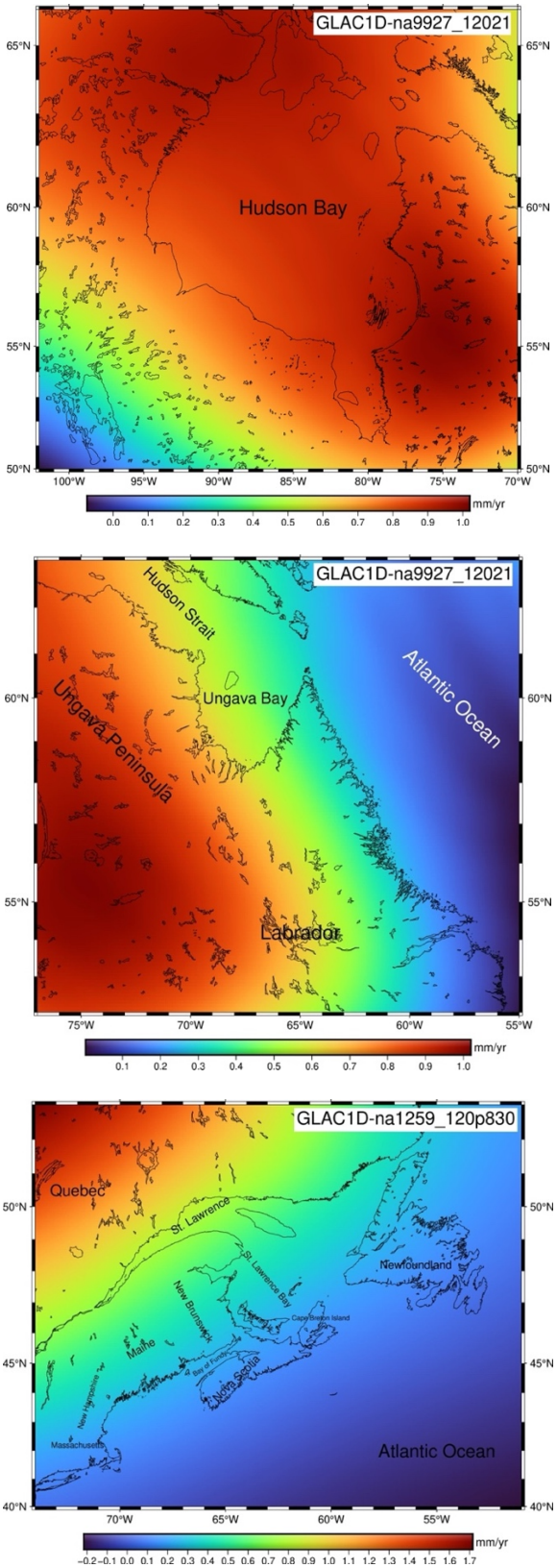


Figure 3.S24. Present-day rates (mm/year) of GIA-induced geoid changes based on optimal regional models. For Hudson Bay (top panel) and the Ungava Peninsula and Labrador (middle panel), the GLAC1D-na9927_12021 model was used, while the GLAC1D-na1259_120p830 model was applied to other subregions (NSNM) along the eastern coast (bottom panel).

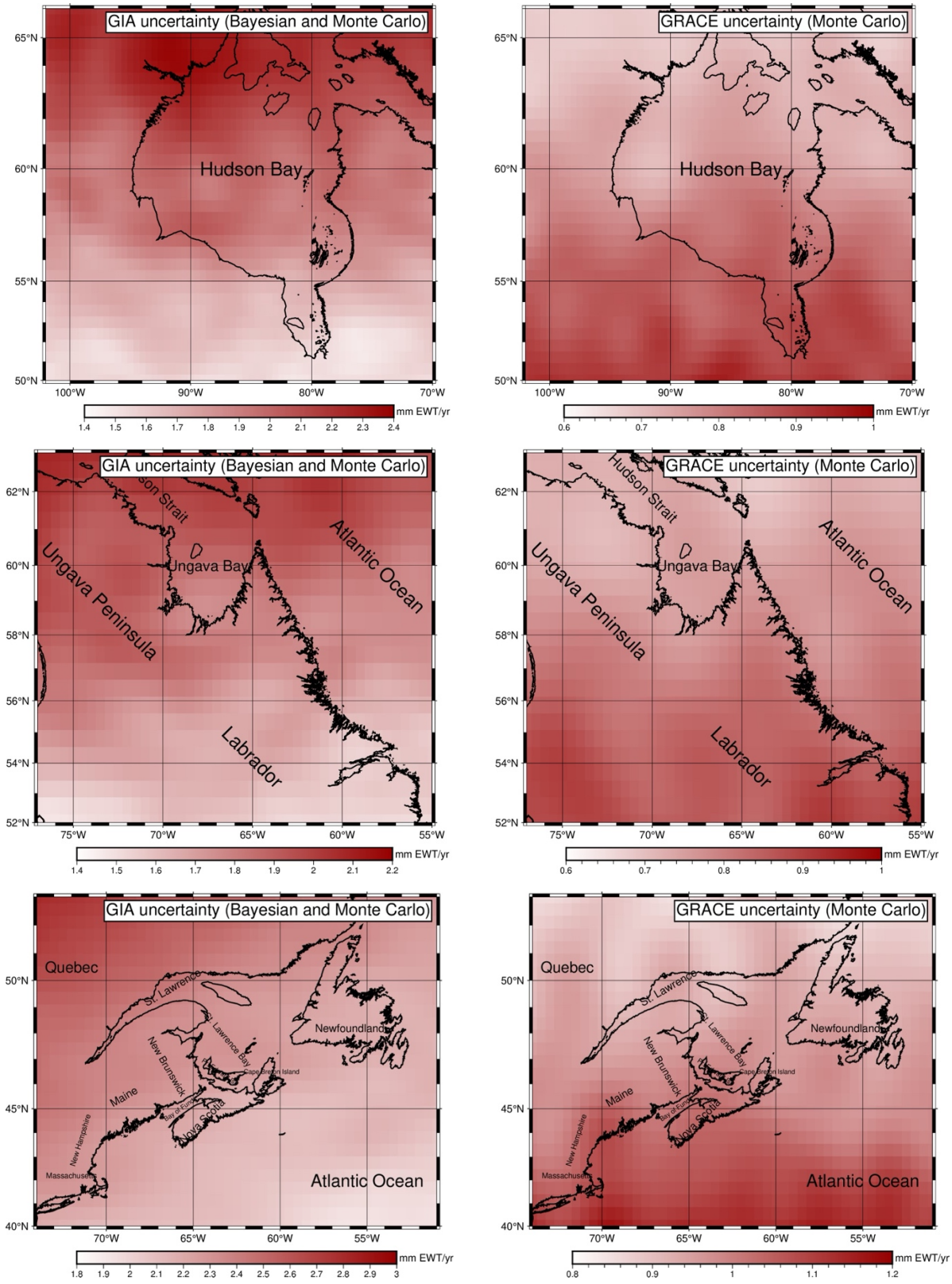


Figure 3.S25. This figure illustrates two primary, independent sources of uncertainty in the GRACE analysis: (1) the uncertainty of the GRACE SHCs, calculated based on the standard deviation of the time-series residuals after removing linear, quadratic, annual, and semi-annual trends; and (2) the uncertainty of the GIA signal, which is the dominant source of uncertainty in our study region, constrained by the sub-ensemble of highest-probability GIA models determined using a Bayesian approach. Both sources of uncertainty are converted into mass changes (in EWT) and quantified in the spatial domain using a Monte Carlo sampling approach. The

uncertainty maps correspond to three subregions: (1) Hudson Bay (top panel); (2) the Ungava Peninsula and Labrador (middle panel); and (3) NSNM, which includes Newfoundland, the St. Lawrence Corridor, New Brunswick, Nova Scotia, Maine, and Massachusetts (bottom panel).

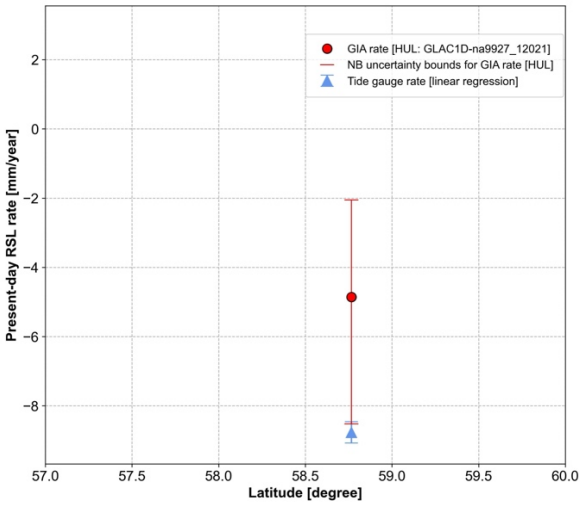


Figure 3.S26. This figure compares RSL rates from CHURCHILL tide gauge observations (blue triangles) and GIA model predictions (red circles) at site #1 in Hudson Bay. The error bars indicate 1σ uncertainty bounds for each estimate. The GIA-induced rate corresponds to the locations of tide gauge.

4

Improved projections of sea-level change and nuisance flooding in central eastern North America: The importance of GIA-induced land motion

Soran Parang [(1)], Makan A. Karegar [(2)], Glenn A. Milne [(1)]

[(1)] Department of Earth and Environmental Sciences, University of Ottawa, Ottawa, Canada
[(2)] Institute of Geodesy and Geoinformation, University of Bonn, Bonn, Germany

Statement of Contribution

This manuscript is my original work, conducted under the supervision of Prof. Glenn A. Milne, who planned and guided the research and provided several rounds of feedback during manuscript preparation. Makan A. Karegar supervised the nuisance flooding section, provided feedback on the harmonic analysis, and contributed to the planning of this part of the research. I carried out all analyses and created all figures presented in the manuscript.

Abstract

Sea-level rise (SLR) associated with recent and future climate warming and anthropogenic climate change is one of the major environmental issues of our generation. Although global mean sea level is rising at roughly 3 mm/yr, mainly driven by land ice melt and ocean thermal expansion, local and regional relative sea level (RSL) trends can differ considerably from this global average, with vertical land motion (VLM) being a key contributing factor. Assessing future coastal flood risk requires accurate projections of RSL that account for both ocean surface changes and land motion. Along the Atlantic coast of Canada and the northeastern United States, glacial isostatic adjustment (GIA) is a dominant driver of long-term VLM, leading to subsidence and enhanced RSL rise in many areas. This study investigates the role of GIA-induced VLM in projections of regional mean sea-level change and nuisance flooding frequency across 25 tide gauges in southeastern Canada and the northeastern United States for the years 2050, 2100, and 2150 CE. We develop projections under three Shared Socioeconomic Pathway (SSP) scenarios, including SSP1-1.9, SSP3-7.0, and SSP5-8.5, and evaluate them across three distinct projection cases: (1) IPCC projections including all components of sea-level change, (2) IPCC projections excluding VLM, and (3) IPCC projections excluding VLM but incorporating a regionally optimized GIA-induced VLM signal with model uncertainty bounds. The results indicate that GIA-induced VLM substantially alters projected mean sea-level changes and nuisance flooding frequencies across the study region. At Atlantic coast locations such as Halifax, Boston, and Saint John, where GIA-induced subsidence dominates, projections that include VLM show higher RSL rise and significantly greater flooding frequencies than projections that exclude it. In contrast, sites located near or within the former ice sheet core, such as Churchill, Rimouski, and Sept Îles, experience land uplift from GIA, resulting in lower projected sea-level changes and reductions in future nuisance flooding frequency. Chronic nuisance flooding (≥50 days/year) is projected to occur at nearly all subsiding tide gauges with historical nuisance flooding (during the IPCC temporal baseline 1995–2014) by 2050 under SSP1-1.9, with many locations exceeding 300 days/year by 2100 under high-emission scenarios when VLM is included. Uncertainty analysis shows that the projections incorporating regionally constrained GIA signals often produce wider uncertainty ranges than the IPCC projections, especially by 2100 and 2150. However, the median (optimal) results from GIA-integrated projections generally align well with those from the IPCC. The approach applied in this study allows mean sea-level projections to be extended to areas lacking dense tide gauge or GNSS coverage, thereby enhancing coastal adaptation planning for GIA-active regions.

Keywords: Glacial isostatic adjustment, Vertical land motion, Relative sea level, Nuisance flooding, Harmonic analysis, Nodal corrections, Sea-level projections, Flood frequency projections, Atlantic coast of North America

4.1. Introduction

The socio-economic impact of sea-level rise (SLR) is one of the major challenges associated with global warming due to the large and growing population density in coastal regions and the high costs associated with coastal infrastructure development and adaptation (Wong et al., 2014). Future projections of sea-level changes at regional to local scales are required by policymakers to develop strategies to minimize the financial and societal impacts of this hazard. However, improving the accuracy of these projections is difficult due to the variety of processes affecting SLR over different spatial and temporal scales (Milne et al., 2009). SLR is influenced by both the vertical motion of the sea surface and the vertical motion of the land in coastal areas. Any processes causing motion of either

surface contribute to sea-level change. However, the Earth's rheology and solid Earth processes are often poorly quantified, even though they can dominate in some regions (Allison et al., 2016). There are two types of sea-level projection: changes in mean (time-averaged) sea level and changes in the frequency (or recurrence time) of high-water events. When the latter occurs, the potential for flooding is at its highest. However, predicting the recurrence time of high-water events requires, as input, an estimate of mean sea level at a given location and time (Woodworth et al., 2011). High-water events range from regular high tide levels to extreme, but much less frequent, storm surges.

Extreme sea-level events are the most destructive, making it essential to accurately estimate how their recurrence time will decrease as mean sea levels continue to rise in most areas. The sea-level hazard associated with lower amplitude high-water events is only now becoming clear, with new research indicating that minor but more frequent flood events (so-called “nuisance flooding”) can have significant long-term impacts. These include the effects of saltwater exposure on coastal infrastructure, groundwater and freshwater ecosystems, and public health risks (Moftakhari et al., 2015; Spanger-Siegfried et al., 2014; Sweet & Park, 2014; ten Veldhuis et al., 2010). Many coastal cities are already experiencing climate-related coastal flooding due to processes that result in land subsidence, thereby enhancing relative sea-level (RSL) rise (Karegar et al., 2015). Much of the Atlantic coast of North America has been sinking for thousands of years, at a maximum rate of ~20 cm per century, due to solid Earth deformation in response to the deglaciation of the North American ice sheets (between about 18,000 and 7,000 years ago). This process, known as glacial isostatic adjustment (GIA), has had a long-lasting impact on regional sea levels (Love et al., 2016; Parang et al., 2024; Spada, 2017). To put this into perspective, global mean SLR during this century is projected to range between 29–110 cm, incorporating dominant processes such as ocean thermal expansion and melting of ice sheets and glaciers (Oppenheimer et al., 2019). The coastal regions of Newfoundland, New Brunswick, and Nova Scotia have been identified as the most vulnerable parts of Canada to coastal flooding, due in part to long-term land subsidence associated with GIA (Greenan et al., 2019). Tide gauge data demonstrate large regional variations in the rate of sea-level change in Eastern Canada, primarily reflecting the influence of long-term vertical land motion (VLM) associated with GIA on the spatial variability of RSL change (Zhai et al., 2015). For example, RSL is falling at rates of about –9 mm/yr in western Hudson Bay due to rapid land uplift, whereas in Halifax, it is rising at approximately 3 mm/yr, illustrating the strong regional contrasts driven by GIA (Dmitrenko et al., 2021; Zhai et al., 2015).

Despite the increasing awareness of flood risks and costs, there is currently limited literature on how SLR and its contributing factors affect nuisance flooding in high-risk regions of Eastern Canada. Recent studies have demonstrated that nuisance flooding is becoming more common along the Atlantic coast of the United States due to SLR and VLM (Karegar et al., 2017; Moftakhari et al., 2015). However, the extent to which different coastal regions in Eastern Canada are currently exposed to recurrent tidal flooding, and how this exposure is expected to evolve in the future, remains largely uncertain. This study aims to improve understanding of the role of GIA-induced VLM in projections of both mean sea-level change and nuisance flooding frequency across southeastern Canada and the northeastern United States. This aim is timely, given that Eastern Canada is experiencing an accelerated rate of SLR due to changes in ocean dynamics (Ezer & Atkinson, 2014; Yin, 2023) and increasing ice mass loss (Hamlington et al., 2020; IMBIE team, 2018). In addition, studies analyzing both global and regional sea-level records have identified large-scale changes in the long-term trends of diurnal and semidiurnal constituents of tidal high water (Schindelegger et al., 2018), which could potentially affect the frequency of nuisance flooding in Eastern Canada. The combination of these factors places this region at an increasing risk of both nuisance and storm surge flooding.

A critical aspect of this study is to assess the contribution of the VLM signal to projected changes in regional mean sea level and the evolution of nuisance flooding frequency, and specifically to improve understanding of the role of GIA-induced VLM in shaping these projections at 25 tide gauges for the time horizons of 2050, 2100, and 2150 CE. To evaluate these projections, three cases are considered: (1) Intergovernmental Panel on Climate Change (IPCC) estimates incorporating all components of sea-level change (Intergovernmental Panel on Climate Change (IPCC), 2023)**,** (2) IPCC estimates without the VLM signal, and (3) IPCC estimates that exclude the VLM signal but integrate a regionally optimized GIA-induced VLM signal with model uncertainty bounds. These projections are developed under three Shared Socioeconomic Pathway (SSP) scenarios: SSP1-1.9, SSP3-7.0, and SSP5-8.5, ensuring comprehensive assessments under different climate and socio-economic conditions. Furthermore, all projections include uncertainty bounds to account for model limitations and uncertainties in future climate forcing. The outcomes of this study serve as a valuable tool for policymakers and coastal management agencies aiming to develop effective mitigation strategies in response to increasing flood risks across eastern Canada and the northeastern United States Atlantic coast. Importantly, our model outputs, through the integration of a regionally constrained GIA signal into the IPCC projection, enhance the utility of existing projections by refining and extending regional mean sea-level change projections in areas with limited observational coverage of contemporary VLM (e.g., from GNSS and tide gauges) within GIA-active regions.

In Section 4.2, we present the methodology used to project regional mean sea-level changes and nuisance flooding frequency. Section 4.3 outlines the results of our projections, organized into projected regional mean sea-level change and nuisance flooding frequency across 25 tide gauge sites. Section 4.4 discusses the broader implications of our findings and highlights limitations that may guide future research. The projected regional mean sea-level changes with uncertainty bounds (Appendix 1), as well as the projected nuisance flooding days with uncertainty bounds (Appendix 2), both provided at 25 tide gauges for three projection cases under three SSP scenarios and for the time horizons of 2050, 2100, and 2150 CE, are made available for our study region.

4.2. Data and methodology

The methodology is structured around three main components. First, GIA modeling is used to estimate present-day VLM rates with uncertainty bounds, based on a wide range of Earth–ice model input parameter sets and paleo sea-level records. Second, regional sea-level projections are developed for three time horizons (2050, 2100, and 2150 CE) under three SSP scenarios, with three projection cases that vary in how the VLM signal is treated. Third, projections of nuisance flooding frequency are generated at 25 tide gauge locations by applying tidal harmonic analysis to historical hourly still water level observations, accounting for secular changes and local nodal corrections for three major tidal constituents (M2, N2, and K1), and based on the projected regional mean sea-level changes.

4.2.1 GIA-induced VLM signal

To estimate the VLM signal driven by GIA across our study region, we use the regionally optimized GIA model outputs developed in Chapter 2. These models were constrained using recent paleo-RSL observations, including both sea-level index points and limiting data points (marine and terrestrial), and are based on a broad parameter space for lithospheric thickness, upper and lower mantle viscosity, and ice history models. For the Hudson Bay, Ungava Peninsula, and Labrador subregions, the selected optimal model configuration is based on the GLAC1D-na9927 ice history model (Tarasov et al., 2012),

with parameters lithospheric thickness (LT) = 120 km, upper mantle viscosity (UMV) = 2×10^{21} Pas, and lower mantle viscosity (LMV) = 10^{21} Pas. For subregions along the eastern coast—including Newfoundland, the St. Lawrence Corridor, New Brunswick and Nova Scotia, and Maine and Massachusetts—we employed the GLAC1D-na1259 ice history model with LT = 120 km, UMV = 0.8×10^{21} Pas, and LMV = 30×10^{21} Pas. Figure 4.1 shows present-day VLM rates derived from these regionally optimized GIA models, highlighting uplift and associated RSL fall in Hudson Bay, and land subsidence accompanied by RSL rise along the Atlantic coastal subregions.

The selection of these region-specific model parameters reflects regional variations in Earth structure and ice loading history, accounting for the presence of lateral viscosity structure confirmed by the 3D GIA modeling in Chapter 2. Model uncertainty bounds were estimated using a Bayesian approach based on a sub-ensemble of the highest-probability Earth-ice model input parameter sets (refer to Table 2.2 in Chapter 2), allowing us to robustly characterize the parametric uncertainty in present-day GIA-induced VLM rates. These GIA-induced VLM estimates are applied in projections of regional mean sea-level change in this analysis. Note that the VLM associated with GIA influences sea surface height through local geoid changes and the syphoning effect. These smaller contributions are included in the GIA signal added to the IPCC results.

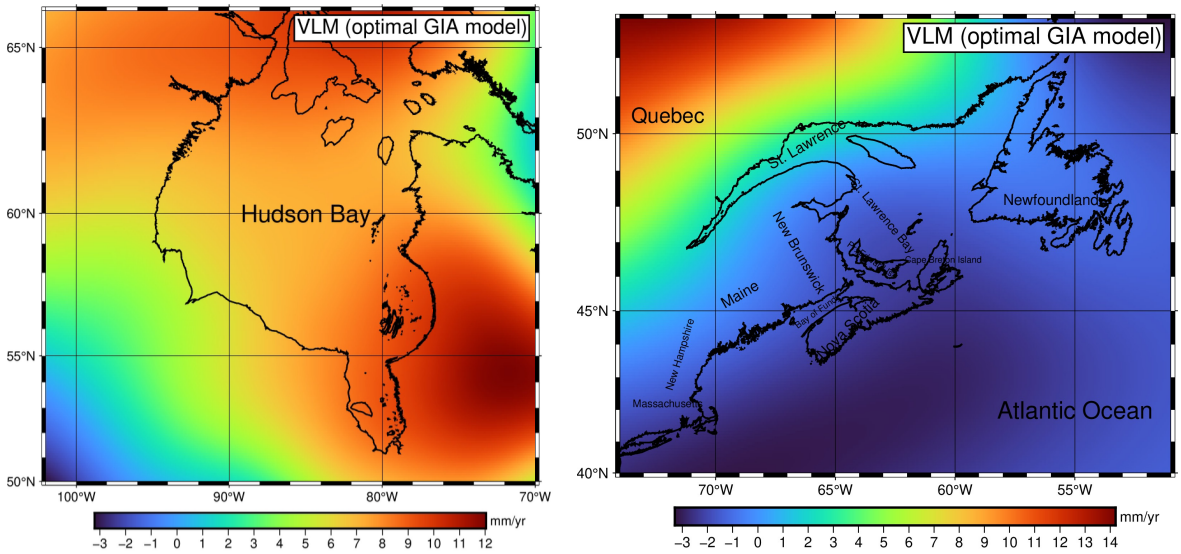


Figure 4.1. Present-day VLM rates from regionally optimized GIA models for two subregions. Left is Hudson Bay, experiencing uplift and RSL fall, and right is the Atlantic coast subregion, which is subject to ongoing land subsidence and RSL rise.

4.2.2. Regional mean sea-level projections

To project future changes in regional mean sea level across southeastern Canada and the northeastern United States, we considered three future time horizons: 2050, 2100, and 2150 CE. Projections were developed under three SSP scenarios from the IPCC Sixth Assessment Report: SSP1-1.9, SSP3-7.0, and SSP5-8.5. These scenarios represent a range of greenhouse gas emission pathways and associated warming levels (Fox-Kemper et al., 2023; Meinshausen et al., 2020): SSP1-1.9 corresponds to the most optimistic mitigation scenario, in which global temperatures stabilize or even slightly decline in the second half of the century, with projected warming ranging from 0.13 °C to 1.25 °C by 2081–2100 relative to the 1995–2014 baseline. SSP3-7.0 represents a high-risk pathway, with projected warming between 1.95 °C and 4.38 °C, while SSP5-8.5 reflects a very high-emissions trajectory, associated with

the greatest warming, ranging from 2.40 °C to 5.57 °C over the same period (see Figure 1.7 in Chapter 1).

The regional sea-level projections from the IPCC include contributions from sterodynamic sea-level change, land water storage, and mass loss from glaciers and the Greenland and Antarctic ice sheets, along with the VLM signal, which is inferred from spatio-temporal statistical modeling based on long-term trends in tide gauge records (Jevrejeva et al., 2019; Kopp et al., 2014, 2017). In this model, tide gauge records are decomposed into three components: a globally uniform term, a regionally varying linear trend, and a regionally varying nonlinear term. The linear component is interpreted as the VLM signal applied in the IPCC projections, reflecting long-term non-climatic processes such as GIA, tectonics, and anthropogenic subsidence. This estimate is assumed to remain constant in future projections. It should be noted that this approach does not explicitly separate GIA from other local effects and assumes linearity even for processes that may vary over time, such as fluid withdrawal or tectonic activity (see Section 2.5 in Kopp et al., 2014).

To assess the role of VLM and its GIA-induced component, we consider three projection cases: (1) IPCC projections including all components, (2) IPCC projections excluding the VLM component, and (3) IPCC projections excluding the generic VLM component but including the RSL signal from our regionally optimized GIA models (Section 4.2.1). While several recent studies incorporate VLM into sea-level projections (e.g., Govorcin et al., 2025; Sherpa et al., 2023; Zhai et al., 2025), our framework distinguishes between two key aspects: case (2) highlights the influence of VLM by showing the outcome when it is omitted, whereas case (3) isolates the contribution of regionally constrained GIA-induced land motion using our optimized models. This design enables us to assess both the necessity of VLM and the added value of improved GIA modeling in sea-level projections. The IPCC projections use a temporal baseline of 20 years from 1995 to 2014, with a midpoint year of 2005; the GIA-induced RSL signal is integrated into the projections by calculating the cumulative VLM from the baseline year to each projection year (2050, 2100, and 2150), assuming a constant linear trend in the GIA signal. The IPCC projections are provided with 1σ uncertainty estimates. The uncertainty in the projections that incorporate regionally constrained GIA signal is quantified using error propagation that integrates the IPCC projection uncertainties with the uncertainty bounds associated with the GIA signal, derived using the Bayesian approach (see Section 4.2.1 and Chapter 2).

4.2.3. Nuisance flooding analysis

To assess how future sea-level change will impact the frequency of high-tide or nuisance flooding, we analyzed hourly still water level records from 25 tide gauge stations distributed across southeastern Canada and the northeastern United States. These stations were selected based on two criteria: (1) availability of site-specific IPCC sea-level projections and (2) at least 70% data completeness over the IPCC temporal baseline (1995–2014), which spans 20 years and is considered sufficient to capture long-term tidal and non-tidal variability (Fox-Kemper et al., 2023; Haigh et al., 2011; Sweet et al., 2018; Thompson et al., 2019). The observational data were obtained from the Global Extreme Sea Level Analysis (GESLA) version 3 database (Haigh et al., 2023; Woodworth et al., 2016), which provides quality-controlled, long-duration time series suitable for assessing trends in high water levels. The considered tide gauge stations include 13 in Canada and 12 in the United States (Figure 4.2). The station names corresponding to the numbered locations on the map are listed in Table 4.S1.

Still water level is defined as the combination of mean sea level, astronomical tides, and meteorological surges (such as wind-driven or pressure-induced variations), and is typically

representative of total water level fluctuations in sheltered coastal environments (Serafin et al., 2017). As such, tide gauge observations serve as a reasonable approximation of still water levels and are widely used in flood frequency analysis. The nuisance flooding analysis in this study focuses on the exceedance of locally defined minor flood thresholds by non-extreme but recurrent high-water events, which can impose chronic stress on coastal infrastructure even in the absence of major storms (Moftakhari et al., 2015; Sweet et al., 2018). To project how the frequency of these events will evolve under future sea-level change, we integrate the results of tidal harmonic analysis over the IPCC temporal baselines with regional mean sea-level projections for the years 2050, 2100, and 2150 across multiple SSP scenarios.

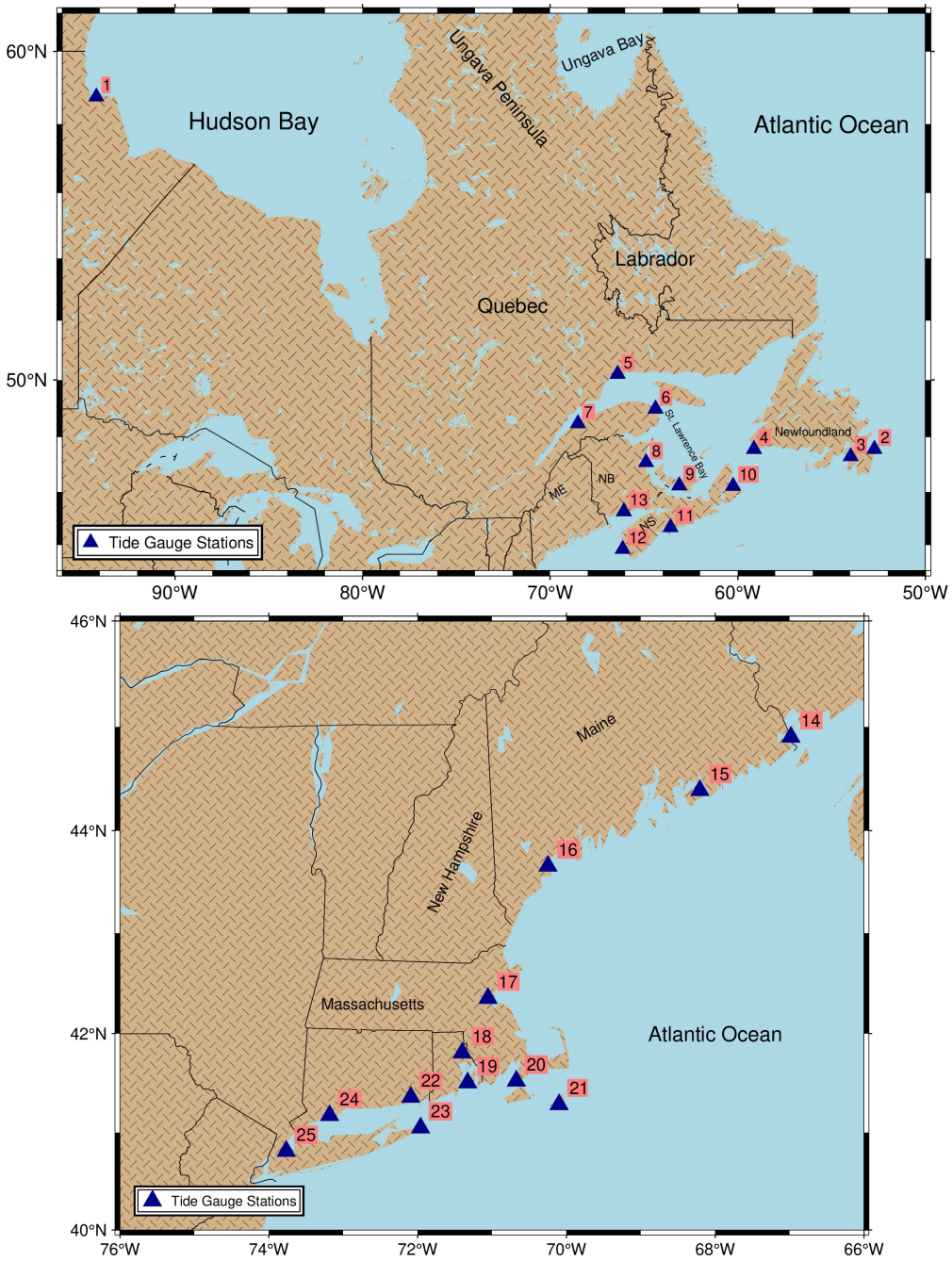


Figure 4.2. Locations of the 25 tide gauge stations used in this study. The top panel shows the 13 Canadian stations, and the bottom panel shows the 12 U.S. stations. Tide gauges are indicated by blue triangles. Station names associated with the numbered locations are listed in Table 4.S1.

To reconstruct hourly tide levels, harmonic analysis was conducted at all 25 tide gauges using the UTide algorithm (Codiga, 2011). UTide provides a unified and robust implementation of classical tidal harmonic analysis, performing a least-squares adjustment to estimate unknown model parameters by fitting the observed still water levels to a sum of sinusoidal constituents, each characterized by frequency, amplitude, and phase lag. The amplitude and phase lag are treated as unknowns and are estimated along with their corresponding 95% confidence intervals. The tidal signal is modeled as:

$$\hat{y}(t) = Z + \sum_{n=1}^{N} H_n f_n(t) \cos(\omega_n t - \phi_n + u_n(t) + V_n(t)) \quad (4.1)$$

where $\hat{y}(t)$ is the predicted tide level at time t; Z is the mean sea level; H_n, ω_n, ϕ_n are the amplitude, angular frequency, and phase lag of the nth tidal constituent (from a total of N applied tidal constituents), respectively; f_n and u_n are nodal corrections for amplitude and phase lag, respectively; and V_n is the astronomical phase argument (Greenwich phase). Across all tide gauges, 68 tidal constituents were detected using a decision-tree-based algorithm implemented in UTide. This algorithm estimates uncertainties through a Monte Carlo approach, which propagates noise characteristics in the residuals to provide confidence intervals on tidal amplitudes and phases. This procedure ensures that the reconstructed tidal signal reflects statistically robust components.

Standard nodal corrections based on equilibrium tide theory are commonly applied to tidal constituents to account for the 18.6-year lunar nodal cycle (Pugh & Woodworth, 2014). These corrections are typically considered globally constant, assuming a uniform astronomical response across ocean basins (Trupin & Wahr, 1990; Woodworth, 2012). However, in shallow-water, friction-dominated, or geomorphologically complex regions, such as estuaries and shelf seas, nonlinear interactions and energy transfer across tidal frequencies distort the expected nodal behavior, causing standard corrections to break down (Amin, 1985; Feng et al., 2015; Hagen et al., 2021; Ku et al., 1985; Ray & Foster, 2016). In these areas, local nodal corrections provide a more accurate representation of tidal modulations. To address this, we applied station-specific nodal corrections to the three major lunar constituents, including M2 (principal lunar semidiurnal), N2 (larger lunar elliptic semidiurnal), and K1 (luni-solar diurnal), based on long-term observational records from each tide gauge in our study region. This approach follows the methodology of Ray & Foster (2016), who demonstrated that applying locally determined nodal modulations for M2, N2, and K1, infers significantly more realistic projections of tide-sufficient flooding at coastal sites such as Boston, where standard corrections fail due to complex regional tidal dynamics.

We applied a two-step approach to account for both secular changes and local nodal modulations within a physically consistent, observation-based framework (Feng et al., 2015; Hagen et al., 2021; Ray & Foster, 2016). First, for each tide gauge, harmonic analysis was performed separately for each year (within the full observational period) that had at least 70% data completeness. In this step, annual amplitudes and Greenwich phase lags, with their associated confidence intervals, were estimated for each constituent (M2, N2, and K1) without applying any nodal corrections. This yielded time series of yearly amplitude and phase values for each constituent, along with their 1σ uncertainties. In the second step, these time series were modeled using a least-squares fit to a function combining a linear trend and a nodal component (represented by an 18.6-year sinusoid):

$$\eta(t) = a + bt + c\sin\left(\frac{2\pi}{18.6}t\right) + d\cos\left(\frac{2\pi}{18.6}t\right) \quad (4.2)$$

where $\eta(t)$ represents either the annual amplitude or Greenwich phase lag at year t, as estimated in the first step; a is the intercept (constant value); b is the secular trend (linear rate of change); and c and d define the nodal modulation as a sinusoid with a period of 18.6 years (full lunar nodal cycle). This approach allows for the simultaneous estimation of both the secular change and periodic nodal variability. From the fitted parameters, we calculated nodal modulations in amplitude (A_m) and phase lag (P_m) for each constituent using the following equations:

$$A_m = \frac{\sqrt{c^2+d^2}}{a+bt_{mid}} \times 100 \text{ (unitless, percent)} \quad (4.3)$$

$$P_m = \sqrt{c^2 + d^2} \text{ (in degrees)} \quad (4.4)$$

Here, t_{mid} is the midpoint time of the analyzed time series. The parameters a, b, c, and d in Equation 4.3 were obtained from the weighted least-squares adjustment applied to the annual amplitude estimates inferred from the first step. Similarly, c and d in Equation 4.4 were derived by fitting the model defined in Equation 4.2 to the annual Greenwich phase lag values.

Figure 4.3 illustrates secular changes and station-specific nodal modulations for the M2 tidal constituent at two tide gauges: Boston (tide gauge #17 in Figure 4.2; left panels) and Churchill (tide gauge #1; right panels). In Boston, the amplitude of M2 shows a positive secular trend of 2.64 ± 0.27 cm/century, with a nodal modulation of 2.92 ± 0.18%. The corresponding phase lag exhibits a negative secular trend of –1.50 ± 0.11 degrees/century and a nodal modulation of 2.31 ± 0.04°. At Churchill, the secular change in amplitude is noticeably large, with a trend of –22.86 ± 1.25 cm/century, which can be primarily attributed to a high rate of GIA-induced sea-level fall in this region. Churchill also shows a nodal amplitude modulation of 3.32 ± 0.80%, a positive secular trend in phase lag of 5.61 ± 0.49 degrees/century, and a nodal phase modulation of 2.31 ± 0.12°.

In addition to VLM and GIA, other contributing factors influencing M2 include changes in large-scale ocean dynamics, local bathymetry, water-column stratification, and the morphological evolution of coastal and estuarine systems, all of which can modulate tidal amplitude and phase lag (Devlin et al., 2017; Mawdsley et al., 2015; Schindelegger et al., 2018; Talke & Jay, 2020). For example, the long-term amplification of M2 at Boston likely reflects regional oceanographic processes rather than land motion alone. In the Gulf of Maine, variations in M2 amplitude have been linked to changes in water-column stratification that influence the exchange of energy between surface (barotropic) and internal (baroclinic) tides. Enhanced stratification promotes greater conversion of barotropic energy into internal tides, reducing surface amplitudes, while weaker stratification has the opposite effect. Consistent with this interpretation, global altimetry records show widespread declines in barotropic M2 amplitudes associated with increased stratification, providing broader context for the Gulf of Maine behavior (Ray & Schindelegger, 2025; Schindelegger et al., 2022).

The local nodal modulations in M2 amplitude and phase lag at Boston and Churchill deviate from the standard modulation values of 3.7% for amplitude and 2.1° for phase lag derived from equilibrium tidal theory (Ray & Foster, 2016). These differences demonstrate the necessity of applying site-specific nodal corrections when reconstructing tidal levels under projected regional mean sea-level changes. The complete set of results for all 25 tide gauges and for M2, N2, and K1, including secular trends and nodal modulation values with 1σ uncertainties for both amplitude and phase lag, is provided in Figures 4.S1–4.S3.

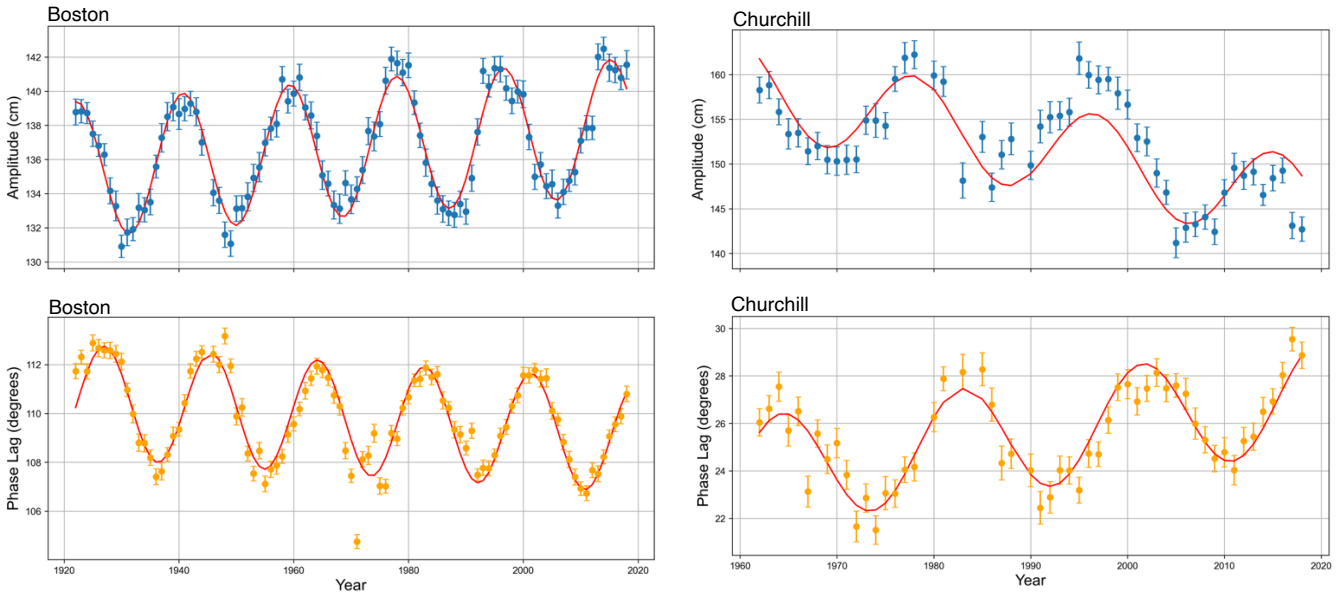


Figure 4.3. Secular changes and local nodal modulations in the M2 tidal constituent at two tide-gauge stations. Left panels: Boston; right panels: Churchill. The top panels show annual amplitude (blue points with uncertainty bars), and the bottom panels show annual Greenwich phase lag (orange points with uncertainty bars), both estimated from harmonic analysis of each year with at least 70% data completeness. Red curves indicate the best-fit model combining a linear trend and an 18.61-year sinusoidal nodal cycle.

To assess future minor tide-sufficient (nuisance) flooding risks in our study region, we applied the impact-based flood threshold approach developed by Sweet et al. (2018), and widely adopted in subsequent global assessments (e.g., Hague et al., 2023). This method estimates flood thresholds (minor, moderate, and major) using regression relationships with the local tidal range, specifically, the greater tidal range (GT), defined as the difference between mean higher high water (MHHW) and mean lower low water (MLLW), to provide consistent, site-specific thresholds for high-tide flooding. Both MHHW and MLLW were estimated from predicted tide levels derived from harmonic analysis over the IPCC temporal baseline for each tide gauge. Unlike methods relying on global digital elevation models, which can have vertical RMSE errors exceeding 2 m (Farr et al., 2007; Kulp & Strauss, 2019; Yamazaki et al., 2017), this approach results in decimeter-scale accuracy for flood thresholds and captures a broader set of flood mechanisms, including tidal overflow, groundwater intrusion, and backflow through drainage systems (Hague et al., 2023; Moore & Obradovich, 2020; Sweet et al., 2018). The minor flood threshold (relative to MLLW) is estimated using the following formula (Sweet et al., 2018):

$$Minor\ flood\ threshold\ \approx 1.04 \times GT + 0.5 \quad (4.5)$$

To quantify historical flooding exposure, we calculated the number of nuisance flooding days during the IPCC 20-year temporal baseline. A day was classified as a nuisance flooding day if the daily maximum predicted tide level equaled or exceeded the local minor flood threshold. Future hourly tide levels were projected for 2050, 2100, and 2150 CE by incorporating (1) tidal predictions from harmonic analysis over the IPCC temporal baseline, (2) secular changes in amplitude and phase lag for M2, N2, and K1, and (3) projected regional mean sea-level changes under three SSP scenarios (see Section 4.2.2). The projected mean sea-level changes were considered under three distinct cases: (1) IPCC projections including all components, (2) IPCC projections excluding VLM, and (3) IPCC projections excluding VLM but incorporating a regionally optimized GIA-induced RSL signal with associated uncertainty bounds. The projected daily maximum tide levels were compared to the local minor flood

thresholds to estimate the number of nuisance flooding days for each scenario and projection year, with all frequency projections presented alongside corresponding upper and lower uncertainty bounds.

4.3. Results and discussion

4.3.1. Projections of regional mean sea-level changes

Figure 4.4 shows the results at four representative tide gauges–Churchill (#1 in Figure 4.2), Rimouski (#7), Halifax (#11), and Boston (#17)–which span eastern and Atlantic Canada as well as the northeastern United States (see Figure 4.2 and Table 4.S1). Projections of regional mean sea-level change under all scenarios generally show an increase in projected values over time, with larger magnitudes by 2100 and 2150 compared to 2050. Across all three projection cases (IPCC, IPCC-noVLM, and IPCC-noVLM + Regional GIA), higher emission scenarios (e.g., SSP5-8.5) generally yield greater projected sea-level change than lower emission scenarios (e.g., SSP1-1.9) for each time horizon. In addition, the uncertainty bounds associated with the projections broaden with time, reflecting increasing uncertainty in long-term climate forcing and model components. Among the three projection cases, projections under case 3 (IPCC-noVLM + Regional GIA) generally exhibit wider uncertainty ranges. This is primarily due to the large uncertainty associated with the GIA signal across the study region and its cumulative effect over time.

The influence of VLM varies across the four tide gauges presented in Figure 4.4. At Halifax and Boston, a similar pattern emerges, where the projected median SLR (indicated by the black horizontal line within each bar) is consistently higher after accounting for the VLM signal, when comparing projection cases 1 (IPCC) and 3 (IPCC-noVLM + Regional GIA) to case 2 (IPCC-noVLM) for a given year and SSP scenario. Although the differences in median sea-level projections across these cases may appear small, they can be significant when evaluating nuisance flooding frequency, where even small increases in water level can determine whether predicted tide levels exceed local minor flood thresholds. The higher projected mean SLR at Halifax and Boston after accounting for VLM confirms that land subsidence is a significant contributor to future RSL along the Atlantic coast. Comparison of the results for cases 1 and 3 indicates that the contribution from non-GIA processes to the VLM signal is minor.

At Rimouski, the projected regional mean SLR is consistently smaller after accounting for the VLM signal for any given projection year and SSP scenario. This behavior is evident in the median values (black horizontal lines in Figure 4.4) and reflects the effect of land uplift, resulting in RSL fall. The difference between projections that include VLM (cases 1 and 3) and those that exclude it (case 2) increases over time, from 2050 to 2150, reflecting the secular (linear) influence of VLM on RSL. As for Boston and Halifax, the results for cases 1 and 3 across all time horizons and SSPs are broadly consistent, indicating that GIA signal is the dominant contributor to VLM at this site. Moreover, the values of projected mean sea-level change at Rimouski show positive RSL under all projection cases and SSP scenarios, except in projection case 3 under SSP1-1.9, where the lower bound indicates a small sea-level fall of ~40 mm by 2150.

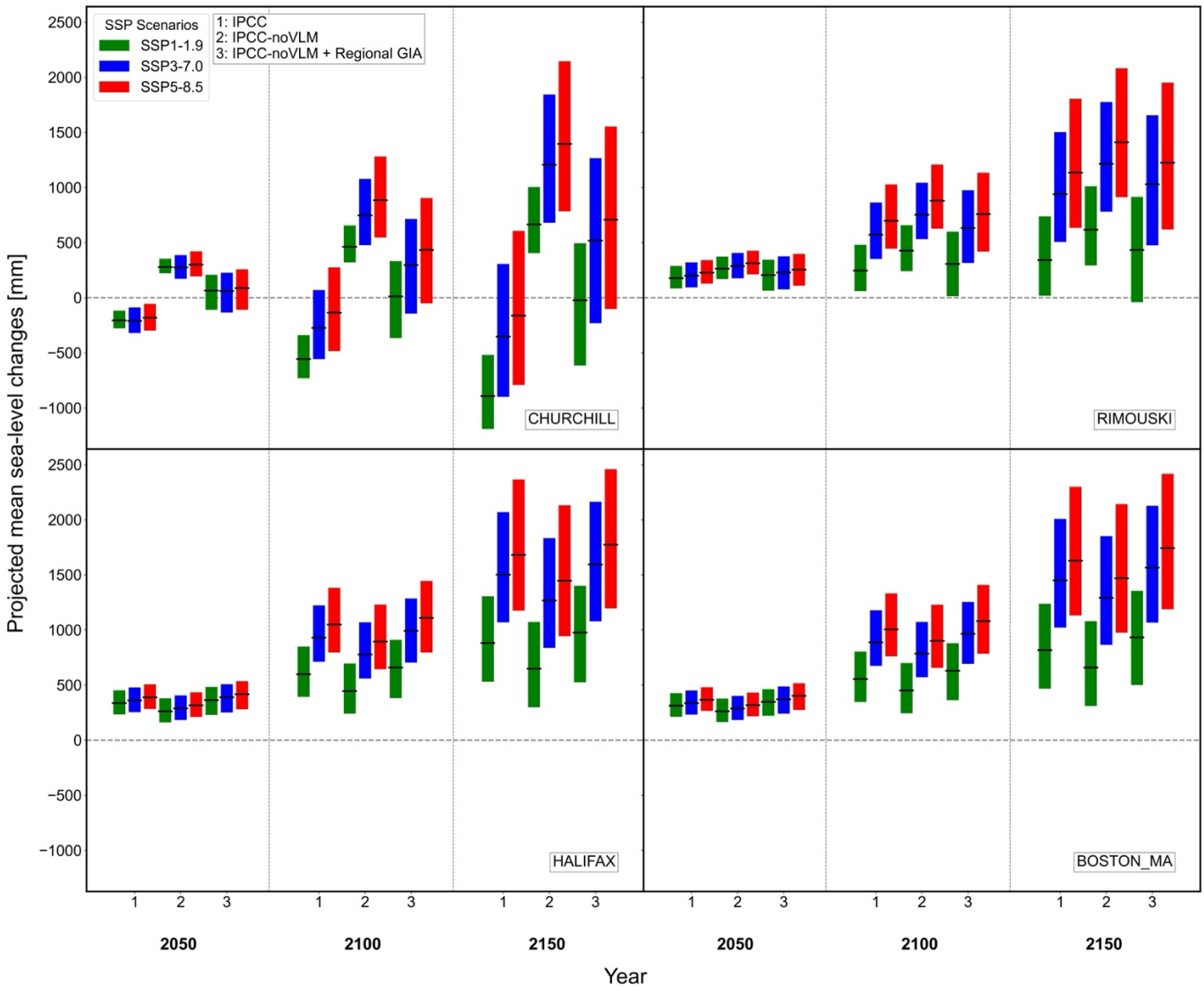


Figure 4.4. Projected regional mean sea-level changes (in mm) relative to the IPCC temporal baseline (1995–2014) at four representative tide gauges: Churchill (#1 in Figure 4.2), Rimouski (#7), Halifax (#11), and Boston (#17). Projections are shown for the years 2050, 2100, and 2150 under three SSP scenarios: SSP1-1.9 (green), SSP3-7.0 (blue), and SSP5-8.5 (red). For each year, results are presented for three projection cases: 1 = IPCC projections including all components (IPCC), 2 = IPCC projections excluding VLM (IPCC-noVLM), and 3 = IPCC projections excluding VLM but incorporating a regionally optimized GIA-induced VLM signal with uncertainty bounds (IPCC-noVLM + Regional GIA). All projections are provided with upper and lower 1σ uncertainty bars, and the median values are indicated by horizontal black lines within colored bars. Axis ranges are fixed across all panels to enable direct comparison among stations.

At Churchill, the largest impact of VLM on projected RSL for the sites considered is evident. The results for cases 1 and 3 show a striking contrast compared to those for case 2. This difference reflects the strong GIA signal at Churchill, which is situated near the thickest part of the ancient Laurentide Ice Sheet. The resulting land uplift dominates the regional sea-level trend at this site. For case 2 (no VLM), projections show positive SLR that increases over time from 2050 to 2150, both in the median and 1σ uncertainty ranges, for all three SSP scenarios. After incorporating the IPCC-based VLM signal (case 1, IPCC), the median values (black horizontal lines) of projected mean sea-level change are negative across all projection years and SSP scenarios. The lower bounds for case 1 remain negative across all years and scenarios, indicating the possibility of sea-level fall within uncertainty. When considering the

upper uncertainty bounds, values also remain negative except for SSP3-7.0 and SSP5-8.5 in 2100 and 2150, where a positive RSL is projected.

For case 3, the median values of projections for Churchill are positive for all SSPs and projection years, with one exception: SSP1-1.9 in 2150, which yields –23.6 mm. For instance, under SSP5-8.5 in 2150, the median value reaches approximately +707 mm. These results indicate that the projected mean SLR in case 3 is considerably larger than that in case 1, despite both accounting for VLM, highlighting differences in the VLM signal applied. When comparing case 3 to case 2, the projections under case 3 are significantly lower due to the effect of the GIA-induced VLM signal, which introduces a substantial RSL fall. However, they remain higher than those for case 1, indicating that the IPCC-based VLM signal (case 1) reflects stronger land uplift and thus greater RSL fall at Churchill than the regionally constrained GIA (case 3).

The IPCC-based VLM signal gives an RSL rate of about –10.7 ± 0.8 mm/yr. In contrast, our regionally optimized GIA model yields a rate of about –4.8 mm/yr, with uncertainty bounds of –8.4 mm/yr (lower) and –2 mm/yr (upper). The long-term trend from the tide gauge records (~1940-2020, based on PSMSL database) gives a rate of –8.8 mm/yr (see Figure 4.S4), which aligns closely with the lower bound of our GIA model (It should be noted that the trend shows a departure from linearity and may include non-GIA signals and fingerprints, such as steric sea-level changes). Additionally, as discussed in Chapter 3 (Sections 3.3.1.1 and 3.4), the average VLM rate derived from three nearby GPS stations is 9.661 ± 0.550 mm/yr, which is more consistent with the IPCC-based VLM estimate, particularly when considering the associated 1σ uncertainty. This highlights the discrepancy between the regionally optimized GIA signal and the IPCC-based VLM component, which, as discussed in Section 4.2.2, is derived as a regionally varying linear trend, estimated from tide gauge records using a Gaussian process model. This trend reflects GIA and other long-term non-climatic processes (global climate-driven sea-level signal is not included). Part of this discrepancy may stem from limitations in the GIA modeling. Specifically, the uncertainty estimates used in this study are derived using a Bayesian approach, which accounts for parametric uncertainty but does not capture structural uncertainty in the modeling (see Chapter 2 for alternative approaches). Moreover, although other potential contributors, such as hydrological mass changes, may influence contemporary VLM rates, our GRACE-based analysis (see Section 3.3.2 in Chapter 3) indicates no significant long-term change in total water storage over the period from April 2002 to November 2023. Given these considerations, the potential role of long-term non-GIA processes, including pre-GRACE hydrological mass changes, remains an open question and warrants further investigation.

Results for the remaining 10 Canadian tide gauges (Figure 4.S5) exhibit a pattern similar to those at Halifax. After accounting for the VLM signal (cases 1 and 3), the projected regional mean SLR is consistently larger than that derived for case 2. Also, the results for cases 1 and 3 are compatible, reflecting the dominance of GIA on VLM at these sites. Similar results are evident across the additional U.S. tide gauges (Figure 4.S6), which closely resemble those for Boston: higher projected SLR after accounting for the VLM signal, driven by RSL rise associated with, primarily, GIA-induced land subsidence. In contrast, the Sept Îles tide gauge (#5 in Figure 4.2), located within the St. Lawrence Corridor, displays a pattern closely resembling the projections at Rimouski. However, note that the median values of projections from case 3 are lower than those from case 1, which is opposite to the trend observed at Rimouski (and Churchill). However, the uncertainty bounds of case 3 capture the results from case 1, indicating general consistency between the two VLM modeling approaches used in projection cases 1 and 3.

4.3.2. Nuisance flooding

4.3.2.1 Historic baseline

To evaluate historical flood exposure, we estimated the frequency of nuisance flooding events over the 20-year IPCC temporal baseline (1995–2014) at each of the 25 tide gauges (Figure 4.2). The results presented here provide a baseline characterization of historical nuisance flooding frequency and are used as a reference for evaluating future changes in tide-sufficient flooding frequency under various projection scenarios. Nuisance flooding was observed at only 9 locations during the IPCC temporal baseline, highlighting spatial variability in historical tidal flood exposure. The highest cumulative frequencies were recorded at Rimouski (#7 in Figure 4.2, 579 days), Saint John (#13, 552 days), and Eastport (#14, 513 days), where frequent exceedance of local flood thresholds occurred over multiple years (Figure 4.5). In contrast to the more frequently affected stations, locations such as Portland (#16, 1 day) and Boston (#17, 13 days) experienced very few events, possibly due to higher local flood thresholds or lower tidal amplitudes.

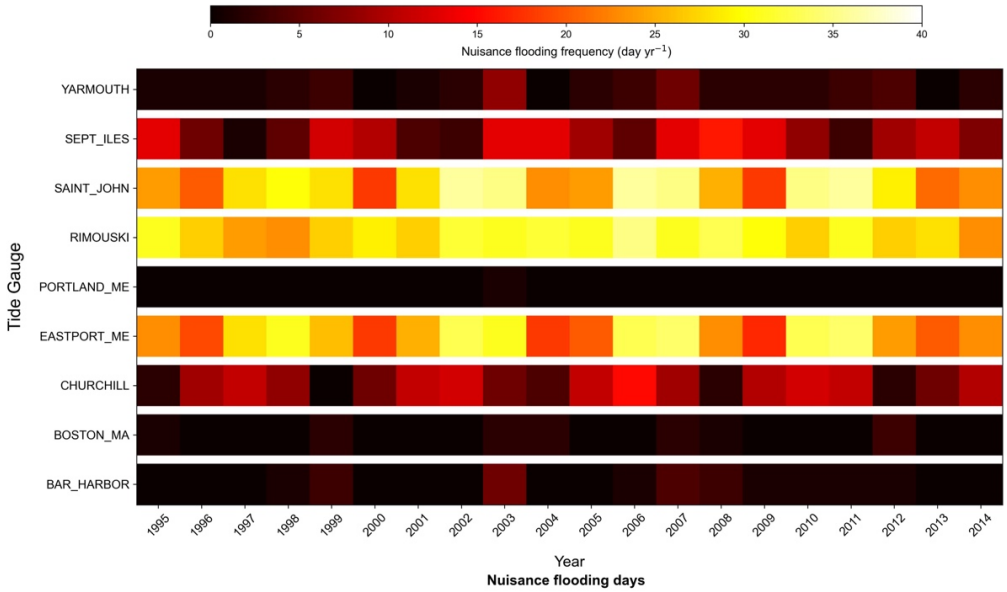


Figure 4.5. Year-by-year distribution of nuisance flooding frequency (days per year) at nine tide gauges from 1995 to 2014 (the IPCC temporal baseline). Colors indicate the number of nuisance flooding days per year, defined by the exceedance of local minor flood thresholds. Out of 25 tide gauges analyzed, only nine experienced nuisance flooding during this period.

4.3.2.2. Projections

Figure 4.6 presents the projected changes in annual nuisance flooding days, relative to the 2005 baseline year (midpoint of the IPCC temporal baseline of 1995–2014), under SSP1-1.9 for the nine tide gauges that experienced historical nuisance flooding over the baseline period (Figure 4.5). After accounting for the VLM signal (projection cases 1 and 3), the number of nuisance flooding days increases compared to projections that exclude VLM (case 2) for six Atlantic coast sites, including Boston (#17 in Figure 4.2), Portland (#16), Bar Harbor (#15), Eastport (#14), Saint John (#13), and Yarmouth (#12), due to GIA-induced land subsidence (see Section 4.3.1). Chronic nuisance flooding, defined as nuisance flooding occurring on 50 or more days per year (Gold et al., 2023; Hague et al.,

2023; Thompson et al., 2019), is projected to occur by 2050 at Boston, Bar Harbor, and Yarmouth under both cases 1 and 3, and at Portland under case 3. Eastport and Saint John, which had the highest baseline frequencies (see Figure 4.5 and Table 4.S2), are projected to experience chronic flooding under all three projection cases by 2050. The influence of VLM grows with time; for example, at Yarmouth, under projection case 3, nuisance flooding increases by ~20 days/year by 2050, ~70 days/year by 2100, and ~140 days/year by 2150. Furthermore, projections under case 3 generally show higher flood frequencies than IPCC, consistent with larger projected regional mean SLR in this case (see Section 4.3.1); differences can exceed 40 days/year (e.g., Portland in 2100 and 2150; Eastport and Saint John in 2150). By 2150, after accounting for the VLM signal, nuisance flooding frequency exceeds baseline values by more than 170 days per year at all six sites, surpassing 300 days per year at Boston, Portland, and Yarmouth after integration of the regional GIA signal from optimal models into the IPCC projections.

In contrast, at Rimouski (#7), Sept Îles (#5), and Churchill (#1), regions experiencing GIA-induced uplift, nuisance flooding frequencies decrease after accounting for the VLM signal. This reduction becomes more pronounced over time, reaching up to 130 fewer flooding days per year at Sept Îles under cases 1 and 3 by 2150. Notably, Churchill is projected to experience zero nuisance flooding days (baseline frequency: 11 days/year) under IPCC projections in all future time frames and under case 3 for both 2100 and 2150, due to the strong GIA-induced uplift signal. Although Rimouski is also projected to experience reductions in flooding frequency, it will still exceed the threshold for chronic flooding by 2050 (baseline: 31 days/year). The differences between cases 1 and 3 directly reflect the differences in regional mean sea-level projections (Section 4.3.1). For example, projections under case 3 at Rimouski are approximately 20 days per year higher than those under the IPCC in 2150, while at Sept Îles, case 3 projects roughly 8 fewer flood days per year.

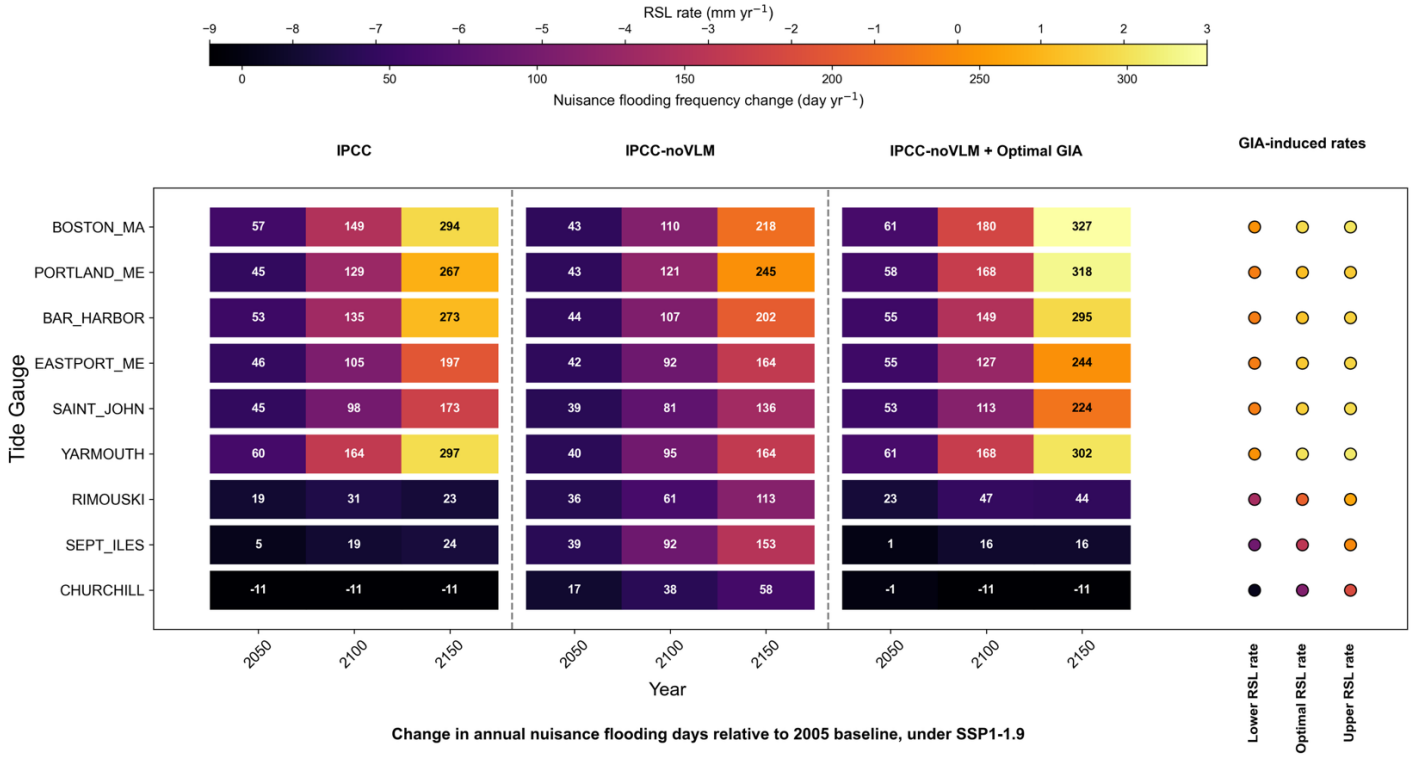


Figure 4.6. Projected change in annual nuisance flooding days (relative to the 2005) under SSP1-1.9 for the nine tide gauges that experienced historical nuisance flooding during the IPCC temporal baseline. Results are based on three projection cases: (1) IPCC (including all components), (2) IPCC-noVLM, and (3) IPCC-noVLM + Optimal GIA. Values are shown for the years 2050, 2100, and 2150. Positive values indicate an increase in nuisance flooding days relative to the baseline, while negative values indicate a decrease.

The right panel displays the present-day GIA-induced RSL rate at each station, based on optimal, lower, and upper bounds from regionally constrained GIA models.

The projection results for nuisance flooding frequency under SSP1-1.9 for the eight Canadian and eight U.S. tide gauges without historical nuisance flooding days during the IPCC temporal baseline are presented in Figures 4.7 and 4.8, respectively. All sites are located along the Atlantic coast, where regionally optimized GIA models indicate RSL rise due to GIA-induced land subsidence (see right side of the figure for optimal GIA-induced RSL rates). As a result, nuisance flooding is projected to occur at significantly higher frequencies in cases that incorporate the VLM signal (cases 1 and 3), relative to projections excluding VLM (case 2). For example, at sites in Canada, the largest increase for 2050 is observed at Halifax (#11 in Figure 4.2), where the frequency under case 3 is 34 days per year higher than case 2. By 2100, North Sydney exhibits over 220 more days per year of nuisance flooding in cases 1 and 3 relative to case 2. Rivière-au-Renard (#6) shows a notably smaller difference across projection cases, as its regionally constrained GIA model yields only ~0.35 mm/yr of RSL rise (the projected frequency in case 3 is just 8–32 days/year higher than case 2 across all projection years). None of the eight Canadian stations experience chronic nuisance flooding by 2050, but by 2100 all locations experience at least ~100 days/year, with North Sydney (#10) reaching 310 days. By 2150, most Canadian sites are projected to flood nearly every day of the year after accounting for VLM. In most cases, the projected frequency is higher under case 3 than under case 1 (e.g., a 10-day and 58-day increase at Halifax in 2050 and 2100, respectively, and a 61-day increase at St. John's in (#2) 2150), consistent with the relatively greater projected SLR discussed in Section 4.3.1. The minimum difference is observed at North Sydney, where cases 1 and 3 yield nearly identical frequencies from 2050 to 2150.

For the eight U.S. sites with no historical nuisance flooding, Montauk (#23), New London (#22), and Nantucket Island (#21) show zero nuisance flooding days in 2050 under case 2, but experience flooding when the VLM signal is included (up to 33 days/year at Nantucket Island in case 3). Chronic flooding is projected by 2050 at Bridgeport (#24), Newport (#19), and Providence (#18) under case 3, while under case 1 their frequencies remain just below the chronic threshold (35–41 days/year). The difference in projected flooding frequency between cases 2 and 3 exceeds 30 days per year by 2050 for many U.S. tide gauges and grows substantially by 2100, for example, over 250 days per year more at Montauk and New London. However, this difference narrows by 2150 as most sites reach the maximum flood frequency of 365 days per year. In comparison, the difference between cases 1 and 2 is smaller. In general, similar to the Canadian tide gauges shown in Figure 4.7, the projected frequencies after integration of the GIA-induced VLM signal into the projections exceed those from the IPCC (case 1).

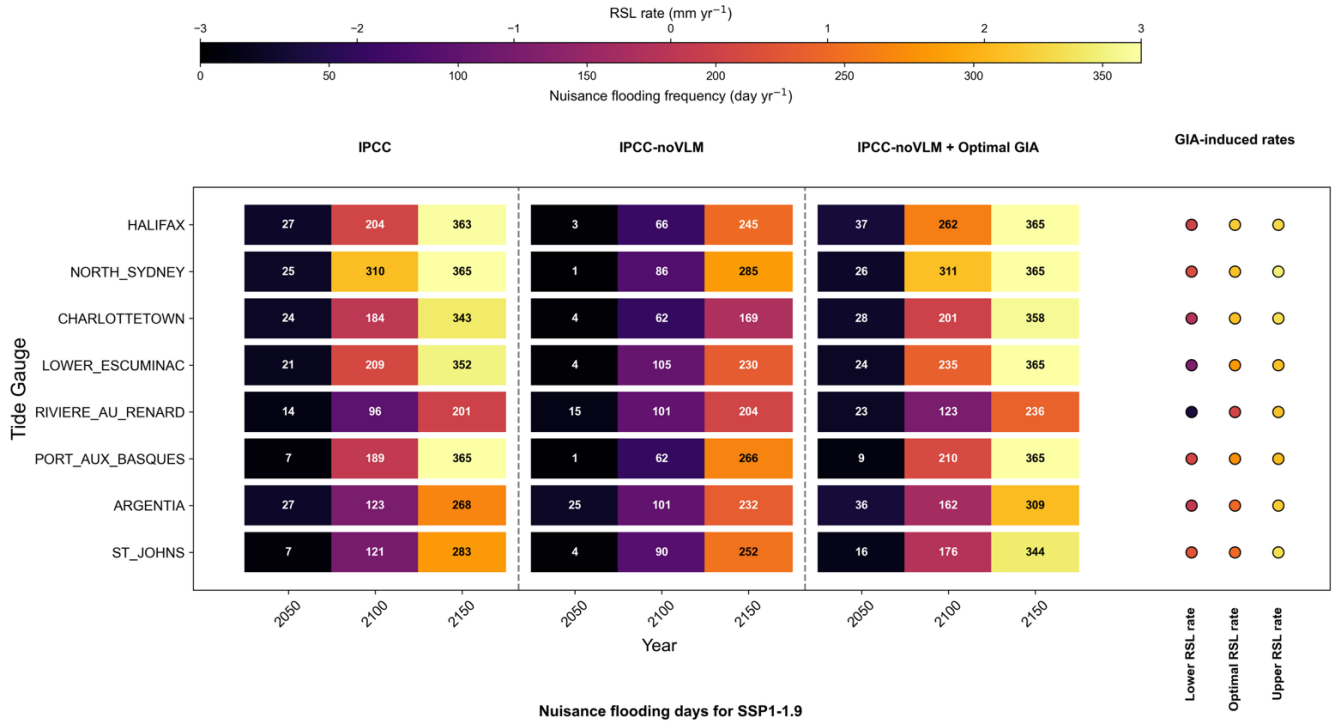


Figure 4.7. Projected annual nuisance flooding frequency (days per year) under SSP1-1.9 for the eight Canadian tide gauges that did not experience historical nuisance flooding over the IPCC temporal baseline (1995–2014). Results are shown for three projection cases: (1) IPCC (all components), (2) IPCC-noVLM (excluding VLM), and (3) IPCC-noVLM + Optimal GIA (excluding VLM but including regionally optimized GIA-induced VLM). Projections are presented for the years 2050, 2100, and 2150. The right panel shows the present-day GIA-induced RSL rate for each station based on optimal, lower, and upper bounds from regionally constrained GIA models.

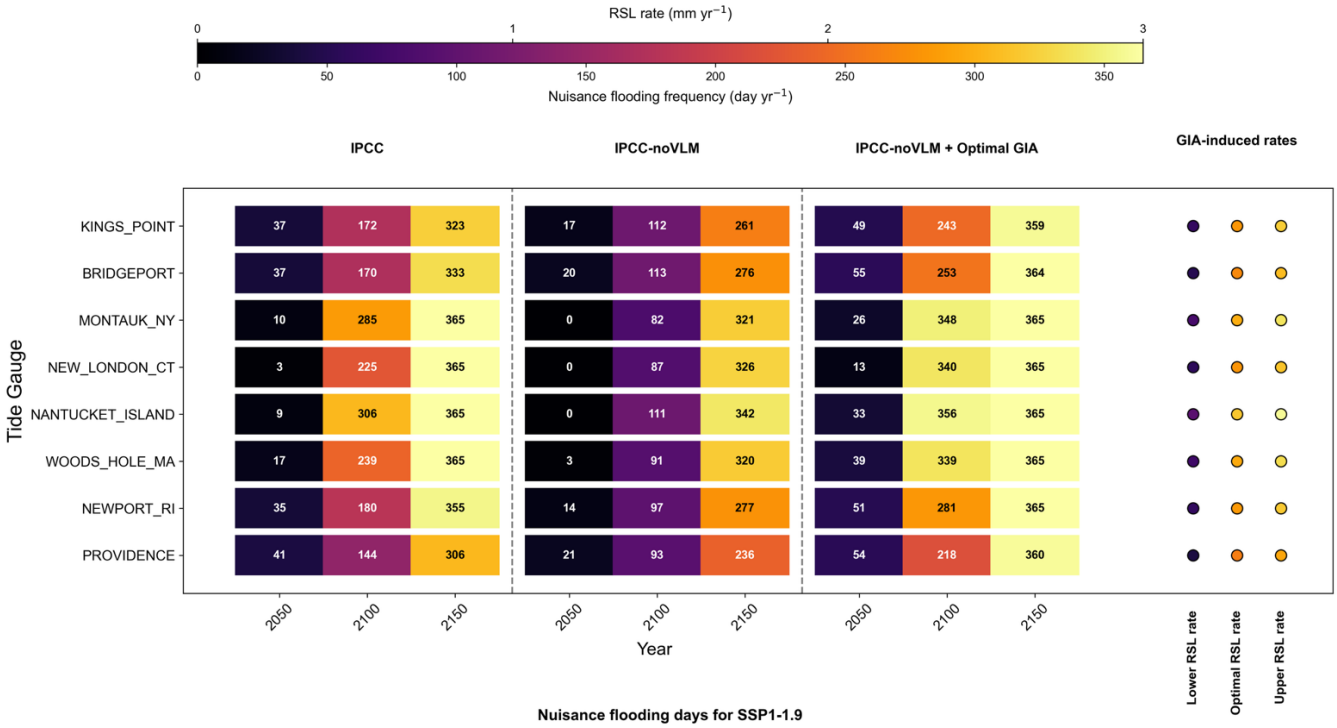


Figure 4.8. Projected annual nuisance flooding frequency (days per year) under SSP1-1.9 for the eight U.S. tide gauges that did not experience historical nuisance flooding over the IPCC temporal baseline (1995–2014). Results are shown for three projection

cases: (1) IPCC (all components), (2) IPCC-noVLM (excluding VLM), and (3) IPCC-noVLM + Optimal GIA (excluding VLM but including regionally optimized GIA-induced VLM). Projections are presented for the years 2050, 2100, and 2150. The right panel shows the present-day GIA-induced RSL rate for each station based on optimal, lower, and upper bounds from regionally constrained GIA models.

Figure 4.9 presents the projected changes in annual nuisance flooding days relative to the 2005 baseline under SSP3-7.0 for the nine tide gauges that experienced nuisance flooding over the IPCC temporal baseline. Consistent with the results discussed for SSP1-1.9 (see Figure 4.6), nuisance flooding frequency increases for the six tide gauges along the Atlantic coast (Boston, Portland, Bar Harbor, Eastport, Saint John, and Yarmouth) after accounting for the VLM signal under projection cases 1 (IPCC) and 3 (IPCC-noVLM + Optimal GIA), reflecting the GIA-induced RSL rise shown in the right-hand side of the figure. A similar trend is evident in projections under SSP5-8.5 (see Figure 4.S7). For a given projection year and case, projected nuisance flooding frequency increases progressively from SSP1-1.9 to SSP5-8.5, driven by a corresponding increase in regional mean SLR. Under SSP3-7.0, nuisance flooding becomes chronic by 2050 (≥50 days/year) at all six Atlantic tide gauges for projection cases 1 and 3. Moreover, by 2050 under SSP5-8.5, chronic flooding is projected at all six sites even under IPCC-noVLM (case 2), highlighting the growing impact of other contributors to SLR. For both SSP3-7.0 and SSP5-8.5, projected nuisance flooding frequency is consistently higher in case 3 than in case 1, due to the larger regional mean SLR associated with projection case 3 (see Section 4.3.1). For SSP3-7.0, flooding reaches and exceeds ~300 days/year by 2100 at Boston, Portland, Bar Harbor, and Yarmouth under cases 1 and 3. At Eastport and Saint John, nuisance flooding exceeds 200 days/year under the same conditions. By 2150, all six sites are projected to experience nuisance flooding on nearly every day of the year under both projection cases 1 and 3. Projections under SSP5-8.5 follow this trend. By 2100, nuisance flooding occurs almost daily at Boston, Portland, Bar Harbor, and Yarmouth under cases 1 and 3, and even under case 2 (IPCC-noVLM), flooding frequency exceeds 300 days/year at Boston, Portland, and Bar Harbor. By 2150, all six Atlantic tide gauges are projected to experience near-continuous flooding under all projection cases, regardless of whether VLM is included.

At the sites experiencing land uplift–Rimouski, Sept Îles, and Churchill–nuisance flooding occurs less frequently in projection cases 1 and 3 compared to projections excluding VLM (case 2), consistent with the SSP1-1.9 results. The strongest VLM signal is at Churchill, where projections under IPCC (case 1) indicate zero nuisance flooding for both SSP3-7.0 and SSP5-8.5 across all projected time frames. In contrast, under case 2 (IPCC-noVLM), projected nuisance flooding reaches ~300 days/year by 2150 for SSP3-7.0 and more than 200 days/year by 2100 for SSP5-8.5. Incorporating the regionally optimized GIA signal into IPCC-noVLM projections (case 3) results in projected nuisance flooding frequencies at Churchill of 1 day/year less than the baseline for SSP3-7.0 and no change for SSP5-8.5 by 2050. By 2100 under SSP3-7.0, flooding increases slightly (2 days/year more than baseline), and by 2150, reaches 18 days/year, still far below the IPCC-noVLM results. For SSP5-8.5, nuisance flooding increases to 30 days/year by 2100 and 74 days/year (relative to the baseline frequency) by 2150 under case 3. The largest discrepancy between cases 1 and 3 occurs under SSP5-8.5, reaching 41 days in 2100 and 85 days in 2150 (as discussed in Section 4.3.1, this discrepancy arises from differences in the applied VLM signal).

For Rimouski and Sept Îles, the nuisance flooding days significantly increase for SSP3-7.0 and SSP5-8.5 by 2100 compared to SSP1-1.9 under projection cases 1 and 3. For example, at Rimouski and Sept Îles, the projected frequency can be ~180 days and more than 200 days greater, respectively, by 2150 under SSP3-7.0 for both projection cases that incorporate the VLM signal. In addition, nuisance

flooding is projected to occur at least ~300 days/year under SSP5-8.5 after accounting for the VLM signal at both Rimouski and Sept Îles. Similar to the results for SSP1-1.9, the projected frequency under case 3 is relatively larger than that from case 1 for Rimouski and smaller for Sept Îles. This is consistent with the projected mean sea-level changes discussed in Section 4.3.1. The maximum difference is observed in 2150 under SSP3-7.0, where the projected frequency for Rimouski under case 3 is 32 days higher than under case 1, while for Sept Îles, it is 21 days lower.

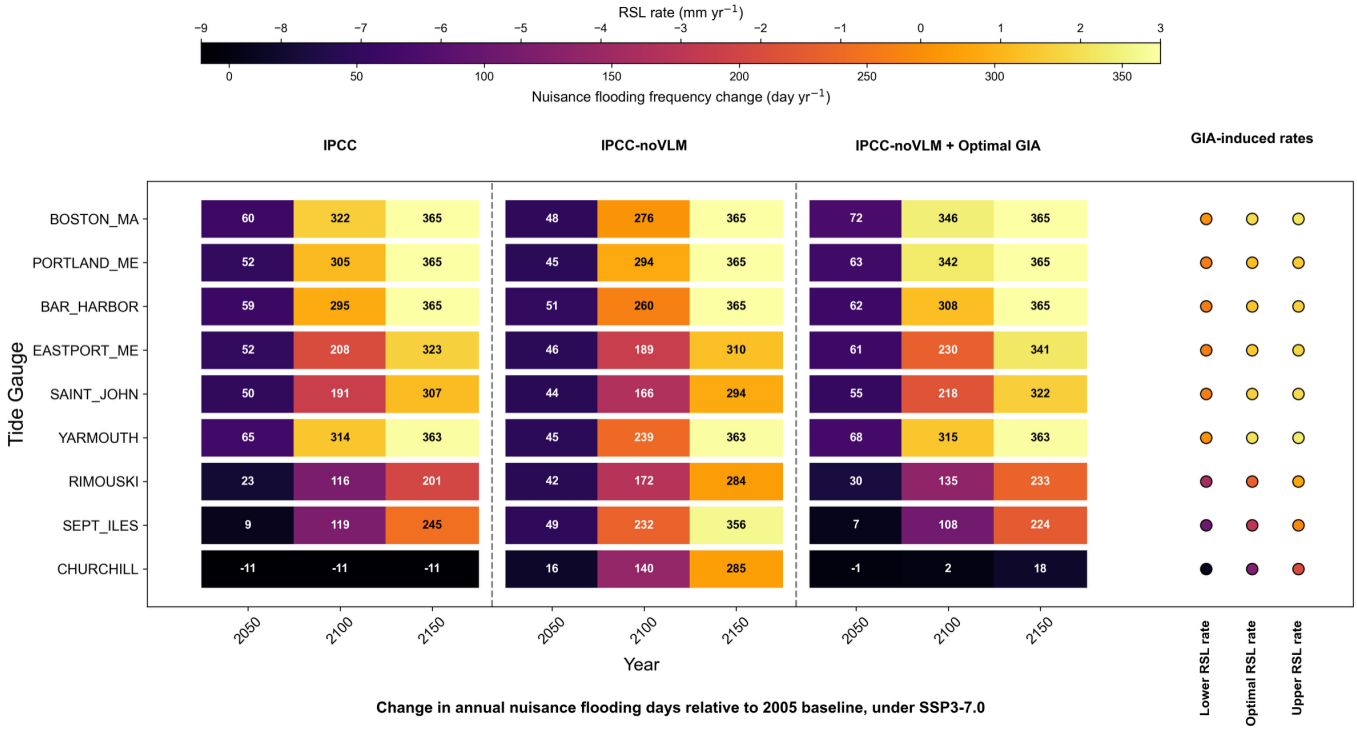


Figure 4.9. Projected change in annual nuisance flooding days (relative to the 2005 baseline) under SSP3-7.0 for the nine tide gauges that experienced historical nuisance flooding during the IPCC temporal baseline. Results are based on three projection cases: (1) IPCC (including all components), (2) IPCC-noVLM (excluding VLM), and (3) IPCC-noVLM + Optimal GIA (excluding VLM but incorporating regionally optimized GIA-induced VLM). Values are shown for the years 2050, 2100, and 2150. Positive values indicate an increase in nuisance flooding days relative to the baseline, while negative values indicate a decrease. The right panel displays the present-day GIA-induced RSL rate at each station, based on optimal, lower, and upper bounds from regionally constrained GIA models.

As shown in Figures 4.S8 and 4.S9, which present projections under SSP3-7.0 and SSP5-8.5, respectively, for Canadian tide gauges without historical nuisance flooding over the IPCC temporal baseline, nuisance flooding frequency increases substantially after accounting for the VLM signal (cases 1 and 3). At all eight analyzed Canadian tide gauges, chronic nuisance flooding does not occur under SSP3-7.0 across any projection case by 2050. However, under SSP5-8.5, chronic nuisance flooding is projected to occur at Halifax (#11 in Figure 4.2), North Sydney (#10), Charlottetown (#9), Lower Escuminac (#8), Argentia (#3), and St. John's (#2) when integrating the regionally optimized GIA signal into IPCC projections (under IPCC (case 1), only North Sydney reaches chronic flooding). For U.S. tide gauges without historical nuisance flooding, the same trend is observed under SSP3-7.0 and SSP5-8.5 (see Figures 4.S10 and 4.S11). Nuisance flooding does not occur at New London (#22) and Nantucket Island (#21) under SSP3-7.0 by 2050 when excluding VLM (case 2), whereas projections incorporating VLM (cases 1 and 3) show frequencies of 7–46 days per year. As indicated in Figures 4.S10 and 4.S11, nuisance flooding is projected to be chronic by 2050 at Kings Point (#25), Bridgeport (#24), Woods Hole (#20), Newport (#19), and Providence (#18) under SSP3-7.0 for

projection case 3, and at all eight U.S. sites by 2050 under SSP5-8.5. Under IPCC projections (case 1) for SSP5-8.5, chronic flooding is expected by 2050 at Kings Point, Bridgeport, Newport, and Providence. In addition, for both SSP3-7.0 and SSP5-8.5, nuisance flooding is projected to occur nearly every day of the year by 2100 across all Canadian and U.S. tide gauges without historical nuisance flooding, regardless of whether VLM is included in the projections.

To assess the uncertainty in projected nuisance flooding frequency, all projections discussed throughout this study are provided with corresponding upper and lower uncertainty bounds. These bounds are derived from the uncertainty in projected regional mean sea-level changes for a given SSP scenario and time frame under each projection case: (1) IPCC, (2) IPCC-noVLM, and (3) IPCC-noVLM + Regional GIA (see Section 4.2.2). Figure 4.10 presents the lower bound of projected changes in annual nuisance flooding days (relative to the baseline) under SSP1-1.9 for nine tide gauges with historical nuisance flooding, derived from the lower bound of projected regional mean sea-level change for each projection case. Similarly, Figures 4.11 and 4.S12 show the upper bounds of projected changes in nuisance flooding frequency under SSP3-7.0 and SSP5-8.5, respectively, also based on the upper bounds of regional mean sea-level projections. If each uncertainty bound is considered separately, a consistent trend is observed with the findings discussed for Figures 4.6, 4.9, and 4.S7: after accounting for the VLM signal through projection cases 1 and 3, the frequency of nuisance flooding increases at the six Atlantic tide gauges where GIA-induced RSL rise occurs and decreases at Rimouski (#7), Sept Îles (#5), and Churchill (#1) due to GIA-induced RSL fall, relative to the IPCC-noVLM projection case. The projected median (optimal) nuisance flooding frequencies lie within the lower and upper uncertainty bounds presented in Figures 4.10, 4.11, and 4.S12.

The uncertainty range of the projected frequency inferred from the integration of GIA-induced VLM into the IPCC-noVLM projections (projection case 3) broadly captures the range of the IPCC projection case. The upper bounds (Figures 4.11 and 4.S12) indicate that nuisance flooding will reach at least ~300 days per year by 2100 at all sites except Churchill. At Churchill, the lower bound for both cases that include VLM indicates zero nuisance flooding frequency for all time frames. Moreover, the upper bound under SSP3-7.0 (Figure 4.11) for the IPCC case also projects zero nuisance flooding, while case 3 projects 120 and 300 days per year by 2100 and 2150, respectively. As discussed in Section 4.3.1, this discrepancy stems from the differing VLM estimates. Despite this, the uncertainty range of case 3 encompasses both the projected median values and the uncertainty range, though the upper bounds for 2100 and 2150 show considerable spread due to the cumulative effect of the linearly applied VLM signal. In contrast, the uncertainty range is narrower for 2050. For example, the upper bound for case 3 shows a projected increase of 12 and 15 nuisance flooding days at Churchill by 2050 under SSP3-7.0 and SSP5-8.5, respectively. The upper bound under SSP5-8.5 (Figure 4.S12) projects chronic nuisance flooding (≥50 days/year) at Churchill by 2150 for the IPCC projection. Projections of the upper and lower bounds for U.S. and Canadian tide gauges without historical nuisance flooding are shown in Figures 4.S13, 4.S14, and 4.S15.

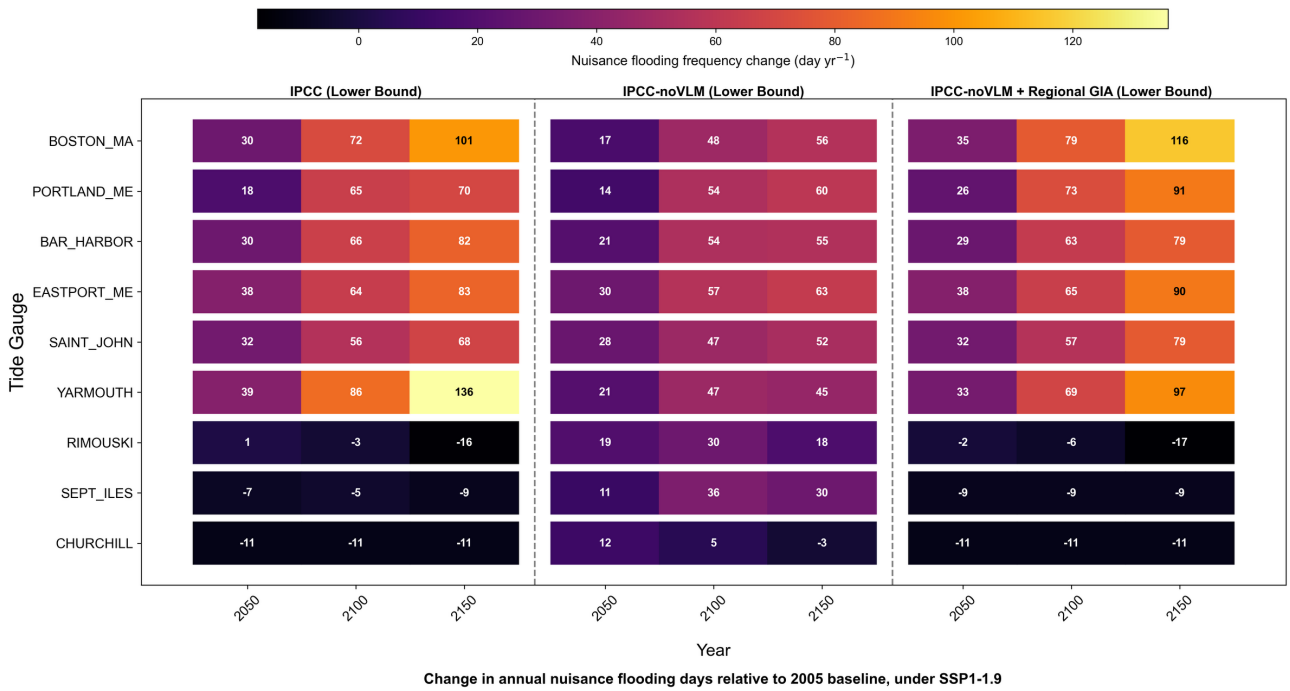


Figure 4.10. Lower bound of projected changes in annual nuisance flooding days (relative to the 2005 baseline) under SSP1-1.9 for the nine tide gauges with historical nuisance flooding over the IPCC temporal baseline. Estimates correspond to the lower bound of projected regional mean sea-level change for each projection case: (1) IPCC, (2) IPCC-noVLM, and (3) IPCC-noVLM + Regional GIA. Projected changes are shown for the years 2050, 2100, and 2150. Positive values indicate an increase in nuisance flooding days relative to the baseline, while negative values indicate a decrease.

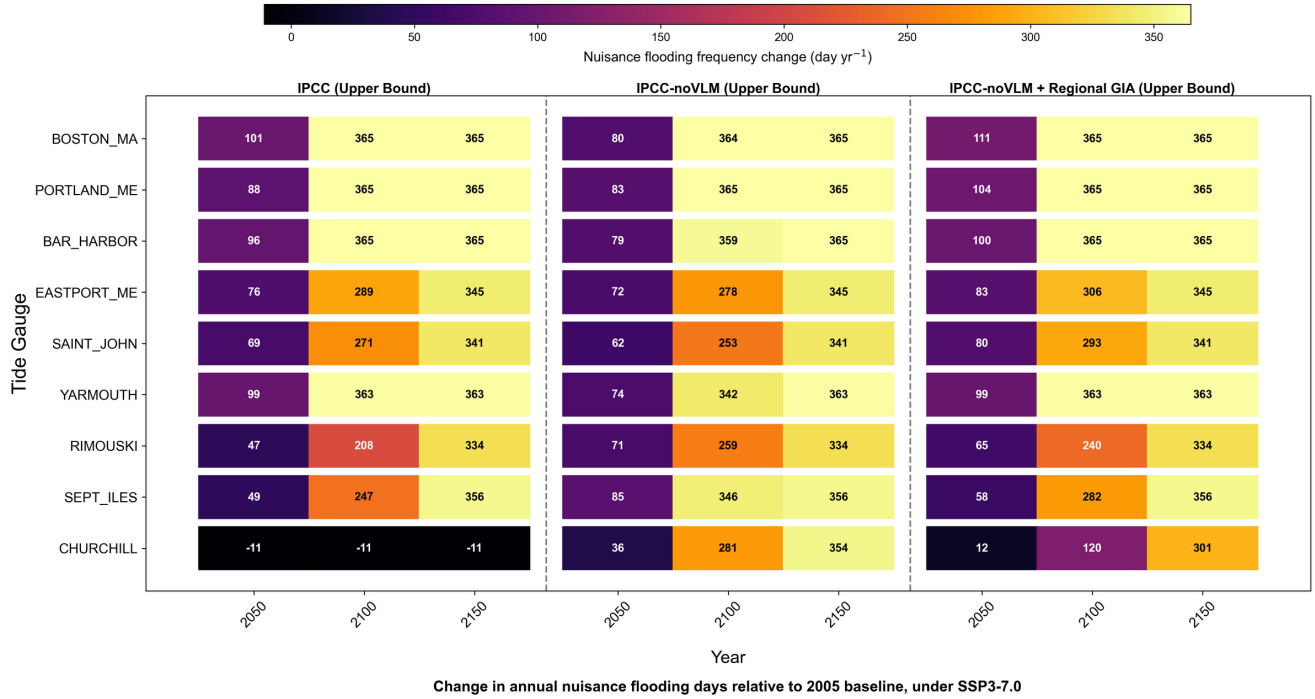


Figure 4.11. Upper bound of projected changes in annual nuisance flooding days (relative to the 2005 baseline) under SSP3-7.0 for the nine tide gauges with historical nuisance flooding over the IPCC temporal baseline. Estimates are based on the upper bound of projected regional mean sea-level change under each projection case: (1) IPCC, (2) IPCC-noVLM, and (3) IPCC-noVLM + Regional GIA. Projected changes are shown for the years 2050, 2100, and 2150. Positive values indicate an increase in nuisance flooding days relative to the baseline, while negative values indicate a decrease.

4.4. General discussion

Projections demonstrate that accounting for VLM significantly increases future SLR and nuisance flooding frequency at Atlantic sites experiencing GIA-induced subsidence. At locations with historical nuisance flooding, the projected frequency under cases 1 and 3 reaches chronic flooding levels (≥50 days/year) by 2050 under SSP1-1.9. Projections under case 3 are often higher than those under case 1 (IPCC), reflecting the relatively greater regional mean SLR (land subsidence) when using the optimized GIA signal. In contrast, at Rimouski, Sept Îles, and Churchill, accounting for the VLM signal reduces future flood frequencies. At Churchill, nuisance flooding does not occur under the IPCC projection and remains minimal under the GIA-integrated case, but reaches as high as 140 days/year under SSP3-7.0 by 2100 in the no-VLM scenario (case 2). This reflects the dominant influence of the GIA signal at this location, where the discrepancy between the IPCC-based and regionally optimized GIA-induced VLM signals results in differences in flood projections of over 80 days/year by 2150 under SSP5-8.5. Uncertainty analysis further supports these findings. Compared to previous studies (Hague et al., 2023; Ray & Foster, 2016), our analysis presents projected mean sea-level changes and nuisance flooding frequencies with 1σ upper and lower uncertainty bounds for each projection case and scenario. The uncertainty range associated with our GIA-based projections is relatively broader than that of the IPCC, due to the larger uncertainty in the GIA signal, especially at sites like Churchill, where the GIA signal is strong. The GIA-integrated projection case (case 3) effectively captures the range of flood frequency outcomes (and regional mean sea-level changes) from the IPCC projection.

The solar annual (SA) and solar semiannual (SSA) constituents are small tidal constituents directly generated by the nonuniform changes in the Sun's declination and distance (Pugh & Woodworth, 2014). They are included in the harmonic analysis to represent the seasonal variation of mean sea level predicted by tidal theory but are more closely related to seasonal changes in weather. To minimize the influence of climate seasonality on the seasonal signals associated with SA and SSA, we first computed residuals. These residuals were calculated by subtracting predicted tidal levels from observed water levels at each tide gauge. These predictions were based on all applied tidal constituents except SA and SSA and included local nodal modulations for the M2, N2, and K1 constituents. Next, we reconstructed the SA and SSA tidal signals using the FES2014 global tide model (Lyard et al., 2021) and subtracted these model-derived SA and SSA values from the initial residuals. This process provided adjusted residuals showing the remaining non-astronomical climate seasonality signal (e.g., effects of freshwater inflow and atmospheric pressure). Finally, we removed these adjusted residuals from the original observations to produce still water-level observations with reduced climate seasonality impact. Figure 4.12 shows the nuisance flooding frequency over the baseline period (1995–2014) at nine tide gauges based on observations with reduced climate seasonality. At all sites, the changes in flooding days are negligible (c.f. Figure 4.5), with a maximum difference of one day in the 2005 baseline year. The exception is Churchill, where the baseline frequency decreases from 11 days to 4 days after reducing climate seasonality, likely due to strong seasonal signals driven by spring/summer freshwater discharge and atmospheric loading. This sensitivity is also reflected in future projections. As shown in Figure 4.S16, under SSP3-7.0 the projected nuisance flooding frequency remains largely unchanged for eight of the nine tide gauges after minimizing the impact of climate seasonality, compared to the results based on the original observations (see Figure 4.9). However, at Churchill, the difference in projected flooding reaches 19 days by 2150 under case 3, even though flooding remains absent for all years under the IPCC projection. For Canadian and U.S. tide gauges without historical nuisance flooding (see Figures 4.S17 and 4.S18), the differences in projected frequency after reducing climate seasonality are generally

minor. However, two sites, North Sydney and St. John's, show larger impacts (~20 days by 2150 under SSP3-7.0).

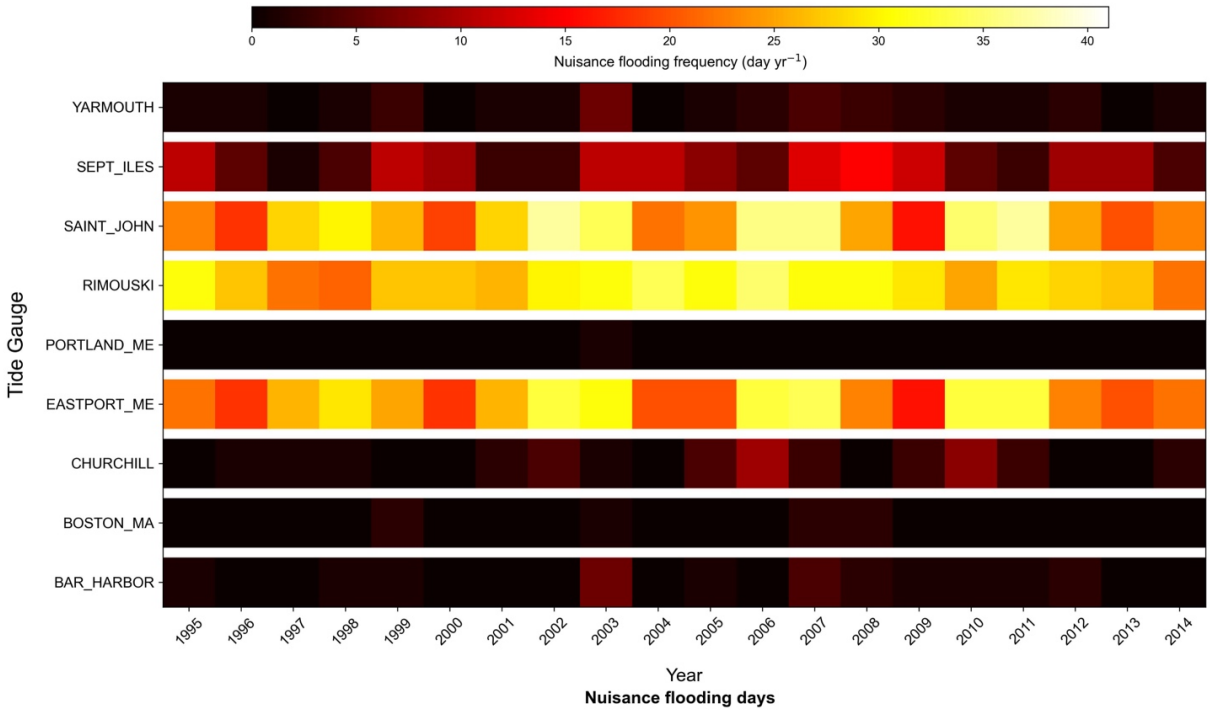


Figure 4.12. Nuisance flooding frequency (days per year) from 1995 to 2014 (IPCC temporal baseline) for the nine tide gauges considered in Figure 4.5, based on water level observations with reduced climate seasonality impact on SA and SSA using FES2014. The largest change is observed at Churchill, where the number of flooding days in 2005 decreases from 11 to 4 after reducing climate seasonality. Changes at the other tide gauges are negligible (c.f. Figure 4.5).

The results of our study show that some regions with historical nuisance flooding may experience zero or reduced flooding in the future due to the counteracting effect of VLM on SLR. This finding contrasts with the results from Hague et al. (2023), which assume SLR at all tide gauges, leading to an increase in nuisance flooding frequency at all locations. In contrast, by incorporating the regionally variable VLM signal, our analysis indicates locations with strong GIA-induced uplift, such as in Hudson Bay (e.g., Churchill), reduces or eliminates risk of nuisance flooding. In addition, tide gauges without historical nuisance flooding may experience chronic nuisance flooding in the future as a result of GIA-induced land subsidence. This pattern is evident at sites along the Atlantic coast of Canada and the northeastern United States, such as Boston and Halifax, where land subsidence amplifies SLR and increases the frequency of projected nuisance flooding. In addition to accounting for VLM, our results improve on Hague et al. (2023) by accounting for site-specific nodal corrections and secular changes in major tidal constituents. These improvements produce significant differences in the results. For instance, at Halifax, Hague et al. (2023) report 51 and 360 minor flooding days for 0.36 m and 0.93 m of SLR, respectively, with 19 days and all 360 days categorized as minor tide-sufficient flooding days. These SLR values are comparable to the projected mean sea-level changes under SSP3-7.0 in our analysis by 2050 and 2100, respectively. Our results show that these same SLR values correspond to 36 nuisance flooding days by 2050 (slightly reduced to 32 days after minimizing the climate seasonality impact on SA and SSA) and 365 days by 2100. Additionally, our projections for Churchill indicate zero nuisance flooding under the IPCC projection (case 1) and zero or only a few flooding days under the GIA-integrated projection (case 3). This differs considerably from the estimates by Hague et al. (2023),

in which minor tide-sufficient flooding at Churchill can occur up to 300 days per year with continuous SLR up to 1 m.

This study addresses a key knowledge gap regarding the evolution of nuisance flooding in eastern Canada, particularly in the context of VLM and GIA. Building on this research, future work could enhance the findings in several aspects. Extending the analysis beyond the IPCC temporal baseline of 1995–2014 to include the full historical record at each tide gauge station would allow for a more comprehensive assessment of long-term nuisance flooding trends and their temporal evolution, as demonstrated by Li et al. (2021) for the U.S. coastline. In addition, while this study used a regression-based scheme developed by Sweet et al. (2018) to define flood thresholds–based on parameters derived from tidal harmonic analysis–this approach is suited to gauged sites and may not fully capture localized variability or be easily transferable to ungauged regions. To address this limitation, future work could explore the use of machine learning approaches to estimate flood thresholds at ungauged sites across by applying multiple predictor variables (Mahmoudi et al., 2024). Furthermore, incorporating uncertainty into flood threshold estimation would improve the representation of local conditions. One promising direction is the use of hierarchical Bayesian models (Piecuch et al., 2025).

Our model outputs are particularly valuable in regions with sparse tide gauge coverage within GIA-active areas. While IPCC-based VLM estimates rely on tide gauge availability and are derived from spatio-temporal statistical modeling of long-term observational trends, the integration of regionally constrained GIA models (including optimal values and uncertainty bounds) into the IPCC estimates through our analysis enables accounting for the VLM signal in projections at any region of interest, including coastal and high-risk areas lacking sufficient observational data (e.g., GNSS and tide gauges). This capability is crucial for providing local mitigation strategies and long-term coastal planning. It should also be noted that our study is limited to projections of tide-sufficient flooding. Future work should consider surge-driven flooding, which, when combined with tidal and mean sea-level changes, could further exacerbate coastal flood risk in various regions.

4.5. Conclusion

This study highlights the critical role of the GIA signal in VLM across eastern North America and its consequent influence on projections of regional mean sea-level change and nuisance flooding frequency. Our analysis, based on a suite of projection cases and scenarios, demonstrates that GIA is the dominant contributor to the long-term VLM signal in the study region, and its inclusion (or exclusion) has a substantial impact on both regional sea-level projections and estimates of nuisance flooding exposure at 25 tide gauge locations. Overall, the applied regionally optimized GIA models yield VLM signals that generally align with IPCC-based VLM estimates, with differences largely falling within their respective uncertainty bounds.

The results of regional mean sea-level projections across 25 tide gauges highlight the spatial variability in the influence of VLM, particularly the contribution from the GIA signal. At most locations, especially along the Atlantic coast of Canada and the U.S., GIA-driven land subsidence leads to higher projected SLR when VLM is incorporated, as shown in projection cases 1 and 3. In contrast, locations situated within or near the former ice sheet core, such as Churchill, Rimouski, and Sept Îles, exhibit the opposite behavior, with GIA-induced uplift producing lower projected mean sea-level changes relative to scenarios that exclude VLM. The integration of GIA-induced VLM slightly increases the projected sea-level change at many sites. Even small differences in median sea-level

projections, despite falling within the uncertainty bounds, can affect the projected frequency of nuisance flooding, particularly at locations sensitive to threshold exceedance.

As discussed in Section 4.3.1, projections at Churchill show the largest sensitivity to the impact of VLM signal. Projections that exclude VLM (case 2) show increasing SLR through 2150 across all SSPs, while those that incorporate VLM (cases 1 and 3) indicate dominant RSL fall. Under case 1, median (optimal) and lower bounds of sea-level change are negative for all years and SSPs, with upper bounds remaining negative except under SSP3-7.0 and SSP5-8.5 in 2100 and 2150. In contrast, projections based on the regionally optimized GIA signal (case 3) yield higher sea-level values than case 1, with median values mostly positive, highlighting the influence of the applied VLM rate: the IPCC estimate implies ~10.7 ± 0.8 mm/yr RSL fall, while the GIA model yields –4.8 mm/yr (range: –8.4 to –2 mm/yr). This divergence may reflect structural uncertainty in GIA modeling, which is not captured in the applied uncertainty estimates, and potential long-term non-GIA processes (e.g., pre-GRACE hydrological mass changes), which require further investigation.

Our nuisance flooding projections indicate that, for Atlantic tide gauges with historical nuisance flooding, flooding frequency increases significantly after accounting for VLM (projection cases 1 and 3). Chronic flooding (≥50 days/year) is projected by 2050 at several locations under SSP1-1.9 (e.g., Boston, Bar Harbor, and Yarmouth in both cases 1 and 3). By 2150, after accounting for the VLM signal, nuisance flooding frequency exceeds baseline values by more than 170 days/year at all six sites. These increases reflect GIA-induced RSL rise from forebulge collapse and land subsidence. Moreover, projections from case 3 often yield higher flood frequencies than those from case 1, with differences exceeding 40 days/year at some stations by 2150. In contrast, tide gauges located near the former Laurentide Ice Sheet center, including Rimouski, Sept Îles, and Churchill, show reduced future nuisance flooding frequency under cases 1 and 3 due to GIA-induced RSL fall. Churchill is projected to experience zero flooding days under IPCC projections in all future timeframes and under case 3 in both 2100 and 2150. At Rimouski, despite overall reductions relative to case 2, projections still exceed the chronic flooding threshold by 2050. At Canadian and U.S. tide gauges without historical nuisance flooding during the baseline, flooding frequencies are projected to increase substantially after accounting for the VLM signal. In Canada, all eight analyzed tide gauges reach ~100 days/year or more by 2100 under SSP1-1.9 after accounting for the VLM signal. For U.S. stations, nuisance flooding is projected to become chronic by 2050 at sites such as Bridgeport, Newport, and Providence under case 3. Uncertainty analysis confirms that projected nuisance flooding frequencies increase or decrease consistently based on the inclusion of VLM and the GIA signal. Uncertainty bounds widen for longer projection horizons (e.g., 2100 and 2150), particularly under projection case 3 due to the larger uncertainty in the GIA signal. The uncertainty bounds of the GIA-integrated projections broadly capture the range of IPCC projections.

References

Allison, M., Yuill, B., Törnqvist, T., Amelung, F., Dixon, T., Erkens, G., et al. (2016). Global Risks and Research Priorities for Coastal Subsidence. *Eos*, *97*. https://doi.org/10.1029/2016EO055013

Amin, M. (1985). Temporal variations of tides on the west coast of Great Britain. *Geophysical Journal International*, *82*(2), 279–299. https://doi.org/10.1111/j.1365-246X.1985.tb05138.x

Codiga, D. L. (2011). Unified tidal analysis and prediction using the utide matlab functions. *Technical Report, Graduate School of Oceanography, University of Rhode Island*.

Devlin, A. T., Jay, D. A., Zaron, E. D., Talke, S. A., Pan, J., & Lin, H. (2017). Tidal Variability Related to Sea Level Variability in the Pacific Ocean. *Journal of Geophysical Research: Oceans*, *122*(11), 8445–8463. https://doi.org/10.1002/2017JC013165

Dmitrenko, I. A., Volkov, D. L., Stadnyk, T. A., Tefs, A., Babb, D. G., Kirillov, S. A., et al. (2021). Atmospherically forced sea-level variability in western Hudson Bay, Canada. *Ocean Science*, *17*(5), 1367–1384. https://doi.org/10.5194/os-17-1367-2021

Ezer, T., & Atkinson, L. P. (2014). Accelerated flooding along the U.S. East Coast: On the impact of sea-level rise, tides, storms, the Gulf Stream, and the North Atlantic Oscillations. *Earth's Future*, *2*(8), 362–382. https://doi.org/10.1002/2014EF000252

Farr, T. G., Rosen, P. A., Caro, E., Crippen, R., Duren, R., Hensley, S., et al. (2007). The Shuttle Radar Topography Mission. *Reviews of Geophysics*, *45*(2). https://doi.org/10.1029/2005RG000183

Feng, X., Tsimplis, M. N., & Woodworth, P. L. (2015). Nodal variations and long-term changes in the main tides on the coasts of <scp>C</scp> hina. *Journal of Geophysical Research: Oceans*, *120*(2), 1215–1232. https://doi.org/10.1002/2014JC010312

Fox-Kemper, B., Hewitt, H. T., Xiao, C., Aðalgeirsdóttir, G., Drijfhout, S. S., Edwards, T. L., et al. (2023). Ocean, Cryosphere and Sea Level Change. In *Climate Change 2021 – The Physical Science Basis* (pp. 1211–1362). Cambridge University Press. https://doi.org/10.1017/9781009157896.011

Gold, A., Anarde, K., Grimley, L., Neve, R., Srebnik, E. R., Thelen, T., et al. (2023). Data From the Drain: A Sensor Framework That Captures Multiple Drivers of Chronic Coastal Floods. *Water Resources Research*, *59*(4). https://doi.org/10.1029/2022WR032392

Govorcin, M., Bekaert, D. P. S., Hamlington, B. D., Sangha, S. S., & Sweet, W. (2025). Variable vertical land motion and its impacts on sea level rise projections. *Science Advances*, *11*(5). https://doi.org/10.1126/sciadv.ads8163

Greenan, B. J. W., James, T. S., Loder, J. W., Pepin, P., Azetsu-Scott, K., Ianson, D., et al. (2019). Changes in oceans surrounding Canada. *Chapter 7 in (Eds.) Bush and Lemmen, Canada's Changing Climate Report, Government of Canada, Ottawa, Ontario*, 343–423.

Hagen, R., Plüß, A., Jänicke, L., Freund, J., Jensen, J., & Kösters, F. (2021). A Combined Modeling and Measurement Approach to Assess the Nodal Tide Modulation in the North Sea. *Journal of Geophysical Research: Oceans*, *126*(3). https://doi.org/10.1029/2020JC016364

Hague, B. S., McGregor, S., Jones, D. A., Reef, R., Jakob, D., & Murphy, B. F. (2023). The Global Drivers of Chronic Coastal Flood Hazards Under Sea-Level Rise. *Earth's Future*, *11*(8). https://doi.org/10.1029/2023EF003784

Haigh, I. D., Eliot, M., & Pattiaratchi, C. (2011). Global influences of the 18.61 year nodal cycle and 8.85 year cycle of lunar perigee on high tidal levels. *Journal of Geophysical Research*, *116*(C6), C06025. https://doi.org/10.1029/2010JC006645

Hamlington, B. D., Gardner, A. S., Ivins, E., Lenaerts, J. T. M., Reager, J. T., Trossman, D. S., et al. (2020). Understanding of Contemporary Regional Sea-Level Change and the Implications for the Future. *Reviews of Geophysics*, *58*(3). https://doi.org/10.1029/2019RG000672

Holgate, S. J., Matthews, A., Woodworth, P. L., Rickards, L. J., Tamisiea, M. E., Bradshaw, E., et al. (2012). New Data Systems and Products at the Permanent Service for Mean Sea Level. *Journal of Coastal Research*, *29*(3), 493–504. https://doi.org/10.2112/JCOASTRES-D-12-00175.1

IMBIE team. (2018). Mass balance of the Antarctic Ice Sheet from 1992 to 2017. *Nature*, *558*(7709), 219–222. https://doi.org/10.1038/s41586-018-0179-y

Intergovernmental Panel on Climate Change (IPCC). (2023). *Climate Change 2021 – The Physical Science Basis*. Cambridge University Press. https://doi.org/10.1017/9781009157896

Jevrejeva, S., Frederikse, T., Kopp, R. E., Le Cozannet, G., Jackson, L. P., & van de Wal, R. S. W. (2019). Probabilistic Sea Level Projections at the Coast by 2100. *Surveys in Geophysics*, *40*(6), 1673–1696. https://doi.org/10.1007/s10712-019-09550-y

Karegar, M. A., Dixon, T. H., & Malservisi, R. (2015). A three-dimensional surface velocity field for the Mississippi Delta: Implications for coastal restoration and flood potential. *Geology*, *43*(6), 519–522. https://doi.org/10.1130/G36598.1

Karegar, M. A., Dixon, T. H., Malservisi, R., Kusche, J., & Engelhart, S. E. (2017). Nuisance Flooding and Relative Sea-Level Rise: the Importance of Present-Day Land Motion. *Scientific Reports*, *7*(1), 11197. https://doi.org/10.1038/s41598-017-11544-y

Kopp, R. E., Horton, R. M., Little, C. M., Mitrovica, J. X., Oppenheimer, M., Rasmussen, D. J., et al. (2014). Probabilistic 21st and 22nd century sea-level projections at a global network of tide-gauge sites. *Earth's Future*, *2*(8), 383–406. https://doi.org/10.1002/2014EF000239

Kopp, R. E., DeConto, R. M., Bader, D. A., Hay, C. C., Horton, R. M., Kulp, S., et al. (2017). Evolving Understanding of Antarctic Ice-Sheet Physics and Ambiguity in Probabilistic Sea-Level Projections. *Earth's Future*, *5*(12), 1217–1233. https://doi.org/10.1002/2017EF000663

Ku, L.-F., Greenberg, D. A., Garrett, C. J. R., & Dobson, F. W. (1985). Nodal Modulation of the Lunar Semidiurnal Tide in the Bay of Fundy and Gulf of Maine. *Science*, *230*(4721), 69–71. https://doi.org/10.1126/science.230.4721.69

Kulp, S. A., & Strauss, B. H. (2019). New elevation data triple estimates of global vulnerability to sea-level rise and coastal flooding. *Nature Communications*, *10*(1), 4844. https://doi.org/10.1038/s41467-019-12808-z

Li, S., Wahl, T., Talke, S. A., Jay, D. A., Orton, P. M., Liang, X., et al. (2021). Evolving tides aggravate nuisance flooding along the U.S. coastline. *Science Advances*, *7*(10). https://doi.org/10.1126/sciadv.abe2412

Love, R., Milne, G. A., Tarasov, L., Engelhart, S. E., Hijma, M. P., Latychev, K., et al. (2016). The contribution of glacial isostatic adjustment to projections of sea-level change along the Atlantic and Gulf coasts of North America. *Earth's Future*, *4*(10), 440–464. https://doi.org/10.1002/2016EF000363

Lyard, F. H., Allain, D. J., Cancet, M., Carrère, L., & Picot, N. (2021). FES2014 global ocean tide atlas: design and performance. *Ocean Science*, *17*(3), 615–649. https://doi.org/10.5194/os-17-615-2021

Mahmoudi, S., Moftakhari, H., Muñoz, D. F., Sweet, W., & Moradkhani, H. (2024). Establishing flood thresholds for sea level rise impact communication. *Nature Communications*, *15*(1), 4251. https://doi.org/10.1038/s41467-024-48545-1

Mawdsley, R. J., Haigh, I. D., & Wells, N. C. (2015). Global secular changes in different tidal high water, low water and range levels. *Earth's Future*, *3*(2), 66–81. https://doi.org/10.1002/2014EF000282

Meinshausen, M., Nicholls, Z. R. J., Lewis, J., Gidden, M. J., Vogel, E., Freund, M., et al. (2020). The shared socio-economic pathway (SSP) greenhouse gas concentrations and their extensions to 2500. *Geoscientific Model Development*, *13*(8), 3571–3605. https://doi.org/10.5194/gmd-13-3571-2020

Milne, G. A., Gehrels, W. R., Hughes, C. W., & Tamisiea, M. E. (2009). Identifying the causes of sea-level change. *Nature Geoscience*, *2*(7), 471–478. https://doi.org/10.1038/ngeo544

Moftakhari, H. R., AghaKouchak, A., Sanders, B. F., Feldman, D. L., Sweet, W., Matthew, R. A., & Luke, A. (2015). Increased nuisance flooding along the coasts of the United States due to sea level rise: Past and future. *Geophysical Research Letters*, *42*(22), 9846–9852. https://doi.org/10.1002/2015GL066072

Moore, F. C., & Obradovich, N. (2020). Using remarkability to define coastal flooding thresholds. *Nature Communications*, *11*(1), 530. https://doi.org/10.1038/s41467-019-13935-3

Oppenheimer, M., Glavovic, B. C., Hinkel, J., van de Wal, R., Magnan, A. K., Abd-Elgawad, A., et al. (2019). Sea level rise and implications for low-lying islands, coasts and communities. In H.-O. Pörtner, D. C. Roberts, V. Masson-Delmotte, P. Zhai, M. Tignor, E. Poloczanska, et al. (Eds.), *IPCC Special Report on the Ocean and Cryosphere in a Changing*

Climate (pp. 321–445). Intergovernmental Panel on Climate Change (IPCC). Retrieved from https://www.ipcc.ch/srocc/

Parang, S., Milne, G. A., Tarasov, L., Love, R., Yousefi, M., & Vacchi, M. (2024). Constraining models of glacial isostatic adjustment in eastern North America. *Quaternary Science Reviews*, *334*, 108708. https://doi.org/10.1016/j.quascirev.2024.108708

Piecuch, C. G., Das, S. B., Gorrell, L., Dangendorf, S., Hamlington, B. D., Thompson, P. R., & Wahl, T. (2025). Impact-Based Thresholds for Investigation of High-Tide Flooding in the United States. *Earth's Future*, *13*(4). https://doi.org/10.1029/2024EF005850

Pugh, D., & Woodworth, P. (2014). *Sea-Level Science*. Cambridge University Press. https://doi.org/10.1017/CBO9781139235778

Ray, R. D., & Foster, G. (2016). Future nuisance flooding at Boston caused by astronomical tides alone. *Earth's Future*, *4*(12), 578–587. https://doi.org/10.1002/2016EF000423

Ray, R. D., & Schindelegger, M. (2025). Trends in the M$$_2$$ ocean tide observed by satellite altimetry in the presence of systematic errors. *Journal of Geodesy*, *99*(2), 11. https://doi.org/10.1007/s00190-025-01935-9

Schindelegger, M., Green, J. A. M., Wilmes, S. -B., & Haigh, I. D. (2018). Can We Model the Effect of Observed Sea Level Rise on Tides? *Journal of Geophysical Research: Oceans*, *123*(7), 4593–4609. https://doi.org/10.1029/2018JC013959

Schindelegger, Michael, Kotzian, D. P., Ray, R. D., Green, J. A. M., & Stolzenberger, S. (2022). Interannual Changes in Tidal Conversion Modulate M $_2$ Amplitudes in the Gulf of Maine. *Geophysical Research Letters*, *49*(24). https://doi.org/10.1029/2022GL101671

Serafin, K. A., Ruggiero, P., & Stockdon, H. F. (2017). The relative contribution of waves, tides, and nontidal residuals to extreme total water levels on U.S. West Coast sandy beaches. *Geophysical Research Letters*, *44*(4), 1839–1847. https://doi.org/10.1002/2016GL071020

Sherpa, S. F., Shirzaei, M., & Ojha, C. (2023). Disruptive Role of Vertical Land Motion in Future Assessments of Climate Change-Driven Sea-Level Rise and Coastal Flooding Hazards in the Chesapeake Bay. *Journal of Geophysical Research: Solid Earth*, *128*(4). https://doi.org/10.1029/2022JB025993

Spada, G. (2017). Glacial Isostatic Adjustment and Contemporary Sea Level Rise: An Overview. *Surveys in Geophysics*, *38*(1), 153–185. https://doi.org/10.1007/s10712-016-9379-x

Spanger-Siegfried, E., Fitzpatrick, M. F., & Dahl, K. (2014). Encroaching tides: How sea level rise and tidal flooding threaten U.S. East and Gulf Coast communities over the next 30 years. *Cambridge, MA: Union of Concerned Scientists*.

Sweet, W. V., & Park, J. (2014). From the extreme to the mean: Acceleration and tipping points of coastal inundation from sea level rise. *Earth's Future*, *2*(12), 579–600. https://doi.org/10.1002/2014EF000272

Sweet, W. V., Dusek, G., Obeysekera, J., & Marra, J. J. (2018). Patterns and projections of high tide flooding along the U.S. coastline using a common impact threshold. *NOAA Technical Report* .

Talke, S. A., & Jay, D. A. (2020). Changing Tides: The Role of Natural and Anthropogenic Factors. *Annual Review of Marine Science*, *12*(1), 121–151. https://doi.org/10.1146/annurev-marine-010419-010727

Tarasov, L., Dyke, A. S., Neal, R. M., & Peltier, W. R. (2012). A data-calibrated distribution of deglacial chronologies for the North American ice complex from glaciological modeling. *Earth and Planetary Science Letters*, *315–316*, 30–40. https://doi.org/10.1016/j.epsl.2011.09.010

Thompson, P. R., Widlansky, M. J., Merrifield, M. A., Becker, J. M., & Marra, J. J. (2019a). A Statistical Model for Frequency of Coastal Flooding in Honolulu, Hawaii, During the 21st Century. *Journal of Geophysical Research: Oceans*, *124*(4), 2787–2802. https://doi.org/10.1029/2018JC014741

Thompson, P. R., Widlansky, M. J., Merrifield, M. A., Becker, J. M., & Marra, J. J. (2019b). A Statistical Model for Frequency of Coastal Flooding in Honolulu, Hawaii, During the 21st Century. *Journal of Geophysical Research: Oceans*, *124*(4), 2787–2802. https://doi.org/10.1029/2018JC014741

Trupin, A., & Wahr, J. (1990). Spectroscopic analysis of global tide gauge sea level data. *Geophysical Journal International*, *100*(3), 441–453. https://doi.org/10.1111/j.1365-246X.1990.tb00697.x

ten Veldhuis, J. A. E., Clemens, F. H. L. R., Sterk, G., & Berends, B. R. (2010). Microbial risks associated with exposure to pathogens in contaminated urban flood water. *Water Research*, *44*(9), 2910–2918. https://doi.org/10.1016/j.watres.2010.02.009

Wong, P.-P. ;, Losada, I. J. ;, Gattuso, J. P. ;, Hinkel J.;, Khattabi, A. ;, McInnes, K. L. ;, et al. (2014). Coastal Systems and Low-Lying Areas. In C. B. Field, V. R. Barros, D. J. Dokken, K. J. Mach, & M. D. Mastrandrea (Eds.), *Climate Change 2014 Impacts, Adaptation, and Vulnerability* (pp. 361–410). Cambridge: Cambridge University Press. https://doi.org/10.1017/CBO9781107415379.010

Woodworth, P. L. (2012). A Note on the Nodal Tide in Sea Level Records. *Journal of Coastal Research*, *280*, 316–323. https://doi.org/10.2112/JCOASTRES-D-11A-00023.1

Woodworth, P. L., Menéndez, M., & Roland Gehrels, W. (2011). Evidence for Century-Timescale Acceleration in Mean Sea Levels and for Recent Changes in Extreme Sea Levels. *Surveys in Geophysics*, *32*(4–5), 603–618. https://doi.org/10.1007/s10712-011-9112-8

Woodworth, P. L., Hunter, J. R., Marcos Moreno, M., Caldwell, P. C., Menendez, M., & Haigh, I. D. (2016). GESLA (Global Extreme Sea Level Analysis) high frequency sea level dataset - Version 2. *British Oceanographic Data Centre - Natural Environment Research Council, UK.*

Yamazaki, D., Ikeshima, D., Tawatari, R., Yamaguchi, T., O'Loughlin, F., Neal, J. C., et al. (2017). A high-accuracy map of global terrain elevations. *Geophysical Research Letters*, *44*(11), 5844–5853. https://doi.org/10.1002/2017GL072874

Yin, J. (2023). Rapid Decadal Acceleration of Sea Level Rise along the U.S. East and Gulf Coasts during 2010–22 and Its Impact on Hurricane-Induced Storm Surge. *Journal of Climate*, *36*(13), 4511–4529. https://doi.org/10.1175/JCLI-D-22-0670.1

Zhai, L., Greenan, B. J. W., Hunter, J., James, T. S., Han, G., MacAulay, P., & Henton, J. A. (2015). Estimating Sea-Level Allowances for Atlantic Canada using the Fifth Assessment Report of the IPCC. *Atmosphere-Ocean*, *53*(5), 476–490. https://doi.org/10.1080/07055900.2015.1106401

Zhai, L., Lu, Y., & Greenan, B. (2025). Evaluation of the Budget of Local Sea Level Trends Along the Coast of Canada and Northern USA During 1958–2015. *Journal of Geophysical Research: Oceans*, *130*(3). https://doi.org/10.1029/2024JC021000

Supplementary figures and tables of Chapter 4

Contents of this section

Tables 4.S1 and 4.S2 and Figures 4.S1–4.S18. This supplemental section contains additional tables and figures that complement material in the main text. All of the tables and figures below are referred to in the main text. See captions for further details.

Table 4.S1. Latitude, longitude, and station name for each tide gauge corresponding to the numbered locations shown in Figure 4.2.

Tide Gauge Number	Tide Gauge Name	Latitude	Longitude
1	CHURCHILL	58.7667	-94.1833
2	ST_JOHNS	47.5667	-52.7167
3	ARGENTIA	47.3000	-53.9833
4	PORT_AUX_BASQUES	47.5667	-59.1333
5	SEPT_ILES	50.2000	-66.4000
6	RIVIERE_AU_RENARD	49.0000	-64.3833
7	RIMOUSKI	48.4833	-68.5167
8	LOWER_ESCUMINAC	47.0833	-64.8833
9	CHARLOTTETOWN	46.2333	-63.1167
10	NORTH_SYDNEY	46.2167	-60.2500
11	HALIFAX	44.6667	-63.5833
12	YARMOUTH	43.8333	-66.1333
13	SAINT_JOHN	45.2667	-66.0667
14	EASTPORT_ME	44.9033	-66.9817
15	BAR_HARBOR	44.3917	-68.2050
16	PORTLAND_ME	43.6567	-70.2467
17	BOSTON_MA	42.3533	-71.0533
18	PROVIDENCE	41.8067	-71.4000
19	NEWPORT_RI	41.5050	-71.3267
20	WOODS_HOLE_MA	41.5233	-70.6717
21	NANTUCKET_ISLAND	41.2850	-70.0967
22	NEW_LONDON_CT	41.3600	-72.0900
23	MONTAUK_NY	41.0483	-71.9600
24	BRIDGEPORT	41.1733	-73.1817
25	KINGS_POINT	40.8100	-73.7650

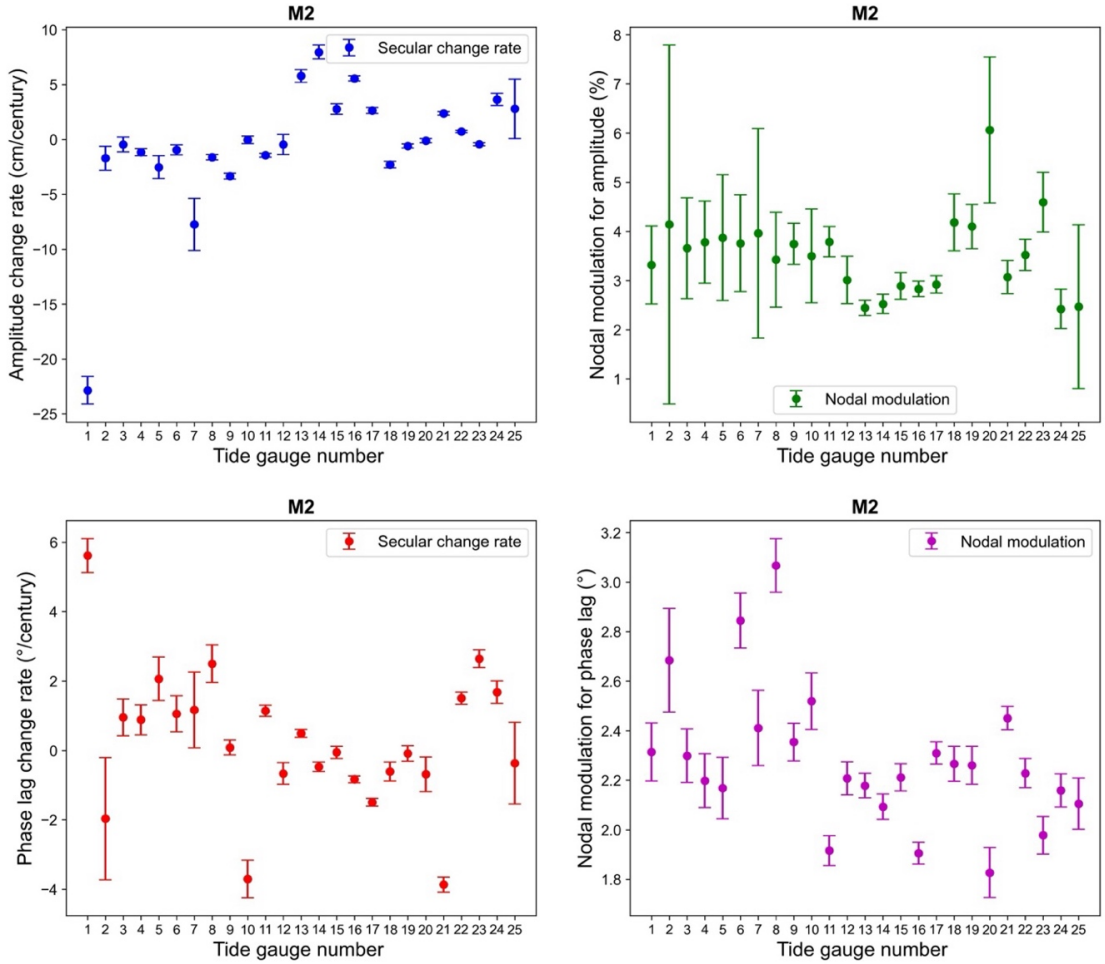


Figure 4.S1. Secular changes and local nodal modulations for the M2 tidal constituent at 25 tide gauges. Each panel presents the results of site-specific regression fits applied to annual amplitude and phase lag estimates. Top left: Secular change in amplitude (cm/century). Top right: Nodal modulation in amplitude (%), calculated as the percentage variation due to the 18.6-year lunar nodal cycle. Bottom left: Secular change in Greenwich phase lag (degrees/century). Bottom right: Nodal modulation in phase lag (°), representing the phase variation over the nodal cycle. Error bars indicate ±1σ uncertainties, derived from the least-squares regression fits. Tide gauge numbers correspond to stations provided in Table 4.S1. Results show significant spatial variability in both secular and nodal trends, emphasizing the need for local corrections in tidal projections.

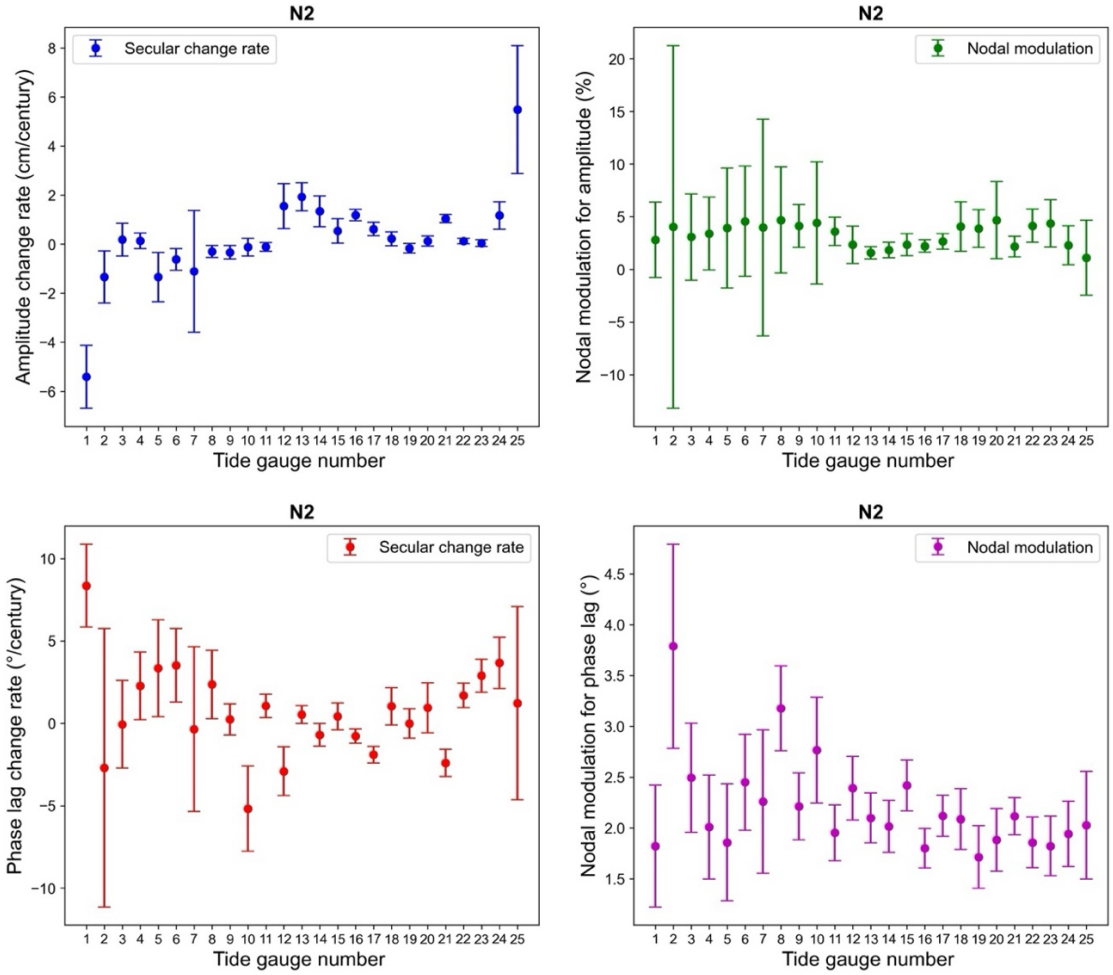


Figure 4.S2. Secular changes and local nodal modulations for the N2 tidal constituent at 25 tide gauges. Each panel presents the results of site-specific regression fits applied to annual amplitude and phase lag estimates. Top left: Secular change in amplitude (cm/century). Top right: Nodal modulation in amplitude (%), calculated as the percentage variation due to the 18.6-year lunar nodal cycle. Bottom left: Secular change in Greenwich phase lag (degrees/century). Bottom right: Nodal modulation in phase lag (°), representing the phase variation over the nodal cycle. Error bars indicate ±1σ uncertainties, derived from the least-squares regression fits. Tide gauge numbers correspond to stations provided in Table 4.S1. Results show significant spatial variability in both secular and nodal trends, emphasizing the need for local corrections in tidal projections.

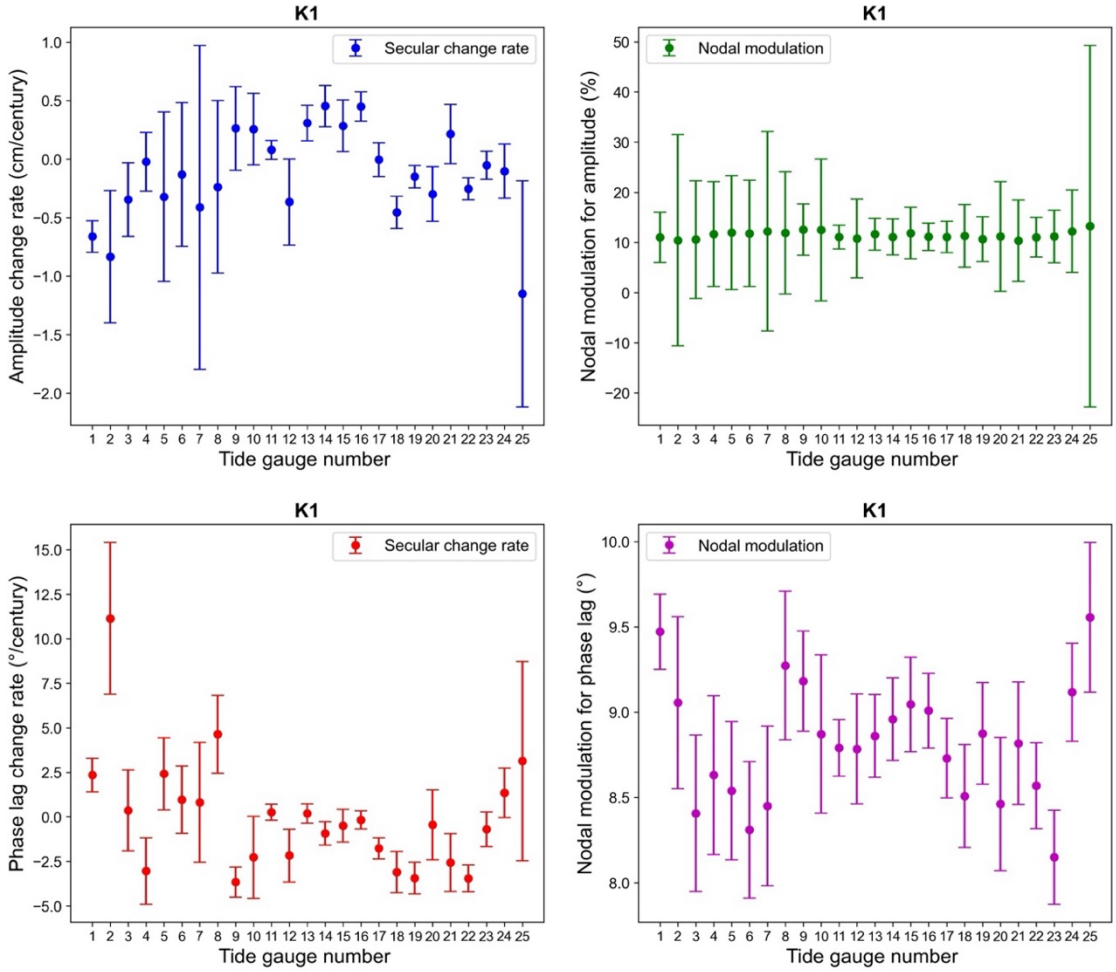


Figure 4.S3. Secular changes and local nodal modulations for the K1 tidal constituent at 25 tide gauges. Each panel presents the results of site-specific regression fits applied to annual amplitude and phase lag estimates. Top left: Secular change in amplitude (cm/century). Top right: Nodal modulation in amplitude (%), calculated as the percentage variation due to the 18.6-year lunar nodal cycle. Bottom left: Secular change in Greenwich phase lag (degrees/century). Bottom right: Nodal modulation in phase lag (°), representing the phase variation over the nodal cycle. Error bars indicate ±1σ uncertainties, derived from the least-squares regression fits. Tide gauge numbers correspond to stations provided in Table 4.S1. Results show significant spatial variability in both secular and nodal trends, emphasizing the need for local corrections in tidal projections.

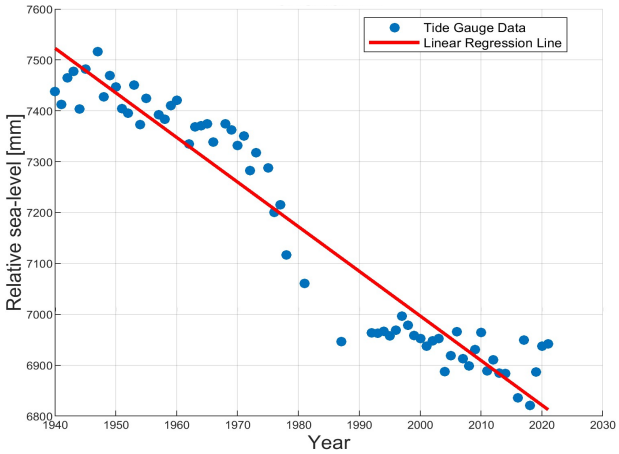


Figure 4.S4. Time series of relative sea level at Churchill, derived from annual tide gauge observations from the Permanent Service for Mean Sea Level (PSMSL). The blue dots represent observed RSL values, and the

red line shows the linear regression fit to the data. The estimated long-term rate of RSL change is –8.76 ± 0.3 mm/yr.

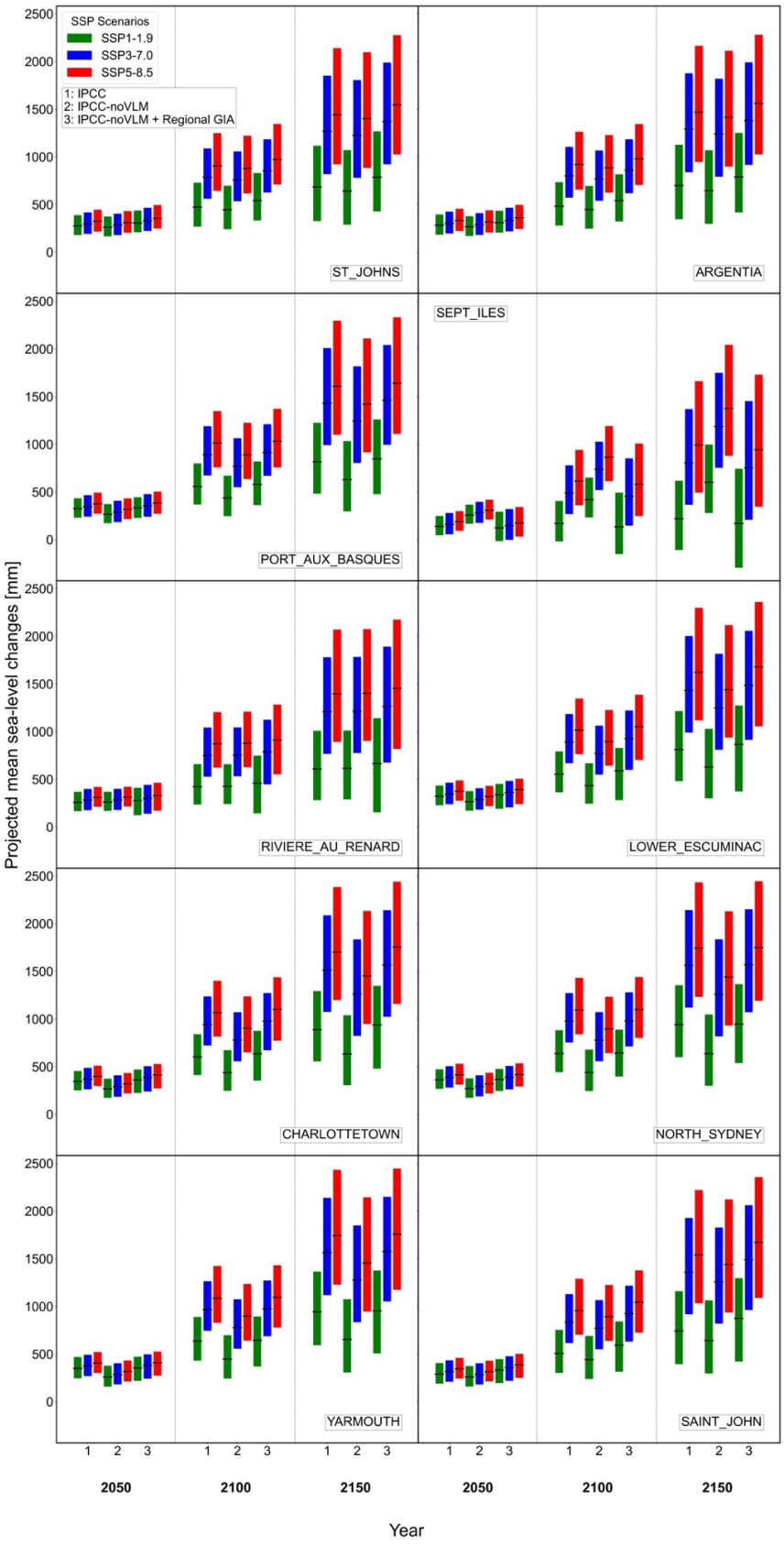


Figure 4.S5. Projected regional mean sea-level changes (in mm) relative to the IPCC temporal baseline (1995–2014) at 10 Canadian tide gauges (see Figure 4.2 and Table 4.S1). Projections are shown for the years 2050,

2100, and 2150 under three SSP scenarios: SSP1-1.9 (green), SSP3-7.0 (blue), and SSP5-8.5 (red). For each year, results are presented for three projection cases: 1 = IPCC projections including all components (IPCC), 2 = IPCC projections excluding VLM (IPCC-noVLM), and 3 = IPCC projections excluding VLM but incorporating a regionally optimized GIA-induced VLM signal with uncertainty bounds (IPCC-noVLM + Regional GIA). All projections are provided with upper and lower 1σ uncertainty bars, and the median values are indicated by horizontal black lines within colored bars. Axis ranges are fixed across all panels to enable direct comparison among stations.

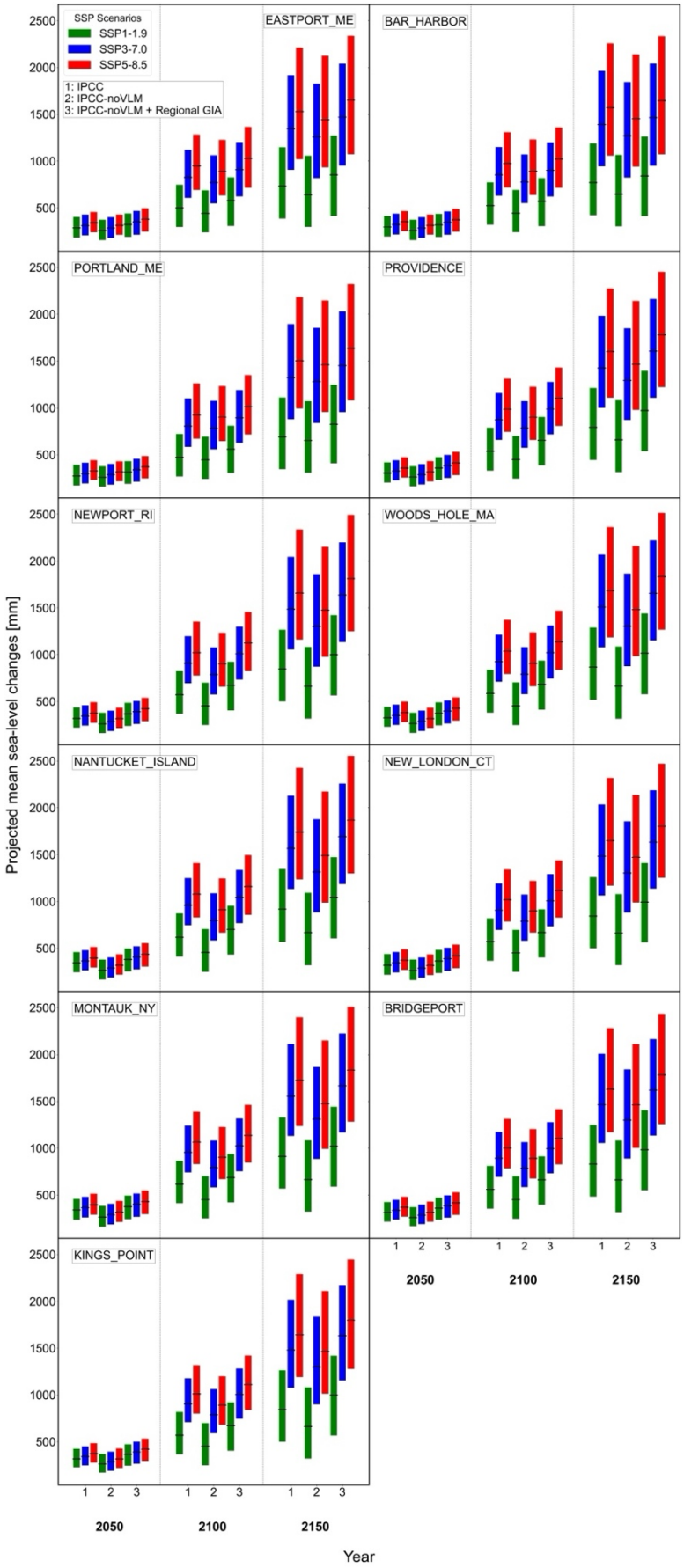


Figure 4.S6. Projected regional mean sea-level changes (in mm) relative to the IPCC temporal baseline (1995–2014) at 11 U.S. tide gauges (see Figure 4.2 and Table 4.S1). Projections are shown for the years 2050, 2100,

and 2150 under three SSP scenarios: SSP1-1.9 (green), SSP3-7.0 (blue), and SSP5-8.5 (red). For each year, results are presented for three projection cases: 1 = IPCC projections including all components (IPCC), 2 = IPCC projections excluding VLM (IPCC-noVLM), and 3 = IPCC projections excluding VLM but incorporating a regionally optimized GIA-induced VLM signal with uncertainty bounds (IPCC-noVLM + Regional GIA). All projections are provided with upper and lower 1σ uncertainty bars, and the median values are indicated by horizontal black lines within colored bars. Axis ranges are fixed across all panels to enable direct comparison among stations.

Table 4.S2. Number of nuisance flooding days in 2005 (the midpoint of the IPCC temporal baseline, 1995–2014) at the nine tide gauges that experienced historical nuisance flooding (see Figure 4.5).

Tide Gauge	Nuisance Flooding Days in 2005
YARMOUTH	2
SEPT_ILES	9
SAINT_JOHN	24
RIMOUSKI	31
PORTLAND_ME	0
EASTPORT_ME	20
CHURCHILL	11
BOSTON_MA	0
BAR_HARBOR	0

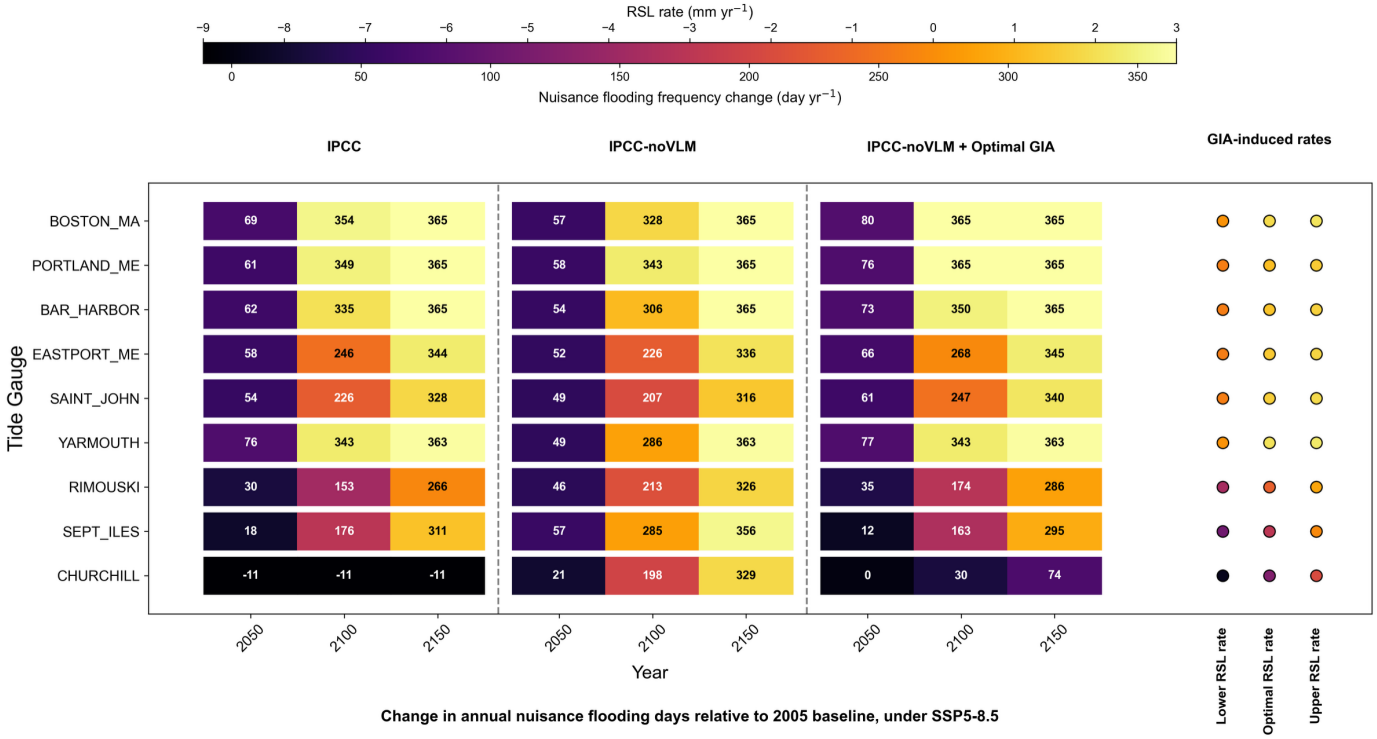


Figure 4.S7. Projected change in annual nuisance flooding days (relative to the 2005 baseline) under SSP5-8.5 for the nine tide gauges that experienced historical nuisance flooding during the IPCC temporal baseline. Results are based on three projection cases: (1) IPCC (including all components), (2) IPCC-noVLM (excluding VLM), and (3) IPCC-noVLM + Optimal GIA (excluding VLM but incorporating regionally optimized GIA-induced VLM). Values are shown for the years 2050, 2100, and 2150. Positive values indicate an increase in nuisance flooding days relative to the baseline, while negative values indicate a decrease. The right panel

displays the present-day GIA-induced RSL rate at each station, based on optimal, lower, and upper bounds from regionally constrained GIA models.

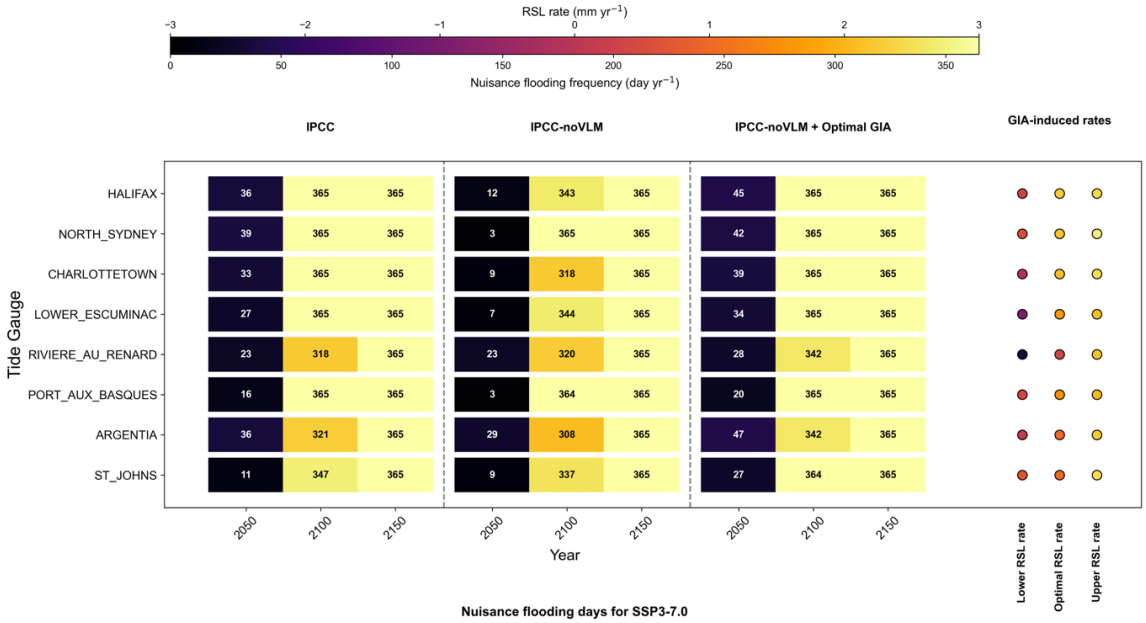


Figure 4.S8. Projected annual nuisance flooding frequency (days per year) under SSP3-7.0 for the eight Canadian tide gauges that did not experience historical nuisance flooding over the IPCC temporal baseline (1995–2014). Results are shown for three projection cases: (1) IPCC (all components), (2) IPCC-noVLM (excluding VLM), and (3) IPCC-noVLM + Optimal GIA (excluding VLM but including regionally optimized GIA-induced VLM). Projections are presented for the years 2050, 2100, and 2150. The right panel shows the present-day GIA-induced RSL rate for each station based on optimal, lower, and upper bounds from regionally constrained GIA models.

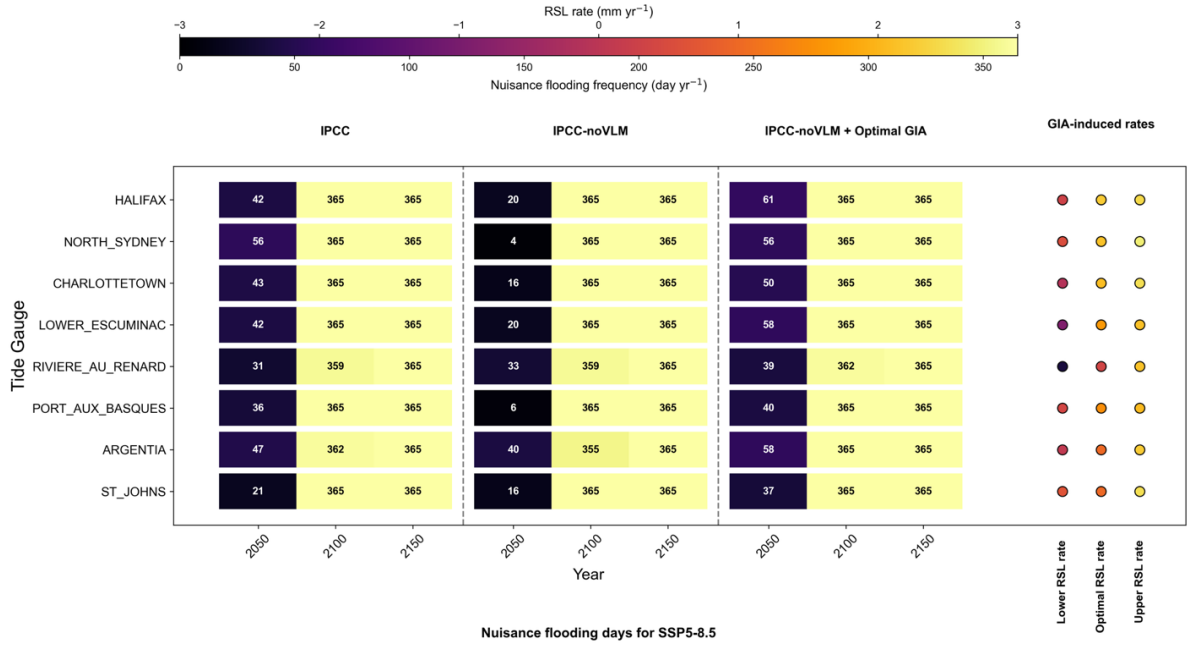


Figure 4.S9. Projected annual nuisance flooding frequency (days per year) under SSP5-8.5 for the eight Canadian tide gauges that did not experience historical nuisance flooding over the IPCC temporal baseline (1995–2014). Results are shown for three projection cases: (1) IPCC (all components), (2) IPCC-noVLM (excluding VLM), and (3) IPCC-noVLM + Optimal GIA (excluding VLM but including regionally optimized GIA-induced VLM). Projections are presented for the years 2050, 2100, and 2150. The right panel shows the present-day GIA-induced RSL rate for each station based on optimal, lower, and upper bounds from regionally constrained GIA models.

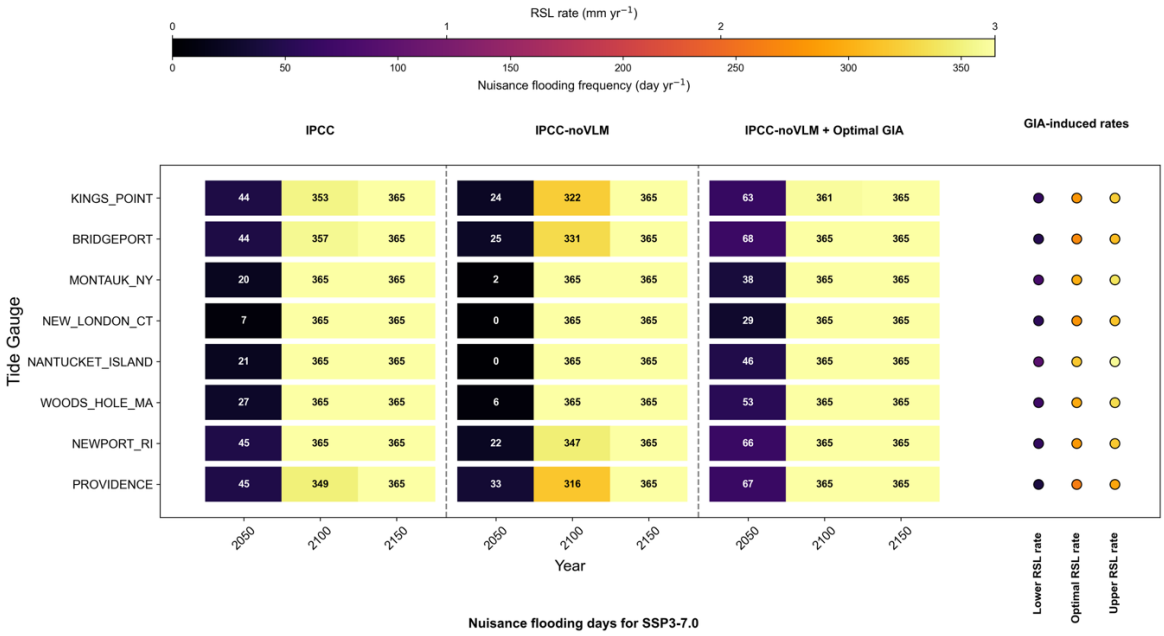


Figure 4.S10. Projected annual nuisance flooding frequency (days per year) under SSP3-7.0 for the eight U.S. tide gauges that did not experience historical nuisance flooding over the IPCC temporal baseline (1995–2014). Results are shown for three projection cases: (1) IPCC (all components), (2) IPCC-noVLM (excluding VLM), and (3) IPCC-noVLM + Optimal GIA (excluding VLM but including regionally optimized GIA-induced VLM). Projections are presented for the years 2050, 2100, and 2150. The right panel shows the present-day GIA-induced RSL rate for each station based on optimal, lower, and upper bounds from regionally constrained GIA models.

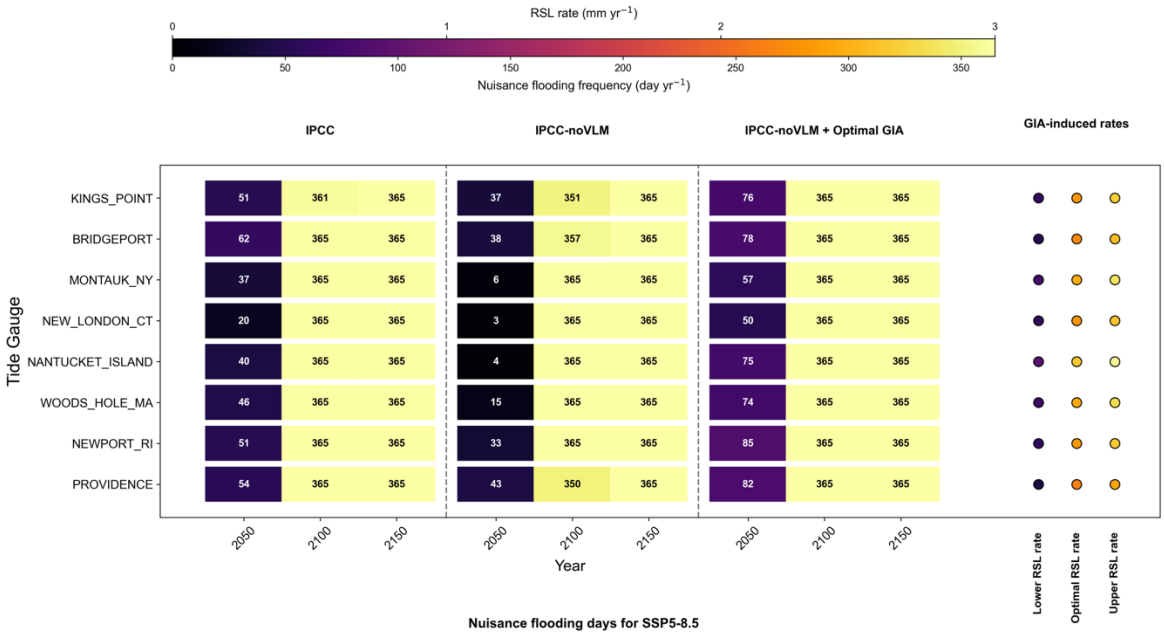


Figure 4.S11. Projected annual nuisance flooding frequency (days per year) under SSP5-8.5 for the eight U.S. tide gauges that did not experience historical nuisance flooding over the IPCC temporal baseline (1995–2014). Results are shown for three projection cases: (1) IPCC (all components), (2) IPCC-noVLM (excluding VLM), and (3) IPCC-noVLM + Optimal GIA (excluding VLM but including regionally optimized GIA-induced VLM). Projections are presented for the years 2050, 2100, and 2150. The right panel shows the present-day GIA-induced RSL rate for each station based on optimal, lower, and upper bounds from regionally constrained GIA models.

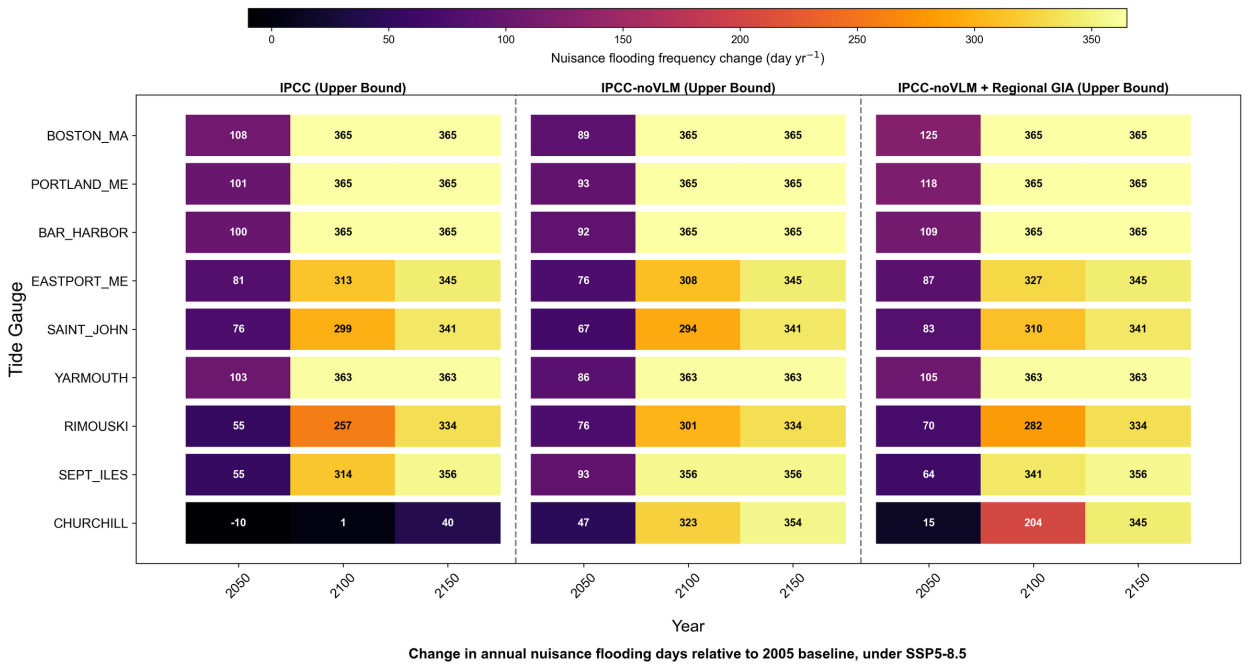


Figure 4.S12. Upper bound of projected changes in annual nuisance flooding days (relative to the 2005 baseline) under SSP5-8.5 for the nine tide gauges with historical nuisance flooding over the IPCC temporal baseline. Estimates are based on the upper bound of projected regional mean sea-level change under each projection case: (1) IPCC, (2) IPCC-noVLM, and (3) IPCC-noVLM + Regional GIA. Projected changes are shown for the years 2050, 2100, and 2150. Positive values indicate an increase in nuisance flooding days relative to the baseline, while negative values indicate a decrease.

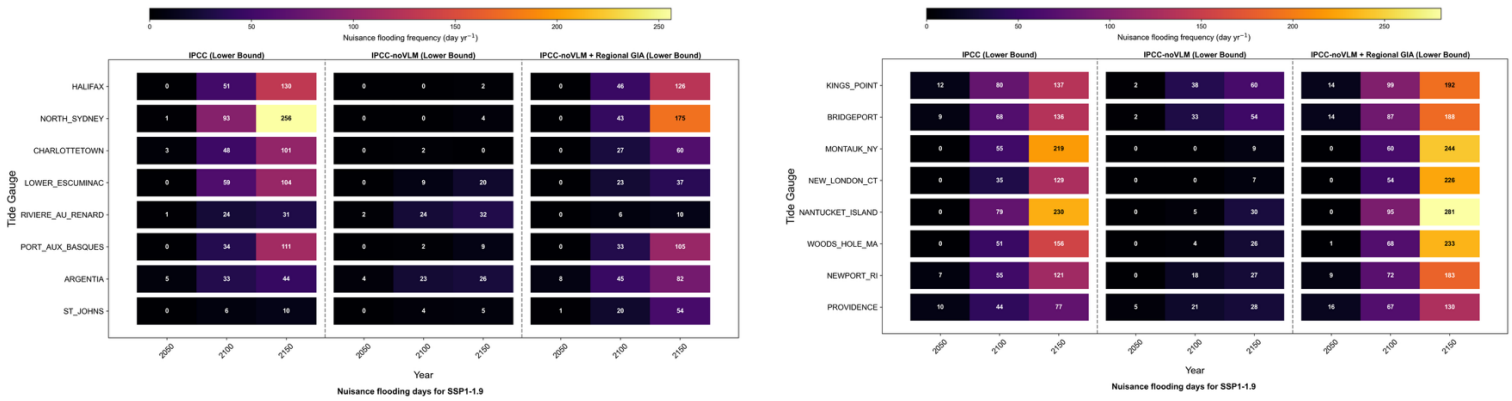


Figure 4.S13. Lower bound of projected annual nuisance flooding frequency (days per year) under SSP1-1.9 for tide gauges that did not experience historical nuisance flooding over the IPCC temporal baseline. The left panel corresponds to Canadian tide gauges, and the right panel to U.S. tide gauges. Estimates are based on the lower bound of projected regional mean sea-level change for each projection case: (1) IPCC, (2) IPCC-noVLM, and (3) IPCC-noVLM + Regional GIA. Projected changes are shown for the years 2050, 2100, and 2150.

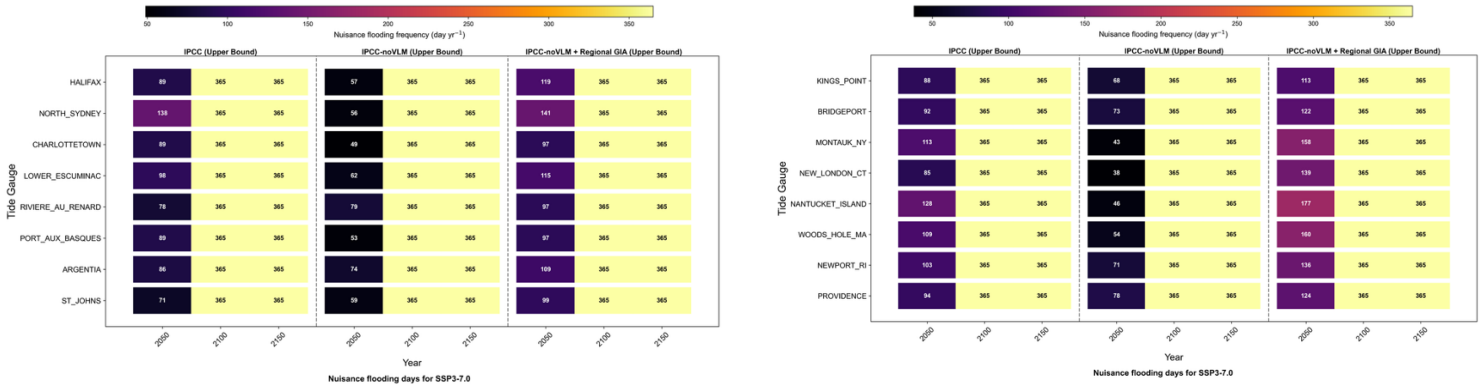


Figure 4.S14. Upper bound of projected annual nuisance flooding frequency (days per year) under SSP3-7.0 for tide gauges that did not experience historical nuisance flooding over the IPCC temporal baseline. The left panel corresponds to Canadian tide gauges, and the right panel to U.S. tide gauges. Estimates are based on the upper bound of projected regional mean sea-level change for each projection case: (1) IPCC, (2) IPCC-noVLM, and (3) IPCC-noVLM + Regional GIA. Projected changes are shown for the years 2050, 2100, and 2150.

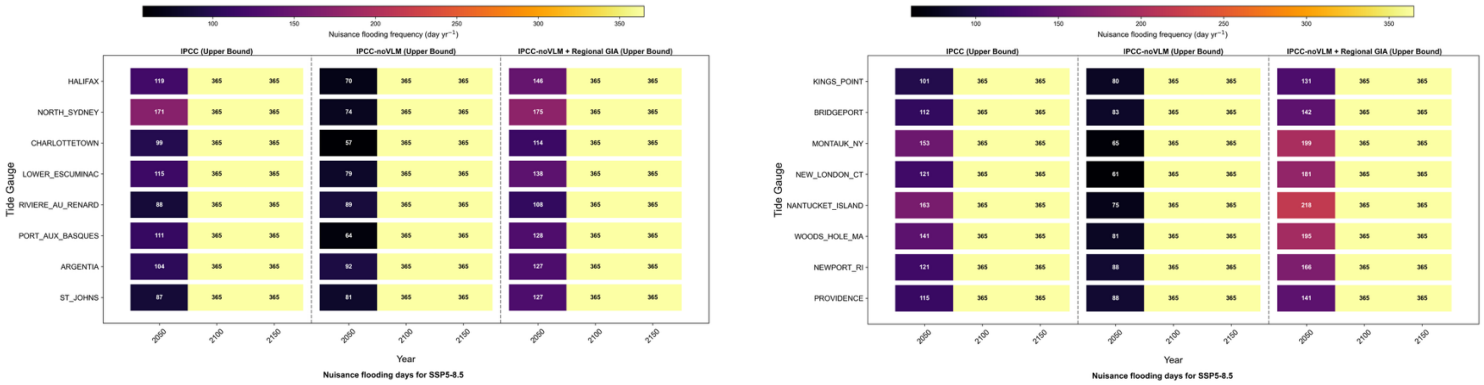


Figure 4.S15. Upper bound of projected annual nuisance flooding frequency (days per year) under SSP5-8.5 for tide gauges that did not experience historical nuisance flooding over the IPCC temporal baseline. The left panel corresponds to Canadian tide gauges, and the right panel to U.S. tide gauges. Estimates are based on the upper bound of projected regional mean sea-level change for each projection case: (1) IPCC, (2) IPCC-noVLM, and (3) IPCC-noVLM + Regional GIA. Projected changes are shown for the years 2050, 2100, and 2150.

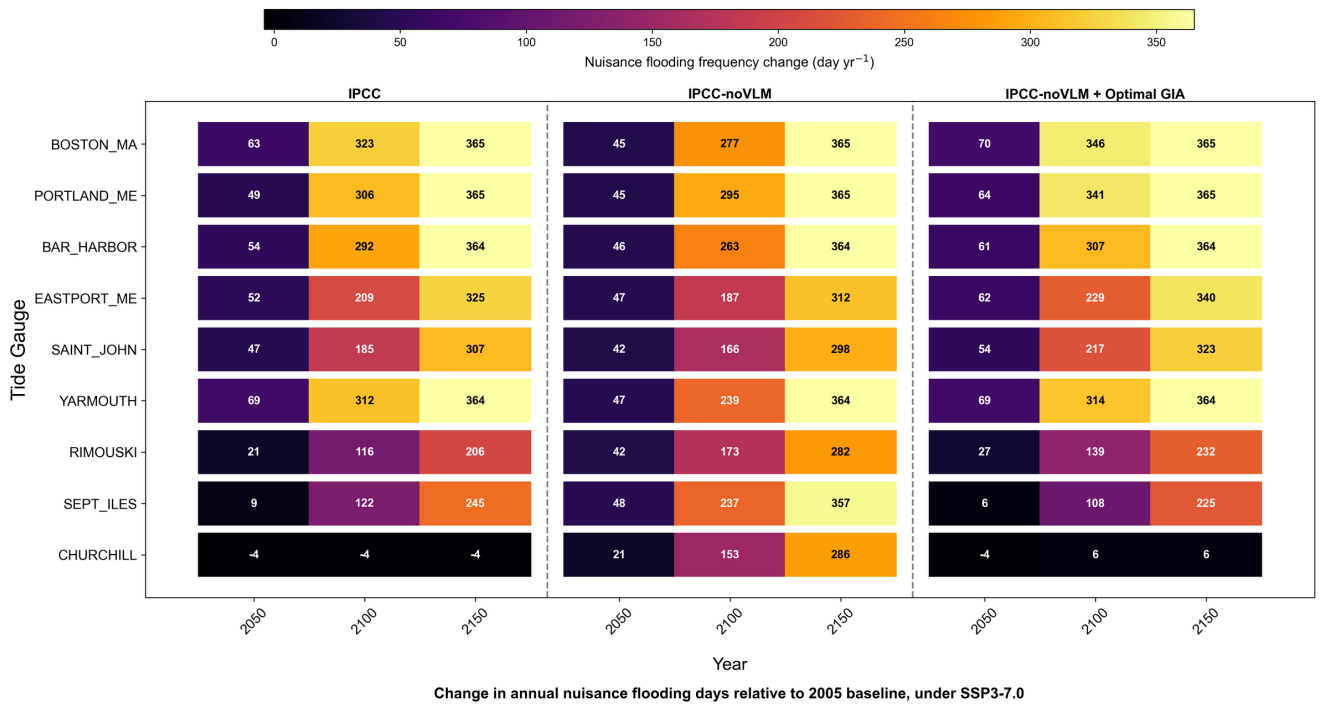


Figure 4.S16. Projected changes in annual nuisance flooding days (relative to the 2005 baseline) under SSP3-7.0 for the nine tide gauges with historical nuisance flooding, based on observations with minimized climate seasonality effects on SA and SSA using FES2014. Results are shown for three projection cases: (1) IPCC (all components), (2) IPCC-noVLM, and (3) IPCC-noVLM + Optimal GIA. Differences from results based on original observations (see Figure 4.9) are negligible at most sites, except at Churchill, where projections differ by up to 19 days by 2150 under case 3.

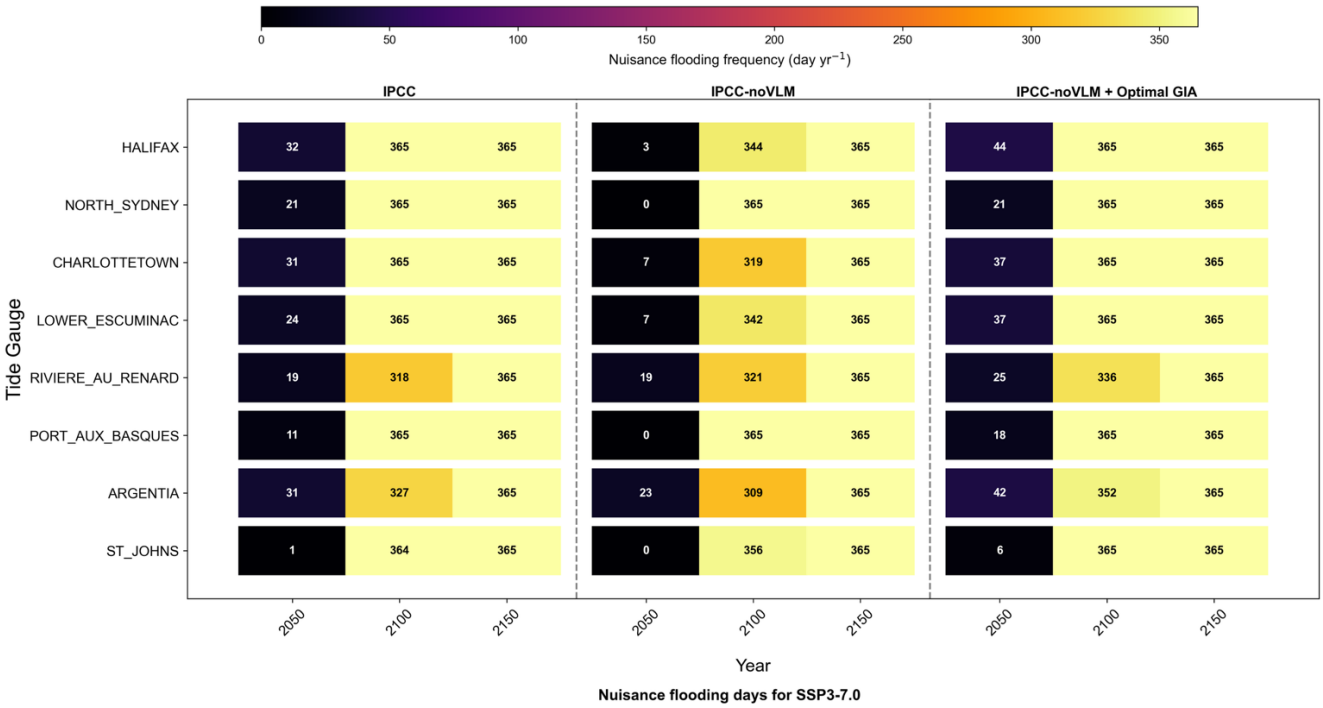


Figure 4.S17. Projected annual nuisance flooding frequency (days per year) under SSP3-7.0 for the eight Canadian tide gauges without historical nuisance flooding, based on observations with minimized climate seasonality effects on SA and SSA using FES2014. Results are shown for three projection cases: (1) IPCC (all components), (2) IPCC-noVLM, and (3) IPCC-noVLM

+ Optimal GIA. Differences from results based on original observations (see Figure 4.S8) are negligible at most sites, except at North Sydney and St. John's, where projections differ by up to ~20 days by 2150 under case 3.

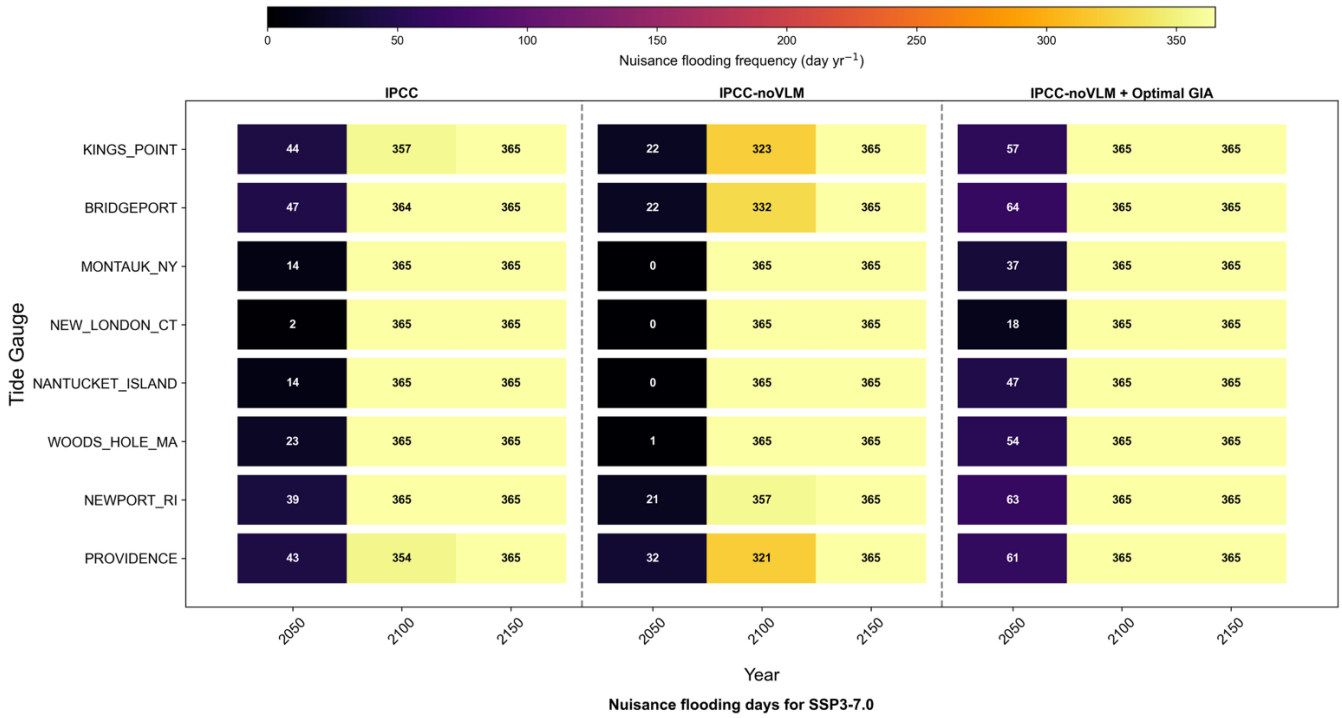


Figure 4.S18. Projected annual nuisance flooding frequency (days per year) under SSP3-7.0 for the eight U.S. tide gauges without historical nuisance flooding, based on observations with minimized climate seasonality effects on SA and SSA using FES2014. Results are shown for three projection cases: (1) IPCC (all components), (2) IPCC-noVLM, and (3) IPCC-noVLM + Optimal GIA. Differences from results based on original observations (see Figure 4.S10) are negligible at most sites.

5

Conclusion

For my Ph.D., I have completed three research projects, all aimed at the overarching goal of improving the quantification and understanding of processes contributing to contemporary and future vertical land motion (VLM) and gravity change in eastern North America. This understanding is essential for producing more accurate projections of mean sea-level change and nuisance flooding over the coming decades. The methodology and results associated with each research project are presented in Chapters 2, 3, and 4 of this thesis. In this concluding chapter, I summarise the key findings from each chapter within a broader context and discuss their implications for potential future work.

Chapter 2 focused on constraining the glacial isostatic adjustment (GIA) signal and its associated uncertainty across southeastern Canada and the northeastern United States, one of the most GIA-affected regions in North America. Accurate representation of GIA in this area is critical, as it dominates the long-term VLM signal and plays a key role in shaping both historical and future relative sea-level (RSL) trends. To address this, we employed a comprehensive paleo sea-level dataset consisting of 1,013 RSL data points from 38 sites, compiled from two regional databases containing 544 sea-level index points (SLIPs), 232 marine limiting points, and 237 terrestrial limiting points. These data were compared to the output from 14,960 forward GIA model simulations based on a suite of 1D (spherically symmetric) earth models and 34 distinct reconstructions of the North American ice sheet history. From this extensive ensemble, we identified optimal Earth-ice model parameter sets that best reproduced the observed RSL data across the region and within spatial subsets. Different subregions require distinct Earth-ice model parameters for optimal RSL fits but some share similar viscosity space and ice history models. As a result, the study region was partitioned into two larger subregions: (1) HUL, near the center and thickest part of the Laurentide Ice Sheet (Hudson Bay, Ungava Peninsula, and Labrador), and (2) NSNM, along the Atlantic coast near the former ice margin (Newfoundland, St. Lawrence Corridor, New Brunswick and Nova Scotia, and Maine and Massachusetts).

The results revealed spatial variability in earth structure, with higher upper mantle viscosity (UMV) beneath the HUL subregion compared to the NSNM subregion. Conversely, lower mantle viscosity (LMV) was inferred to be very low in HUL and high in NSNM. These contrasting model parameter sets reflect the importance of lateral earth structure in driving regional differences in the GIA response, which cannot be adequately represented by a single 1D earth model. Indeed, no single combination of 1D parameters produced high-quality fits to the full RSL dataset, even when tested against a wide range of ice sheet reconstructions, underscoring that the inferred spatial variations are robustly linked to earth structure. This interpretation was supported by 3D GIA model simulations, based on two shear-wave tomographic models, which confirmed the regional sensitivity to lateral variations in viscosity, although

they did not yield significant improvements in data–model fit, likely due to limitations in the accuracy of the adopted 3D viscosity models and/or a bias in the ice history models, which are all based on the assumption of radial (1D) earth structure.

Therefore, an important aim for future work is to develop more accurate 3D earth models for this region. One approach involves constructing 3D GIA models that incorporate composite mantle rheology alongside laterally varying temperature fields derived from regional models, as demonstrated by van der Wal et al. (2013). Another avenue is to apply LitMod (Afonso et al., 2016), a probabilistic (Bayesian) inversion framework that can consider multiple datasets, such as seismic velocity, surface heat flow, topography, and gravity anomalies, in order to construct more accurate temperature models and, consequently, improved 3D viscosity models. These models could then be integrated into GIA modeling to assess their consistency with both paleo RSL data and contemporary GNSS-derived velocities, potentially leading to improved fits in this GIA-active region. A primary limiting factor of 3D-Earth GIA modelling is the high computational cost associated with these models, which limits the ability to conduct extensive parameter space exploration. In this study, the 3D models were constructed using the 1D viscosity structure derived from our analysis; however, this approach may introduce bias if the applied 1D structure is not optimal for the adopted laterally variable earth structure. Emerging strategies to address this challenge include the use of artificial neural networks to emulate the output of computationally expensive 3D GIA simulations (Love et al., 2024) and the application of adjoint methods to determine the optimal earth structure will fewer forward runs (Crawford et al., 2018).

Another avenue for future work to improve the results from 3D GIA modeling involves addressing limitations in the ice history models themselves. The ice models applied in this study were originally developed using 1D earth structures, which do not account for lateral variations in mantle viscosity. As a result, these ice histories may be inaccurate when used within a 3D GIA framework. Developing and incorporating ice models that are consistent with laterally varying earth structures would enhance the physical realism of the modeling and potentially improve data–model fits. The adjoint method noted above can also be applied for this purpose (e.g., Lloyd et al., 2024). Another approach involves coupling glaciological ice sheet models to 3D-Earth GIA models, which has been done for the Antarctic ice sheets (Gomez et al., 2018; van Calcar et al., 2023) but not the North American ice sheets.

Further improvements in GIA modeling can be achieved by incorporating more realistic rheological representations of Earth's mantle, such as non-Newtonian rheology. For example, Kang et al. (2022) demonstrate that RSL changes simulated using non-Newtonian rheology show more rapid sea-level fall following deglaciation around ~14 ka BP, compared to those produced by Newtonian models. This is followed by more gradual sea-level fluctuations for sites close to the near-field area, and another gradual sea level fall during the mid-to-late Holocene for sites close to the ice margins. For instance, RSL observations in the St. Lawrence Corridor are better explained by a non-Newtonian rheological model, which yields improved fits relative to models based on Newtonian viscoelastic rheology. The improved performance is largely attributed to the lower upper mantle viscosity characteristic of non-Newtonian rheology when mantle stresses are high, which better captures the rapid RSL fall during deglaciation at sites such as 21–24 in our study region (Chapter 2).

Another important direction for advancing GIA modeling is improving the quality and spatial coverage of paleo RSL observations. In contrast to previous studies, which rely mainly on SLIPs, our analysis incorporates both SLIPs and limiting data points to more comprehensively constrain the GIA signal with uncertainty. Enhancing the reliability and density of both types of data, particularly in data-sparse subregions like the Ungava Peninsula and Labrador, where SLIPs are limited, would

significantly improve model constraints, thereby yielding more accurate GIA predictions across the study region.

A central component of the Chapter 2 analysis is the estimation of model uncertainty, which is essential for evaluating the robustness of GIA model predictions. Three distinct methods were employed to quantify this uncertainty, including heuristic, nominal Bayesian, and history matching approaches. Each method offers specific strengths and limitations. The nominal Bayesian approach estimates uncertainty bounds based on the spread of predicted RSL values across a sub-ensemble of the highest-probability model parameter sets, while ignoring the structural uncertainty in the model physics. Notably, both the heuristic and history matching methods yield uncertainty bounds that are derived from individual forward model simulations, ensuring physical consistency. The history matching approach takes this a step further by constraining the model space based on a single ice sheet chronology, allowing for a more targeted exploration of plausible parameter combinations. The preliminary implementation of the history matching approach in this study demonstrates strong potential for improving GIA model uncertainty estimates by accounting for both parametric and structural uncertainties in the modeling. However, because this is a partial implementation of the method, certain limitations became apparent. For instance, model bounds generated from the history matching approach (and the heuristic method) occasionally cross over time at specific sites, which limits their interpretability for certain periods. Additionally, the current history matching analysis was affected by a simplified treatment of model structural error and a limited sampling of ice sheet chronologies. Moreover, in defining RSL bounds based on a single ice sheet chronology, we have ignored the structural uncertainty associated with this component of the GIA model. As a result, the model bounds are too narrow in some regions or are incompatible with a portion of the limiting data in other areas. A more robust application of history matching would necessitate joint sampling of both earth model parameters and ice sheet chronologies, a comprehensive assessment of model structural uncertainties, and the use of statistical emulators to enable efficient exploration of the parameter space across multiple sampling waves, as outlined in Tarasov & Goldstein (2023).

A major contribution of Chapter 3 is the utilization of optimal regional GIA models, accompanied by model uncertainty bounds, to more precisely constrain GIA-induced VLM rates across eastern North America, building directly on the work presented in Chapter 2. A comprehensive uncertainty analysis for the VLM signal is presented, addressing gaps that remained in previous studies. In addition, this chapter marks the first time that uncertainty in GRACE mass change estimates is quantified by explicitly accounting for uncertainty in the GIA signal. This refinement plays a critical role in the interpretation of GRACE-derived secular mass changes, as it reduces potential biases associated with GIA correction. The analysis presented in this chapter builds on the complementary timescales of the datasets, paleo RSL reconstructions providing millennial-scale VLM rates, and GNSS and GRACE observations presenting contemporary, decadal-scale estimates. By comparing paleo and contemporary VLM rates, this study identifies potential changes in land motion over time, allowing for the reliable detection of rate discrepancies. These residuals can be interpreted as resulting from other non-GIA processes, with contemporary hydrological mass change, estimated independently from GRACE, as the dominant contributor. Incorporating both VLM estimates and GRACE-derived mass change enables a consistency check that strengthens our understanding of the sources and magnitudes of VLM in the region and allows for a more robust separation of GIA-induced trends from other geophysical signals. This integrated framework improves confidence in the interpretation of observed mass change signals and supports the broader goal of refining regional sea-level projections.

Our findings improve upon the work of Karegar et al. (2017), who suggested that anthropogenic impacts from the James Bay Hydroelectric Project led to significant water mass accumulation in southeastern Hudson Bay, causing deviations between contemporary and long-term GIA-induced VLM rates along parts of the Atlantic coast. However, our uncertainty-inclusive approach shows broad compatibility between contemporary and paleo VLM rates across subregions. Our GRACE estimates reveal no substantial hydrological mass changes in Hudson Bay or other subregions that could result in contemporary land subsidence along the Atlantic seaboard. Our results indicate that GIA as the dominant driver of VLM in the region during the late Holocene and for the past few decades, with minimal influence from hydrological processes.

In addition to the improvements and new contributions presented in this study, several limitations should be acknowledged. A key limitation is the sparse distribution of GNSS stations in the study region, particularly in Hudson Bay, the Ungava Peninsula, and Labrador, which limits our ability to analyze localized variations in decadal-scale VLM rates. Although the station selection criteria minimize spatial bias between GPS- and RSL-derived VLM rates, so that any differences primarily reflect temporal variations, the relatively short length of some GNSS time series may introduce additional biases in the inferred rates. Another limitation is the low number (or absence) of SLIPs older than 4 ka BP at certain sites. For example, the postglacial decay time analysis, which is a more reliable model for Hudson Bay, is hindered by the lack of SLIPs over 4 ka BP. Consequently, VLM estimates at these sites are based on linear fits to SLIPs younger than 2 ka BP, which may introduce bias. Moreover, in areas such as the Ungava Peninsula and Labrador, there are currently no SLIPs available that can be used to estimate late-Holocene RSL changes, and the corresponding paleo VLM rates are derived solely from regionally constrained GIA models. Future studies should aim to enhance the spatial and temporal resolution of contemporary VLM measurements by expanding GNSS networks and incorporating InSAR-based estimates, while also collecting new SLIPs in the data-sparse regions to improve constraints on paleo VLM rates and late-Holocene RSL change.

While there is broad compatibility between recent decadal-scale and millennial-scale VLM rates across the study region, a few sites require further investigation. For instance, at site #1 in western Hudson Bay, both GNSS-derived uplift rates and those inferred from late-Holocene RSL change (when considering their corresponding uncertainties) are up to ~5 mm/yr higher than the GIA-induced rate from the optimal regional model. However, the GPS rate is captured by the upper bound of the GIA-induced estimate, highlighting the importance of uncertainty quantification. Similarly, the rate of RSL fall captured by the tide gauge at Churchill, co-located with the GPS station, exceeds the optimal GIA model rate, though the lower bound encompasses the observed value. This discrepancy between optimal values may reflect significant hydrological mass changes occurring prior to the GRACE observation period (April 2002 – November 2023). To better understand such discrepancies, future work should also focus on developing high-resolution regional or local hydrological models that extend the temporal coverage of total water storage variations in the study region to periods before GRACE.

Chapter 4 highlights the critical role of the VLM signal, specifically its GIA component, in projecting regional mean sea-level change and nuisance flooding frequency across eastern North America, based on multiple projection cases and SSP scenarios. Its inclusion or exclusion substantially alters sea-level projections and flood exposure estimates at 25 tide gauge locations. The regionally optimized GIA models developed in Chapter 2 produce VLM rates that generally align with IPCC-based estimates, with most differences falling within their respective uncertainty bounds. At Atlantic tide gauge sites such as Halifax and Boston, land subsidence due to GIA-induced forebulge collapse amplifies RSL rise, resulting in higher projected mean sea-level change and increased nuisance flooding

frequency. Under both IPCC-based and GIA-integrated projections, historically flood-prone sites are projected to reach the chronic nuisance flooding level as early as 2050 under the low-emissions scenario. In contrast, uplift-dominated sites such as Rimouski, Sept Îles, and particularly Churchill exhibit reduced sea-level rise due to GIA-induced uplift and RSL fall. At Churchill, the largest sensitivity to VLM is observed: projections that exclude VLM indicate rising sea levels through 2150, whereas those that incorporate VLM show dominant RSL fall. Under IPCC projections, the median of sea-level change remains negative across all SSPs and time horizons. In contrast, projections using the regionally optimized GIA signal yield higher values, with mostly positive medians, underscoring the influence of the applied VLM rate and its connection to the discrepancy discussed in Chapter 3. Consistent with this trend, projected nuisance flooding at Churchill is nonexistent (or minimal) after accounting for the GIA signal, illustrating how the GIA signal mitigates future flood risk in areas near the former ice sheet core.

The Chapter 4 results demonstrate that regions with historical nuisance flooding may experience reduced or no future flooding due to GIA-induced uplift, whereas regions without a history of flooding may reach chronic flooding levels as a result of GIA-induced subsidence. These findings contrast to those in studies that assume sea-level rise across all tide gauges (e.g., Hague et al., 2023), which may, therefore, overestimate flood risk in regions experiencing GIA-induced uplift and underestimate it in areas undergoing GIA-induced subsidence. The model outputs are particularly valuable for regions with limited tide gauge coverage in GIA-affected areas. Unlike IPCC-based VLM estimates that depend on tide gauge availability, our integration of regionally constrained GIA models enables projections to be generated at any location, including vulnerable coastal areas lacking direct observations. As noted above, our projections study is limited to tide-sufficient flooding. Future work should include surge-driven flooding, which, when combined with tidal and mean sea-level changes, would further increase coastal flood risk. Additionally, for future work, extending the analysis to the full historical record at each tide gauge, beyond the IPCC temporal baseline of 1995–2014 used in this study, would enable a more comprehensive assessment of long-term nuisance flooding trends, as demonstrated in studies such as Li et al. (2021).

The spatial and temporal trends in high-tide flooding can be sensitive to the choice of flood threshold. In this study, the threshold was determined using a regression-based scheme developed by Sweet et al. (2018), which relies on parameters derived from tidal harmonic analysis at tide gauge stations. While effective at gauged sites, this method may not fully capture localized variability or extend reliably to ungauged coastal regions. For future work, machine learning techniques could be explored to estimate flood thresholds across the study region by learning from multiple predictor variables to complement point-based and linear methods. Such models could enable estimation of flood thresholds and nuisance flooding frequency at ungauged locations, similar to the recent work by Mahmoudi et al. (2024). Another direction is the estimation of flood thresholds with associated uncertainties, which allows for a better representation of local conditions, based on alternative approaches such as the hierarchical Bayesian method recently introduced by Piecuch et al. (2025).

The broader significance of the research presented in this thesis lies in its contribution to uncertainty quantification and its combined use of complementary datasets to evaluate our understanding of both paleo and contemporary contributors to VLM and gravity change. By assessing paleo RSL data alongside contemporary GNSS, tide gauge, and GRACE observations, this work demonstrates how multiple observational constraints, along with their associated uncertainty estimates, can be used to more accurately identify and interpret residual signals. This thesis highlights that accurate interpretation of various geodetic and geological records requires well-constrained GIA model predictions. Improving

data control in GIA model assessment is essential, particularly in regions of Canada where sea-level data and GNSS coverage can be sparse. In such areas, GRACE measurements provide valuable constraints on both the GIA signal and hydrological mass changes. GRACE-derived estimates of total water storage variations are critical for calibrating regional hydrological models; however, as demonstrated in this thesis, accurate interpretation requires prior removal of the GIA signal using regionally constrained models to avoid bias. Conversely, when GRACE data are used to constrain GIA models, the hydrological signal must be estimated (e.g., from hydrological models) and removed. In future work, as GIA and hydrological models improve, there is clear potential to use GRACE observations to constrain and improve both GIA and hydrological models via iterative, joint inversion approaches.

The inclusion of GRACE observations in the research presented in this thesis is further motivated by their relevance to the Canada1Water initiative (canada1water.ca), a national-scale project launched in 2021 to improve the understanding of water resource sustainability in Canada. A core objective of this initiative is to assess large-scale hydrological change and water security across the country under various climate scenarios, using physics-based numerical models such as HydroGeoSphere (aquanty.com) to simulate surface and groundwater dynamics. Importantly, the improved GIA models, which enhance the accuracy of GRACE-derived estimates of total water storage variations, support a key aim of Canada1Water by providing more reliable observational constraints for hydrological modeling and future projections. In this way, the present work contributes to the broader national effort to evaluate and manage water resources in the context of climate change and long-term sustainability.

As the community seeks to develop more reliable regional GIA models, particularly in areas with complex earth structure and sparse observational data, the methodological foundation developed in this thesis can be extended to constrain GIA models for all of Canada. In addition, as addressed in the preceding paragraphs, various models and approaches (e.g., machine learning-based emulators and joint inversions of geophysical datasets) can provide improved characterization of lateral earth structure and ice loading history. These advancements not only provide improved sea-level projections and estimates of hydrological mass change across Canada but also support important applications such as the calibration of national vertical datums. More accurate estimates of VLM are essential for geoid determination and precise positioning, which are fundamental to geodetic reference systems.

Bibliography

Afonso, J. C., Rawlinson, N., Yang, Y., Schutt, D. L., Jones, A. G., Fullea, J., & Griffin, W. L. (2016). 3-D multiobservable probabilistic inversion for the compositional and thermal structure of the lithosphere and upper mantle: III. Thermochemical tomography in the Western-Central U.S. *Journal of Geophysical Research: Solid Earth*, *121*(10), 7337–7370. https://doi.org/10.1002/2016JB013049

Argus, D. F., Peltier, W. R., Drummond, R., & Moore, A. W. (2014). The Antarctica component of postglacial rebound model ICE-6G_C (VM5a) based on GPS positioning, exposure age dating of ice thicknesses, and relative sea level histories. *Geophysical Journal International*, *198*(1), 537–563. https://doi.org/10.1093/gji/ggu140

Bettadpur, S. (2018). CSR Level-2 processing standards document for product release 06. *GRACE 327–742, Revision 5.0, The GRACE Project, Center for Space Research, University of Texas at Austin*.

Blewitt, G., Kreemer, C., Hammond, W. C., & Gazeaux, J. (2016). MIDAS robust trend estimator for accurate GPS station velocities without step detection. *Journal of Geophysical Research: Solid Earth*, *121*(3), 2054–2068. https://doi.org/10.1002/2015JB012552

Blewitt, G., Hammond, W., & Kreemer, C. (2018). Harnessing the GPS Data Explosion for Interdisciplinary Science. *Eos*, *99*. https://doi.org/10.1029/2018EO104623

Boon, J. D., Mitchell, M., Loftis, J. D., & Malmquist, D. L. (2018). Anthropocene Sea Level Change: A History of Recent Trends Observed in the U.S. East, Gulf, and West Coast Regions. *Special Report in Applied Marine Science and Ocean Engineering (SRAMSOE), Virginia Institute of Marine Science, William & Mary*, *467*.

van Calcar, C. J., van de Wal, R. S. W., Blank, B., de Boer, B., & van der Wal, W. (2023). Simulation of a fully coupled 3D glacial isostatic adjustment – ice sheet model for the Antarctic ice sheet over a glacial cycle. *Geoscientific Model Development*, *16*(18), 5473–5492. https://doi.org/10.5194/gmd-16-5473-2023

Calvin, K., Dasgupta, D., Krinner, G., Mukherji, A., Thorne, P. W., Trisos, C., et al. (2023). *IPCC, 2023: Climate Change 2023: Synthesis Report. Contribution of Working Groups I, II and III to the Sixth Assessment Report of the Intergovernmental Panel on Climate Change [Core Writing Team, H. Lee and J. Romero (eds.)]. IPCC, Geneva, Switzerland.* https://doi.org/10.59327/IPCC/AR6-9789291691647

Caron, L., Métivier, L., Greff-Lefftz, M., Fleitout, L., & Rouby, H. (2017). Inverting Glacial Isostatic Adjustment signal using Bayesian framework and two linearly relaxing rheologies. *Geophysical Journal International*, *209*(2), 1126–1147. https://doi.org/10.1093/gji/ggx083

Cazenave, A., & Llovel, W. (2010). Contemporary Sea Level Rise. *Annual Review of Marine Science*, *2*(1), 145–173. https://doi.org/10.1146/annurev-marine-120308-081105

Cherqui, F., Belmeziti, A., Granger, D., Sourdril, A., & Le Gauffre, P. (2015). Assessing urban potential flooding risk and identifying effective risk-reduction measures. *Science of The Total Environment*, *514*, 418–425. https://doi.org/10.1016/j.scitotenv.2015.02.027

Church, J. A., Clark, P. U., Cazenave, A., Gregory, J. M., Jevrejeva, S., Levermann, A., et al. (2013). Sea Level Change. *Climate Change 2013: The Physical Science Basis. Contribution of Working Group I to the Fifth Assessment Report of the Intergovernmental Panel on Climate Change (IPCC), Cambridge University Press, Cambridge, United Kingdom and New York, NY, USA*.

Clark, J. A., Farrell, W. E., & Peltier, W. R. (1978). Global Changes in Postglacial Sea Level: A Numerical Calculation. *Quaternary Research*, *9*(3), 265–287. https://doi.org/10.1016/0033-5894(78)90033-9

Crawford, O., Al-Attar, D., Tromp, J., Mitrovica, J. X., Austermann, J., & Lau, H. C. P. (2018). Quantifying the sensitivity of post-glacial sea level change to laterally varying viscosity. *Geophysical Journal International*, *214*(2), 1324–1363. https://doi.org/10.1093/gji/ggy184

Crétaux, J., Soudarin, L., Davidson, F. J. M., Gennero, M., Bergé-Nguyen, M., & Cazenave, A. (2002). Seasonal and interannual geocenter motion from SLR and DORIS measurements: Comparison with surface loading data. *Journal of Geophysical Research: Solid Earth*, *107*(B12). https://doi.org/10.1029/2002JB001820

Crowley, J. W., & Huang, J. (2020). A least-squares method for estimating the correlated error of GRACE models. *Geophysical Journal International*, *221*(3), 1736–1749. https://doi.org/10.1093/gji/ggaa104

Dahle, C., Murböck, M., Flechtner, F., Dobslaw, H., Michalak, G., Neumayer, K., et al. (2019). The GFZ GRACE RL06 Monthly Gravity Field Time Series: Processing Details and Quality Assessment. *Remote Sensing*, *11*(18), 2116. https://doi.org/10.3390/rs11182116

Dalca, A. V., Ferrier, K. L., Mitrovica, J. X., Perron, J. T., Milne, G. A., & Creveling, J. R. (2013). On postglacial sea level—III. Incorporating sediment redistribution. *Geophysical Journal International*, *194*(1), 45–60. https://doi.org/10.1093/gji/ggt089

Daly, R. A. (1925). Pleistocene changes of level. *American Journal of Science*, *5(10)*, 281–313.

van Dam, T., Wahr, J., & Lavallée, D. (2007). A comparison of annual vertical crustal displacements from GPS and Gravity Recovery and Climate Experiment (GRACE) over Europe. *Journal of Geophysical Research: Solid Earth*, *112*(B3). https://doi.org/10.1029/2006JB004335

Davis, J. L., Tamisiea, M. E., Elósegui, P., Mitrovica, J. X., & Hill, E. M. (2008). A statistical filtering approach for Gravity Recovery and Climate Experiment (GRACE) gravity data. *Journal of Geophysical Research: Solid Earth*, *113*(B4). https://doi.org/10.1029/2007JB005043

Dziewonski, A. M., & Anderson, D. L. (1981). Preliminary reference Earth model. *Physics of the Earth and Planetary Interiors*, *25*(4), 297–356. https://doi.org/10.1016/0031-9201(81)90046-7

Edwards, R. J. (2013). SEA LEVEL STUDIES | Sedimentary Indicators of Relative Sea-Level Changes – Low Energy. In *Encyclopedia of Quaternary Science* (pp. 396–408). Elsevier. https://doi.org/10.1016/B978-0-444-53643-3.00136-9

Engelhart, S. E., & Horton, B. P. (2012). Holocene sea level database for the Atlantic coast of the United States. *Quaternary Science Reviews*, *54*, 12–25. https://doi.org/10.1016/j.quascirev.2011.09.013

Ezer, T., & Atkinson, L. P. (2014). Accelerated flooding along the U.S. East Coast: On the impact of sea-level rise, tides, storms, the Gulf Stream, and the North Atlantic Oscillations. *Earth's Future*, *2*(8), 362–382. https://doi.org/10.1002/2014EF000252

Farrell, W. E., & Clark, J. A. (1976). On Postglacial Sea Level. *Geophysical Journal of the Royal Astronomical Society*, *46*(3), 647–667. https://doi.org/10.1111/j.1365-246X.1976.tb01252.x

Forster, P., Storelvmo, T., Armour, K., Collins, W., Dufresne, J.-L., Frame, D., et al. (2021). The Earth's Energy Budget, Climate Feedbacks and Climate Sensitivity. In *Climate Change 2021 – The Physical Science Basis* (pp. 923–1054). Cambridge University Press. https://doi.org/10.1017/9781009157896.009

Fox-Kemper, B., Hewitt, H. T., Xiao, C., Aðalgeirsdóttir, G., Drijfhout, S. S., Edwards, T. L., et al. (2023). Ocean, Cryosphere and Sea Level Change. In *Climate Change 2021 – The Physical Science Basis* (pp. 1211–1362). Cambridge University Press. https://doi.org/10.1017/9781009157896.011

Gazeaux, J., Williams, S., King, M., Bos, M., Dach, R., Deo, M., et al. (2013). Detecting offsets in GPS time series: First results from the detection of offsets in GPS experiment. *Journal of Geophysical Research: Solid Earth*, *118*(5), 2397–2407. https://doi.org/10.1002/jgrb.50152

Gomez, N., Latychev, K., & Pollard, D. (2018). A Coupled Ice Sheet–Sea Level Model Incorporating 3D Earth Structure: Variations in Antarctica during the Last Deglacial Retreat. *Journal of Climate*, *31*(10), 4041–4054. https://doi.org/10.1175/JCLI-D-17-0352.1

Greenan, B. J. W., James, T. S., Loder, J. W., Pepin, P., Azetsu-Scott, K., Ianson, D., et al. (2019). Changes in oceans surrounding Canada. *Chapter 7 in (Eds.) Bush and Lemmen, Canada's Changing Climate Report, Government of Canada, Ottawa, Ontario*, 343–423.

Gregory, J. M., Griffies, S. M., Hughes, C. W., Lowe, J. A., Church, J. A., Fukimori, I., et al. (2019). Concepts and Terminology for Sea Level: Mean, Variability and Change, Both Local and Global. *Surveys in Geophysics*, *40*(6), 1251–1289. https://doi.org/10.1007/s10712-019-09525-z

Griffiths, J., & Ray, J. (2016). Impacts of GNSS position offsets on global frame stability. *Geophysical Journal International*, *204*(1), 480–487. https://doi.org/10.1093/gji/ggv455

Griggs, G. (2021). Rising Seas in California — An Update on Sea-Level Rise Science (pp. 105–111). https://doi.org/10.1142/9789811213960_0016

Guérou, A., Meyssignac, B., Prandi, P., Ablain, M., Ribes, A., & Bignalet-Cazalet, F. (2023). Current observed global mean sea level rise and acceleration estimated from satellite altimetry and the associated measurement uncertainty. *Ocean Science*, *19*(2), 431–451. https://doi.org/10.5194/os-19-431-2023

Hague, B. S., McGregor, S., Jones, D. A., Reef, R., Jakob, D., & Murphy, B. F. (2023). The Global Drivers of Chronic Coastal Flood Hazards Under Sea-Level Rise. *Earth's Future*, *11*(8). https://doi.org/10.1029/2023EF003784

Hallegatte, S., Green, C., Nicholls, R. J., & Corfee-Morlot, J. (2013). Future flood losses in major coastal cities. *Nature Climate Change*, *3*(9), 802–806. https://doi.org/10.1038/nclimate1979

Han, S.-C., Shum, C. K., Jekeli, C., Kuo, C.-Y., Wilson, C., & Seo, K.-W. (2005). Non-isotropic filtering of GRACE temporal gravity for geophysical signal enhancement. *Geophysical Journal International*, *163*(1), 18–25. https://doi.org/10.1111/j.1365-246X.2005.02756.x

Hill, E. M., Davis, J. L., Tamisiea, M. E., & Lidberg, M. (2010). Combination of geodetic observations and models for glacial isostatic adjustment fields in Fennoscandia. *Journal of Geophysical Research: Solid Earth*, *115*(B7). https://doi.org/10.1029/2009JB006967

IMBIE team. (2018). Mass balance of the Antarctic Ice Sheet from 1992 to 2017. *Nature*, *558*(7709), 219–222. https://doi.org/10.1038/s41586-018-0179-y

Jamieson, T. F. (1865). On the History of the Last Geological Changes in Scotland. *Quarterly Journal of the Geological Society of London*, *21*, 161–203.

Kang, K., Zhong, S., Geruo, A., & Mao, W. (2022). The effects of non-Newtonian rheology in the upper mantle on relative sea level change and geodetic observables induced by glacial isostatic adjustment process. *Geophysical Journal International*, *228*(3), 1887–1906. https://doi.org/10.1093/gji/ggab428

Karato, S., & Wu, P. (1993). Rheology of the Upper Mantle: A Synthesis. *Science*, *260*(5109), 771–778. https://doi.org/10.1126/science.260.5109.771

Karegar, M. A., Dixon, T. H., Malservisi, R., Kusche, J., & Engelhart, S. E. (2017). Nuisance Flooding and Relative Sea-Level Rise: the Importance of Present-Day Land Motion. *Scientific Reports*, *7*(1), 11197. https://doi.org/10.1038/s41598-017-11544-y

Kaufmann, G., Wu, P., & Ivins, E. R. (2005). Lateral viscosity variations beneath Antarctica and their implications on regional rebound motions and seismotectonics. *Journal of Geodynamics*, *39*(2), 165–181. https://doi.org/10.1016/j.jog.2004.08.009

Kemp, A. C., & Horton, B. P. (2013). Contribution of relative sea-level rise to historical hurricane flooding in New York City. *Journal of Quaternary Science*, *28*(6), 537–541. https://doi.org/10.1002/jqs.2653

Khan, N. S., Ashe, E., Shaw, T. A., Vacchi, M., Walker, J., Peltier, W. R., et al. (2015). Holocene Relative Sea-Level Changes from Near-, Intermediate-, and Far-Field Locations. *Current Climate Change Reports*, *1*(4), 247–262. https://doi.org/10.1007/s40641-015-0029-z

Khan, S. A., Sasgen, I., Bevis, M., van Dam, T., Bamber, J. L., Wahr, J., et al. (2016). Geodetic measurements reveal similarities between post–Last Glacial Maximum and present-day mass loss from the Greenland ice sheet. *Science Advances*, *2*(9). https://doi.org/10.1126/sciadv.1600931

King, M. A., Altamimi, Z., Boehm, J., Bos, M., Dach, R., Elosegui, P., et al. (2010). Improved Constraints on Models of Glacial Isostatic Adjustment: A Review of the Contribution of Ground-Based Geodetic Observations. *Surveys in Geophysics*, *31*(5), 465–507. https://doi.org/10.1007/s10712-010-9100-4

Kuchar, J., Milne, G., Hill, A., Tarasov, L., & Nordman, M. (2019). An investigation into the sensitivity of postglacial decay times to uncertainty in the adopted ice history. *Geophysical Journal International*. https://doi.org/10.1093/gji/ggz512

Kusche, J., & Schrama, E. J. O. (2005). Surface mass redistribution inversion from global GPS deformation and Gravity Recovery and Climate Experiment (GRACE) gravity data. *Journal of Geophysical Research: Solid Earth*, *110*(B9). https://doi.org/10.1029/2004JB003556

Kusche, J., Schmidt, R., Petrovic, S., & Rietbroek, R. (2009). Decorrelated GRACE time-variable gravity solutions by GFZ, and their validation using a hydrological model. *Journal of Geodesy*, *83*(10), 903–913. https://doi.org/10.1007/s00190-009-0308-3

Kusche, Jürgen. (2007). Approximate decorrelation and non-isotropic smoothing of time-variable GRACE-type gravity field models. *Journal of Geodesy*, *81*(11), 733–749. https://doi.org/10.1007/s00190-007-0143-3

Lambeck, K., & Nakada, M. (1990). Late Pleistocene and Holocene sea-level change along the Australian coast. *Global and Planetary Change*, *3*(1–2), 143–176. https://doi.org/10.1016/0921-8181(90)90060-P

Lambeck, K., Rouby, H., Purcell, A., Sun, Y., & Sambridge, M. (2014). Sea level and global ice volumes from the Last Glacial Maximum to the Holocene. *Proceedings of the National Academy of Sciences*, *111*(43), 15296–15303. https://doi.org/10.1073/pnas.1411762111

Landerer, F. W., Flechtner, F. M., Save, H., Webb, F. H., Bandikova, T., Bertiger, W. I., et al. (2020a). Extending the Global Mass Change Data Record: GRACE Follow-On Instrument and Science Data Performance. *Geophysical Research Letters*, *47*(12). https://doi.org/10.1029/2020GL088306

Landerer, F. W., Flechtner, F. M., Save, H., Webb, F. H., Bandikova, T., Bertiger, W. I., et al. (2020b). Extending the Global Mass Change Data Record: GRACE Follow-On Instrument and Science Data Performance. *Geophysical Research Letters*, *47*(12). https://doi.org/10.1029/2020GL088306

Latychev, K., Mitrovica, J. X., Tromp, J., Tamisiea, M. E., Komatitsch, D., & Christara, C. C. (2005). Glacial isostatic adjustment on 3-D Earth models: a finite-volume formulation. *Geophysical Journal International*, *161*(2), 421–444. https://doi.org/10.1111/j.1365-246X.2005.02536.x

Lee, J.-Y., Marotzke, J., Bala, G., Cao, L., Corti, S., Dunne, J. P., et al. (2023). Future Global Climate: Scenario-based Projections and Near-term Information. In *Climate Change 2021 – The Physical Science Basis* (pp. 553–672). Cambridge University Press. https://doi.org/10.1017/9781009157896.006

Leo, K. L., Gillies, C. L., Fitzsimons, J. A., Hale, L. Z., & Beck, M. W. (2019). Coastal habitat squeeze: A review of adaptation solutions for saltmarsh, mangrove and beach habitats. *Ocean & Coastal Management*, *175*, 180–190. https://doi.org/10.1016/j.ocecoaman.2019.03.019

Li, J., Chen, J. L., & Wilson, C. R. (2016). Topographic effects on coseismic gravity change for the 2011 Tohoku-Oki earthquake and comparison with GRACE. *Journal of Geophysical Research: Solid Earth*, *121*(7), 5509–5537. https://doi.org/10.1002/2015JB012407

Li, S., Wahl, T., Talke, S. A., Jay, D. A., Orton, P. M., Liang, X., et al. (2021). Evolving tides aggravate nuisance flooding along the U.S. coastline. *Science Advances*, *7*(10). https://doi.org/10.1126/sciadv.abe2412

Lidberg, M., Johansson, J. M., Scherneck, H.-G., & Davis, J. L. (2007). An improved and extended GPS-derived 3D velocity field of the glacial isostatic adjustment (GIA) in Fennoscandia. *Journal of Geodesy*, *81*(3), 213–230. https://doi.org/10.1007/s00190-006-0102-4

Lidberg, M., Johansson, J. M., Scherneck, H.-G., & Milne, G. A. (2010). Recent results based on continuous GPS observations of the GIA process in Fennoscandia from BIFROST. *Journal of Geodynamics*, *50*(1), 8–18. https://doi.org/10.1016/j.jog.2009.11.010

Lloyd, A. J., Crawford, O., Al-Attar, D., Austermann, J., Hoggard, M. J., Richards, F. D., & Syvret, F. (2023). GIA imaging of 3-D mantle viscosity based on palaeo sea level observations – Part I: Sensitivity kernels for an Earth with laterally varying viscosity. *Geophysical Journal International*, *236*(2), 1139–1171. https://doi.org/10.1093/gji/ggad455

Loomis, B. D., Rachlin, K. E., & Luthcke, S. B. (2019). Improved Earth Oblateness Rate Reveals Increased Ice Sheet Losses and Mass-Driven Sea Level Rise. *Geophysical Research Letters*, *46*(12), 6910–6917. https://doi.org/10.1029/2019GL082929

Loomis, B. D., Luthcke, S. B., & Sabaka, T. J. (2019). Regularization and error characterization of GRACE mascons. *Journal of Geodesy*, *93*(9), 1381–1398. https://doi.org/10.1007/s00190-019-01252-y

Love, R., Milne, G. A., Tarasov, L., Engelhart, S. E., Hijma, M. P., Latychev, K., et al. (2016). The contribution of glacial isostatic adjustment to projections of sea-level change along the Atlantic and Gulf coasts of North America. *Earth's Future*, *4*(10), 440–464. https://doi.org/10.1002/2016EF000363

Love, R., Milne, G. A., Ajourlou, P., Parang, S., Tarasov, L., & Latychev, K. (2024). A fast surrogate model for 3D Earth glacial isostatic adjustment using Tensorflow (v2.8.0) artificial neural networks. *Geoscientific Model Development*, *17*(23), 8535–8551. https://doi.org/10.5194/gmd-17-8535-2024

Mahmoudi, S., Moftakhari, H., Muñoz, D. F., Sweet, W., & Moradkhani, H. (2024). Establishing flood thresholds for sea level rise impact communication. *Nature Communications*, *15*(1), 4251. https://doi.org/10.1038/s41467-024-48545-1

Milne, G., & Shennan, I. (2013). SEA LEVEL STUDIES | Isostasy: Glaciation-Induced Sea-Level Change. In *Encyclopedia of Quaternary Science* (pp. 452–459). Elsevier. https://doi.org/10.1016/B978-0-444-53643-3.00135-7

Milne, G. A., Davis, J. L., Mitrovica, J. X., Scherneck, H.-G., Johansson, J. M., Vermeer, M., & Koivula, H. (2001). Space-Geodetic Constraints on Glacial Isostatic Adjustment in Fennoscandia. *Science*, *291*(5512), 2381–2385. https://doi.org/10.1126/science.1057022

Milne, Glenn A., & Mitrovica, J. X. (1998). Postglacial sea-level change on a rotating Earth. *Geophysical Journal International*, *133*(1), 1–19. https://doi.org/10.1046/j.1365-246X.1998.1331455.x

Milne, Glenn A., Mitrovica, J. X., Scherneck, H., Davis, J. L., Johansson, J. M., Koivula, H., & Vermeer, M. (2004). Continuous GPS measurements of postglacial adjustment in Fennoscandia: 2. Modeling results. *Journal of Geophysical Research: Solid Earth*, *109*(B2). https://doi.org/10.1029/2003JB002619

Milne, Glenn A., Gehrels, W. R., Hughes, C. W., & Tamisiea, M. E. (2009). Identifying the causes of sea-level change. *Nature Geoscience*, *2*(7), 471–478. https://doi.org/10.1038/ngeo544

Mitrovica, J. X., Forte, A. M., & Simons, M. (2000). A reappraisal of postglacial decay times from Richmond Gulf and James Bay, Canada. *Geophysical Journal International*, *142*(3), 783–800. https://doi.org/10.1046/j.1365-246x.2000.00199.x

Mitrovica, Jerry X., & Milne, G. A. (2003). On post-glacial sea level: I. General theory. *Geophysical Journal International*, *154*(2), 253–267. https://doi.org/10.1046/j.1365-246X.2003.01942.x

Mitrovica, J.X., & Milne, G. A. (2002). On the origin of late Holocene sea-level highstands within equatorial ocean basins. *Quaternary Science Reviews*, *21*(20–22), 2179–2190. https://doi.org/10.1016/S0277-3791(02)00080-X

Moftakhari, H. R., AghaKouchak, A., Sanders, B. F., Feldman, D. L., Sweet, W., Matthew, R. A., & Luke, A. (2015). Increased nuisance flooding along the coasts of the United States due to sea level rise: Past and future. *Geophysical Research Letters*, *42*(22), 9846–9852. https://doi.org/10.1002/2015GL066072

Nansen, F. (1921). The strandflat and isostasy. *Videnskapsselskapets Skrifter. I. Matematisk-Naturhistorisk Klasse, Jacob Dybwad*.

Nerem, R. S., Beckley, B. D., Fasullo, J. T., Hamlington, B. D., Masters, D., & Mitchum, G. T. (2018). Climate-change–driven accelerated sea-level rise detected in the altimeter era. *Proceedings of the National Academy of Sciences*, *115*(9), 2022–2025. https://doi.org/10.1073/pnas.1717312115

Nield, G. A., Barletta, V. R., Bordoni, A., King, M. A., Whitehouse, P. L., Clarke, P. J., et al. (2014). Rapid bedrock uplift in the Antarctic Peninsula explained by viscoelastic response to recent ice unloading. *Earth and Planetary Science Letters*, *397*, 32–41. https://doi.org/10.1016/j.epsl.2014.04.019

Oppenheimer, M., Glavovic, B. C., Hinkel, J., van de Wal, R., Magnan, A. K., Abd-Elgawad, A., et al. (2019). Sea level rise and implications for low-lying islands, coasts and communities. In H.-O. Pörtner, D. C. Roberts, V. Masson-Delmotte, P. Zhai, M. Tignor, E. Poloczanska, et al. (Eds.), *IPCC Special Report on the Ocean and Cryosphere in a Changing Climate* (pp. 321–445). Intergovernmental Panel on Climate Change (IPCC). Retrieved from https://www.ipcc.ch/srocc/

Paulson, A., Zhong, S., & Wahr, J. (2005). Modelling post-glacial rebound with lateral viscosity variations. *Geophysical Journal International*, *163*(1), 357–371. https://doi.org/10.1111/j.1365-246X.2005.02645.x

Peltier, W. R. (1974). The impulse response of a Maxwell Earth. *Reviews of Geophysics*, *12*(4), 649. https://doi.org/10.1029/RG012i004p00649

Peltier, W. R. (1998). Postglacial variations in the level of the sea: Implications for climate dynamics and solid-Earth geophysics. *Reviews of Geophysics*, *36*(4), 603–689. https://doi.org/10.1029/98RG02638

Peltier, W. R. (2004). GLOBAL GLACIAL ISOSTASY AND THE SURFACE OF THE ICE-AGE EARTH: The ICE-5G (VM2) Model and GRACE. *Annual Review of Earth and Planetary Sciences*, *32*(1), 111–149. https://doi.org/10.1146/annurev.earth.32.082503.144359

Peltier, W. R., & Drummond, R. (2008). Rheological stratification of the lithosphere: A direct inference based upon the geodetically observed pattern of the glacial isostatic adjustment of the North American continent. *Geophysical Research Letters*, *35*(16). https://doi.org/10.1029/2008GL034586

Peltier, W. R., & Fairbanks, R. G. (2006). Global glacial ice volume and Last Glacial Maximum duration from an extended Barbados sea level record. *Quaternary Science Reviews*, *25*(23–24), 3322–3337. https://doi.org/10.1016/j.quascirev.2006.04.010

Peltier, W. R., Argus, D. F., & Drummond, R. (2015). Space geodesy constrains ice age terminal deglaciation: The global ICE-6G_C (VM5a) model. *Journal of Geophysical Research: Solid Earth*, *120*(1), 450–487. https://doi.org/10.1002/2014JB011176

Piecuch, C. G., Das, S. B., Gorrell, L., Dangendorf, S., Hamlington, B. D., Thompson, P. R., & Wahl, T. (2025). Impact-Based Thresholds for Investigation of High-Tide Flooding in the United States. *Earth's Future*, *13*(4). https://doi.org/10.1029/2024EF005850

Ranalli, G. (1995). Rheology of the Earth. *Chapman and Hall*, *2nd Ed.*

Ray, R. D., & Foster, G. (2016). Future nuisance flooding at Boston caused by astronomical tides alone. *Earth's Future*, *4*(12), 578–587. https://doi.org/10.1002/2016EF000423

Reager, J. T., Gardner, A. S., Famiglietti, J. S., Wiese, D. N., Eicker, A., & Lo, M.-H. (2016). A decade of sea level rise slowed by climate-driven hydrology. *Science*, *351*(6274), 699–703. https://doi.org/10.1126/science.aad8386

Reguero, B. G., Losada, I. J., Díaz-Simal, P., Méndez, F. J., & Beck, M. W. (2015). Effects of Climate Change on Exposure to Coastal Flooding in Latin America and the Caribbean. *PLOS ONE*, *10*(7), e0133409. https://doi.org/10.1371/journal.pone.0133409

Riva, R. E. M., Gunter, B. C., Urban, T. J., Vermeersen, B. L. A., Lindenbergh, R. C., Helsen, M. M., et al. (2009). Glacial Isostatic Adjustment over Antarctica from combined ICESat and GRACE satellite data. *Earth and Planetary Science Letters*, *288*(3–4), 516–523. https://doi.org/10.1016/j.epsl.2009.10.013

Ruddiman, WF. (2014). Earth's Climate Past and Future. *W.H. Freeman and Company, New York*, *3rd edition*.

Santamaría-Gómez, A., Rietbroek, R., Rebischung, P., Frederikse, T., & Legrand, J. (2024). Combined Global GNSS Velocity Field. https://doi.org/10.1007/1345_2024_263

Sasgen, I., Martinec, Z., & Fleming, K. (2006). Wiener optimal filtering of GRACE data. *Studia Geophysica et Geodaetica*, *50*(4), 499–508. https://doi.org/10.1007/s11200-006-0031-y

Schindelegger, M., Green, J. A. M., Wilmes, S. -B., & Haigh, I. D. (2018). Can We Model the Effect of Observed Sea Level Rise on Tides? *Journal of Geophysical Research: Oceans*, *123*(7), 4593–4609. https://doi.org/10.1029/2018JC013959

Sella, G. F., Stein, S., Dixon, T. H., Craymer, M., James, T. S., Mazzotti, S., & Dokka, R. K. (2007). Observation of glacial isostatic adjustment in "stable" North America with GPS. *Geophysical Research Letters*, *34*(2). https://doi.org/10.1029/2006GL027081

Seo, K.-W., Wilson, C. R., Chen, J., & Waliser, D. E. (2008). GRACE's spatial aliasing error. *Geophysical Journal International*, *172*(1), 41–48. https://doi.org/10.1111/j.1365-246X.2007.03611.x

Serafin, K. A., Ruggiero, P., & Stockdon, H. F. (2017). The relative contribution of waves, tides, and nontidal residuals to extreme total water levels on U.S. West Coast sandy beaches. *Geophysical Research Letters*, *44*(4), 1839–1847. https://doi.org/10.1002/2016GL071020

Shackleton, N. J., & Opdyke, N. D. (1973). Oxygen Isotope and Palaeomagnetic Stratigraphy of Equatorial Pacific Core V28-238: Oxygen Isotope Temperatures and Ice Volumes on a 10 5 Year and 10 6 Year Scale. *Quaternary Research*, *3*(1), 39–55. https://doi.org/10.1016/0033-5894(73)90052-5

Shennan, I. (2015). Handbook of sea-level research. In *Handbook of Sea-Level Research* (pp. 3–25). Wiley. https://doi.org/10.1002/9781118452547.ch2

Spada, G. (2017). Glacial Isostatic Adjustment and Contemporary Sea Level Rise: An Overview. *Surveys in Geophysics*, *38*(1), 153–185. https://doi.org/10.1007/s10712-016-9379-x

Spanger-Siegfried, E., Fitzpatrick, M. F., & Dahl, K. (2014). Encroaching tides: How sea level rise and tidal flooding threaten U.S. East and Gulf Coast communities over the next 30 years. *Cambridge, MA: Union of Concerned Scientists*.

Suarez, P., Anderson, W., Mahal, V., & Lakshmanan, T. R. (2005). Impacts of flooding and climate change on urban transportation: A systemwide performance assessment of the Boston Metro Area. *Transportation Research Part D: Transport and Environment*, *10*(3), 231–244. https://doi.org/10.1016/j.trd.2005.04.007

Sweet, W., Park, J., Marra, J., Zervas, C., & Gill, S. (2014). Sea level rise and nuisance flood frequency changes around the United States. *NOAA Technical Report NOS CO-OPS*, *073*.

Sweet, W. V., & Park, J. (2014). From the extreme to the mean: Acceleration and tipping points of coastal inundation from sea level rise. *Earth's Future*, *2*(12), 579–600. https://doi.org/10.1002/2014EF000272

Sweet, W. V., Dusek, G., Obeysekera, J., & Marra, J. J. (2018). Patterns and projections of high tide flooding along the U.S. coastline using a common impact threshold. *NOAA Technical Report* .

Swenson, S., & Wahr, J. (2002). Methods for inferring regional surface-mass anomalies from Gravity Recovery and Climate Experiment (GRACE) measurements of time-variable gravity. *Journal of Geophysical Research: Solid Earth*, *107*(B9). https://doi.org/10.1029/2001JB000576

Swenson, S., & Wahr, J. (2006). Post-processing removal of correlated errors in GRACE data. *Geophysical Research Letters*, *33*(8). https://doi.org/10.1029/2005GL025285

Swenson, S., Chambers, D., & Wahr, J. (2008). Estimating geocenter variations from a combination of GRACE and ocean model output. *Journal of Geophysical Research: Solid Earth*, *113*(B8). https://doi.org/10.1029/2007JB005338

Tamisiea, M. E., Mitrovica, J. X., & Davis, J. L. (2007). GRACE Gravity Data Constrain Ancient Ice Geometries and Continental Dynamics over Laurentia. *Science*, *316*(5826), 881–883. https://doi.org/10.1126/science.1137157

Tapley, B. D., Bettadpur, S., Ries, J. C., Thompson, P. F., & Watkins, M. M. (2004). GRACE Measurements of Mass Variability in the Earth System. *Science*, *305*(5683), 503–505. https://doi.org/10.1126/science.1099192

Tapley, B. D., Watkins, M. M., Flechtner, F., Reigber, C., Bettadpur, S., Rodell, M., et al. (2019). Contributions of GRACE to understanding climate change. *Nature Climate Change*, *9*(5), 358–369. https://doi.org/10.1038/s41558-019-0456-2

Tarasov, L., & Goldstein, M. (2023). Assessing uncertainty in past ice and climate evolution: overview, stepping-stones, and challenges. *EGUsphere [Preprint]*. https://doi.org/https://doi.org/10.5194/egusphere-2022-1410

Tarasov, L., Dyke, A. S., Neal, R. M., & Peltier, W. R. (2012). A data-calibrated distribution of deglacial chronologies for the North American ice complex from glaciological modeling. *Earth and Planetary Science Letters*, *315–316*, 30–40. https://doi.org/10.1016/j.epsl.2011.09.010

Tebaldi, C., Debeire, K., Eyring, V., Fischer, E., Fyfe, J., Friedlingstein, P., et al. (2021). Climate model projections from the Scenario Model Intercomparison Project (ScenarioMIP) of CMIP6. *Earth System Dynamics*, *12*(1), 253–293. https://doi.org/10.5194/esd-12-253-2021

Thomas, I. D., King, M. A., Bentley, M. J., Whitehouse, P. L., Penna, N. T., Williams, S. D. P., et al. (2011). Widespread low rates of Antarctic glacial isostatic adjustment revealed by GPS observations. *Geophysical Research Letters*, *38*(22), n/a-n/a. https://doi.org/10.1029/2011GL049277

Vacchi, M., Engelhart, S. E., Nikitina, D., Ashe, E. L., Peltier, W. R., Roy, K., et al. (2018). Postglacial relative sea-level histories along the eastern Canadian coastline. *Quaternary Science Reviews*, *201*, 124–146. https://doi.org/10.1016/j.quascirev.2018.09.043

Vardić, K., Clarke, P. J., & Whitehouse, P. L. (2022). A GNSS velocity field for crustal deformation studies: The influence of glacial isostatic adjustment on plate motion models. *Geophysical Journal International*, *231*(1), 426–458. https://doi.org/10.1093/gji/ggac047

ten Veldhuis, J. A. E., Clemens, F. H. L. R., Sterk, G., & Berends, B. R. (2010). Microbial risks associated with exposure to pathogens in contaminated urban flood water. *Water Research*, *44*(9), 2910–2918. https://doi.org/10.1016/j.watres.2010.02.009

Velicogna, I., Mohajerani, Y., A, G., Landerer, F., Mouginot, J., Noel, B., et al. (2020). Continuity of Ice Sheet Mass Loss in Greenland and Antarctica From the GRACE and GRACE Follow-On Missions. *Geophysical Research Letters*, *47*(8). https://doi.org/10.1029/2020GL087291

Wahr, J., Molenaar, M., & Bryan, F. (1998). Time variability of the Earth's gravity field: Hydrological and oceanic effects and their possible detection using GRACE. *Journal of Geophysical Research: Solid Earth*, *103*(B12), 30205–30229. https://doi.org/10.1029/98JB02844

Wahr, J., Swenson, S., Zlotnicki, V., & Velicogna, I. (2004). Time-variable gravity from GRACE: First results. *Geophysical Research Letters*, *31*(11). https://doi.org/10.1029/2004GL019779

van der Wal, W., Barnhoorn, A., Stocchi, P., Gradmann, S., Wu, P., Drury, M., & Vermeersen, B. (2013). Glacial isostatic adjustment model with composite 3-D Earth rheology for Fennoscandia. *Geophysical Journal International*, *194*(1), 61–77. https://doi.org/10.1093/gji/ggt099

van der Wal, W., Whitehouse, P. L., & Schrama, E. J. O. (2015). Effect of GIA models with 3D composite mantle viscosity on GRACE mass balance estimates for Antarctica. *Earth and Planetary Science Letters*, *414*, 134–143. https://doi.org/10.1016/j.epsl.2015.01.001

Walcott, R. I. (1972). Past Sea Levels, Eustasy and Deformation of the Earth. *Quaternary Research*, *2*(1), 1–14. https://doi.org/10.1016/0033-5894(72)90001-4

Wang, H., Xiang, L., Jia, L., Jiang, L., Wang, Z., Hu, B., & Gao, P. (2012). Load Love numbers and Green's functions for elastic Earth models PREM, iasp91, ak135, and modified models with refined crustal structure from Crust 2.0. *Computers & Geosciences*, *49*, 190–199. https://doi.org/10.1016/j.cageo.2012.06.022

Wang, H., Jia, L., Steffen, H., Wu, P., Jiang, L., Hsu, H., et al. (2013). Increased water storage in North America and Scandinavia from GRACE gravity data. *Nature Geoscience*, *6*(1), 38–42. https://doi.org/10.1038/ngeo1652

Watkins, M. M., Wiese, D. N., Yuan, D., Boening, C., & Landerer, F. W. (2015). Improved methods for observing Earth's time variable mass distribution with GRACE using spherical cap mascons. *Journal of Geophysical Research: Solid Earth*, *120*(4), 2648–2671. https://doi.org/10.1002/2014JB011547

Watson, C. S., White, N. J., Church, J. A., King, M. A., Burgette, R. J., & Legresy, B. (2015). Unabated global mean sea-level rise over the satellite altimeter era. *Nature Climate Change*, *5*(6), 565–568. https://doi.org/10.1038/nclimate2635

Wdowinski, S., Bray, R., Kirtman, B. P., & Wu, Z. (2016). Increasing flooding hazard in coastal communities due to rising sea level: Case study of Miami Beach, Florida. *Ocean & Coastal Management*, *126*, 1–8. https://doi.org/10.1016/j.ocecoaman.2016.03.002

Whitehouse, P. L. (2018). Glacial isostatic adjustment modelling: historical perspectives, recent advances, and future directions. *Earth Surface Dynamics*, *6*(2), 401–429. https://doi.org/10.5194/esurf-6-401-2018

Williams, K., Stamps, D. S., Melini, D., & Spada, G. (2024). Vertical Displacements and Sea-Level Changes in Eastern North America Driven by Glacial Isostatic Adjustment: An Ensemble Modeling Approach. *Journal of Geophysical Research: Solid Earth*, *129*(10). https://doi.org/10.1029/2023JB028250

Williams, S. D. P. (2003). Offsets in Global Positioning System time series. *Journal of Geophysical Research: Solid Earth*, *108*(B6). https://doi.org/10.1029/2002JB002156

Wong, P.-P. ;, Losada, I. J. ;, Gattuso, J. P. ;, Hinkel J.;, Khattabi, A. ;, McInnes, K. L. ;, et al. (2014). Coastal Systems and Low-Lying Areas. In C. B. Field, V. R. Barros, D. J. Dokken, K. J. Mach, & M. D. Mastrandrea (Eds.), *Climate Change 2014 Impacts, Adaptation, and Vulnerability* (pp. 361–410). Cambridge: Cambridge University Press. https://doi.org/10.1017/CBO9781107415379.010

Woodworth, P. L., Menéndez, M., & Roland Gehrels, W. (2011). Evidence for Century-Timescale Acceleration in Mean Sea Levels and for Recent Changes in Extreme Sea Levels. *Surveys in Geophysics*, *32*(4–5), 603–618. https://doi.org/10.1007/s10712-011-9112-8

Wu, P. (2005). Effects of lateral variations in lithospheric thickness and mantle viscosity on glacially induced surface motion in Laurentia. *Earth and Planetary Science Letters*, *235*(3–4), 549–563. https://doi.org/10.1016/j.epsl.2005.04.038

Yokoyama, Y., & Purcell, A. (2021). On the geophysical processes impacting palaeo-sea-level observations. *Geoscience Letters*, *8*(1), 13. https://doi.org/10.1186/s40562-021-00184-w

Yousefi, M., Milne, G., Li, S., Wang, K., & Bartholet, A. (2020). Constraining Interseismic Deformation of the Cascadia Subduction Zone: New Insights From Estimates of Vertical Land Motion Over Different Timescales. *Journal of Geophysical Research: Solid Earth*, *125*(3). https://doi.org/10.1029/2019JB018248